An Estimation-Theoretic Technique for Motion-Compensated Synthetic-Aperture Array Imaging

Cedric Leonard Logan

An Estimation-Theoretic Technique for Motion-Compensated Synthetic-Aperture Array Imaging

by

Cedric Leonard Logan

B.S.E.E. The University of Alabama (1989)
S.M. Massachusetts Institute of Technology (1993)
E.E. Massachusetts Institute of Technology (1993)

Submitted to the Department of
Electrical Engineering and Computer Science
in Partial Fulfillment of the Requirements
for the Degree of

Doctor of Science

at the
MASSACHUSETTS INSTITUTE OF TECHNOLOGY
February 2000

Signature of Author _____
Department of Electrical Engineering and Computer Science
January 31, 2000

Certified by _____
Professor Alan S. Willsky
Department of Electrical Engineering and Computer Science
Thesis Supervisor

Certified by _____
Hamid Krim
Assistant Professor of ECE, North Carolina State University
Thesis Supervisor

Accepted by _____
Professor Arthur C. Smith
Chairman, Department Committee on Graduate Students

An Estimation-Theoretic Technique for Motion-Compensated Synthetic-Aperture Array Imaging

by

Cedric Leonard Logan

Submitted to the Department of Electrical Engineering and Computer Science
on January 31, 2000 in Partial Fulfillment of the
Requirements for the Degree of Doctor of Science

Abstract

Synthetic-Aperture Radar (SAR) is an imaging technique that achieves high azimuth resolution by using coherent processing to exploit the relative motion between an airborne or spaceborne radar antenna and the imaged target field (effectively synthesizing the effect of a larger aperture array). From an estimation-theoretic perspective, this thesis addresses the following limitations of conventional imaging techniques for the spotlight-mode version of SAR: *sidelobe imaging artifacts and loss of resolution for stationary SAR scenes containing high-amplitude scatterers,* and *blurring and object-displacement artifacts in the presence of moving targets.*

First, this thesis presents a generalized estimation-theoretic SAR imaging framework which exploits the idea of L_1-norm regularization. Some results are included which demonstrate the utility of this approach for reducing sidelobes and improving resolution for stationary SAR images. A parameterized L_1-norm-based moving-target imaging technique is also presented. For the case of a single moving target, this technique is able to compensate for the blurring due to temporally-constant velocity rigid-body motion (even if the target scatterers are closely-spaced). However, the motion-induced object-displacement compensation performance of this technique is significantly affected by velocity estimation errors.

This thesis also presents an estimation-theoretic moving-target SAR imaging framework which uses a multi-dimensional matched-filter for computing a set of scatterer-velocity estimates which are used as initial conditions for an L_1-norm-based estimation algorithm which assumes that the target scatterers have temporally-constant spatially-independent velocities. Therefore, this framework is able to image a moving target and nearby high-amplitude stationary clutter simultaneously. This framework also shows potential for imaging targets with non-rigid body motion. However, the motion-induced object-displacement compensation performance of this approach is significantly affected by cross-scatterer interference effects.

Thesis Supervisor: Alan S. Willsky
Title: Professor of Electrical Engineering, Massachusetts Institute of Technology

Thesis Supervisor: Hamid Krim
Title: Assistant Professor of Electrical Engineering, North Carolina State University

Thesis Committee Member: Ronald D. Chaney
Title: Associate Division Manager, Alphatech, Inc.

Thesis Committee Member: Jeffery H. Shapiro
Title: Professor of Electrical Engineering, Massachusetts Institute of Technology

Acknowledgments

Next, I would like to thank my thesis supervisor, **Professor Alan S. Willsky**, for allowing me the privilege and opportunity to work closely with him as a member of the Stochastic Systems Group (SSG). I have benefited immensely from his insight, wisdom, suggestions, comments, and constructive criticism of my work. I especially thank him for teaching me how to see the "big picture", as related to my research. I also thank Alan for teaching me how to explain my work in a straightforward fashion (rather than getting caught up in unnecessary details). Along with his outstanding intellectual qualities, Alan shows true compassion, patience, and concern for his students (especially when they deserve it the least). If I ever became a university professor, Alan would be my role model.

I would also like to thank my thesis co-supervisor, **Professor Hamid Krim**, for his friendship, support, and encouragement (as well as our many stimulating intellectual discussions). I especially thank him for his advice and expertise in the area of array-processing (such that I was able to gain a different, but needed, perspective on my research).

In addition, I would like to thank my remaining two thesis committee members, **Dr. Ron Chaney**, and **Professor Jeff Shapiro** for their expertise and advice, especially as related to SAR and ATR. I especially thank Ron for being a great mentor to me during the periods I did research at Lincoln Laboratory (and for his patience in helping to understand the mechanics of the Lincoln Laboratory ADTS SAR system). In addition to being on my thesis committee, Jeff also acted as my academic advisor during the entire course of my graduate studies at MIT. His advice and counsel were crucial for helping me to navigate the MIT EECS doctoral process.

I would like to thank my parents, **Sidney Jr. and Earlean Logan**, for their love, support, and encouragement during my graduate studies. Mere words cannot begin to express how much I love and appreciate them (and admire their example of hard work, sacrifice, and perseverance). I especially thank them for their financial support during the last few months of my graduate studies at MIT (as well as their help which allowed

me to purchase a car in order to travel to my new workplace). I also thank my sisters and brothers for their love and encouragement: **Arnell Jones, Mildred Murray, Sidney Logan III, Rodney Logan, Winfred Logan, Cassandra Logan,** and **Marcella Logan**. In addition, I thank my grandparents, **Callum and Hildra Hayes**, for their love and encouragement as well.

It has truly been a privilege to interact with my fellow members of the Stochastic Systems Group. First of all, I would like to thank my fellow "SAR Boyz", **Andrew Kim** and **John Richards**, for our many fun times hanging out and discussing just about anything under the sun, for our many trips to the Food Trucks (especially the BBQ truck, operated by **Butch Harris**), for being fellow Founders and Keepers of the SSG Manifesto Board, and for their patience with my strange, bizarre, and sometimes unending stream of jokes and *non sequiturs*. Andrew also deserves praise for his excellent job of maintaining the SSG computer system (otherwise I would be doing my thesis research using slide-rules and abacuses). Next, I would like to thank **Taylore Kelly** for being a great friend, and for being there to listen during those (very rare) occasions when I air one of my latest gripes. In addition, she has helped us "MIT" types at the SSG to "lighten up" a little and enjoy life.

I would like to thank the rest of the SSG (past and present) for many fond memories over the last few years: **Terrence Ho** (for being a great friend, as well as clearing a path through the SSG doctoral "pipeline", especially the "Chapter 5 bottleneck"), **W. Clem Karl** (for his encouragement and advice during the first couple of years I was in the SSG), **Rachel Learned** (for "pestering" me to come and interview with Lockheed Sanders, and for "going to bat" for me during the interview process. Otherwise, I probably wouldn't have a job...), **Mike Daniel, Seema Jaggi, John Fisher** (even if he did graduate from the U. of FL), **Andy Tsai** (aka PK), **Dewey Tucker** (for not going "postal" on the rest of the SSG when our jokes got a little out of hand), **Charlie Fosgate, Bill Irving, Austin Frakt, Mike Schneider** (for our many fruitful discussions on the absurdities of American politics), **Paul Fieguth** (whom I want to express congratulations on getting married, even though that is one of the signs that the End Times foretold in the book of Revelation is upon us...), **Ilya Pollak, Ron Dror** (winner of the SSG Golden Plunger Award), **Martin Wainwright, Alex Ihler, Erik Sudderth, Junmo Kim, Ben Halpern** (for going out of his way to help with SSG computer system, in addition to his many duties with Alan), **Paula Place, Jerry Weinstein, Gerald Spica, Susan Sheldon, Eric Miller, Mickey Bhatia, Lori Belcastro, Mark Luettgen, Jun Zhang, Khalid Daoudi,** and **Tony Yezzi**.

I have also had many fond memories and fruitful interactions with many others (past and present) in the Laboratory for Information and Decision Systems (LIDS) (which the SSG is a part). First, I would like to thank **Kathleen O'Sullivan** for her concern and care (including, for many years, ensuring that we had enough coffee (and food) to do our research) for the LIDS students (as well as the LIDS faculty). Here is to a happy and well-deserved retirement. I also want to thank **Prof. Vincent Chan, Fifa Monserrate, Doris Inslee,** and **Kathy Sullivan** for their concern and support of the LIDS students as well (and for ensuring that the administrative "wheels" of LIDS are greased and run smoothly). I would like to thank **Mike Branicky, Mitch Livstone, Prof. Steve Massaquoi** (for his friendship and encouragement, especially during my thesis writing), **Pierre-Arthur Elysee, Mike**

6

...Well, I don't know what will happen now. We've got some difficult days ahead. But it really doesn't matter with me now. Because I've been to the mountain top. And I don't mind. Like anybody, I would like to live a long life. Longevity has its place. But I'm not concerned about that now. I just want to do God's will. And He's allowed me to go up to the mountain. And I've looked over. And I've seen the Promised Land. I may not get there with you. But I want you to know tonight, that we, as a people, will get to the Promised Land. So I am happy tonight. I'm not worried about anything. I'm not fearing any man. Mine eyes have seen the glory of the coming of the LORD.

Excerpts from the
last public address of
Dr. Martin Luther King Jr.
Memphis, TN
April 3, 1968

Who shall separate us from the love of Christ? Shall trouble or hardship or persecution or famine or nakedness or danger or sword? As it is written: "For your sake we face death all day long; we are considered as sheep to be slaughtered." No, in all these things we are more than conquerors through Him who loved us. For I am convinced that neither death nor life, neither angels nor demons, neither the present nor the future, nor any powers, neither height nor depth, nor anything else in all creation, will be able to separate us from the love of God that is in Christ Jesus our LORD.

Romans 8:35-39 (NIV)

Contents

List of Figures

18

21

22

24

31

List of Tables

Chapter 1

Introduction

$\mathbf{S}$ YNTHETIC-APERTURE RADAR(SAR) is an imaging technique that achieves high azimuth resolution by exploiting the relative motion between a (airborne or spaceborne) vehicle-mounted radar antenna and the observed target field[10, 13, 18]. This is done by coherently processing the returned radar signals so as to synthesize the effect of a larger aperture array laid out along the vehicle's path of motion.

Most SAR systems tend to have two main modes of operation. In *Strip-Map* Mode, the physical antenna has a constant orientation relative to the radar platform. The radar's "footprint" is dragged along with platform, as shown in Figure 1.1 . In *Spotlight* Mode, the physical antenna is oriented such as to illuminate the same segment of the target area over the SAR's "dwell" time. The radar's footprint is stationary with respect to the ground, as also shown in Figure 1.1. An example of a typical spotlight-mode SAR image shown in Figure 1.2 (which is part of a data set collected by Sandia National Laboratory in 1995 under DARPA's Moving and Stationary Target Acquisition and Recognition (MSTAR) program). This image consists of a T-72 tank (from the former Soviet Union) in a grass clutter background (with an approximate resolution of $0.25m$ in range and $0.25m$ in azimuth).

One important application of the SAR imaging technique is as a front-end sensor for the purposes of Automatic Target Recognition (ATR) [12]. For a SAR-based automatic target recognition system, the fundamental goal is to detect and recognize objects of interest (targets) in a noisy environment (clutter). As shown in Figure 1.3, a typical SAR-based ATR system is usually divided into three main subsystems: a prescreener, a discriminator, and a classifier. The prescreener searches for high-amplitude regions over the collection of images generated by the SAR image-formation process (which may represent several square kilometers of terrain), and outputs a series of sub-images called regions-of-interest (ROI). These ROI's correspond to rough guesses of target locations in the SAR images. The discriminator then refines the rough guesses of the prescreener by sorting out the ROI's that correspond to false alarms caused by high-amplitude natural clutter, such as trees. Lastly, the classifier sorts the remaining ROI's into a set of predefined target categories (or into a none-of-the-above man-made clutter category, such as the ROI's corresponding to buildings). This classification is usually done by comparing the number and configuration of the higher-amplitude feature scatterers in the ROI's to the corresponding feature scatterers found in some pre-determined database of target images.

34
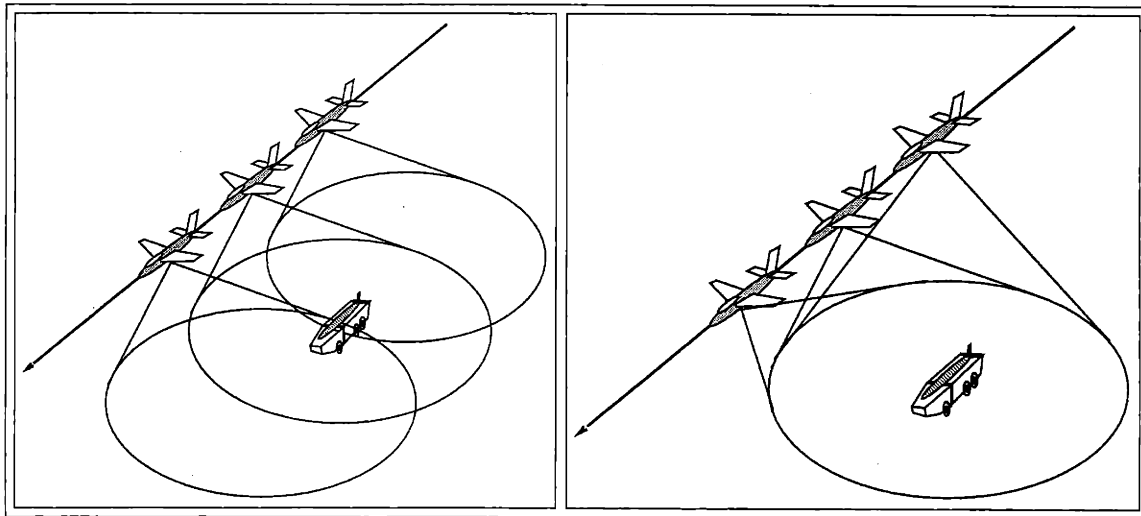
Figure 1.1: Strip-Map Mode and Spotlight-Mode SAR Imaging Configurations
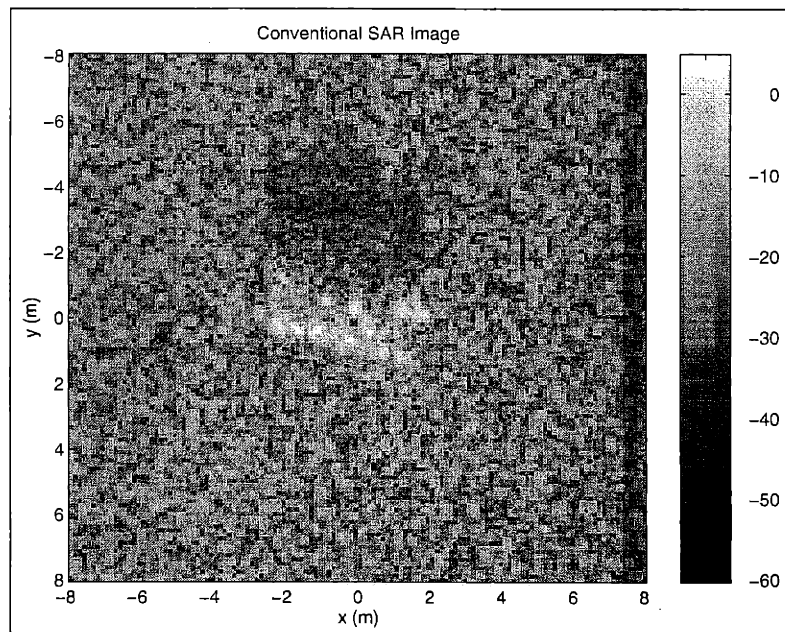
Figure 1.2: Spotlight-Mode SAR Image of a Soviet T-72 Tank
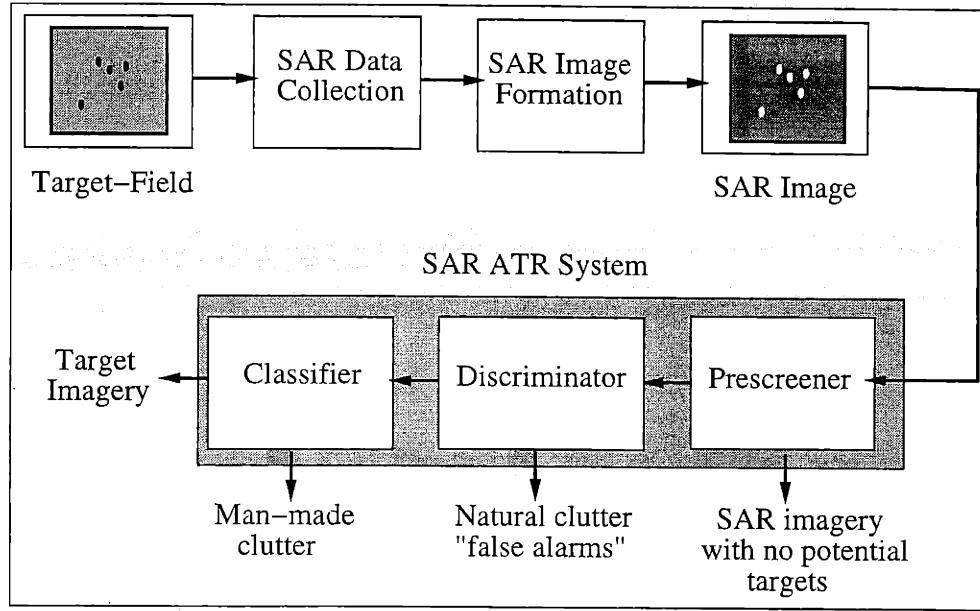
Figure 1.3: Typical SAR-based Automatic Target Recognition System

1.1 Problem Motivation: Moving-Target SAR Imaging

In 1983, Munson [28] formulated a relationship between spotlight-mode SAR imaging and *tomography*. Now, the goal of tomography is to reconstruct a 2-D function $A(x, y)$ from its *Radon Transform*, $p_\theta(u)$ [6, 24], which is defined by the following *Projection Integral*

$$p_\theta(u) = \int A(u \cos\theta - v \sin\theta, u \sin\theta + v \cos\theta) dv \ . \tag{1.1}$$

From Figure 1.4, we see that the value of the Radon transform at a given point $u = u_o$ is equal to the line integral of $A(x, y)$ along the path parallel to the v-axis that passes through $u = u_o$.

The basic idea behind Munson's formulation is that *we can describe a given received spotlight-mode radar signal as the convolution of the corresponding transmitted signal with the tomographic projection $p_k(r)$ (where the look-angle θ of the SAR system is proportional to the integer k) of the illuminated target-field's complex-reflectivity density $A(x, y)$*, as shown in Figure 1.5. In other words, we can think of the spotlight-mode SAR imaging problem as a (very) limited-angle tomographic reconstruction problem (since for most SAR systems, the total range of the look angle θ is usually less than 10 degrees).

In the context of tomography, if we let **A** be a (lexicographically-ordered) vector of samples of the (time-invariant) 2-D function $A(x, y)$, and we let **p** be a (lexicographically-ordered) vector of samples of the projections, $p_\theta(u)$, the tomographic data can be represented by the following estimation-theoretic model

$$\mathbf{p} = \mathbf{PA} + \eta \ , \tag{1.2}$$

where **P** is a "projection matrix" and η is a vector of additive noise. Then the tomographic-reconstruction problem is equivalent to the corresponding estimation-theoretic inverse prob-
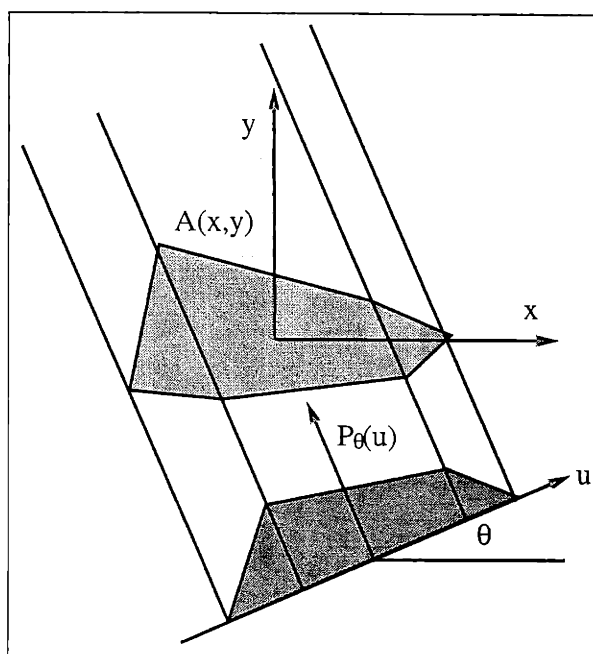
Figure 1.4: Tomographic Projection Geometry
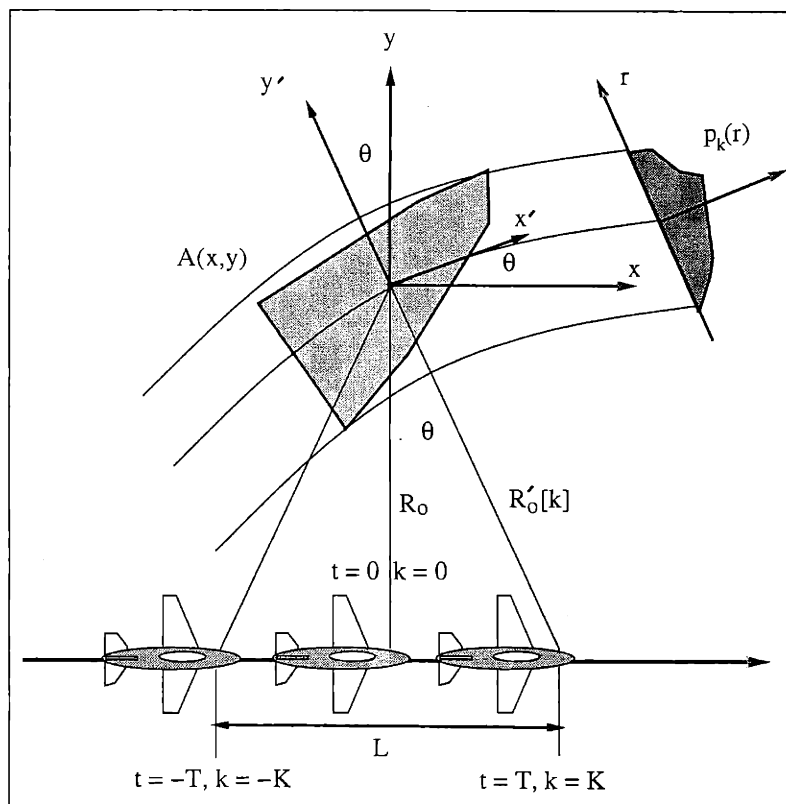
Figure 1.5: Relationship between Tomography and Spotlight-Mode SAR

lem of estimating the vector $\mathbf{A}$, given the vector of noisy measurements $\mathbf{p}$. Because of the previously-mentioned relationship between spotlight-mode imaging and tomography, if we let $\mathbf{A}$ be a (lexicographically-ordered) vector of samples of the (time-invariant) target-field reflectivity function $A(x,y)$ and we let $\mathbf{f}$ be a (lexicographically-ordered) vector of samples of the (complex-valued) received SAR data (after the appropriate demodulation operations by the radar system's receiver hardware), the spotlight-mode SAR data can be expressed in a similar fashion by the following estimation-theoretic model

$$\mathbf{f} = \mathbf{FA} + \eta .\tag{1.3}$$

For this case, $\mathbf{F}$ is a matrix composed of (approximately-orthogonal) complex-exponential basis functions, while η is again a vector of additive noise. This particular model essentially says that the demodulated received SAR data is given by a limited-support scaled 2-D Fourier Transform of the sampled target-field reflectivity function. From this model, the goal of spotlight-mode SAR is *to solve the estimation-theoretic inverse problem of estimating the vector $\mathbf{A}$, given the vector of noisy measurements $\mathbf{f}$.*

The maximum-likelihood least-squares solution to the spotlight-mode SAR inverse problem (for zero-mean circularly-complex Gaussian noise with a spatial-correlation matrix, $\mathbf{K}_\eta = \mathbf{E}[\eta\eta^{\mathbf{H}}]$) is given by

$$\hat{\mathbf{A}} = \left(\mathbf{F}^H \mathbf{K}_\eta^{-1} \mathbf{F} \right)^{-1} \mathbf{F}^H \mathbf{K}_\eta^{-1} \mathbf{f} .\tag{1.4}$$

If the noise is also spatially-statistically independent and isotropic, (which is usually the case) the noise spatial-correlation matrix is given by $\mathbf{K}_\eta = \sigma_\eta^2 \mathbf{I}$. Therefore, the maximum-likelihood least-squares solution is given by

$$\hat{\mathbf{A}} = \left(\frac{1}{\sigma_\eta^2} \mathbf{F}^H \mathbf{F} \right)^{-1} \frac{1}{\sigma_\eta^2} \mathbf{F}^H \mathbf{f} = \left(\mathbf{F^H F} \right)^{-1} \mathbf{F^H f} .\tag{1.5}$$

However, a direct computation of the maximum-likelihood solution to the spotlight-mode SAR inverse problem (using the inverse of $\mathbf{F}^H \mathbf{F}$) can be computationally intensive, even for a relatively moderate-sized SAR scene. In order to reduce this computational load, most conventional spotlight-mode SAR imaging techniques make the following simplifying assumption (which is equivalent to assuming that the complex-exponential basis-functions corresponding to the columns of $\mathbf{F}$ are orthogonal)

$$\mathbf{F}^H \mathbf{F} \approx \mathbf{I} .\tag{1.6}$$

Given this assumption, the maximum-likelihood least-squares solution is approximately given by

$$\hat{\mathbf{A}} \approx \mathbf{F}^H \mathbf{f} .\tag{1.7}$$

This is equivalent to using a limited-support scaled inverse 2-D Fourier Transform to (approximately) recover the target-field reflectivities from the demodulated SAR data. However, a side effect of this assumption is the *introduction of artifacts such as sidelobes into*
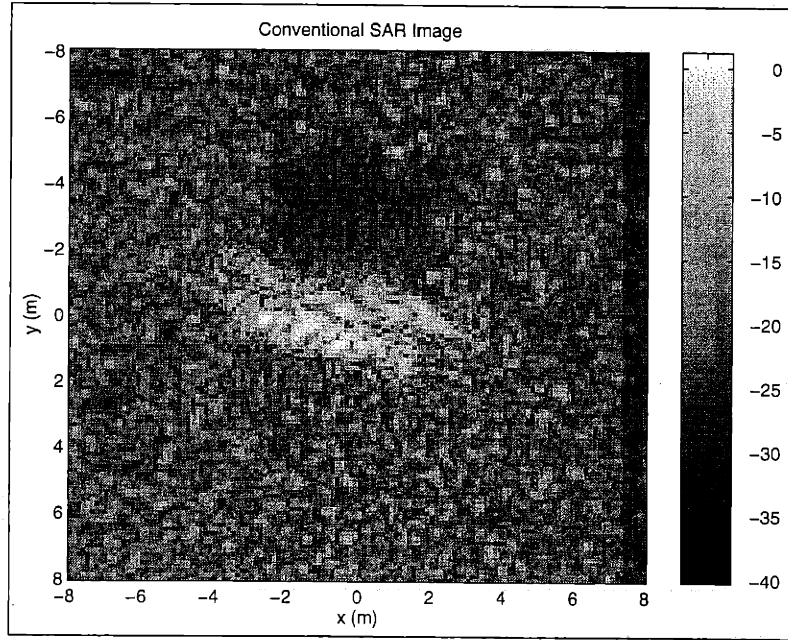
Figure 1.6: Simulated Conventional Spotlight-mode SAR Image of a Moving Soviet T-72 Tank

the conventional SAR image for high-amplitude scatterers. In addition, *the SAR image will also be limited in resolution.*

If there is target motion in the SAR scene, the target-field reflectivity function $A(x, y)$ will no longer be strictly time-invariant. However, if we now let the vector $\mathbf{A}$ correspond to samples of the target-field reflectivity function *at some initial time* t_0, (usually the midpoint of the SAR's dwell-time interval) we can still represent the SAR data by the following parameterized estimation-theoretic model

$$\mathbf{f} = \mathbf{F}(\mathbf{v})\mathbf{A} + \eta \tag{1.8}$$

Here, the complex-exponential basis-functions of the estimation-theoretic spotlight-mode SAR model are (nonlinear) functions of a set of motion parameters $\mathbf{v}$. Because of these motion parameters, the *corresponding inverse problem of estimating the vector* $\mathbf{A}$ *(given the vector of noisy measurements* $\mathbf{f}$*) will be in general ill-posed (i.e., we will not have a unique least-squares solution for both* $\mathbf{A}$ *and* $\mathbf{v}$*).* If we again assume that there is no motion in the SAR scene, and use the conventional SAR estimator for $\mathbf{A}$ (i.e., a scaled inverse 2-D Fourier Transform), the non-orthogonality of the velocity-dependent basis-functions in $\mathbf{F}(\mathbf{v})$ will cause *the resulting conventional SAR image to exhibit significant blurring and object-displacement artifacts* [10, 37]. This is illustrated in the simulated spotlight-mode moving-target image of a Soviet T-72 tank (which is a moving version of the T-72 target shown in the conventional MSTAR image of Figure 1.2) shown in Figure 1.6. From the standpoint of ATR applications, if we have moving targets, this ultimately implies that we will have a degradation in the performance of any ATR system based upon conventional SAR processing.

Given these limitations of conventional SAR imaging techniques, the main issues of this research are the following:

- *Reducing sidelobe imaging artifacts and improving resolution for stationary SAR scenes containing high-amplitude scatterers.*

- *Improving the spotlight-mode SAR image formation process (without significantly increasing the computational burden) in the presence of moving targets* (so as to minimize the performance degradation of applications such as SAR-based ATR).

1.2   Previous Work

There have been a variety of research efforts in the literature dealing with the moving-target SAR imaging problem. Most approaches to this problem assume that a given SAR scene is entirely composed of a single rigid-body moving target. This implies that these approaches cannot image both a moving target and nearby stationary clutter simultaneously. In addition, some of these techniques require the tracking of high-amplitude prominent-point scatterers in order to estimate the motion of the rigid-body target. Here, we briefly describe some of these approaches (some of which are discussed in greater detail in Appendix A) They can be divided into four distinct subclasses: *prominent-point* techniques , *phase-estimation* techniques, *space-time-frequency* techniques, and *polynomial-phase* techniques.

1.2.1   Prominent-Point SAR Motion-Compensation Techniques

The prominent-point class of SAR motion-compensation algorithms essentially correct for target motion by tracking a number of bright (i.e., high signal-to-noise ratio) target scatterers. The Range-Migration ISAR (RMI) technique [16] developed by Lincoln Laboratory focuses the SAR image by subtracting out the complex phase of the highest-amplitude scatterer (which is assumed to be from the moving target) from the demodulated SAR data. This technique can compensate for both *unknown, purely translational* motion and *known, constant rotational* motion. The Geometric-Analysis Automated Imaging (GAI) technique [39], developed by the Environmental Research Institute of Michigan (ERIM), is a somewhat more sophisticated multiple prominent-point cousin of the Lincoln Lab Range-Migration ISAR algorithm. Whereas the Lincoln Lab algorithm only compensates for pure translational motion (and known rotational motion), the Geometric Analysis technique also compensates for *unknown* rotational motion and other complicated target motions (again with the assumption that the target is a rigid body).

1.2.2   Phase-Estimation SAR Motion-Compensation Techniques

The phase-estimation techniques are similar to the Lincoln Laboratory RMI technique, in that they assume that each target scatterer has the same motion-induced complex-phase error (i.e., purely translational rigid body motion). Unlike the RMI technique, however, this class of algorithms assume that the motion-induced phase error is purely in azimuth (i.e., no range-walk[10]). But since they do not require the tracking of bright prominent-point scatterers, they tend to be more robust to noise. Phase-Gradient Autofocusing (PGA)[7],

developed by Sandia Laboratory, is an imaging technique where the *derivative* of the motion-induced phase error is first estimated from the SAR data. Once the phase error is obtained by integrating the estimated phase-error derivative, it is then used to correct the original SAR imagery. Shear-Averaging [14], is an imaging technique where the pulse-to-pulse *difference* of the motion-induced phase error is first estimated from the SAR data. Once the phase error is obtained by a recursive sum of the estimated phase-error differences, it is then used to correct the original SAR imagery. As with the PGA algorithm discussed earlier, the Shear-Averaging technique corresponds to the case where we assume that each target scatterer has the same phase error.

1.2.3   Space-Time-Frequency SAR Motion-Compensation Techniques

Just like the previously-mentioned phase-estimation techniques the space-time-frequency[1, 2, 3] class of SAR motion-compensation algorithms assume that each target scatterer has the same motion-induced phase error (i.e., purely translational rigid body motion), and they assume that this phase error is purely in azimuth (i.e., no range-walk). The space-time-frequency techniques also do not require the tracking of bright prominent-point scatterers, thus they are somewhat more robust to noise than the prominent-point techniques. Unlike the phase-estimation techniques, the space-time-frequency techniques estimate the phase-error by integrating the instantaneous Doppler frequency (from pulse to pulse) of the target (which is dependent upon the relative velocity between the target and the SAR antenna). This Doppler-frequency estimation is usually performed by using the *Wigner-Ville time-frequency distribution* $F_s(t,\omega)$[2], which for a complex-valued $1-D$ time-domain signal $s(t)$ is defined as

$$F_s(t,\omega) = \int_{-\infty}^{+\infty} s\left(t+\frac{\tau}{2}\right) s^*\left(t-\frac{\tau}{2}\right) e^{-j\omega\tau} d\tau \qquad (1.9)$$

1.2.4   Polynomial-Phase SAR Motion-Compensation Techniques

Another class of phase-estimation algorithms are the *polynomial-phase algorithms* [4, 33]. Just like the phase-estimation techniques and the space-time-frequency techniques, the polynomial phase algorithms assume that each target scatterer has the same motion-induced phase error, and they assume that this phase error is purely in azimuth. Unlike these two classes of motion-compensation algorithms, the polynomial-phase algorithms assume that the phase error is a *parametric polynomial function* with respect to time. In the literature, the parameters of this polynomial function are usually estimated by using the so-called *Higher-Order Ambiguity* function [33].

1.3   Thesis Organization and Main Contributions

Here, we summarize the remainder of this thesis, along with the main contributions.

Chapter 2, Spotlight-Mode SAR Model

In this chapter, we present a series of estimation-theoretic models for the spotlight-mode version of SAR. First, we derive a general-motion data model for our spotlight-mode SAR imaging geometry with the following set of five fundamental ideas: tomographic convolution, two-dimensional slant-plane, far-field plane-wave, ideal isotropic point-scatterers, and transmitted chirp pulse with quadrature demodulation. From this general-motion model, we develop an estimation-theoretic model for the conventional zero-velocity case. We also develop estimation-theoretic models for the special cases of spatially-varying temporally-constant velocity (where each scatterer can have independent temporally-constant motions) and rigid-body temporally-constant velocity (where we have a single moving-target with temporally-constant translational velocities and a temporally-constant rotation rate).

Chapter 3, L_1-Norm Based SAR Processing

In this chapter, we develop a generalized SAR imaging framework which exploits the idea of L_1-norm regularization in order to compensate for the non-orthogonality of the spotlight-mode SAR basis functions. In this chapter, we also address the research issue of sidelobe imaging artifacts and resolution for stationary SAR scenes containing high-amplitude scatterers.

For comparison purposes, we first present a brief overview of a conventional SAR processing algorithm. Next, we present an a estimation-theoretic justification for the L_1-norm-based SAR processing framework, from the context of the ill-posed over-complete basis-pursuit estimation problem in the literature. We also present a means for implementing an L_1-norm-based algorithm by using a coordinate-descent line-minimization scheme. We then present some results for some stationary SAR scenes in order to demonstrate the utility of an L_1-norm based approach for enhancing feature scatterers in SAR images by reducing sidelobes and improving resolution.

Chapter 4, Matched-Filter SAR Processing

In this chapter, we address the issue of SAR imaging in the presence of moving targets, in the context of imaging both a moving target and nearby stationary clutter simultaneously. Here, we present the Matched-Filter SAR processing technique, which uses a multi-dimensional matched-filter as a means of computing a set of scatterer-velocity estimates which are used as initial conditions for an L_1-norm based estimation algorithm derived for the spatially-varying temporally-constant velocity (SVTCV) SAR model (which assumes that the imaged target field consists of a $2 - D$ array of ideal point scatterers with spatially independent velocities). The matched filter also computes a target detection statistic for determining which spatial locations in a particular SAR scene correspond to actual moving scatterers (allowing a reduction in the computational intensity of the SVTCV L_1-norm based estimation algorithm).

We first present the SVTCV L_1-norm based algorithm for estimating the scatterer velocities, along with a standard least-squares algorithm for estimating the scatterer amplitudes. Next, we present the matched filter algorithm itself, along with a discussion of the methods it uses to compute the scatterer-velocity estimates and the target-detection statistic. We also discuss some of the issues encountered in the actual implementation of the matched-filter algorithm. In addition, we discuss methods for reducing cross-scatterer interference effects in the matched-filter scatterer-velocity estimates. Then, we present a Monte Carlo analysis of the detection and velocity-estimation performance of the matched-filter algorithm. Lastly, we present some results for both synthetic point scatterers embedded in real clutter, and a synthetic-motion real target embedded in real clutter. From these results, we show that this approach can image a moving target and nearby high-amplitude stationary clutter simultaneously.

Chapter 5, Rigid-Body L_1-Norm SAR Processing

In this chapter, we again address the issue of SAR imaging in the presence of moving targets. Here, we present an estimation-theoretic L_1-norm based approach for imaging constant-velocity rigid-body moving targets. First, we detail the development of the rigid-body SAR processing algorithm. We also discuss some of the implementation issues associated with this algorithm. Lastly, we present some results for both synthetic moving point-scatterers embedded in real clutter and synthetic-motion real targets embedded in real clutter.

Chapter 6, Contributions and Suggestions for Further Research

In this chapter, we briefly summarize the contributions of this thesis and we present the overall conclusions which can be derived from the results of our research. We also present some suggestions for extending this work.

Chapter 2

Spotlight-Mode SAR Model

FOR our research, we first focus on developing an estimation-theoretic model for the spotlight-mode version of SAR. First, we derive a general-motion data model for our spotlight-mode SAR imaging geometry with the following set of "fundamental" ideas (which we will describe more fully in the later sections): *tomographic convolution* (i.e., we describe a given received spotlight-mode radar signal as the convolution of the corresponding transmitted signal with the tomographic projection of the illuminated target-field's so-called complex-reflectivity density), *two-dimensional slant-plane* (i.e., we "throw away" all height information about the target field, and we approximate the actual three-dimensional imaging geometry by a two-dimensional imaging geometry), *far-field plane-wave* (i.e.,we assume that the distance from the SAR antenna to the illuminated target-field is "large" compared to both the length of the synthetic aperture and the effective radius of the illuminated target-field, which implies that the far-field wavefront from the SAR antenna is a straight line perpendicular to the radar's "line-of-sight"), *ideal isotropic point-scatterers* (i.e.,we approximate the illuminated target-field's complex-reflectivity density by a finite array of complex-amplitude isotropic "ideal" point-scatterers), and *transmitted chirp pulse with quadrature demodulation* (i.e., we assume that the transmitted SAR signal is a series of broadband frequency-modulated "chirp" pulses). From this general-motion model, we develop an estimation-theoretic model for the "conventional" zero-velocity case. We also develop estimation-theoretic models for the special cases of spatially-varying temporally-constant velocity and "rigid-body" temporally-constant velocity.

2.1 General-Motion Spotlight-Mode SAR Data Model

We consider the pulsed spotlight-mode SAR (moving with velocity v, and imaging a target field centered at range R_o from the radar's flight path) shown in Figure 2.1. In Figure 2.1, (X, Y, Z) refer to the *earth-relative* coordinates of the target-field, while (x, y, z) refer to the so-called *slant-plane* coordinates [7, 18] of the target-field. These coordinate systems are related by

$$(X, Y, Z) = (\ x, y\cos(\Psi_E) + z\sin(\Psi_E), z\cos(\Psi_E) - y\sin(\Psi_E)\ )\ , \qquad (2.1)$$

where the *elevation angle* Ψ_E is given by $\Psi_E = \sin^{-1}(\frac{Z_o}{R_o})$ (with Z_o referring to the altitude of the SAR platform). In the context of moving-target imaging, our ultimate goal *is to*
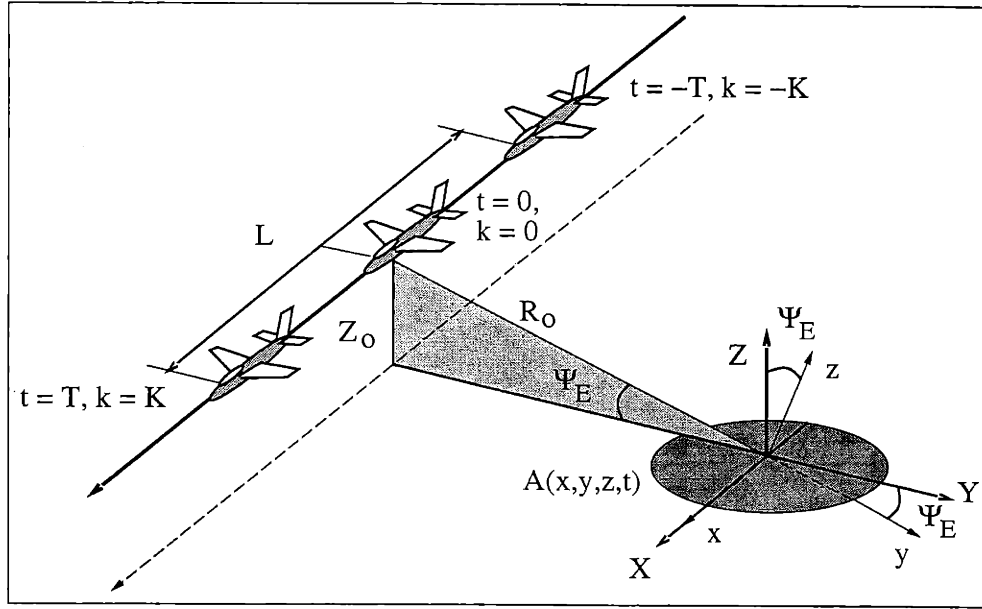
Figure 2.1: Spotlight-Mode SAR Imaging Model

recover the time-varying 3-D complex "reflectivity density" $A(x, y, z, t)$ (in the slant-plane coordinate system) of the illuminated target-field from our received SAR data.

For this pulsed-SAR model, we assume that the SAR system transmits a total of $2K + 1$ pulses over a "dwell" time of $2T$ (which implies that the length of our synthetic antenna array is given by $L = 2vT$). In other words, the SAR system transmits the following pulse-train signal $s_T(t)$

Transmitted Spotlight-Mode SAR Signal

$$s_T(t) = \sum_{k=-K}^{K} s_o(t - t_T[k]) \,, \quad -T \leq k \leq T \tag{2.2}$$

where $s_o(t)$ is a time-limited SAR "mother" pulse (i.e., $s_o(t) = 0$ for $|t| > \frac{T_p}{2}$). Each of the transmitted pulses are centered at the time instants $t_T[k]$, given by

$$t_T[k] \;=\; \frac{2T}{2K} k \;=\; \frac{k}{f_{PRF}} \;=\; \tau_{PRF}\, k \,. \quad -K \leq k \leq K \tag{2.3}$$

(where in the SAR literature[7, 18], $f_{PRF} = \frac{2K}{2T}$ is known as the *Pulse-Repetition Frequency*). Note that the duration T_p of the SAR "mother" pulse $s_o(t)$ is assumed to be much less than the time τ_{PRF} between pulse transmissions, given by $\tau_{PRF} = \frac{1}{f_{PRF}}$. Given the pulsed-SAR imaging geometry shown in Figure 2.1, we can develop a model for the pulsed spotlight-mode SAR data with the set of fundamental ideas previously discussed.

2.1.1   Tomographic Convolution

In 1983, Munson [28] formulated a relationship between the tomographic reconstruction problem and the spotlight-mode SAR imaging problem. The basic idea behind his formulation was that *we can describe a given received spotlight-mode radar signal as the convolution of the corresponding transmitted signal with the tomographic projection of the illuminated target-field's complex-reflectivity density.*

In the context of our SAR imaging model, when the SAR system transmits the pulse-train signal $s_T(t)$, the corresponding (delayed) received signal $s_R(t)$ is given by the following convolution (where $c = 3 \times 10^8$ m/s, and $v \ll c$)

Received Spotlight-Mode SAR Signal

$$s_R(t) = \sum_{k=-K}^{K} \int_{r\,\in\,Target\;Field} p_k(r,t)\, s_o\left(t - t_T[k] - \tfrac{2}{c}r\right) dr \; , \qquad (2.4)$$

where the tomographic projection $p_k(r,t)$ of the time-varying 3-D target-field reflectivity density $A(x,y,z,t)$ in the slant-plane coordinate system is given by

$$p_k(r,t) = \int\int\int_{x,y,z\,\in\,Target\;Field} A(x,y,z,t)\, \delta\left(r - \sqrt{(x - vt_T[k])^2 + (y + R_o)^2 + z^2}\right) dx\,dy\,dz \; .$$

$$(2.5)$$

From this equation, we see that the value of $p_k(r,t)$, (usually referred to in the SAR literature as a *range profile*) at a given range $r = r_o$ is equal to the surface integral of $A(x,y,z,t)$ over a spherical surface of radius r_o, centered at the SAR antenna location at $t = t_T[k]$. In other words, we can think of the value of $p_k(r,t)$ at a given range as being the superposition of all illuminated target-field scatterers located at that particular range from the SAR antenna. Note that we are assuming that the received signal is amplified by the radar hardware in such a manner that the magnitude of $p_k(r,t)$ is not dependent upon the range (i.e., we compensate for the $\frac{1}{r^2}$ propagation attenuation of the radar pulse).

2.1.2   Two-Dimensional Slant-Plane

If we make the assumption that the slant-plane height, z, of each target in the illuminated target field is much less than the center range distance R_o (and if we neglect target occlusion and "shadowing" effects), we can approximate the projection $p_k(r,t)$ by

$$p_k(r,t) \;\approx\; \int\int \left[\int A(x,y,z,t)dz\right] \delta\left(r - \sqrt{(x - vt_T[k])^2 + (y + R_o)^2}\right) dx\,dy$$

$$= \;\int\int A(x,y,t)\, \delta\left(r - \sqrt{(x - vt_T[k])^2 + (y + R_o)^2}\right) dx\,dy \; . \qquad (2.6)$$

Here, we see that the time-varying 2-D reflectivity density $A(x,y,t)$ is given by the projection of the time-varying 3-D reflectivity density $A(x,y,z,t)$ upon the slant-plane given by $z = 0$. In other words, *we are throwing away all height information about the target field.* The key implication of the "slant-plane" assumption *is that we can approximate the actual three-dimensional imaging geometry of Figure 2.1 by the two-dimensional geometry*
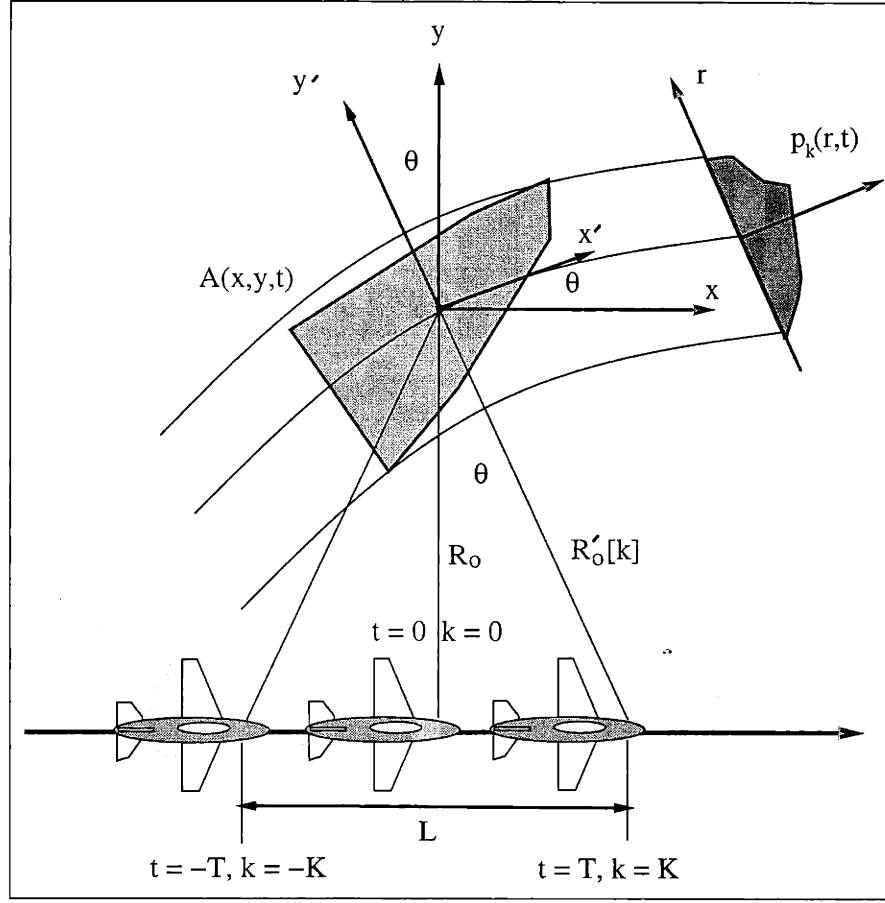
Figure 2.2: Slant-Plane Spotlight-Mode SAR Imaging Model

shown in Figure 2.2. The value of the range profile $p_k(r,t)$ at $r = r_o$ is now equal to the line integral of $A(x,y,t)$ along a circular path of radius r_o, centered at the SAR antenna location at $t = t_T[k]$.

If we substitute the projection equation into the SAR received-signal convolution equation, and simplify by integrating with respect to the range variable r, we can express $s_R(t)$ by

$$s_R(t) = \sum_{k=-K}^{K} \int \int A(x,y,t) \, s_o \left(t - t_T[k] - \frac{2}{c}\sqrt{(x - vt_T[k])^2 + (y + R_o)^2} \right) dx\,dy \; . \quad (2.7)$$

Let $R_o'[k] = \sqrt{(vt_T[k])^2 + (R_o)^2}$ be the range to the center of the target field (as a function of pulse number k), and let (x', y') be the rotated coordinates with respect to the SAR's "line of sight", as shown in Figure 2.2. Then we can express $s_R(t)$ as

Received SAR Signal (2-D Slant-Plane)

$$s_R(t) = \sum_{k=-K}^{K} \int \int A_k'(x', y', t) \, s_o \left(t - t_T[k] - \frac{2}{c}\sqrt{(x')^2 + (y' + R_o'[k])^2} \right) dx'\,dy' \; . \quad (2.8)$$

where the slant-plane coordinates (x, y) and the rotated coordinates (x', y') (for a given k) are related by

$$x = x' \cos(\theta[k]) - y' \sin(\theta[k]) \tag{2.9}$$

$$y = y' \cos(\theta[k]) + x' \sin(\theta[k]) , \tag{2.10}$$

and where the rotated 2-D reflectivity density $A_k'(x', y', t)$ is given by

$$A_k'(x', y', t) = A(x' \cos(\theta[k]) - y' \sin(\theta[k]), y' \cos(\theta[k]) + x' \sin(\theta[k]), t) . \tag{2.11}$$

Note that the angle $\theta[k]$ refers to the so-called SAR "look angle", which is given by

$$\theta[k] = \tan^{-1} \left(\frac{v t_T[k]}{R_o} \right) \tag{2.12}$$

For most SAR systems, the angle $\theta[k]$ is usually assumed to be "small" (less than 10 degrees), so we can approximate it by

$$\theta[k] \approx \frac{v}{R_o} \, t_T[k] = \dot{\theta} t_T[k] \tag{2.13}$$

where the "look angle rotation rate" $\dot{\theta}$ is given by $\dot{\theta} = \frac{v}{R_o}$.

2.1.3   Far-field Plane-Wave

We assume that the distance R_o is "large" compared to both the length of the synthetic aperture and the effective radius of our illuminated target-field. This implies that we can approximate the center range $R_o'[k]$ by

$$R_o'[k] \approx R_o + \frac{(v t_T[k])^2}{2 R_o} . \tag{2.14}$$

This also implies that we can approximate the received signal equation $s_R(t)$ by

$$s_R(t) \approx$$

$$\sum_{k=-K}^{K} \int \int A_k'(x', y', t) \, s_o \left(t - t_T[k] - \frac{2}{c} \left(R_o'[k] + y' + \frac{(x')^2}{2(R_o'[k] + y')} \right) \right) dx' dy'$$

$$\approx \sum_{k=-K}^{K} \int \int A_k'(x', y', t) \, s_o \left(t - t_T[k] - \frac{2}{c} \left(R_o'[k] + y' \right) \right) dx' dy'$$

$$\approx \sum_{k=-K}^{K} \int \left[\int A_k'(x', y', t) \, dx' \right] s_o \left(t - t_T[k] - \frac{2}{c} \left(R_o'[k] + y' \right) \right) dy'$$

$$\approx \sum_{k=-K}^{K} \int \left[p_k(y', t) \right] \, s_o \left(t - t_T[k] - \frac{2}{c} \left(R_o'[k] + y' \right) \right) dy' . \tag{2.15}$$

Here, we see that the value of the projection $p_k(y', t)$ at a given "relative range" $y' = y \cos(\theta[k]) - x \sin(\theta[k])$ is given by the line integral of $A(x, y, t)$ along the line $x' = x \cos(\theta[k]) + y \sin(\theta[k])$, as shown in Figure 2.3. We are essentially assuming that the far-field wavefront from the SAR antenna is a straight line perpendicular to the radar's "line-of-sight".
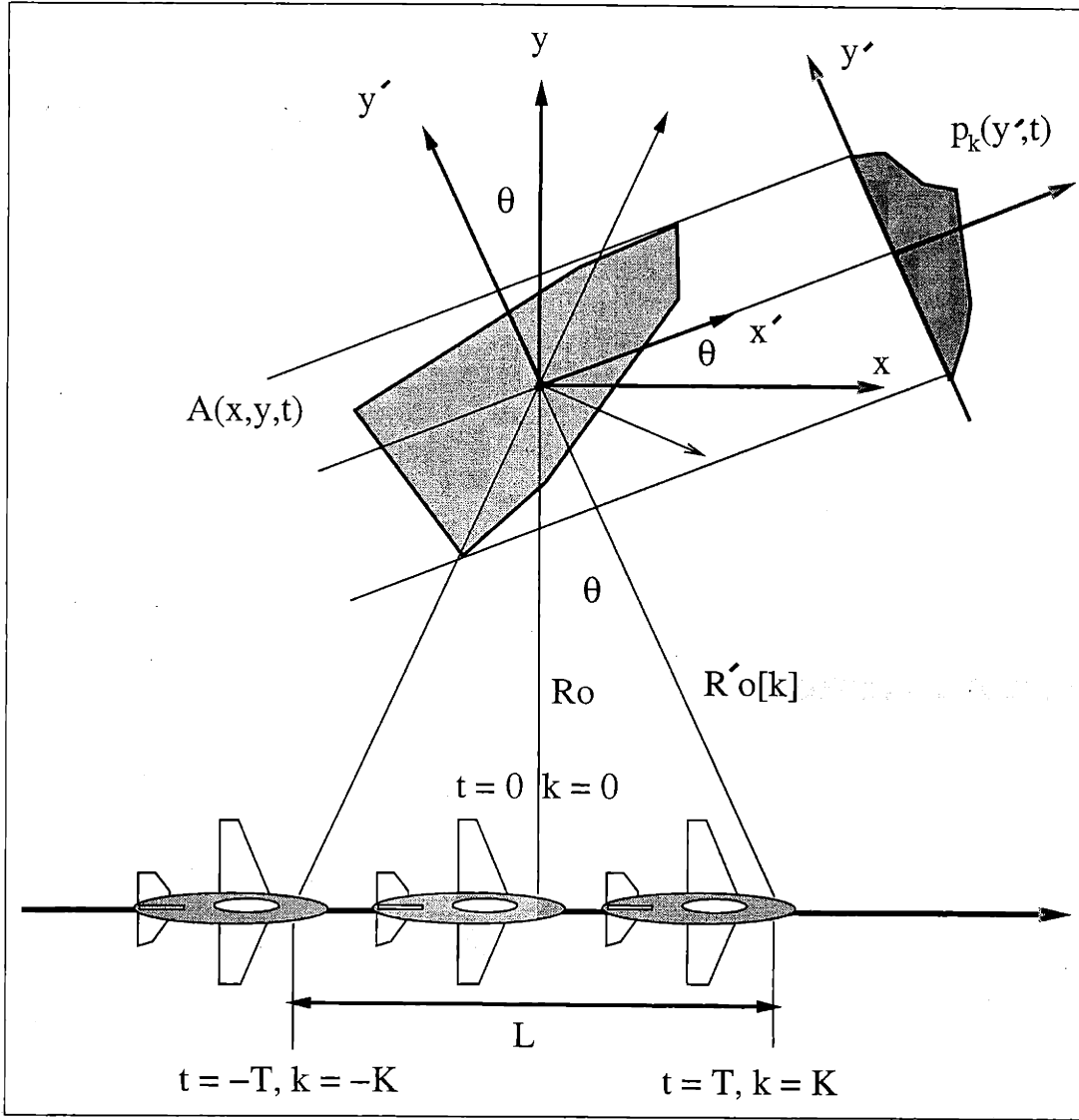
Figure 2.3: Far-Field Slant-Plane Spotlight-Mode SAR Imaging Model

2.1.4   Ideal Point-Scatterers

Up to this point in the derivation of the SAR received-signal equation $s_R(t)$, we have implicitly assumed that the target-field's time-varying $3-D$ reflectivity density $A(x,y,z,t)$ (and its $2-D$ projection $A(x,y,t)$) was *continuous*. From the SAR literature [7, 18], one way of simplifying this equation even further (as will be shown here) is to approximate the 2-D projection of the time-varying illuminated target-field by a *2-D finite array* of complex-amplitude *isotropic "ideal" point-scatterers*, i.e.,

$$A(x,y,t) \;=\; \sum_{n_x}\sum_{n_y} A[n_x,n_y] \; \delta(x - x_{n_x n_y}(t), y - y_{n_x n_y}(t)) \,.$$

$$\{x_{n_x n_y}(t), y_{n_x n_y}(t)\} \in Target\ Field \tag{2.16}$$

Here, $(x_{n_x n_y}(t), y_{n_x n_y}(t))$ refer to the $2 - D$ trajectories of the (possibly moving) point scatterers. For this point-scatterer array, we assume that the initial positions of the point scatterers are located at the following *sampled spatial positions*

$$
\begin{align}
x_{n_x n_y}(0) &= \Delta_x n_x \quad \{n_x, n_y\} \in Target\ Field \tag{2.17}\\
y_{n_x n_y}(0) &= \Delta_y n_y . \quad \{n_x, n_y\} \in Target\ Field \tag{2.18}
\end{align}
$$

where Δ_x and Δ_y are the *spatial sampling-interval constants* (whose values we will derive later in Chapter 3). We also assume that the received signal is amplified by the radar hardware in such a manner that the magnitudes of the *complex* elements of $A[n_x, n_y]$ are only dependent upon the reflectivity intensity(but not the range) of the corresponding point scatterers in the $2 - D$ array (i.e., we compensate for the $\frac{1}{r^2}$ propagation attenuation). The phases of the elements of $A[n_x, n_y]$ are the phase shifts between the incident and reflected signals at the corresponding point scatterers. Since we assume that the velocities of the point-scatterers are much less than the speed of light, then for each pulse transmit time $t_T[k]$, we can express the $2 - D$ projection of the time-varying reflectivity in the rotated-coordinate system (x', y') by

$$
A'_k(x', y') = \sum_{n_x} \sum_{n_y} A[n_x, n_y]\ \delta(x' - x'[n_x, n_y, k], y' - y'[n_x, n_y, k]) , \tag{2.19}
$$

where trajectories $(x'[n_x, n_y, k], y'[n_x, n_y, k])$ of the point-scatterers in the rotated coordinate system are given by

$$
\begin{align}
x'[n_x, n_y, k] &= x_{n_x n_y}(t_T[k]) \cos(\theta[k]) + y_{n_x n_y}(t_T[k]) \sin(\theta[k]) \tag{2.20}\\
y'[n_x, n_y, k] &= y_{n_x n_y}(t_T[k]) \cos(\theta[k]) - x_{n_x n_y}(t_T[k]) \sin(\theta[k]) . \tag{2.21}
\end{align}
$$

If we substitute $A'_k(x', y')$ into the plane-wave approximation for the SAR received signal equation, we get the following expression for $s_R(t)$

$$
\begin{align}
s_R(t) &\approx \sum_{k=-K}^{K} \int \left[\int A'_k(x', y')\ dx' \right] s_o \left(t - t_T[k] - \frac{2}{c} \left(R'_o[k] + y' \right) \right) dy' \\
&\approx \sum_{k=-K}^{K} \sum_{n_x} \sum_{n_y} A[n_x, n_y]\ s_o \left(t - t_T[k] - \frac{2}{c} \left(R'_o[k] + y'[n_x, n_y, k] \right) \right) . \tag{2.22}
\end{align}
$$

Therefore, we see that the isotropic "ideal" point-scatterer assumption allows us to approximate the SAR received-signal equation $s_R(t)$ by a "simple" *superposition of delayed versions of the SAR "mother" pulse $s_o(t)$*.

2.1.5   Chirp-Pulse with Quadrature Demodulation

For our SAR imaging model, we consider the case where the SAR "mother" pulse $s_o(t)$ is a broadband complex "chirp" signal of the form

$$
s_o(t) = e^{j2\pi \left(f_c t + \frac{\alpha t^2}{2} \right)} \mathrm{rect} \left(\frac{t}{T_p} \right) . \tag{2.23}
$$

Here, T_p is the pulse-width, f_c is the "center" frequency, and α is the chirp rate. The "rectangle" function $\text{rect}(t)$ is defined to be

$$\text{rect}(t) = \begin{cases} 1 & -\frac{1}{2} \leq t \leq \frac{1}{2} \\ 0 & \text{otherwise} \end{cases} . \tag{2.24}$$

The actual transmitted (real-valued) pulse-train signal $s_T(t)$ is then given by

$$s_T(t) = \text{Re}\left[\sum_{k=-K}^{K} s_o(t - t_T[k])\right] . \quad -T \leq k \leq T \tag{2.25}$$

For an array of "ideal" point scatterers with complex reflectivities given by $A[n_x, n_y]$, the received signal is approximately given by the following (real-valued) superposition of delayed versions of the SAR "mother" pulse $s_o(t)$

$$s_R(t) \approx \text{Re}\left[\sum_{k=-K}^{K} \sum_{n_x} \sum_{n_y} A[n_x, n_y]\, s_o\left(t - t_T[k] - \frac{2}{c}\left(R'_o[k] + y'[n_x, n_y, k]\right)\right)\right] \tag{2.26}$$

The center range $R'_o[k]$ and the relative range $y'[n_x, n_y, k]$ are given by the following expressions

$$R'_o[k] = R_o + \frac{(vt_T[k])^2}{2R_o} \tag{2.27}$$

$$y'[n_x, n_y, k] = y_{n_x n_y}(t_T[k])\cos(\theta[k]) - x_{n_x n_y}(t_T[k])\sin(\theta[k]) . \tag{2.28}$$

Let the signal $s_{R_o}(t)$ be a complex "reference chirp" pulse-train given by

$$s_{R_o}(t) = \sum_{k=-K}^{K} s_o\left(t - t_T[k] - \frac{2R'_o[k]}{c}\right)$$

$$= \sum_{k=-K}^{K} e^{j2\pi\left(f_c\left(t - t_T[k] - \frac{2R'_o[k]}{c}\right) + \frac{\alpha}{2}\left(t - t_T[k] - \frac{2R'_o[k]}{c}\right)^2\right)} \text{rect}\left(\frac{t - t_T[k] - \frac{2R'_o[k]}{c}}{T_p}\right) . \tag{2.29}$$

The real part of this complex reference signal describes a return signal from a unit-intensity point scatterer located at the origin of the target-field coordinate system. If we now assume that the *relative round-trip travel time* $\tau'[n_x, n_y, k] - \tau'_o[k]$, given by

$$\tau'[n_x, n_y, k] - \tau'_o[k] = \left(\frac{2(R'_o[k] + y'[n_x, n_y, k])}{c}\right) - \left(\frac{2R'_o[k]}{c}\right) , \tag{2.30}$$

is "small" (compared to the pulse-width T_p) for all scatterers in the target-field, we can express the received signal $s_R(t)$ as

$$s_R(t) = Re[s^*_{R_o}(t)\, f(t)] . \tag{2.31}$$
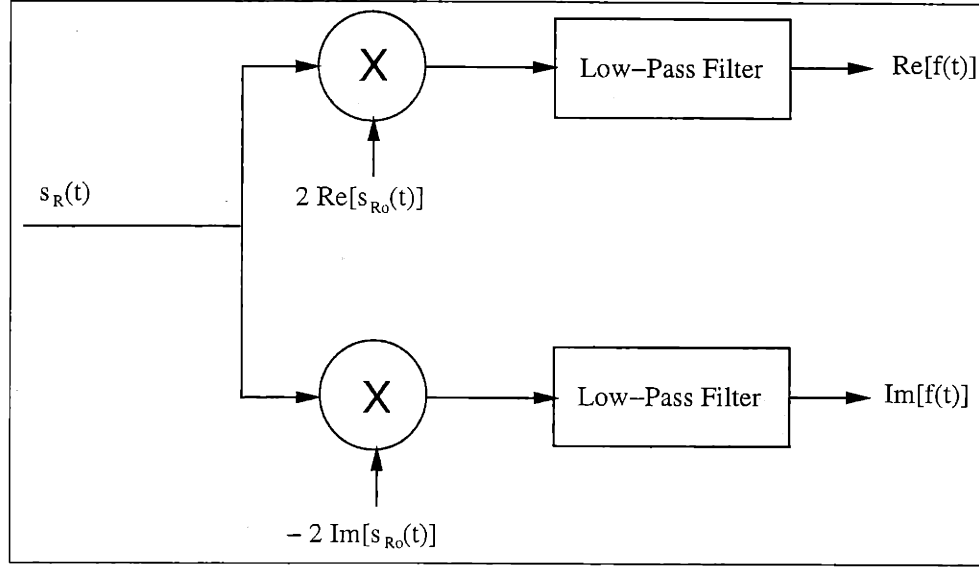
Figure 2.4: SAR Quadrature-Demodulation System

The signal $f(t)$ is an (analog) complex "baseband" pulse-train given by

$$f(t) = \sum_{k=-K}^{K} \sum_{n_x} \sum_{n_y} A[n_x, n_y] \, e^{-j2\pi\left(f_c\left(\frac{2y'[n_x,n_y,k]}{c}\right) + 2\alpha(t-t_T[k])\left(\frac{y'[n_x,n_y,k]}{c}\right) + \phi_{RVP}[n_x,n_y,k]\right)}$$
$$\times \text{rect}\left(\frac{t - t_T[k] - \frac{2R'_o[k]}{c}}{T_p}\right) , \tag{2.32}$$

where $\phi_{RVP}[n_x, n_y, k]$ is a nonlinear phase term (usually referred to in the literature as the Residual Video Phase (RVP)[7]) given by

$$\phi_{RVP}[n_x, n_y, k] = \frac{\alpha}{2}\left(\left(\frac{2R'_o[k]}{c}\right)^2 - \left(\frac{2(R'_o[k] + y'[n_x, n_y, k])}{c}\right)^2\right) . \tag{2.33}$$

This residual phase term can usually be neglected (since $|y'[n_x, n_y, k]| \ll R'_o[k]$). For many SAR imaging systems[7], the baseband signal $f(t)$ is obtained by *quadrature-demodulating* the return signals with the reference "chirp" (as shown in Figure 2.4).

If we shift the demodulated baseband pulses by the round-trip travel times $\tau'_o[k] = \frac{2R'_o[k]}{c}$ of the reference chirp pulses (so as to get rid of the dependence upon $R'_o[k]$), we can express $f(t)$ as

$$f(t) = \sum_{k=-K}^{K} \sum_{n_x} \sum_{n_y} A[n_x, n_y] \, e^{-j2\pi\left(f_c\left(\frac{2y'[n_x,n_y,k]}{c}\right) + 2\alpha(t-t_T[k])\left(\frac{y'[n_x,n_y,k]}{c}\right)\right)}$$
$$\times \text{rect}\left(\frac{t - t_T[k]}{T_p}\right) . \tag{2.34}$$

Note that we also neglected the Residual Video Phase term $\phi_{RVP}[n_x, n_y, k]$ as well. Simplifying this expression even further, we obtain

$$
\begin{aligned}
f(t) &= \sum_{k=-K}^{K} \sum_{n_x} \sum_{n_y} A[n_x, n_y]\, e^{-j\,\frac{4\pi}{c}[f_c(y'[n_x,n_y,k]) + \alpha(t-t_T[k])(y'[n_x,n_y,k])]} \mathrm{rect}\left(\frac{t - t_T[k]}{T_p}\right)\\
&= \sum_{k=-K}^{K} \sum_{n_x} \sum_{n_y} A[n_x, n_y]\, e^{-j\,\frac{4\pi}{c}[(f_c + \alpha(t-t_T[k]))(y'[n_x,n_y,k])]} \mathrm{rect}\left(\frac{t - t_T[k]}{T_p}\right)\\
&= \sum_{k=-K}^{K} \sum_{n_x} \sum_{n_y} A[n_x, n_y]\, e^{-j\,\frac{4\pi}{\lambda_c}\left[\left(1 + \frac{\alpha T_p}{f_c}\frac{(t-t_T[k])}{T_p}\right)(y'[n_x,n_y,k])\right]} \mathrm{rect}\left(\frac{t - t_T[k]}{T_p}\right). (2.35)
\end{aligned}
$$

Here, $\lambda_c = \frac{c}{f_c}$ is the "center" wavelength of the transmitted chirp pulses.

Define the "pulse-relative" *continuous* time variable $\hat{t}$ as $\hat{t} = t - t_T[k]$ (with $\frac{-T_p}{2} \leq \hat{t} \leq \frac{T_p}{2}$). If we sample the "pulse-relative" time variable $\hat{t}$ at time instants

$$
\hat{t}[n] = \frac{T_p n}{N}, \qquad \frac{-N}{2} \leq n \leq \frac{N}{2} \tag{2.36}
$$

(where for this case, the integer N is assumed to be even) we can rearrange the *one-dimensional* pulse train $f(t)$ into the following equivalent *discrete two-dimensional* SAR data function $f[n, k]$

$$
f[n,k] = f(\hat{t}[n] + t_T[k]) = \sum_{n_x} \sum_{n_y} A[n_x, n_y]\, e^{-j\,\frac{4\pi}{\lambda_c}\left[\left(1 + \frac{\alpha T_p}{f_c}\frac{\hat{t}[n]}{T_p}\right)(y'[n_x,n_y,k])\right]}.
$$

$$
-K \leq k \leq K\,, \quad \frac{-N}{2} \leq n \leq \frac{N}{2} \tag{2.37}
$$

In the SAR literature, the (discrete) sampled "pulse-relative" time variable $\hat{t}[n]$ is usually referred to as the "fast" sampling time [7, 10], while the (discrete) pulse-transmit time $t_T[k] = \frac{2Tk}{2K}$ is usually referred to as the "slow" sampling time.

If we let $y'[n_x, n_y, k] = y_{n_x n_y}(t_T[k]) \cos(\theta[k]) - x_{n_x n_y}(t_T[k]) \sin(\theta[k])$ (the plane-wave relative range relation with $\theta[k] = \tan^{-1}(\frac{v}{R_o} t_T[k]) \approx \frac{v}{R_o} t_T[k]$), we can express the complex baseband signal by the following relation (where the "look-angle" rotation rate $\dot{\theta}$ is given by $\dot{\theta} = \frac{v}{R_o}$)

$$
\boxed{
\begin{aligned}
&\underline{\textit{General-Motion SAR Data Model}}\\
f[n,k] &= \sum_{n_x} \sum_{n_y} A[n_x, n_y]\\
&\times e^{-j\,\frac{4\pi}{\lambda_c}\left[\left(1 + \frac{\alpha T_p}{f_c}\frac{\hat{t}[n]}{T_p}\right)\left(y_{n_x n_y}(t_T[k])\cos(\dot{\theta}t_T[k]) - x_{n_x n_y}(t_T[k])\sin(\dot{\theta}t_T[k])\right)\right]}.\\
&\qquad -K \leq k \leq K \quad -\frac{N}{2} \leq n \leq \frac{N}{2}
\end{aligned}
} \tag{2.38}
$$

Note that we have not as yet made any assumptions about the trajectories $(x_{n_x n_y}(t), y_{n_x n_y}(t))$ of the point-scatterers (other than the previous assumption that the point-scatterers do not move significantly over the duration of a single pulse).

2.2   General-Motion Estimation Theoretic SAR Model

Suppose we assume that the trajectories $(x_{n_x n_y}(t), y_{n_x n_y}(t))$ of the point-scatterers are also functions of a *general-motion parameter vector* $\mathbf{v}$,i.e., $(x_{n_x n_y}(t, \mathbf{v}), y_{n_x n_y}(t, \mathbf{v}))$. Here, $\mathbf{v}$ can represent translational motion parameters, rotational motion parameters, velocity basis-function coefficients, etc. In its most general form, $\mathbf{v}$ can represent the velocities of all of the point scatterers for all pulse transmit times $t_T[k]$. We can now write a general-motion estimation-theoretic model of the complex SAR data by substituting the general-motion parameterized trajectories into the general-motion SAR data model (and include an additive-noise term $\eta[n, k]$)

$$
\boxed{
\begin{aligned}
&\underline{\textit{General-Motion Estimation-Theoretic SAR Model}} \\
&f[n,k] = \sum_{n_x}\sum_{n_y} A[n_x, n_y] \\
&\times e^{-j\frac{4\pi}{\lambda_c}\left[\left(1+\frac{\alpha T_p}{f_c}\frac{\hat{t}[n]}{T_p}\right)\left(y_{n_x n_y}(t_T[k],\mathbf{v})\cos(\dot{\theta}t_T[k]) - x_{n_x n_y}(t_T[k],\mathbf{v})\sin(\dot{\theta}t_T[k])\right)\right]} + \eta[n,k] \\
&= \sum_{n_x}\sum_{n_y} A[n_x, n_y] s_{\mathbf{v}}[n_x, n_y, n, k] + \eta[n,k] \ . \\
&\qquad\qquad -K \leq k \leq K \qquad -\frac{N}{2} \leq n \leq \frac{N}{2}
\end{aligned}
}
\tag{2.39}
$$

The additive noise is modeled as zero-mean and *circularly-complex Gaussian*, i.e.,

$$
\mathrm{Re}\,[\,\eta[n,k]\,] \sim \mathrm{N}(0, \sigma_\eta^2/2) \tag{2.40}
$$

$$
\mathrm{Im}\,[\,\eta[n,k]\,] \sim \mathrm{N}(0, \sigma_\eta^2/2) \tag{2.41}
$$

$$
\mathrm{E}\,[\,\mathrm{Re}\,[\,\eta[n,k]\,]\,\mathrm{Im}\,[\,\eta[n,k]\,]\,] = 0 \ . \tag{2.42}
$$

We can also express the general-motion estimation-theoretic model in the following matrix form

$$
\mathbf{f} = \mathbf{F}(\mathbf{v})\mathbf{A} + \eta, \tag{2.43}
$$

where $\mathbf{f}$ is the SAR data, and $\mathbf{v}$ is the general-motion parameter vector. The vector $\mathbf{A}$ is the vector of scatterer intensities, given by

$$
\mathbf{A} = \begin{bmatrix} \vdots \\ A[0,0] \\ A[0,1] \\ \vdots \end{bmatrix} \ . \tag{2.44}
$$

and η is the additive Gaussian noise. The matrix $\mathbf{F}(\mathbf{v})$ has the form

$$
\mathbf{F}(\mathbf{v}) = \begin{bmatrix} \ldots & \mathbf{s}_{\mathbf{v}}[0,0] & \mathbf{s}_{\mathbf{v}}[0,1] & \ldots \end{bmatrix} , \tag{2.45}
$$

where each column vector $\mathbf{s_v}[n_x, n_y]$ corresponds to a lexicographical ordering of the $2-D$ complex-exponential basis-function given by $s_{\mathbf{v}}[n_x, n_y, n, k]$. If we assume that the additive noise η is spatially statistically-independent, then its spatial-correlation matrix is given by

$$\mathbf{K}_\eta = E\left[\eta\eta^H\right] = \sigma_\eta^2 \mathbf{I}\,. \tag{2.46}$$

2.3 Zero-Velocity Estimation-Theoretic SAR Model

If we make the assumption that the SAR "look" angle $\theta[k]$ is "small", and if we make the assumption that the center frequency f_c is much greater than the chirp bandwidth BW $= \alpha T_p$, then for a *stationary* array of point scatterers (where $(x_{n_x n_y}(t_T[k]), y_{n_x n_y}(t_T[k])) = (\Delta_x n_x, \Delta_y n_y)$), we can write the sampled complex baseband signal $f[n, k]$ as

$$
\begin{aligned}
f[n,k] \quad &= \sum_{n_x}\sum_{n_y} A[n_x, n_y]\, e^{-j\frac{4\pi}{\lambda_c}\Delta_y n_y}\, e^{-j\frac{4\pi}{\lambda_c}\left[\Delta_y n_y \frac{\alpha T_p}{f_c}\frac{\dot{t}[n]}{T_p} - \Delta_x n_x \dot{\theta} t_T[k]\right]}\,.\\[4pt]
&\quad -\frac{N}{2} \leq n \leq \frac{N}{2} \quad -K \leq k \leq K
\end{aligned}
\tag{2.47}
$$

where, again, the "look-angle" rotation rate $\dot{\theta}$ is given by $\dot{\theta} = \frac{v}{R_o}$. If we merge the constant-phase term $e^{-j\frac{4\pi}{\lambda_c}\Delta_y n_y}$ into the complex phase of $A[n_x, n_y]$ (since for most SAR imaging applications, we are generally more interested in the amplitude of the target-field complex reflectivity density rather than its phase), the complex baseband signal for the stationary-scatterer zero-velocity case can be written as

$$
\boxed{
\begin{aligned}
&\qquad\qquad \textit{Zero-Velocity SAR Data Model}\\
&f[n,k] \;=\; \sum_{n_x}\sum_{n_y} A[n_x, n_y]\, e^{-j\frac{4\pi}{\lambda_c}\left[\Delta_y n_y \frac{\alpha T_p}{f_c}\frac{\dot{t}[n]}{T_p}\right]}\, e^{j\frac{4\pi}{\lambda_c}[\Delta_x n_x \dot{\theta} t_T[k]]}\\[6pt]
&\qquad\;\; =\; \sum_{n_x}\sum_{n_y} A[n_x, n_y] s_y[n_y, n] s_x[n_x, k]\,. \quad -\frac{N}{2} \leq n \leq \frac{N}{2} \quad -K \leq k \leq K
\end{aligned}
}
\tag{2.48}
$$

Here, we see that the SAR data for the zero-velocity case is essentially given by a *limited-support scaled 2-D Fourier Transform of the imaged target field.*

From this result, we can write our estimation-theoretic model of the zero-velocity complex SAR data by simply including an additive-noise term $\eta[n, k]$ to the SAR data model.

$$
\boxed{
\begin{aligned}
&\qquad\qquad \textit{Zero-Velocity Estimation-Theoretic SAR Data Model}\\
&f[n,k] \;=\; \sum_{n_x}\sum_{n_y} A[n_x, n_y] s_y[n_y, n] s_x[n_x, k] + \eta[n, k]\,.\\[6pt]
&\qquad\qquad\qquad -\frac{N}{2} \leq n \leq \frac{N}{2} \quad -K \leq k \leq K
\end{aligned}
}
\tag{2.49}
$$
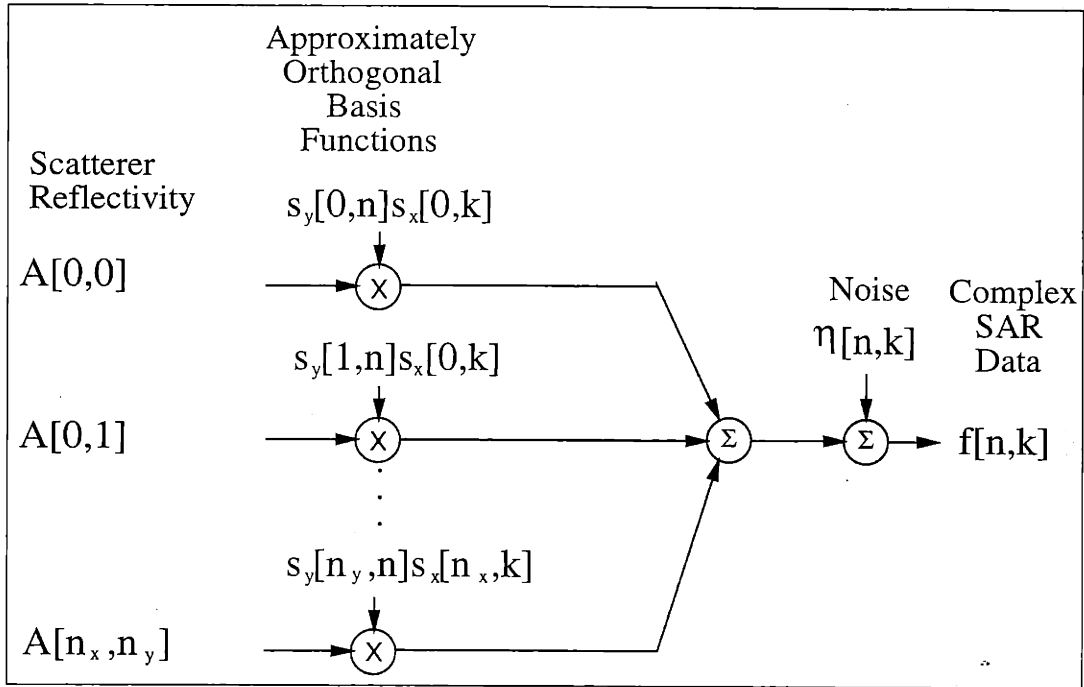
Figure 2.5: Zero-Velocity Estimation-Theoretic SAR Data Model

The additive noise is modeled as zero-mean and *circularly-complex Gaussian*, i.e.,

$$\text{Re}[\,\eta[n,k]\,] \sim \text{N}(0,\sigma_\eta^2/2) \tag{2.50}$$

$$\text{Im}[\,\eta[n,k]\,] \sim \text{N}(0,\sigma_\eta^2/2) \tag{2.51}$$

$$\text{E}[\,\text{Re}[\,\eta[n,k]\,]\,\text{Im}[\,\eta[n,k]\,]\,] = 0 \;. \tag{2.52}$$

From this framework, we can think of the SAR imaging problem as an estimation problem where we are "transmitting " a set of complex-valued coefficients (parameterized by the scatterer reflectivities $A[n_x, n_y]$) by using a set of *approximately* orthogonal basis-functions (given by the limited-support scaled 2-D Fourier Transform, and parameterized by the initial scatterer positions $(\Delta_x n_x, \Delta_y n_y)$), over a " noisy" channel, as shown in Figure 2.5.

We can also express the zero-velocity estimation-theoretic model in the following matrix form

$$\mathbf{f} = \mathbf{FA} + \eta, \tag{2.53}$$

where $\mathbf{f}$ is the SAR data and η is the additive Gaussian noise. For a set of ideal point scatterers located at the sampled spatial positions $(\Delta_x n_x, \Delta_y n_y)$, the vector $\mathbf{A}$ of scatterer intensities is given by

$$\mathbf{A} = \begin{bmatrix} \vdots \\ A[0,0] \\ A[0,1] \\ \vdots \end{bmatrix}, \tag{2.54}$$

The matrix $\mathbf{F}$ has the form

$$\mathbf{F} = \begin{bmatrix} \ldots & \mathbf{s}[0,0] & \mathbf{s}[0,1] & \ldots \end{bmatrix} , \tag{2.55}$$

where each column vector $\mathbf{s}[n_x, n_y]$ correspond to a lexicographical ordering of the $2-D$ complex-exponential basis-function given by $s_y[n_y, n]s_x[n_x, k]$. If we assume that the additive noise η is *spatially statistically-independent*, then its spatial-correlation matrix is given by

$$\mathbf{K}_\eta = E\left[\eta\eta^H\right] = \sigma_\eta^2 \mathbf{I} . \tag{2.56}$$

2.4 Spatially-Varying Temporally-Constant Velocity (SVTCV) Estimation Theoretic SAR Model

If we assume that the velocity of each moving point scatterer is constant over the SAR's "dwell time" $-T \leq t \leq T$ (but *independent from scatterer to scatterer*), then the scatterer trajectories are given by the following relations

$$x_{n_x n_y}(t) = \Delta_x n_x + \dot{x}[n_x, n_y]t \tag{2.57}$$

$$y_{n_x n_y}(t) = \Delta_y n_y + \dot{y}[n_x, n_y]t , \tag{2.58}$$

where $\dot{x}[n_x, n_y]$ and $\dot{y}[n_x, n_y]$ are the respective azimuth velocities and range velocities of the point scatterers corresponding to $A[n_x, n_y]$. Recall from Section 2.1.5 that the SAR relative-range equation $y'[n_x, n_y, k]$ was given by

$$y'[n_x, n_y, k] = y_{n_x n_y}(t_T[k]) \cos(\dot{\theta}t_T[k]) - x_{n_x n_y}(t_T[k]) \sin(\dot{\theta}t_T[k]) . \tag{2.59}$$

We can also think of this equation as being a discrete-time version (for $t = t_T[k]$) of the following *continuous-time* SAR relative-range equation

$$y'_{n_x n_y}(t) = y_{n_x n_y}(t) \cos(\dot{\theta}t) - x_{n_x n_y}(t) \sin(\dot{\theta}t) . \tag{2.60}$$

(i.e., $y'[n_x, n_y, k] = y'_{n_x n_y}(t_T[k])$). If we substitute the SVTCV trajectory relations into the continuous-time SAR relative-range equation, we obtain the following third-order polynomial approximation about $t = 0$,

$$y'_{n_x n_y}(t) \approx y'_{n_x n_y}(0) + \frac{\partial y'_{n_x n_y}(0)}{\partial t}t + \frac{1}{2!}\frac{\partial^2 y'_{n_x n_y}(0)}{\partial^2 t}t^2 + \frac{1}{3!}\frac{\partial^3 y'_{n_x n_y}(0)}{\partial^3 t}t^3 , \tag{2.61}$$

where

$$y'_{n_x n_y}(0) = \Delta_y n_y \tag{2.62}$$

$$\frac{\partial y'_{n_x n_y}(0)}{\partial t} = \left(\dot{y}[n_x, n_y] - \Delta_x n_x \dot{\theta}\right) \tag{2.63}$$

$$\frac{\partial^2 y'_{n_x n_y}(0)}{\partial^2 t} = -\left(2\dot{x}[n_x, n_y]\dot{\theta} + \Delta_y n_y \dot{\theta}^2\right) \tag{2.64}$$

$$\frac{\partial^3 y'_{n_x n_y}(0)}{\partial^3 t} = \left(-3\dot{y}[n_x, n_y]\dot{\theta}^2 + \Delta_x n_x \dot{\theta}^3\right) . \tag{2.65}$$

Note that for our case of a constant "look-angle" rotation rate $\dot{\theta} = \frac{v}{R_o}$, the mapping from the scatterer's motion parameters to the relative-range derivatives is both *linear* and *non-singular*. Rearranging terms, the polynomial approximation to the relative-range can be written in the following form

$$
\begin{aligned}
y'_{n_x n_y}(t) \approx & \left(\frac{1}{6}\dot{\theta}^3 t^3 - \dot{\theta}t \right) \Delta_x n_x + \left(1 - \frac{1}{2}\dot{\theta}^2 t^2 \right) \Delta_y n_y \\
& - \dot{\theta}t^2 \dot{x}[n_x, n_y] + \left(t - \frac{1}{2}\dot{\theta}^2 t^3 \right) \dot{y}[n_x, n_y] \, .
\end{aligned} \tag{2.66}
$$

Therefore, we can write the original discrete-time relative-range equation $y'[n_x, n_y, k]$ as

$$
\begin{aligned}
y'[n_x, n_y, k] = & \; y'_{n_x n_y}(t_T[k]) \\
= & \; y'_{n_x n_y}\left(\frac{Tk}{K} \right) \\
\approx & \left(\frac{1}{6}\dot{\theta}^3 \left(\frac{Tk}{K} \right)^3 - \dot{\theta}\left(\frac{Tk}{K} \right) \right) \Delta_x n_x + \left(1 - \frac{1}{2}\dot{\theta}^2 \left(\frac{Tk}{K} \right)^2 \right) \Delta_y n_y \\
& - \dot{\theta}\left(\frac{Tk}{K} \right)^2 \dot{x}[n_x, n_y] + \left(\left(\frac{Tk}{K} \right) - \frac{1}{2}\dot{\theta}^2 \left(\frac{Tk}{K} \right)^3 \right) \dot{y}[n_x, n_y] \, . \tag{2.67}
\end{aligned}
$$

This implies that we can express the sampled demodulated $2-D$ SAR data function for the spatially-varying temporally-constant velocity case as

$$
f[n, k] = \sum_{n_x} \sum_{n_y} A[n_x, n_y] \, e^{\, j \, \left[\phi_x[n,k]\Delta_x n_x + \phi_y[n,k]\Delta_y n_y + \phi_{\dot{x}}[n,k]\dot{x}[n_x,n_y] + \phi_{\dot{y}}[n,k]\dot{y}[n_x,n_y] \right]} \, , \tag{2.68}
$$

where

$$
\phi_x[n, k] = -\frac{4\pi}{\lambda_c} \left(1 + \frac{\alpha T_p}{f_c} \frac{n}{N} \right) \left[\frac{1}{6}\dot{\theta}^3 \left(\frac{Tk}{K} \right)^3 - \dot{\theta}\left(\frac{Tk}{K} \right) \right] \tag{2.69}
$$

$$
\phi_y[n, k] = -\frac{4\pi}{\lambda_c} \left(1 + \frac{\alpha T_p}{f_c} \frac{n}{N} \right) \left[1 - \frac{1}{2}\dot{\theta}^2 \left(\frac{Tk}{K} \right)^2 \right] \tag{2.70}
$$

$$
\phi_{\dot{x}}[n, k] = \frac{4\pi}{\lambda_c} \left(1 + \frac{\alpha T_p}{f_c} \frac{n}{N} \right) \left[\dot{\theta}\left(\frac{Tk}{K} \right)^2 \right] \tag{2.71}
$$

$$
\phi_{\dot{y}}[n, k] = -\frac{4\pi}{\lambda_c} \left(1 + \frac{\alpha T_p}{f_c} \frac{n}{N} \right) \left[\left(\frac{Tk}{K} \right) - \frac{1}{2}\dot{\theta}^2 \left(\frac{Tk}{K} \right)^3 \right] \, . \tag{2.72}
$$

In a similar fashion to the generalized-motion case, we can write an estimation-theoretic model for the spatially-varying temporally-constant velocity (SVTCV) SAR data by includ-

ing an additive-noise term $\eta[n,k]$,

$$
\begin{array}{|l|}
\hline
\\
\textit{Spatially-Varying Temporally-Constant Velocity} \\
\textit{(SVTCV) Estimation-Theoretic SAR Data Model} \\
\\
f[n,k] = \quad \sum_{n_x}\sum_{n_y} A[n_x,n_y]s_{\mathbf{v}}[n_x,n_y,n,k] + \eta[n,k] \;, \\
\\
\qquad\qquad -\dfrac{N}{2}\le n \le \dfrac{N}{2} \;\; -K \le k \le K \\
\\
\hline
\end{array}
\tag{2.73}
$$

where the velocity-parameter vector $\mathbf{v}$ consists of the azimuth velocities and range velocities of the point scatterers

$$
\mathbf{v} = \begin{bmatrix} \vdots \\ \dot{x}[0,0] \\ \dot{x}[0,1] \\ \vdots \\ \dot{y}[0,0] \\ \dot{y}[0,1] \\ \vdots \end{bmatrix} .
\tag{2.74}
$$

We model the additive noise as zero-mean and circularly-complex Gaussian, i.e.,

$$
\mathrm{Re}\,[\,\eta[n,k]\,] \sim \mathrm{N}(0,\sigma_\eta^2/2)
\tag{2.75}
$$

$$
\mathrm{Im}\,[\,\eta[n,k]\,] \sim \mathrm{N}(0,\sigma_\eta^2/2)
\tag{2.76}
$$

$$
\mathrm{E}\,[\,\mathrm{Re}\,[\,\eta[n,k]\,]\,\mathrm{Im}\,[\,\eta[n,k]\,]\,] = 0 \;.
\tag{2.77}
$$

We see that the SVTCV estimation-theoretic SAR data model is composed of *non-orthogonal* basis-functions, which are parameterized by both the scatterer initial positions and the scatterer velocities, as shown in Figure 2.6.

Just as with the generalized-motion model discussed previously, we can express the SVTCV estimation-theoretic model in the following matrix form

$$
\mathbf{f} = \mathbf{F}(\mathbf{v})\mathbf{A} + \eta,
\tag{2.78}
$$

where $\mathbf{f}$ is the SAR data. The vector $\mathbf{A}$ is the vector of scatterer intensities, given by

$$
\mathbf{A} = \begin{bmatrix} \vdots \\ A[0,0] \\ A[0,1] \\ \vdots \end{bmatrix} .
\tag{2.79}
$$

Again, the vector $\mathbf{v}$ is the vector of the corresponding scatterer velocities, and η is the additive Gaussian noise. The matrix $\mathbf{F}(\mathbf{v})$ has the form

$$
\mathbf{F}(\mathbf{v}) = \begin{bmatrix} \dots \mathbf{s}_{\mathbf{v}}[0,0] & \mathbf{s}_{\mathbf{v}}[0,1] & \dots \end{bmatrix} ,
\tag{2.80}
$$
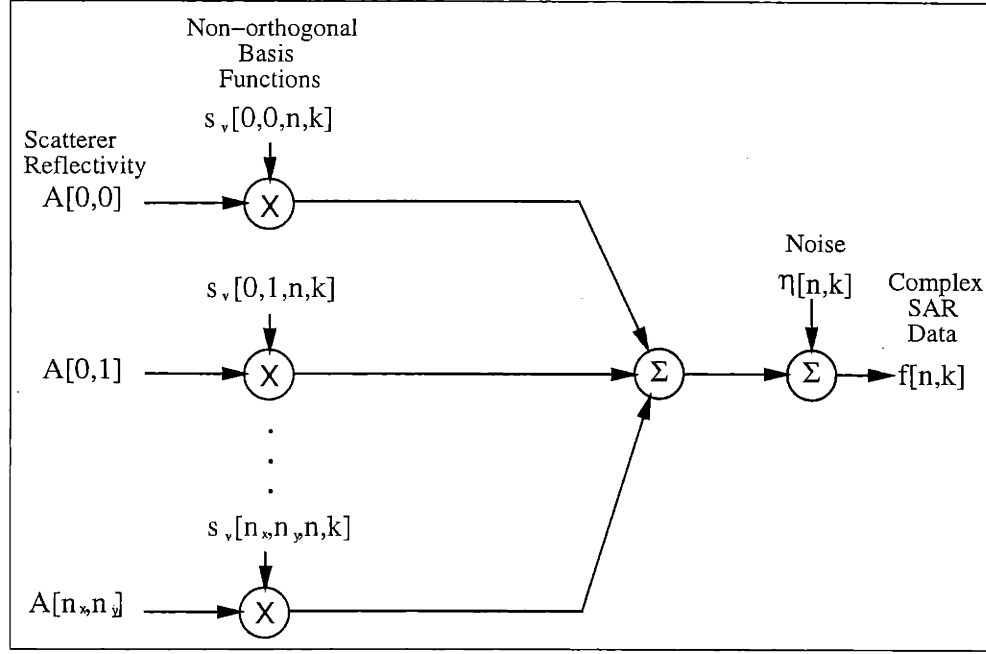
Figure 2.6: Spatially-Varying Temporally-Constant Velocity Estimation-Theoretic SAR Data Model

where each column vector $\mathbf{s_v}[n_x, n_y]$ corresponds to a lexicographical ordering of the complex-exponential basis-function given by $s_v[n_x, n_y, n, k]$. If we assume that the additive noise η is spatially statistically-independent, then its spatial-correlation matrix is given by

$$\mathbf{K}_\eta = E\left[\eta\eta^H\right] = \sigma_\eta^2 \mathbf{I} \,. \tag{2.81}$$

2.5 Rigid-Body Temporally-Constant Velocity Estimation Theoretic SAR Model

Here, we now consider the case where the $2-D$ array of point scatterers belong to a *rotating, translating rigid-body target*, i.e., the scatterers have the following trajectories

$$x_{n_x n_y}(t) = x_{RB} + \dot{x}_{RB}t + (\Delta_x n_x - x_{RB})\cos(\dot{\psi}_{RB}t) + (\Delta_y n_y - y_{RB})\sin(\dot{\psi}_{RB}t) \tag{2.82}$$

$$y_{n_x n_y}(t) = y_{RB} + \dot{y}_{RB}t + (\Delta_y n_y - y_{RB})\cos(\dot{\psi}_{RB}t) - (\Delta_x n_x - x_{RB})\sin(\dot{\psi}_{RB}t) \,. \tag{2.83}$$

As before, $(\Delta_x n_x, \Delta_y n_y)$ are the initial positions (at $t = 0$) of the point-scatterers, and (x_{RB}, y_{RB}) is the initial position (at $t = 0$) of the center-of-rotation. The velocities $(\dot{x}_{RB}, \dot{y}_{RB})$ are the initial velocities of the center-of-rotation, and $\dot{\psi}_{RB}$ is the target rotation rate. If we assume that $\dot{\psi}_{RB}$ is "small", we can simplify these expressions to

$$x_{n_x n_y}(t) = \Delta_x n_x + \left(\dot{x}_{RB} + (\Delta_y n_y - y_{RB})\dot{\psi}_{RB}\right)t \tag{2.84}$$

$$y_{n_x n_y}(t) = \Delta_y n_y + \left(\dot{y}_{RB} - (\Delta_x n_x - x_{RB})\dot{\psi}_{RB}\right)t \,. \tag{2.85}$$

This implies that the scatterer velocities are approximately given by

$$\dot{x}[n_x, n_y] = \dot{x}_{RB} + (\Delta_y n_y - y_{RB})\dot{\psi}_{RB} \tag{2.86}$$

$$\dot{y}[n_x, n_y] = \dot{y}_{RB} - (\Delta_x n_x - x_{RB})\dot{\psi}_{RB} \ . \tag{2.87}$$

Just as with the general SVTCV estimation theoretic model, we are essentially assuming that the velocity of each moving point scatterer is constant over the SAR's "dwell time" $-T \leq t \leq T$. However, the scatterer velocities are now correlated by the rigid-body equations.

For the simplified rigid-body scatterer-velocity equations derived here, suppose we are given $(x_{RB}, y_{RB}, \dot{x}_{RB}, \dot{y}_{RB}) = (x_{RB_o}, y_{RB_o}, 0, 0)$. We see that for $\dot{\psi}_{RB} \neq 0$, this is is equivalent to $(x_{RB}, y_{RB}, \dot{x}_{RB}, \dot{y}_{RB}) = (0, 0, -y_{RB_o}\dot{\psi}_{RB}, x_{RB_o}\dot{\psi}_{RB})$. This implies that the center-of-rotation position variables (x_{RB}, y_{RB}) are *redundant* variables. This also implies that we can simplify the scatterer-velocity equations by "merging" the terms $-y_{RB}\dot{\psi}_{RB}$ and $x_{RB}\dot{\psi}_{RB}$ into $(\dot{x}_{RB}, \dot{y}_{RB})$

$$\dot{x}[n_x, n_y] = \dot{x}_{RB} + \dot{\psi}_{RB}\Delta_y n_y \tag{2.88}$$

$$\dot{y}[n_x, n_y] = \dot{y}_{RB} - \dot{\psi}_{RB}\Delta_x n_x \ . \tag{2.89}$$

If we substitute the expressions for the scatterer velocities into the SVTCV $2-D$ SAR data function derived in the previous section, we get the following expression for the rigid-body SAR data

$$
\begin{aligned}
f[n, k] &= e^{\, j\, \left[(\phi_x[n,k] - \phi_{\dot{y}}[n,k]\dot{\psi}_{RB})\Delta_x n_x + (\phi_y[n,k] + \phi_{\dot{x}}[n,k]\dot{\psi}_{RB})\Delta_y n_y \right]} \\
&\times e^{\, j\, \left[\phi_{\dot{x}}[n,k]\dot{x}_{RB} + \phi_{\dot{y}}[n,k]\dot{y}_{RB} \right]} \ .
\end{aligned}
\tag{2.90}
$$

We can write an estimation-theoretic model for the rigid-body temporally-constant velocity (RBTCV) SAR data by including an additive-noise term $\eta[n, k]$,

$$
\begin{array}{|c|}
\hline
\\
\underline{\textit{Rigid-Body Temporally-Constant Velocity (RBTCV)}} \\
\underline{\textit{Estimation-Theoretic SAR Data Model}} \\
f[n, k] = \sum_{n_x} \sum_{n_y} A[n_x, n_y] s_{\dot{\psi}_{RB}}[n_x, n_y, n, k] s_{\dot{x}_{RB} \, \dot{y}_{RB}}[n, k] + \eta[n, k] \ . \\
-\frac{N}{2} \leq n \leq \frac{N}{2} \quad -K \leq k \leq K \\
\\
\hline
\end{array}
\tag{2.91}
$$

We model the additive noise as zero-mean and circularly-complex Gaussian, i.e.,

$$\text{Re}\,[\,\eta[n, k]\,] \sim N(0, \sigma_\eta^2/2) \tag{2.92}$$

$$\text{Im}\,[\,\eta[n, k]\,] \sim N(0, \sigma_\eta^2/2) \tag{2.93}$$

$$E\,[\,\text{Re}\,[\,\eta[n, k]\,]\,\text{Im}\,[\,\eta[n, k]\,]\,] = 0 \ . \tag{2.94}$$

We can also express the RBTCV estimation-theoretic model in the following matrix form

$$\mathbf{f} = \mathbf{F}(\mathbf{v})\mathbf{A} + \eta, \tag{2.95}$$

where $\mathbf{f}$ is the SAR data. The vector $\mathbf{A}$ is the vector of scatterer intensities, given by

$$\mathbf{A} = \begin{bmatrix} \vdots \\ A[0,0] \\ A[0,1] \\ \vdots \end{bmatrix} . \qquad (2.96)$$

The vector $\mathbf{v}$ is the vector of the rigid-body scatterer-velocity parameters,

$$\mathbf{v} = \begin{bmatrix} \dot{x}_{RB} \\ \dot{y}_{RB} \\ \dot{\psi}_{RB} \end{bmatrix} . \qquad (2.97)$$

and η is the additive Gaussian noise. The matrix $\mathbf{F}(\mathbf{v})$ has the form

$$\mathbf{F}(\mathbf{v}) = \begin{bmatrix} \dots & \mathbf{s_v}[0,0] & \mathbf{s_v}[0,1] & \dots \end{bmatrix} , \qquad (2.98)$$

where each column vector $\mathbf{s_v}[n_x, n_y]$ corresponds to a complex exponential basis function given by $s_{\dot{\psi}_{RB}}[n_x, n_y, n, k] s_{\dot{x}_{RB} \, \dot{y}_{RB}}[n, k]$. If we assume that the additive noise η is spatially statistically-independent, then its spatial-correlation matrix is given by

$$\mathbf{K}_\eta = E\left[\eta\eta^H\right] = \sigma_\eta^2 \mathbf{I} . \qquad (2.99)$$

Chapter 3

L_1-Norm Based SAR Processing

IN this chapter, we present a generalized SAR imaging framework which exploits the idea of L_1-norm regularization in order to address the limitations of conventional SAR imaging (e.g., blurring to motion, sidelobe artifacts, and loss of scatterer resolution). For comparison purposes, we first present a brief overview of a conventional SAR processing algorithm. Next, we present an a estimation-theoretic justification for the L_1-norm-based SAR processing framework, from the context of the ill-posed over-complete basis-pursuit estimation problem. We also present a means for implementing an L_1-norm-based algorithm by using a coordinate-descent line-minimization scheme. Later in Chapter 5, we will present a parameterized estimation-theoretic L_1-norm regularized approach for imaging rigid-body moving targets. In this chapter, we also present some results in order to demonstrate the utility of an L_1-norm regularized approach for reducing sidelobes and improving resolution for stationary SAR images.

3.1 Conventional Spotlight-Mode SAR Processing

In the previous chapter, we derived the following zero-velocity estimation-theoretic model for the quadrature-demodulated sampled "baseband" SAR data $f[n,k]$ (where we have a $2-D$ array of stationary isotropic "ideal" point-scatterers)

$$
\begin{aligned}
\textit{Zero-Velocity SAR Model} \\
f[n,k] &= \sum_{n_x}\sum_{n_y} A[n_x,n_y]\, e^{-j\frac{4\pi}{\lambda_c}\left[\Delta_y n_y \frac{\alpha T_p}{f_c}\frac{\ell[n]}{T_p}\right]}\, e^{j\frac{4\pi}{\lambda_c}\left[\Delta_x n_x \dot{\theta} t_T[k]\right]} + \eta[n,k] \\
&= \sum_{n_x}\sum_{n_y} A[n_x,n_y] s_y[n_y,n] s_x[n_x,k] + \eta[n,k]\ . \\
&\qquad -\frac{N}{2} \le n \le \frac{N}{2} \quad -K \le k \le K
\end{aligned}
$$

(3.1)

Recall that we assumed that ideal point-scatterers were located at the following *sampled spatial positions*

$$x_{n_x n_y}(t) = \Delta_x n_x \quad \{n_x, n_y\} \in Target\ Field \tag{3.2}$$

$$y_{n_x n_y}(t) = \Delta_y n_y \ . \quad \{n_x, n_y\} \in Target\ Field \tag{3.3}$$

where Δ_x and Δ_y are *spatial sampling-interval constants* (whose values we will derive later in this chapter). Also recall that the set of corresponding point-scatterer reflectivities were given by the $2-D$ function $A[n_x, n_y]$. For this zero-velocity case, we see that the SAR data is essentially given by a *limited-support scaled 2-D Fourier Transform of the imaged target field*. This implies that we can simply *use a limited-support scaled inverse 2-D Fourier Transform to (approximately) recover the target-field reflectivities $A[n_x, n_y]$ from the demodulated SAR data $f[n, k]$.*

From the previous chapter, we can express the zero-velocity estimation-theoretic model in the following matrix form

$$\mathbf{f} = \mathbf{FA} + \eta, \tag{3.4}$$

where $\mathbf{f}$ is the SAR data and η is the additive Gaussian noise. For a set of ideal point scatterers located at the sampled spatial positions $(\Delta_x n_x, \Delta_y n_y)$, the vector $\mathbf{A}$ of scatterer intensities is given by

$$\mathbf{A} = \begin{bmatrix} \vdots \\ A[0,0] \\ A[0,1] \\ \vdots \end{bmatrix} . \tag{3.5}$$

The matrix $\mathbf{F}$ has the form

$$\mathbf{F} = \begin{bmatrix} \ldots & \mathbf{s}[0,0] & \mathbf{s}[0,1] & \ldots \end{bmatrix} , \tag{3.6}$$

where each column vector $\mathbf{s}[n_x, n_y]$ corresponds to a lexicographical ordering of the complex-exponential basis-function given by $s_y[n_y, n]s_x[n_x, k]$. Since we assume that the additive noise η is *spatially statistically-independent*, then its spatial-correlation matrix is given by

$$\mathbf{K}_\eta = E\left[\eta\eta^H\right] = \sigma_\eta^2 \mathbf{I} . \tag{3.7}$$

For the matrix zero-velocity model presented here, the maximum-likelihood estimate for the scatterer vector $\mathbf{A}$ is given by

$$\hat{\mathbf{A}}_{ML} = \left(\mathbf{F}^H \mathbf{K}_\eta^{-1} \mathbf{F}\right)^{-1} \mathbf{F}^H \mathbf{K}_\eta^{-1} \mathbf{f} . \tag{3.8}$$

This is equivalent to minimizing the following standard least-squares cost function $J(\mathbf{A})$

$$J(\mathbf{A}) = ||\mathbf{f} - \mathbf{FA}||_{\mathbf{K}_\eta^{-1}}^2 = (\mathbf{f} - \mathbf{FA})^H \mathbf{K}_\eta^{-1} (\mathbf{f} - \mathbf{FA}) . \tag{3.9}$$

For the case where the noise η is spatially statistically-independent and isotropic, the maximum-likelihood estimate can be simplified to

$$\hat{\mathbf{A}}_{ML} = \left(\frac{1}{\sigma_\eta^2}\mathbf{F}^H\mathbf{F}\right)^{-1}\frac{1}{\sigma_\eta^2}\mathbf{F}^H\mathbf{f} = \left(\mathbf{F}^H\mathbf{F}\right)^{-1}\mathbf{F}^H\mathbf{f} . \tag{3.10}$$

However, direct calculation of the inverse of the matrix $\mathbf{F}^H\mathbf{F}$ can be computationally intensive, even for a moderately sized SAR scene. Therefore, the following approximation is typically made to the so-called ambiguity-function matrix $\mathbf{F}^H\mathbf{F}$ (where the ambiguity function[42] refers to the response of the maximum-likelihood estimator to a unit-amplitude point-scatterer located at the center of the imaged target-field)

$$\mathbf{F}^H\mathbf{F} \approx \mathbf{I} . \tag{3.11}$$

Thus, the conventional-SAR maximum-likelihood estimate is given by

$$\hat{\mathbf{A}}_{ML} \approx \mathbf{F}^H\mathbf{f} , \tag{3.12}$$

which is essentially the inverse Fourier Transform (with limited support) of the demodulated SAR data. The effect of this approximation is the introduction of sidelobes into the final SAR image for high-amplitude scatterers (since the ambiguity function for an estimator based upon the limited-extent Fourier-Transform is approximately a scaled sinc function). This approximation also limits the conventional SAR image in resolution.

In terms of the original sampled 2-D target-field reflectivity $A[n_x, n_y]$, the approximation to the maximum-likelihood estimate is given by

$$\hat{A}[n_x, n_y] \approx \frac{1}{(2K)(N)} \sum_{k=-K}^{K} \sum_{n=-\frac{N}{2}}^{\frac{N}{2}} f[n, k]\, e^{j\frac{4\pi}{\lambda_c}\left[\Delta_y n_y \frac{\alpha T_p}{f_c}\frac{\hat{t}[n]}{T_p}\right]}\, e^{-j\frac{4\pi}{\lambda_c}[\Delta_x n_x \dot{\theta} t_T[k]]}$$

$$= \frac{1}{(2K)(N)} \sum_{k=-K}^{K} \sum_{n=-\frac{N}{2}}^{\frac{N}{2}} f[n, k]\, h_y[n_y, n]\, h_x[n_x, k] . \tag{3.13}$$

The (sampled) scaled inverse Fourier-Transform basis-functions ($h_x[n_x, k]$ and $h_y[n_y, n]$) are given by the respective complex-conjugates of the zero-velocity SAR model basis-functions $s_x[n_x, k]$ and $s_y[n_y, n]$.

In the literature[7, 10], this conventional SAR processing algorithm is usually divided into two main steps, *range-processing* and *azimuth processing*. The first part of the so-called range-processing step is the quadrature-demodulation process (plus the required analog-to-digital conversion) used to obtain the complex baseband SAR data, $f[n, k]$, from the received "chirp" signals reflected from the point scatterers. This part of the range-processing is performed by the radar hardware at each pulse-transmit time $t_T[k]$. After $f[n, k]$ is obtained, the next part of the range-processing step is a scaled $1 - D$ Fourier-transform with respect to the "fast" sampling time $\hat{t}[n] = \frac{T_p n}{N}$. This forms a series of so-called *Relative-Range Profiles* (RRP). Then, the azimuth-processing step is simply a scaled $1 - D$ Fourier Transform "across" the relative-range profile data with respect to the "slow time" (pulse-transmit time) $t_T[k] = \frac{T k}{K}$. This gives us the final complex SAR image $\hat{A}[n_x, n_y]$. One interpretation of the conventional range and azimuth processing algorithms presented in the literature is as a *row-column decomposition of the 2-D inverse scaled Fourier Transform*.

Range Resolution and Azimuth Resolution

Here, we derive values for the spatial sampling intervals, Δ_x and Δ_y. In the literature[18], these sampling intervals are usually some fraction of the corresponding "inherent" azimuth and range resolutions, δ_x and δ_y, of the SAR system (whose values we will derive here).

Suppose we are given the following noiseless zero-velocity SAR data set $f[n,k]$, which corresponds to an array of ideal point scatterers with initial positions at $(\delta_x n_x', \delta_y n_y')$ (where $\{n_x', n_y'\} \in Target\ Field$).

$$f[n,k] = \sum_{n_x'} \sum_{n_y'} A[n_x', n_y']\, e^{-j\,\frac{4\pi}{\lambda_c}\left[\frac{\alpha T_p}{f_c}\frac{\hat{t}[n]}{T_p}\delta_y n_y'\right]}\, e^{\,j\,\frac{4\pi}{\lambda_c}\left[\dot{\theta}t_T[k]\delta_x n_x'\right]}\ .$$

$$-\frac{N}{2} \le n \le \frac{N}{2} \qquad -K \le k \le K \qquad\qquad (3.14)$$

Again, $f[n,k]$ is a scaled Fourier Transform of the imaged target field reflectivity. This scaled Fourier Transform can also be expressed in the following form

$$f[n,k] = \sum_{n_x'} \sum_{n_y'} A[n_x', n_y']\, e^{\,j\,k\Delta\omega_x \delta_x n_x'}\, e^{-j\,n\Delta\omega_y \delta_y n_y'}\ ,$$

$$-\frac{N}{2} \le n \le \frac{N}{2} \qquad -K \le k \le K \qquad\qquad (3.15)$$

where the *spatial frequencies* $(k\Delta\omega_x, n\Delta\omega_y)$ are given by

$$k\Delta\omega_x \;=\; \frac{4\pi\dot{\theta}t_T[k]}{\lambda_c} = \frac{4\pi\dot{\theta}}{\lambda_c}\left[\frac{k(2T)}{2K}\right] \qquad\qquad (3.16)$$

$$n\Delta\omega_y \;=\; \frac{4\pi}{\lambda_c}\left[\frac{\alpha T_p}{f_c}\frac{\hat{t}[n]}{T_p}\right] = \frac{4\pi\alpha\hat{t}[n]}{c} = \frac{4\pi\alpha}{c}\left[\frac{nT_p}{N}\right]\ . \qquad\qquad (3.17)$$

As shown in Figure 3.1, this Fourier-Transform equation essentially says that *the SAR data is contained within a $2K\Delta\omega_x \times N\Delta\omega_y$ subset of the target-field's 2-D Fourier Transform* [28], where the dimensions of this subset, $2K\Delta\omega_x$ and $N\Delta\omega_y$, are given by

$$2K\Delta\omega_x \;=\; \frac{8\pi\dot{\theta}T}{\lambda_c} \qquad\qquad (3.18)$$

$$N\Delta\omega_y \;=\; \frac{4\pi\alpha T_p}{c}\ . \qquad\qquad (3.19)$$

The variables (ω_x, ω_y) shown in Figure 3.1 are the spatial frequencies corresponding to (x, y). Therefore, the noiseless-data maximum-likelihood estimate, $\hat{A}[n_x, n_y]$ (using (3.11), which is the discrete scaled inverse Fourier Transform of $f[n,k]$) is approximately given by the following set of scaled *sampled 2-D sinc functions* (where the spatial sampling intervals are again given by Δ_x and Δ_y)

$$\hat{A}[n_x, n_y] = \frac{1}{(2K)(N)} \sum_{k=-K}^{K} \sum_{n=-\frac{N}{2}}^{\frac{N}{2}} f[n,k]\, e^{-j\,k\Delta\omega_x\Delta_x n_x}\, e^{\,j\,n\Delta\omega_y\Delta_y n_y}$$

$$\approx \sum_{n'_x} \sum_{n'_y} A[n'_x, n'_y] \text{sinc}\left(\frac{2K\Delta\omega_x(\Delta_x n_x - \delta_x n'_x))}{2}\right) \text{sinc}\left(\frac{N\Delta\omega_y(\Delta_y n_y - \delta_y n'_y))}{2}\right) .$$

$$(3.20)$$

In order for the sinc-function mainlobe "peaks" (corresponding to each point scatterer) to be distinct, the initial positions $(\delta_x n'_x, \delta_y n'_y)$ of the ideal point scatterers must be separated by an azimuth distance and a range distance equal to the corresponding azimuth and range widths of the mainlobes of the scaled sampled sinc functions. This implies that the ultimate SAR azimuth resolution δ_x and range resolution δ_y are given by the following expressions

<div style="border:1px solid">

SAR Azimuth Resolution and Range Resolution

$$\delta_x = 2\frac{\pi}{\left(\frac{2K\Delta\omega_x}{2}\right)} = \frac{\lambda_c}{2\theta T}$$

$$\delta_y = 2\frac{\pi}{\left(\frac{N\Delta\omega_y}{2}\right)} = \frac{c}{\alpha T_p} .$$

</div>

$$(3.21)$$

We see that the range resolution δ_y *is inversely proportional to the approximate bandwidth* αT_p *of the transmitted "chirp" signals*, while the azimuth resolution δ_x *is inversely proportional to the length of the radar's "synthetic-aperture angle"* $2\dot\theta T$. As stated earlier, in the literature[18], the spatial sampling-interval constants, Δ_x and Δ_y, are usually chosen to be some fraction of δ_x and δ_y (e.g., $\Delta_x = 0.5\delta_x$ and $\Delta_y = 0.5\delta_y$).

Range Walk and the Polar Format Algorithm

In order for the Fourier-Transform based conventional SAR processing technique to produce acceptable results, the relative-range variations of the target-field point scatterers must be less than the range sampling interval Δ_y. In terms of the general-motion SAR relative-range equation derived in the previous chapter, the following condition must be satisfied for the set of stationary scatterers with trajectories given by $(x_{n_x n_y}(t_T[k]), y_{n_x n_y}(t_T[k])) = (\Delta_y n_y, \Delta_y n_y)$

$$\left(\Delta_y n_y - \frac{\Delta_y}{2}\right) \le (y_{n_x n_y}(t_T[k])\cos(\theta[k]) - x_{n_x n_y}(t_T[k])\sin(\theta[k])) \le \left(\Delta_y n_y + \frac{\Delta_y}{2}\right) .$$

$$(3.22)$$

This condition can also be written as

<div style="border:1px solid">

SAR Range-Walk Condition

$$\left(\Delta_y n_y - \frac{\Delta_y}{2}\right) \le (\Delta_y n_y \cos(\theta[k]) - \Delta_x n_x \sin(\theta[k])) \le \left(\Delta_y n_y + \frac{\Delta_y}{2}\right) .$$

</div>

$$(3.23)$$

If this condition is violated, the final SAR image will be degraded by an effect known as *range-walk*, where the energy from a given point-scatterer is dispersed over several spatial
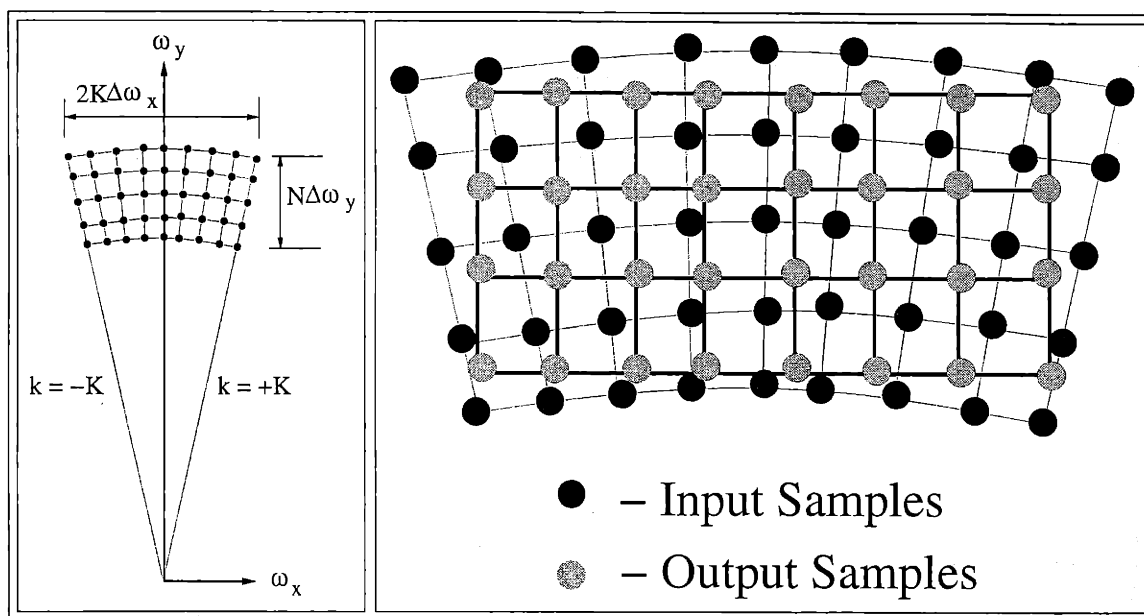
Figure 3.1: Fourier Data Domain for SAR Imaging Geometry and Polar Format Resampling

sampling-interval "cells". Even for stationary targets, range walk can still occur for higher-resolution SAR systems (with smaller range sampling-interval constants Δ_y and/or larger look angle extents, $\theta[K] - \theta[-K] = 2\dot{\theta}T$). This essentially arises from our assumption that our data samples correspond to an approximately rectangular portion of the 2-D Fourier Transform of the target-field reflectivity density, when in reality, it is an *angular* section. One common means of compensating for range-walk (without sacrificing range resolution) is to resample the demodulated SAR data by interpolating from a polar grid to a rectangular grid, as shown in Figure 3.1.

For the experimental results presented later in this chapter for the enhancement of stationary SAR scenes, we found that we did not have to consider range-walk as an issue, since the SAR's look angle extent was relatively small (about 0.036 radians). Therefore, we did not need to use polar-format resampling for these particular examples. However, for the L_1-Norm based SAR processing technique presented in Chapter 5 for the rigid-body motion case, we used a polar-format resampling based algorithm in order to compensate for *target* rotation (which is equivalent to having a larger SAR look angle extent).

3.2 General-Motion L₁-Norm Based SAR Processing Algorithm

Recall from Chapter 2 that we derived the following general-motion parameterized estimation-theoretic model

$$
\begin{aligned}
\underline{\textit{General-Motion Estimation-Theoretic SAR Model}} \\
f[n,k] = \sum_{n_x}\sum_{n_y} A[n_x,n_y] \\
\times e^{-j\frac{4\pi}{\lambda_c}\left[\left(1+\frac{\alpha T_p}{f_c}\frac{i[n]}{T_p}\right)\left(y_{n_x n_y}(t_T[k],\mathbf{v})\cos(\dot\theta t_T[k])-x_{n_x n_y}(t_T[k],\mathbf{v})\sin(\dot\theta t_T[k])\right)\right]} + \eta[n,k] \\
= \sum_{n_x}\sum_{n_y} A[n_x,n_y]s_{\mathbf{v}}[n_x,n_y,n,k] + \eta[n,k]\ . \\
-K \le k \le K \quad -\frac{N}{2} \le n \le \frac{N}{2}
\end{aligned}
\tag{3.24}
$$

The vector $\mathbf{v}$ is a general-motion parameter vector which can represent translational motion parameters, rotational motion parameters, velocity basis-function coefficients, etc. We can also express the general-motion estimation-theoretic model in the following matrix form

$$\mathbf{f} = \mathbf{F}(\mathbf{v})\mathbf{A} + \eta, \tag{3.25}$$

where $\mathbf{f}$ is the SAR data. The vector $\mathbf{A}$ is the vector of scatterer intensities, given by

$$\mathbf{A} = \begin{bmatrix} \vdots \\ A[0,0] \\ A[0,1] \\ \vdots \end{bmatrix}. \tag{3.26}$$

and η is the additive Gaussian noise. The matrix $\mathbf{F}(\mathbf{v})$ has the form

$$\mathbf{F}(\mathbf{v}) = \begin{bmatrix} \cdots & \mathbf{s_v}[0,0] & \mathbf{s_v}[0,1] & \cdots \end{bmatrix}, \tag{3.27}$$

where each column vector $\mathbf{s_v}[n_x,n_y]$ corresponds to a lexicographical ordering of the $2-D$ complex-exponential basis-function given by $s_{\mathbf{v}}[n_x,n_y,n,k]$. If we assume that the additive noise η is spatially statistically-independent and isotropic, then its spatial-correlation matrix is given by

$$\mathbf{K}_\eta = E\left[\eta\eta^H\right] = \sigma_\eta^2\mathbf{I}\ . \tag{3.28}$$

Given the general-motion estimation-theoretic model with the form, $\mathbf{f} = \mathbf{F}(\mathbf{v})\mathbf{A}+\eta$, the maximum likelihood estimate for the scatterer-amplitude vector $\mathbf{A}$ and scatterer-velocity vector $\mathbf{v}$ is equivalent to finding the scatterer amplitudes $\hat{\mathbf{A}}$ and velocity-parameters $\hat{\mathbf{v}}$ which minimizes the following standard least-squares cost function $J(\mathbf{A},\mathbf{v})$

$$J(\mathbf{A},\mathbf{v}) = \|\mathbf{f}-\mathbf{F}(\mathbf{v})\mathbf{A}\|^2_{\mathbf{K}_\eta^{-1}} = (\mathbf{f}-\mathbf{F}(\mathbf{v})\mathbf{A})^H\mathbf{K}_\eta^{-1}(\mathbf{f}-\mathbf{F}(\mathbf{v})\mathbf{A})\ . \tag{3.29}$$

From this cost function, the maximum-likelihood estimate for the scatterer-amplitude vector $\mathbf{A}$ is given by

$$\hat{\mathbf{A}}_{ML} = \left(\mathbf{F}^H(\hat{\mathbf{v}}_{ML})\mathbf{K}_\eta^{-1}\mathbf{F}(\hat{\mathbf{v}}_{ML})\right)^{-1}\mathbf{F}^H(\hat{\mathbf{v}}_{ML})\mathbf{K}_\eta^{-1}\mathbf{f} , \tag{3.30}$$

where the maximum-likelihood estimate $\hat{\mathbf{v}}_{ML}$ of the velocity-parameter vector $\mathbf{v}$ is given by

$$\hat{\mathbf{v}}_{ML} = \arg\max_{\mathbf{v}} [\, ||\left(\mathbf{F}^H(\mathbf{v})\mathbf{K}_\eta^{-1}\mathbf{F}(\mathbf{v})\right)^{-1}\mathbf{F}^H(\mathbf{v})\mathbf{K}_\eta^{-1}\mathbf{f}||_2^2\,] . \tag{3.31}$$

However, for many moving-target SAR imaging applications, our estimation problem will be ill-posed (i.e., we will not have a unique solution for both $\hat{\mathbf{A}}_{ML}$ and $\hat{\mathbf{v}}_{ML}$), which implies that we must add some type of regularization to this problem. In the literature[21], one common means of regularizing an estimation problem of this form is to add a quadratic penalty upon the vector $\mathbf{A}$ to the cost function $J(\mathbf{A}, \mathbf{v})$, e.g.,

$$J(\mathbf{A}, \mathbf{v}) = ||\mathbf{f} - \mathbf{F}(\mathbf{v})\mathbf{A}||_{\mathbf{K}_\eta^{-1}}^2 + \gamma_A \mathbf{A}^H \mathbf{A} . \tag{3.32}$$

The corresponding solution to this so-called L_2 *regularized problem* is then given by

$$\hat{\mathbf{A}}_{ML} = \left(\mathbf{F}^H(\hat{\mathbf{v}}_{ML})\mathbf{K}_\eta^{-1}\mathbf{F}(\hat{\mathbf{v}}_{ML}) + \gamma_A\mathbf{I}\right)^{-1}\mathbf{F}^H(\hat{\mathbf{v}}_{ML})\mathbf{K}_\eta^{-1}\mathbf{f} , \tag{3.33}$$

where, in a similar fashion to before, the maximum-likelihood estimate $\hat{\mathbf{v}}_{ML}$ is given by

$$\hat{\mathbf{v}}_{ML} = \arg\max_{\mathbf{v}} [\, ||\left(\mathbf{F}^H(\mathbf{v})\mathbf{K}_\eta^{-1}\mathbf{F}(\mathbf{v}) + \gamma_A\mathbf{I}\right)^{-1}\mathbf{F}^H(\mathbf{v})\mathbf{K}_\eta^{-1}\mathbf{f}||_2^2\,] . \tag{3.34}$$

For a given set of velocity parameters $\mathbf{v}$, it can be shown [19, 21, 27] that the quadratic L_2 penalty $\gamma_A\mathbf{A}^H\mathbf{A}$ is equivalent to the following zero-mean circularly-complex Gaussian prior model for the scatterer amplitudes $A[n_x, n_y]$

$$\text{Re}\,[\,A[n_x, n_y]\,] \sim \text{N}(0, \gamma_A^{-1}/2) \tag{3.35}$$

$$\text{Im}\,[\,A[n_x, n_y]\,] \sim \text{N}(0, \gamma_A^{-1}/2) \tag{3.36}$$

$$\text{E}\,[\,\text{Re}\,[\,A[n_x, n_y]\,]\,\text{Im}\,[\,A[n_x, n_y]\,]\,] = 0 . \tag{3.37}$$

Note that this particular prior model also assumes that the scatterer amplitudes are spatially statistically-independent, which implies that the spatial-correlation matrix for $\mathbf{A}$ is given by

$$\mathbf{K_A} = E\left[\mathbf{A}\mathbf{A}^H\right] = \gamma_A^{-1}\mathbf{I} . \tag{3.38}$$

In the SAR literature[19, 29], it has been shown that this type of Gaussian L_2 prior model gives a very good statistical description for the scatterer amplitudes of "natural" clutter, such as trees or grass. However, for a scene containing a "man-made" target, the SAR image will also contain a small number of relatively high-amplitude elements (corresponding to the target scatterers), which would appear as statistical "outliers" to the Gaussian prior model. This implies that the L_2 regularized estimator will try to "smooth out" the portions of the SAR image containing the target-scatterer amplitudes, (which is clearly undesirable for

SAR automatic-target recognition applications, since it is usually the target portions of the SAR image that are the most important). In other words, if we think of a target-containing SAR image as being approximately *sparse* (i.e., containing only a small number of non-zero elements), *the L_2 regularized estimator will try to approximate each high-amplitude target scatterer by a non-sparse (spatially-distributed) superposition of smaller amplitude elements in the SAR image.*

In addition, for moving-target applications, the (nonlinear) estimation of the velocity parameters $\mathbf{v}$ is directly dependent upon the prior model for the scatterer amplitudes. This implies that the L_2 regularized estimator may not give good estimates for these parameters, which implies that *the L_2 regularized $\hat{\mathbf{A}}_{ML}$ and $\hat{\mathbf{v}}_{ML}$ may not correspond to a focused image of the target-field.*

Even if there is no target motion, the L_2 regularized estimator will also suffer from the following problems (due to the non-orthogonality of the complex-exponential basis-functions contained in the columns of $\mathbf{F}(\mathbf{v})$): *the high-amplitude target portions of the SAR image will contain artifacts such as sidelobes, and the SAR image will be resolution-limited by the so-called ambiguity-function matrix* $\mathbf{F}^H(\mathbf{v})\mathbf{F}(\mathbf{v})$.

In many respects, this type of ill-posed estimation problem has many similarities to the so-called *over-complete basis-pursuit problem* in the literature [8, 9, 11]. For basis pursuit, the goal is to represent a given signal or image by a *sparse* superposition of scaled basis functions taken from some (possibly non-orthogonal) basis-function "dictionary". If this basis-function dictionary is over-complete, this essentially means that some of its basis functions can also be represented by a superposition of other basis functions found in the dictionary. This implies that a given signal or image will not have a unique representation with an over-complete basis-function dictionary. Therefore, if we do not regularize the scaling coefficients of the basis functions, we will not necessarily get a sparse representation. The basis pursuit technique tries to achieve a sparse representation for this case by *regularizing the L_1 norm of the set of basis-function scaling coefficients.*

If we think of the set of generalized-parameter complex-exponential basis-functions given by $s_{\mathbf{v}}[n_x, n_y, n, k]$ (for all possible combinations of velocity-parameters $\mathbf{v}$) as being an over-complete basis-function dictionary (with the estimated scatterer amplitudes being the basis-function scaling coefficients), we can use the L_1-norm regularization idea from basis pursuit to obtain a (hopefully) sparse estimate to the scatterer amplitudes (which for our SAR imaging application, implies that we will correctly recover the high-amplitude target portions of the SAR image). In the context of our estimation problem, this is done by computing the $\hat{\mathbf{A}}$ and $\hat{\mathbf{v}}$ which minimizes the following L_1*-norm regularized cost function* $J(\mathbf{A}, \mathbf{v})$

$$J(\mathbf{A}, \mathbf{v}) = ||\mathbf{f} - \mathbf{F}(\mathbf{v})\mathbf{A}||^2_{\mathbf{K}_\eta^{-1}} + \gamma_A ||\mathbf{A}||_1 + J_{\mathbf{v}}(\mathbf{v}) \ . \tag{3.39}$$

This cost function is a standard least-squares cost function for $\mathbf{f} = \mathbf{F}(\mathbf{v})\mathbf{A} + \eta$, augmented by a L_1 penalty upon the scatterer amplitudes (with an optional penalty $J_{\mathbf{v}}(\mathbf{v})$ upon the velocity parameters). This type of L_1-norm based formation also has many similarities to the so-called *total-variation* imaging techniques in the literature [32, 35, 36] (which remove noise by minimizing the L_1-norm of the intensity gradient of a given image).

For the case where the noise η is spatially statistically-independent and isotropic, the

cost function can be simplified to

$$J(\mathbf{A}, \mathbf{v}) = \frac{1}{\sigma_\eta^2} ||\mathbf{f} - \mathbf{F}(\mathbf{v})\mathbf{A}||_2^2 + \gamma_A ||\mathbf{A}||_1 + J_\mathbf{v}(\mathbf{v}) . \tag{3.40}$$

Since the location of the minimum of this cost-function is unaffected by multiplication by a constant, we see that varying the assumed noise variance σ_η^2 is equivalent to varying the L_1 weighting γ_A (along with the optional penalty $J_\mathbf{v}(\mathbf{v})$). Therefore, we can normalize the cost function by assuming that the noise variance is unity (i.e., $\sigma_\eta^2 = 1$), and just vary the L_1 weighting γ_A (along with the optional penalty $J_\mathbf{v}(\mathbf{v})$), i.e.,

$$J(\mathbf{A}, \mathbf{v}) = ||\mathbf{f} - \mathbf{F}(\mathbf{v})\mathbf{A}||_2^2 + \gamma_A ||\mathbf{A}||_1 + J_\mathbf{v}(\mathbf{v}) . \tag{3.41}$$

3.3   Implementation Issues

In the literature [8, 9, 11, 20], the basis-pursuit L_1-minimization over the set of basis-function scaling coefficients is usually computed by recasting the problem as a linear programming problem. However, for a large-scale estimation problem such as our SAR imaging problem, the linear-programming techniques used by basis-pursuit can be somewhat computationally intensive. Here, we present an alternative method for performing the L_1 minimization for our SAR imaging estimation problem. This method involves calculation of the *approximate* gradient of the L_1 cost function.

3.3.1   Continuous Approximation to the L$_1$-Norm

For our SAR imaging problem, the gradient, sgn[$\mathbf{A}$], of the L_1-norm of $\mathbf{A}$ is *discontinuous* at $\mathbf{A} = \mathbf{0}$, which implies that any type of calculation based upon this gradient will be ill-posed for "small" values of $\mathbf{A}$. In order to avoid this type of computational difficulty, we first make the following continuous approximation to the L_1-norm of $\mathbf{A}$ (where the parameter ϵ_A is an L_1 *approximation constant*)

$$\begin{aligned}
||\mathbf{A}||_1 &= \sum_{n_x} \sum_{n_y} |A[n_x, n_y]| \\
&\approx \sum_{n_x} \sum_{n_y} \sqrt{A[n_x, n_y]A^*[n_x, n_y] + \epsilon_A^2} .
\end{aligned} \tag{3.42}$$

Then the corresponding continuous approximation asgn[$\mathbf{A}$] to the gradient, sgn[$\mathbf{A}$], is given by

$$\begin{aligned}
[\text{sgn}[\mathbf{A}]]_{n_x n_y} &\approx [\text{asgn}[\mathbf{A}]]_{n_x n_y} \\
&= \text{asgn}(A[n_x, n_y]) \\
&= \frac{A[n_x, n_y]}{\sqrt{A[n_x, n_y]A^*[n_x, n_y] + \epsilon_A^2}} .
\end{aligned} \tag{3.43}$$

For small values of $\mathbf{A}$ (i.e., $|A[n_x, n_y]| \ll \epsilon_A$), asgn($A[n_x, n_y]$) is approximately given by

$$\text{asgn}(A[n_x, n_y]) \approx \frac{A[n_x, n_y]}{\epsilon_A} . \tag{3.44}$$

This implies that an estimation scheme based upon this type of approximation will exhibit (well-posed) L_2 regularization behavior for small values of $\mathbf{A}$ (since the gradient of the L_2 quadratic penalty $\gamma_A \mathbf{A}^H \mathbf{A}$ is given by $\gamma_A \mathbf{A}$).

3.3.2 Gradient-Descent

Once we have the continuous approximation to the L_1-norm of $\mathbf{A}$ (and its gradient), the most straightforward method for performing the L_1 minimization for the normalized cost function is to use the following recursive gradient-descent algorithm

$$
\begin{aligned}
\hat{\mathbf{A}}_{m+1} &= \hat{\mathbf{A}}_m - \alpha_A \left[\frac{\partial J(\mathbf{A}, \mathbf{v})}{\partial \mathbf{A}} \right]^H \Bigg|_{\mathbf{A}=\hat{\mathbf{A}}_m,\, \mathbf{v}=\hat{\mathbf{v}}_m} \\
&= \hat{\mathbf{A}}_m + \alpha_A \mathbf{F}^H(\hat{\mathbf{v}}_m)[\mathbf{f} - \mathbf{F}(\hat{\mathbf{v}}_m)\hat{\mathbf{A}}_m] - \alpha_A \gamma_A sgn[\hat{\mathbf{A}}_m]
\end{aligned}
\tag{3.45}
$$

$$
\begin{aligned}
\hat{\mathbf{v}}_{m+1} &= \hat{\mathbf{v}}_m - \alpha_{\mathbf{v}} \frac{1}{2} \Re \left[\frac{\partial J(\mathbf{A}, \mathbf{v})}{\partial \mathbf{v}} \right] \Bigg|_{\mathbf{A}=\hat{\mathbf{A}}_m,\, \mathbf{v}=\hat{\mathbf{v}}_m} \\
&= \hat{\mathbf{v}}_m + \alpha_{\mathbf{v}} \Re \left[\hat{\mathbf{A}}_m^H \frac{\partial \mathbf{F}^H(\hat{\mathbf{v}}_m)}{\partial \mathbf{v}} [\mathbf{f} - \mathbf{F}(\hat{\mathbf{v}}_m)\hat{\mathbf{A}}_m] \right] - \alpha_{\mathbf{v}} \frac{\partial J_{\mathbf{v}}(\mathbf{v})}{\partial \mathbf{v}} \Bigg|_{\mathbf{v}=\hat{\mathbf{v}}_m} .
\end{aligned}
\tag{3.46}
$$

Here, we are simultaneously estimating both $\mathbf{A}$ and $\mathbf{v}$. The constants α_A and $\alpha_{\mathbf{v}}$ control the rate of convergence (and stability) of the gradient-descent algorithm.

3.3.3 Coordinate-Descent Line Minimization

One major disadvantage of the gradient-descent implementation is its sensitivity to the presence of local minima in the cost function $J(\mathbf{A}, \mathbf{v})$. For our SAR imaging application, this implies that the gradient-descent algorithm may converge to a solution set $\hat{\mathbf{A}}$ and $\hat{\mathbf{v}}$ where the gradient of $J(\mathbf{A}, \mathbf{v})$ is locally small, but where the SAR image is not focused.

One way of reducing this sensitivity to local minima is by using the following *coordinate-descent line minimization* based algorithm. For this algorithm (given the normalized L_1 cost function $J(\mathbf{A}, \mathbf{v})$), we first define the following set of velocity-dependent target-scatterer amplitudes, $\mathbf{A}(\mathbf{v})$

$$
\mathbf{A}(\mathbf{v}) = \arg \min_{\mathbf{A}} [J(\mathbf{A}, \mathbf{v})] .
\tag{3.47}
$$

In other words, for a given set of velocity parameters $\mathbf{v}$, $\mathbf{A}(\mathbf{v})$ is defined as the set of scatterer amplitudes which minimizes the L_1 cost function $J(\mathbf{A}, \mathbf{v})$. We can evaluate $\mathbf{A}(\mathbf{v})$ (for a given $\mathbf{v}$) by the following version of the previously-presented gradient-descent algorithm (which incorporates the continuous approximation, asgn[$\mathbf{A}$], to the gradient of the L_1 norm of $\mathbf{A}$)

$$
\hat{\mathbf{A}}_{m+1}(\mathbf{v}) = \hat{\mathbf{A}}_m(\mathbf{v}) + \alpha_A \mathbf{F}^H(\mathbf{v})[\mathbf{f} - \mathbf{F}(\mathbf{v})\hat{\mathbf{A}}_m(\mathbf{v})] - \alpha_A \gamma_A \text{asgn}[\hat{\mathbf{A}}_m(\mathbf{v})] .
\tag{3.48}
$$

For a given set of velocity parameters $\mathbf{v}$ (and velocity-dependent target-scatterer amplitudes $\mathbf{A}(\mathbf{v})$), the real part of the gradient (with respect to the velocity parameters $\mathbf{v}$) of

the L_1 cost-function $J(\mathbf{A}, \mathbf{v})$ evaluated at $\mathbf{A} = \mathbf{A}(\mathbf{v})$ is given by

$$\Re \left[\frac{\partial J(\mathbf{A}, \mathbf{v})}{\partial \mathbf{v}} \right] \bigg|_{\mathbf{A} = \mathbf{A}(\mathbf{v})} = -2\Re \left[\mathbf{A}^H(\mathbf{v}) \frac{\partial \mathbf{F}^H(\mathbf{v})}{\partial \mathbf{v}} [\mathbf{f} - \mathbf{F}(\mathbf{v})\mathbf{A}(\mathbf{v})] \right] . \qquad (3.49)$$

The coordinate-descent line-minimization algorithm uses this gradient to minimize the L_1 cost function in the following manner:

I. For a set of given initial velocity-parameters $\mathbf{v}_0$, we first compute the following search direction, $\mathbf{d}_0$, given by the negative of the real part of the gradient (with respect to the velocity parameters) of the L_1 cost-function $J(\mathbf{A}, \mathbf{v})$ evaluated at $\mathbf{A} = \mathbf{A}(\mathbf{v}_0)$ and $\mathbf{v} = \mathbf{v}_0$

$$\mathbf{d}_0 = -\frac{1}{2} \Re \left[\frac{\partial J(\mathbf{A}, \mathbf{v})}{\partial \mathbf{v}} \right] \bigg|_{\mathbf{A} = \mathbf{A}(\mathbf{v}_0), \mathbf{v} = \mathbf{v}_0} . \qquad (3.50)$$

This quantity is then used as the initial condition for a set of recursive *coordinate-descent 1-D line minimizations*[5, 15].

II. For each iteration m (given the corresponding set of velocity-parameters, $\mathbf{v}_m$, and given the corresponding direction vector $\mathbf{d}_m$):

    A. We perform the following $1 - D$ minimization over the scalar λ

$$\hat{\lambda}_m = \arg \min_\lambda \left[J(\mathbf{A}(\mathbf{v}_m + \lambda \mathbf{d}_m), \mathbf{v}_m + \lambda \mathbf{d}_m) \right] . \qquad (3.51)$$

    Essentially, we are searching the velocity-parameter space $\mathbf{v}$ along a $1 - D$ line (parameterized by the scalar λ) defined by $\mathbf{v} = \mathbf{v}_m + \lambda \mathbf{d}_m$ for a new value of $\mathbf{v}$ which minimizes the L_1 cost function.

    B. Once we obtain this new minimum, given by

$$\mathbf{v}_{m+1} = \mathbf{v}_m + \hat{\lambda}_m \mathbf{d}_m , \qquad (3.52)$$

    we then compute a new direction vector, $\mathbf{d}_{m+1}$, which we use in the next iteration of this algorithm to start a new search for a lower minimum.

$$\mathbf{d}_{m+1} = -\frac{1}{2} \Re \left[\frac{\partial J(\mathbf{A}, \mathbf{v})}{\partial \mathbf{v}} \right] \bigg|_{\substack{\mathbf{A} = \mathbf{A}(\mathbf{v}_{m+1}), \\ \mathbf{v} = \mathbf{v}_{m+1}}} + \mu_m \mathbf{d}_m . \qquad (3.53)$$

In the literature[5, 15], the scalar μ_m for the coordinate-descent line-minimization algorithm is generally given by the following ratio of vector inner products

$$\mu_m = \frac{\left(\frac{1}{2} \Re \left[\frac{\partial J(\mathbf{A}, \mathbf{v})}{\partial \mathbf{v}} \right] \big|_{\substack{\mathbf{A} = \mathbf{A}(\mathbf{v}_{m+1}), \\ \mathbf{v} = \mathbf{v}_{m+1}}} \right)^T \frac{1}{2} \Re \left[\frac{\partial J(\mathbf{A}, \mathbf{v})}{\partial \mathbf{v}} \right] \big|_{\substack{\mathbf{A} = \mathbf{A}(\mathbf{v}_{m+1}), \\ \mathbf{v} = \mathbf{v}_{m+1}}}}{\left(\frac{1}{2} \Re \left[\frac{\partial J(\mathbf{A}, \mathbf{v})}{\partial \mathbf{v}} \right] \big|_{\substack{\mathbf{A} = \mathbf{A}(\mathbf{v}_m), \\ \mathbf{v} = \mathbf{v}_m}} \right)^T \frac{1}{2} \Re \left[\frac{\partial J(\mathbf{A}, \mathbf{v})}{\partial \mathbf{v}} \right] \big|_{\substack{\mathbf{A} = \mathbf{A}(\mathbf{v}_m), \\ \mathbf{v} = \mathbf{v}_m}}} . \qquad (3.54)$$

However, for some of the results presented in this thesis (in Chapter 5), we used the following alternative form for μ_m (which has been shown in the literature [5] to be less sensitive to the presence of local minima in the L_1 cost function)

$$
\mu_m =
$$
$$
\frac{\left(\frac{1}{2}\Re\left[\frac{\partial J(\mathbf{A},\mathbf{v})}{\partial \mathbf{v}}\right]\Big|_{\substack{\mathbf{A}=\mathbf{A}(\mathbf{v}_{m+1}),\\ \mathbf{v}=\mathbf{v}_{m+1}}}\right)^T \left(\frac{1}{2}\Re\left[\frac{\partial J(\mathbf{A},\mathbf{v})}{\partial \mathbf{v}}\right]\Big|_{\substack{\mathbf{A}=\mathbf{A}(\mathbf{v}_{m+1}),\\ \mathbf{v}=\mathbf{v}_{m+1}}} - \frac{1}{2}\Re\left[\frac{\partial J(\mathbf{A},\mathbf{v})}{\partial \mathbf{v}}\right]\Big|_{\substack{\mathbf{A}=\mathbf{A}(\mathbf{v}_m),\\ \mathbf{v}=\mathbf{v}_m}}\right)}{\left(\frac{1}{2}\Re\left[\frac{\partial J(\mathbf{A},\mathbf{v})}{\partial \mathbf{v}}\right]\Big|_{\substack{\mathbf{A}=\mathbf{A}(\mathbf{v}_m),\\ \mathbf{v}=\mathbf{v}_m}}\right)^T \frac{1}{2}\Re\left[\frac{\partial J(\mathbf{A},\mathbf{v})}{\partial \mathbf{v}}\right]\Big|_{\substack{\mathbf{A}=\mathbf{A}(\mathbf{v}_m),\\ \mathbf{v}=\mathbf{v}_m}}} .
$$

$$(3.55)$$

For the coordinate-descent line-minimization algorithm, it can be shown[5, 15] that each new direction vector $\mathbf{d}_{m+1}$ is approximately orthogonal to the previous direction vector $\mathbf{d}_m$. As compared to the direct gradient-descent algorithm, we see that this algorithm has a somewhat more robust "global" minima search strategy.

Once we have obtained a convergent estimate $\hat{\mathbf{v}}$ of the velocity-parameters, the (hopefully) focused SAR image is given by $\hat{\mathbf{A}} = \mathbf{A}(\hat{\mathbf{v}})$. Now, for higher values of the L_1 weighting γ_A, the sparseness assumption of the L_1 imaging technique implies that most of the target scatterers will be attenuated, except for the "brighter" higher-amplitude feature scatterers (which would be advantageous for some automatic target recognition applications). However, if we want to attenuate the target scatterers as little as possible(for the sake of comparison to the conventional SAR imaging techniques), we can compute the scatterer amplitudes by finding the $\hat{\mathbf{A}}$ which minimizes the (normalized) standard least-squares cost function (given that we have obtained a convergent estimate $\hat{\mathbf{v}}$ of the velocity-parameters from the before-mentioned coordinate-descent line-minimization algorithm),i.e.,

$$
\hat{\mathbf{A}} = \arg\min_{\mathbf{A}}\left[J(\mathbf{A},\hat{\mathbf{v}})\right] = \arg\min_{\mathbf{A}}\left[||\mathbf{f} - \mathbf{F}(\hat{\mathbf{v}})\mathbf{A}||_2^2\right] . \tag{3.56}
$$

Note that this is equivalent to $\gamma_A = 0$. This computation can be done by the following recursive gradient-descent algorithm (with $\hat{\mathbf{A}}_0 = \mathbf{0}$)

$$
\begin{aligned}
\hat{\mathbf{A}}_{m+1} &= \hat{\mathbf{A}}_m - \alpha\left[\frac{\partial J(\mathbf{A},\hat{\mathbf{v}})}{\partial \mathbf{A}}\right]^H\Bigg|_{\mathbf{A}=\hat{\mathbf{A}}_m} \\
&= \hat{\mathbf{A}}_m + \alpha\mathbf{F}^H(\hat{\mathbf{v}})[\mathbf{f} - \mathbf{F}(\hat{\mathbf{v}})\hat{\mathbf{A}}_m] .
\end{aligned} \tag{3.57}
$$

3.4   Example Problem: Feature and Resolution Enhancement of Stationary SAR Scenes

For many types of SAR-based automatic target recognition (ATR) algorithms found in the literature[12, 19, 23, 29, 44], the stated fundamental goal is to detect and recognize objects of interest (targets) in a noisy environment (clutter). After a potential target has been detected, the ATR system must then determine whether it belongs to a given set of targets (usually by comparing it to a database of test target images). However, the target-recognition performance of many SAR ATR schemes presented in the literature generally depend upon both the number and the configuration of the so-called *feature scatterers* (i.e., the brighter scatterers) of the target of interest. This implies that the performance of most of these SAR ATR schemes will be affected by the previously mentioned effects of the nonorthogonality of the complex-exponential SAR model basis-functions (i.e., blurring due to scatterer motion, imaging artifacts (sidelobes), and loss of scatterer resolution).

In Chapter 5, we will present a method for using the L_1-norm based approach presented in this chapter to correct for blurring due to motion in the SAR images, thereby potentially improving SAR ATR performance. Here, we present some results for some stationary SAR scenes in order to demonstrate the utility of the L_1-norm based approach for enhancing feature scatterers in SAR images by reducing sidelobes and improving resolution.

3.4.1 L_1 Enhancement Algorithm

From Chapter 2 (and Section 3.1), recall that we can express the SAR data for the stationary target case by the following zero-velocity estimation-theoretic model

$$
\begin{aligned}
\textit{Zero-Velocity SAR Model} \\
f[n,k] &= \sum_{n_x}\sum_{n_y} A[n_x,n_y]\, e^{-j\frac{4\pi}{\lambda_c}\left[\Delta_y n_y \frac{\alpha T_p}{f_c}\frac{t[n]}{T_p}\right]}\, e^{j\frac{4\pi}{\lambda_c}\left[\Delta_x n_x \dot\theta t_T[k]\right]} + \eta[n,k] \\
&= \sum_{n_x}\sum_{n_y} A[n_x,n_y]\, s_y[n_y,n]\, s_x[n_x,k] + \eta[n,k]\,. \\
&\qquad -\frac{N}{2}\le n \le \frac{N}{2}\quad -K\le k \le K
\end{aligned}
\tag{3.58}
$$

We can also express the zero-velocity estimation-theoretic model in the following matrix form

$$
\mathbf{f} = \mathbf{FA} + \eta,
\tag{3.59}
$$

where $\mathbf{f}$ is the SAR data and η is the additive Gaussian noise. For a set of ideal point scatterers located at the sampled spatial positions $(x[n_x], y[n_y])$, the vector $\mathbf{A}$ of scatterer

intensities is given by

$$\mathbf{A} = \begin{bmatrix} \vdots \\ A[0,0] \\ A[0,1] \\ \vdots \end{bmatrix}, \tag{3.60}$$

The matrix $\mathbf{F}$ has the form

$$\mathbf{F} = \begin{bmatrix} \ldots & \mathbf{s}[0,0] & \mathbf{s}[0,1] & \ldots \end{bmatrix}, \tag{3.61}$$

where each column vector $\mathbf{s}[n_x, n_y]$ corresponds to a to a lexicographical ordering of the complex-exponential basis-function given by $s_y[n_y, n]s_x[n_x, k]$.

For this zero-velocity estimation-theoretic model, our goal is to minimize the following normalized-noise L_1 cost function (without the optional regularization upon the velocity-parameters which we essentially assume are known, i.e. the velocity-parameters are zero)

$$J(\mathbf{A}) = ||\mathbf{f} - \mathbf{F}\mathbf{A}||_2^2 + \gamma_A ||\mathbf{A}||_1 . \tag{3.62}$$

Therefore, we can use the following recursive gradient-descent algorithm (with the continuous approximation to the discontinuous gradient of the L_1 norm)

$$\hat{\mathbf{A}}_{m+1} = \hat{\mathbf{A}}_m + \alpha_A \mathbf{F}^H[\mathbf{f} - \mathbf{F}\hat{\mathbf{A}}_m] - \alpha_A \gamma_A \text{asgn}[\hat{\mathbf{A}}_m] \tag{3.63}$$

$$\begin{aligned}
[\text{asgn}[\hat{\mathbf{A}}_m]]_{n_x n_y} &= \text{asgn}(\hat{A}_m[n_x, n_y]) \\
&= \frac{\hat{A}_m[n_x, n_y]}{\sqrt{\hat{A}_m[n_x, n_y]\hat{A}_m^*[n_x, n_y] + \epsilon_A^2}},
\end{aligned} \tag{3.64}$$

which is well-posed for the known (zero) velocity parameters.

3.4.2 Experimental Results

Here, we present some examples of the feature enhancement imaging capabilities of the L_1-based algorithm. For these results, we were given two conventional complex SAR data sets (in the discrete $2-D$ form $A_{CONV}[n_x, n_y]$). We converted these data sets into "raw" demodulated SAR data $\mathbf{f}$ by normalizing the data sets (by their respective maximum magnitude over n_x and n_y, denoted by A_{MAX}) and performing a scaled Fourier Transform corresponding to the "conventional" zero-velocity SAR model, i.e.,

$$\mathbf{f} = \frac{1}{A_{MAX}} \mathbf{F} \mathbf{A}_{CONV} . \tag{3.65}$$

We also used the normalized conventional SAR data as the "initial-condition" for the L_1 gradient-descent recursion, i.e., $\hat{\mathbf{A}}_0 = \frac{1}{A_{MAX}} \mathbf{A}_{CONV}$. After the L_1 gradient-descent converged to a final value, we then post-multiplied this final value by A_{MAX} in order to obtain the final L_1 processed SAR image.

F_c	Center Frequency	33.5 GHz
λ_c	Center Wavelength	0.009 m
αT_p	Chirp Bandwidth	1.2 GHz
f_{PRF}	Pulse Repetition Frequency	512 pulse/s
N	Complex Samples per Range Profile	512
$2K$	Pulses per Synthetic Aperture	512
R_o	Center Slant-Range	2778 M
v	SAR Platform Velocity	100 m/s
$\dot{\theta}$	Look-Angle Rotation Rate	0.036 rad/s
$2T$	Dwell Time	1.0 s
L	Synthetic-Aperture Length	100 m
Δ_y	Range Sampling Interval	0.125 m
Δ_x	Azimuth Sampling Interval	0.125 m
δ_y	Range Resolution	0.25 m
δ_x	Azimuth Resolution	0.25 m

Table 3.1: System Parameters for First L_1 SAR Processing Example

Clutter Scene

For the first example, we have a 512×512 pixel "clutter" scene consisting mainly of trees and grass (with an approximate resolution in range and azimuth of of $\delta_y = 0.25m$ and $\delta_x = 0.25m$). As shown in the conventional SAR image of Figure 3.2, we also have two man-made high-amplitude "corner-reflector" scatterers. An azimuthal cross-section of the SAR image (at a range of $y = -5.7m$, which includes the corner reflector located at $(x, y) = (-8.8m, -5.7m)$) is shown in Figure 3.3. For the corner reflector (with a mainlobe peak of about $30dB$), we have two "dominant" sidelobes at about $10dB$, and several smaller sidelobes at about $0dB$.

The SAR image was also "oversampled" in both range and azimuth, i.e., the values of the range and azimuth sampling interval constants, Δ_y and Δ_x, were one-half the approximate resolution of of the image. The parameters of our zero-velocity SAR model were chosen to be as similar as possible to the 33.5 GHz Lincoln Laboratory Advanced Detection and Tracking System (ADTS)[16] system operating in spotlight mode, as shown in Table 3.1.

The results of the L_1 enhancement algorithm are shown in Figures 3.4 through 3.11. For these experiments, we found that it was best to chose the L_1 approximation constant ϵ_A as the product of α_A and the L_1 weight parameter γ_A. For $\gamma_A = 0.001$, we see that the resulting SAR image is slightly more "grainy" than the conventional image, with a somewhat higher contrast. The tree "shadows" and the road begin to become more apparent.

For $\gamma_A = 0.01$, the two "corner-reflectors" begin to dominate the SAR image. However, we also begin to see more clearly the boundary between the trees and the grassy field (due to the enhancement of the slightly brighter tree scatterers). We also see this enhancement effect in the azimuthal cross-section plot, where the "nulls" between the smaller azimuthal sidelobes of the corner reflector are more pronounced (by about $20dB$). The mainlobe width of the corner reflector is still approximately the same as the conventional image.

For $\gamma_A = 0.1$, the two corner reflectors are virtually the only features left in the SAR

image (which is very desirable from a target detection point-of-view). From the azimuthal cross-section plot, we see that all of the sidelobes (including the two dominant sidelobes) from the corner reflector are significantly reduced (by about $20dB$). However, the mainlobe width of the corner reflector is still approximately the same as the conventional image, which implies that the feature-scatterer resolving performance is about the same.

For $\gamma_A = 0.5$, the sidelobes from the two corner-reflectors are reduced even further (by about $40dB$ from the conventional image). We also see that the width of the mainlobe of the corner reflector has been reduced by half. This implies that for this value of γ_A, the L_1 enhancement algorithm can now resolve feature scatterers at about half the azimuth resolving distance of the conventional SAR imaging algorithm. Later in this section, we will illustrate this further with a synthetic-data example. However, note that the mainlobe height has decreased from about $32dB$ to about $27dB$. This implies that if we increased γ_A beyond 0.5 for this example, the resulting SAR image of the two corner-reflectors would be significantly attenuated. Thus, we see that there is a limit to the resolution improvement attainable with the L_1 enhancement algorithm.
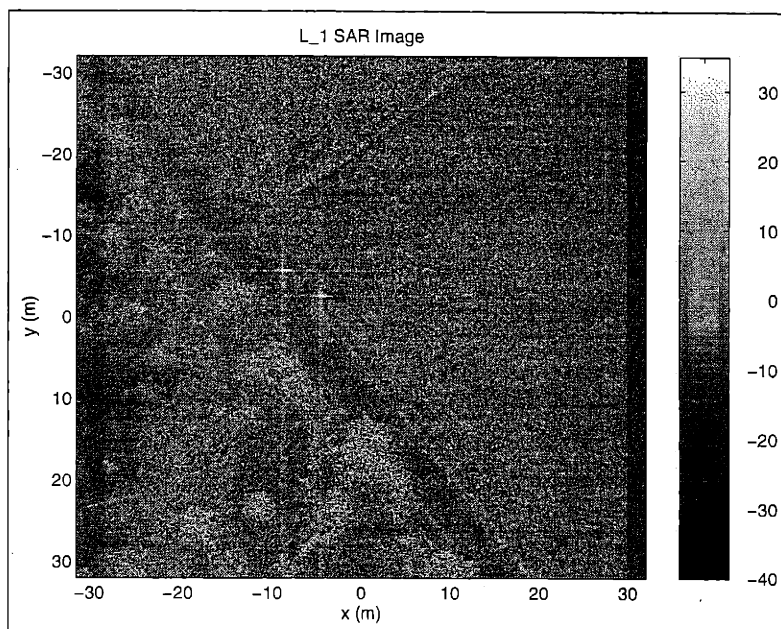
Figure 3.2: Conventional SAR Image
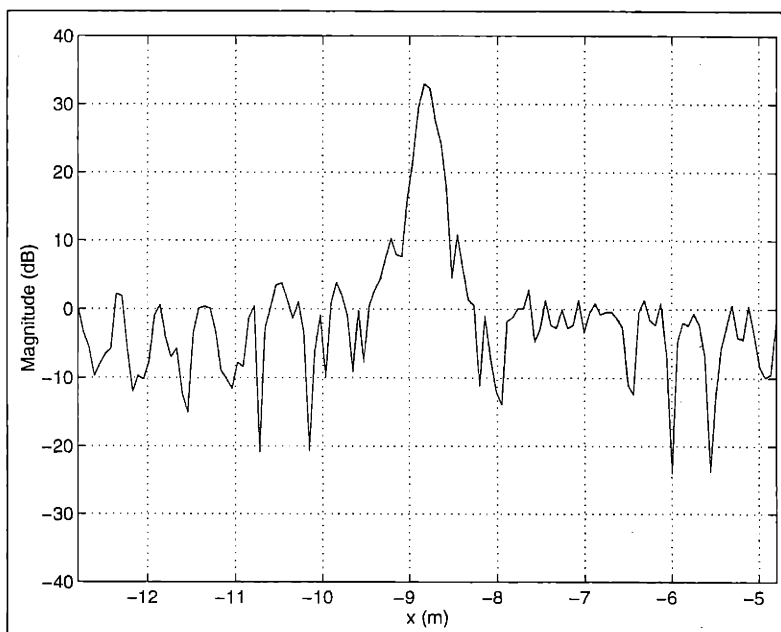
Figure 3.3: Azimuthal Cross-section of Conventional SAR Image at $y = -5.7m$
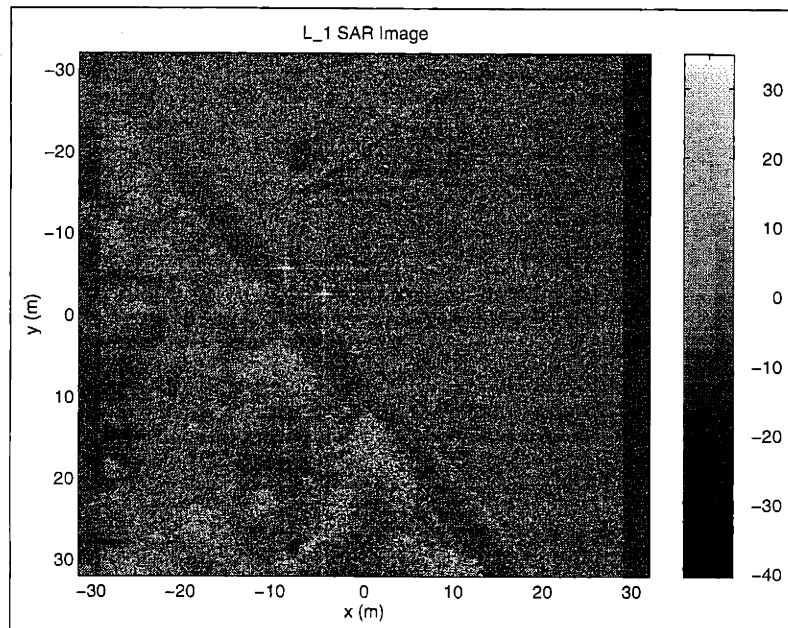
Figure 3.4: L_1 SAR Image for $\alpha_A = 0.1, \gamma_A = 0.001, \epsilon_A = 0.0001, m = 20$
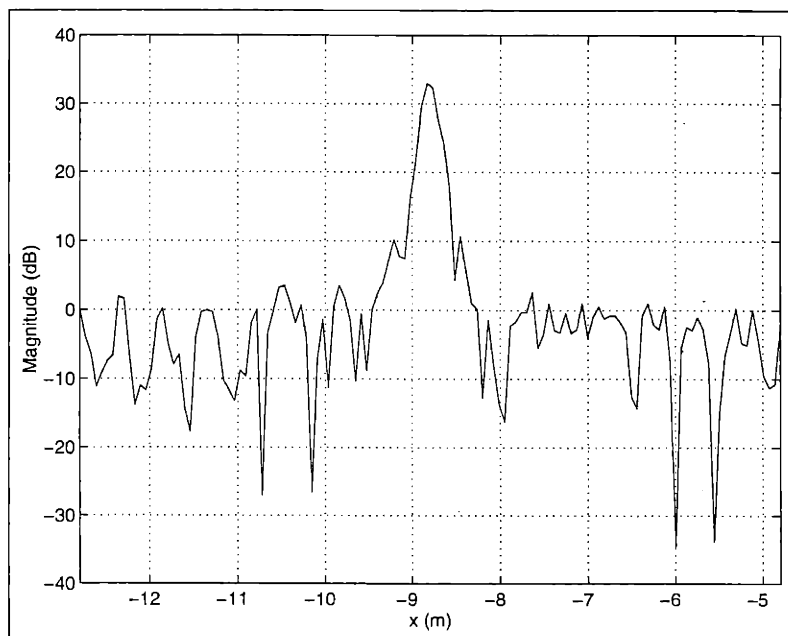
Figure 3.5: Azimuthal Cross-section of L_1 SAR Image at $y = -5.7m$ for $\alpha_A = 0.1, \gamma_A = 0.001, \epsilon_A = 0.0001, m = 20$
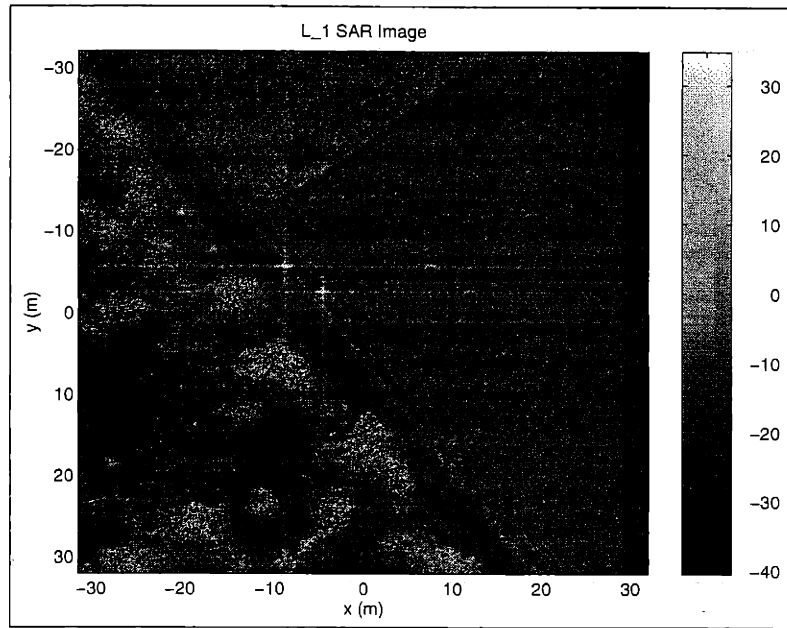
Figure 3.6: L_1 SAR Image for $\alpha_A = 0.1, \gamma_A = 0.01, \epsilon_A = 0.001, m = 20$
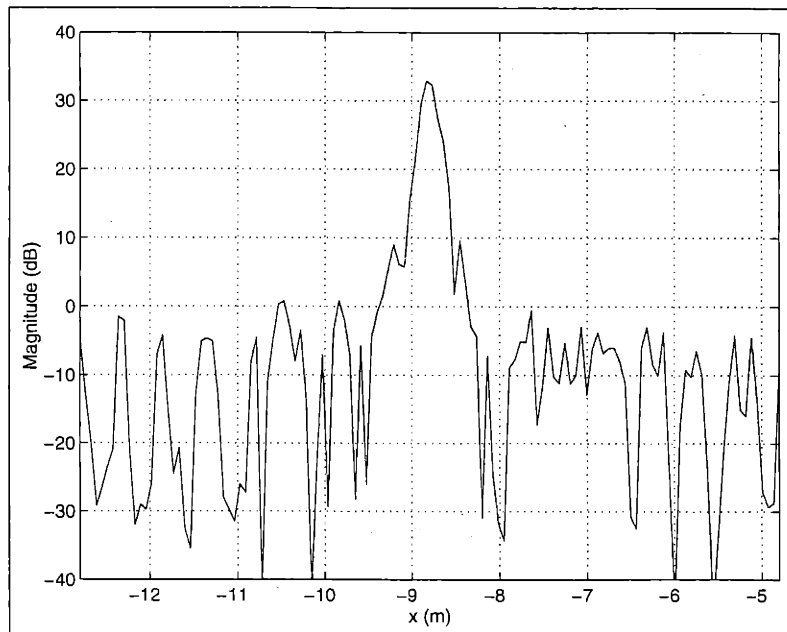
Figure 3.7: Azimuthal Cross-section of L_1 SAR Image at $y = -5.7m$ for $\alpha_A = 0.1, \gamma_A = 0.01, \epsilon_A = 0.001, m = 20$
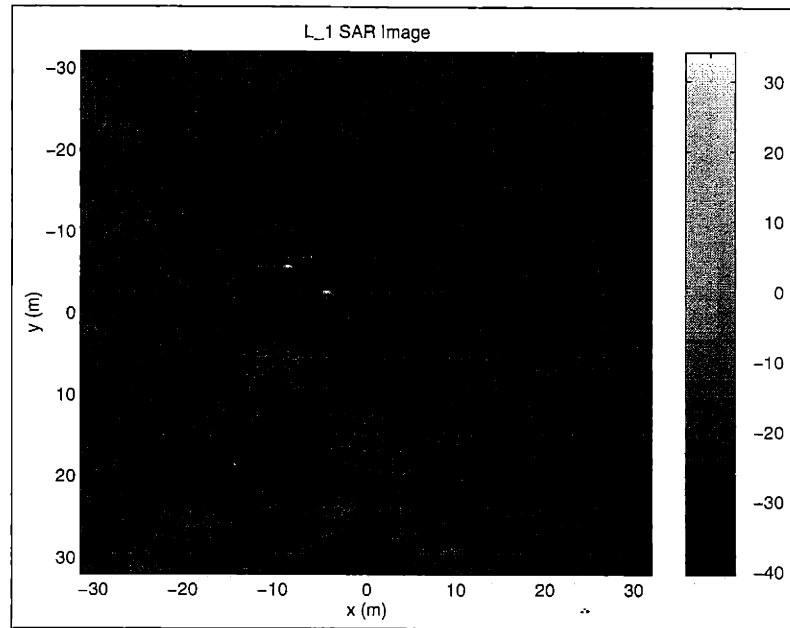
Figure 3.8: L_1 SAR Image for $\alpha_A = 0.1, \gamma_A = 0.1, \epsilon_A = 0.01, m = 20$
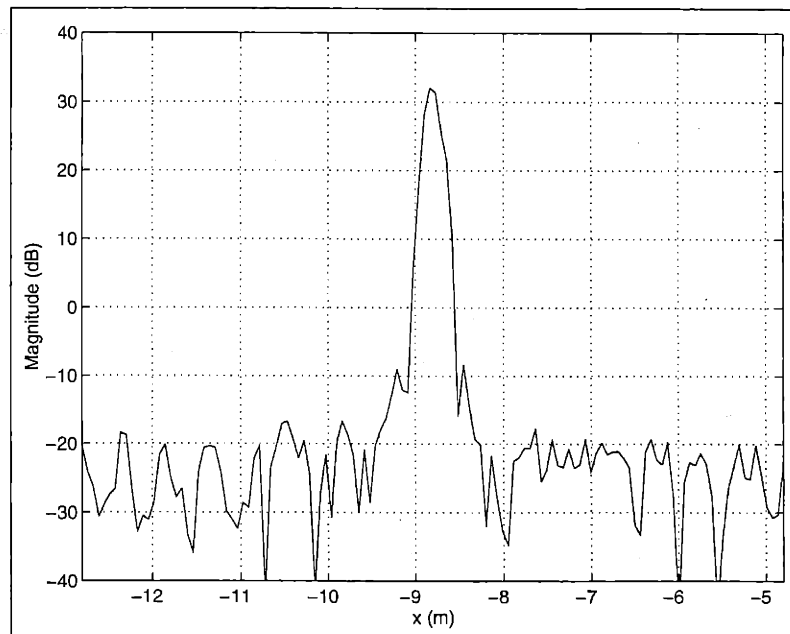
Figure 3.9: Azimuthal Cross-section of L_1 SAR Image at $y = -5.7m$ for $\alpha_A = 0.1, \gamma_A = 0.1, \epsilon_A = 0.01, m = 20$
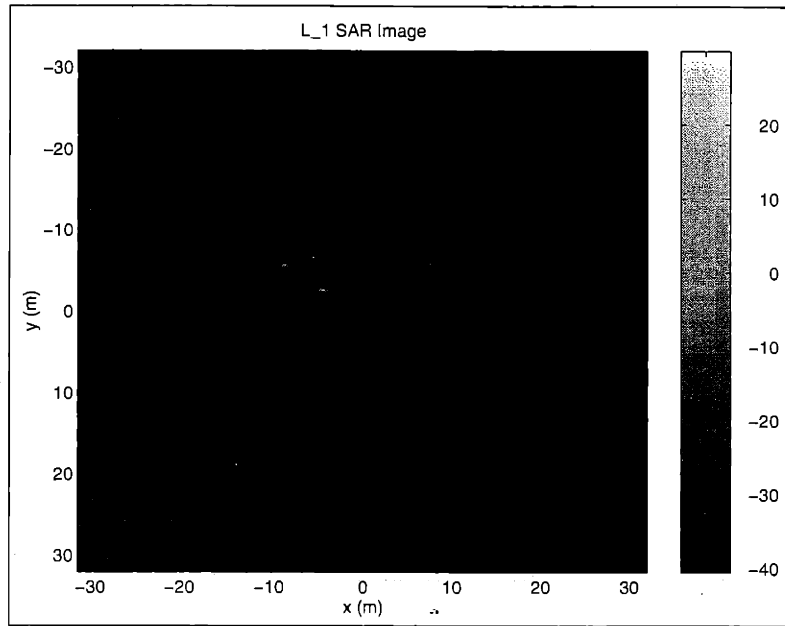
Figure 3.10: L_1 SAR Image for $\alpha_A = 0.01, \gamma_A = 0.5, \epsilon_A = 0.005, m = 200$
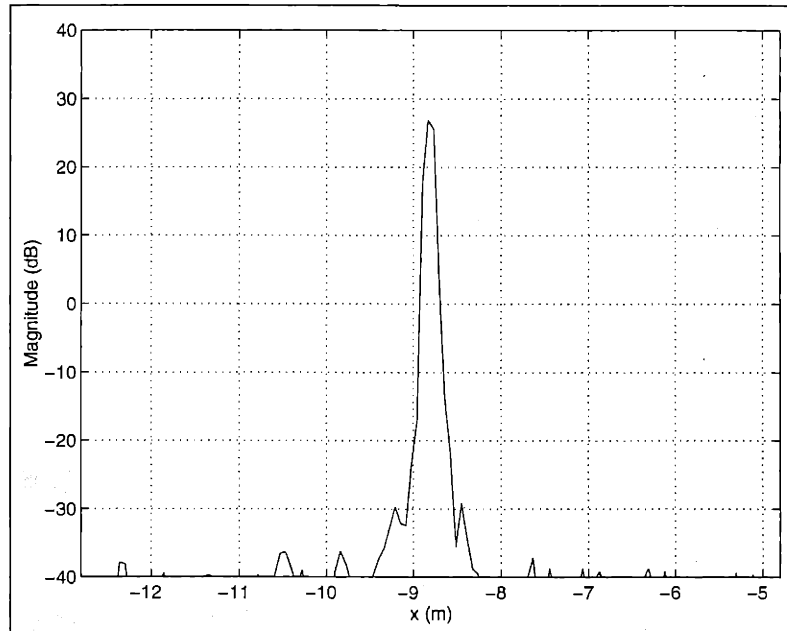
Figure 3.11: Azimuthal Cross-section of L_1 SAR Image at $y = -5.7m$ for $\alpha_A = 0.01, \gamma_A = 0.5, \epsilon_A = 0.005, m = 200$

F_c	Center Frequency	33.5 GHz
λ_c	Center Wavelength	0.009 m
αT_p	Chirp Bandwidth	1.2 GHz
f_{PRF}	Pulse Repetition Frequency	128 pulse/s
N	Complex Samples per Range Profile	128
$2K$	Pulses per Synthetic Aperture	128
R_o	Center Slant-Range	2778 M
v	SAR Platform Velocity	100 m/s
$\dot{\theta}$	Look-Angle Rotation Rate	0.036 rad/s
$2T$	Dwell Time	1.0 s
L	Synthetic-Aperture Length	100 m
Δ_y	Range Sampling Interval	0.125 m
Δ_x	Azimuth Sampling Interval	0.125 m
δ_y	Range Resolution	0.25 m
δ_x	Azimuth Resolution	0.25 m

Table 3.2: System Parameters for Second L_1 SAR Processing Example

Target Scene

For our next example, we have a 128×128 pixel "typical" target scene (with an approximate resolution in range and azimuth of of $\delta_y = 0.25m$ and $\delta_x = 0.25m$) consisting of a T-72 tank from the former Soviet Union, in a grass clutter background (shown in Figure 3.12). This particular image was part of a spotlight-mode SAR data set collected by Sandia National Laboratory in 1995 under DARPA's Moving and Stationary Target Acquisition and Recognition (MSTAR) program.

An azimuthal cross-section (at a range of $0.45m$) of the target image is shown in Figure 3.13 (which shows some of the feature scatterers corresponding to the tank's treads centered at approximately $(x, y) = (-1m, 0.45m)$). Just as with the previous "clutter" scene, this image was also "oversampled" in both range and azimuth, i.e., the values of the range and azimuth sampling resolution constants, Δ_y and Δ_x were one-half the approximate range and azimuth resolutions of the image. The parameters of our zero-velocity SAR model were again chosen to be as similar as possible to the 33.5 GHz Lincoln Laboratory ADTS system operating in spotlight mode, as shown in Table 3.2.

The results of the L_1 enhancement algorithm are shown in Figures 3.14 through 3.21. For these cases, the L_1 approximation constant ϵ_A was again chosen to be the product of α_A and the L_1 weight parameter γ_A. For comparison purposes, we show the azimuthal cross-sections at a range of $0.45m$ (which contain the set of feature scatterers corresponding to the tank's treads centered at approximately $(x, y) = (-1m, 0.45m)$).

For $\gamma_A = 0.01$, the resulting SAR image is somewhat more "grainy" than the conventional image. The tank's shadow begins to become more apparent.

For $\gamma_A = 0.1$, the outline of the target is clearly seen. From the azimuthal cross-section plot, we see that most of the background grass-clutter scatterers are significantly attenuated (by about $20dB$). From the azimuthal cross-section, we also see that the "nulls" between the target feature scatterers are somewhat more pronounced (by about $10dB$).

For $\gamma_A = 0.5$, we begin to see a "sharpening" of the target "feature" scatterers from the treads and turret of the T-72 tank. The clutter scatterers have been attenuated by over $40dB$.

Finally, for $\gamma_A = 0.7$, we see which of the target feature scatterers are dominant (which should be quite useful for target detection and classification). However, note that the mainlobe height of the brightest dominant target-scatterer at $(x, y) = (1.3m, 0.45m)$ has decreased from about $3dB$ to about $-5dB$. In a similar fashion to the previous clutter-scene example, this implies that if we increased γ_A beyond 0.7, the resulting SAR image of this dominant target-scatterer would be significantly attenuated. Again, we see that there is a limit to the resolution improvement attainable with the L_1 enhancement algorithm.
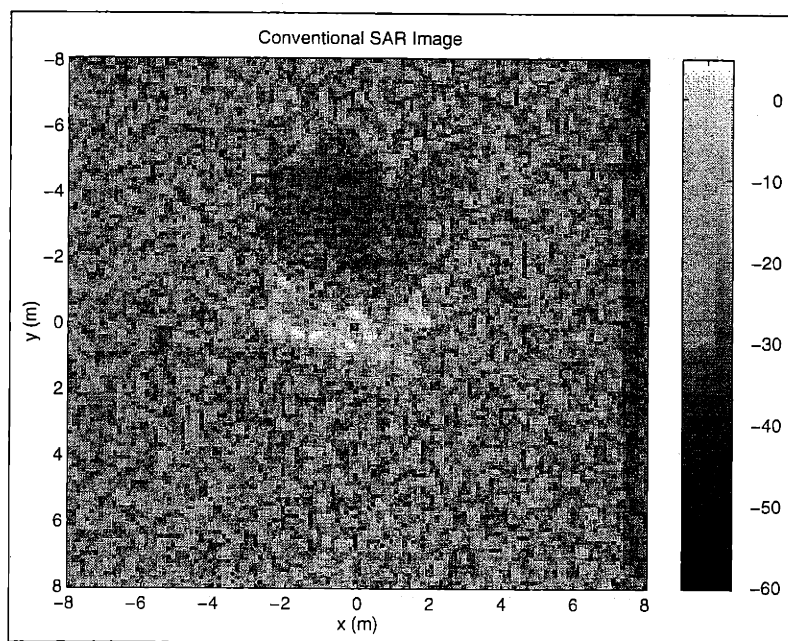
Figure 3.12: Conventional SAR Image
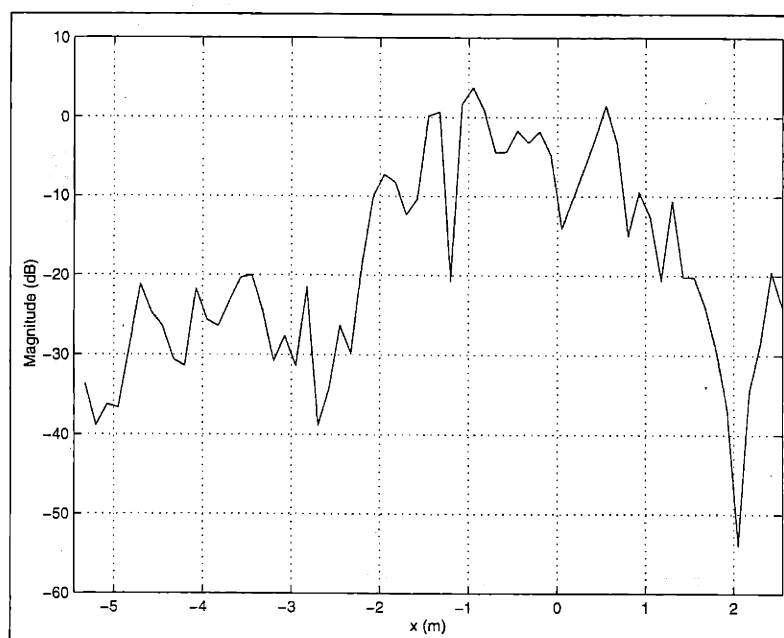
Figure 3.13: Azimuthal Cross-section of Conventional SAR Image at $y = 0.45m$
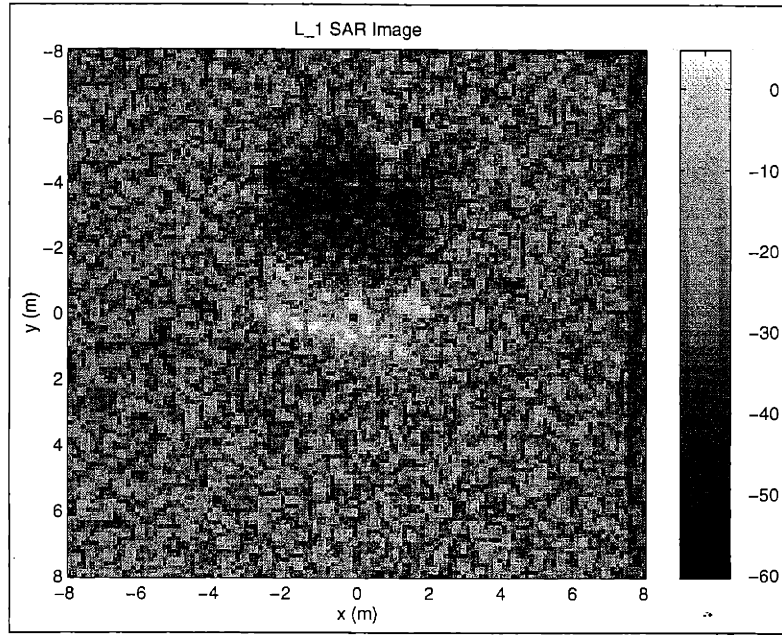
Figure 3.14: L_1 SAR Image for $\alpha_A = 0.1, \gamma_A = 0.01, \epsilon_A = 0.001, m = 20$
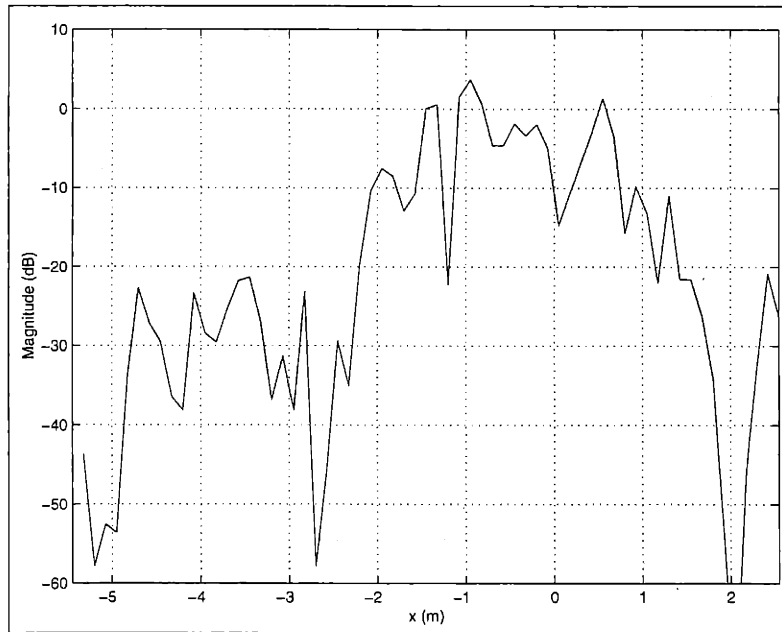
Figure 3.15: Azimuthal Cross-section of L_1 SAR Image at $y = 0.45m$ for $\alpha_A = 0.1, \gamma_A = 0.01, \epsilon_A = 0.001, m = 20$
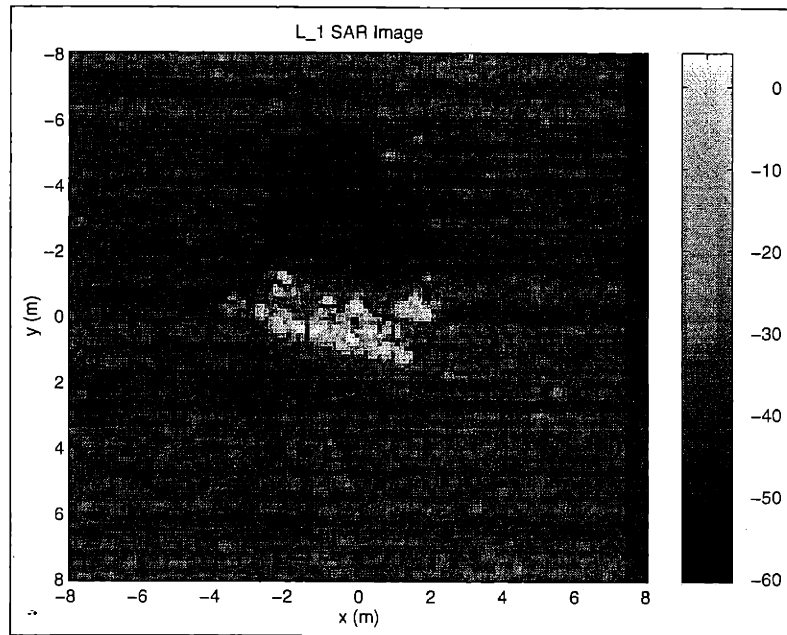
Figure 3.16: L_1 SAR Image for $\alpha_A = 0.1, \gamma_A = 0.1, \epsilon_A = 0.01, m = 20$
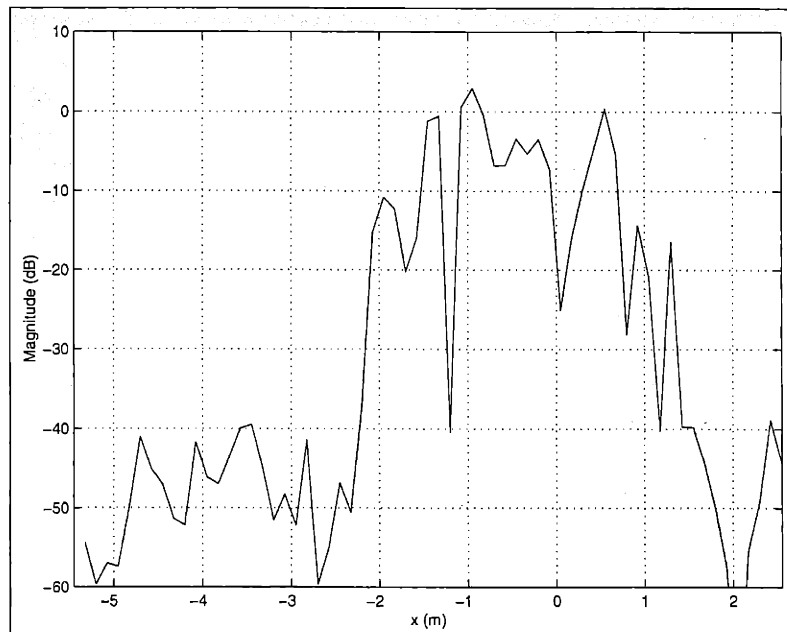
Figure 3.17: Azimuthal Cross-section of L_1 SAR Image at $y = 0.45m$ for $\alpha_A = 0.1, \gamma_A = 0.1, \epsilon_A = 0.01, m = 20$
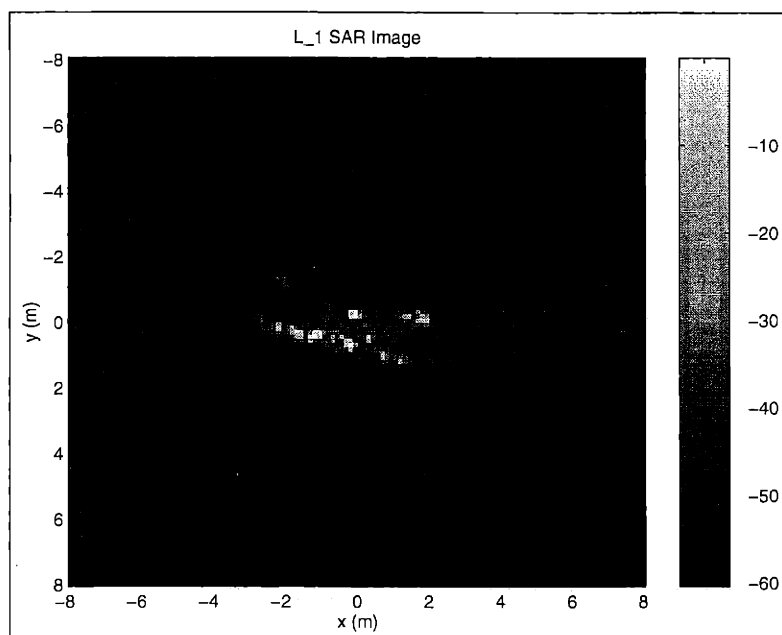
Figure 3.18: L_1 SAR Image for $\alpha_A = 0.01, \gamma_A = 0.5, \epsilon_A = 0.005, m = 200$
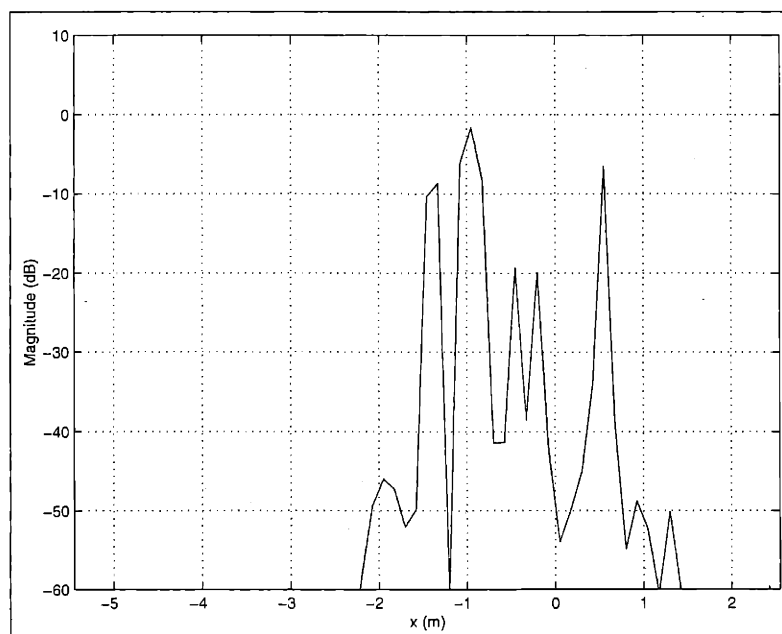
Figure 3.19: Azimuthal Cross-section of L_1 SAR Image at $y = 0.45m$ for $\alpha_A = 0.01, \gamma_A = 0.5, \epsilon_A = 0.005, m = 200$
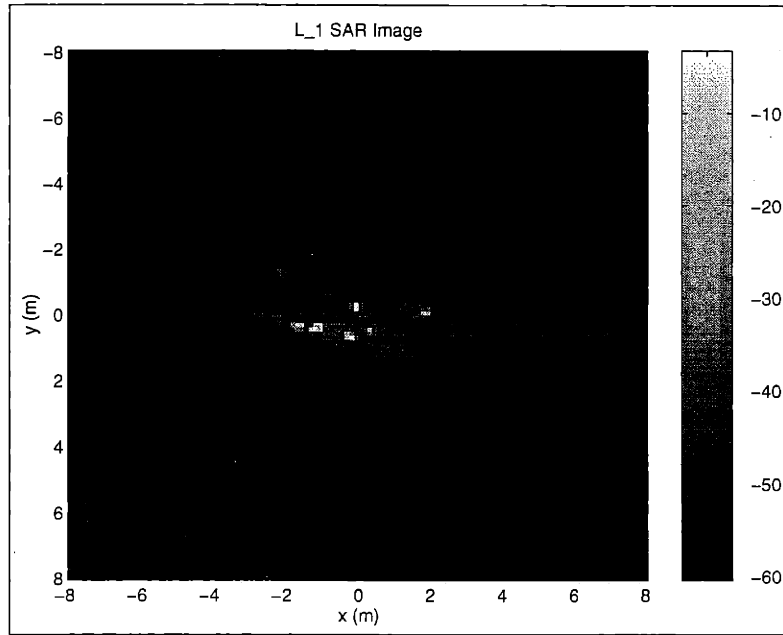
Figure 3.20: L_1 SAR Image for $\alpha_A = 0.01, \gamma_A = 0.7, \epsilon_A = 0.007, m = 200$
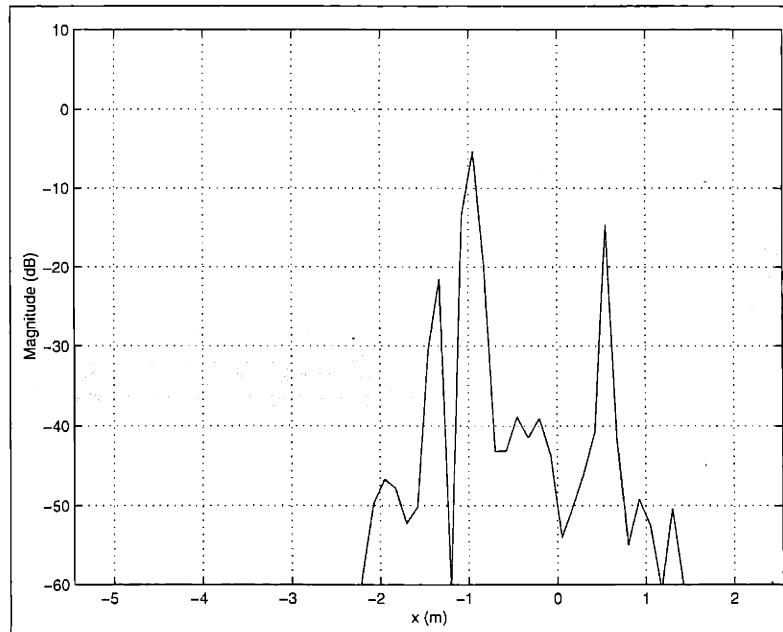
Figure 3.21: Azimuthal Cross-section of L_1 SAR Image at $y = 0.45m$ for $\alpha_A = 0.01, \gamma_A = 0.7, \epsilon_A = 0.007, m = 200$

F_c	Center Frequency	33.5 GHz
λ_c	Center Wavelength	0.009 m
αT_p	Chirp Bandwidth	1.2 GHz
f_{PRF}	Pulse Repetition Frequency	64 pulse/s
N	Complex Samples per Range Profile	64
$2K$	Pulses per Synthetic Aperture	64
R_o	Center Slant-Range	2778 M
v	SAR Platform Velocity	100 m/s
$\dot{\theta}$	Look-Angle Rotation Rate	0.036 rad/s
$2T$	Dwell Time	0.5 s
L	Synthetic-Aperture Length	50 m
Δ_y	Range Sampling Interval	0.125 m
Δ_x	Azimuth Sampling Interval	0.125 m
δ_y	Range Resolution	0.25 m
δ_x	Azimuth Resolution	0.5 m

Table 3.3: System Parameters for Third L_1 SAR Processing Example

Synthetic-Data Example

For our last example, we have a 64 × 64 pixel data set generated by the general-motion SAR data model presented in Chapter 2. In order to illustrate the resolution enhancement capabilities of the L_1 algorithm, the azimuth resolution of this data was deliberately degraded (as compared to the previous data sets) by reducing the dwell time to $0.5s$, as shown in Table 3.3 (which gives an approximate resolution in azimuth of of $\delta_x = 0.5m$). The range resolution $\delta_y = 0.25m$ was the same as the previous examples. Using these system parameters, we generated synthetic data sets with two stationary unit-amplitude (random-phase) synthetic point-scatterers (with one scatterer at $(x, y) = (0m, 0m)$, and the other scatterer at $(x, y) = (\delta_0, 0m)$). We added circularly-complex spatially statistically-independent, isotropic, zero-mean Gaussian noise with a variance $\sigma_\eta^2 = 0.1^2$, which implied that the signal-to-noise ratio (SNR), given by $SNR = 20 \log_{10} \frac{\text{mean}_{n_x,n_y} |A[n_x,n_y]|}{\sigma_\eta}$ for this example was $20dB$.

The results (SAR images and azimuthal cross-sections) of the L_1 enhancement algorithm for a scatterer azimuth separation of $\delta_0 = \delta_x = 0.5m$ are shown in Figure 3.22 for $\gamma_A = \{0, 0.5, 0.7, 1\}$ (with increasing γ_A from top to bottom). Here, we see that even for the conventional imaging case ($\gamma_A = 0$), the two scatterers are resolved. However, we do see a decrease in the width of the mainlobes as we increase γ_A (as well as a reduction in the amplitudes of the sidelobes).

The results for a scatterer azimuth separation of $\delta_0 = 0.75\delta_x = 0.375m$ are shown in Figure 3.23 for $\gamma_A = \{0, 0.5, 0.7, 1\}$ (with increasing γ_A from top to bottom). Here, we see that for the conventional imaging case ($\gamma_A = 0$), the two scatterers are barely resolved in azimuth(with a "null" of less than $4dB$ between the scatterers). In contrast, these same scatterers are clearly resolved in azimuth by the L_1 enhancement algorithm at the higher weightings (with a "null" of about $20dB$ at $\gamma_A = 1$). In addition, the sidelobes are reduced as well, even for the smaller weightings.

The results for a scatterer azimuth separation of $\delta_0 = 0.5\delta_x = 0.25m$ are shown in Figure 3.24 for $\gamma_A = \{0, 0.5, 0.7, 1\}$ (with increasing γ_A from top to bottom). Here, we see that for the conventional imaging case ($\gamma_A = 0$), the two scatterers are not resolved at all. Again, in contrast, these same scatterers are clearly resolved in azimuth by the L_1 enhancement algorithm at the higher weightings (with a "null" of about $10dB$ at $\gamma_A = 1$). Therefore, we see that the L_1 enhancement algorithm can significantly improve the inherent imaging resolution of the SAR system for relatively "bright" feature scatterers with a relatively high SNR (greater than or equal to $20dB$). This improvement in imaging resolution may not hold true for lower $SNR's$.
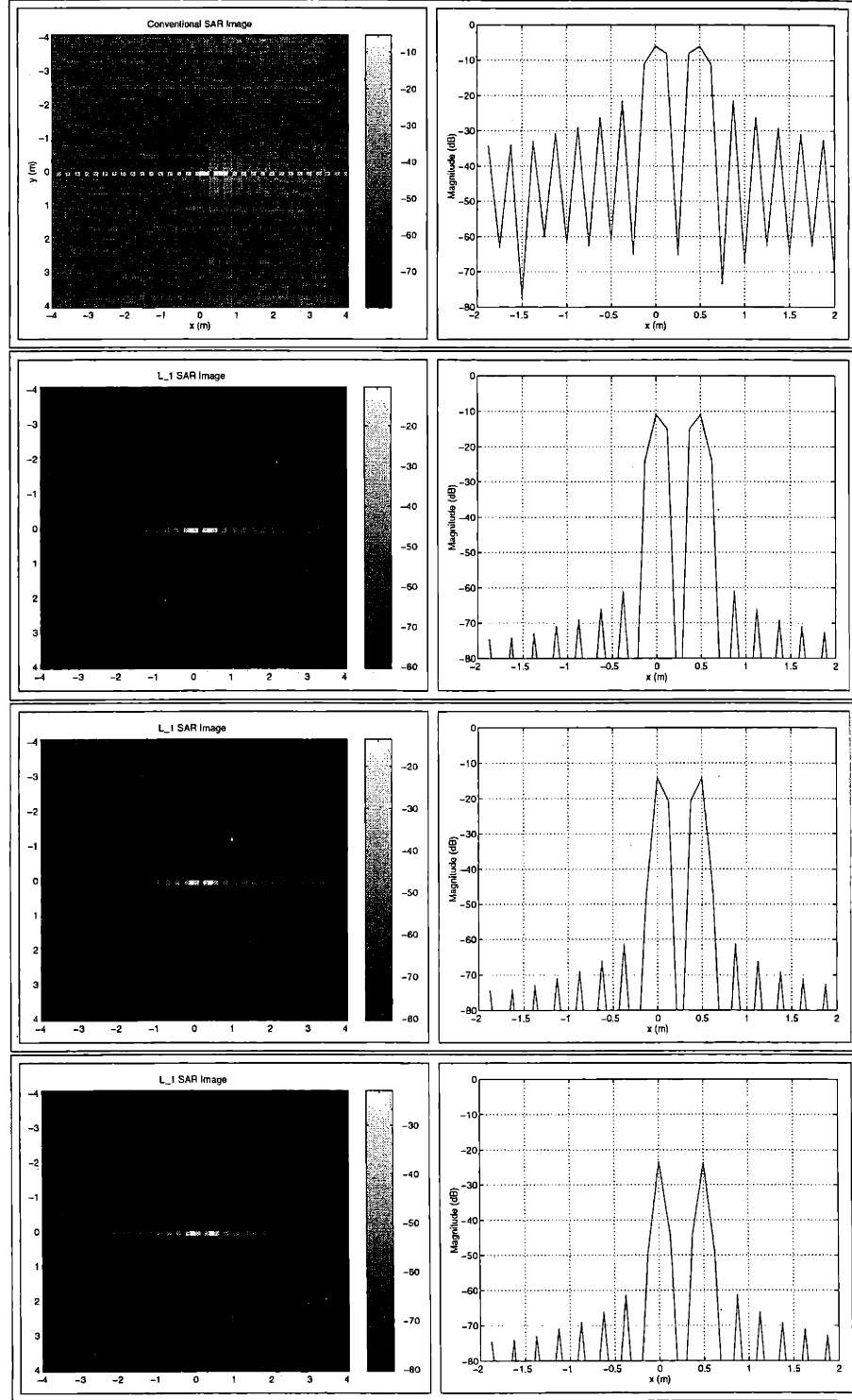
Figure 3.22: L_1 SAR   Images   and   Azimuthal   Cross-sections   (at y = $0m$)   for $\gamma_A = \{0, 0.5, 0.7, 1\}$ and $\alpha_A = 0.01, \epsilon_A = 0.01\gamma_A, m = 200$ $(\delta_0 = 0.5m)$
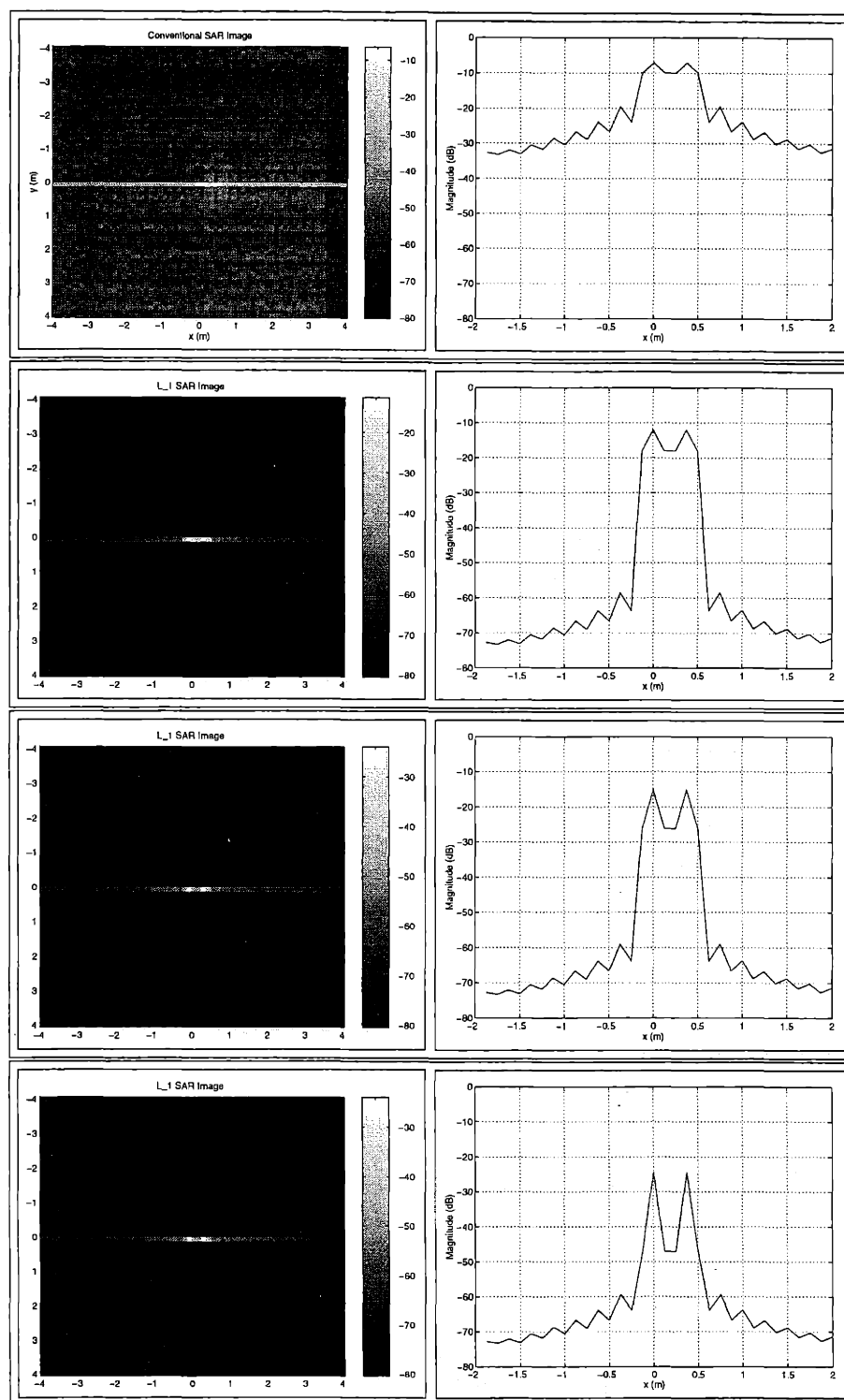
Figure 3.23: L_1 SAR Images and Azimuthal Cross-sections (at $y = 0m$) for $\gamma_A = \{0, 0.5, 0.7, 1\}$ and $\alpha_A = 0.01, \epsilon_A = 0.01\gamma_A, m = 200$ ($\delta_0 = 0.375m$)
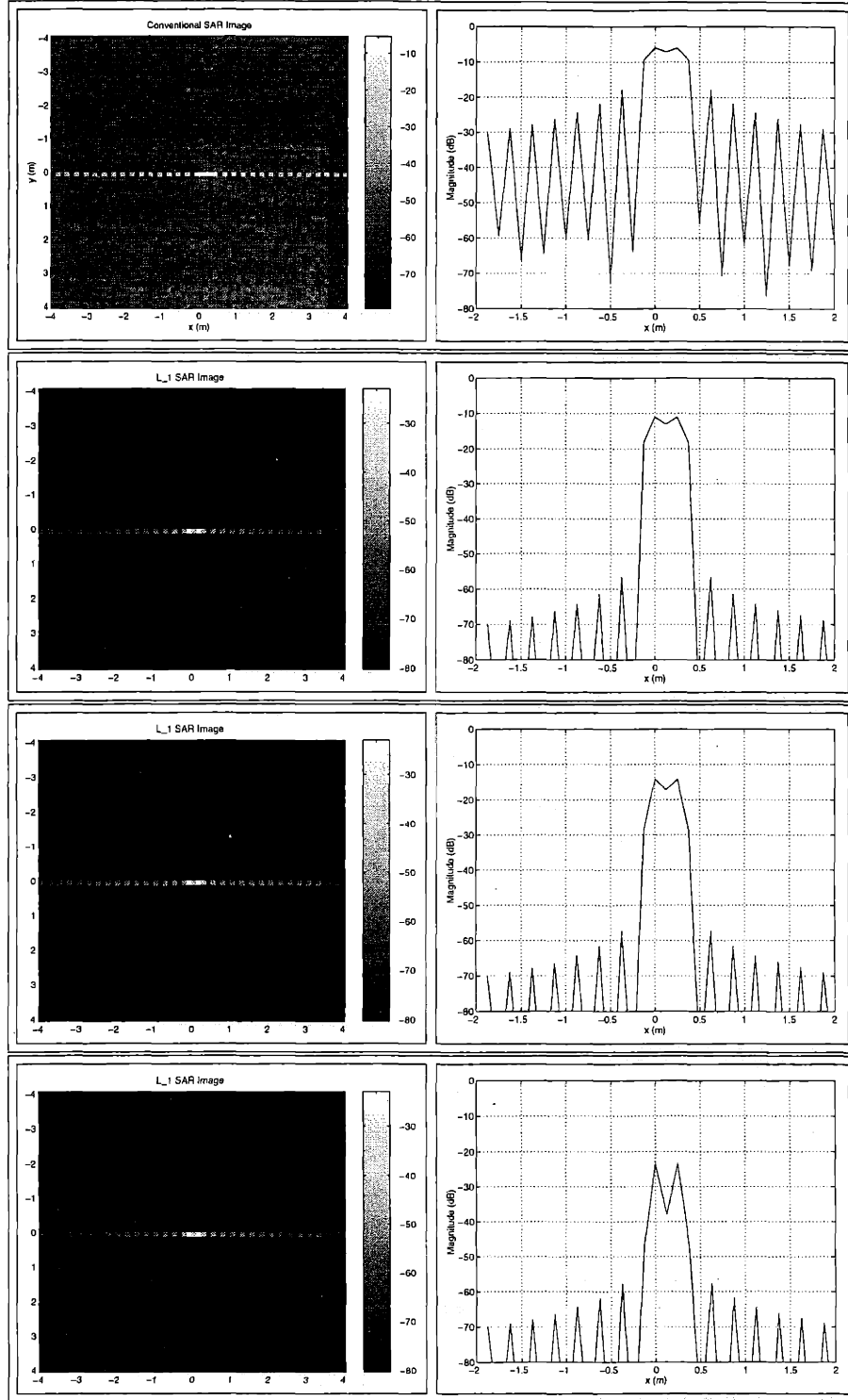
Figure 3.24: L_1 SAR Images and Azimuthal Cross-sections (at y = $0m$) for $\gamma_A = \{0, 0.5, 0.7, 1\}$ and $\alpha_A = 0.01, \epsilon_A = 0.01\gamma_A, m = 200$ ($\delta_0 = 0.25m$)

Chapter 4

Matched-Filter SAR Processing

IN this chapter, we present the Matched-Filter SAR processing technique, which uses a multi-dimensional matched-filter as a means of computing a set of scatterer-velocity estimates which are used as initial conditions for an L_1-norm based estimation algorithm derived for the spatially-varying temporally-constant velocity (SVTCV) SAR model presented in Chapter 2 (which assumes that the target field consists of a $2-D$ array of ideal point scatterers with spatially independent velocities). The matched filter also computes a target detection statistic for determining which spatial locations in a particular SAR scene correspond to actual moving scatterers (allowing a reduction in the computational intensity of the SVTCV L_1-norm based estimation algorithm).

First, we present the SVTCV L_1-norm based algorithm for estimating the scatterer velocities, along with a standard least-squares algorithm for estimating the scatterer amplitudes. In this presentation, we also discuss the motivation for the development of the matched filter. Next, we present the matched filter algorithm itself, along with a discussion of the methods it uses to compute the scatterer-velocity estimates and the target-detection statistic. We also discuss some of the issues encountered in the actual implementation of the matched-filter algorithm. In addition, we discuss methods for reducing cross-scatterer interference effects. Then, we present a Monte Carlo analysis of the detection and velocity-estimation performance of the matched-filter algorithm. Lastly, we present some results for both synthetic point-scatterers embedded in real clutter, and a synthetic-motion real target embedded in real clutter.

4.1 Motivation: The Spatially-Varying Temporally-Constant Velocity (SVTCV) SAR Estimation Problem

Recall from Chapter 2 that for the spatially-varying temporally-constant velocity (SVTCV) case, we assumed that the target field consists of a $2-D$ array of ideal point scatterers, with reflectivities given by $A[n_x, n_y]$. The corresponding SVTCV trajectories of these point scatterers were given by the following relations, where Δ_x and Δ_y are the so-called spatial sampling-interval constants (whose values we derived in (3.19) of Chapter 3)

$$x_{n_x n_y}(t) = \Delta_x n_x + \dot{x}[n_x, n_y]t \qquad (4.1)$$

$$y_{n_x n_y}(t) = \Delta_y n_y + \dot{y}[n_x, n_y]t . \qquad (4.2)$$

Here, $\dot{x}[n_x, n_y]$ and $\dot{y}[n_x, n_y]$ are the respective azimuth velocities and range velocities of the point scatterers. From Chapter 2, recall that the corresponding SVTCV estimation-theoretic SAR data model was given by

$$\underline{\textit{Spatially-Varying Temporally-Constant Velocity}}$$
$$\underline{\textit{(SVTCV) Estimation-Theoretic SAR Data Model}}$$
$$f[n,k] = \sum_{n_x}\sum_{n_y} A[n_x,n_y]s_{\mathbf{v}}[n_x,n_y,n,k] + \eta[n,k]$$
$$-\frac{N}{2} \leq n \leq \frac{N}{2} \quad -K \leq k \leq K. \tag{4.3}$$

The *non-orthogonal* basis-functions $s_{\mathbf{v}}[n_x, n_y, n, k]$ are given by

$$s_{\mathbf{v}}[n_x,n_y,n,k] = e^{j\left[\phi_x[n,k]\Delta_x n_x + \phi_y[n,k]\Delta_y n_y + \phi_{\dot{x}}[n,k]\dot{x}[n_x,n_y] + \phi_{\dot{y}}[n,k]\dot{y}[n_x,n_y]\right]}. \tag{4.4}$$

The corresponding velocity-parameter vector $\mathbf{v}$ consists of the azimuth velocities and range velocities of the point scatterers

$$\mathbf{v} = \begin{bmatrix} \vdots \\ \dot{x}[0,0] \\ \dot{x}[0,1] \\ \vdots \\ \dot{y}[0,0] \\ \dot{y}[0,1] \\ \vdots \end{bmatrix}. \tag{4.5}$$

The SVTCV estimation-theoretic model can also be expressed in the following general matrix form

$$\mathbf{f} = \mathbf{F}(\mathbf{v})\mathbf{A} + \eta, \tag{4.6}$$

where $\mathbf{f}$ is the SAR data. The vector $\mathbf{A}$ is the vector of scatterer intensities, given by

$$\mathbf{A} = \begin{bmatrix} \vdots \\ A[0,0] \\ A[0,1] \\ \vdots \end{bmatrix}. \tag{4.7}$$

Again, the vector $\mathbf{v}$ is the vector of the corresponding scatterer velocities, and η is the additive Gaussian noise. The matrix $\mathbf{F}(\mathbf{v})$ has the form

$$\mathbf{F}(\mathbf{v}) = \begin{bmatrix} \dots \mathbf{s}_{\mathbf{v}}[0,0] & \mathbf{s}_{\mathbf{v}}[0,1] & \dots \end{bmatrix}, \tag{4.8}$$

where each column vector $\mathbf{s_v}[n_x, n_y]$ correspond to a lexicographical ordering of the complex exponential basis-function given by $s_\mathbf{v}[n_x, n_y, n, k]$. As before, the additive noise η is assumed to be zero-mean, spatially statistically-independent, and isotropic, which implies that its spatial-correlation matrix is given by

$$\mathbf{K}_\eta = E\left[\eta\eta^H\right] = \sigma_\eta^2 \mathbf{I} \tag{4.9}$$

For the matrix SVTCV model presented here, the maximum-likelihood estimates for the scatterer-amplitude vector and the scatterer-velocity vector are given by the $\mathbf{A}$ and $\mathbf{v}$ which minimize the following standard least-squares cost function

$$\begin{aligned} J(\mathbf{A}, \mathbf{v}) &= ||\mathbf{f} - \mathbf{F}(\mathbf{v})\mathbf{A}||_{\mathbf{K}_\eta^{-1}}^2 \\ &= \frac{1}{\sigma_\eta^2}||\mathbf{f} - \mathbf{F}(\mathbf{v})\mathbf{A}||_2^2 \ . \end{aligned} \tag{4.10}$$

Since the location of the minimum of this cost function is unaffected by a constant scaling, we can normalize it by setting $\sigma_\eta^2 = 1$, which gives the following expression

$$J(\mathbf{A}, \mathbf{v}) = ||\mathbf{f} - \mathbf{F}(\mathbf{v})\mathbf{A}||_2^2 \ . \tag{4.11}$$

From this minimization of the (normalized) cost function, it can be shown[21] that the closed-form expression for the maximum-likelihood estimate of the scatterer-amplitude vector $\mathbf{A}$ is given by

$$\hat{\mathbf{A}}_{ML} = \left(\mathbf{F}^H(\hat{\mathbf{v}}_{ML})\mathbf{F}(\hat{\mathbf{v}}_{ML})\right)^{-1}\mathbf{F}^H(\hat{\mathbf{v}}_{ML})\mathbf{f} \ , \tag{4.12}$$

where the maximum-likelihood estimate $\hat{\mathbf{v}}_{ML}$ of the scatterer-velocity vector $\mathbf{v}$ is given by

$$\hat{\mathbf{v}}_{ML} = \arg\max_\mathbf{v} \left[\ || \left(\mathbf{F}^H(\mathbf{v})\mathbf{F}(\mathbf{v})\right)^{-1}\mathbf{F}^H(\mathbf{v})\mathbf{f}||_2^2 \ \right] . \tag{4.13}$$

However, direct calculation of the closed-form solutions for $\hat{\mathbf{A}}_{ML}$ and $\hat{\mathbf{v}}_{ML}$ (using the inverse of the matrix $\mathbf{F}^H(\mathbf{v})\mathbf{F}(\mathbf{v})$) can be computationally intensive even for a moderately sized SAR scene (since the dimensions of these vectors are directly proportional to the total number of scatterers in the $2 - D$ target-scatterer array).

If we are given the maximum-likelihood estimate $\hat{\mathbf{v}}_{ML}$ of the scatterer-velocity vector, we can compute the maximum-likelihood estimate $\hat{\mathbf{A}}_{ML}$ of the scatterer-amplitude vector by the following recursive gradient-descent algorithm for the normalized least-squares cost function (with $\hat{\mathbf{A}}_0 = \mathbf{0}$)

$$\begin{aligned} \hat{\mathbf{A}}_{m+1} &= \hat{\mathbf{A}}_m - \alpha \frac{\partial J(\mathbf{A}, \hat{\mathbf{v}}_{ML})}{\partial \mathbf{A}}\bigg|_{\mathbf{A}=\hat{\mathbf{A}}_m} \\ &= \hat{\mathbf{A}}_m + \alpha \mathbf{F}^H(\hat{\mathbf{v}}_{ML})[\mathbf{f} - \mathbf{F}(\hat{\mathbf{v}}_{ML})\hat{\mathbf{A}}_m] \ . \end{aligned} \tag{4.14}$$

However, if we try to use this technique to minimize the least-squares cost function over *both* $\mathbf{A}$ and $\mathbf{v}$, the corresponding gradient-descent algorithm may converge to a solution which does not result in a focused SAR image (since this cost function is a nonlinear

function of the scatterer velocity vector $\mathbf{v}$, which implies that it may have local minima). In Chapter 3, we presented the L_1-norm based SAR processing technique, which was based upon finding the scatterer velocity and amplitude estimates which minimized the following L_1 *-norm regularized cost function*

$$J(\mathbf{A}, \mathbf{v}) = ||\mathbf{f} - \mathbf{F}(\mathbf{v})\mathbf{A}||_2^2 + \gamma_A ||\mathbf{A}||_1 + J_\mathbf{v}(\mathbf{v}) , \qquad (4.15)$$

which the standard (normalized) least-squares cost function augmented by an L_1 penalty upon the scatterer amplitude estimates (plus an (optional) regularization penalty upon the velocity estimates). The solution for this cost function can be computed by the following gradient-descent algorithm

$$\begin{aligned}
\hat{\mathbf{v}}_{m+1} &= \hat{\mathbf{v}}_m - \alpha_\mathbf{v} \left.\frac{\partial J(\mathbf{A}, \mathbf{v})}{\partial \mathbf{v}}\right|_{\mathbf{A}=\hat{\mathbf{A}}_m, \, \mathbf{v}=\hat{\mathbf{v}}_m} \\
&= \hat{\mathbf{v}}_m + \alpha_\mathbf{v} 2\Re\left(\hat{\mathbf{A}}_m^H \frac{\partial \mathbf{F}^H(\hat{\mathbf{v}}_m)}{\partial \mathbf{v}}[\mathbf{f} - \mathbf{F}(\hat{\mathbf{v}}_m)\hat{\mathbf{A}}_m]\right) - \frac{\partial J_\mathbf{v}(\mathbf{v}_m)}{\partial \mathbf{v}} \qquad (4.16)
\end{aligned}$$

$$\begin{aligned}
\hat{\mathbf{A}}_{m+1} &= \hat{\mathbf{A}}_m - \alpha \left.\frac{\partial J(\mathbf{A}, \hat{\mathbf{v}}_m)}{\partial \mathbf{A}}\right|_{\mathbf{A}=\hat{\mathbf{A}}_m} \\
&= \hat{\mathbf{A}}_m + \alpha \mathbf{F}^H(\hat{\mathbf{v}}_m)[\mathbf{f} - \mathbf{F}(\hat{\mathbf{v}}_m)\hat{\mathbf{A}}_m] - \alpha\gamma_A \mathrm{asgn}[\hat{\mathbf{A}}_m] , \qquad (4.17)
\end{aligned}$$

where $\mathrm{asgn}[\mathbf{A}]$ is the following *continuous* approximation to the *discontinuous* gradient $\mathrm{sgn}[\mathbf{A}]$ of the L_1-norm of $\mathbf{A}$

$$\begin{aligned}
[\mathrm{asgn}[\mathbf{A}]]_{n_x n_y} &= \frac{A[n_x, n_y]}{\sqrt{A[n_x, n_y]A^*[n_x, n_y] + \epsilon_A^2}} \\
&\approx \mathrm{sgn}(A[n_x, n_y]) . \qquad (4.18)
\end{aligned}$$

As discussed in Chapter 3, this technique essentially tries to find an $\mathbf{A}$ and $\mathbf{v}$ where the estimated SAR image $\mathbf{A}$ is *sparse* (i.e., the image has only a small number of scatterers with non-zero amplitudes). This implies that the L_1-norm gradient-descent algorithm would be more likely to converge to a solution for the scatterer velocities $\mathbf{v}$ which results a focused SAR image. Therefore, we can use the L_1-norm based technique to estimate $\mathbf{v}$, then use the least-squares gradient-descent algorithm (with this L_1 estimate of $\mathbf{v}$) to estimate the scatterer amplitudes $\mathbf{A}$.

However, even though the L_1-norm based algorithm may converge to a more acceptable solution for $\mathbf{v}$ than a least-squares based algorithm, the underlying L_1-norm regularized cost-function may still exhibit some local minima. Thus, it would be beneficial for the the L_1-norm based algorithm to start with a good initial condition $\hat{\mathbf{v}}_0$ for the scatterer velocities.

In addition, for many SAR scenes containing moving targets, it is usually the case that only a relatively small number of scatterers in the scene actually have a non-zero velocity. This implies that the scatterer-velocity vector $\mathbf{v}$ will in general be sparse (i.e., most of its elements can be assumed to be zero). In other words, if we knew which scatterers are moving, we can decompose the scatterer-velocity vector $\mathbf{v}$ and the scatterer-amplitude vector $\mathbf{A}$ into

the following forms (by multiplying them by a pair of "segmentation-projection" matrices $\mathbf{P_V}$ and $\mathbf{P_A}$)

$$\mathbf{P_v v} = \left[\begin{array}{c} \mathbf{v}_T \\ \hline \mathbf{v}_C \end{array} \right] = \left[\begin{array}{c} \mathbf{v}_T \\ \hline \mathbf{0} \end{array} \right] \qquad (4.19)$$

$$\mathbf{P_A A} = \left[\begin{array}{c} \mathbf{A}_T \\ \hline \mathbf{A}_C \end{array} \right] . \qquad (4.20)$$

In these expressions, $\mathbf{v}_T$ is a (reduced-order) vector of target scatterer velocities, $\mathbf{v}_C = \mathbf{0}$ is a corresponding vector of (zero) clutter scatterer velocities, $\mathbf{A}_T$ is a reduced-order vector of target scatterer amplitudes, and $\mathbf{A}_C$ is the corresponding vector of (zero-velocity) clutter scatterer amplitudes. Note that the segmentation-projection matrices consist solely of 0's and 1's, and have the properties

$$\mathbf{P_v}^T \mathbf{P_v} = \left[\begin{array}{c|c} \mathbf{I} & \mathbf{0} \\ \hline \mathbf{0} & \mathbf{0} \end{array} \right] \qquad (4.21)$$

$$\mathbf{P_A}^T \mathbf{P_A} = \mathbf{I} . \qquad (4.22)$$

Again, if we know the location of the target scatterers in the SAR scene (i.e., we know $\mathbf{P_v}$ and $\mathbf{P_A}$), we can express the SVTCV SAR model in the following matrix form

$$\begin{aligned} \mathbf{f} &= \mathbf{F}_T(\mathbf{v}_T)\mathbf{A}_T + \mathbf{F}_C(\mathbf{v}_C)\mathbf{A}_C + \eta \\ &= \mathbf{F}_T(\mathbf{v}_T)\mathbf{A}_T + \mathbf{F}_C(\mathbf{0})\mathbf{A}_C + \eta \\ &= \mathbf{F}_T(\mathbf{v}_T)\mathbf{A}_T + \mathbf{F}_C\mathbf{A}_C + \eta , \end{aligned} \qquad (4.23)$$

The matrix $\mathbf{F}_T(\mathbf{v}_T)$ corresponds to a reduced-order set of target-scatterer complex exponential SVTCV basis-functions, while the matrix $\mathbf{F}_C$ corresponds to the set of (zero velocity) clutter-scatterer complex-exponential SVTCV basis-functions (which is essentially the conventional SAR scaled Fourier Transform of $\mathbf{F}_C$). For this form of the SVTCV SAR model, the L_1-norm regularized cost function is given by

$$J(\mathbf{A}_T, \mathbf{A}_C, \mathbf{v}_T) = ||\mathbf{f} - \mathbf{F}_T(\mathbf{v}_T)\mathbf{A}_T - \mathbf{F}_C\mathbf{A}_C||_2^2 + \gamma_A \left(||\mathbf{A}_T||_1 + ||\mathbf{A}_C||_1 \right) + J_\mathbf{v}(\mathbf{v}_T) , \quad (4.24)$$

which implies that the resulting reduced-order L_1-norm gradient-descent algorithm is given by

$$\begin{aligned} [\hat{\mathbf{v}}_T]_{m+1} &= [\hat{\mathbf{v}}_T]_m + \alpha_\mathbf{v} 2\Re \left([\hat{\mathbf{A}}_T]_m^H \frac{\partial \mathbf{F}_T^H([\hat{\mathbf{v}}_T]_m)}{\partial \mathbf{v}_T} [\mathbf{f} - \mathbf{F}_T([\hat{\mathbf{v}}_T]_m)[\hat{\mathbf{A}}_T]_m - \mathbf{F}_C[\mathbf{A}_C]_m] \right) \\ &\quad - \frac{\partial J_{\mathbf{v}_T}([\mathbf{v}_T]_m)}{\partial \mathbf{v}_T} \end{aligned} \qquad (4.25)$$

$$
\begin{aligned}
[\hat{\mathbf{A}}_T]_{m+1} &= [\hat{\mathbf{A}}_T]_m + \alpha\mathbf{F}_T^H([\hat{\mathbf{v}}_T]_m)[\mathbf{f} - \mathbf{F}_T([\hat{\mathbf{v}}_T]_m)[\hat{\mathbf{A}}_T]_m - \mathbf{F}_C[\mathbf{A}_C]_m] \\
&\quad - \alpha\gamma_A\,\mathrm{asgn}[[\hat{\mathbf{A}}_T]_m]
\end{aligned}
\tag{4.26}
$$

$$
\begin{aligned}
[\hat{\mathbf{A}}_C]_{m+1} &= [\hat{\mathbf{A}}_C]_m + \alpha\mathbf{F}_C^H[\mathbf{f} - \mathbf{F}_T([\hat{\mathbf{v}}_T]_m)[\hat{\mathbf{A}}_T]_m - \mathbf{F}_C[\mathbf{A}_C]_m] \\
&\quad - \alpha\gamma_A\,\mathrm{asgn}[[\hat{\mathbf{A}}_C]_m]\;.
\end{aligned}
\tag{4.27}
$$

Once the (reduced-order) L_1-norm target-scatterer velocity estimates $\hat{\mathbf{v}}_T$ are obtained, we can compute the target-scatterer amplitudes $\hat{\mathbf{A}}_T$ and the clutter-scatterer amplitudes $\hat{\mathbf{A}}_C$ by the following recursive gradient-descent least-squares estimation algorithm

$$
[\hat{\mathbf{A}}_T]_{m+1} = [\hat{\mathbf{A}}_T]_m + \alpha\mathbf{F}_T^H(\hat{\mathbf{v}}_T)[\mathbf{f} - \mathbf{F}_T(\hat{\mathbf{v}}_T)[\hat{\mathbf{A}}_T]_m - \mathbf{F}_C[\mathbf{A}_C]_m]
\tag{4.28}
$$

$$
[\hat{\mathbf{A}}_C]_{m+1} = [\hat{\mathbf{A}}_C]_m + \alpha\mathbf{F}_C^H[\mathbf{f} - \mathbf{F}_T(\hat{\mathbf{v}}_T)[\hat{\mathbf{A}}_T]_m - \mathbf{F}_C[\mathbf{A}_C]_m]\;.
\tag{4.29}
$$

Note that this algorithm is essentially trying to minimize the following version of the least-squares cost function over $\mathbf{A}_T$ and $\mathbf{A}_C$ (for a given $\hat{\mathbf{v}}_T$)

$$
J(\mathbf{A}_T, \mathbf{A}_C, \hat{\mathbf{v}}_T) = \|\mathbf{f} - \mathbf{F}_T(\hat{\mathbf{v}}_T)\mathbf{A}_T - \mathbf{F}_C\mathbf{A}_C\|_2^2\;.
\tag{4.30}
$$

We see that since the dimension of the reduced-order $\mathbf{F}_T(\mathbf{v}_T)$ is less than the dimension of the full matrix $\mathbf{F}(\mathbf{v})$ (and the matrices $\mathbf{F}_C$ and $\mathbf{F}_C^H$ can be computed by fast FFT algorithms), the reduced-order algorithms will be computationally less intensive than the previous full-order versions (which assumed that every spatial location in a particular SAR scene corresponded to a moving scatterer). However, for the reduced-order algorithms, we still need to have some type of target detection scheme which would be able to tell whether a particular spatial location in a SAR scene corresponds to a moving target or not (i.e., we are able to compute $\mathbf{P}_\mathbf{v}$ and $\mathbf{P}_\mathbf{A}$).

4.2   The Matched-Filter Algorithm

Here, we present a matched-filter based algorithm which computes a set of initial velocity-estimates for the L_1-norm based gradient-descent algorithm. In addition, this matched-filter algorithm generates a target-detection statistic for determining which spatial locations in a SAR scene correspond to target scatterers, thus allowing us to use the reduced-order gradient-descent estimation algorithms presented in the previous section.

Recall from the previous section that the closed-form solution for the maximum-likelihood estimate $\hat{\mathbf{v}}_{ML}$ of the scatterer-velocity vector $\mathbf{v}$ for the normalized least-squares cost function was given by

$$
\hat{\mathbf{v}}_{ML} = \arg\max_{\mathbf{v}} \left[\,\|\left(\mathbf{F}^H(\mathbf{v})\mathbf{F}(\mathbf{v})\right)^{-1}\mathbf{F}^H(\mathbf{v})\mathbf{f}\|_2^2\,\right]\;.
\tag{4.31}
$$

Also recall that a direct calculation of the closed-form solution for $\hat{\mathbf{v}}_{ML}$ (using the inverse of the matrix $\mathbf{F}^H(\mathbf{v})\mathbf{F}(\mathbf{v})$) can be computationally intensive even for a "moderately" sized SAR scene. Therefore, in a similar fashion to the conventional imaging algorithm presented in Section 3.1, we make the following approximation to the ambiguity function matrix

$\mathbf{F}^H(\mathbf{v})\mathbf{F}(\mathbf{v})$ (where the "ambiguity" function[42] refers to the response of the maximum-likelihood estimator to a unit-amplitude point-scatterer located at the center of the imaged target-field)

$$\mathbf{F}^H(\mathbf{v})\mathbf{F}(\mathbf{v}) \approx \mathbf{I} \ . \tag{4.32}$$

We can then approximate the maximum-likelihood estimate $\hat{\mathbf{v}}_{ML}$ of the scatterer-velocity vector $\mathbf{v}$ by the output of the following *matched-filter*

$$\hat{\mathbf{v}}_{ML} \approx \arg\max_{\mathbf{v}} \left[\ ||\mathbf{F}^H(\mathbf{v})\mathbf{f}||_2^2 \ \right] \ . \tag{4.33}$$

However, since the matrix $\mathbf{F}(\mathbf{v})$ actually consists of a set of non-orthogonal basis-functions, this implies that the matched-filter will suffer from *scatterer cross-interference effects* (i.e., the matched-filter velocity estimates for a particular scatterer will be corrupted by the presence of nearby scatterers. Later, in Section 4.4, we will discuss ways of reducing these scatterer cross-interference effects. Here, we discuss in more detail the computation of the matched-filter velocity estimates and the matched-filter target-detection statistic.

4.2.1 Matched-Filter Velocity Estimation

In order to perform the matched-filter velocity estimation, we first represent the SVTCV point-scatterer azimuth-velocity and range-velocity functions, $\dot{x}[n_x, n_y]$ and $\dot{y}[n_x, n_y]$, in the following quantized form

$$\dot{x}[n_x, n_y] = n_{\dot{x}}[n_x, n_y]\Delta_{\dot{x}} \tag{4.34}$$

$$\dot{y}[n_x, n_y] = n_{\dot{y}}[n_x, n_y]\Delta_{\dot{y}} \ . \tag{4.35}$$

Here, the parameters $\Delta_{\dot{x}}$ and $\Delta_{\dot{y}}$ are *velocity-quantization constants*, while the functions $n_{\dot{x}}[n_x, n_y]$ and $n_{\dot{y}}[n_x, n_y]$ are *2 − D integer-valued azimuth-velocity and range-velocity functions*(i.e., $\{n_{\dot{x}}[n_x, n_y], n_{\dot{y}}[n_x, n_y]\} \in \{\ldots, -2, -1, 0, 1, 2, \ldots\}$). Then the matched-filter computation is equivalent to the following maximization over the integer-valued "free" parameters $n_{\dot{x}}$ and $n_{\dot{y}}$ (which have the same domain as $n_{\dot{x}}[n_x, n_y]$ and $n_{\dot{y}}[n_x, n_y]$)

$$(n_{\dot{x}_{ML}}[n_x, n_y], n_{\dot{y}_{ML}}[n_x, n_y]) = \arg\max_{n_{\dot{x}}, n_{\dot{y}}} \left[\ \left|\hat{A}[n_x, n_y, n_{\dot{x}}, n_{\dot{y}}]\right| \ \right] \ , \tag{4.36}$$

where $|\cdot|$ is the standard magnitude operator. The function $\hat{A}[n_x, n_y, n_{\dot{x}}, n_{\dot{y}}]$ is a *4 − D SVTCV quantized likelihood function* given by the following integral summation

$$\hat{A}[n_x, n_y, n_{\dot{x}}, n_{\dot{y}}] = \frac{1}{(2K)(N)} \sum_n \sum_k f[n, k]h[n_x, n_y, n_{\dot{x}}, n_{\dot{x}}, n, k] \ ,$$

$$\tag{4.37}$$

where the *SVTCV quantized basis-functions* $h[n_x, n_y, n_{\dot{x}}, n_{\dot{y}}, n, k]$ are given by

$$h[n_x, n_y, n_{\dot{x}}, n_{\dot{y}}, n, k] = e^{-j\left[\phi_x[n,k]n_x\Delta_x + \phi_y[n,k]n_y\Delta_y + \phi_{\dot{x}}[n,k]n_{\dot{x}}\Delta_{\dot{x}} + \phi_{\dot{y}}[n,k]n_{\dot{y}}\Delta_{\dot{y}}\right]} \ . \tag{4.38}$$

Note that $h[n_x, n_y, n_{\dot{x}}, n_{\dot{y}}, n, k]$ is equivalent to the complex-conjugate of the original non-orthogonal SVTCV basis function $s_{\mathbf{v}}[n_x, n_y, n, k]$ (with the discretized azimuth velocities

and range velocities parameterized by the "free" parameters, $n_{\dot{x}}$ and $n_{\dot{y}}$). After we compute $n_{\dot{x}_{ML}}[n_x, n_y]$ and $n_{\dot{y}_{ML}}[n_x, n_y]$, the corresponding matched-filter maximum-likelihood estimates of the scatterer velocities are simply given by

$$\hat{\dot{x}}_{ML}[n_x, n_y] = n_{\dot{x}_{ML}}[n_x, n_y]\Delta_{\dot{x}} \qquad (4.39)$$

$$\hat{\dot{y}}_{ML}[n_x, n_y] = n_{\dot{y}_{ML}}[n_x, n_y]\Delta_{\dot{y}} \ . \qquad (4.40)$$

In other words, *for a given range location, $n_y\Delta_y$, and a given azimuth location, $n_x\Delta_x$, the estimated scatterer velocities are proportional to the location of the maximum of the likelihood function over the velocities $n_{\dot{x}}\Delta_{\dot{x}}$ and $n_{\dot{y}}\Delta_{\dot{y}}$.*

4.2.2   Matched-Filter Target-Detection Statistic

Recall from Section 4.1 that in order to use the reduced-order gradient-descent algorithms (with their attendant computational savings), we need to have some type of target detection scheme which would be able to tell whether a particular spatial location in a SAR scene corresponds to a moving target or not. In addition, for the matched filter algorithm, it would be useful to compute a measure of the validity of its estimates. In a sense, one would like to know whether the matched-filter has detected an actual moving target scatterer at a given spatial location, or have its estimates been corrupted by the interference from a nearby scatterer. Here, we present a method for computing such a measure.

Suppose we are given the matched-filter quantized likelihood function $\hat{A}[n_x, n_y, n_{\dot{x}}, n_{\dot{y}}]$ for a given spatial location $(\Delta_x n_x, \Delta_y n_y)$). Recall from Section 4.2.1 that the matched-filter maximum-likelihood estimates of the scatterer velocities are given by

$$\hat{\dot{x}}_{ML}[n_x, n_y] = n_{\dot{x}_{ML}}[n_x, n_y]\Delta_{\dot{x}} \qquad (4.41)$$

$$\hat{\dot{y}}_{ML}[n_x, n_y] = n_{\dot{y}_{ML}}[n_x, n_y]\Delta_{\dot{y}} \ , \qquad (4.42)$$

where

$$(n_{\dot{x}_{ML}}[n_x, n_y], n_{\dot{y}_{ML}}[n_x, n_y]) = \arg\max_{n_{\dot{x}}, n_{\dot{y}}} \left[\left| \hat{A}[n_x, n_y, n_{\dot{x}}, n_{\dot{y}}] \right| \right] \ . \qquad (4.43)$$

Let $\hat{A}_{MAX}[n_x, n_x]$ be the maximum magnitude of $\hat{A}[n_x, n_y, n_{\dot{x}}, n_{\dot{y}}]$ over $n_{\dot{x}}$ and $n_{\dot{y}}$

$$\hat{A}_{MAX}[n_x, n_y] = \max_{n_{\dot{x}}, n_{\dot{y}}} \left[\left| \hat{A}[n_x, n_y, n_{\dot{x}}, n_{\dot{y}}] \right| \right] \ . \qquad (4.44)$$

This is also the approximate magnitude of the maximum-likelihood estimate for the scatterer amplitude $\hat{A}[n_x, n_y]$ at the spatial location $(\Delta_x n_x, \Delta_y n_y)$. Given this estimate, we make use of the following empirical observation: *For a given moving scatterer, the maximum amplitude of the scatterer in a focused SAR image will be greater than the amplitude of the spatially-distributed blur region corresponding to this scatterer in a conventional SAR image.* This implies that we can determine whether a particular spatial location contains a moving target by comparing $\hat{A}_{MAX}[n_x, n_x]$ to the average amplitude of the blur region in the corresponding conventional SAR image given by $\hat{A}_{CONV}[n_x, n_x]$.

Another empirical observation is that *the blur region due to a moving scatterer in the conventional SAR image tends to be spatially localized around the initial spatial position of*

that moving scatterer. This implies that for a given spatial location $(\Delta_x n_x, \Delta_y n_y)$, we only need to compare $\hat{A}_{MAX}[n_x, n_x]$ to the average blur amplitude within a spatially-localized "window" region $\hat{A}_W[n_x, n_y, n'_x, n'_y]$ around this spatial location in the conventional image, where this window region is given by the following expression (where (n'_x, n'_y) are a set of "dummy" discrete parameters with the same domain as (n_x, n_y))

$$\hat{A}_W[n_x, n_y, n'_x, n'_y] = \hat{A}_{CONV}[n'_x + n_x, n'_y + n_y] w[n'_x, n'_y] \,, \tag{4.45}$$

where the "window" function $w[n_x, n_y]$ (of azimuth width Δ_{W_x} and range width Δ_{W_y}) is given by

$$w[n_x, n_y] = \begin{cases} 1 & |n_x \Delta_x| \le \frac{\Delta_{W_x}}{2} \quad |n_y \Delta_y| \le \frac{\Delta_{W_y}}{2} \\ 0 & \text{otherwise} \end{cases} . \tag{4.46}$$

Let $\hat{A}_{MEAN}[n_x, n_y]$ be the mean magnitude of the windowed SAR image $\hat{A}_W[n_x, n_y, n'_x, n'_y]$ over n'_x and n'_y

$$\hat{A}_{MEAN}[n_x, n_y] = \underset{n'_x, n'_y}{\text{mean}} \; [\, |\hat{A}_W[n_x, n_y, n'_x, n'_y]| \,] \,. \tag{4.47}$$

Also, let $\sigma_{\hat{A}}[n_x, n_y]$ be the standard deviation of the magnitudes of the elements of the windowed SAR image $\hat{A}_W[n_x, n_y, n'_x, n'_y]$ over n'_x and n'_y

$$\sigma_{\hat{A}}[n_x, n_y] = \underset{n'_x, n'_y}{\sigma} \; [\, |\hat{A}_W[n_x, n_y, n'_x, n'_y]| \,] \,. \tag{4.48}$$

Then, we can compute the following detection statistic $\chi[n_x, n_y]$

$$\boxed{\chi[n_x, n_y] = \frac{\hat{A}_{MAX}[n_x, n_y] - \hat{A}_{MEAN}[n_x, n_y]}{\sigma_{\hat{A}}[n_x, n_y]} \,.} \tag{4.49}$$

For a given spatial location $(\Delta_x n_x, \Delta_y n_y)$, we are comparing the maximum magnitude $\hat{A}_{MAX}[n_x, n_y]$ of the quantized likelihood function with the mean magnitude $\hat{A}_{MEAN}[n_x, n_y]$ of the corresponding windowed conventional image (scaled by the standard deviation $\sigma_{\hat{A}}[n_x, n_y]$ of the windowed image, so as to lessen the dependence of the detection statistic upon the absolute amplitudes of the target point-scatterers). Recall that the matched-filter velocity estimates for a given spatial location are proportional to the spatial location of the maximum magnitude of $\hat{A}[n_x, n_y, n_{\dot{x}}, n_{\dot{y}}]$ over $n_{\dot{x}}$ and $n_{\dot{y}}$. If there actually is a strong scatterer at the given spatial location $(\Delta_x n_x, \Delta_y n_y)$, then the maximum magnitude $\hat{A}_{MAX}[n_x, n_y]$ will be significantly greater than the average magnitude of the blur region in the conventional image. In other words, the detection statistic $\chi[n_x, n_y]$ *gives a measure of how sharply focused is the scatterer as compared to the original conventional SAR image.*

If the statistic $\chi[n_x, n_y]$ at a particular spatial location, $(\Delta_x n_x, \Delta_y n_y)$, is above some threshold χ_{MAX}, we state that a target scatterer has been detected, which implies that the maximum of the magnitudes of the matched-filter quantized likelihood-function over $n_{\dot{x}}$ and $n_{\dot{y}}$ (whose location is used to estimate the range and azimuth velocities of the

point scatterer) is due to the presence of an actual target scatterer at $(\Delta_x n_x, \Delta_y n_y)$, rather than due to other types of variations (such as those caused by either additive noise or the interference of a nearby scatterer). Therefore, we can classify the scatterer at this particular spatial location as a valid target scatterer, which means that we assume that the corresponding matched-filter velocity estimates are also valid. Otherwise, we assume that the scatterer velocity is zero, since most scatterers in typical SAR image are stationary (as stated earlier in Section 4.1). In other words, if we define χ as the vector of target-detection statistics, given by

$$\chi = \begin{bmatrix} \vdots \\ \chi[0,0] \\ \chi[0,1] \\ \vdots \end{bmatrix}, \tag{4.50}$$

then the segmentation-projection matrices, $\mathbf{P_v}$ (used to decompose the scatterer-velocity vector $\mathbf{v}$ into a (reduced-dimension) target-scatterer velocity vector, $\mathbf{v}_T$, and a clutter-scatterer velocity-vector $\mathbf{v}_C = \mathbf{0}$) and $\mathbf{P_A}$ (used to decompose the scatterer-amplitude vector $\mathbf{A}$ into a (reduced-dimension) target-scatterer amplitude vector, $\mathbf{A}_T$, and a clutter-scatterer amplitude-vector $\mathbf{A}_C$) are functions of both χ and χ_{MAX}, i.e.,

$$\mathbf{P_v}(\chi, \chi_{MAX})\mathbf{v} = \begin{bmatrix} \mathbf{v}_T \\ - \\ \mathbf{v}_C \end{bmatrix} = \begin{bmatrix} \mathbf{v}_T \\ - \\ \mathbf{0} \end{bmatrix} \tag{4.51}$$

$$\mathbf{P_A}(\chi, \chi_{MAX})\mathbf{A} = \begin{bmatrix} \mathbf{A}_T \\ - \\ \mathbf{A}_C \end{bmatrix}. \tag{4.52}$$

Note that the number of spatial locations classified as "targets" will depend upon the threshold on $\chi[n_x, n_y]$. In the detection-theoretic literature, this particular detection statistic has many similarities to the so-called *Constant False-Alarm Rate*(CFAR) detection statistic (which is solely dependent upon the *relative intensities* of the scatterer to the additive noise).

4.3 Matched-Filter Implementation Issues

In this section, we discuss some of the significant issues encountered in the actual implementation of the matched-filter algorithm. First, we discuss a "fast" method for computing the matched-filter likelihood function integral (by using the Fourier Transform). Then we discuss a method for modifying the matched-filter algorithm so as to compensate for range-velocity induced azimuth displacement.

4.3.1 Fast Computation of the Matched-Filter Likelihood Function

Rather than evaluating the matched-filter quantized likelihood function directly (which can be computationally prohibitive), the following fast and easily implementable solution can be used (with equivalent performance). First, we rewrite the quantized likelihood function $\hat{A}[n_x, n_y, n_{\dot{x}}, n_{\dot{x}}]$ in the following form

$$\hat{A}[n_x, n_y, n_{\dot{x}}, n_{\dot{y}}] = \frac{1}{(2K)(N)} \sum_k \sum_n f[n_x, n_y, n, k] h[n_{\dot{x}}, n_{\dot{y}}, n, k] \ . \tag{4.53}$$

Here, the *phased-shifted SAR data* $f[n_x, n_y, n, k]$ and the quantized basis-functions $h[n_{\dot{x}}, n_{\dot{y}}, n, k]$ are given by

$$f[n_x, n_y, n, k] = f[n, k] e^{-j[\phi_x[n,k]n_x \Delta_x + \phi_y[n,k]n_y \Delta_y]} \tag{4.54}$$

$$h[n_{\dot{x}}, n_{\dot{y}}, n, k] = e^{-j[\phi_{\dot{x}}[n,k]n_{\dot{x}} \Delta_{\dot{x}} + \phi_{\dot{y}}[n,k]n_{\dot{y}} \Delta_{\dot{y}}]} \ . \tag{4.55}$$

Let $(k_{\dot{x}}, k_{\dot{y}})$ be a set of *discrete* spatial-frequencies (i.e., $\{k_{\dot{x}}, k_{\dot{y}}\} \in \{\ldots, -2, -1, 0, 1, 2, \ldots\}$). For a given azimuth and range location, $(n_x \Delta_x, n_y \Delta_y)$, we reparameterize the phased-shifted SAR data to form the following discrete space-time multi-dimensional signal (where the function $\delta[k_{\dot{x}}, k_{\dot{y}}]$ is the usual $2-D$ Kronecker delta-function)

$$f[k_{\dot{x}}, k_{\dot{y}}, n_x, n_y, n, k] = f[n_x, n_y, n, k] \delta[k_{\dot{x}} - \phi_{\dot{x}}[n, k]\Delta_{k_{\dot{x}}}^{-1}, k_{\dot{y}} - \phi_{\dot{y}}[n, k]\Delta_{k_{\dot{y}}}^{-1}] \ . \tag{4.56}$$

The parameters $(\Delta_{k_{\dot{x}}}, \Delta_{k_{\dot{y}}})$ determines the sampling rate of the SVTCV phase functions $(\phi_{\dot{x}}[n, k], \phi_{\dot{y}}[n, k])$ to $(k_{\dot{x}}, k_{\dot{y}})$. For the results presented in this chapter, we chose $(\Delta_{k_{\dot{x}}}, \Delta_{k_{\dot{y}}})$ such that the phase-shifted SAR data had approximately the same spatial extent in $(k_{\dot{x}}, k_{\dot{y}})$ space as it had in (k, n) space, i.e.,

$$\Delta_{k_{\dot{x}}} = \frac{\max\limits_{n,k} \phi_{\dot{x}}[n, k] - \min\limits_{n,k} \phi_{\dot{x}}[n, k]}{2K} \tag{4.57}$$

$$\Delta_{k_{\dot{y}}} = \frac{\max\limits_{n,k} \phi_{\dot{y}}[n, k] - \min\limits_{n,k} \phi_{\dot{y}}[n, k]}{N} \ . \tag{4.58}$$

It can be shown that for a given azimuth and range location, $(n_x \Delta_x, n_y \Delta_y)$, the quantized likelihood function $\hat{A}[n_x, n_y, n_{\dot{x}}, n_{\dot{x}}]$ is exactly equivalent to the following multi-dimensional spatio-temporal Fourier Transform[21]

$$F[n_x, n_y, n_{\dot{x}}, n_{\dot{y}}] =$$

$$\frac{1}{(2K)(N)} \sum_{k_{\dot{x}}} \sum_{k_{\dot{y}}} \sum_n \sum_k f[k_{\dot{x}}, k_{\dot{y}}, n_x, n_y, n, k] e^{-j\left[k_{\dot{x}} \Delta_{k_{\dot{x}}} n_{\dot{x}} \Delta_{\dot{x}} + k_{\dot{y}} \Delta_{k_{\dot{y}}} n_{\dot{y}} \Delta_{\dot{y}}\right]} \ . \tag{4.59}$$
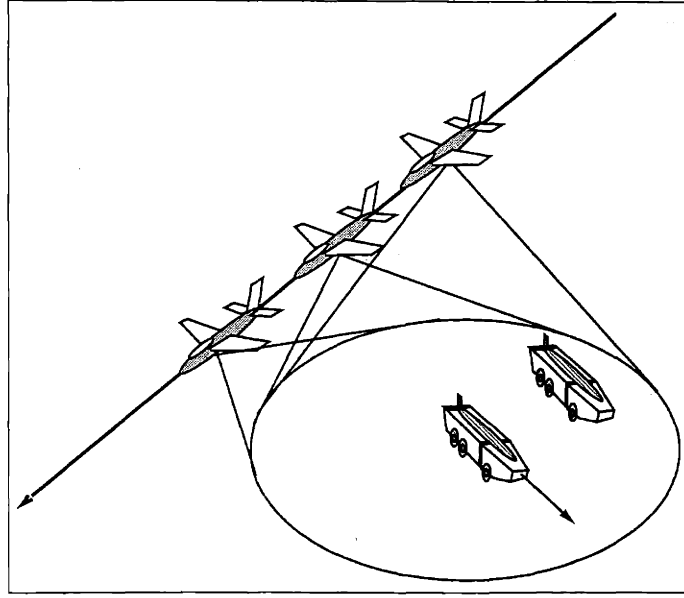
Figure 4.1: Ambiguity Between Azimuth Position and Range Velocity

This reformulation clearly improves the computational efficiency of the motion compensated SAR technique, since the spatio-temporal FT can be calculated by standard "fast" multi-dimensional FFT algorithms.

4.3.2   Compensation of Range-Velocity Induced Azimuth-Displacement

Recall from Chapter 2 that the polynomial approximation to the SVTCV phase functions were given by

$$\phi_x[n,k] \;=\; -\,\frac{4\pi}{\lambda_c}\left(1+\frac{\alpha T_p}{f_c}\frac{n}{N}\right)\left[\frac{1}{6}\dot\theta^3\left(\frac{Tk}{K}\right)^3-\dot\theta\left(\frac{Tk}{K}\right)\right] \tag{4.60}$$

$$\phi_y[n,k] \;=\; -\,\frac{4\pi}{\lambda_c}\left(1+\frac{\alpha T_p}{f_c}\frac{n}{N}\right)\left[1-\frac{1}{2}\dot\theta^2\left(\frac{Tk}{K}\right)^2\right] \tag{4.61}$$

$$\phi_{\dot x}[n,k] \;=\; \frac{4\pi}{\lambda_c}\left(1+\frac{\alpha T_p}{f_c}\frac{n}{N}\right)\left[\dot\theta\left(\frac{Tk}{K}\right)^2\right] \tag{4.62}$$

$$\phi_{\dot y}[n,k] \;=\; -\,\frac{4\pi}{\lambda_c}\left(1+\frac{\alpha T_p}{f_c}\frac{n}{N}\right)\left[\left(\frac{Tk}{K}\right)-\frac{1}{2}\dot\theta^2\left(\frac{Tk}{K}\right)^3\right]. \tag{4.63}$$

Upon closer inspection, we see that for $\dot\theta$ small, $\phi_{\dot y}[n,k] \approx -\phi_x[n,k]/\dot\theta$. For a given scatterer (with an initial spatial position given by $(\Delta_x n_x, \Delta_y n_y)$), this implies that *a matched filter based upon these phase functions will have difficulty distinguishing between the initial azimuth position $\Delta_x n_x$ and the range-velocity induced displacement $x_{DISP}(\dot y[n_x, n_y]) = -\dot y[n_x, n_y]/\dot\theta$* (as illustrated in Figure 4.1).

We can alleviate this problem for the matched-filter algorithm in the following manner. First, we remove the linear portion of the polynomial approximation to the range-velocity

phase function, $\phi_{\dot{y}}[n,k]$, which leaves the following "leftover" dominant term

$$\phi_{\dot{y}}[n,k] \approx -\frac{4\pi}{\lambda_c} \left(\frac{\alpha T_p}{f_c}\frac{n}{N}\right)\left[\left(\frac{Tk}{K}\right)\right].$$

(4.64)

In the literature[18], this dominant cross-phase term between n and k corresponds to motion-induced *range-walk* (i.e., when we perform a Fourier Transform with respect to the "fast-time" index n, we have a displacement in range proportional to the "slow-time" index k). Next, we use the matched-filter algorithm (with the modified range-velocity phase function) to obtain maximum-likelihood estimates, $n_{\dot{x}_{ML}}[n_x, n_y]$ and $n_{\dot{y}_{ML}}[n_x, n_y]$, of the $2-D$ integer-valued velocity functions, from which we get the following maximum-likelihood estimates of the scatterer velocities

$$\hat{\dot{x}}_{ML}[n_x, n_y] = n_{\dot{x}_{ML}}[n_x, n_y]\Delta_{\dot{x}}$$

(4.65)

$$\hat{\dot{y}}_{ML}[n_x, n_y] = n_{\dot{y}_{ML}}[n_x, n_y]\Delta_{\dot{y}}\ .$$

(4.66)

These maximum-likelihood estimates are used as initial conditions by the L_1-based velocity-estimation algorithm (which was discussed earlier in Section 4.1). This algorithm then produces a set of velocity-estimates which are used by the least-squares algorithm to obtain an uncorrected estimate, $\hat{A}_U[n_x, n_y]$, of the amplitudes of the $2-D$ point-scatterer array. Since we removed the linear portion of the polynomial approximation to the range-velocity phase function, the matched-filter is essentially estimating the range-velocities *solely* from the range-walk induced blurring. Lastly, we use the L_1 range-velocity estimates to correct the amplitude estimates for the azimuth displacement

$$\hat{A}[n_x, n_y] = \hat{A}_U\left[n_x - \frac{1}{\Delta_x}\frac{1}{\dot{\theta}}\hat{\dot{y}}[n_x, n_y], n_y\right]\ ,$$

(4.67)

since we assume that we know the look-angle rotation rate $\dot{\theta}$.

4.4 Reduction of Scatterer Cross-Interference Effects

Recall from Section 3.2 that we simplified the expression for the matched-filter maximum-likelihood estimate by making the following approximation to the so-called ambiguity function matrix $\mathbf{F}^H(\mathbf{v})\mathbf{F}(\mathbf{v})$

$$\mathbf{F}^H(\mathbf{v})\mathbf{F}(\mathbf{v}) \approx \mathbf{I} \,. \tag{4.68}$$

Since the matrix $\mathbf{F}(\mathbf{v})$ actually consists of a set of non-orthogonal basis-functions, this implies that the matched-filter algorithm (as presented up to this point) will suffer from *scatterer cross-interference effects* (i.e., the matched-filter velocity estimates for a particular scatterer will be corrupted by the presence of nearby scatterers.

First, we present two algorithms, image-windowing and clutter-nulling, for reducing scatterer cross-interference effects. The image-windowing algorithm starts with a conventional SAR image (with the polar-format resampling technique discussed in Section 3.1) $\hat{A}_{CONV}[n_x, n_y]$, and assumes that the motion-induced blur energy for a given point scatterer in this image is localized about the scatterer's initial spatial position $(\Delta_x n_x, \Delta_y n_y)$. By windowing this conventional SAR image about the motion-induced blur of the given scatterer (and converting this windowed image back into the original SAR data domain with a scaled Fourier Transform), the image-windowing algorithm sharply reduces interference effects from scatterers outside of the motion-induced blur area. For the SAR image window generated by the image-windowing algorithm for a given point-scatterer, the clutter-nulling algorithm reduces interference from nearby strong stationary scatterers (within the image window) by zeroing out all portions of the image window that have a higher magnitude than a threshold proportional to the magnitude of the conventional SAR image at the initial spatial location $(\Delta_x n_x, \Delta_y n_y)$ of the given point-scatterer. Lastly, we present a prefiltering algorithm for the matched-filter which uses median filtering[24] in order to eliminate high-value spurious velocity estimates caused by cross-scatterer interference.

4.4.1 Image Windowing

For the matched-filter algorithm, we are essentially estimating the motion of a given moving-target scatterer from its motion-induced blurring. However, one implicit assumption of the matched-filter algorithm is that the motion-induced blurring due to a single scatterer can be distributed over the *entire* SAR image (since we are using all of the SAR data $f[n, k]$). Generally (for target velocities much smaller than the velocity of the SAR antenna platform), the motion-induced blur tends to be localized around the initial position of the moving-target scatterer. Here, we present a windowing method which exploits this spatial localization effect in order to sharply reduce interference effects from scatterers outside of the motion-induced blur area.

As illustrated in Figure 4.3, we begin with a conventional SAR image $\hat{A}_{CONV}[n_x, n_y]$, computed from the SAR data $f[n, k]$ by the standard Fourier-Transform based processing algorithm presented in Section 3.1, with polar-format resampling. Let (k_x, k_y) be a set of *discrete* spatial-frequencies (i.e., $\{k_x, k_y\} \in \{\ldots, -2, -1, 0, 1, 2, \ldots\}$), and let (n', k') be a set of discrete parameters with the same domain as the SAR fast sampling time n and the SAR slow time k. Then the conventional image (with polar-format resampling) is equivalent to

the following Fourier Transform

$$
\begin{aligned}
\hat{A}_{CONV}[n_x, n_y] \quad &= \sum_{k_x} \sum_{k_y} \sum_{n'} \sum_{k'} f[n', k'] \delta \left[k_x - \frac{\phi_x[n', k']}{\Delta_{k_x}}, k_y - \frac{\phi_y[n', k']}{\Delta_{k_y}} \right] \\
&\times e^{-j\left[k_x \Delta_{k_x} \Delta_x n_x + k_y \Delta_{k_y} \Delta_y n_y \right]} \\
&= \sum_{n'} \sum_{k'} f[n', k'] e^{-j\left[\phi_x[n', k'] \Delta_x n_x + \phi_y[n', k'] \Delta_y n_y \right]} ,
\end{aligned} \tag{4.69}
$$

where $\delta[k_x, k_y]$ is the usual two-dimensional Kronecker delta-function. The constants Δ_{k_x} and Δ_{k_y} control the sampling of the SVTCV phase functions $\phi_x[n, k]$ and $\phi_y[n, k]$ to k_x and k_y. For the results presented in this thesis, the values of $(\Delta_{k_x}, \Delta_{k_y})$ were chosen such that the remapped SAR data had approximately the same spatial extent in (k_x, k_y) space as it had in (k', n') space, i.e.,

$$
\Delta_{k_x} = \frac{\max\limits_{n', k'} \phi_x[n', k'] - \min\limits_{n', k'} \phi_x[n', k']}{2K} \tag{4.70}
$$

$$
\Delta_{k_y} = \frac{\max\limits_{n', k'} \phi_y[n', k'] - \min\limits_{n', k'} \phi_y[n', k']}{N} . \tag{4.71}
$$

Let (n'_x, n'_y) be a set of "dummy" discrete parameters with the same domain as (n_x, n_y). For a given scatterer location $(n_x \Delta_x, n_y \Delta_y)$, we first "window" the conventional SAR image $\hat{A}_{CONV}[n'_x, n'_y]$ to produce $\hat{A}_W[n_x, n_y, n'_x, n'_y]$, given by

$$
\hat{A}_W[n_x, n_y, n'_x, n'_y] = \hat{A}_{CONV}[n'_x + n_x, n'_y + n_y] w[n'_x, n'_y] , \tag{4.72}
$$

where the "window" function $w[n_x, n_y]$ (of azimuth width Δ_{W_x} and range width Δ_{W_y}) is given by

$$
w[n_x, n_y] = \begin{cases} 1 & |n_x \Delta_x| \leq \frac{\Delta_{W_x}}{2} \quad |n_y \Delta_y| \leq \frac{\Delta_{W_y}}{2} \\ 0 & \text{otherwise} \end{cases} . \tag{4.73}
$$

Therefore, if an interfering scatterer is located outside the window, its energy will be eliminated from $\hat{A}_W[n_x, n_y, n'_x, n'_y]$. In terms of the Fourier Transform equation for $\hat{A}_{CONV}[n_x, n_y]$, the windowed SAR image, $\hat{A}_W[n_x, n_y, n'_x, n'_y]$, is given by

$$
\begin{aligned}
\hat{A}_W[n_x, n_y, n'_x, n'_y] \quad &= \sum_{n'} \sum_{k'} f[n', k'] e^{-j\left[\phi_x[n', k'] \Delta_x n_x + \phi_y[n', k'] \Delta_y n_y \right]} \\
&\times w[n'_x, n'_y] e^{-j\left[\phi_x[n', k'] \Delta_x n'_x + \phi_y[n', k'] \Delta_y n'_y \right]} \\
&= \sum_{n'} \sum_{k'} f[n_x, n_y, n', k'] w[n'_x, n'_y] e^{-j\left[\phi_x[n', k'] \Delta_x n'_x + \phi_y[n', k'] \Delta_y n'_y \right]} .
\end{aligned}
$$

$$
\tag{4.74}
$$

where $f[n_x, n_y, n, k]$ is the phase-shifted data set presented in Section 4.2.1.

Let (k_x', k_y') be a set of discrete spatial-frequencies with the same domain as (k_x, k_y). Then the inverse Fourier-Transform of the windowed image (with respect to the "dummy" spatial-parameters (n_x', n_y')) is given by

$$
\begin{aligned}
F_W[n_x, n_y, k_x', k_y'] \quad &= \sum_{n_x'} \sum_{n_y'} \hat{A}_W[n_x, n_y, n_x', n_y'] e^{j\left[k_x' \Delta_{k_x} \Delta_x n_x + k_y' \Delta_{k_y} \Delta_y n_y\right]} \\[2mm]
&= \sum_{n_x'} \sum_{n_y'} \sum_{n'} \sum_{k'} f[n_x, n_y, n', k'] w[n_x', n_y'] e^{-j\left[\phi_x[n', k'] \Delta_x n_x' + \phi_y[n', k'] \Delta_y n_y'\right]} \\
&\quad \times e^{j\left[k_x' \Delta_{k_x} \Delta_x n_x + k_y' \Delta_{k_y} \Delta_y n_y\right]} \\[2mm]
&= \sum_{n_x' = -\frac{\Delta_{W_x}}{2\Delta_x}}^{\frac{\Delta_{W_x}}{2\Delta_x}} \sum_{n_y' = -\frac{\Delta_{W_y}}{2\Delta_y}}^{\frac{\Delta_{W_y}}{2\Delta_y}} \sum_{n'} \sum_{k'} f[n_x, n_y, n', k'] \\
&\quad \times e^{-j\left[\phi_x[n', k'] \Delta_x n_x' + \phi_y[n', k'] \Delta_y n_y'\right]} e^{j\left[k_x' \Delta_{k_x} \Delta_x n_x + k_y' \Delta_{k_y} \Delta_y n_y\right]} \\[2mm]
&= \sum_{n'} \sum_{k'} f[n_x, n_y, n', k'] \\
&\quad \times \mathrm{sinc}\left(\frac{\Delta_{W_x}(k_x' \Delta_{k_x} - \phi_x[n', k'])}{2}\right) \mathrm{sinc}\left(\frac{\Delta_{W_y}(k_y' \Delta_{k_y} - \phi_y[n', k'])}{2}\right).
\end{aligned}
$$

$$(4.75)$$

The final phase-shifted data set $f_W[n_x, n_y, n, k]$ is given by the following interpolation within the inverse Fourier Transform $F_W[n_x, n_y, k_x, k_y]$

$$
\begin{aligned}
f_W[n_x, n_y, n, k] \quad &= F_W\left[n_x, n_y, \frac{\phi_x[n', k']}{\Delta_{k_x}}, \frac{\phi_y[n', k']}{\Delta_{k_y}}\right] \\[2mm]
&= \sum_{n'} \sum_{k'} f[n_x, n_y, n', k'] \\
&\quad \times \mathrm{sinc}\left(\frac{\Delta_{W_x}(\phi_x[n, k] - \phi_x[n', k'])}{2}\right) \mathrm{sinc}\left(\frac{\Delta_{W_y}(\phi_y[n, k] - \phi_y[n', k'])}{2}\right).
\end{aligned}
$$

$$(4.76)$$

Recall from Chapter 2 that the polynomial approximations to the SVTCV phase functions were given by

$$
\phi_x[n, k] = -\frac{4\pi}{\lambda_c}\left(1 + \frac{\alpha T_p}{f_c}\frac{n}{N}\right)\left[\frac{1}{6}\dot{\theta}^3\left(\frac{Tk}{K}\right)^3 - \dot{\theta}\left(\frac{Tk}{K}\right)\right] \tag{4.77}
$$

$$
\phi_y[n, k] = -\frac{4\pi}{\lambda_c}\left(1 + \frac{\alpha T_p}{f_c}\frac{n}{N}\right)\left[1 - \frac{1}{2}\dot{\theta}^2\left(\frac{Tk}{K}\right)^2\right]. \tag{4.78}
$$

For $\dot{\theta}$ and $\frac{\alpha T_p}{f_c}$ "small", the dominant terms in the SVTCV phase functions are given by

$$\phi_x[n,k] \approx \frac{4\pi}{\lambda_c}\dot{\theta}\left(\frac{Tk}{K}\right) \tag{4.79}$$

$$\phi_y[n,k] \approx -\frac{4\pi}{\lambda_c}\left(1+\frac{\alpha T_p}{f_c}\frac{n}{N}\right) . \tag{4.80}$$

This implies that $f_W[n_x, n_y, n, k]$ is approximately equal to the convolution of $f[n_x, n_y, n, k]$ with a $2-D$ sinc function whose mainlobe widths are inversely proportional to the azimuth and range widths of the window function $w[n_x, n_y]$. Thus, $f_W[n_x, n_y, n, k]$ is approximately equivalent to a *lowpass-filtered version of the original phase-shifted data set* $f[n_x, n_y, n, k]$. In addition, we can downsample $f_W[n_x, n_y, n, k]$, such that *the fast computation of the subsequent matched-filter likelihood function need only involve Fourier transforms on the order of the size of the data window* (rather than on the order of the size of the entire SAR image). Therefore, we can significantly improve the computational efficiency of the matched-filter algorithm.

4.4.2 Clutter Nulling

Even after we perform the windowing operation for a given scatterer at the spatial location $(n_x\Delta_x, n_y\Delta_y)$, we can still get significant interference from nearby bright stationary clutter scatterers (whose amplitudes are on the order of the amplitude of the given scatterer) located within the image window. However, we can reduce the effects of these types of scatterers by taking advantage of the following empirical observation: *Given a conventional SAR image containing two scatterers of equal amplitudes (with one moving and one stationary), the maximum magnitude of the spatially-distributed blur region corresponding to the moving scatterer in the conventional SAR image will be less than the maximum magnitude of the stationary scatterer in the conventional image* (as illustrated with the example shown in Figure 4.2, where we have a unit-amplitude stationary scatterer and a unit-amplitude moving scatterer with an azimuth velocity of $1m/s$). This implies that for the SAR image window generated by the image-windowing algorithm for a given point-scatterer, we can reduce interference from nearby "strong" stationary scatterers (within the image window) by zeroing out all portions of the image window that have a higher magnitude than a "clutter-nulling" threshold , $A_{CN}[n_x, n_y]$ (which is proportional to the magnitude of the conventional SAR image at the initial spatial location $(\Delta_x n_x, \Delta_y n_y)$ of the given point-scatterer),i.e.,

$$\hat{A}_W[n_x, n_y, n'_x, n'_y] =$$
$$\begin{cases} \hat{A}_{CONV}[n'_x + n_x, n'_y + n_y]w[n'_x, n'_y] & |\hat{A}_{CONV}[n'_x + n_x, n'_y + n_y]| \leq A_{CN}[n_x, n_y] \\ 0 & \text{otherwise} \end{cases}$$

$$\tag{4.81}$$
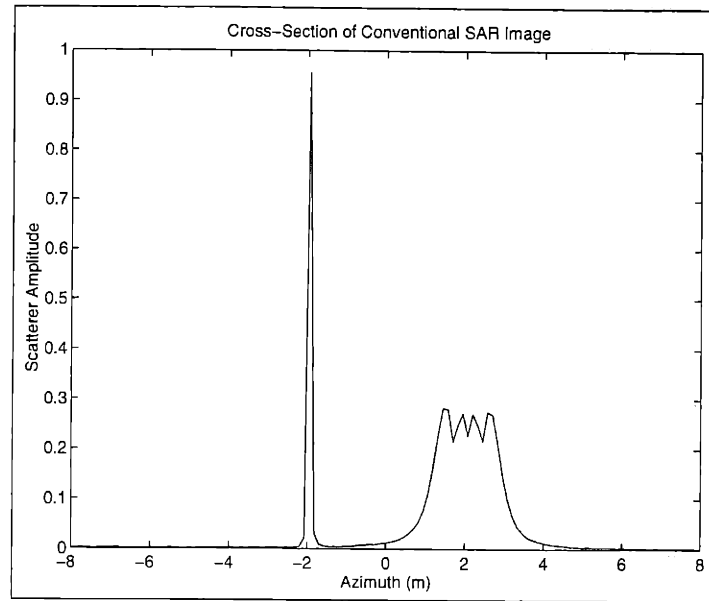
Figure 4.2: Azimuthal Cross-section of Conventional SAR Image Containing Both a Stationary Scatterer and a Moving Scatterer (with Equal Amplitudes)
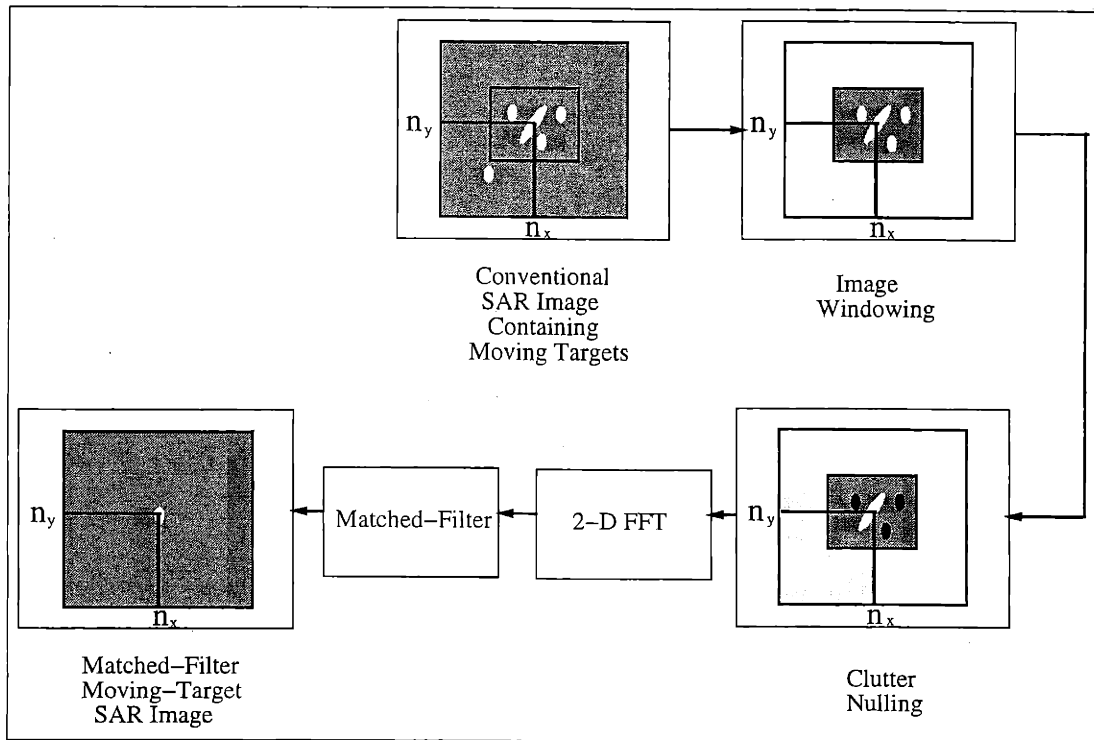
Figure 4.3: Image Windowing and Clutter Nulling (for a Point-Scatterer with Initial Spatial Location $(\Delta_x n_x, \Delta_y n_y)$)

4.4.3 Median Prefiltering of Matched-Filter Velocity Estimates

In the previous sections, we presented two methods, image-windowing and clutter-nulling, for reducing scatter cross-interference effects in the matched-filter velocity estimates. However, these two techniques do not completely eliminate these effects, especially for closely-spaced moving scatterers of relatively equal amplitudes (but different velocities). Empirically, we found that one major effect of scatterer cross-interference was the introduction of large-valued spurious velocity-estimates into the results of the matched filter. These spurious estimates have many similarities to so-called impulsive "salt-and-pepper" noise in the image-processing literature[24]. From the image-processing literature, one relatively effective method for reducing this type of noise (while minimizing distortion of spatial discontinuities in the velocity estimates, unlike linear lowpass filtering) is the so-called *median filtering* technique[24], where the filtered image value at a given spatial location is given by the median of the original image values over some region surrounding that location. This implies that we can use a median filter as a "prefilter" in order to eliminate high-value spurious matched-filter velocity estimates (before they are used as initial conditions for the L_1-norm based velocity estimation algorithm.

Recall from Section 4.2.1 that the matched-filter maximum-likelihood estimates of the scatterer velocities are given by

$$\hat{\dot{x}}_{ML}[n_x, n_y] = n_{\dot{x}_{ML}}[n_x, n_y]\Delta_{\dot{x}} \tag{4.82}$$

$$\hat{\dot{y}}_{ML}[n_x, n_y] = n_{\dot{y}_{ML}}[n_x, n_y]\Delta_{\dot{y}} \, , \tag{4.83}$$

where

$$(n_{\dot{x}_{ML}}[n_x, n_y], n_{\dot{y}_{ML}}[n_x, n_y]) = \arg \max_{n_{\dot{x}}, n_{\dot{y}}} \left[\left| \hat{A}[n_x, n_y, n_{\dot{x}}, n_{\dot{y}}] \right| \right] \, . \tag{4.84}$$

For a given spatial location $(\Delta_x n_x, \Delta_y n_y)$, the corresponding median filtered velocity estimates are given by following median of the matched-filter maximum-likelihood velocity-estimates over a spatial "region-of-interest" (ROI) surrounding this location (where (n_x'', n_y'') are a set of "dummy" discrete parameters with the same domain as (n_x, n_y))

$$\hat{\dot{x}}_{MED}[n_x, n_y] = \underset{n_x'', n_y'' \in \text{ROI}}{\text{median}} \hat{\dot{x}}_{ML}[n_x + n_x'', n_y + n_y''] \tag{4.85}$$

$$\hat{\dot{y}}_{MED}[n_x, n_y] = \underset{n_x'', n_y'' \in \text{ROI}}{\text{median}} \hat{\dot{y}}_{ML}[n_x + n_x'', n_y + n_y''] \, . \tag{4.86}$$

For all of the matched-filter results presented in this chapter, we used an ROI of $0.5m \times 0.5m$ for the median velocity filters.

4.5   Summary of the Matched-Filter SAR Processing Algorithm

Here, we present a summary of the overall matched-filter SAR processing algorithm discussed in this chapter, with the following notational conventions:

Symbol	Definition
$\hat{A}_U[n_x, n_y]$	Matched-Filter Least-Squares SAR Image Before Azimuth-Compensation
$\hat{A}_{AC}[n_x, n_y]$	Matched-Filter Least-Squares Image After Azimuth-Compensation
$\hat{A}[n_x, n_y, n_{\dot{x}}, n_{\dot{x}}]$	Quantized Likelihood Function
$\hat{A}_{MAX}[n_x, n_y]$	Maximum Magnitude of $\hat{A}[n_x, n_y, n_{\dot{x}}, n_{\dot{y}}]$ over $(n_{\dot{x}}, n_{\dot{y}})$
$\hat{A}_{CONV}[n_x, n_y]$	Conventional SAR Image
$A_{CN}[n_x, n_y]$	Clutter-Nulling Threshold
$\hat{A}_W[n_x, n_y, n'_x, n'_y]$	Windowed Conventional SAR Image
$\hat{A}_{MEAN}[n_x, n_y]$	Mean Magnitude of $\hat{A}_W[n_x, n_y, n'_x, n'_y]$ over (n'_x, n'_y)
$\sigma_{\hat{A}}[n_x, n_y]$	Std. Dev. of the Magnitudes of $\hat{A}_W[n_x, n_y, n'_x, n'_y]$ over (n'_x, n'_y)
$F_W[n_x, n_y, k'_x, k'_y]$	Fourier Transform of $\hat{A}_W[n_x, n_y, n'_x, n'_y]$ (with respect to (n'_x, n'_y))
$f_W[n_x, n_y, n, k]$	Windowed Phased-Shifted SAR Data
$f[k_{\dot{x}}, k_{\dot{y}}, n_x, n_y, n, k]$	Discrete Space-Time multi-dimensional SAR data
$\chi[n_x, n_y]$	Matched-Filter Detection Statistic
χ	Vector of Matched-Filter Detection Statistics
$(\hat{\dot{x}}_{ML}[n_x, n_y], \hat{\dot{y}}_{ML}[n_x, n_y])$	ML velocity estimates
$(\hat{\dot{x}}_{MED}[n_x, n_y], \hat{\dot{y}}_{MED}[n_x, n_y])$	Median-Filtered ML Velocity Estimates
$\hat{\mathbf{v}}_{MED}$	Vector of Median-Filtered ML Velocity Estimates
χ_{MAX}	Detection-Statistic Threshold
$\mathbf{P_v}(\chi, \chi_{MAX}), \mathbf{P_A}(\chi, \chi_{MAX})$	Projection-Segmentation Matrices
$[\hat{\mathbf{v}}_T]_m$	Reduced-Order Vector of Target-Scatterer Velocity Estimates
$\hat{\mathbf{v}}_C$	Vector of (zero) Target-Scatterer Velocity Estimates
$[\hat{\mathbf{A}}_T]_m$	Reduced-Order Vector of Target-Scatterer Amplitude Estimates
$[\hat{\mathbf{A}}_C]_m$	Vector of Clutter-Scatterer Amplitude Estimates
$\hat{\mathbf{v}}_{L_1}$	(Sparse) Full-Order Vector of L_1 Scatterer-Velocity Estimates

As illustrated by Figure 4.4, the overall matched-filter based SAR processing algorithm consists of the following steps:

I. Form a conventional SAR image $\hat{A}_{CONV}[n_x, n_y]$ from the demodulated SAR data $f[n, k]$ by a scaled Fourier Transform (with polar-format resampling).

II. For each initial scatterer spatial location, $(n_x \Delta_x, n_y \Delta_y)$

    A. Window the conventional SAR image $\hat{A}_{CONV}[n_x, n_y]$ around the spatial location $(\Delta_x n_x, \Delta_y n_y)$ to produce $\hat{A}_W[n_x, n_y, n'_x, n'_y]$, given by

$$\hat{A}_W[n_x, n_y, n'_x, n'_y] = \hat{A}_{CONV}[n'_x, n'_y] w[n'_x - n_x, n'_y - n_y] . \qquad (4.87)$$

    B. Apply the "clutter nulling" algorithm by zeroing out all portions of the windowed image $\hat{A}_W[n_x, n_y, n'_x, n'_y]$ that have an amplitude greater than the clutter-nulling threshold $A_{CN}[n_x, n_y]$ (which is proportional to the magnitude of $\hat{A}_{CONV}[n_x, n_y]$).

    C. Fourier-Transform the windowed image $\hat{A}_W[n_x, n_y, n'_x, n'_y]$ (with respect to n'_x and n'_y) to produce $F_W[n_x, n_y, k'_x, k'_y]$, then interpolate within $F_W[n_x, n_y, k'_x, k'_y]$ (using the SVTCV phase functions) to produce the windowed phase-shifted data set $f_W[n_x, n_y, n, k]$.

    D. Reparameterize the windowed phased-shifted SAR data to form the following discrete space-time multi-dimensional signal (with the linear portion of the range-velocity phase-function $\phi_{\dot{y}}[n, k]$ removed)

$$f[k_{\dot{x}}, k_{\dot{y}}, n_x, n_y, n, k] = f_W[n_x, n_y, n, k] \delta \left[k_{\dot{x}} - \phi_{\dot{x}}[n, k] \Delta_{k_{\dot{x}}}^{-1}, k_{\dot{y}} - \phi_{\dot{y}}[n, k] \Delta_{k_{\dot{y}}}^{-1} \right] . $$

$$(4.88)$$

    E. Compute the quantized likelihood function $\hat{A}[n_x, n_y, n_{\dot{x}}, n_{\dot{y}}]$ by using the following Fourier Transform

$$\hat{A}[n_x, n_y, n_{\dot{x}}, n_{\dot{y}}] = $$
$$\frac{1}{(2K)(N)} \sum_{k_{\dot{x}}} \sum_{k_{\dot{y}}} \sum_{n} \sum_{k} f[k_{\dot{x}}, k_{\dot{y}}, n_x, n_y, n, k] e^{-j \left[k_{\dot{x}} \Delta_{k_{\dot{x}}} n_{\dot{x}} \Delta_{\dot{x}} + k_{\dot{y}} \Delta_{k_{\dot{y}}} n_{\dot{y}} \Delta_{\dot{y}} \right]} . $$

$$(4.89)$$

    F. Compute the maximum-likelihood estimates of the $2 - D$ discrete integer-valued initial-velocity functions at (n_x, n_y), given by

$$(n_{\dot{x}_{ML}}[n_x, n_y], n_{\dot{y}_{ML}}[n_x, n_y]) = \arg \max_{n_{\dot{x}}, n_{\dot{y}}} \left[\left| \hat{A}[n_x, n_y, n_{\dot{x}}, n_{\dot{y}}] \right| \right] . \qquad (4.90)$$

    G. Compute the detection statistic $\chi[n_x, n_y]$

$$\chi[n_x, n_y] = \frac{\hat{A}_{MAX}[n_x, n_y] - \hat{A}_{MEAN}[n_x, n_y]}{\sigma_{\hat{A}}[n_x, n_y]} , \qquad (4.91)$$

    where

$$\hat{A}_{MAX}[n_x, n_y] = \max_{n_{\dot{x}}, n_{\dot{y}}} \left[|\hat{A}[n_x, n_y, n_{\dot{x}}, n_{\dot{y}}]| \right] \qquad (4.92)$$

$$\hat{A}_{MEAN}[n_x, n_y] = \underset{n_x', n_y'}{\text{mean}} \ \ [\,|\hat{A}_W[n_x, n_y, n_x', n_y']|\,] \tag{4.93}$$

$$\sigma_{\hat{A}}[n_x, n_y] = \underset{n_x', n_y'}{\sigma} \ \ [\,|\hat{A}_W[n_x, n_y, n_x', n_y']|\,] \, . \tag{4.94}$$

III. Median-filter the maximum-likelihood estimates of the scatterer velocities to produce $\hat{\dot{x}}_{MED}[n_x, n_y]$ and $\hat{\dot{y}}_{MED}[n_x, n_y]$

$$\hat{\dot{x}}_{MED}[n_x, n_y] = \underset{n_x'', n_y'' \in \text{ROI}}{\text{median}} \ \hat{\dot{x}}_{ML}[n_x + n_x'', n_y + n_y''] \tag{4.95}$$

$$\hat{\dot{y}}_{MED}[n_x, n_y] = \underset{n_x'', n_y'' \in \text{ROI}}{\text{median}} \ \hat{\dot{y}}_{ML}[n_x + n_x'', n_y + n_y''] \, , \tag{4.96}$$

of the maximum-likelihood estimates given by

$$\hat{\dot{x}}_{ML}[n_x, n_y] = n_{\dot{x}_{ML}}[n_x, n_y]\Delta_{\dot{x}} \tag{4.97}$$

$$\hat{\dot{y}}_{ML}[n_x, n_y] = n_{\dot{y}_{ML}}[n_x, n_y]\Delta_{\dot{y}} \, . \tag{4.98}$$

IV. Given the vector of median-prefiltered velocity estimates $\hat{\mathbf{v}}_{MED}$, given by

$$\hat{\mathbf{v}}_{MED} = \begin{bmatrix} \vdots \\ \hat{\dot{x}}_{MED}[0, 0] \\ \hat{\dot{x}}_{MED}[0, 1] \\ \vdots \\ \hat{\dot{y}}_{MED}[0, 0] \\ \hat{\dot{y}}_{MED}[0, 1] \\ \vdots \end{bmatrix} , \tag{4.99}$$

and the vector of detection statistics χ given by

$$\chi = \begin{bmatrix} \vdots \\ \chi[0, 0] \\ \chi[0, 1] \\ \vdots \end{bmatrix} , \tag{4.100}$$

along with the detection threshold χ_{MAX}, decompose $\hat{\mathbf{v}}_{MED}$ into a (reduced-order) "target" scatterer velocity vector, $[\hat{\mathbf{v}}_T]_0$, and a "clutter" scatterer velocity-vector $\hat{\mathbf{v}}_C = \mathbf{0}$ by using the segmentation-projection matrix $\mathbf{P}_{\mathbf{v}}(\chi, \chi_{MAX})$

$$\mathbf{P}_{\mathbf{v}}(\chi, \chi_{MAX})\hat{\mathbf{v}}_{MED} = \begin{bmatrix} [\hat{\mathbf{v}}_T]_0 \\ - \\ \hat{\mathbf{v}}_C \end{bmatrix} = \begin{bmatrix} \hat{\mathbf{v}}_T \\ - \\ \mathbf{0} \end{bmatrix} . \tag{4.101}$$

In other words, for $\chi[n_x, n_y]$ greater than the threshold χ_{MAX}, the spatial location $(n_x\Delta_x, n_y\Delta_y)$ is classified as belonging to a target scatterer, with velocities given by the median prefiltered values. Otherwise, the scatterer velocities are assumed to be zero.

V. Use $[\hat{\mathbf{v}}_T]_0$ as an initial condition for following recursive reduced-order gradient-descent L_1-based velocity-estimation algorithm (where $0 \leq m \leq M_1 - 1$, with $[\hat{\mathbf{A}}_T]_0 = \mathbf{0}$ and $[\hat{\mathbf{A}}_C]_0 = \mathbf{0}$)

$$
\begin{aligned}
[\hat{\mathbf{v}}_T]_{m+1} &= [\hat{\mathbf{v}}_T]_m + \alpha_{\mathbf{v}} 2\Re \left([\hat{\mathbf{A}}_T]_m^H \frac{\partial \mathbf{F}_T^H([\hat{\mathbf{v}}_T]_m)}{\partial \mathbf{v}_T} [\mathbf{f} - \mathbf{F}_T([\hat{\mathbf{v}}_T]_m)[\hat{\mathbf{A}}_T]_m - \mathbf{F}_C[\mathbf{A}_C]_m] \right) \\
&\quad - \frac{\partial J_{\mathbf{v}_T}([\mathbf{v}_T]_m)}{\partial \mathbf{v}_T}
\end{aligned}
\tag{4.102}
$$

$$
\begin{aligned}
[\hat{\mathbf{A}}_T]_{m+1} &= [\hat{\mathbf{A}}_T]_m + \alpha \mathbf{F}_T^H([\hat{\mathbf{v}}_T]_m)[\mathbf{f} - \mathbf{F}_T([\hat{\mathbf{v}}_T]_m)[\hat{\mathbf{A}}_T]_m - \mathbf{F}_C[\mathbf{A}_C]_m] \\
&\quad - \alpha \gamma_A \operatorname{asgn}[[\hat{\mathbf{A}}_T]_m] \,,
\end{aligned}
\tag{4.103}
$$

$$
\begin{aligned}
[\hat{\mathbf{A}}_C]_{m+1} &= [\hat{\mathbf{A}}_C]_m + \alpha \mathbf{F}_C^H[\mathbf{f} - \mathbf{F}_T([\hat{\mathbf{v}}_T]_m)[\hat{\mathbf{A}}_T]_m - \mathbf{F}_C[\mathbf{A}_C]_m] \\
&\quad - \alpha \gamma_A \operatorname{asgn}[[\hat{\mathbf{A}}_C]_m] \,.
\end{aligned}
\tag{4.104}
$$

VI. Once the (reduced-order) L_1-norm target-scatterer velocity estimates $[\hat{\mathbf{v}}_T]_{M_1}$ are obtained, compute the target-scatterer amplitudes $\hat{\mathbf{A}}_T$ and the clutter-scatterer amplitudes $\hat{\mathbf{A}}_C$ by the following recursive reduced-order gradient-descent least-squares estimation algorithm (where $M_1 \leq m \leq M_2 - 1$, with $[\hat{\mathbf{A}}_T]_{M_1} = \mathbf{0}$ and $[\hat{\mathbf{A}}_C]_{M_1} = \mathbf{0}$)

$$
[\hat{\mathbf{A}}_T]_{m+1} = [\hat{\mathbf{A}}_T]_m + \alpha \mathbf{F}_T^H([\hat{\mathbf{v}}_T]_{M_1})[\mathbf{f} - \mathbf{F}_T([\hat{\mathbf{v}}_T]_{M_1})[\hat{\mathbf{A}}_T]_m - \mathbf{F}_C[\mathbf{A}_C]_m]
\tag{4.105}
$$

$$
[\hat{\mathbf{A}}_C]_{m+1} = [\hat{\mathbf{A}}_C]_m + \alpha \mathbf{F}_C^H[\mathbf{f} - \mathbf{F}_T([\hat{\mathbf{v}}_T]_{M_1})[\hat{\mathbf{A}}_T]_m - \mathbf{F}_C[\mathbf{A}_C]_m] \,.
\tag{4.106}
$$

VII. Given the full-order scatterer-velocity estimates $\hat{\mathbf{v}}_{L_1}$ (given by the following remapping of the reduced-order velocity estimates $[\hat{\mathbf{v}}_T]_{M_1}$ generated by the L_1-norm algorithm)

$$
\hat{\mathbf{v}}_{L_1} = \mathbf{P}_{\mathbf{v}}^T(\chi, \chi_{MAX}) \begin{bmatrix} [\hat{\mathbf{v}}_T]_{M_1} \\ - \\ \mathbf{0} \end{bmatrix} = \begin{bmatrix} \vdots \\ \hat{x}_{L_1}[0,0] \\ \hat{x}_{L_1}[0,1] \\ \vdots \\ \hat{y}_{L_1}[0,0] \\ \hat{y}_{L_1}[0,1] \\ \vdots \end{bmatrix} ,
\tag{4.107}
$$

and the "uncorrected" scatterer-amplitude estimates $\hat{\mathbf{A}}_U$ (given by the following remapping of the scatterer-amplitude estimates generated by the least-squares algorithm)

$$
\hat{\mathbf{A}}_U = \mathbf{P}_{\mathbf{A}}^T(\chi, \chi_{MAX}) \begin{bmatrix} [\hat{\mathbf{A}}_T]_{M_2} \\ - \\ [\hat{\mathbf{A}}_C]_{M_2} \end{bmatrix} = \begin{bmatrix} \vdots \\ \hat{A}_U[0,0] \\ \hat{A}_U[0,1] \\ \vdots \end{bmatrix} ,
\tag{4.108}
$$

use the range-velocity estimates to correct the target-scatterer amplitude estimates for azimuth displacement

$$\hat{A}_{AC}[n_x, n_y] = \hat{A}_U \left[n_x - \frac{1}{\Delta_x} \frac{1}{\hat{\theta}} \hat{y}_{L_1}[n_x, n_y], n_y \right] \ . \tag{4.109}$$
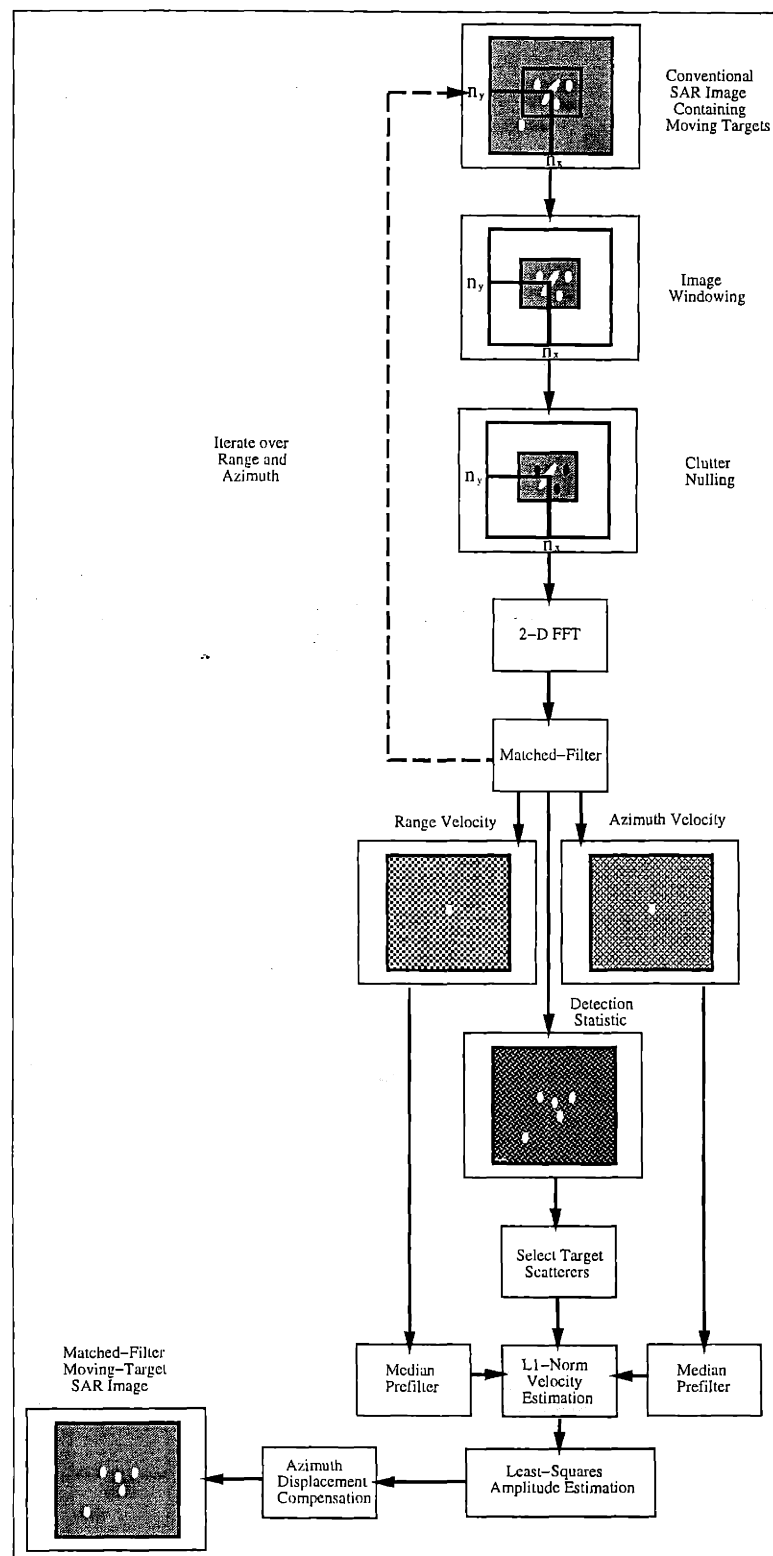
Figure 4.4: Matched-Filter Algorithm

4.6   Performance Analysis

As presented in this chapter, the matched-filter SAR processing technique uses the following decision rule (based upon the detection statistic $\chi[n_x, n_y]$)

$$\chi[n_x, n_y] \overset{Target}{\underset{Clutter}{\gtrless}} \chi_{MAX} , \tag{4.110}$$

for determining the presence of a "target" point-scatterer at a given spatial location $(n_x\Delta_x, n_y\Delta_y)$. If this rule decides that a (possibly moving) target is present, the matched filter then provides estimates of both the range velocity and azimuth velocity of this point-scatterer (otherwise, the matched-filter assumes that the point-scatterer at this spatial location corresponds to stationary clutter, with both a range velocity and an azimuth velocity of zero). These scatterer-velocity estimates are then used as an initial estimate by the L_1-norm based velocity-estimation algorithm.

Ultimately, we would like to use the results of the matched-filter SAR processing algorithm for the purpose of automatic target recognition. For this particular purpose, it would be useful to analyze (and quantify) both the detection performance and the estimation performance of the matched-filter algorithm. In this section, we present such a performance analysis (first for the presence of additive noise, then for the presence of interfering scatterers).

4.6.1   Monte Carlo Performance Analysis

In order to analyze the detection and estimation performance of the matched filter, we consider the following *binary hypothesis problem* for the demodulated SAR data $f[n, k]$

$$H_1 : \quad f[n, k] = A[0, 0]e^{-j\left[\phi_{\dot{x}}[n,k]n_{\dot{x}}[0,0]\Delta_{\dot{x}} + \phi_{\dot{y}}[n,k]n_{\dot{y}}[0,0]\Delta_{\dot{y}}\right]} +$$

$$\sum_{n_x \neq 0}\sum_{n_y \neq 0} A[n_x, n_y]e^{-j\left[\phi_x[n,k]n_x\Delta_x + \phi_y[n,k]n_y\Delta_y + \phi_{\dot{x}}[n,k]n_{\dot{x}}[n_x,n_y]\Delta_{\dot{x}} + \phi_{\dot{y}}[n,k]n_{\dot{y}}[n_x,n_y]\Delta_{\dot{y}}\right]}$$

$$+\eta[n, k]$$

$$H_0 : \quad f[n, k] =$$

$$\sum_{n_x \neq 0}\sum_{n_y \neq 0} A[n_x, n_y]e^{-j\left[\phi_x[n,k]n_x\Delta_x + \phi_y[n,k]n_y\Delta_y + \phi_{\dot{x}}[n,k]n_{\dot{x}}[n_x,n_y]\Delta_{\dot{x}} + \phi_{\dot{y}}[n,k]n_{\dot{y}}[n_x,n_y]\Delta_{\dot{y}}\right]}$$

$$+\eta[n, k] , \tag{4.111}$$

where the additive noise $\eta[n, k]$ is circularly-complex spatially-independent Gaussian noise (with variance σ_η^2). We also have a set of interfering scatterers with initial spatial-locations $(n_x\Delta_x, n_y\Delta_y)$ and initial velocities $(\dot{x}[n_y, n_y], \dot{y}[n_x, n_y]) = (n_{\dot{x}}[n_x, n_y]\Delta_{\dot{x}}, n_{\dot{y}}[n_x, n_y]\Delta_{\dot{y}})$. For hypothesis H_1, we have a single "target" point-scatterer at the initial spatial-location $(n_x\Delta_x, n_y\Delta_y) = (0m, 0m)$ (which is not equal to any of the initial spatial-locations of the interfering scatterers) and initial velocity $(\dot{x}[0, 0], \dot{y}[0, 0]) = (n_{\dot{x}}[0, 0]\Delta_{\dot{x}}, n_{\dot{y}}[0, 0]\Delta_{\dot{y}})$. Otherwise, we just have the interfering scatterers, plus the additive noise. In matrix-vector form,

this binary hypothesis problem is given by

$$H_1: \quad \mathbf{f} = A[0,0]\mathbf{s_v}[0,0] + \sum_{n_x \neq 0} \sum_{n_y \neq 0} A[n_x, n_y]\mathbf{s_v}[n_x, n_y] + \eta$$

$$H_0: \quad \mathbf{f} = \sum_{n_x \neq 0} \sum_{n_y \neq 0} A[n_x, n_y]\mathbf{s_v}[n_x, n_y] + \eta \ , \tag{4.112}$$

where the velocity-parameter vector $\mathbf{v}$ is given by

$$\mathbf{v} = \begin{bmatrix} \vdots \\ \dot{x}[0,0] \\ \dot{x}[0,1] \\ \vdots \\ \dot{y}[0,0] \\ \dot{y}[0,1] \\ \vdots \end{bmatrix} = \begin{bmatrix} \vdots \\ n_{\dot{x}}[0,0]\Delta_{\dot{x}} \\ n_{\dot{x}}[0,1]\Delta_{\dot{x}} \\ \vdots \\ n_{\dot{y}}[0,0]\Delta_{\dot{y}} \\ n_{\dot{y}}[0,1]\Delta_{\dot{y}} \\ \vdots \end{bmatrix} . \tag{4.113}$$

The matched-filter target-scatterer decision rule for this problem is given by

$$\chi_0(\mathbf{f}) \underset{H_0}{\overset{H_1}{\gtrless}} \chi_{MAX} \ , \tag{4.114}$$

where $\chi_0(\mathbf{f}) = \chi[0,0]$ is the matched-filter detection statistic corresponding to the initial spatial location, $(n_x\Delta_x, n_y\Delta_y) = (0m, 0m)$.

Since it is assumed that the *a priori* probabilities of the two hypotheses are unknown, we must analyze the the detection performance of the matched-filter decision rule by computing the following *Neyman-Pearson* criterion[21]

$$P_D(\chi_{MAX}) = \int_{\chi_{MAX}}^{+\infty} p_{\chi_0|H_1}(\chi_0|H_1)d\chi_0 \tag{4.115}$$

$$P_F(\chi_{MAX}) = \int_{\chi_{MAX}}^{+\infty} p_{\chi_0|H_0}(\chi_0|H_0)d\chi_0 \ , \tag{4.116}$$

where $P_D(\chi_{MAX})$ is the so-called *probability of detection* (i.e., the probability of the decision rule saying that there is a target point-scatterer when there actually is one), and where $P_F(\chi_{MAX})$ is the so-called *probability of false alarm* (i.e., the probability of the decision rule saying that there is a target point-scatterer when there actually is not).

In order to compute the Neyman-Pearson criterion for the matched-filter decision rule , we need to first determine the conditional probability densities, $p_{\chi_0|H_1}(\chi_0|H_1)$ and $p_{\chi_0|H_0}(\chi_0|H_0)$, of χ_0 given the respective hypotheses H_1 and H_0. However, the detection statistic $\chi_0(\mathbf{f})$ is a *nonlinear function of the target point-scatterer parameters, the interfering point-scatterer parameters and the additive-noise parameters*, which implies that it may not be possible to compute a "closed-form" representation of the conditional probabilities as a function of these parameters. However, we can estimate the Neyman-Pearson criterion

by performing a *Monte Carlo* based simulation analysis of the matched-filter algorithm. For a given set of target point-scatterer parameters, interfering point-scatterer parameters, and noise parameters, we first generate the following synthetic SAR data sets (under hypotheses H_1 and H_0), $\{f_1|H_1, f_2|H_1, \ldots, f_M|H_1\}$ and $\{f_1|H_0, f_2|H_0, \ldots, f_M|H_0\}$, (where M is the number of Monte Carlo "trials"). These synthetic data sets are then used to generate the following sets of detection statistics, $\{\chi_0(f_1|H_1), \chi_0(f_2|H_1), \ldots, \chi_0(f_M|H_1)\}$ and $\{\chi_0(f_1|H_0), \chi_0(f_2|H_0), \ldots, \chi_0(f_M|H_0)\}$. Then the estimate, $\hat{P}_F(\chi_{MAX})$, of the probability-of-detection is given by the number of detection statistics in the set $\{\chi_0(f_1|H_1), \chi_0(f_2|H_1), \ldots, \chi_0(f_M|H_1)\}$ which exceed the threshold χ_{MAX} (divided by the number of Monte Carlo trials, M),i.e.,

$$\hat{P}_D(\chi_{MAX}) = \frac{\#\{\chi_0 \in \{\chi_0(f_1|H_1), \chi_0(f_2|H_1), \ldots, \chi_0(f_M|H_1)\}|\chi_0 \geq \chi_{MAX}\}}{M} . \quad (4.117)$$

The corresponding estimate, $\hat{P}_F(\chi_{MAX})$, of the probability-of-false-alarm is given by the number of detection statistics in the set $\{\chi_0(f_1|H_0), \chi_0(f_2|H_0), \ldots, \chi_0(f_M|H_0)\}$ which exceed the threshold χ_{MAX} (divided by the number of Monte Carlo trials, M),i.e.,

$$\hat{P}_F(\chi_{MAX}) = \frac{\#\{\chi_0 \in \{\chi_0(f_1|H_0), \chi_0(f_2|H_0), \ldots, \chi_0(f_M|H_0)\}|\chi_0 \geq \chi_{MAX}\}}{M} . \quad (4.118)$$

If we plot the probability-of-detection versus the probability-of-false-alarm for a given set of model parameters, we get what is known in the literature[21] as a Receiver Operating Characteristic (ROC) curve for this detection scheme. From the literature[21], it can be shown that the estimates of $P_D(\chi_{MAX})$ and $P_F(\chi_{MAX})$ are unbiased, with error variances approximately given by

$$
\begin{aligned}
\sigma^2\left[\hat{P}_D(\chi_{MAX})\right] &= E\left[\left(\hat{P}_D(\chi_{MAX}) - P_D(\chi_{MAX})\right)^2\right] \\
&= \frac{P_D(\chi_{MAX})(1 - P_D(\chi_{MAX}))}{M} \\
&\approx \frac{\hat{P}_D(\chi_{MAX})(1 - \hat{P}_D(\chi_{MAX}))}{M} \quad (4.119)
\end{aligned}
$$

$$
\begin{aligned}
\sigma^2\left[\hat{P}_F(\chi_{MAX})\right] &= E\left[\left(\hat{P}_F(\chi_{MAX}) - P_F(\chi_{MAX})\right)^2\right] \\
&= \frac{P_F(\chi_{MAX})(1 - P_F(\chi_{MAX}))}{M} \\
&\approx \frac{\hat{P}_F(\chi_{MAX})(1 - \hat{P}_F(\chi_{MAX}))}{M} . \quad (4.120)
\end{aligned}
$$

For the Monte Carlo results presented in this chapter, we used these expressions to compute one-standard-deviation "error bars" for the receiver-operating-characteristic curves. Note that since we are using the estimates $\hat{P}_D(\chi_{MAX})$ and $\hat{P}_F(\chi_{MAX})$ rather than the actual probabilities, $P_D(\chi_{MAX})$ and $P_F(\chi_{MAX})$, these error bars will tend to be smaller than the actual error standard-deviation when either $\hat{P}_D(\chi_{MAX})$ or $\hat{P}_F(\chi_{MAX})$ are near 0 or 1.

Recall that the matched-filter also provides estimates $\dot{x}_{ML}(\mathbf{f}) = \dot{x}_{ML}[0,0] = n_{\dot{x}_{ML}}[0,0]\Delta_{\dot{x}}$ and $\dot{y}_{ML}(\mathbf{f}) = \dot{y}_{ML}[0,0] = n_{\dot{y}_{ML}}[0,0]\Delta_{\dot{y}}$ of both the azimuth velocity and range velocity of the scatterer at $(0,0)$. Given hypothesis H_1 (i.e., we actually have a target point-scatterer with initial spatial-location $(0,0)$ and initial velocity $(\dot{x}[0,0], \dot{y}[0,0]) = (n_{\dot{x}}[0,0]\Delta_{\dot{x}}, n_{\dot{y}}[0,0]\Delta_{\dot{y}})$), we can analyze the velocity-estimation performance of the matched-filter from the following sets of synthetic Monte Carlo velocity data, $\{\dot{x}_{ML}(\mathbf{f}_1|H_1), \dot{x}_{ML}(\mathbf{f}_2|H_1), \ldots, \dot{x}_{ML}(\mathbf{f}_M|H_1)\}$ and $\{\dot{y}_{ML}(\mathbf{f}_1|H_1), \dot{y}_{ML}(\mathbf{f}_2|H_1), \ldots, \dot{y}_{ML}(\mathbf{f}_M|H_1)\}$. For example, given the actual target point-scatterer velocities of $(\dot{x}[0,0], \dot{y}[0,0])$, the approximate *mean-square velocity-estimation errors* are given by

$$
\begin{aligned}
E\left[(\dot{x}_{ML}(\mathbf{f}|H_1) - \dot{x}[0,0])^2\right] &= E\left[(\dot{x}_{ML}(\mathbf{f}|H_1) - E[\dot{x}_{ML}(\mathbf{f}|H_1)])^2\right] \\
&\quad + (E[\dot{x}_{ML}(\mathbf{f}|H_1)] - \dot{x}[0,0]])^2 \\
&= \sigma^2\left[\dot{x}_{ML}(\mathbf{f}|H_1)\right] + (b(\dot{x}_{ML}(\mathbf{f}|H_1)|\dot{x}[0,0])))^2 \quad (4.121)
\end{aligned}
$$

$$
\begin{aligned}
E\left[(\dot{y}_{ML}(\mathbf{f}|H_1) - \dot{y}[0,0])^2\right] &= E\left[(\dot{y}_{ML}(\mathbf{f}|H_1) - E[\dot{y}_{ML}(\mathbf{f}|H_1)])^2\right] \\
&\quad + (E[\dot{y}_{ML}(\mathbf{f}|H_1)] - \dot{y}[0,0]])^2 \\
&= \sigma^2\left[\dot{y}_{ML}(\mathbf{f}|H_1)\right] + (b(\dot{y}_{ML}(\mathbf{f}|H_1)|\dot{y}[0,0])))^2 \quad ,(4.122)
\end{aligned}
$$

where $\sigma^2[.]$ is the sample variance and $b(.)$ is the *estimation bias*.

4.6.2 Performance in the Presence of Additive Noise with No Interfering Scatterers

Here, we present a Monte Carlo analysis of the noisy-data detection and velocity-estimation performance of the matched-filter algorithm (where we have no nearby interfering scatterers). The parameters of the estimation-theoretic model used to generate the synthetic Monte Carlo SAR data (plus the parameters of the matched-filter) are shown in Table 4.1. The estimation-theoretic model parameters were chosen to be as similar as possible to the 33.5 GHz Lincoln Laboratory Advanced Detection and Tracking System (ADTS)[16] system operating in spotlight mode. Since we are interested in the "worst-case" detection and velocity-estimation performance of the matched-filter, we did not use the clutter-nulling algorithm (which was discussed in Section 4.4.2) for reducing cross-scatterer interference.

Stationary Target Scatterer

For this case, the target point-scatterer (which under hypothesis H_1 was located at the center of the illuminated target field, $(n_x\Delta_x, n_y\Delta_y) = (0m, 0m)$) was stationary, i.e., $(n_{\dot{x}}[0,0]\Delta_{\dot{x}}, n_{\dot{y}}[0,0]\Delta_{\dot{y}}) = (0m/s, 0m/s)$. The magnitude of the point-scatterer amplitude was unit-magnitude, i.e., $|A[0,0]| = 1$. For each Monte Carlo trial the phase angle of the target point-scatterer amplitude was a random variable uniformly distributed between 0 and 2π. We ran $M = 100$ Monte Carlo trials (under both hypotheses H_1 and H_0) for *signal-to-noise ratios (SNR)* (defined by $SNR = 20\log_{10}\left(\frac{|A[0,0]|}{\sigma_\eta}\right)$) of $20dB$, $14dB$, $9.5dB$, $6dB$, and $0dB$.

F_c	Center Frequency	33.5 GHz
λ_c	Center Wavelength	0.009 m
αT_p	Chirp Bandwidth	1.2 GHz
f_{PRF}	Pulse Repetition Frequency	128 pulse/s
N	Complex Samples per Range Profile	64
$2K$	Pulses per Synthetic Aperture	128
R_o	Center Slant-Range	2778 M
v	SAR Platform Velocity	100 m/s
$\dot{\theta}$	Look-Angle Rotation Rate	0.036 rad/s
$2T$	Dwell Time	1.0 s
L	Synthetic-Aperture Length	100 m
Δ_y	Range Sampling Interval	0.125 m
Δ_x	Azimuth Sampling Interval	0.125 m
δ_y	Range Resolution	0.25 m
δ_x	Azimuth Resolution	0.25 m
$\Delta_{\dot{y}}$	MF Range-Velocity Quantization	0.25 m/s
$\Delta_{\dot{x}}$	MF Azimuth-Velocity Quantization	0.5 m/s
Δ_{W_y}	Range Width of MF Image-Window	4 m
Δ_{W_x}	Azimuth Width of MF Image-Window	8 m

Table 4.1: System Parameters for Monte Carlo Analysis of Matched-Filter

Figure 4.5 shows a plot of the approximate probability-of-detection and probability-of-false-alarm, versus the detection-rule threshold χ_{MAX}, for an SNR of $20dB$ (with error bars equal to the estimated error standard-deviation). Here, we see that for $6 \leq \chi_{MAX} \leq 22$, $P_D(\chi_{MAX})$ is approximately unity, and $P_F(\chi_{MAX})$ is approximately zero. This implies that for this range of threshold values, the matched-filter detection-rule has *near-perfect discrimination between the hypotheses H_1 and H_0*. Figure 4.6 shows a plot of the approximate probability-of-detection and probability-of-false-alarm, versus the detection-rule threshold χ_{MAX}, for $SNR = 14dB$. We see that the probability-of-false-alarm is essentially the same as the $SNR = 20dB$ case. However, the probability-of-detection is somewhat lower. The range of threshold values that give near-perfect discrimination between the hypotheses H_1 and H_0 is now only $6 \leq \chi_{MAX} \leq 8$.

For an SNR of $9.5dB$ (shown in Figure 4.7), we see that we can no longer pick a detection threshold that has near-perfect discrimination between the hypotheses. However, we can still make a trade-off between the probability-of-detection and the probability-of-false-alarm. For example, if we desire a probability-of-false-alarm of $P_F(\chi_{MAX}) = 0$, we can choose a detection threshold of $\chi_{MAX} = 6$, which gives a probability-of-detection of about $P_D(\chi_{MAX}) = 0.85$. But if we choose a slightly lower detection threshold of $\chi_{MAX} = 5$, we get a slightly higher probability-of-false-alarm of about $P_F(\chi_{MAX}) = 0.1$, and a slightly higher probability-of-detection of about $P_D(\chi_{MAX}) = 0.95$.

For an SNR of $6dB$ (shown in Figure 4.8), the detection performance of the matched-filter begins to fall to somewhat poor levels. For example, if we again choose a detection threshold of $\chi_{MAX} = 5$, we again get a probability-of-false-alarm of about $P_F(\chi_{MAX}) = 0.1$.

SNR	Azimuth Vel. Var.	Azimuth Vel. Bias	Range Vel. Var.	Range Vel. Bias
0 dB	84.58 m^2/s^2	- 1.29 m/s	6.05 m^2/s^2	- 0.01 m/s
6 dB	24.11 m^2/s^2	0.02 m/s	2.00 m^2/s^2	- 0.09 m/s
9.5 dB	4.33 m^2/s^2	- 0.02 m/s	0.19 m^2/s^2	- 0.03 m/s
14 dB	0.00 m^2/s^2	0.00 m/s	0.00 m^2/s^2	0.00 m/s
20 dB	0.00 m^2/s^2	0.00 m/s	0.00 m^2/s^2	0.00 m/s

Table 4.2: Matched-Filter Velocity-Estimation Performance for Noisy-Data, Stationary Target-Scatterer Examples

But we get a probability-of-detection of only about $P_D(\chi_{MAX}) = 0.4$ (which is less than half of the probability-of-detection for the 9.5dB case). And for an SNR of 0dB, the probability-of-false-alarm and the probability-of-detection are approximately equal for all detection thresholds, which implies that *the matched-filter would be unable to discriminate between the two hypotheses*. For comparison purposes, we also show the Receiver Operating Characteristic (ROC) curves in Figure 4.10. Since we have near perfect discrimination for the 20dB and the 14dB cases, both of the corresponding ROC curves will lie along the lines $P_F = 0(0 \leq P_D \leq 1)$ and $P_D = 1(0 \leq P_F \leq 1)$. Again, we see that the performance of the matched-filter detection scheme is marginally acceptable for the 9.5dB case, and drops dramatically for the lower SNR's.

We analyzed the noisy-data stationary-target velocity-estimation performance of the matched-filter (for SNR's of 9.5dB, 6dB, 9.5dB, 6dB,and 0dB) by computing the sample variance and bias of the the Monte Carlo range-velocity and azimuth-estimates, as shown in Table 4.2. For SNR's of 20dB and 14dB, we essentially have zero estimation error in both range velocity and azimuth velocity, which of course implies that the matched-filter will generally do an excellent job of estimating these quantities for a SNR above 14dB. For an SNR of 9.5dB, we begin to see some degradation in the velocity-estimation performance, especially in the azimuth velocity. This also goes along with the fact that we no longer have "perfect" detection (as discussed previously). And for SNR's of 6dB and 0dB, the estimation-performance of the matched-filter has fallen to completely unacceptable levels.
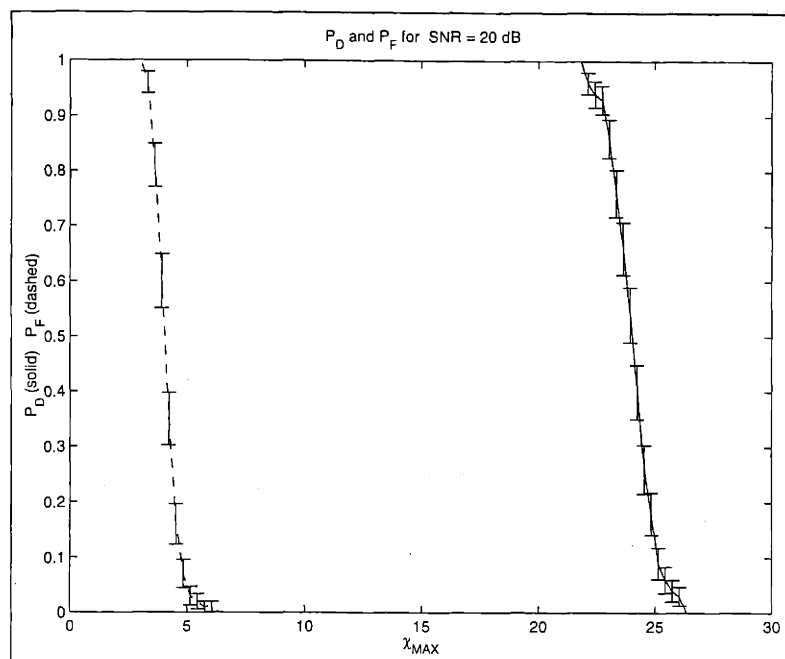
Figure 4.5: $P_D(\chi_{MAX})$ and $P_F(\chi_{MAX})$ for $SNR = 20dB$ (Stationary Target-Scatterer) with One-Standard-Deviation Error Bars
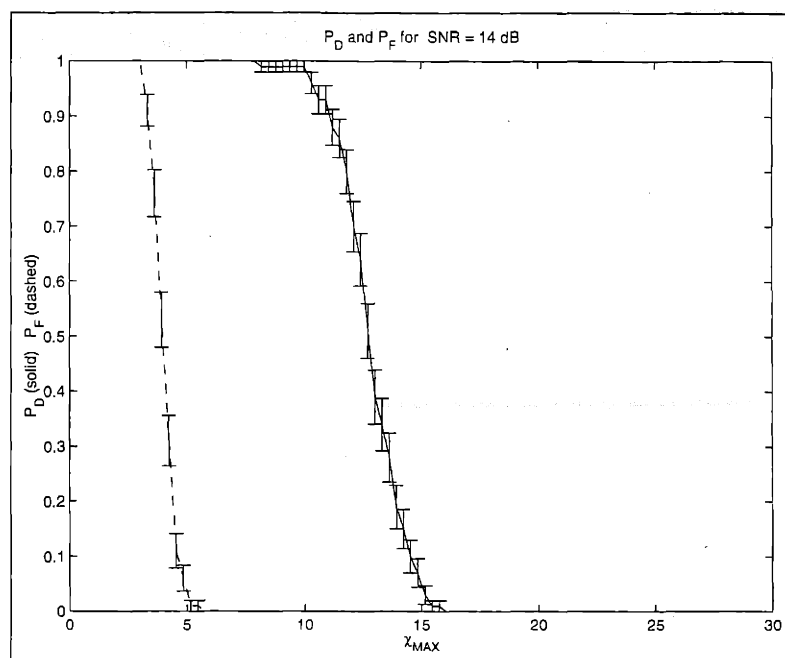
Figure 4.6: $P_D(\chi_{MAX})$ and $P_F(\chi_{MAX})$ for $SNR = 14dB$ (Stationary Target-Scatterer) with One-Standard-Deviation Error Bars
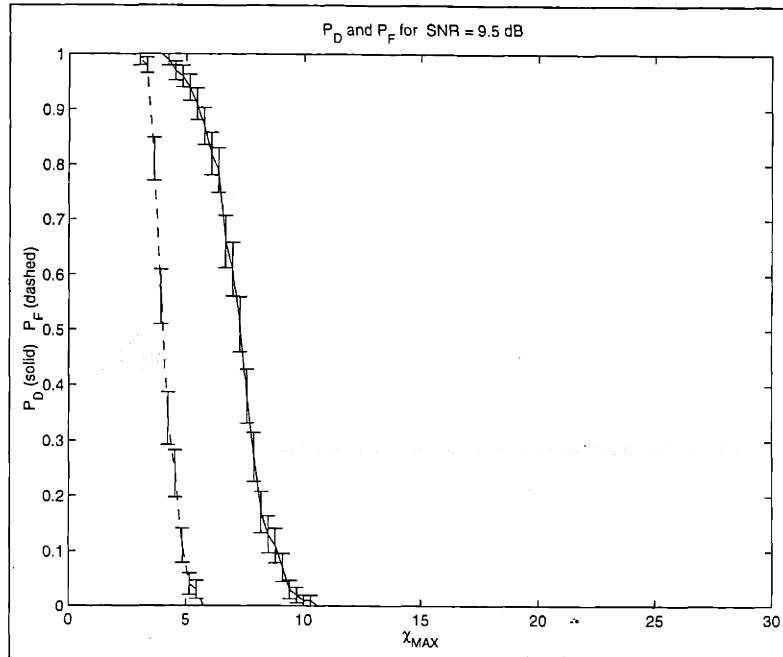
Figure 4.7: $P_D(\chi_{MAX})$ and $P_F(\chi_{MAX})$ for $SNR = 9.5dB$ (Stationary Target-Scatterer) with One-Standard-Deviation Error Bars
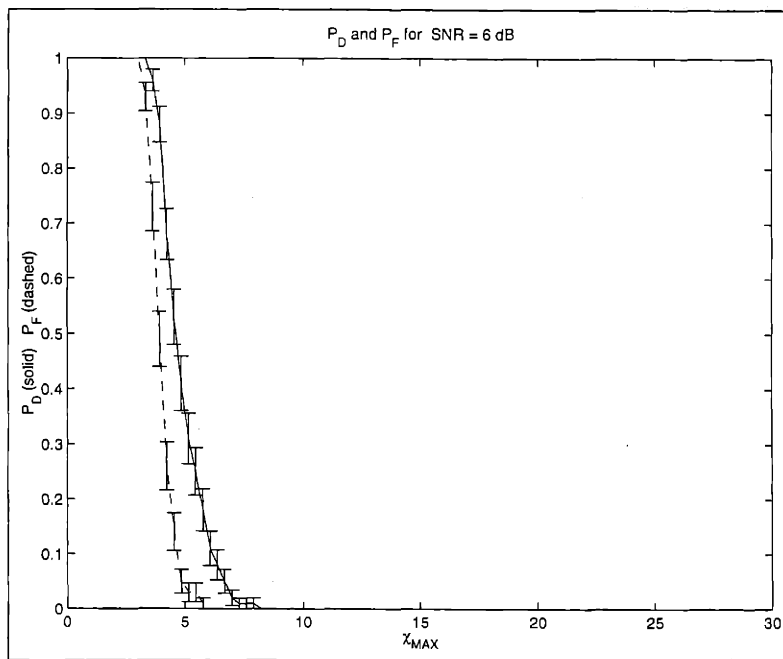
Figure 4.8: $P_D(\chi_{MAX})$ and $P_F(\chi_{MAX})$ for $SNR = 6dB$ (Stationary Target-Scatterer) with One-Standard-Deviation Error Bars
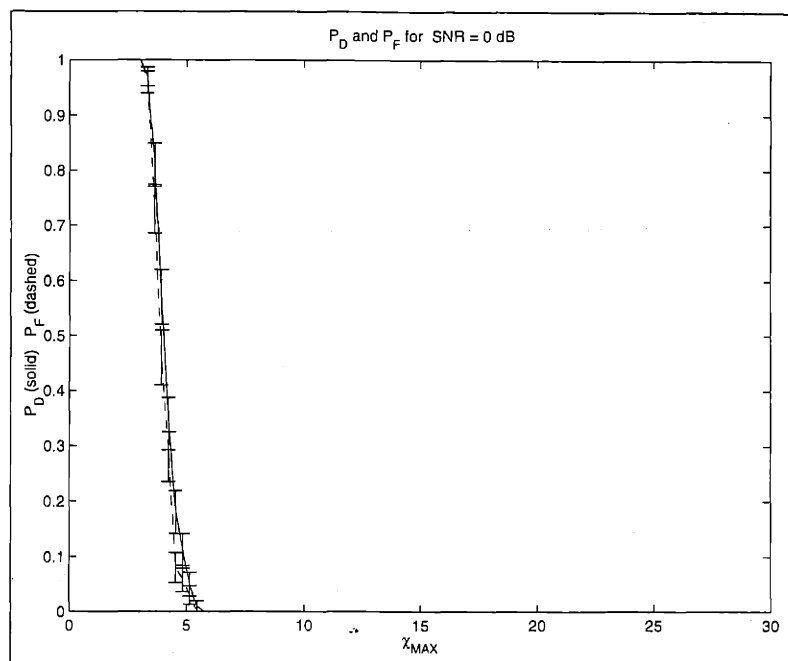
Figure 4.9: $P_D(\chi_{MAX})$ and $P_F(\chi_{MAX})$ for $SNR = 0dB$ (Stationary Target-Scatterer) with One-Standard-Deviation Error Bars
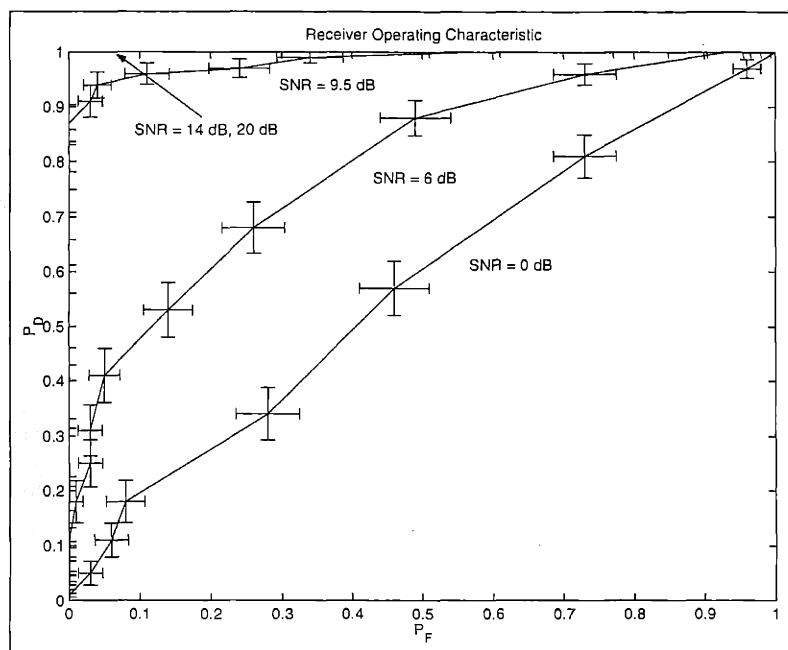
Figure 4.10: Receiver Operating Characteristic (Stationary Target-Scatterer) with One-Standard-Deviation Error Bars

Moving Target Scatterer

For this case, we analyzed the noisy-data detection and velocity-estimation performance of the matched-filter for a moving target point-scatterer. Just as with the previous example, we have no interfering scatterers. Here, the initial-position of the target point-scatterer (under hypothesis H_1) was again located at the center of the illuminated target field, $(n_x\Delta_x, n_y\Delta_y) = (0m, 0m)$. However, the initial velocity of the target point-scatterer was now given by $(\dot{x}[0,0], \dot{y}[0,0]) = (n_{\dot{x}}[0,0]\Delta_{\dot{x}}, n_{\dot{y}}[0,0]\Delta_{\dot{y}}) = (1m/s, 1.152m/s)$. The point-scatterer amplitude was unit-magnitude ($|A[0,0]| = 1$) with a random complex phase angle (uniformly distributed between 0 and 2π for each Monte Carlo trial). We ran $M = 100$ Monte Carlo trials (under both hypotheses H_1 and H_0) for signal-to-noise ratios (SNR) of $20dB$, $14dB$, $9.5dB$, $6dB$, and $0dB$.

Figure 4.11 shows a plot of the approximate probability-of-detection and probability-of-false-alarm, versus the detection-rule threshold χ_{MAX}, for an SNR of $20dB$. Similarly to the stationary target-scatterer case, $P_D(\chi_{MAX})$ is approximately unity, and $P_F(\chi_{MAX})$ is approximately zero (for the range $6 \leq \chi_{MAX} \leq 19$). Therefore, even for the moving target-scatterer case, the matched-filter detection-rule can have *near-perfect discrimination between the hypotheses H_1 and H_0* (though the range of detection-rule thresholds is slightly less than for the stationary target-scatterer case). Figure 4.12 shows a plot of the approximate probability-of-detection and probability-of-false-alarm, versus the detection-rule threshold χ_{MAX}, for $SNR = 14dB$. We see that the probability-of-detection is again somewhat lower than for the $SNR = 20dB$ case. As compared to the stationary target case, the range of threshold values that give near-perfect discrimination between the hypotheses H_1 and H_0 is now only about $6 \leq \chi_{MAX} \leq 7$.

For an SNR of $9.5dB$ (shown in Figure 4.13), we see that just as with the stationary target case, we can no longer pick a detection threshold that has near-perfect discrimination between the hypotheses, but must now make a trade-off between the probability-of-detection and the probability-of-false-alarm. For example, if we desire a probability-of-false-alarm of $P_F(\chi_{MAX}) = 0.1$, we choose a detection threshold of $\chi_{MAX} = 5$, which gives a probability-of-detection of about $P_D(\chi_{MAX}) = 0.65$ (which is significantly lower than the corresponding probability-of-detection $P_D(\chi_{MAX}) = 0.95$ for the stationary target scatterer case). Just as with the stationary target-scatterer case, for SNR's of $6dB$ and $0dB$ (shown in Figure 4.14 and Figure 4.15), the detection performance of the matched-filter begins to fall to fairly poor levels. We also show a plot (in Figure 4.16) of the receiver operating characteristic (ROC) curves. Since we have near perfect discrimination for the $20dB$ and the $14dB$ cases, both the corresponding ROC curves will lie along the lines $P_F = 0(0 \leq P_D \leq 1)$ and $P_D = 1(0 \leq P_F \leq 1)$, just as with the previous stationary-target case. We also see that the performance of the matched-filter detection scheme drops even more dramatically for SNR's less than or equal to $14dB$, as compared to the stationary-target case. In fact, we see in the ROC curve plot of Figure 4.16 that the ROC curve for the $SNR = 0dB$ is no longer strictly convex, but instead nearly lies on the line $P_D = P_F$. This implies that the matched-filter detection scheme performs only marginally better than purely random guessing for this low SNR case.

As shown in Table 4.3, for SNR's of $20dB$ and $14dB$, we essentially have zero estimation error for azimuth velocity. However, we do have a small estimation error for range-velocity

SNR	Azimuth Vel. Var.	Azimuth Vel. Bias	Range Vel. Var.	Range Vel. Bias
0 dB	75.57 m^2/s^2	- 0.76 m/s	5.42 m^2/s^2	- 1.00 m/s
6 dB	47.38 m^2/s^2	- 1.15 m/s	3.74 m^2/s^2	- 0.71 m/s
9.5 dB	7.61 m^2/s^2	0.20 m/s	0.63 m^2/s^2	- 0.12 m/s
14 dB	0.00 m^2/s^2	0.0 m/s	0.01 m^2/s^2	- 0.07 m/s
20 dB	0.00 m^2/s^2	0.0 m/s	0.01 m^2/s^2	- 0.11 m/s

Table 4.3: Matched-Filter Velocity-Estimation Performance for Noisy-Data, Moving Target-Scatterer Examples

(which is caused by the range-velocity quantization of the matched-filter). For a SNR of $9.5dB$, we begin to see some degradation in the velocity-estimation performance. This again goes along with the fact that we no longer have "perfect" detection for this case. And for SNR's of $6dB$ and $0dB$, the estimation-performance of the matched-filter has fallen to completely undesirable levels.
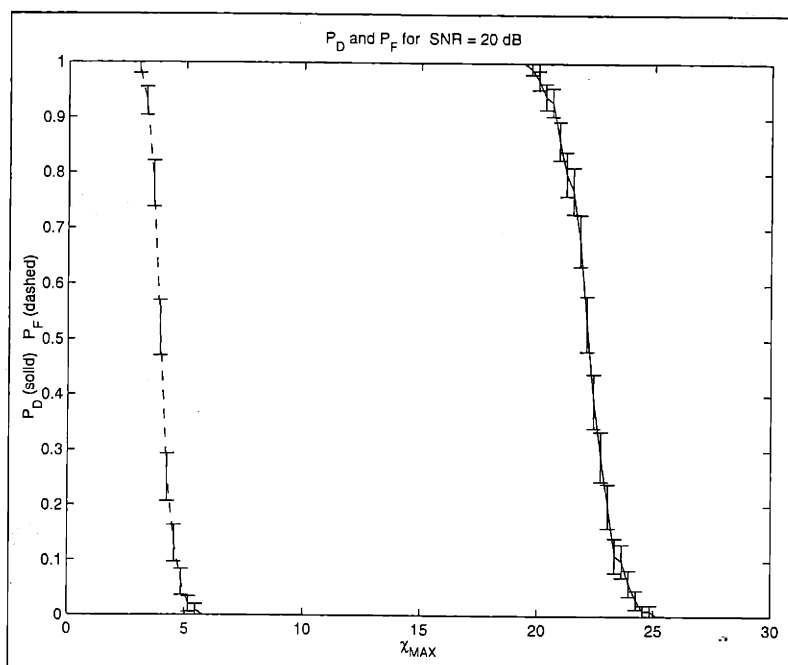
Figure 4.11: $P_D(\chi_{MAX})$ and $P_F(\chi_{MAX})$ for $SNR = 20dB$ (Moving Target-Scatterer) with One-Standard-Deviation Error Bars
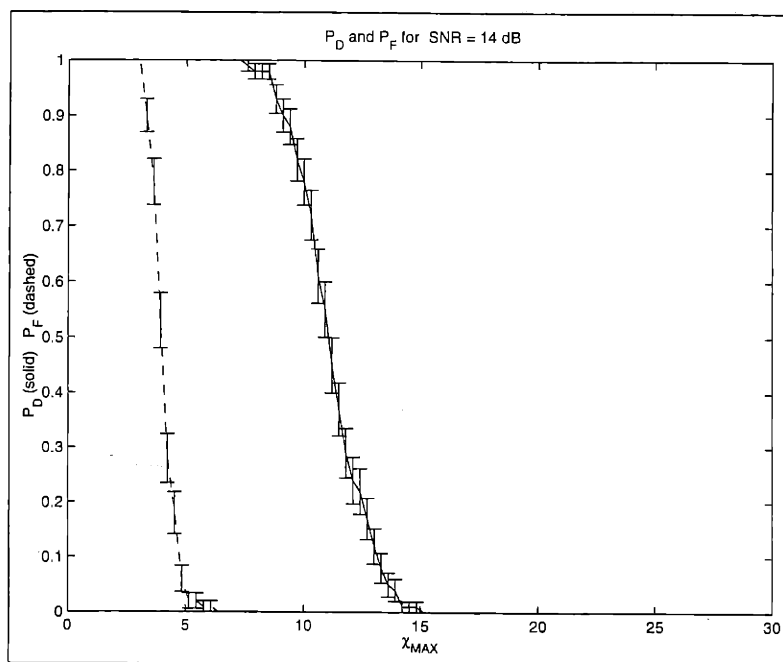
Figure 4.12: $P_D(\chi_{MAX})$ and $P_F(\chi_{MAX})$ for $SNR = 14dB$ (Moving Target-Scatterer) with One-Standard-Deviation Error Bars

Figure 4.13: $P_D(\chi_{MAX})$ and $P_F(\chi_{MAX})$ for $SNR = 9.5dB$ (Moving Target-Scatterer) with One-Standard-Deviation Error Bars

Figure 4.14: $P_D(\chi_{MAX})$ and $P_F(\chi_{MAX})$ for $SNR = 6dB$ (Moving Target-Scatterer) with One-Standard-Deviation Error Bars

Figure 4.15: $P_D(\chi_{MAX})$ and $P_F(\chi_{MAX})$ for $SNR = 0dB$ (Moving Target-Scatterer) with One-Standard-Deviation Error Bars
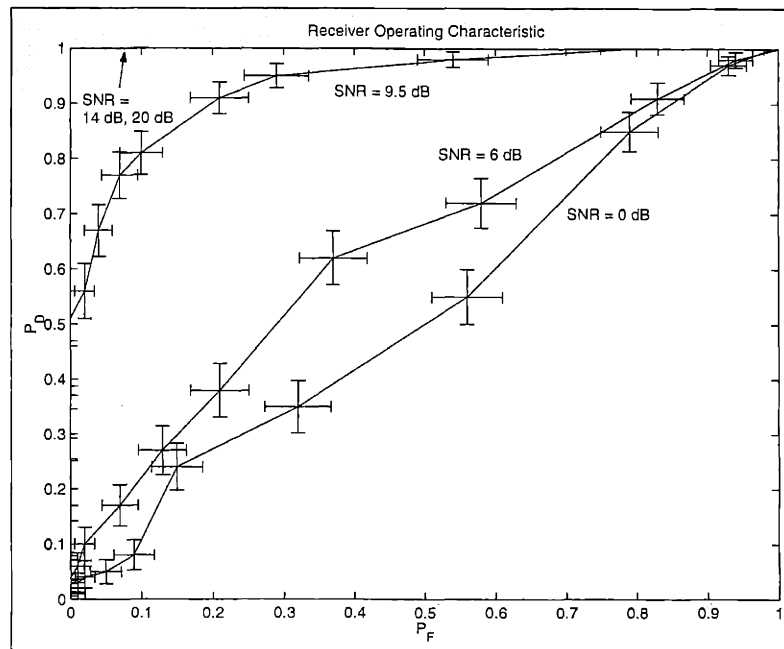
Figure 4.16: Receiver Operating Characteristic (Moving Target-Scatterer) with One-Standard-Deviation Error Bars

4.6.3   Performance in the Presence of Interfering Scatterers

Here, we present a Monte Carlo analysis of the matched-filter's detection and velocity-estimation performance in the presence of interfering point-scatterers. The parameters of the estimation-theoretic model used to generate the synthetic Monte Carlo SAR data (plus the parameters of the matched-filter) are again shown in Table 4.1. As with the previous noisy-data examples, these model parameters were chosen to be as similar as possible to the 33.5 GHz Lincoln Laboratory Advanced Detection and Tracking System (ADTS)[16] system operating in spotlight mode. Again, we did not use the clutter-nulling algorithm for reducing cross-scatterer interference.

For the Monte Carlo analysis presented in this section, the experimental set-up involved a $2 - D$ "square box" (of variable size) of eight interfering scatterers with initial spatial locations surrounding the initial-position of the target point-scatterer. As shown in in Figure 4.17, this box was centered at the spatial location $(n_x \Delta_x, n_y \Delta_y) = (0, 0)$ of the target scatterer. The size of this box was given by 2δ m, which implied that the spatial locations of the interfering scatterers were given by

Scatterer #1: $(n_x \Delta_x, n_y \Delta_y) = (\delta_0 \ m, 0 \ m)$

Scatterer #2: $(n_x \Delta_x, n_y \Delta_y) = (-\delta_0 \ m, 0 \ m)$

Scatterer #3: $(n_x \Delta_x, n_y \Delta_y) = (0 \ m, \delta_0 \ m)$

Scatterer #4: $(n_x \Delta_x, n_y \Delta_y) = (0 \ m, -\delta_0 \ m)$

Scatterer #5: $(n_x \Delta_x, n_y \Delta_y) = (\delta_0 \ m, \delta_0 \ m)$

Scatterer #6: $(n_x \Delta_x, n_y \Delta_y) = (-\delta_0 \ m, \delta_0 \ m)$

Scatterer #7: $(n_x \Delta_x, n_y \Delta_y) = (\delta_0 \ m, -\delta_0 \ m)$

Scatterer #8: $(n_x \Delta_x, n_y \Delta_y) = (-\delta_0 \ m, -\delta_0 \ m)$

As shown Figure 4.17, we see that the spatial separation (in both range and azimuth) between the interfering scatterers and the target scatterer is given by δ_0. Just as with the stationary-target Monte Carlo experiments, the target point-scatterer complex amplitude was unit-magnitude ($|A[0, 0]| = 1$), with a random (uniformly distributed between 0 and 2π) phase-angle for each Monte Carlo trial. The magnitudes of the interfering scatterers' reflectivities were equal (but with spatially statistically-independent random phase-angles uniformly distributed between 0 and 2π)and parameterized by the *signal-to-clutter ratio (SCR)*, defined by

$$SCR = 20 \log_{10} \left(\frac{|A[0, 0]|}{\underset{n_x \neq 0, \ n_y \neq 0}{\mathrm{mean}} |A[n_x, n_y]|} \right) \tag{4.123}$$
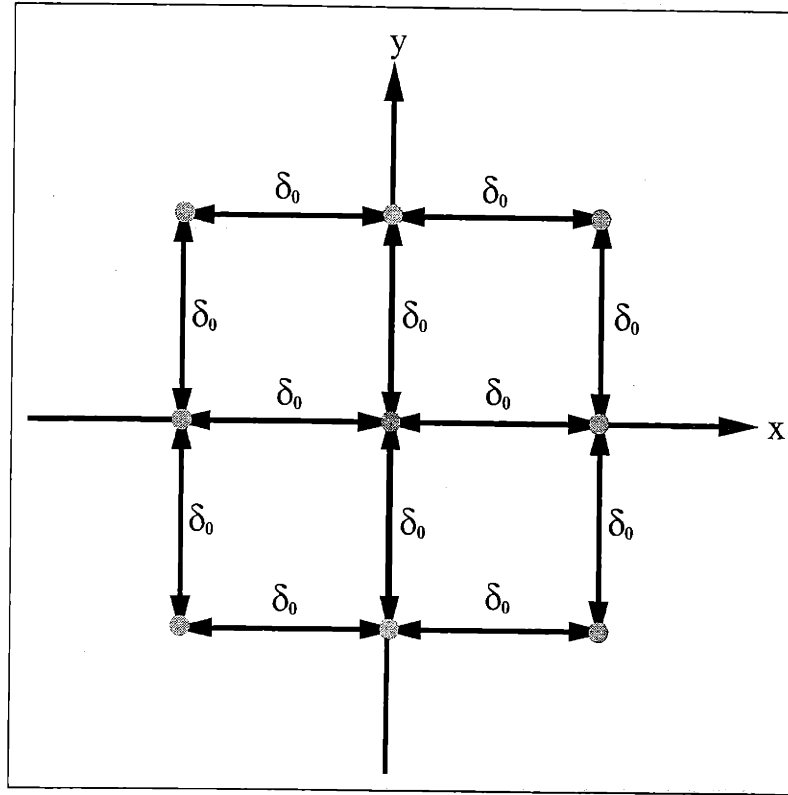
Figure 4.17: Spatial Configuration of Interfering Scatterers for Matched-Filter Monte-Carlo Analysis (with Target Scatterer at $(x, y) = (0, 0)$)

Moving Target Scatterer in the Presence of Stationary Interfering Scatterers with Varying Spatial Separation ($SNR = 20dB$, $SCR = 0dB$)

For this case, we analyzed the effect of varying the scatterer spatial separation δ_0 upon the detection and velocity-estimation performance of the matched-filter (for a moving target point-scatterer with stationary interfering scatterers, i.e., $(\dot{x}[n_x, n_y], \dot{y}[n_x, n_y]) = (0, 0)$ for $n_x \neq 0$ and $n_y \neq 0$). For this particular case, we used a relatively high SNR of $20dB$ (i.e., $\frac{|A[0,0]|}{\sigma_\eta} = 10$). The initial velocity of the moving target point-scatterer was chosen to be the same as the noisy-data moving target-scatterer example of the previous section, i.e., $(\dot{x}[0, 0], \dot{y}[0, 0]) = (n_{\dot{x}}[0, 0]\Delta_{\dot{x}}, n_{\dot{y}}[0, 0]\Delta_{\dot{y}}) = (1m/s, 1.152m/s)$. Both the target point-scatterer amplitude and the interfering scatterer amplitudes were unit-magnitude (which implied that we had an SCR of $0dB$), with random (uniformly distributed between 0 and 2π) complex phase-angles, for each Monte Carlo trial. We ran $M = 100$ Monte Carlo trials (under both hypotheses H_1 and H_0) for scatterer spatial separations, δ_0, of 1.00 m, 0.75 m, 0.50 m, and 0.25 m.

Figure 4.18 shows a plot of the approximate probability-of-detection and probability-of-false-alarm, versus the detection-rule threshold χ_{MAX}, for a δ_0 of $1.00m$. The "perfect-discrimination" detection threshold range is approximately given by $8 \leq \chi_{MAX} \leq 9$. This implies that the detection performance (for detection-rule thresholds within the perfect-

δ_0	Azimuth Vel. Var.	Azimuth Vel. Bias	Range Vel. Var.	Range Vel. Bias
0.25 m	0.16 m^2/s^2	- 0.18 m/s	0.22 m^2/s^2	- 0.27 m/s
0.50 m	0.00 m^2/s^2	0.00 m/s	0.01 m^2/s^2	- 0.07 m/s
0.75 m	0.00 m^2/s^2	0.00 m/s	0.01 m^2/s^2	- 0.10 m/s
1.00 m	0.00 m^2/s^2	0.00 m/s	0.01 m^2/s^2	- 0.10 m/s

Table 4.4: Matched-Filter Velocity-Estimation Performance for a Moving Target-Scatterer with Stationary Interfering Scatterers and an $SNR = 20dB$

discrimination range) of the matched-filter is essentially unaffected by stationary interfering scatterers located at least $1.00m$ away from the target scatterer. Figure 4.19 shows a plot of the approximate probability-of-detection and probability-of-false-alarm, versus the detection-rule threshold χ_{MAX}, for a δ_0 of $0.75m$. We see that the probability-of-detection is slightly less, as compared to the δ_0 of $1.00m$ case. The range of threshold values that give near-perfect discrimination between the hypotheses H_1 and H_0 is again about $8 \leq \chi_{MAX} \leq 9$. This implies that the detection performance (for detection-rule thresholds within the perfect-discrimination range) of the matched-filter is essentially unaffected by stationary interfering scatterers located at least $0.75m$ away from the target scatterer.

For a δ_0 of $0.5m$ (shown in Figure 4.20), we see that the interfering scatterers are now starting to affect the "optimal" detection performance of the matched-filter. For example, if we desire a probability-of-false-alarm of $P_F(\chi_{MAX}) = 0$, we choose a detection threshold of $\chi_{MAX} = 9$, which gives a maximum probability-of-detection of about $P_D(\chi_{MAX}) = 0.95$.

For a δ_0 of $0.25m$ (shown in Figure 4.21), we see that the detection performance of the matched-filter is significantly degraded by the presence of the interfering scatterers. If we again desire a probability-of-false-alarm of $P_F(\chi_{MAX}) = 0$, we must choose a detection threshold of $\chi_{MAX} = 14$, which gives a maximum probability-of-detection of only about $P_D(\chi_{MAX}) = 0.2$. Even if we again chose $\chi_{MAX} = 9$ (which gives a probability-of-false-alarm of about $P_F(\chi_{MAX}) = 0.4$), we would only get a maximum probability-of-detection of about $P_D(\chi_{MAX}) = 0.85$. Therefore, we see that for this case, where we have *distinct and independent scatterer motions*, the matched-filter has an effective detection spatial-resolution of approximately $0.50m$ (for an $SNR = 20dB$ and an $SCR = 0dB$). The receiver operating characteristic (ROC) curves are shown in Figure 4.22. Again, we see the dramatic drop in the detection performance of the matched-filter detection scheme as the spacing between the scatterers decreases.

In Table 4.4, we see that for δ_0's equal to 1.00 m, 0.75 m, and 0.50 m, the velocity-estimation errors are relatively small and are caused by the velocity quantizations of the matched-filter. For a δ_0 of 0.25 m, we do see some degradation in the velocity-estimation performance, though the degradation is within acceptable limits.

Figure 4.18: $P_D(\chi_{MAX})$ and $P_F(\chi_{MAX})$ for $\delta_0 = 1.00m$ (Moving Target-Scatterer with Stationary Interfering Scatterers) with One-Standard-Deviation Error Bars

Figure 4.19: $P_D(\chi_{MAX})$ and $P_F(\chi_{MAX})$ for $\delta_0 = 0.75m$ (Moving Target-Scatterer with Stationary Interfering Scatterers) with One-Standard-Deviation Error Bars

Figure 4.20: $P_D(\chi_{MAX})$ and $P_F(\chi_{MAX})$ for $\delta_0 = 0.50m$ (Moving Target-Scatterer with Stationary Interfering Scatterers) with One-Standard-Deviation Error Bars

Figure 4.21: $P_D(\chi_{MAX})$ and $P_F(\chi_{MAX})$ for $\delta_0 = 0.25m$ (Moving Target-Scatterer with Stationary Interfering Scatterers) with One-Standard-Deviation Error Bars
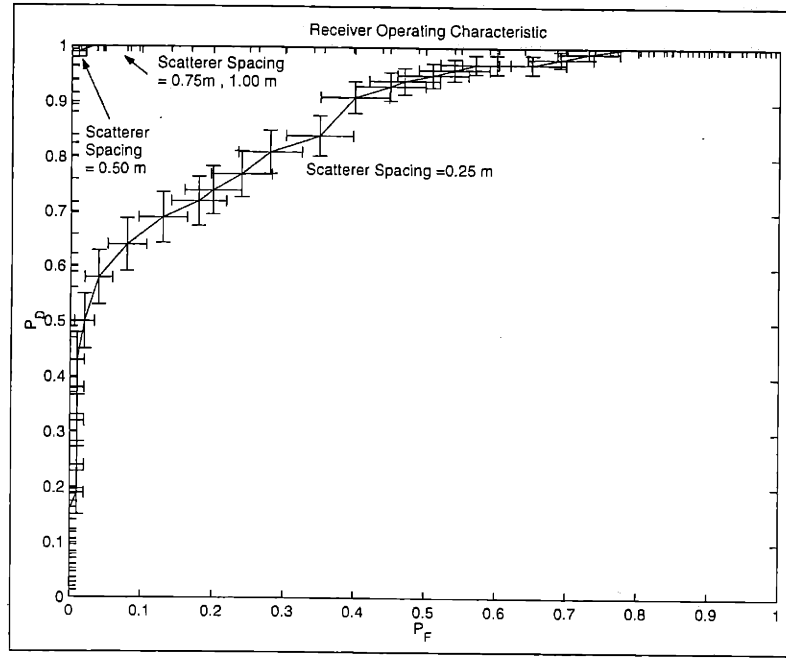
Figure 4.22: Receiver Operating Characteristic (Moving Target-Scatterer with Stationary Interfering Scatterers) with One-Standard-Deviation Error Bars

Moving Target Scatterer in the Presence of Stationary Interfering Scatterers with Varying SCR ($SNR = 20dB$, $\delta_0 = 0.25m$)

For this case, we analyzed the effect of varying the signal-to-clutter ratio (SCR) of the interfering scatterers upon the detection and velocity-estimation performance of the matched-filter. As with the previous example, this was done for a moving target point-scatterer with stationary interfering scatterers (i.e., $(\dot{x}[n_x, n_y], \dot{y}[n_x, n_y]) = (0, 0)$ for $n_x \neq 0$ and $n_y \neq 0$). Again, we used an SNR of $20dB$. The initial velocity of the moving target point-scatterer was chosen to be the same as the noisy-data moving target-scatterer example of the previous section, i.e., $(\dot{x}[0, 0], \dot{y}[0, 0]) = (n_{\dot{x}}[0, 0]\Delta_{\dot{x}}, n_{\dot{y}}[0, 0]\Delta_{\dot{y}}) = (1m/s, 1.152m/s)$. The target point-scatterer amplitude was unit-magnitude, with a random (uniformly distributed between 0 and 2π) phase-angle, for each Monte Carlo trial. Recall from the Monte Carlo experiments presented in the previous section (with stationary interfering scatterers and varying scatterer spacing) that the performance of the matched-filter was seriously degraded for $\delta_0 = 0.25m$ (with an SCR of $0dB$). Therefore, for this set of Monte Carlo experiments, we set the interfering scatterer spacing to $\delta_0 = 0.25m$ and increased the effective SCR (by reducing the amplitudes of the interfering scatterers) in order to see how this degradation decreases with increasing SCR. We ran $M = 100$ Monte Carlo trials (under both hypotheses H_1 and H_0) for SCR's of of $20dB$, $14dB$, $9.5dB$, $6dB$, $3.5dB$, and compared them to the $0dB$ case.

For an increased SCR of $3.5dB$, (shown in Figure 4.24), we begin to see a substantial improvement in the detection performance of the matched-filter, as compared to the $SCR = 0dB$ case. For example, if we desire a probability-of-false-alarm of $P_F(\chi_{MAX}) = 0$, we

SCR	Azimuth Vel. Var.	Azimuth Vel. Bias	Range Vel. Var.	Range Vel. Bias
0 dB	0.16 m^2/s^2	- 0.18 m/s	0.22 m^2/s^2	- 0.27 m/s
3.5 dB	0.01 m^2/s^2	- 0.01 m/s	0.01 m^2/s^2	- 0.09 m/s
6 dB	0.00 m^2/s^2	0.00 m/s	0.01 m^2/s^2	- 0.07 m/s
9.5 dB	0.00 m^2/s^2	0.00 m/s	0.01 m^2/s^2	- 0.10 m/s
14 dB	0.00 m^2/s^2	0.00 m/s	0.01 m^2/s^2	- 0.12 m/s
20 dB	0.00 m^2/s^2	0.00 m/s	0.01 m^2/s^2	- 0.12 m/s

Table 4.5: Matched-Filter Velocity-Estimation Performance (as a Function of SCR) for a Moving Target-Scatterer with Stationary Interfering Scatterers and an $SNR = 20dB$

choose a detection threshold of $\chi_{MAX} = 13$. However, we now get a maximum probability-of-detection of $P_D(\chi_{MAX}) = 0.85$, which is much better than $P_D(\chi_{MAX}) = 0.2$ for the $SCR = 0dB$ case.

For an SCR of $6dB$ (shown in Figure 4.25), we see that the effects of the interfering scatterers upon the detection performance of the matched-filter has been reduced even further. We now have "perfect-discrimination" for the detection threshold $12 \leq \chi_{MAX} \leq 13$.

Figure 4.26, Figure 4.27, and Figure 4.28 show the approximate probability-of-detection and probability of-false-alarm, versus the detection-rule threshold χ_{MAX}, for $SCR = 9.5dB$, $SCR = 14dB$, and $SCR = 20dB$ respectively. For all of these cases, we see that we have approximately "perfect-discrimination" in the detection threshold range of $10 \leq \chi_{MAX} \leq 15$. This implies that the detection performance (for detection-rule thresholds within the perfect-discrimination range) of the matched-filter is essentially unaffected by stationary interfering scatterers with magnitudes less than 30 percent of the magnitude of the target scatterer (and located at least $0.25m$ away from the target scatterer).

The receiver operating characteristic (ROC) curves are shown in Figure 4.29. Again, we see the improvement in the detection performance of the matched-filter as the SCR increases. In addition, we see a similar improvement in the velocity-estimation performance in Table 4.5. For an SCR greater than $6dB$, the performance of the matched-filter is essentially limited by velocity-quantization errors.
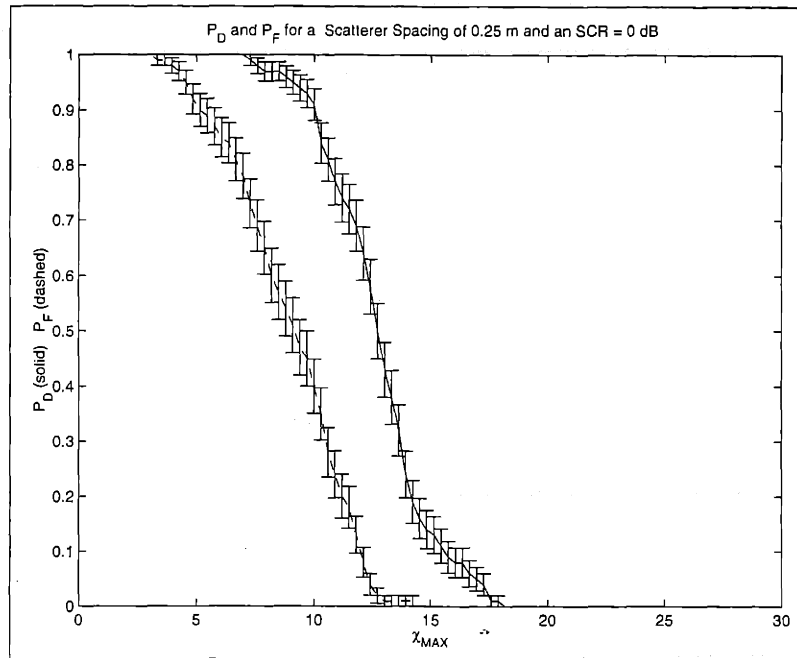
Figure 4.23: $P_D(\chi_{MAX})$ and $P_F(\chi_{MAX})$ for $SCR = 0dB$ (Moving Target-Scatterer with Stationary Interfering Scatterers) with One-Standard-Deviation Error Bars
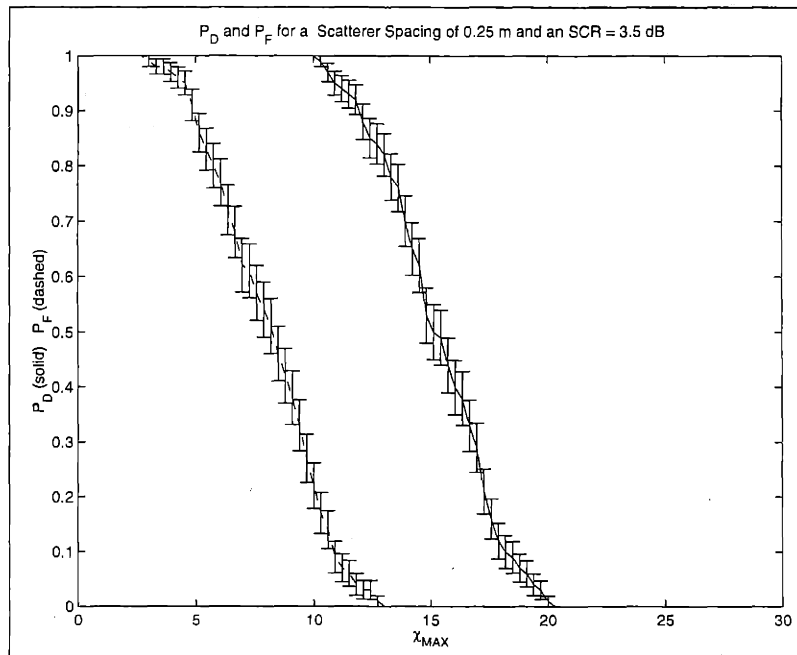
Figure 4.24: $P_D(\chi_{MAX})$ and $P_F(\chi_{MAX})$ for $SCR = 3.5dB$ (Moving Target-Scatterer with Stationary Interfering Scatterers) with One-Standard-Deviation Error Bars
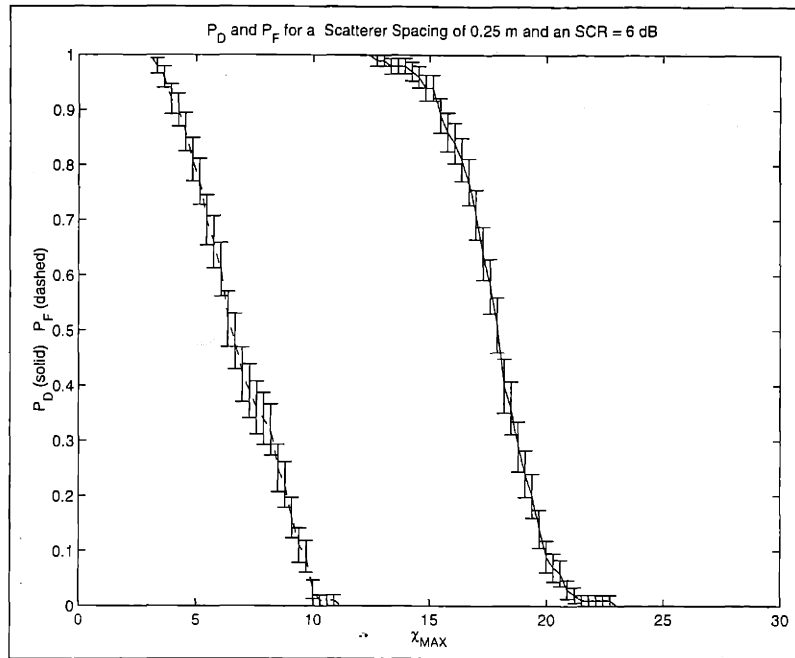
Figure 4.25: $P_D(\chi_{MAX})$ and $P_F(\chi_{MAX})$ for $SCR = 6dB$ (Moving Target-Scatterer with Stationary Interfering Scatterers) with One-Standard-Deviation Error Bars
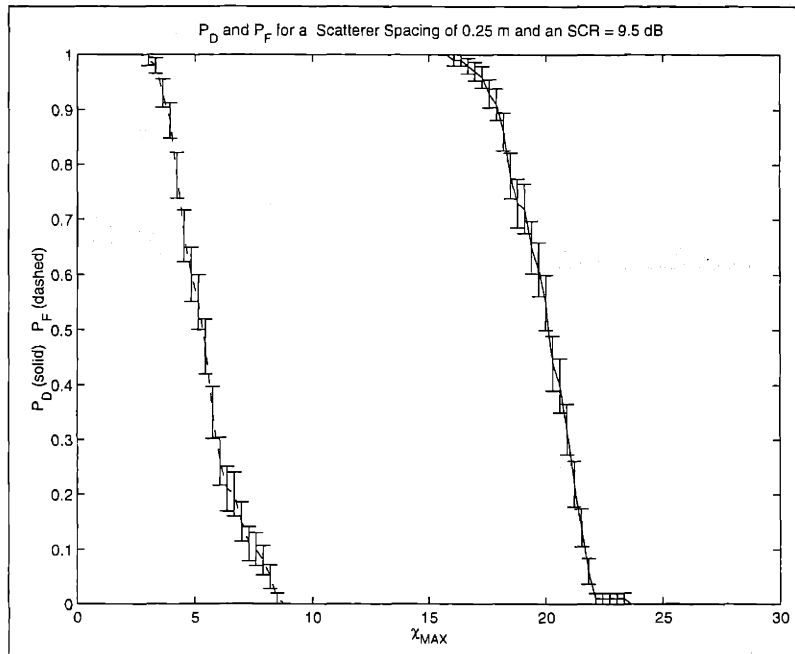
Figure 4.26: $P_D(\chi_{MAX})$ and $P_F(\chi_{MAX})$ for $SCR = 9.5dB$ (Moving Target-Scatterer with Stationary Interfering Scatterers) with One-Standard-Deviation Error Bars
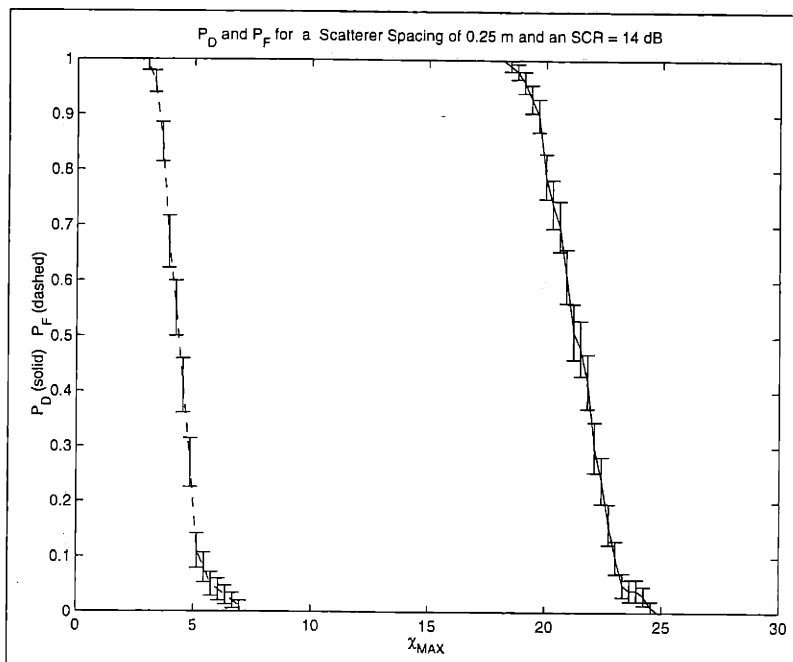
Figure 4.27: $P_D(\chi_{MAX})$ and $P_F(\chi_{MAX})$ for $SCR = 14dB$ (Moving Target-Scatterer with Stationary Interfering Scatterers) with One-Standard-Deviation Error Bars
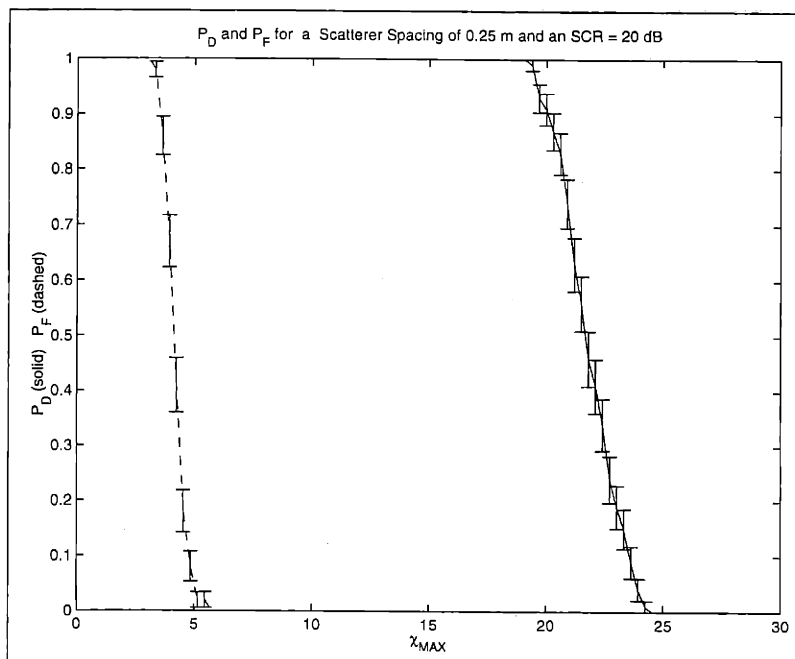
Figure 4.28: $P_D(\chi_{MAX})$ and $P_F(\chi_{MAX})$ for $SCR = 20dB$ (Moving Target-Scatterer with Stationary Interfering Scatterers) with One-Standard-Deviation Error Bars
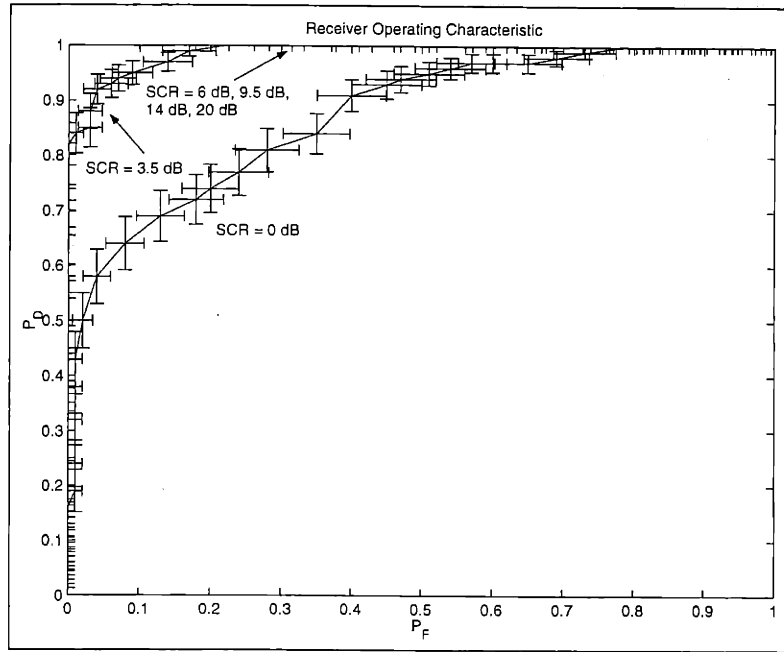
Figure 4.29: Receiver Operating Characteristic (Moving Target-Scatterer with Stationary Interfering Scatterers) with One-Standard-Deviation Error Bars

Moving Target Scatterer in the Presence of Stationary Interfering Scatterers and Varying SNR $(SCR = 0dB, \delta_0 = 0.5m)$

Here, we illustrate the effect of the additive-noise SNR for the case where we have a moving target point-scatterer with stationary interfering scatterers. The initial-position of the target point-scatterer (under hypothesis H_1) was again located at the center of the illuminated target field, $(n_x\Delta_x, n_y\Delta_y) = (0m, 0m)$, with the same initial velocity as the previous cases $(\dot{x}[0,0], \dot{y}[0,0]) = (n_{\dot{x}}[0,0]\Delta_{\dot{x}}, n_{\dot{y}}[0,0]\Delta_{\dot{y}}) = (1m/s, 1.152m/s)$. The target point-scatterer amplitude and the interfering-scatterer amplitudes were unit-magnitude (with implied that we had an SCR of $0dB$), with random (uniformly distributed between 0 and 2π) complex phase-angles, for each Monte Carlo trial. The interfering scatterer spacing was set to $\delta_0 = 0.5m$ (which was the approximate detection resolution of the matched-filter observed in the previous Monte Carlo experiment with $SNR = 20dB$). We ran $M = 100$ Monte Carlo trials (under both hypotheses H_1 and H_0) for SNR's of of $20dB$, $14dB$, $9.5dB$, and $6dB$.

The $SNR = 20dB$ case is shown in Figure 4.30, which is the same as the $\delta_0 = 0.5m$ presented earlier in Figure 4.20. For this case, if we desire a probability-of-false-alarm of $P_F(\chi_{MAX}) = 0$, we choose a detection threshold of $\chi_{MAX} = 9$, which gives a maximum probability-of-detection of about $P_D(\chi_{MAX}) = 0.95$.

For an $SNR = 14dB$, we begin to see a degradation of the matched-filter detection performance due to the noise. For example, if we again desire a probability-of-false-alarm of $P_F(\chi_{MAX}) = 0$, we choose a detection threshold of $\chi_{MAX} = 8$, which gives a maximum probability-of-detection of only about $P_D(\chi_{MAX}) = 0.7$.

SNR	Azimuth Vel. Var.	Azimuth Vel. Bias	Range Vel. Var.	Range Vel. Bias
6 dB	38.91 m^2/s^2	- 0.68 m/s	2.63 m^2/s^2	- 0.87 m/s
9.5 dB	8.04 m^2/s^2	- 0.37 m/s	0.34 m^2/s^2	- 0.18 m/s
14 dB	0.08 m^2/s^2	- 0.05 m/s	0.05 m^2/s^2	- 0.10 m/s
20 dB	0.00 m^2/s^2	0.00 m/s	0.01 m^2/s^2	- 0.07 m/s

Table 4.6: Matched-Filter Velocity-Estimation Performance for Moving Target-Scatterer with Stationary Interfering Scatterers and Additive Noise
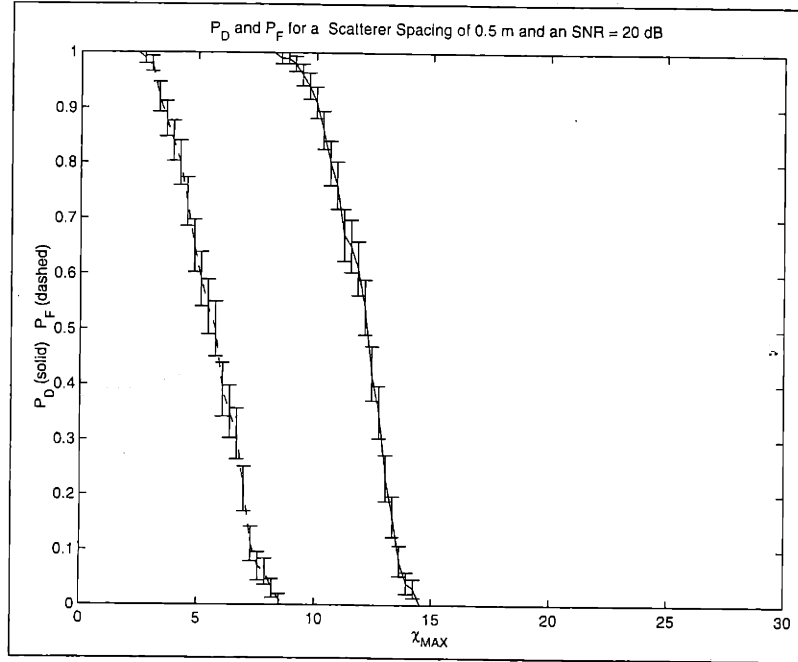
Figure 4.30: $P_D(\chi_{MAX})$ and $P_F(\chi_{MAX})$ for $SNR = 20dB$ (Moving Target-Scatterer with Stationary Interfering Scatterers) with One-Standard-Deviation Error Bars

For lower SNR's, the performance begins to seriously degrade. In fact, for the $SNR = 9.5dB$, as shown in Figure 4.32, the performance has degraded to a level comparable to the $SNR = 20dB$ performance with $\delta_0 = 0.25m$, shown in Figure 4.21. This implies that *the matched-filter has a detection resolution of $\delta_0 = 0.5$ only if the SNR is greater than 14dB* (for an SCR of 0dB). This is confirmed by the ROC curves shown in Figure 4.34 and the velocity-estimation performance shown in Table 4.6.
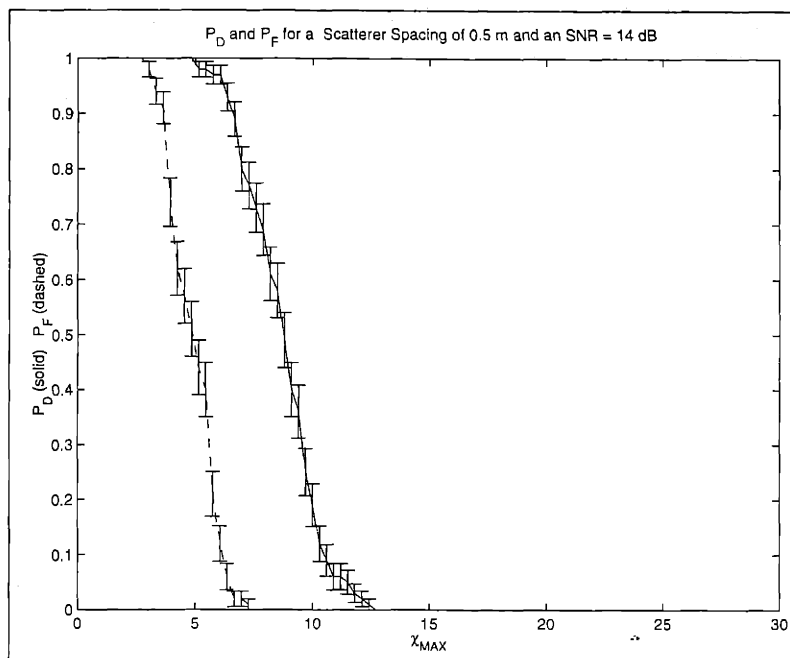
Figure 4.31: $P_D(\chi_{MAX})$ and $P_F(\chi_{MAX})$ for $SNR = 14dB$ (Moving Target-Scatterer with Stationary Interfering Scatterers) with One-Standard-Deviation Error Bars
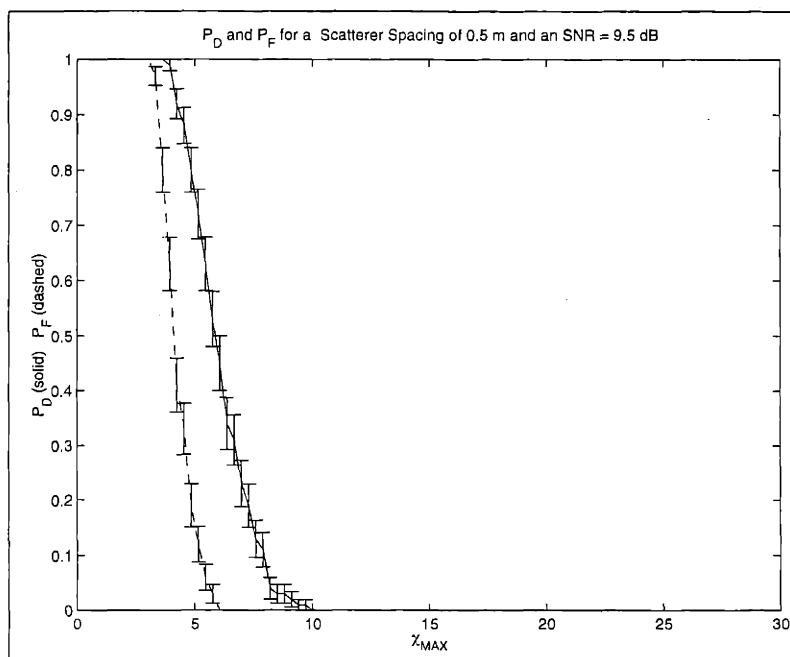
Figure 4.32: $P_D(\chi_{MAX})$ and $P_F(\chi_{MAX})$ for $SNR = 9.5dB$ (Moving Target-Scatterer with Stationary Interfering Scatterers) with One-Standard-Deviation Error Bars
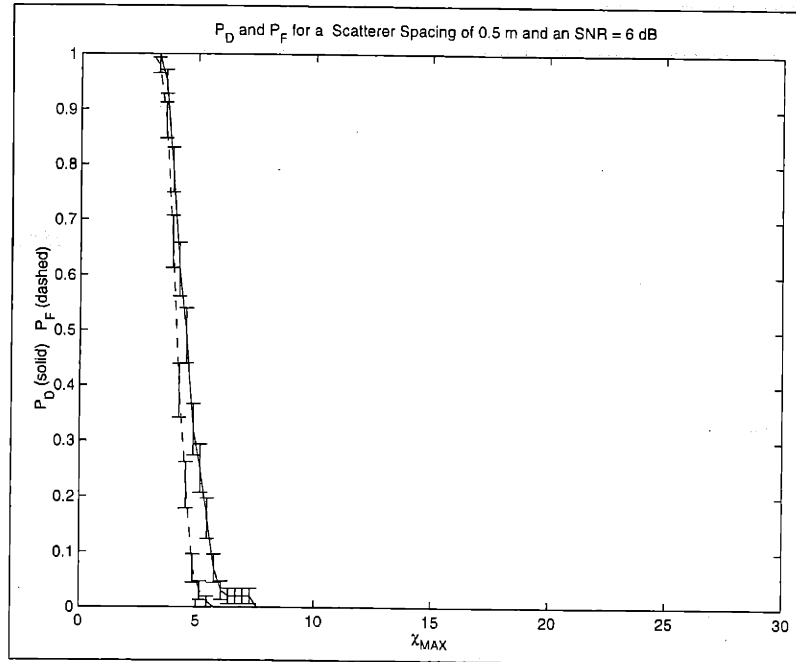
Figure 4.33: $P_D(\chi_{MAX})$ and $P_F(\chi_{MAX})$ for $SNR = 6dB$ (Moving Target-Scatterer with Stationary Interfering Scatterers) with One-Standard-Deviation Error Bars
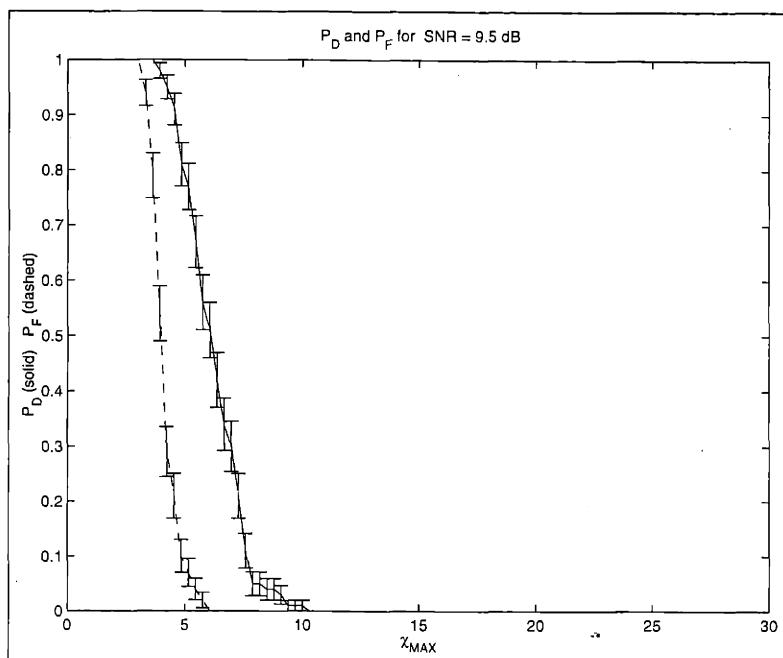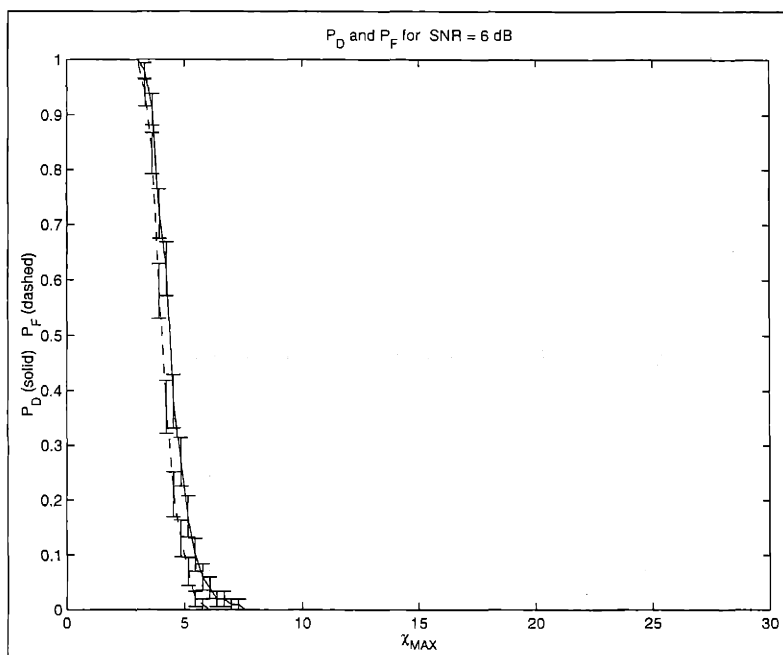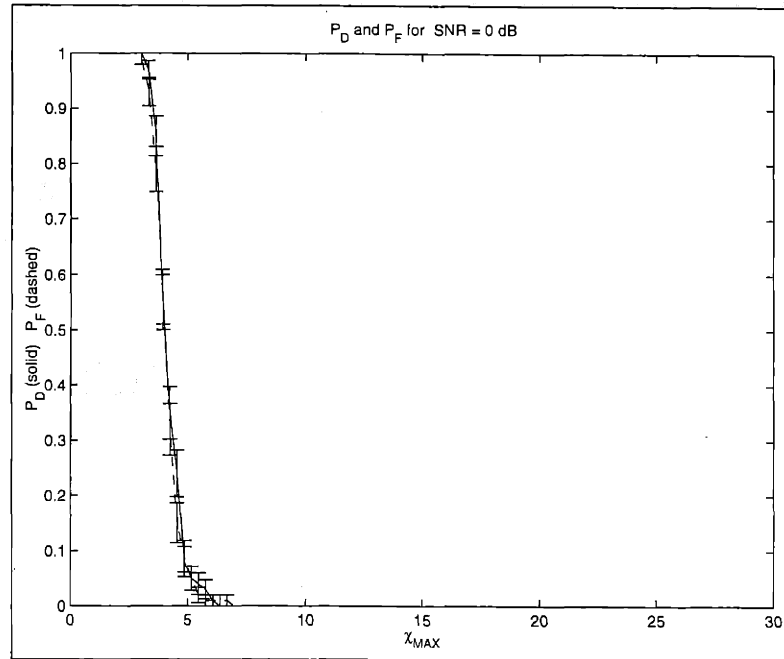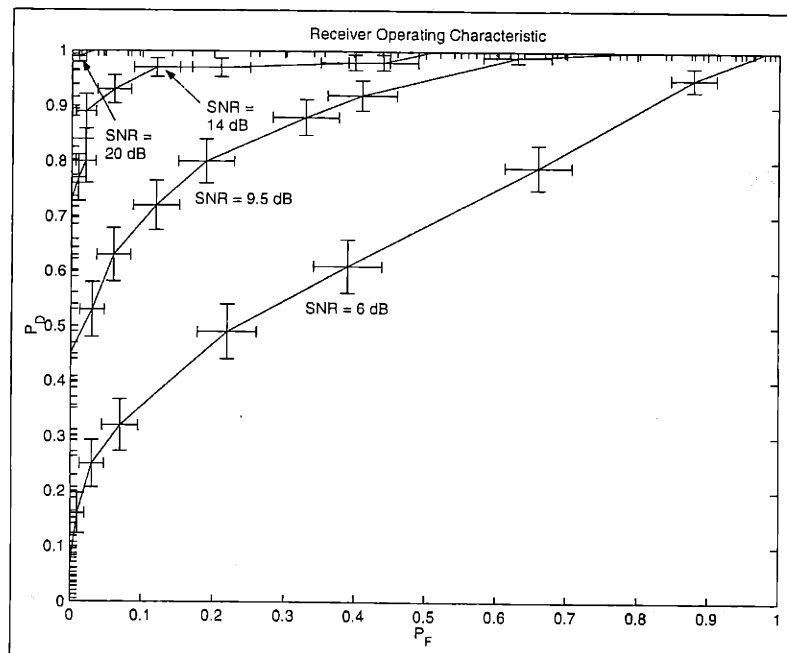

Figure 4.34: Receiver Operating Characteristic for SNR = $20dB$, $14dB$, $9.5dB$, and $6dB$ (Moving Target-Scatterer with Stationary Interfering Scatterers) with One-Standard-Deviation Error Bars

Moving Target Scatterer in the Presence of Moving Interfering Scatterers with Varying Spatial Separation ($SNR = 20dB$, $SCR = 0dB$)

For our next case, we analyzed the detection and velocity-estimation performance of the matched-filter for a moving target point-scatterer with moving interfering scatterers. The initial-position of the target point-scatterer (under hypothesis H_1) was again located at the center of the illuminated target field, $(n_x\Delta_x, n_y\Delta_y) = (0m, 0m)$, with the same initial velocity as the previous stationary interfering-scatterers case $(\dot{x}[0,0], \dot{y}[0,0]) = (n_{\dot{x}}[0,0]\Delta_{\dot{x}}, n_{\dot{y}}[0,0]\Delta_{\dot{y}}) = (1m/s, 1.152m/s)$. We again had eight interfering scatterers with initial spatial locations along the sides and corners of a square "box" (of width $2\delta_0$ m) surrounding the initial-position of the target point-scatterer, as shown previously in Figure 4.17. However, these interfering scatterers now have the same velocities as the target point-scatterer (i.e., $(\dot{x}[n_x, n_y], \dot{y}[n_x, n_y]) = (1m/s, 1.152m/s)$ for $n_x \neq 0$ and $n_y \neq 0$) (which is equivalent to the target scatterer and the interfering scatterers acting together as a "rigid-body" target with purely-translational motion). Both the target point-scatterer amplitude and the interfering-scatterer amplitudes were unit-magnitude ($|A[n_x, n_y]| = 1$ which implied an $SCR = 0dB$), with random (uniformly distributed between 0 and 2π) complex phase-angles, for each Monte Carlo trial. We ran $M = 100$ Monte Carlo trials (under both hypotheses H_1 and H_0) for scatterer spacings, δ_0, of 1.00 m, 0.75 m, 0.50 m, and 0.25 m.

Figure 4.35 shows a plot of the approximate probability-of-detection and probability-of-false-alarm, versus the detection-rule threshold χ_{MAX}, for δ_0 equal to 1.00m. The "perfect-discrimination" detection threshold range is approximately given by $8 \leq \chi_{MAX} \leq 13$, which is slightly larger than for the previous stationary interfering-scatterer case. Again, the detection performance (for detection-rule thresholds within the perfect-discrimination range) of the matched-filter is essentially unaffected by moving interfering scatterers located at least 1.00m away from the target scatterer. Figure 4.36 shows the probability-of-detection and probability-of-false-alarm, versus the detection-rule threshold χ_{MAX}, for δ_0 equal to 0.75m. The range of threshold values that give near-perfect discrimination between the hypotheses H_1 and H_0 is about $8 \leq \chi_{MAX} \leq 12$ which is slightly smaller than the δ_0 of 1.00m case. Again, for detection-rule thresholds within the perfect-discrimination range, the detection performance of the matched-filter is essentially unaffected by moving interfering scatterers located at least 0.75m away from the target scatterer.

For a δ_0 of 0.5m (shown in Figure 4.37), we begin to see the effect of the interfering scatterers upon the "optimal" detection performance of the matched-filter. For instance, if we desire a probability-of-false-alarm of $P_F(\chi_{MAX}) = 0$, we choose a detection threshold of $\chi_{MAX} = 12$, which gives a maximum probability-of-detection of about $P_D(\chi_{MAX}) = 0.95$.

For a δ_0 of 0.25m (shown in Figure 4.38), the detection performance of the matched-filter is significantly degraded by the presence of the interfering scatterers. If we desire a probability-of-false-alarm of $P_F(\chi_{MAX}) = 0$, we must choose a detection threshold of $\chi_{MAX} = 18$, which gives a maximum probability-of-detection of only about $P_D(\chi_{MAX}) = 0.05$.

Thus, in the presence of moving interfering-scatterers, the matched-filter has an effective detection spatial-resolution of approximately 0.50m (for an $SNR = 20dB$ and an $SCR = 0dB$), just as with the stationary interfering-scatterer case. The receiver operating characteristic (ROC) curves are shown in Figure 4.39. Again, we see the dramatic drop in

δ_0	Azimuth Vel. Var.	Azimuth Vel. Bias	Range Vel. Var.	Range Vel. Bias
0.25 m	0.06 m^2/s^2	0.02 m/s	0.04 m^2/s^2	- 0.09 m/s
0.50 m	0.00 m^2/s^2	0.00 m/s	0.01 m^2/s^2	- 0.10 m/s
0.75 m	0.00 m^2/s^2	0.00 m/s	0.01 m^2/s^2	- 0.11 m/s
1.00 m	0.00 m^2/s^2	0.00 m/s	0.01 m^2/s^2	- 0.11 m/s

Table 4.7: Matched-Filter Velocity-Estimation Performance for Moving Target-Scatterer with Moving Interfering Scatterers
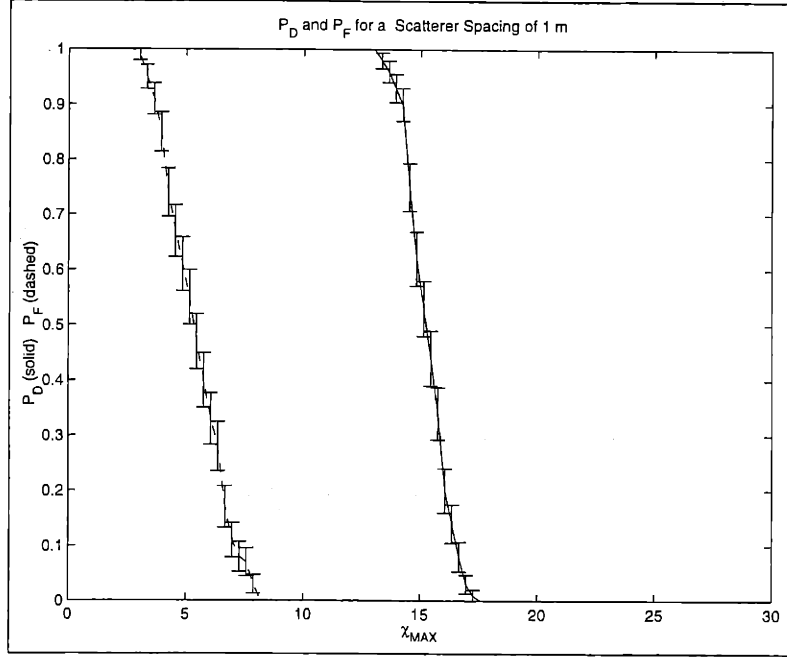
Figure 4.35: $P_D(\chi_{MAX})$ and $P_F(\chi_{MAX})$ for $\delta_0 = 1.00m$ (Moving Target-Scatterer with Moving Interfering Scatterers) with One-Standard-Deviation Error Bars

the detection performance of the matched-filter detection scheme as the spacing between the scatterers decreases below 0.5m.

As shown in Table 4.7, the velocity-estimation errors are relatively small and are caused by the velocity quantizations of the matched-filter. For a δ_0 of 0.25 m, we actually see an overall improvement in the velocity-estimation performance, as compared to the previous stationary interfering-scatterer case shown in Table 4.4. One explanation for this improvement is the fact that the interfering scatterers now have the same velocity as the target scatterer. This implies that the matched filter will exhibit better performance for a moving target with strongly correlated (e.g., rigid-body) motion.

152
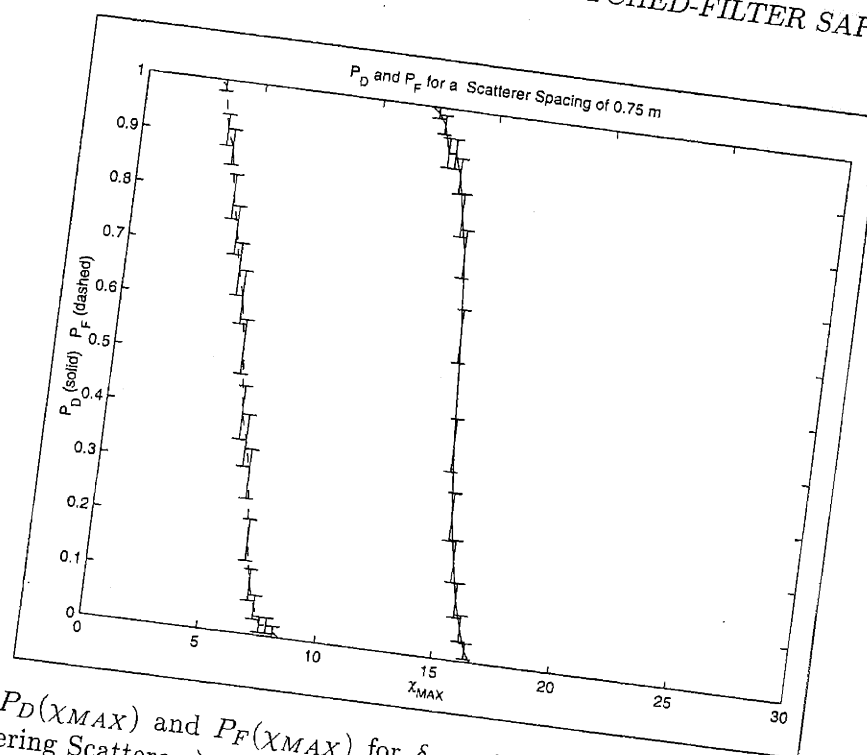
Figure 4.36: $P_D(\chi_{MAX})$ and $P_F(\chi_{MAX})$ for $\delta_0 = 0.75m$ (Moving Target-Scatterer with Moving Interfering Scatterers) with One-Standard-Deviation Error Bars
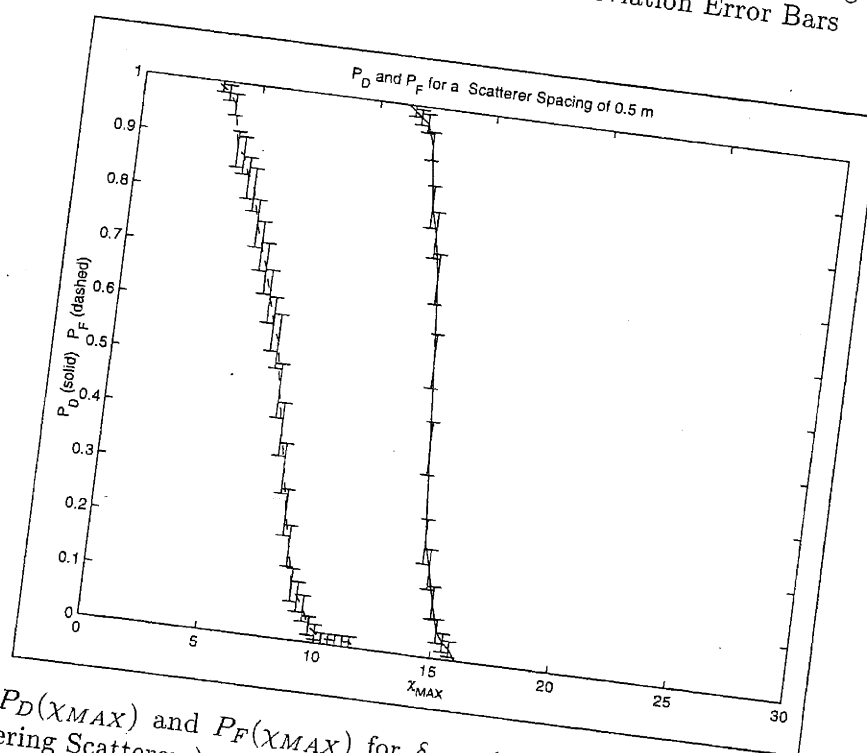
Figure 4.37: $P_D(\chi_{MAX})$ and $P_F(\chi_{MAX})$ for $\delta_0 = 0.50m$ (Moving Target-Scatterer with Moving Interfering Scatterers) with One-Standard-Deviation Error Bars
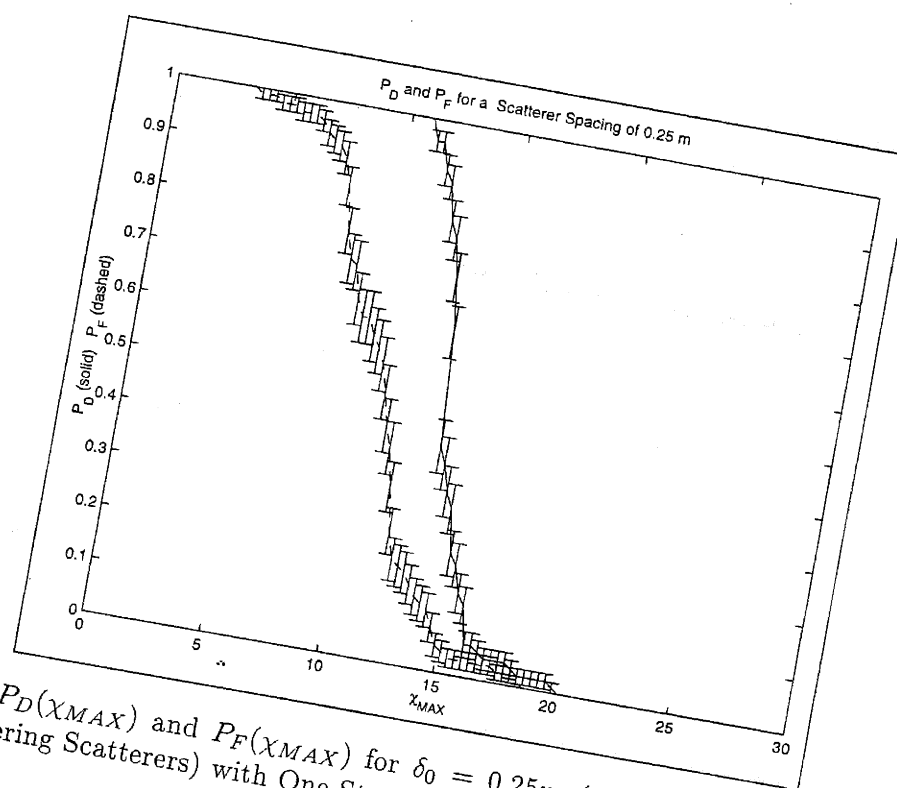
Figure 4.38: $P_D(\chi_{MAX})$ and $P_F(\chi_{MAX})$ for $\delta_0 = 0.25m$ (Moving Target-Scatterer with Moving Interfering Scatterers) with One-Standard-Deviation Error Bars
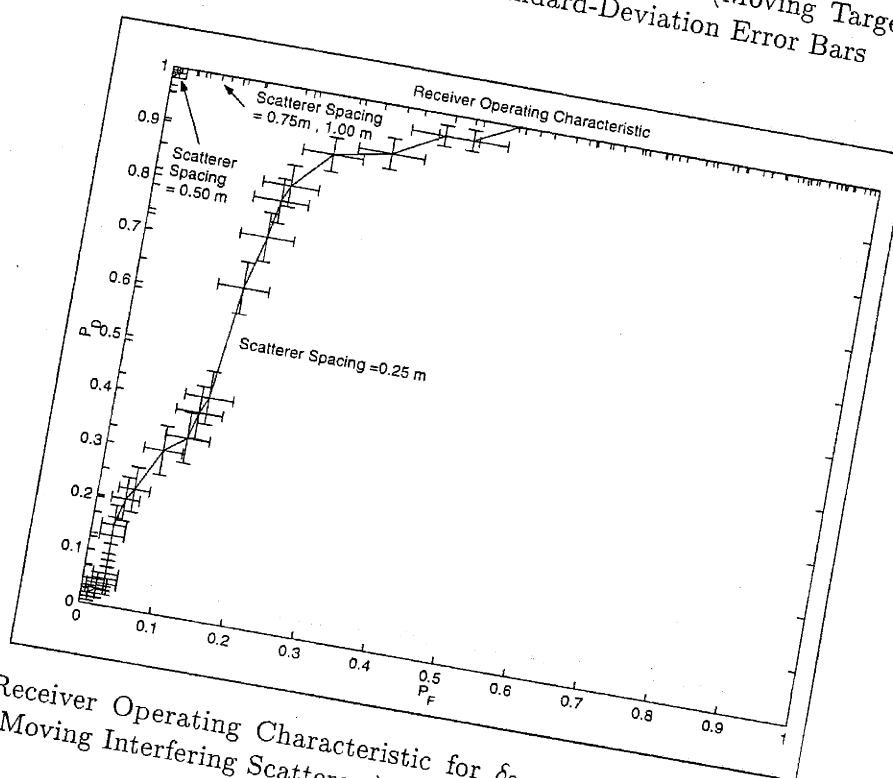
Figure 4.39: Receiver Operating Characteristic for $\delta_0 = 0.25m, 0.50m$ (Moving Target-Scatterer with Moving Interfering Scatterers) with One-Standard-Deviation Error Bars

SNR	Azimuth Vel. Var.	Azimuth Vel. Bias	Range Vel. Var.	Range Vel. Bias
6 dB	47.44 m^2/s^2	- 0.44 m/s	2.05 m^2/s^2	- 0.20 m/s
9.5 dB	19.99 m^2/s^2	- 0.05 m/s	0.99 m^2/s^2	- 0.23 m/s
14 dB	0.01 m^2/s^2	0.01 m/s	0.01 m^2/s^2	- 0.08 m/s
20 dB	0.00 m^2/s^2	0.00 m/s	0.01 m^2/s^2	- 0.10 m/s

Table 4.8: Matched-Filter Velocity-Estimation Performance for Moving Target-Scatterer with Moving Interfering Scatterers and Additive Noise

Moving Target Scatterer in the Presence of Moving Interfering Scatterers and Varying SNR ($SCR = 0dB$, $\delta_0 = 0.5m$)

Here, we illustrate the effects of the SNR upon the performance of the matched-filter where we have a moving target point-scatterer with moving interfering scatterers. The initial-position of the target point-scatterer (under hypothesis H_1) was again located at the center of the illuminated target field, $(n_x\Delta_x, n_y\Delta_y) = (0m, 0m)$, with the same initial velocity as the previous cases $(\dot{x}[0,0], \dot{y}[0,0]) = (n_{\dot{x}}[0,0]\Delta_{\dot{x}}, n_{\dot{y}}[0,0]\Delta_{\dot{y}}) = (1m/s, 1.152m/s)$. The interfering scatterers again had the same velocities as the target point-scatterer (i.e., $(\dot{x}[n_x, n_y], \dot{y}[n_x, n_y]) = (1m/s, 1.152m/s)$ for $n_x \neq 0$ and $n_y \neq 0$) (which, as before, is equivalent to the target scatterer and the interfering scatterers acting together as a "rigid-body" target with purely-translational motion). Both the target point-scatterer amplitude and the interfering-scatterer amplitudes were unit-magnitude (with implied that we had an SCR of $0dB$), with random (uniformly distributed between 0 and 2π) reflectivity phase-angles, for each Monte Carlo trial. Recall from the previous example where we had a moving target-scatterer with moving interfering scatterers that the approximate detection resolution of the matched-filter was $\delta_0 = 0.5m$ (for an $SNR = 20dB$). Therefore, for this example, we also set the scatterer spacing to $\delta_0 = 0.5m$. We ran $M = 100$ Monte Carlo trials (under both hypotheses H_1 and H_0) for SNR's of of $20dB$, $14dB$, $9.5dB$, and $6dB$.

We again show the $SNR = 20dB$ case in Figure 4.40, which is the same as the $\delta_0 = 0.5m$ case presented earlier in Figure 4.37. For this example, if we desire a probability-of-false-alarm of $P_F(\chi_{MAX}) = 0$, we choose a detection threshold of $\chi_{MAX} = 12$, which gives a maximum probability-of-detection of about $P_D(\chi_{MAX}) = 0.95$.

We begin to see the effects of the noise for the $SNR = 14dB$ case. For example, if we desire a probability-of-false-alarm of $P_F(\chi_{MAX}) = 0$, we choose a detection threshold of $\chi_{MAX} = 8$, which gives a maximum probability-of-detection of about $P_D(\chi_{MAX}) = 0.7$.

For lower SNR's, the performance begins to seriously degrade. In fact, for $SNR = 9.5dB$, as shown in Figure 4.42, the performance is comparable to the $SNR = 20dB$ performance with $\delta_0 = 0.25m$, shown in Figure 4.38. Just as with the previous Monte-Carlo example with stationary interfering-scatterers (and varying SNR), we can conclude that *the effective detection resolution of the matched-filter in the presence of moving interfering-scatterers is approximately 0.5m only for an SNR greater than 14dB*. This is confirmed by the ROC curves shown in Figure 4.44 and the velocity-estimation performance shown in Table 4.8.
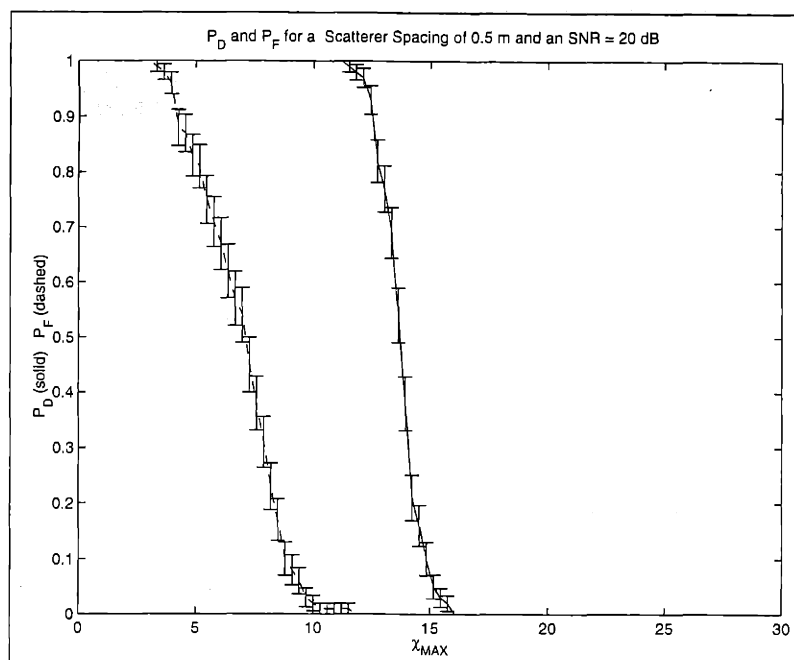
Figure 4.40: $P_D(\chi_{MAX})$ and $P_F(\chi_{MAX})$ for $SNR = 20dB$ (Moving Target-Scatterer with Moving Interfering Scatterers) with One-Standard-Deviation Error Bars
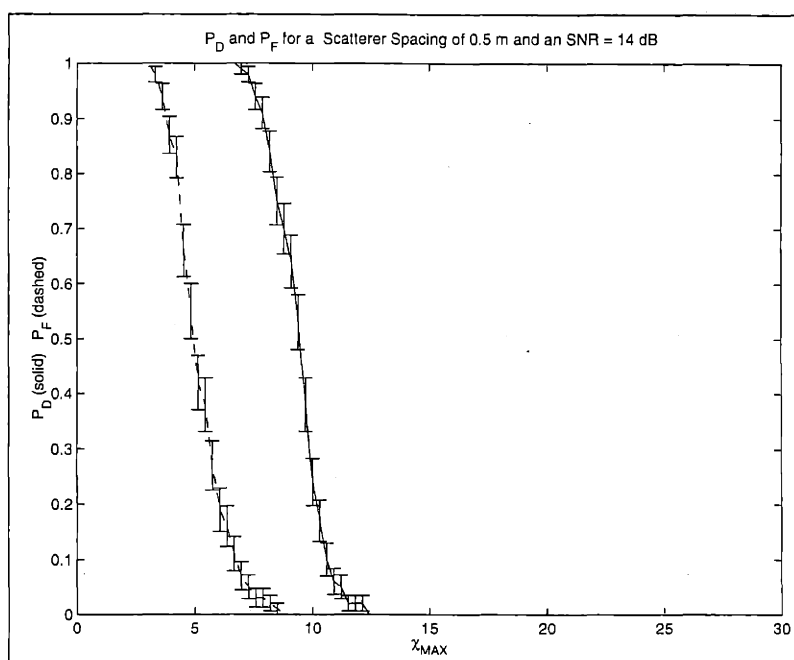
Figure 4.41: $P_D(\chi_{MAX})$ and $P_F(\chi_{MAX})$ for $SNR = 14dB$ (Moving Target-Scatterer with Moving Interfering Scatterers) with One-Standard-Deviation Error Bars
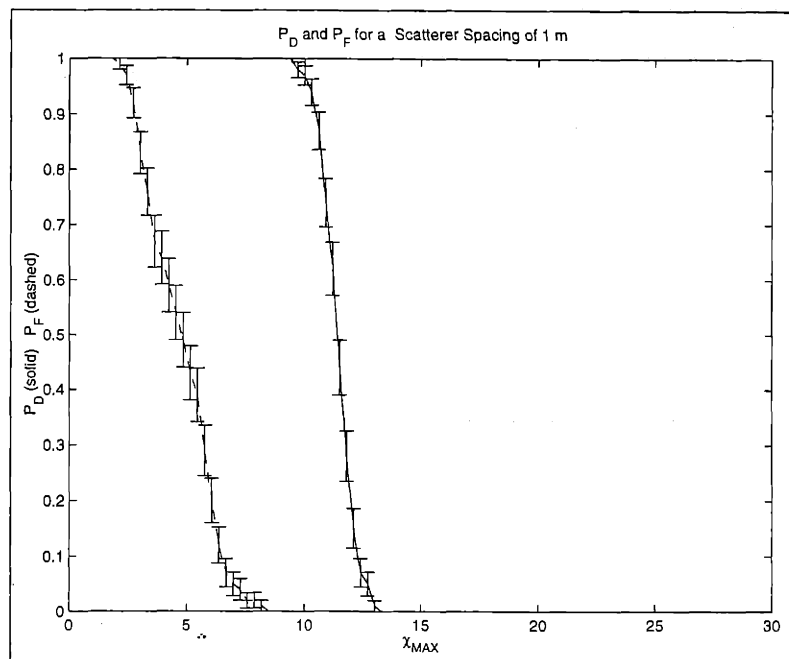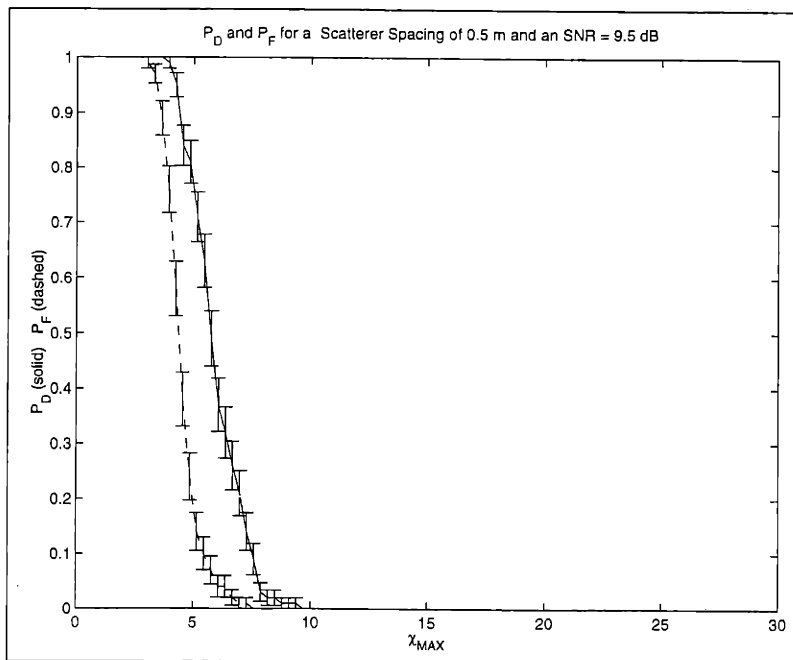
Figure 4.42: $P_D(\chi_{MAX})$ and $P_F(\chi_{MAX})$ for $SNR = 9.5dB$ (Moving Target-Scatterer with Moving Interfering Scatterers) with One-Standard-Deviation Error Bars

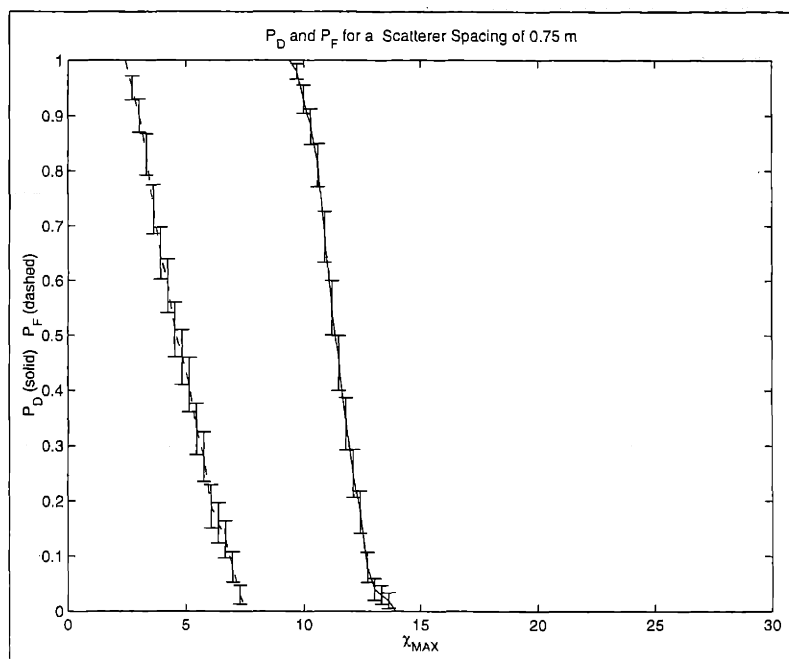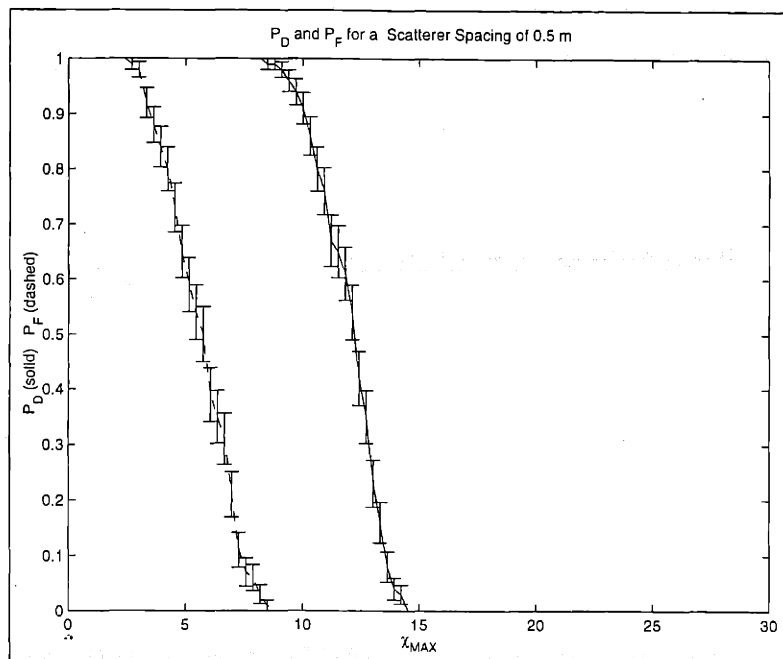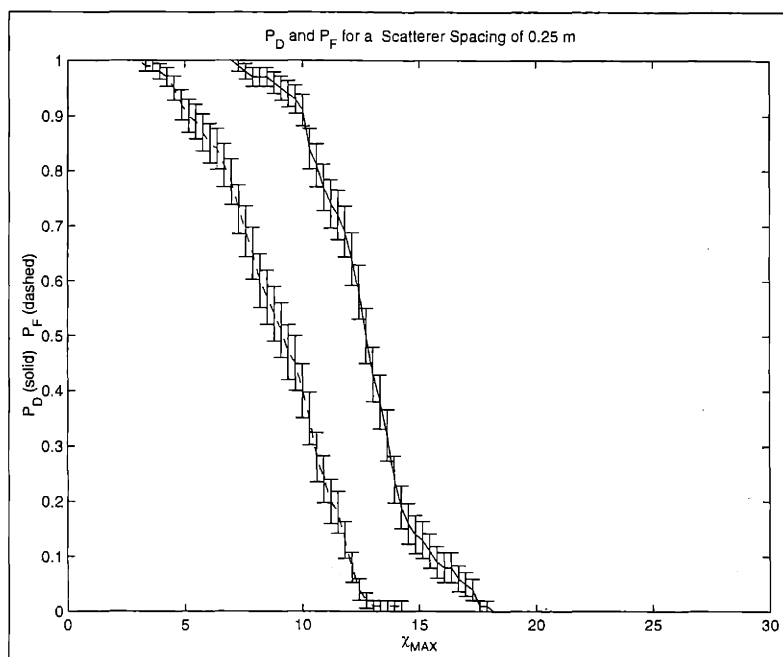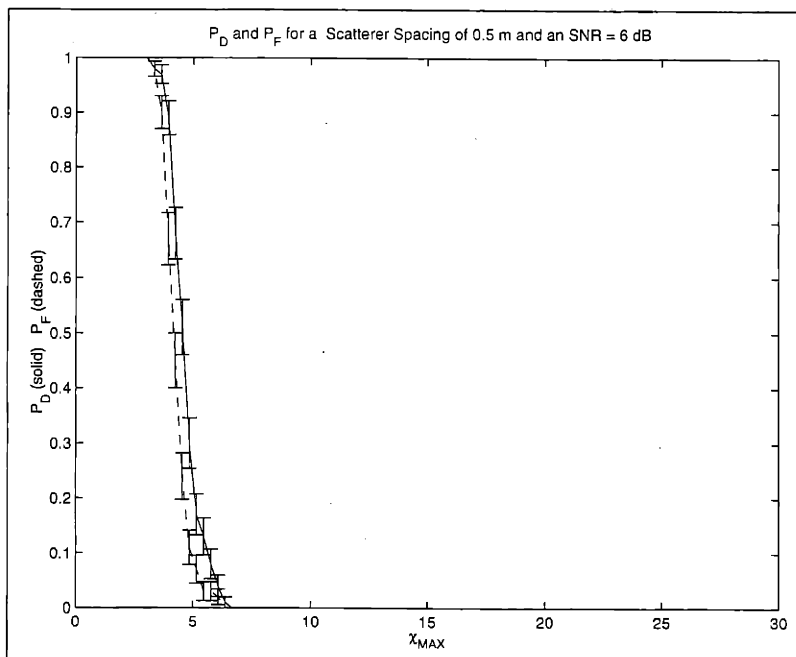Figure 4.43: $P_D(\chi_{MAX})$ and $P_F(\chi_{MAX})$ for $SNR = 6dB$ (Moving Target-Scatterer with Moving Interfering Scatterers) with One-Standard-Deviation Error Bars
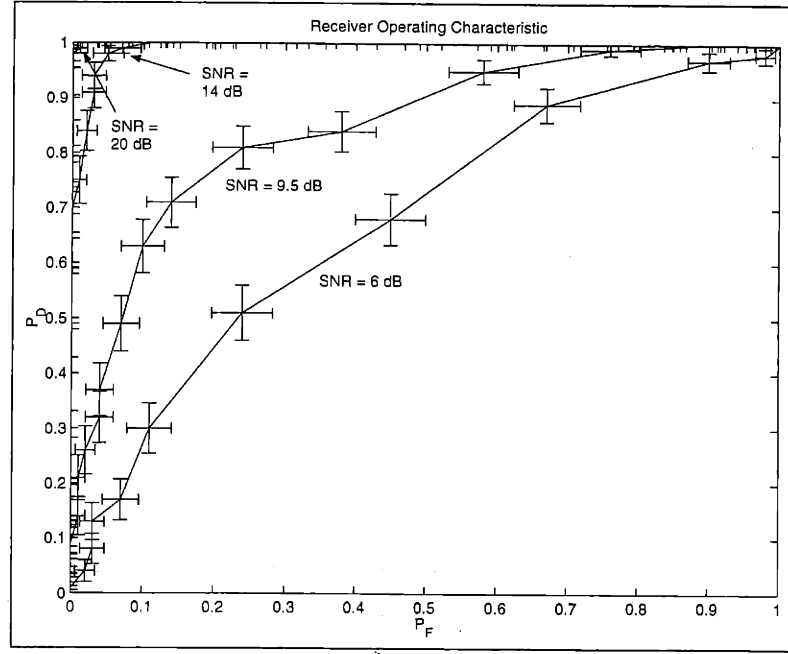
Figure 4.44: Receiver Operating Characteristic for SNR = $20dB$, $14dB$, $9.5dB$, and $6dB$ (Moving Target-Scatterer with Moving Interfering Scatterers) with One-Standard-Deviation Error Bars

4.7 Experimental Results

Here, we present some experimental results in order to illustrate the motion-compensated imaging capabilities of the matched-filter SAR processing algorithm. In Section 4.7.1, we first present some examples where we have synthetic moving point scatterers embedded in an actual stationary-clutter conventional SAR image. Then in Section 4.7.2, we present an example where we (manually) segmented the target portion of the conventional SAR image of an actual (stationary) target, and used it to generate a synthetic-motion moving target.

For these experimental examples, we assumed that we were only given the conventional moving-target (complex) SAR images (in the discrete $2 - D$ form $A_{CONV}[n_x, n_y]$). These images were converted into "raw" demodulated SAR data $\mathbf{f}$ by normalizing the images (by their respective maximum magnitude over n_x and n_y, denoted by A_{MAX}) and performing a scaled Fourier Transform corresponding to the "conventional" zero-velocity SAR model, i.e.,

$$\mathbf{f} = \frac{1}{A_{MAX}}\mathbf{FA}_{CONV} .\qquad(4.124)$$

Once we obtained a focused image from the least-squares amplitude-estimation portion of the matched-filter SAR processing algorithm, we then post-multiplied this image by A_{MAX}.

4.7.1   Synthetic Point Scatterers Embedded in Real Clutter

In this section, we present a set of experimental examples where we have a synthetic moving-target (consisting of a $2-D$ array of ideal point-scatterers) embedded in a real stationary clutter scene. This particular scene consisted mainly of trees and grass, as shown in the conventional SAR image of Figure 4.45 (with an approximate resolution in range and azimuth of of $\delta_y = 0.25m$ and $\delta_x = 0.25m$). In addition, the clutter scene had two man-made high-amplitude scatterers with a magnitude of about $35dB$.

We generated the SAR data for these examples by first performing a scaled Fourier Transform (corresponding to the conventional zero-velocity SAR model) upon the conventional SAR image of the clutter scene. These transformed data sets were then added to the SAR data corresponding to the synthetic target (which as stated earlier, consisted of a $2-D$ array of moving ideal point scatterers). The synthetic-target portion of the SAR data sets was generated using the general-motion estimation-theoretic SAR data model presented in Chapter 2, with parameters chosen to be as similar as possible to the 33.5 GHz Lincoln Laboratory Advanced Detection and Tracking System (ADTS)[16] system operating in spotlight mode (as shown in Table 4.9 for the synthetic target).

For all of the synthetic-target examples presented here, the $2-D$ target-scatterer array consisted of nine synthetic moving point-scatterers. The initial positions of these scatterers were centered near the two "man-made" high-amplitude scatterers in the following configuration about the point $(x, y) = (-6.5m, -4m)$:

Scatterer #0: $(n_x\Delta_x, n_y\Delta_y) = (-6.5m, -4m)$

Scatterer #1: $(n_x\Delta_x, n_y\Delta_y) = (-6.5m - \delta_0, -4m - \delta_0)$

Scatterer #2: $(n_x\Delta_x, n_y\Delta_y) = (-6.5m - \delta_0, -4m)$

Scatterer #3: $(n_x\Delta_x, n_y\Delta_y) = (-6.5m - \delta_0, -4m + \delta_0)$

Scatterer #4: $(n_x\Delta_x, n_y\Delta_y) = (-6.5m + \delta_0, -4m - \delta_0)$

Scatterer #5: $(n_x\Delta_x, n_y\Delta_y) = (-6.5m + \delta_0, -4m)$

Scatterer #6: $(n_x\Delta_x, n_y\Delta_y) = (-6.5m + \delta_0, -4m + \delta_0)$

Scatterer #7: $(n_x\Delta_x, n_y\Delta_y) = (-6.5m, -4m - \delta_0)$

Scatterer #8: $(n_x\Delta_x, n_y\Delta_y) = (-6.5m, -4m + \delta_0)$

We see that the synthetic-target array for this examples had a spatial spacing of $\delta_0 m$ with respect to both range and azimuth,

Rigid-Body Purely-Translational Motion with a Scatterer Spacing of $1m$

For the first synthetic-target example, we have a rigid-body target with purely-translational motion, i.e., all of the nine moving point-scatterers in the 2-D synthetic-target array had a velocity of $(\dot{x}[n_x, n_y], \dot{y}[n_x, n_y]) = (2m/s, 2.304m/s)$. In order to examine the azimuth-displacement compensation performance of the matched-filter SAR processing algorithm

F_c	Center Frequency	33.5 GHz
λ_c	Center Wavelength	0.009 m
αT_p	Chirp Bandwidth	1.2 GHz
f_{PRF}	Pulse Repetition Frequency	512 pulse/s
N	Complex Samples per Range Profile	512
$2K$	Pulses per Synthetic Aperture	512
R_o	Center Slant-Range	2778 M
v	SAR Platform Velocity	100 m/s
$\dot\theta$	Look-Angle Rotation Rate	0.036 rad/s
$2T$	Dwell Time	1.0 s
L	Synthetic-Aperture Length	100 m
Δ_y	Range Sampling Interval	0.125 m
Δ_x	Azimuth Sampling Interval	0.125 m
δ_y	Range Resolution	0.25 m
δ_x	Azimuth Resolution	0.25 m
$\Delta_{\dot y}$	MF Range-Velocity Quantization	0.25 m/s
$\Delta_{\dot x}$	MF Azimuth-Velocity Quantization	0.5 m/s
Δ_{W_y}	Range Width of MF Image-Window	4 m
Δ_{W_x}	Azimuth Width of MF Image-Window	8 m

Table 4.9: System Parameters for Matched-Filter SAR Processing Examples (Synthetic Point Scatterers Embedded in Real Clutter)

separately from its velocity-estimation and image-focusing performance, we chose the range velocities $\dot y[n_x, n_y]$ such the synthetic-target scatterers "wrapped around" to their actual position in the SAR image. This was done for all of the experimental examples presented in this chapter.

For this first example, the spatial spacing $\delta_0 m$ of the scatterers in the synthetic target was chosen to be $1m$. Each of these scatterers had an amplitude of $40dB$, which was slightly greater than the amplitude of the man-made scatterers in the clutter image, as shown in the stationary-target conventional SAR images of Figure 4.46 and Figure 4.47. A cross-section of the stationary-target conventional SAR image (at $y = -4m$) is also shown in Figure 4.48. Here, we see three peaks corresponding to scatterers #'s 0, 2, and 5.

The conventional SAR images of these moving synthetic point-scatterers after being embedded in the background-clutter SAR image are shown in Figure 4.49 and Figure 4.50. A cross-section of the conventional SAR image (at $y = -4m$) is also shown in Figure 4.51. Here, we see that the image of the moving point-scatterers is blurred to the point so as to be essentially useless the purposes of automatic-target recognition (if used directly).

For the matched-filter, we used the clutter-nulling cross-interference reduction algorithm (which was discussed in Section 4.3.3) with a threshold of of $A_T[n_x, n_y] = 10|\hat{A}_{CONV}[n_x, n_y]|$. The resulting target-detection statistic, $\chi[n_x, n_y]$, is shown in Figure 4.52. Here, the locations of the nine moving synthetic scatterers (plus the two stationary "man-made clutter" scatterers) become readily apparent from the "darker" areas of this image. For this matched-filter processing example, we chose a detection-statistic threshold χ_{MAX} of 6, allowing us

to capture any slight initial spatial-location variation in the target scatterers without introducing an unacceptable number of false-alarm target locations. A corresponding image of the scatterer locations which were classified (using this threshold) as belonging to target scatterers is shown in Figure 4.53. We see that the matched-filter detection scheme correctly picked the initial location of all of the synthetic moving point-scatterers, plus the location of the stationary man-made clutter scatterers. we also see that the detection scheme also picked some spurious false-alarm target locations, especially around the the stationary man-made clutter scatterers.

In order to compute the median-prefiltered matched-filter velocity estimates (which were used as the initial conditions for the L_1-Norm based velocity-estimation algorithm) we used median filters with a spatial region-of-interest (ROI) of $0.5m \times 0.5m$. For the reduced-order L_1-Norm based velocity-estimation algorithm, we used an L_1 weighting of $\gamma_A = 1.1$. For the results presented in this chapter, we did not use a regularization penalty upon the velocity estimates, which implied $J_\mathbf{v}(\mathbf{v}) = 0$.

The estimated azimuth velocities and range velocities are shown in Figure 4.54 and Figure 4.55, and in the cross-sections of Figure 4.56 and Figure 4.57. We see from these cross-sections that the L_1-Norm based velocity-estimation algorithm gave reasonable estimates of the velocities of both the synthetic moving point-scatterers and the stationary man-made clutter scatterers. Note that we still had a few spurious velocity estimates at the false-alarm spatial locations.

The resulting SAR images generated by the least-squares amplitude-estimation algorithm are shown in Figure 4.58 and Figure 4.59. We see that all nine of the synthetic moving point-scatterers are now focused and distinct In fact, it compares quite well to the SAR images formed by the least-squares amplitude-estimation algorithm when the scatterer-velocities are known exactly, (shown Figure 4.65 and Figure 4.66). The mainlobe height of the moving-target scatterers in the matched-filter SAR image are approximately $15dB$, as shown in the azimuthal cross-section (at $y = -4m$) of Figure 4.60 (which again compares favorably to the cross-section shown in Figure 4.67 of the exact-velocity image , where the scatterers have a mainlobe height of approximately $20dB$) As compared to some of the moving-target SAR imaging techniques presented in the literature[14, 16, 39], we see that the matched-filter technique can image *both the moving point-scatterers and the stationary clutter scatterers*, even if they are relatively near each other. In terms of automatic target recognition, the matched-filter shows promise for having the ability to focus a moving target, while preserving nearby stationary "landmark" scatterers.

However, we found that if we used the range-velocity induced azimuth-displacement compensation scheme directly (with the velocities generated by the L_1-Norm based velocity-estimation algorithm), we found that the resulting corrected SAR image of the moving target scatterers would exhibit relatively severe distortions in the azimuth positions (due to the fact that *the azimuth displacement errors are proportional to the errors in the range velocities divided by the SAR system's look-angle rotation rate of* $\dot{\theta} = 0.036 rad/s$). In order to reduce these distortions, we averaged the range velocity over a set of "bright" scatterer locations where both the target-detection statistic, $\chi[n_x, n_y]$, was greater than 8.5, and where the magnitude of estimated range-velocity was greater than $0.5m/s$, as shown in Figure 4.61. For this case, the average range velocity for these scatterer locations was computed to be $2.3753m/s$. We then used this velocity to compensate the scatterers at

the previous "target" spatial locations (with $\chi[n_x, n_y] \leq 6$) which had an estimated range-velocity with a magnitude greater than $0.5 m/s$. As shown in Figure 4.63 and Figure 4.64, the resulting azimuth-displacement error for the moving target was approximately $2m$.
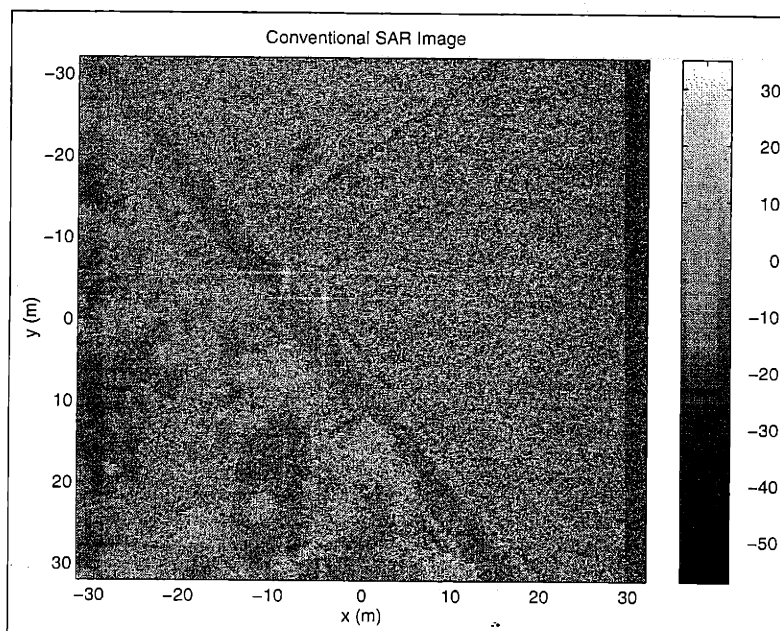
Figure 4.45: Conventional SAR Image of Stationary Clutter Scene used for Synthetic-Target Matched-Filter Experimental Examples
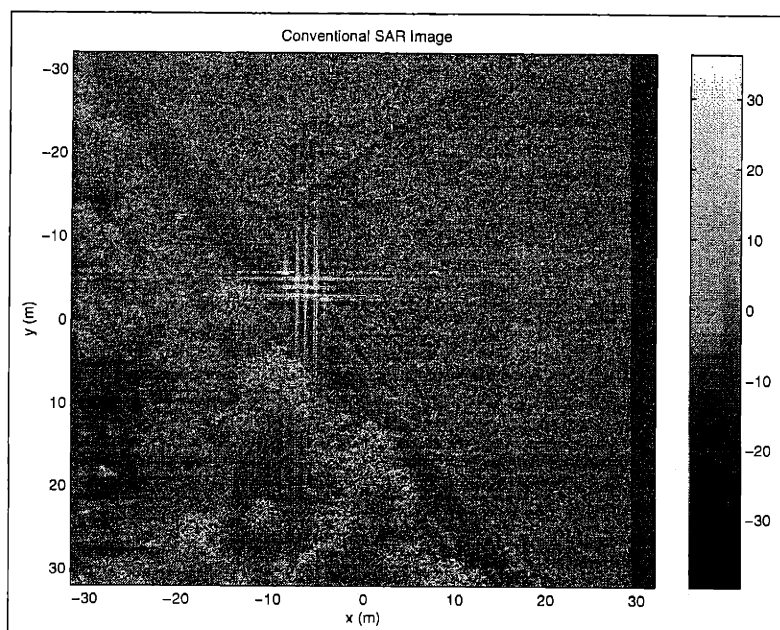
Figure 4.46: Stationary-Target Conventional SAR Image with a Scatterer Spacing of $1m$
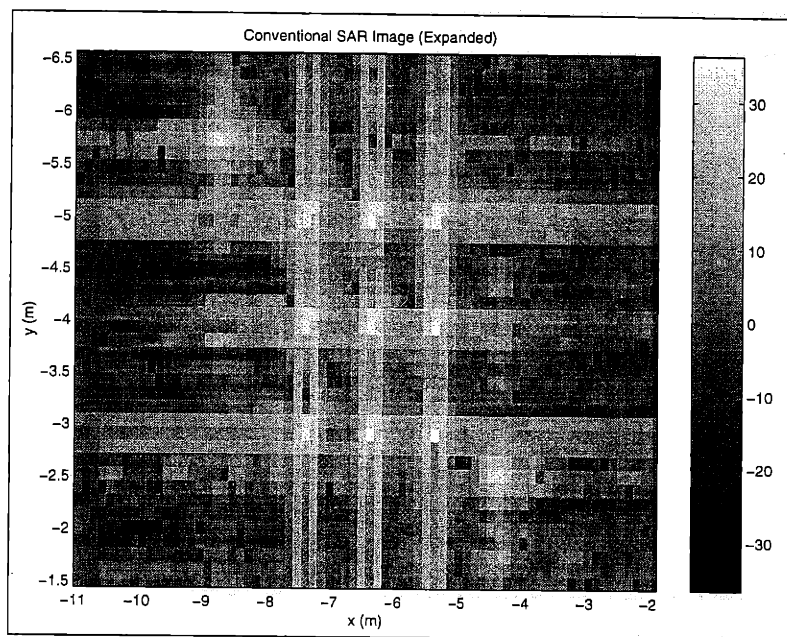
Figure 4.47: Expanded Stationary-Target Conventional SAR Image with a Scatterer Spacing of $1m$
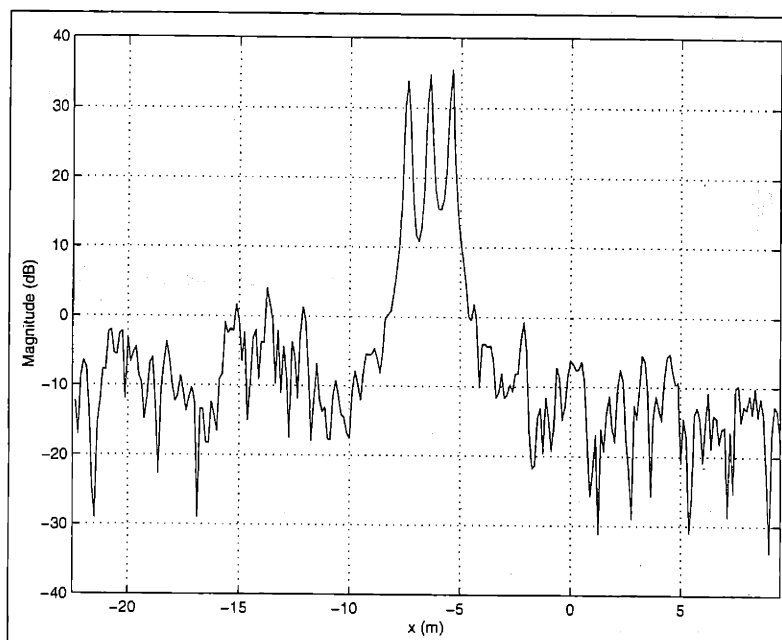
Figure 4.48: Cross-Section of Stationary-Target Conventional SAR Image (at $y = -4m$) with a Scatterer Spacing of $1m$
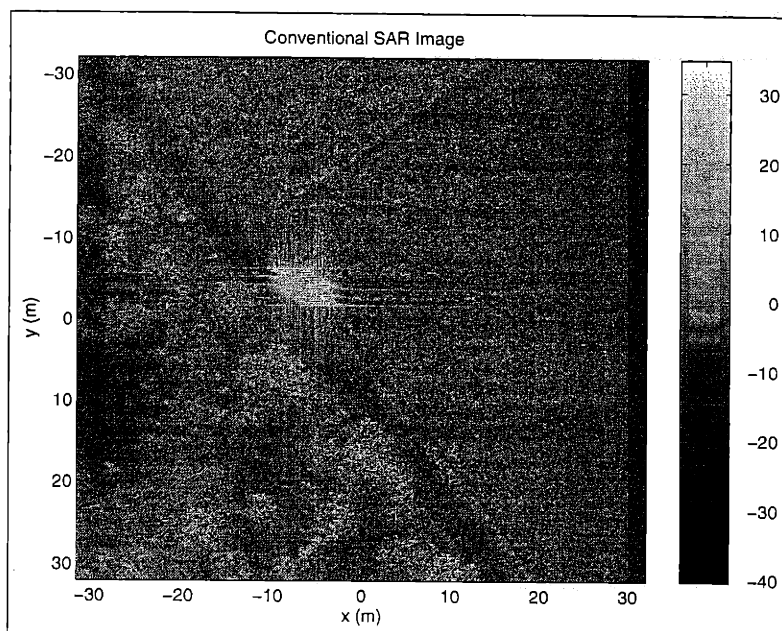
Figure 4.49: Conventional SAR Image for Rigid-Body Purely-Translational Motion with a Scatterer Spacing of $1m$
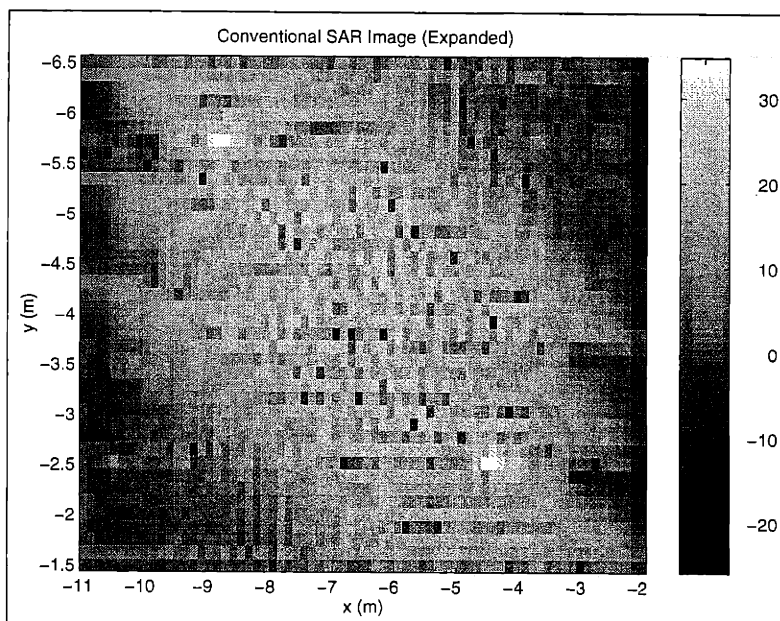
Figure 4.50: Expanded Conventional SAR Image for Rigid-Body Purely-Translational Motion with a Scatterer Spacing of $1m$
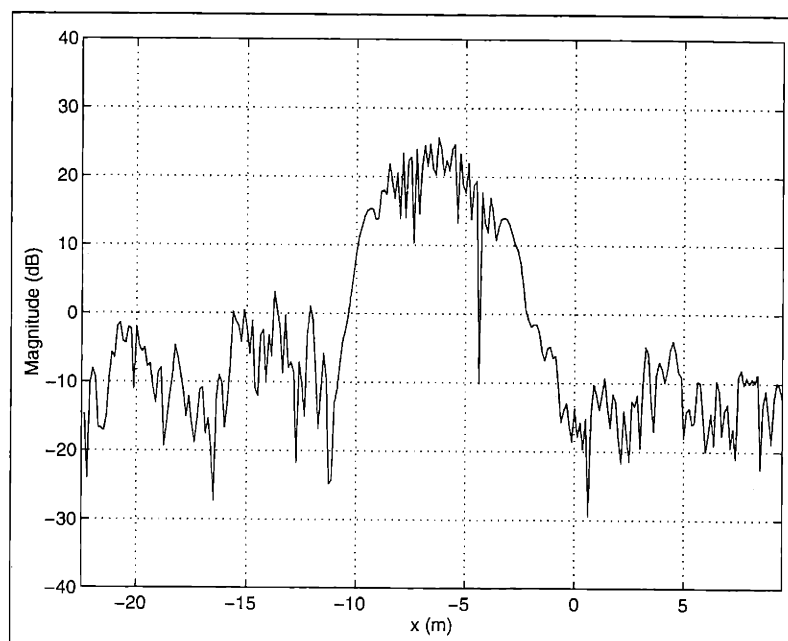
Figure 4.51: Cross-Section of Conventional SAR Image (at $y = -4m$) for Rigid-Body Purely-Translational Motion with a Scatterer Spacing of $1m$
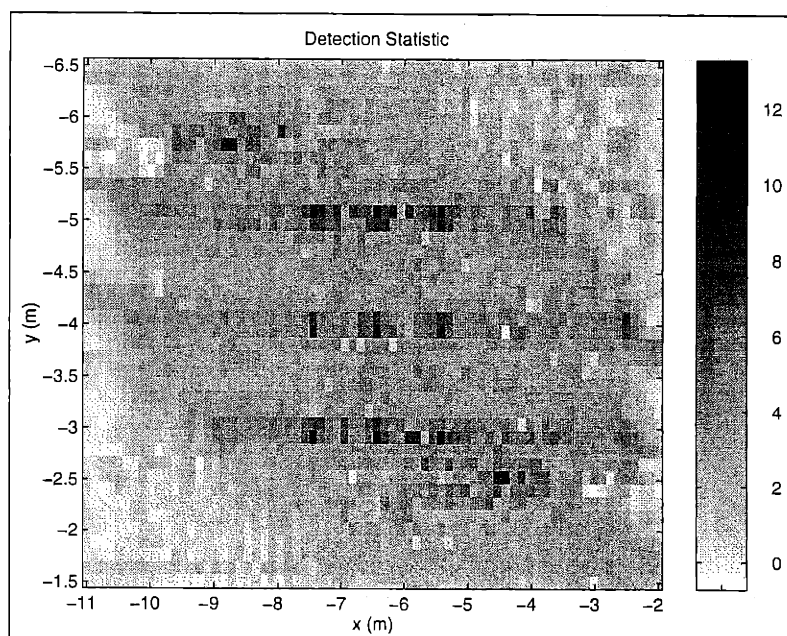
Figure 4.52: Detection Statistic for Rigid-Body Purely-Translational Motion with a Scatterer Spacing of $1m$
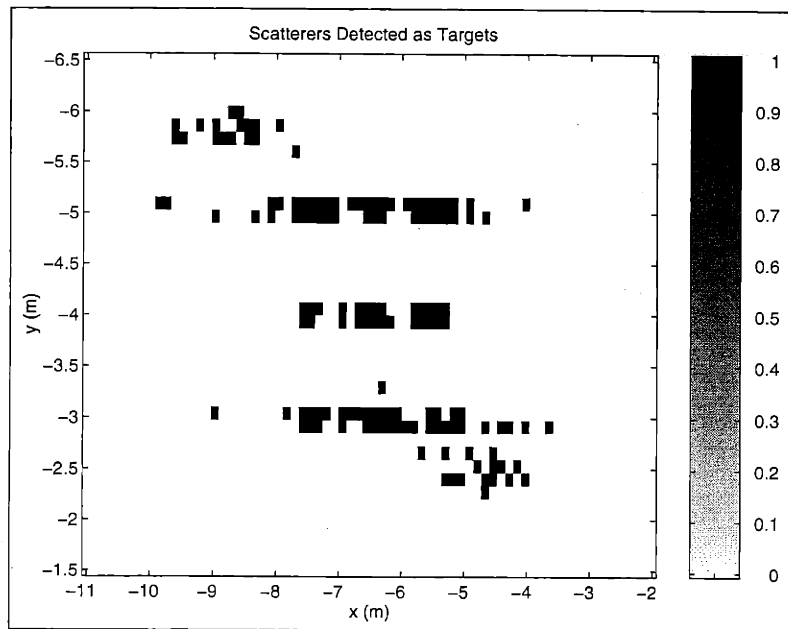
Figure 4.53: Selected Target Scatterers for Rigid-Body Purely-Translational Motion with a Scatterer Spacing of $1m$
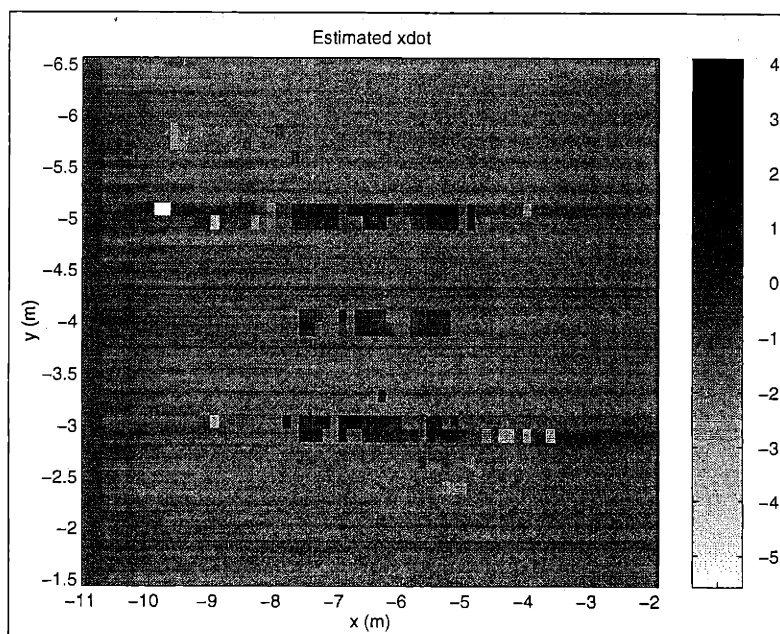
Figure 4.54: Estimated Azimuth-Velocity Field $\dot{x}$ for Rigid-Body Purely-Translational Motion with a Scatterer Spacing of $1m$
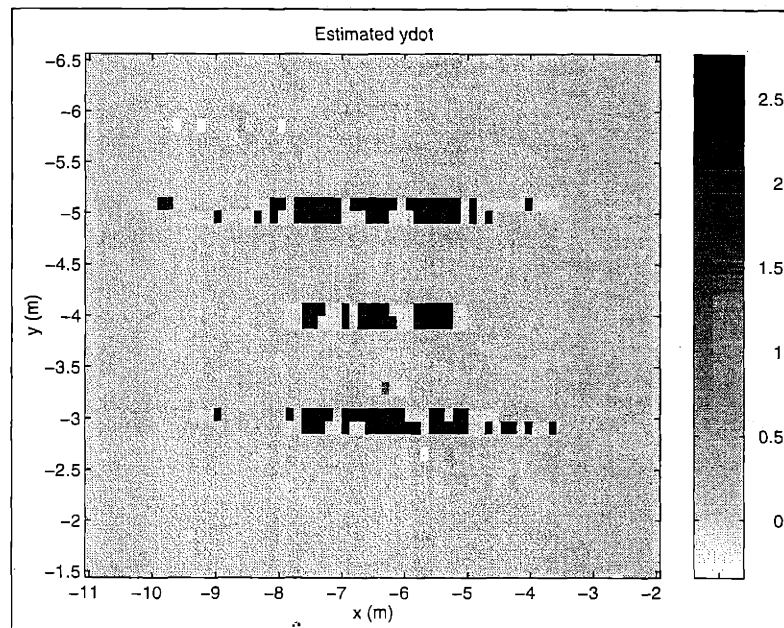
Figure 4.55: Estimated Range-Velocity Field $\dot{y}$ for Rigid-Body Purely-Translational Motion with a Scatterer Spacing of $1m$
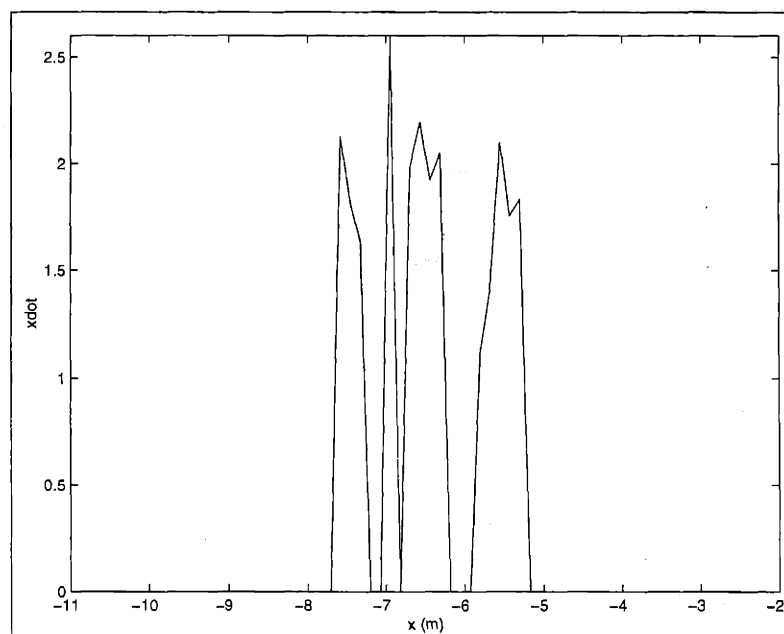
Figure 4.56: Cross-Section of Estimated Azimuth-Velocity Field $\dot{x}$ (at $y = -4m$) for Rigid-Body Purely-Translational Motion with a Scatterer Spacing of $1m$
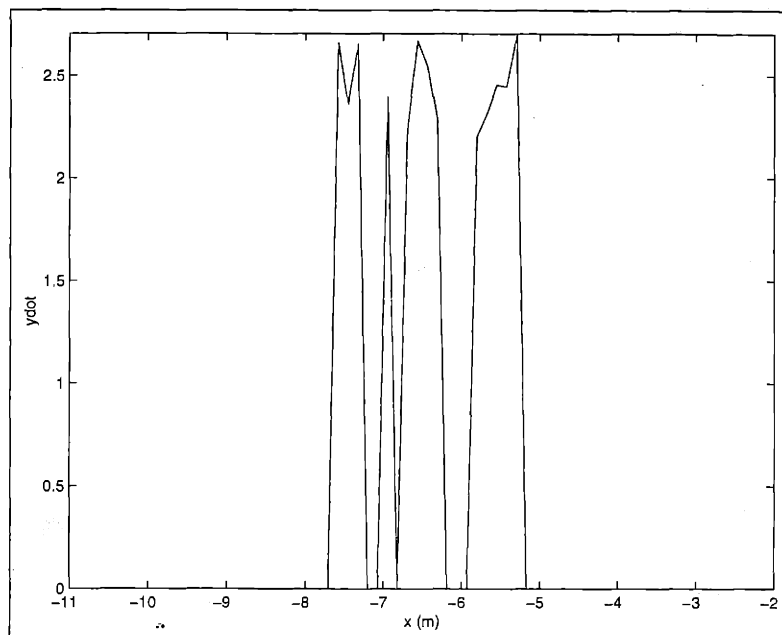
Figure 4.57: Cross-Section of Estimated Range-Velocity Field $\dot{y}$ (at $y = -4m$) for Rigid-Body Purely-Translational Motion with a Scatterer Spacing of $1m$
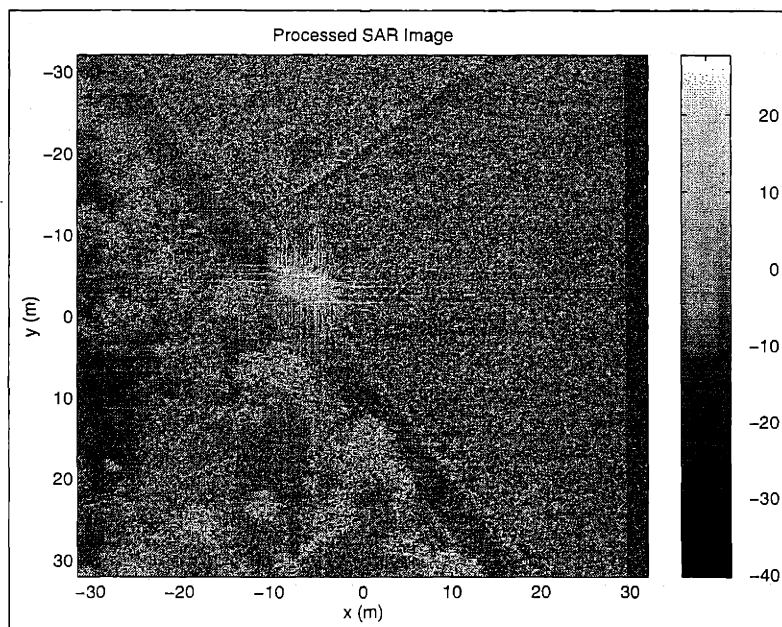
Figure 4.58: Matched-Filter SAR Image for Rigid-Body Purely-Translational Motion with a Scatterer Spacing of $1m$
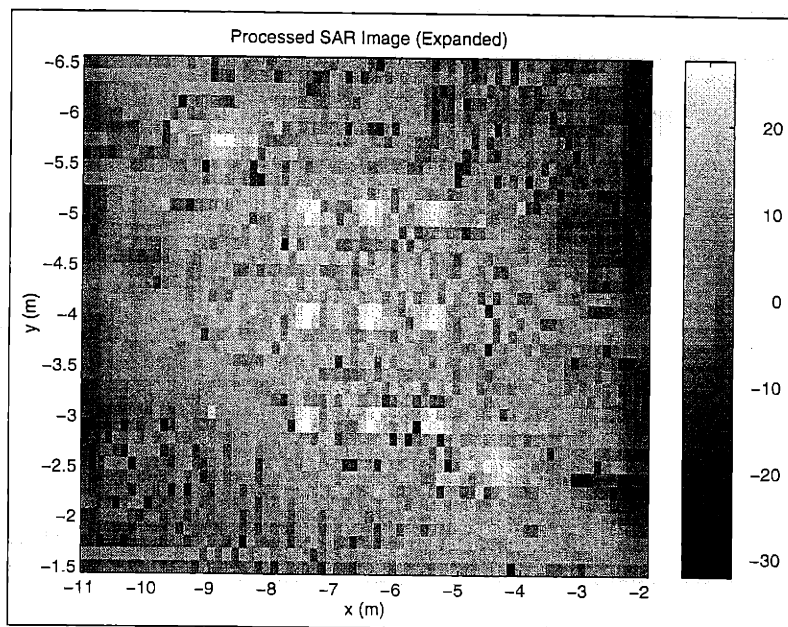
Figure 4.59: Expanded Matched-Filter SAR Image for Rigid-Body Purely-Translational Motion with a Scatterer Spacing of $1m$
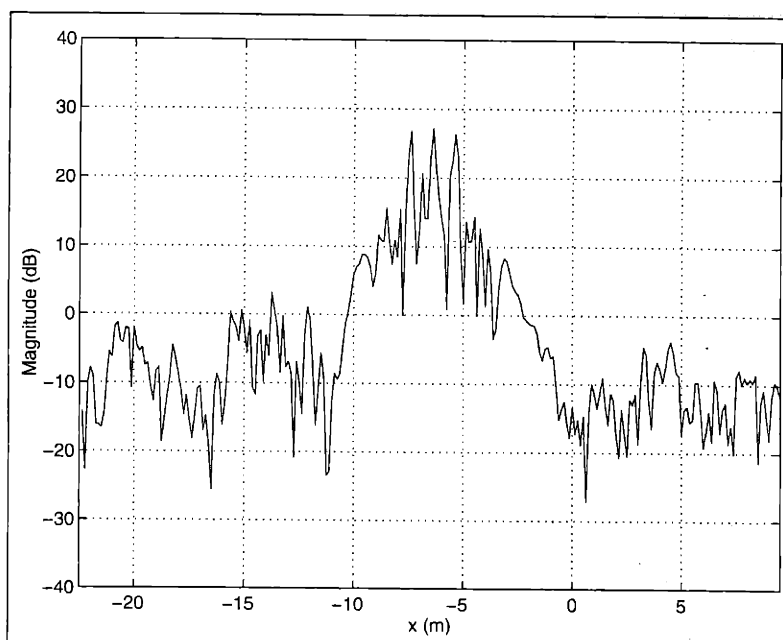
Figure 4.60: Cross-Section of Matched-Filter SAR Image (at $y = -4m$) for Rigid-Body Purely-Translational Motion with a Scatterer Spacing of $1m$
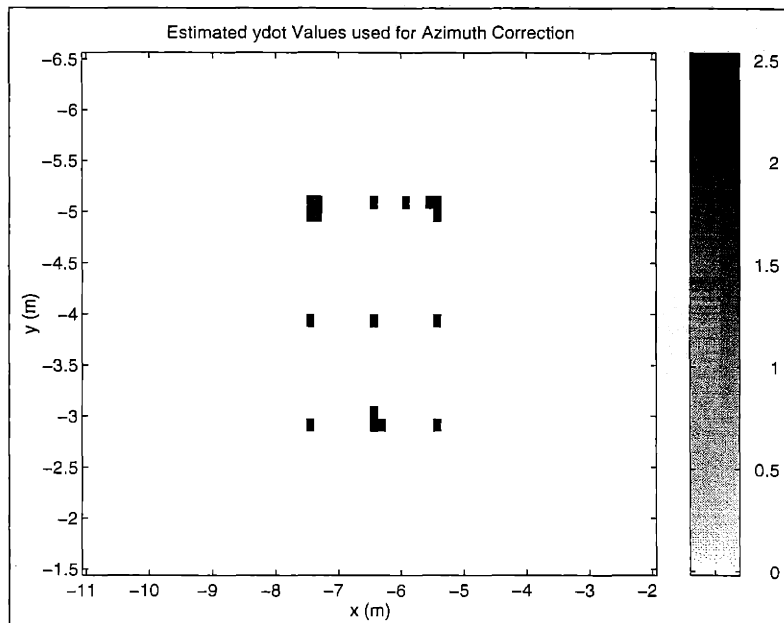
Figure 4.61: Estimated Range-Velocity Values used for Azimuth-Displacement Compensation for Rigid-Body Purely-Translational Motion with a Scatterer Spacing of $1m$
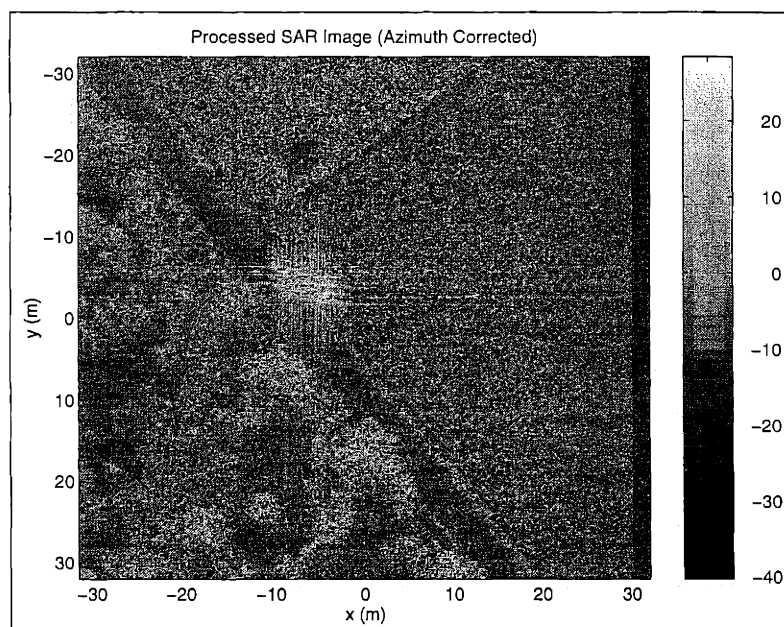
Figure 4.62: Azimuth-Displacement Compensated Matched-Filter SAR Image for Rigid-Body Purely-Translational Motion with a Scatterer Spacing of $1m$
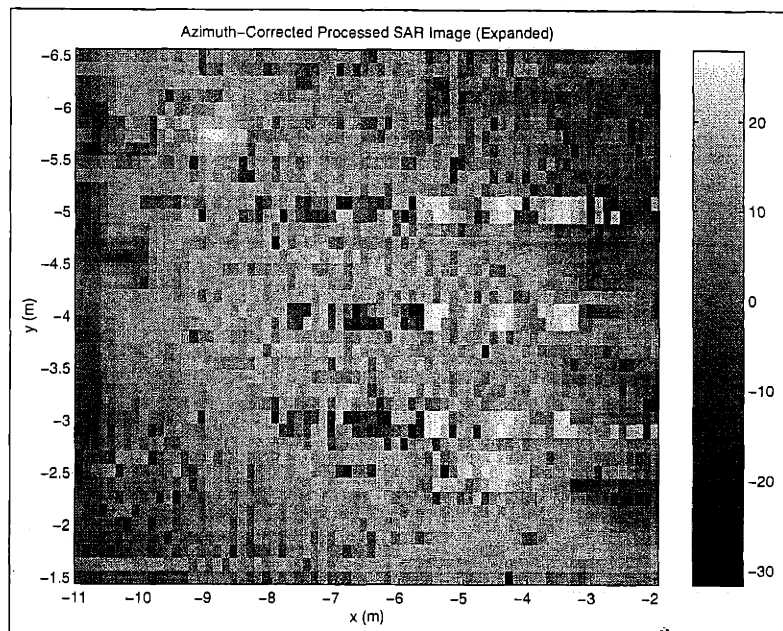
Figure 4.63: Expanded Azimuth-Displacement Compensated Matched-Filter SAR Image for Rigid-Body Purely-Translational Motion with a Scatterer Spacing of $1m$
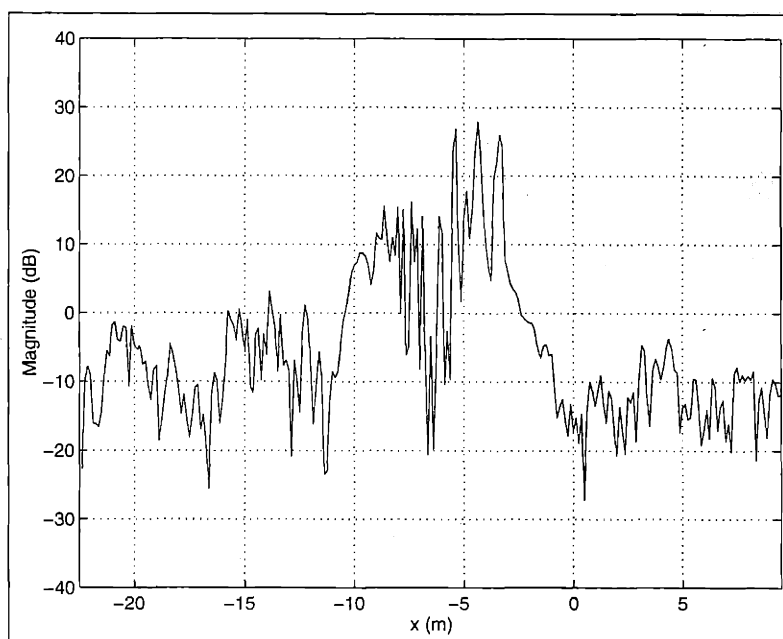
Figure 4.64: Cross-Section of Azimuth-Displacement Compensated Matched-Filter SAR Image (at $y = -4m$) for Rigid-Body Purely-Translational Motion with a Scatterer Spacing of $1m$
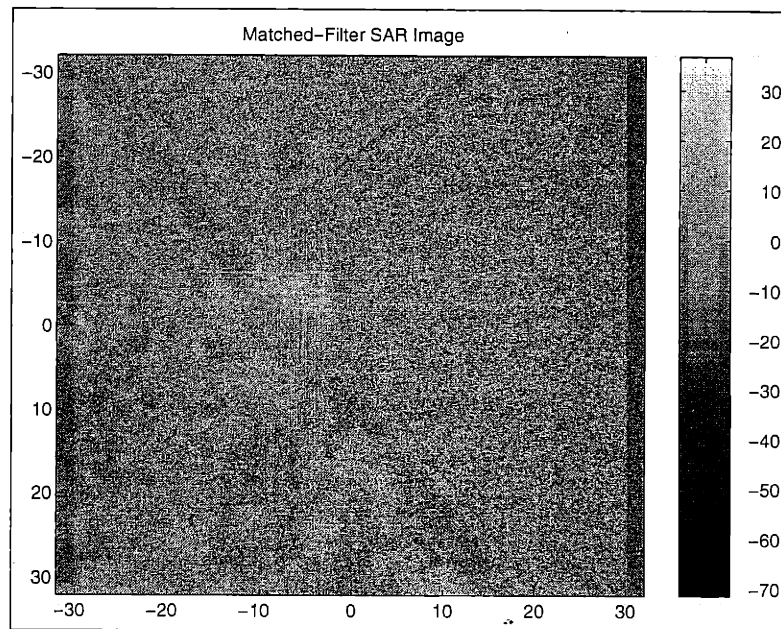
Figure 4.65:   Exact-Velocity Matched-Filter SAR Image for Rigid-Body Purely-Translational Motion with a Scatterer Spacing of $1m$
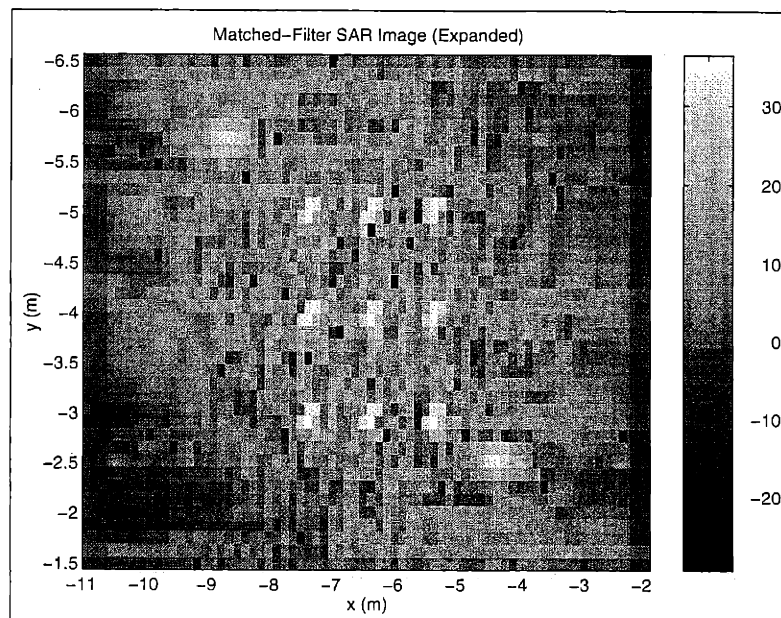
Figure 4.66: Expanded Exact-Velocity Matched-Filter SAR Image for Rigid-Body Purely-Translational Motion with a Scatterer Spacing of $1m$
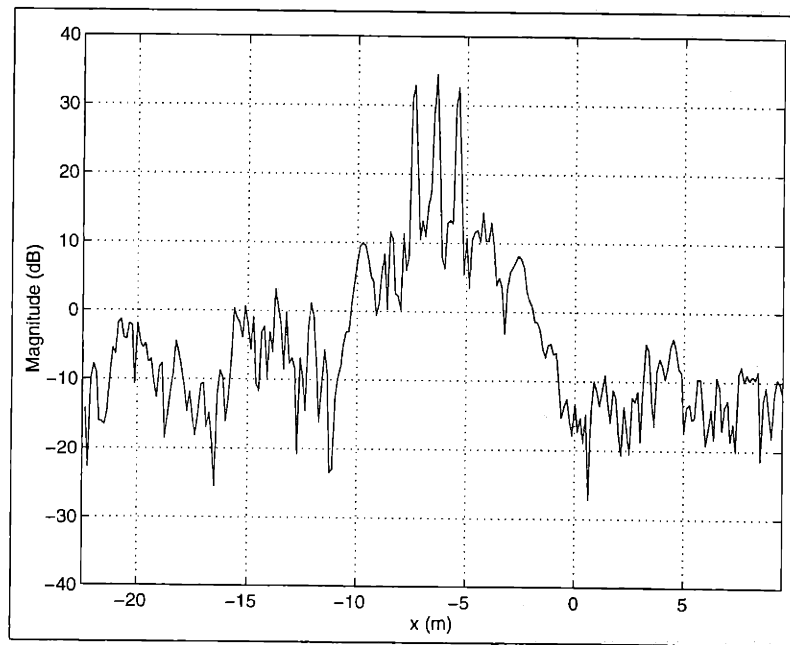
Figure 4.67: Cross-Section of Exact-Velocity Matched-Filter SAR Image (at $y = -4m$) for Rigid-Body Purely-Translational Motion with a Scatterer Spacing of $1m$

Rigid-Body Temporally-Constant Velocity Translational Motion with a Scatterer Spacing of $0.75m$

For this example, we again have nine "synthetic" moving point-scatterers (with an amplitude of $40dB$), with initial positions in a "box" configuration centered at $(x, y) = (-6.5m, -4m)$ near the two "man-made clutter" high-amplitude scatterers, as shown in the stationary-target conventional SAR images of Figure 4.68 and Figure 4.69. A cross-section of the stationary-target conventional SAR image (at $y = -4m$) is also shown in Figure 4.70. Here, we see three peaks corresponding to scatterers #'s 0, 2, and 5. As compared to the previous experimental example, these synthetic scatterers have a slightly smaller spatial separation of $\delta_0 = 0.75m$, in order to illustrate the imaging resolution limitations of the matched-filter algorithm.

We again have rigid-body target purely-translational motion, i.e., all of the nine moving synthetic-target point-scatterers had a velocity of $(\dot{x}[n_x, n_y], \dot{y}[n_x, n_y]) = (2m/s, 2.304m/s)$. As shown in Figures 4.71- 4.73, we see that the conventional SAR image is essentially useless for the purposes of automatic target recognition.

For the matched-filter, we used the clutter-nulling cross-interference reduction algorithm with a threshold of of $A_T[n_x, n_y] = 10|\hat{A}_{CONV}[n_x, n_y]|$. The resulting target-detection statistic is shown in Figure 4.74. Again we see that the locations of the nine synthetic moving point-scatterers (plus the two stationary "man-made clutter" scatterers) are again readily apparent from the "darker" areas of this image. For comparison purposes, we again chose a detection-statistic threshold χ_{MAX} of 6 we used in the previous example. The resulting target scatterer locations are shown in Figure 4.75. As compared to the previous example, we see that the matched-filter detection scheme has generated slightly more spurious false-alarm locations.

In order to compute the median-prefiltered matched-filter velocity estimates , we used median filters with a spatial region-of-interest (ROI) of $0.5m \times 0.5m$. For the reduced-order L_1-Norm based velocity-estimation algorithm, we used an L_1 weighting of $\gamma_A = 1.1$ (which was identical to the first example). The estimated azimuth velocities and range velocities are shown in Figure 4.76 and Figure 4.77, and in the cross-sections of Figure 4.78 and Figure 4.79. As compared to the previous example, we see from the velocity-field cross-sections that the matched-filter has a slightly larger azimuth-velocity error for scatterer # 5.

The matched-filter SAR images are shown in Figure 4.80 and Figure 4.81. Here, we see that all of the target scatterers are focused and distinct. However, from the cross-section plot of Figure 4.82, we see that the scatterers are not as sharply focused as the previous case with the scatterer spacing of $1m$. For this case, we only have a mainlobe height of about $12dB$. The SAR images formed by the least-squares amplitude-estimation algorithm when the scatterer-velocities are known exactly are shown Figure 4.87 and Figure 4.88. Just as with the previous example, the scatterers have a mainlobe height of approximately $20dB$, as shown in Figure 4.89.

For the azimuth-displacement compensation, we again averaged the range velocity over a set of "bright" scatterer locations where both the target-detection statistic, $\chi[n_x, n_y]$, was greater than 8.5, and where the magnitude of estimated range-velocity was greater than $0.5m/s$, as shown in Figure 4.83. For this example, the average range velocity for

these scatterer locations was computed to be $2.2745m/s$, which was slightly better than the average-velocity computed for the previous example One explanation for this smaller error bias is that (unlike for the azimuth velocity, as we saw in the velocity-field cross-section of Figure 4.78), the range-velocity is improved (for purely-translational rigid-body motion) when the scatterer energy is more concentrated (due to the smaller spacing).

We then used this velocity to compensate the scatterers at the previous "target" spatial locations (with $\chi[n_x, n_y] \leq 6$) which had an estimated range-velocity with a magnitude greater than $0.5m/s$. As shown in Figure 4.85 and Figure 4.86, the resulting azimuth-displacement error for the moving target was approximately $1m$, which again was somewhat better than the previous example (due to the smaller average estimation-error in the range velocity).
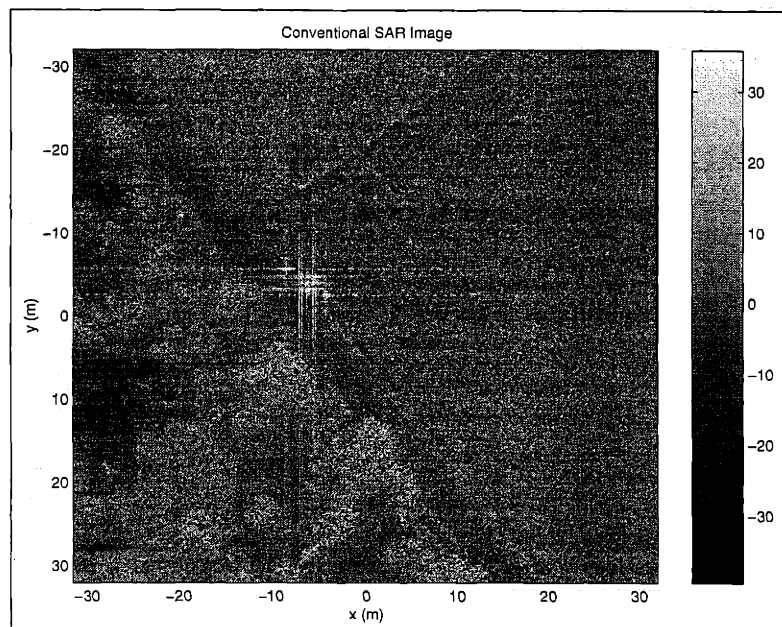
Figure 4.68: Stationary-Target Conventional SAR Image with a Scatterer Spacing of $0.75m$
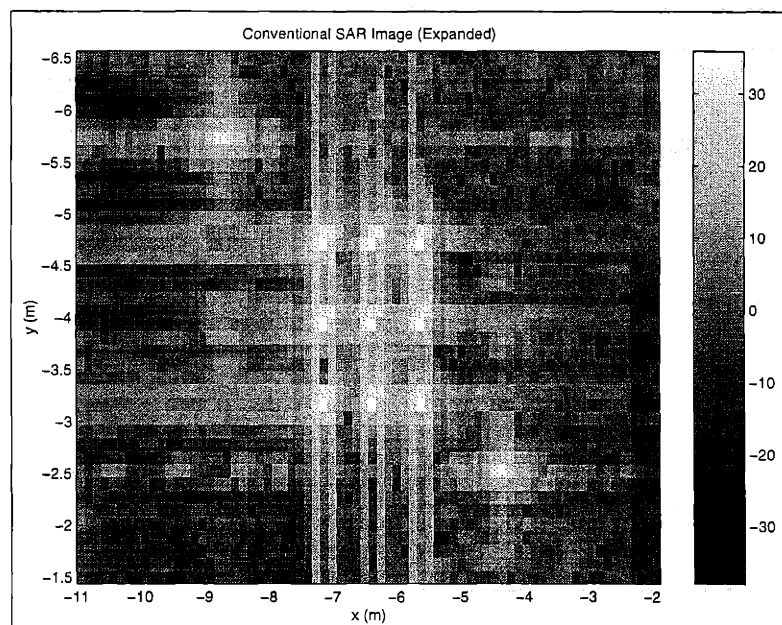
Figure 4.69: Expanded Stationary-Target Conventional SAR Image with a Scatterer Spacing of $0.75m$
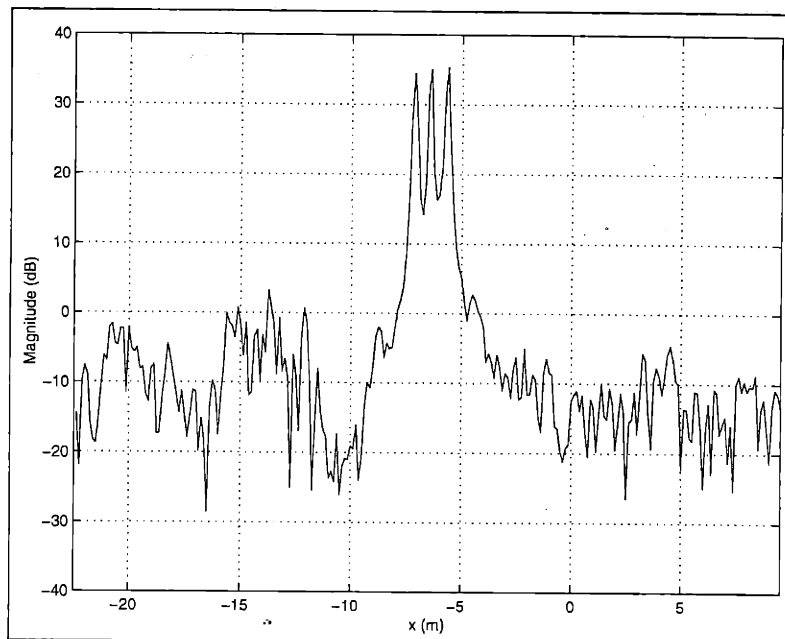
Figure 4.70: Cross-Section of Stationary-Target Conventional SAR Image (at $y = -4m$) with a Scatterer Spacing of $0.75m$
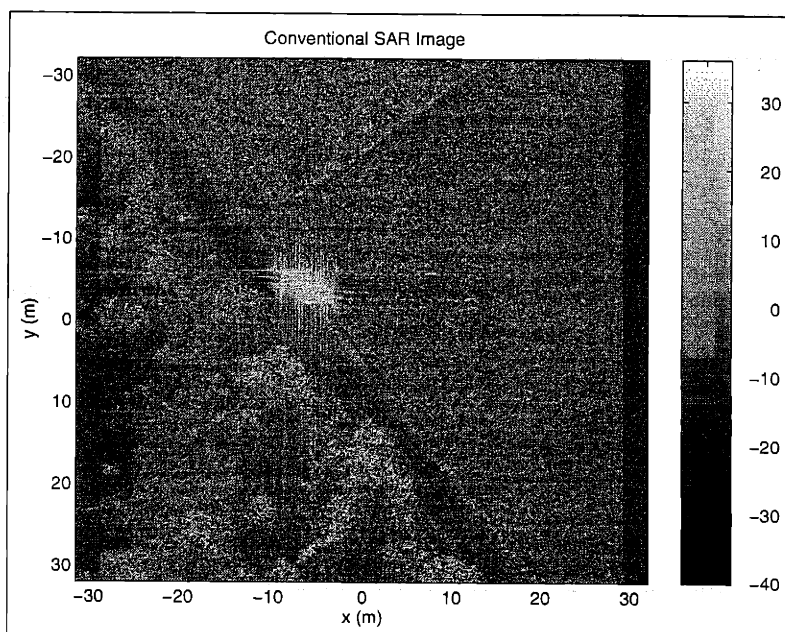
Figure 4.71: Conventional SAR Image for Rigid-Body Purely-Translational Motion with a Scatterer Spacing of $0.75m$
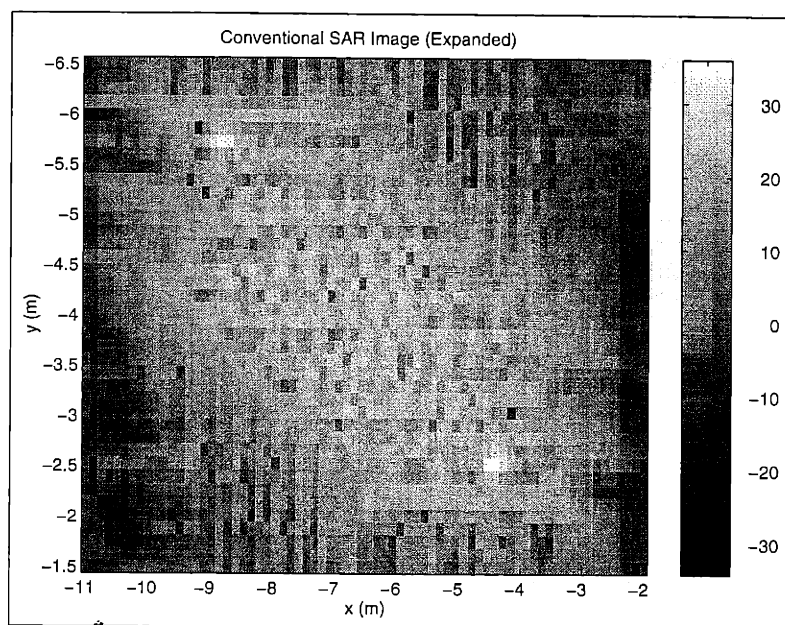
Figure 4.72: Expanded Conventional SAR Image for Rigid-Body Purely-Translational Motion with a Scatterer Spacing of 0.75m
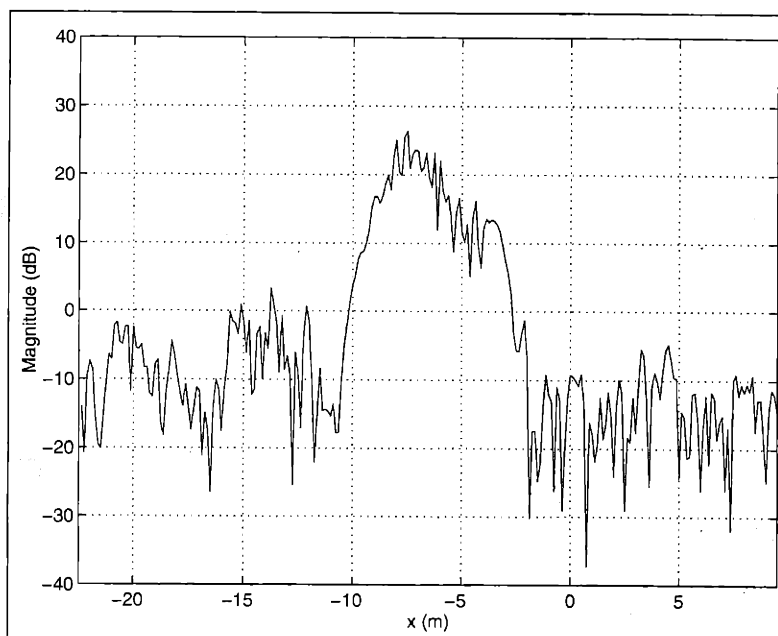
Figure 4.73: Cross-Section of Conventional SAR Image (at $y = -4m$) for Rigid-Body Purely-Translational Motion with a Scatterer Spacing of 0.75m
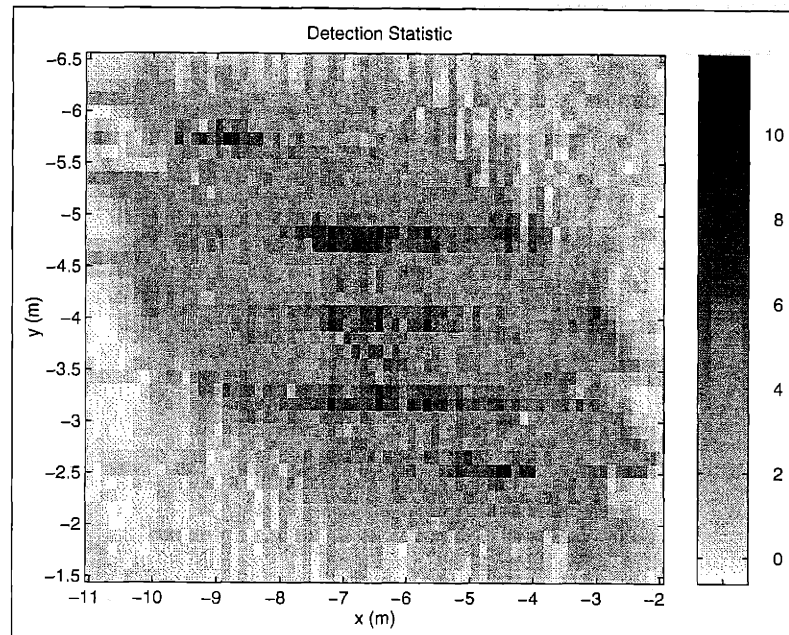
Figure 4.74: Detection Statistic for Rigid-Body Purely-Translational Motion with a Scatterer Spacing of $0.75m$
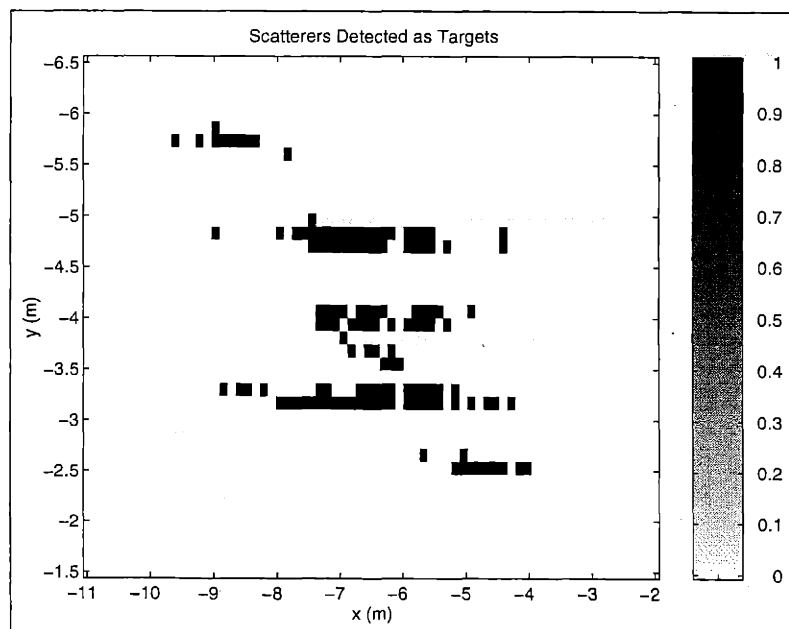
Figure 4.75: Selected Target Scatterers for Rigid-Body Purely-Translational Motion with a Scatterer Spacing of $0.75m$
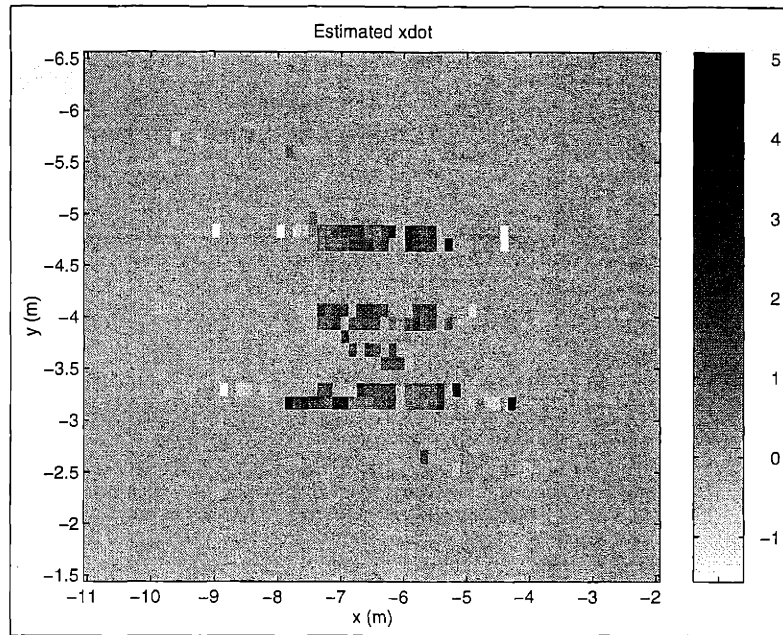
Figure 4.76: Estimated Azimuth-Velocity Field $\dot{x}$ for Rigid-Body Purely-Translational Motion with a Scatterer Spacing of $0.75m$
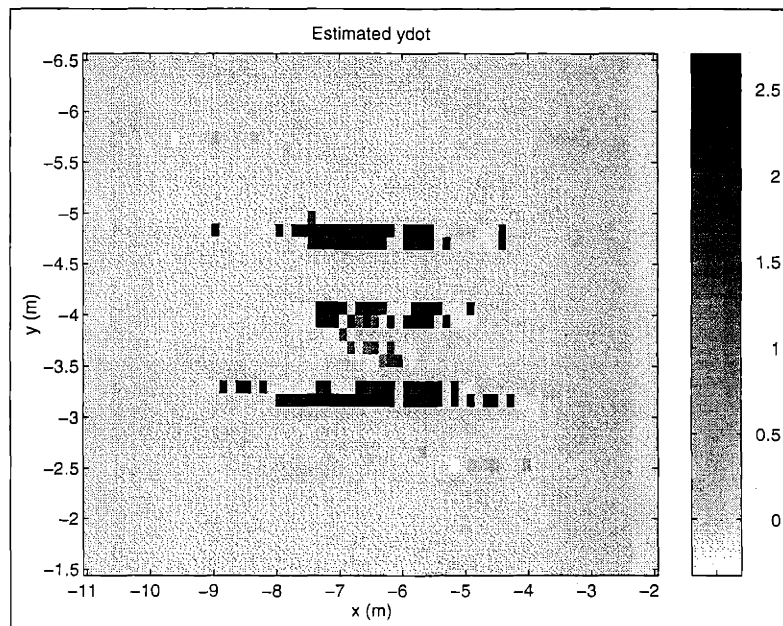
Figure 4.77: Estimated Range-Velocity Field $\dot{y}$ for Rigid-Body Purely-Translational Motion with a Scatterer Spacing of $0.75m$
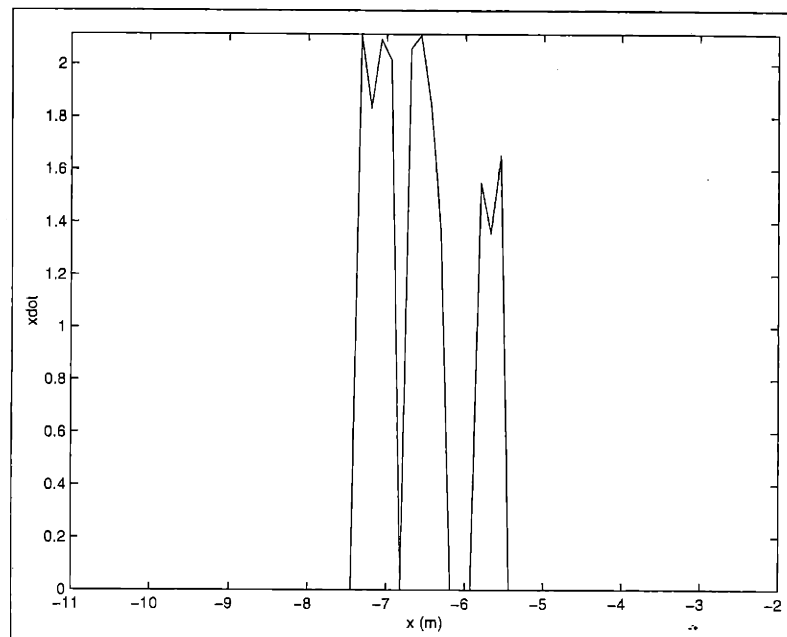
Figure 4.78: Cross-Section of Estimated Azimuth-Velocity Field $\dot{x}$ (at $y = -4m$) for Rigid-Body Purely-Translational Motion with a Scatterer Spacing of $0.75m$
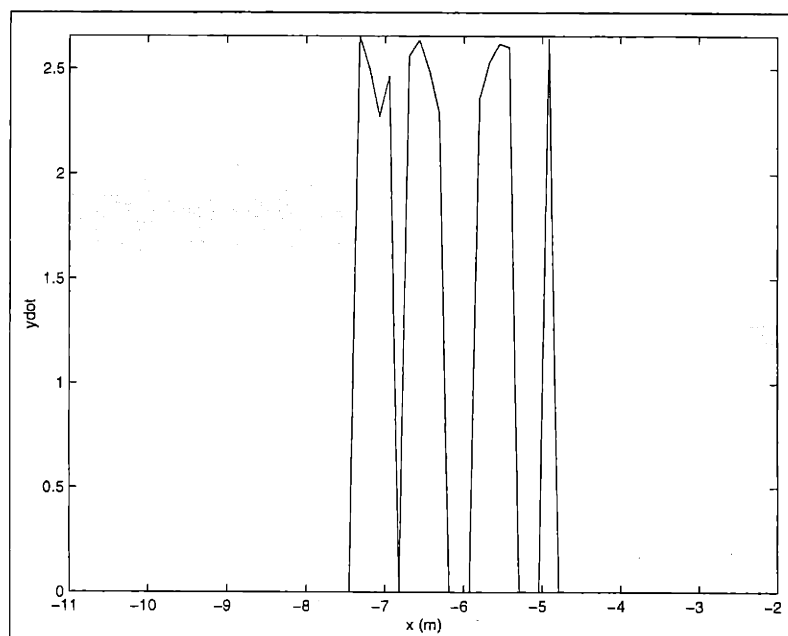
Figure 4.79: Cross-Section of Estimated Range-Velocity Field $\dot{y}$ (at $y = -4m$) for Rigid-Body Purely-Translational Motion with a Scatterer Spacing of $0.75m$
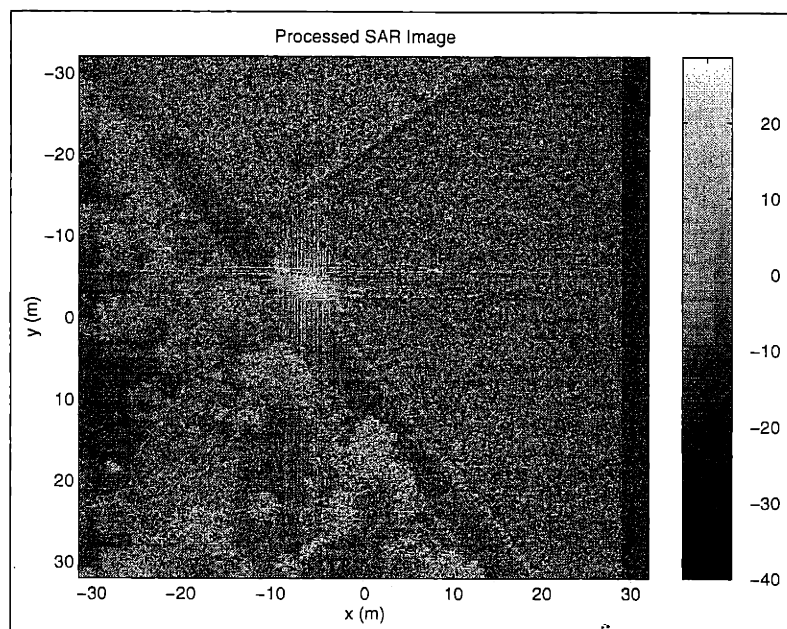
Figure 4.80: Matched-Filter SAR Image for Rigid-Body Purely-Translational Motion with a Scatterer Spacing of $0.75m$
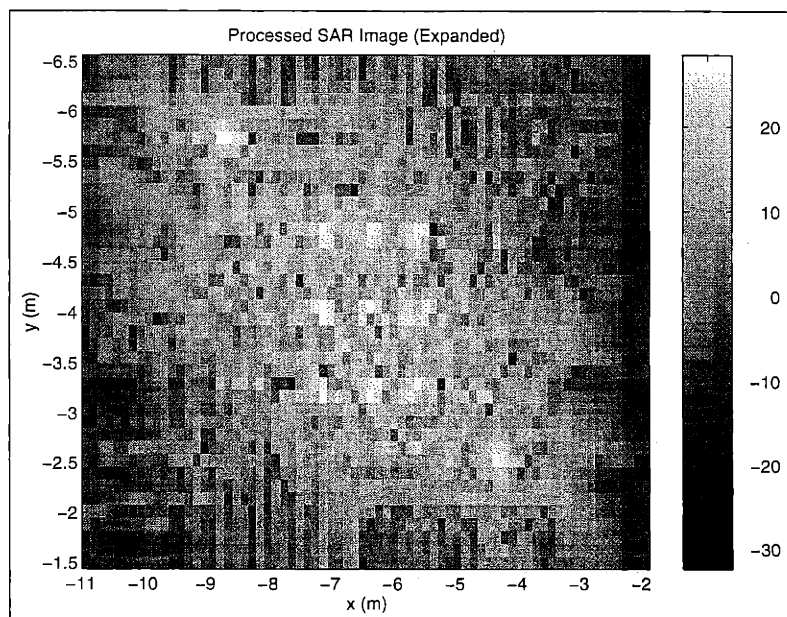
Figure 4.81: Expanded Matched-Filter SAR Image for Rigid-Body Purely-Translational Motion with a Scatterer Spacing of $0.75m$
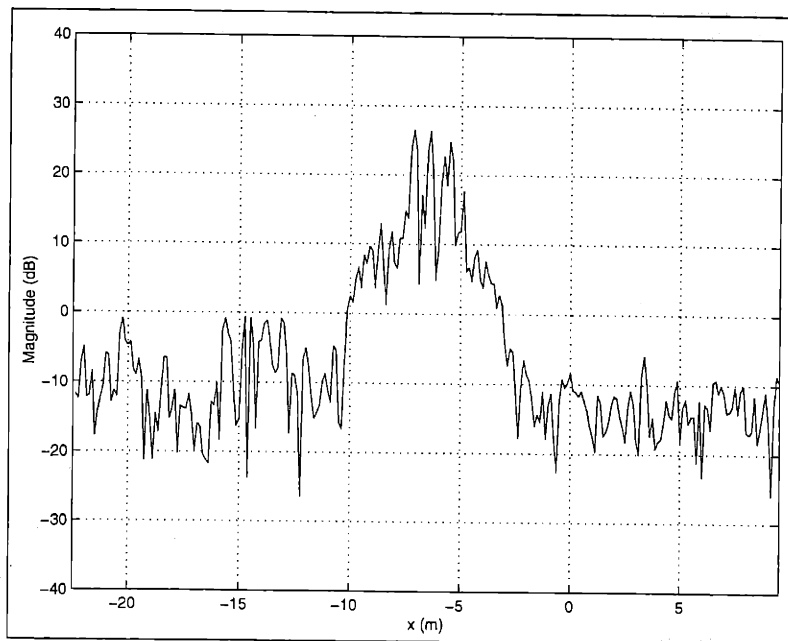
Figure 4.82: Cross-Section of Matched-Filter SAR Image (at $y = -4m$) for Rigid-Body Purely-Translational Motion with a Scatterer Spacing of $0.75m$
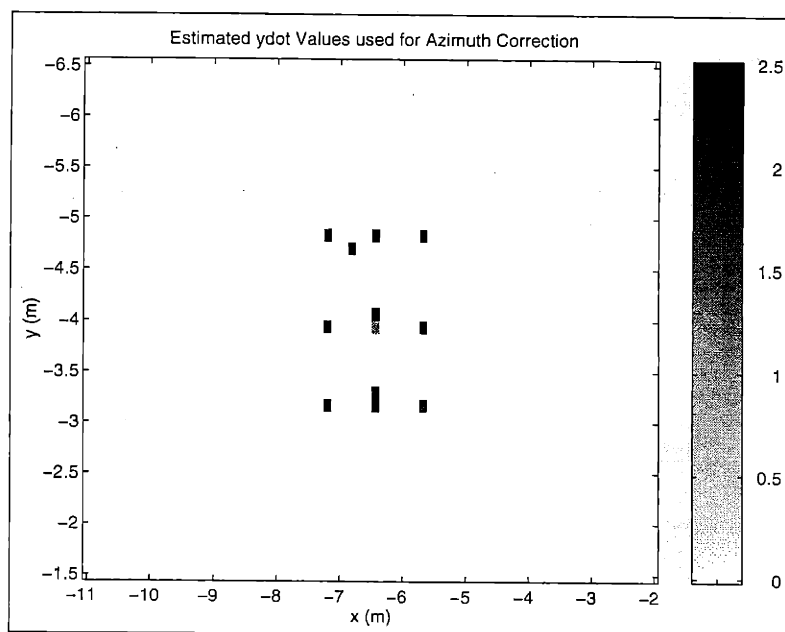
Figure 4.83: Estimated Range-Velocity Values used for Azimuth-Displacement Compensation for Rigid-Body Purely-Translational Motion with a Scatterer Spacing of $0.75m$
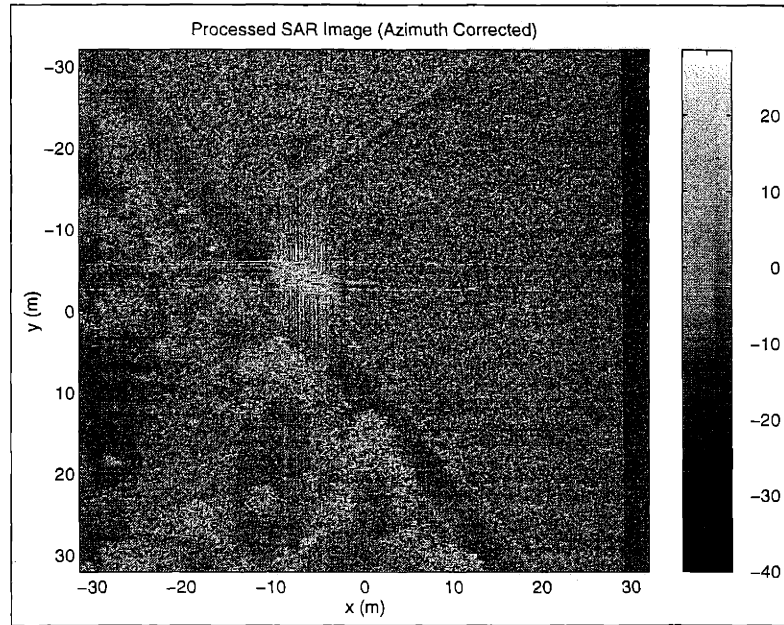
Figure 4.84: Azimuth-Displacement Compensated Matched-Filter SAR Image for Rigid-Body Purely-Translational Motion with a Scatterer Spacing of $0.75m$
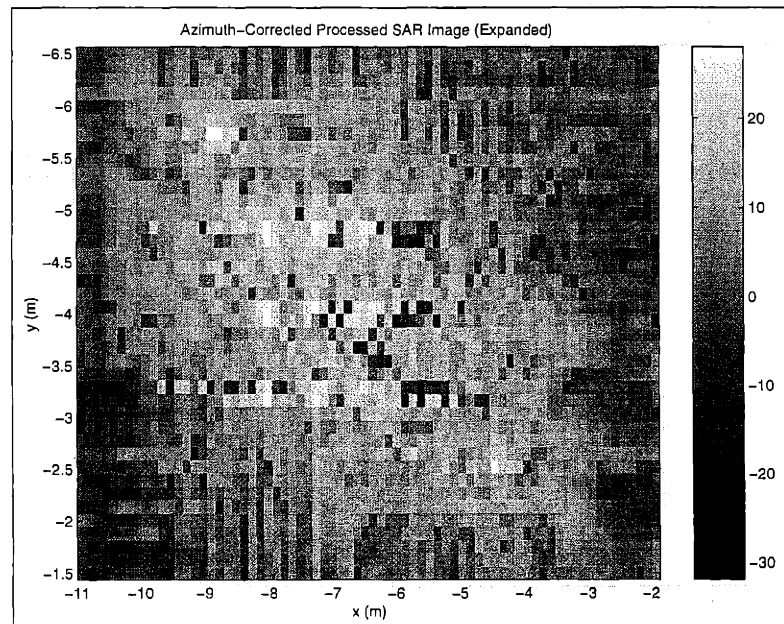
Figure 4.85: Expanded Azimuth-Displacement Compensated Matched-Filter SAR Image for Rigid-Body Purely-Translational Motion with a Scatterer Spacing of $0.75m$
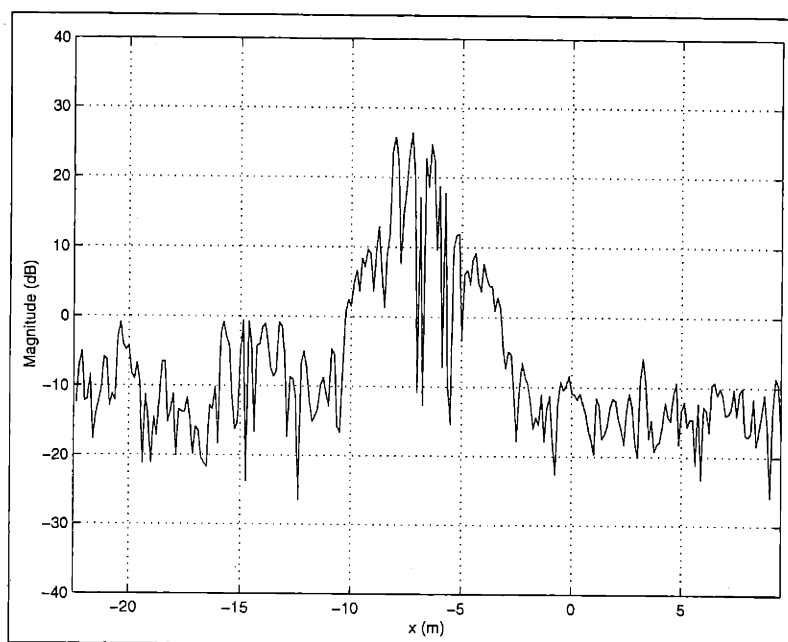
Figure 4.86: Cross-Section of Azimuth-Displacement Compensated Matched-Filter SAR Image (at $y = -4m$) for Rigid-Body Purely-Translational Motion with a Scatterer Spacing of $0.75m$
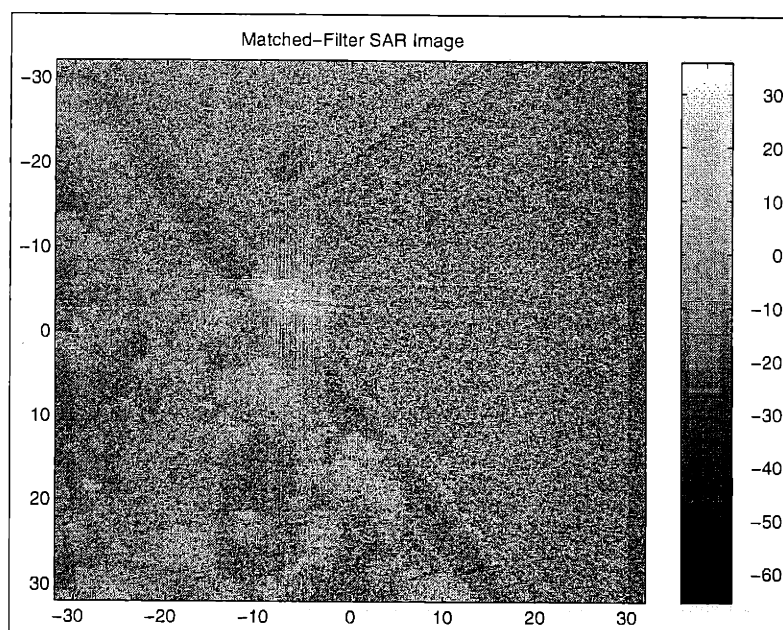
Figure 4.87: Exact-Velocity Matched-Filter SAR Image for Rigid-Body Purely-Translational Motion with a Scatterer Spacing of $0.75m$
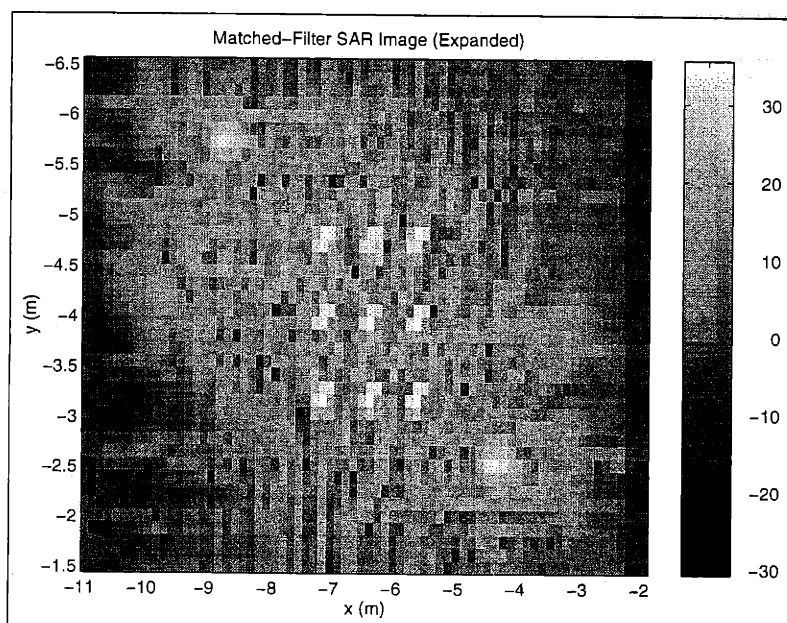
Figure 4.88: Expanded Exact-Velocity Matched-Filter SAR Image for Rigid-Body Purely-Translational Motion with a Scatterer Spacing of $0.75m$
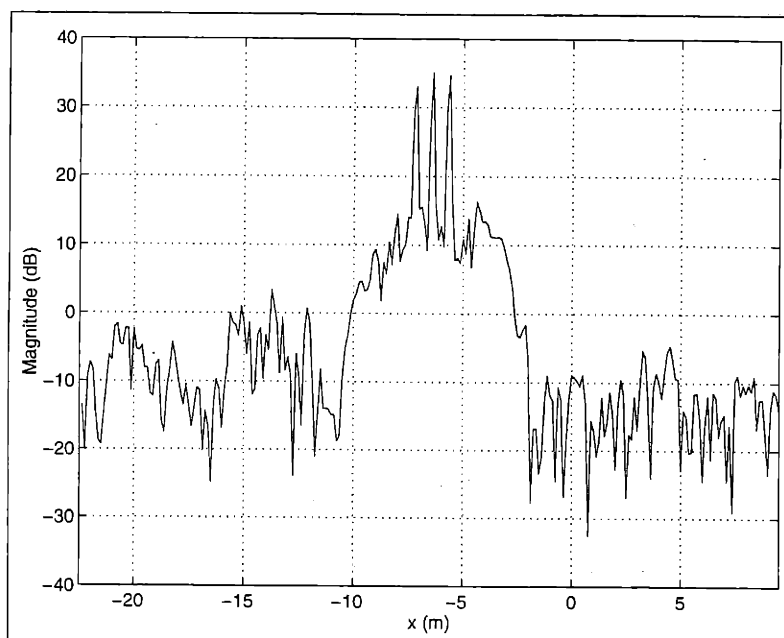
Figure 4.89: Cross-Section of Exact-Velocity Matched-Filter SAR Image (at $y = -4m$) for Rigid-Body Purely-Translational Motion with a Scatterer Spacing of $0.75m$

Non-Rigid Body Motion with a Scatterer Spacing of $1m$

For the previous two experimental examples of matched-filter SAR processing, we strictly dealt with rigid-body, purely translational motion (i.e., all of the synthetic target scatterers had identical velocities). For this example, we examine the effects of "non-rigid body" spatial variations in the azimuthal scatterer velocities. For comparison purposes we again had nine synthetic moving point-scatterers, with initial positions in a "box" configuration centered at $(x, y) = (-6.5m, -4m)$ near the two man-made high-amplitude scatterers. The spatial spacing in the initial positions of the scatterers was chosen to be $1m$, which was identical to the first experimental example. However, we now chose the azimuth velocities to be samples of a Gaussian random variable, with a mean of $2m/s$ and a standard-deviation of $0.5m/s$. We also chose the range velocities to be samples of a Gaussian random variable, with a mean of $2.304m/s$ and a standard-deviation of $0.25m/s$. In particular:

Scatterer #0: $(n_x\Delta_x, n_y\Delta_y, \dot{x}[n_x, n_y], \dot{y}[n_x, n_y]) = (-6.5m, -4m, 2.2071m/s, 2.1224m/s)$

Scatterer #1: $(n_x\Delta_x, n_y\Delta_y, \dot{x}[n_x, n_y], \dot{y}[n_x, n_y]) = (-7.5m, -5m, 2.3747m/s, 2.0380m/s)$

Scatterer #2: $(n_x\Delta_x, n_y\Delta_y, \dot{x}[n_x, n_y], \dot{y}[n_x, n_y]) = (-7.5m, -4m, 2.1588m/s, 2.2517m/s)$

Scatterer #3: $(n_x\Delta_x, n_y\Delta_y, \dot{x}[n_x, n_y], \dot{y}[n_x, n_y]) = (-7.5m, -3m, 2.7581m/s, 2.4445m/s)$

Scatterer #4: $(n_x\Delta_x, n_y\Delta_y, \dot{x}[n_x, n_y], \dot{y}[n_x, n_y]) = (-5.5m, -5m, 1.8760m/s, 2.3415m/s)$

Scatterer #5: $(n_x\Delta_x, n_y\Delta_y, \dot{x}[n_x, n_y], \dot{y}[n_x, n_y]) = (-5.5m, -4m, 1.7467m/s, 2.3919m/s)$

Scatterer #6: $(n_x\Delta_x, n_y\Delta_y, \dot{x}[n_x, n_y], \dot{y}[n_x, n_y]) = (-5.5m, -3m, 2.4426m/s, 2.5872m/s)$

Scatterer #7: $(n_x\Delta_x, n_y\Delta_y, \dot{x}[n_x, n_y], \dot{y}[n_x, n_y]) = (-6.5m, -5m, 1.4893m/s, 2.1508m/s)$

Scatterer #8: $(n_x\Delta_x, n_y\Delta_y, \dot{x}[n_x, n_y], \dot{y}[n_x, n_y]) = (-6.5m, -3m, 1.5111, 2.1927m/sm/s)$

As before, these synthetic point-scatterers were embedded in the background-clutter SAR image as shown in the conventional SAR images of Figure 4.90 and Figure 4.91. As with the previous examples, we cannot use these blurred images directly for automatic-target recognition algorithms. In addition, as compared to the previous two examples, we see severe distortion in the azimuth positions of the nine target scatterers due to the variations in the range velocities.

For the matched-filter, we used the clutter-nulling cross-interference reduction algorithm with a threshold of of $A_T[n_x, n_y] = 10|\hat{A}_{CONV}[n_x, n_y]|$. The target-detection statistic is shown in Figure 4.93. As compared to the rigid-body example with a scatterer spacing of $1m$, we see that the initial locations of the scatterers are not quite as distinct. Consequently, when we used a detection-statistic threshold χ_{MAX} of 6, we see that the detection scheme picked slightly more spurious false-alarm target locations, as shown in Figure 4.94. We again see the effects of the azimuth-position distortion due to the variations in the range-

velocity induced azimuth displacement (caused by the variations in the range velocity). Even though the algorithm was able to detect all nine of the target scatterers, there were relatively large errors in their azimuth positions. (though the detection scheme did correctly pick the location of the two stationary man-made clutter scatterers). For example, due to the range-velocity induced azimuth-displacement, scatterer #'s 0, 2, and 5 were detected at $(x, y) = (-1.5m, -4m)$, $(-6.1m, -4m)$, and $(-7.9m, -4m)$, respectively, rather than at their actual positions of $(x, y) = (-6.5, -4m)$, $(-7.5m, -4m)$, and $(-5.5m, -4m)$ (which meant that the spatial orientation of the scatterers relative to each other was distorted).

For the median-prefiltering, we used median filters with a spatial region-of-interest (ROI) of $0.5m \times 0.5m$. For the reduced-order L_1-Norm based velocity-estimation algorithm, we used an L_1 weighting of $\gamma_A = 1.1$ (which was identical to the first and second examples). The estimated azimuth velocities and range velocities are shown in Figure 4.95 and Figure 4.96 and in the cross-sections of Figure 4.97 and Figure 4.98 (at $y = -4m$, corresponding to scatterers #'s 0, 2, and 5). We see from the cross-section plots that the L_1-Norm based velocity-estimation algorithm was able to capture some of the spatial variations in the velocities of the synthetic moving point-scatterers, though the velocity estimates are still at the apparent locations of these scatterers, rather than at their actual physical location. For example, we see in Figure 4.97 that the estimated azimuth velocities around the apparent azimuth location of scatterer # 5 (at $x = -7.9m$) were slightly lower than the azimuth velocities around the apparent azimuth location of scatterers #'s 0 and 2, which is consistent with the fact that this scatterer had a relatively lower azimuth velocity.

The resulting SAR images generated by the least-squares amplitude-estimation routine are shown in Figure 4.99 and Figure 4.100. Just as with the rigid-body example, the matched-filter was able to focus both the synthetic moving point-scatterers and the stationary man-made clutter scatterers. As shown in the azimuthal cross-section of Figure 4.101, the mainlobe height of the target scatterers was about $13dB$, which was comparable to the previous rigid-body examples. However, we again see that the azimuth positions of these scatterers still have fairly severe distortions. Thus we see that the matched-filter algorithm is able to focus a moving target containing scatterers with relatively-independent velocities, but the resulting image will be distorted in azimuth.

For the azimuth-displacement compensation, we again averaged the range velocity over a set of "bright" scatterer locations where both the target-detection statistic, $\chi[n_x, n_y]$, was greater than 8.5, and where the magnitude of estimated range-velocity was greater than $0.5m/s$, as shown in Figure 4.102. For this example, the average range velocity for these scatterer locations was computed to be $2.3260m/s$, which was relatively close to the target's actual mean azimuth-velocity of $2.304m/s$. We then used this velocity to compensate the scatterers at the previous target spatial locations (with $\chi[n_x, n_y] \leq 6$) which had an estimated range-velocity with a magnitude greater than $0.5m/s$. As shown in Figure 4.104 and Figure 4.105, the resulting average azimuth-displacement error for the moving target was approximately $1m$. However, the standard deviation of the azimuth-displacement error was *approximately* $4.9m$. Thus, we see that even though the algorithm did a reasonable job of centering the target scatterers around the the correct center-location of the target (at $(x, y) = (-6.5, -4m)$), it was not able to correct the relative azimuth distortion of the scatterer positions (since the L_1-Norm based velocity-estimation algorithm did not generate range-velocity estimates of sufficient accuracy). If we knew the velocities exactly, we see that

we actually can correct for most of the azimuth distortions, as shown in the exact-velocity results of Figures 4.106- Figure 4.111.
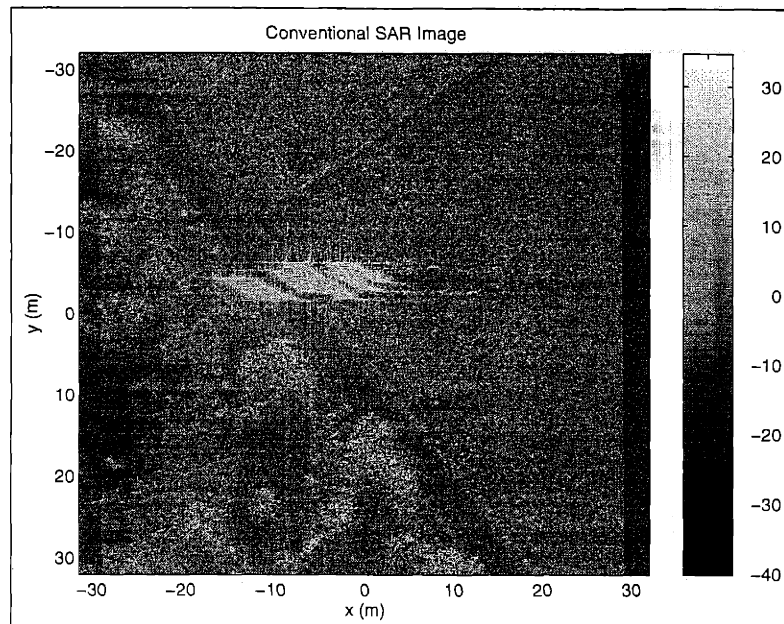
Figure 4.90: Conventional SAR Image for Non-Rigid Body Motion with a Scatterer Spacing of $1m$
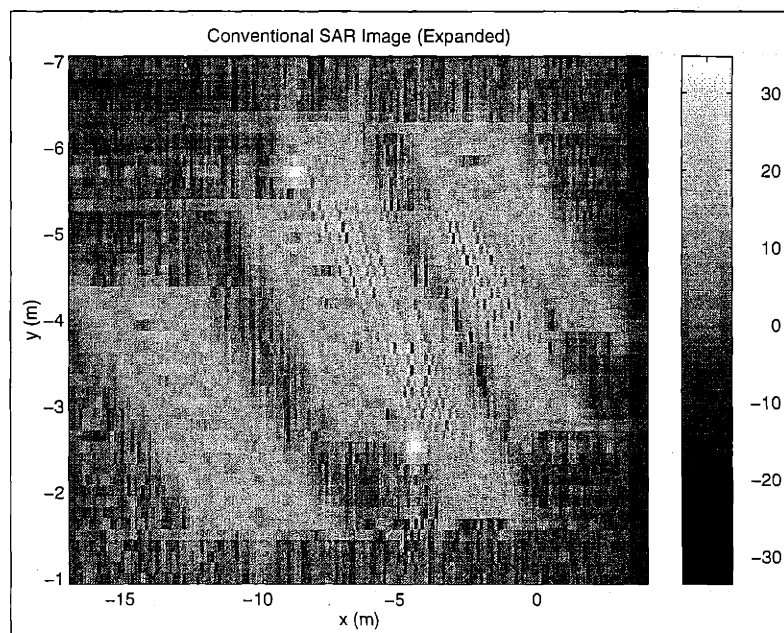
Figure 4.91: Expanded Conventional SAR Image for Non-Rigid Body Motion with a Scatterer Spacing of $1m$
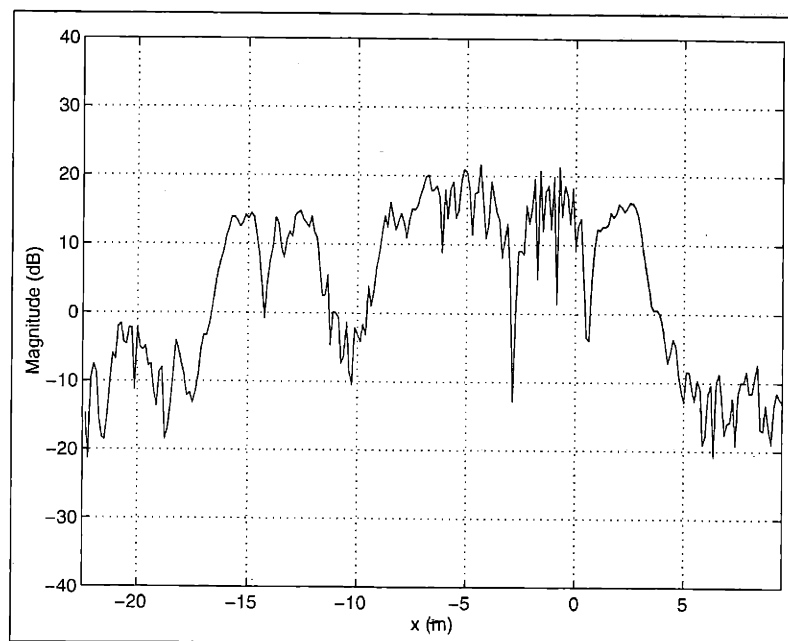
Figure 4.92: Cross-Section of Conventional SAR Image (at $y = -4m$) for Non-Rigid Body Motion with a Scatterer Spacing of $1m$
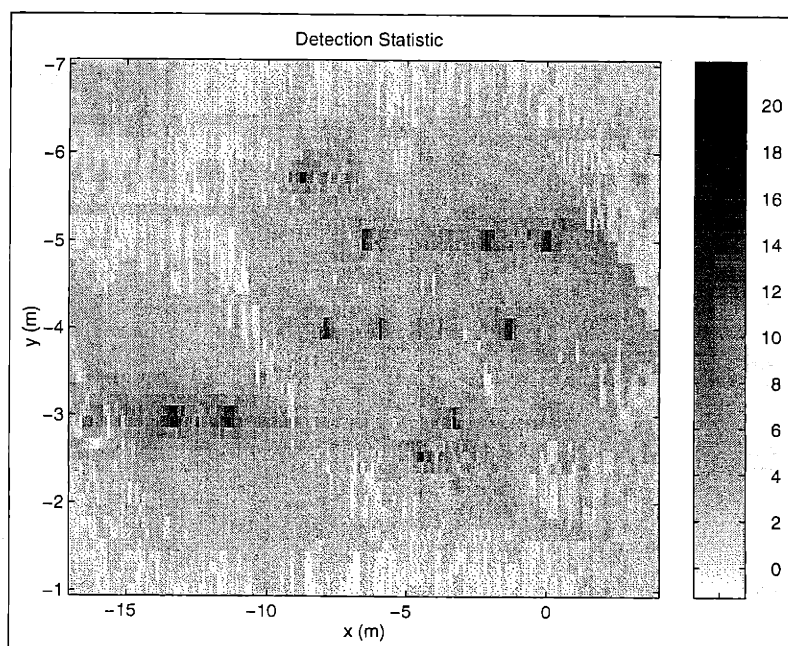
Figure 4.93: Detection Statistic for Non-Rigid Body Motion with a Scatterer Spacing of $1m$
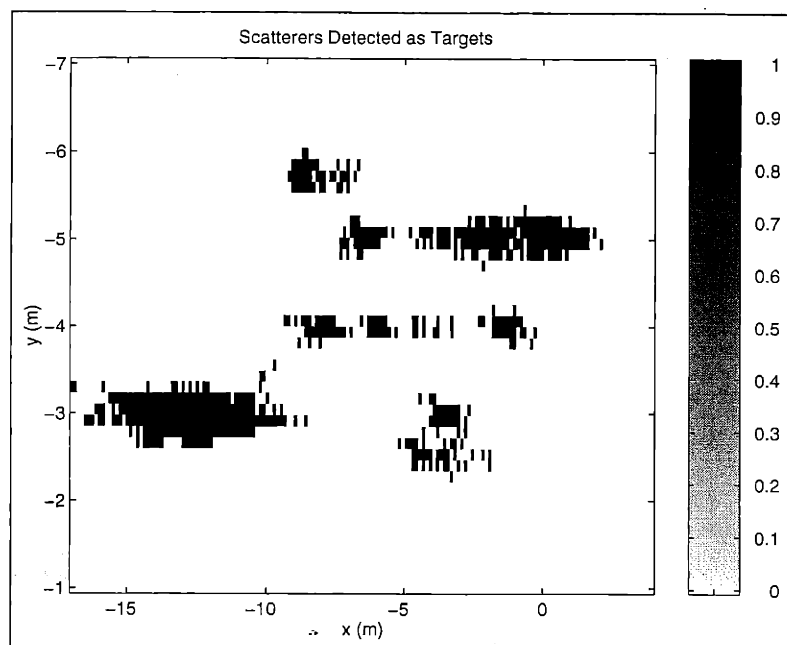
Figure 4.94: Selected Target Scatterers for Non-Rigid Body Motion with a Scatterer Spacing of $1m$
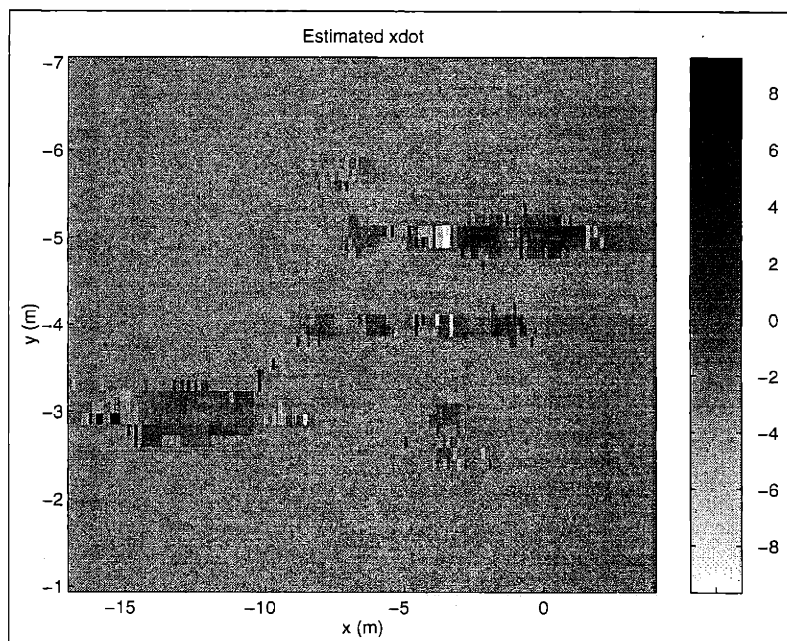
Figure 4.95: Estimated Azimuth-Velocity Field $\dot{x}$ for Non-Rigid Body Motion with a Scatterer Spacing of $1m$
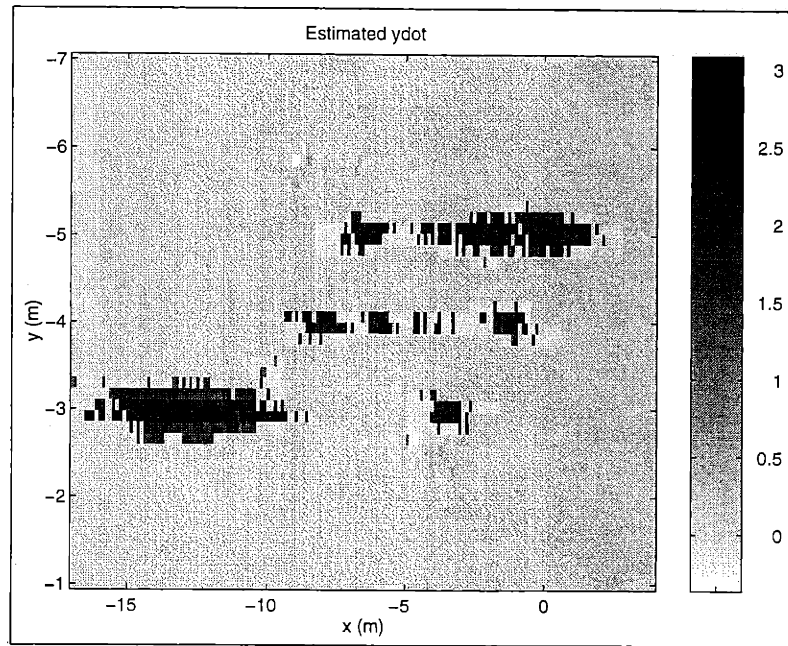
Figure 4.96: Estimated Range-Velocity Field $\dot{y}$ for Non-Rigid Body Motion with a Scatterer Spacing of $1m$
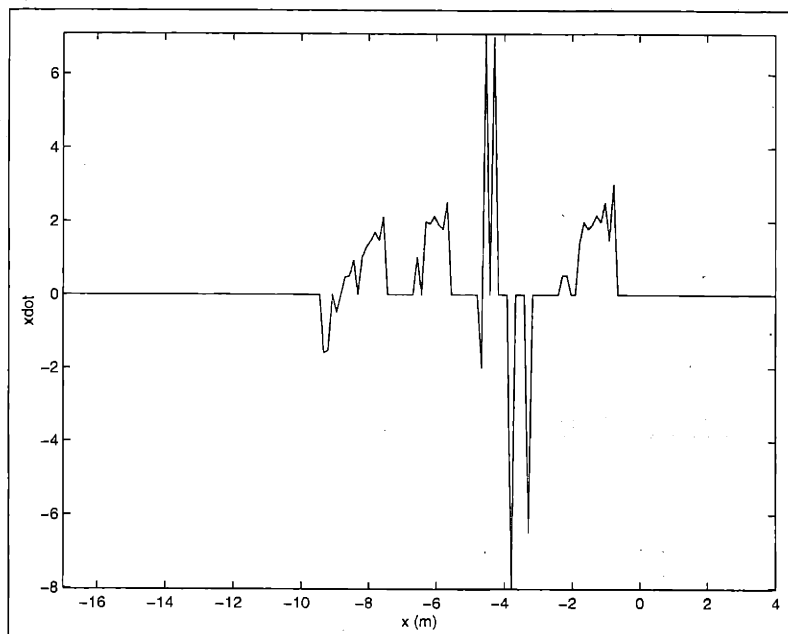
Figure 4.97: Cross-Section of Estimated Azimuth-Velocity Field $\dot{x}$ (at $y = -4m$) for Non-Rigid Body Motion with a Scatterer Spacing of $1m$
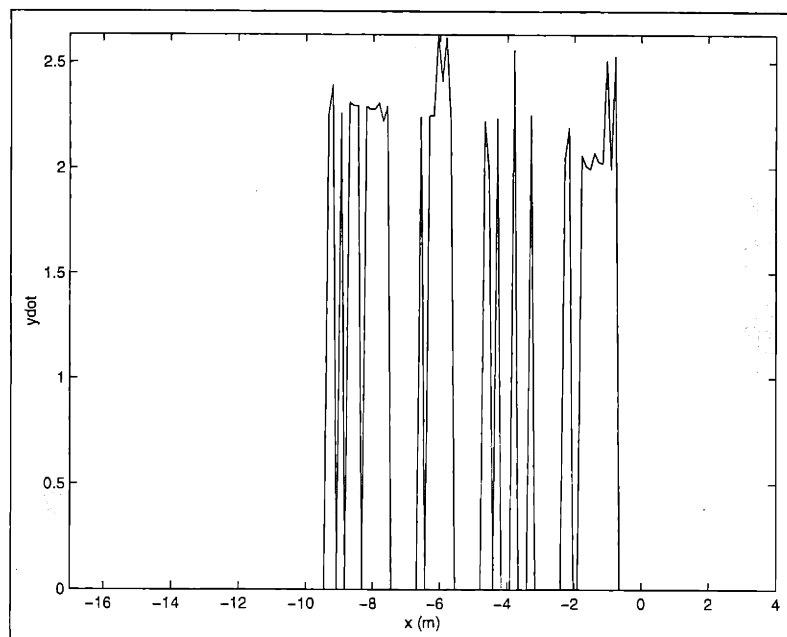
Figure 4.98: Cross-Section of Estimated Range-Velocity Field $\dot{y}$ (at $y = -4m$) for Non-Rigid Body Motion with a Scatterer Spacing of $1m$
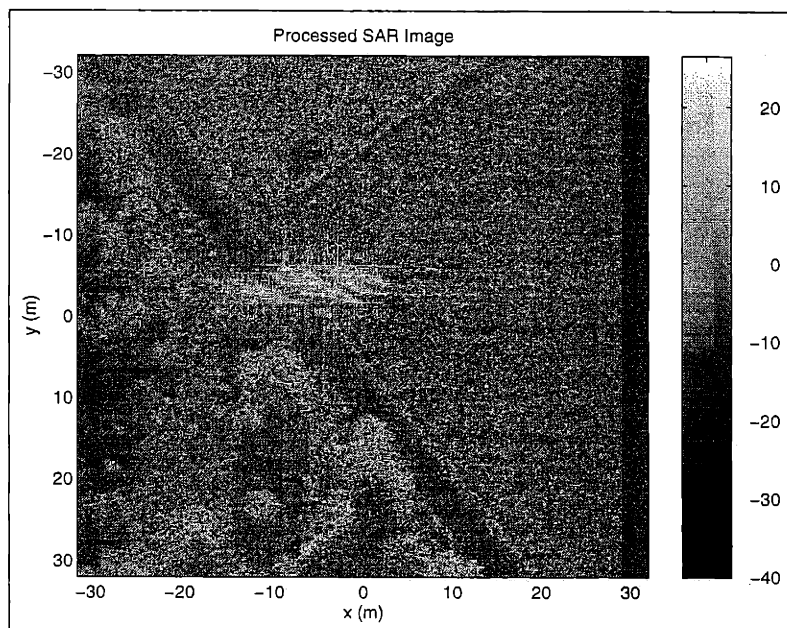
Figure 4.99: Matched-Filter SAR Image for Non-Rigid Body Motion with a Scatterer Spacing of $1m$
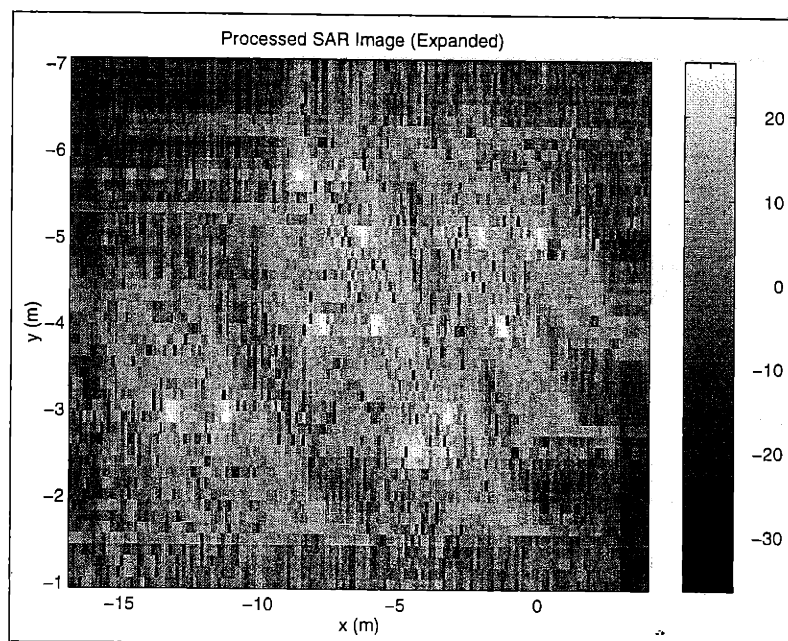
Figure 4.100: Expanded Matched-Filter SAR Image for Non-Rigid Body Motion with a Scatterer Spacing of $1m$
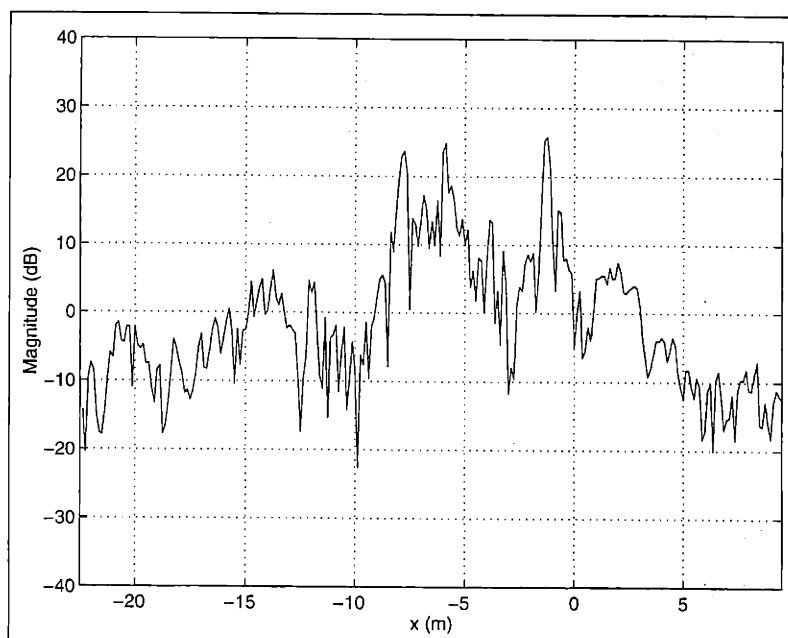
Figure 4.101: Cross-Section of Matched-Filter SAR Image (at $y = -4m$) for Non-Rigid Body Motion with a Scatterer Spacing of $1m$
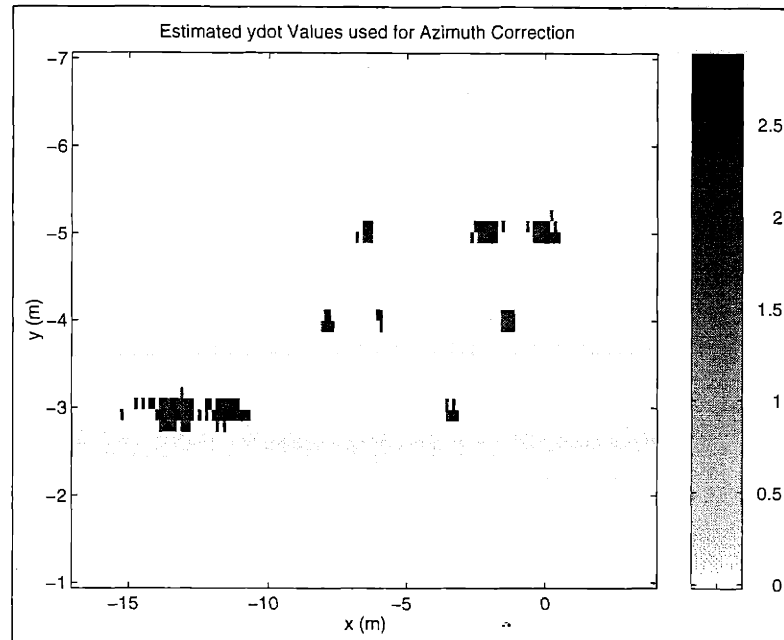
Figure 4.102: Estimated Range-Velocity Values used for Azimuth-Displacement Compensation for Non-Rigid Body Motion with a Scatterer Spacing of $1m$
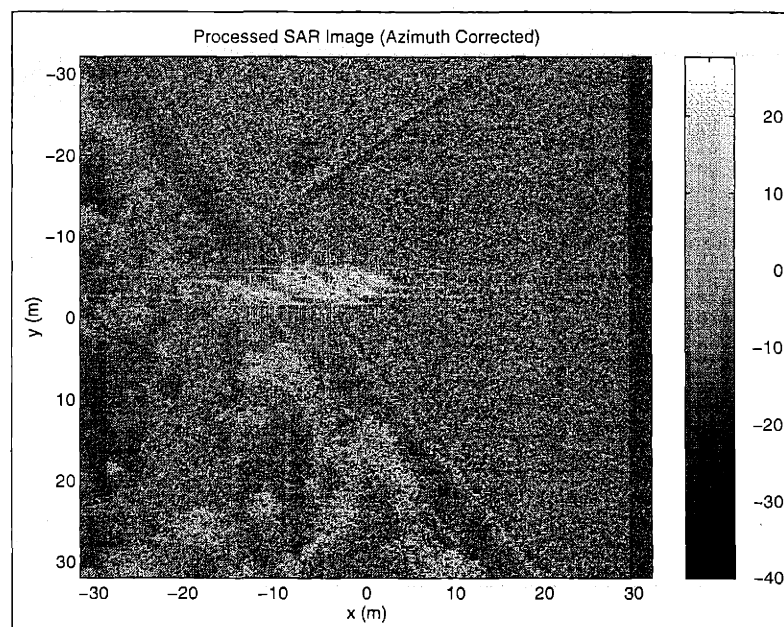
Figure 4.103: Azimuth-Displacement Compensated Matched-Filter SAR Image for Non-Rigid Body Motion with a Scatterer Spacing of $1m$
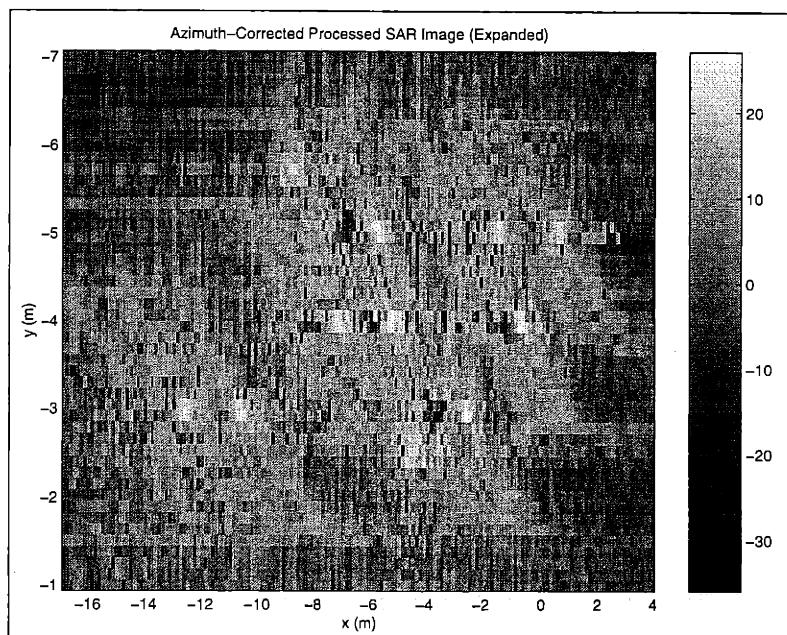
Figure 4.104: Expanded Azimuth-Displacement Compensated Matched-Filter SAR Image for Non-Rigid Body Motion with a Scatterer Spacing of $1m$
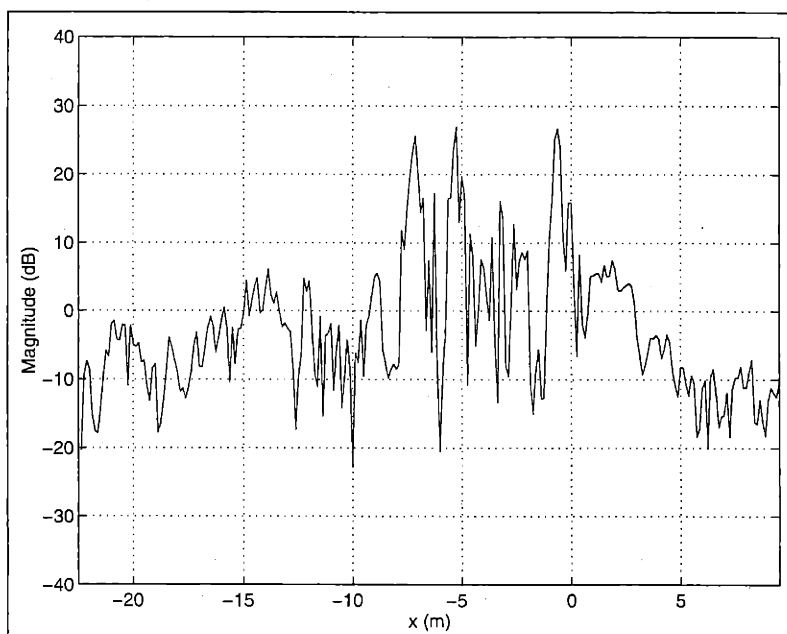
Figure 4.105: Cross-Section of Azimuth-Displacement Compensated Matched-Filter SAR Image (at $y = -4m$) for Non-Rigid Body Motion with a Scatterer Spacing of $1m$
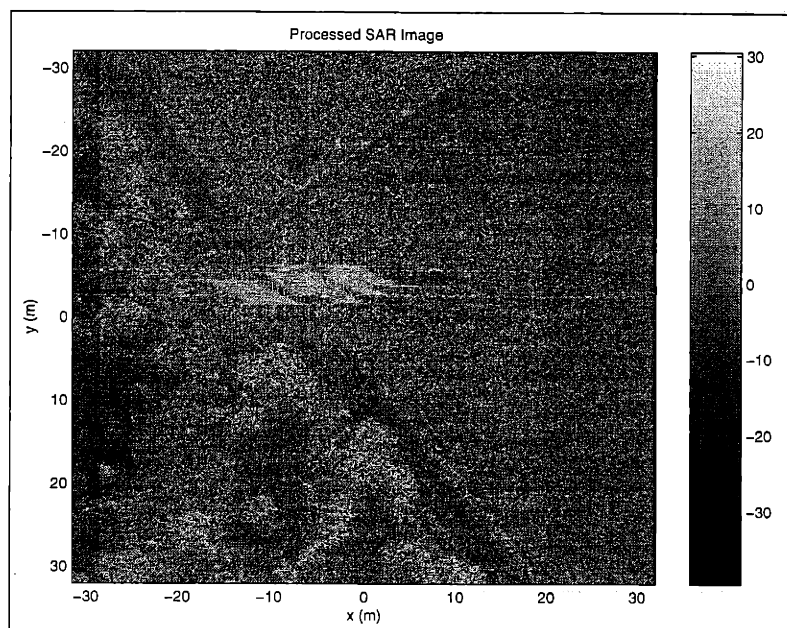
Figure 4.106: Exact-Velocity Matched-Filter SAR Image for Non-Rigid Body Motion with a Scatterer Spacing of $1m$
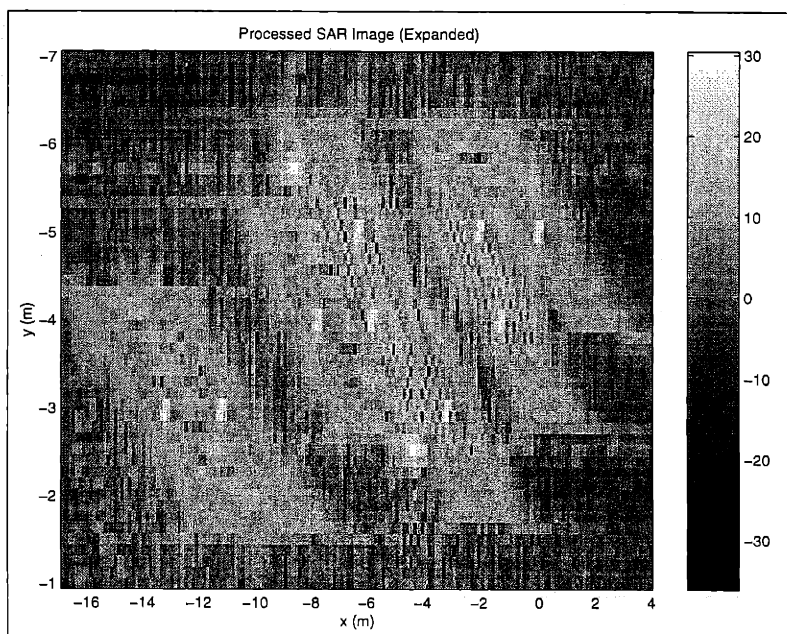
Figure 4.107: Expanded Exact-Velocity Matched-Filter SAR Image for Non-Rigid Body Motion with a Scatterer Spacing of $1m$
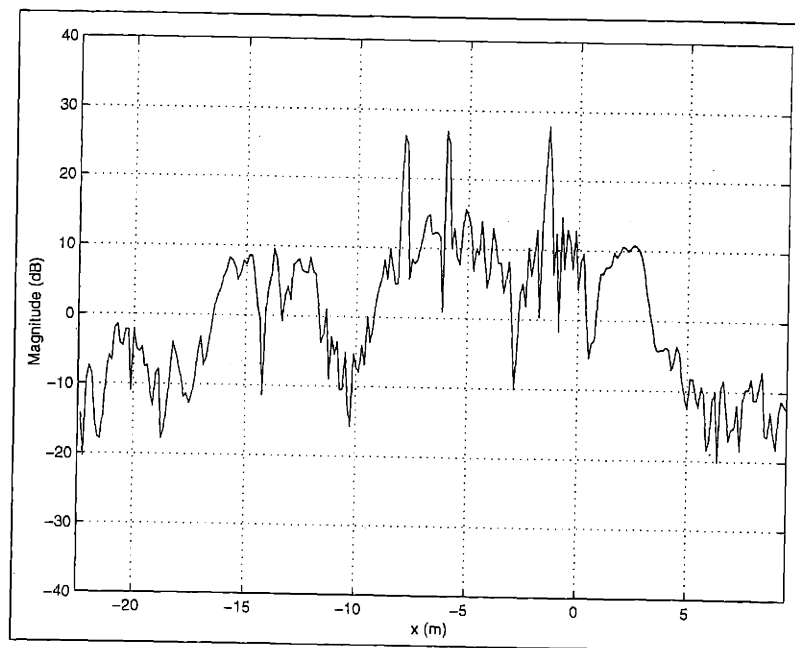
Figure 4.108: Cross-Section of Exact-Velocity Matched-Filter SAR Image (at $y = -4m$) for Non-Rigid Body Motion with a Scatterer Spacing of $1m$
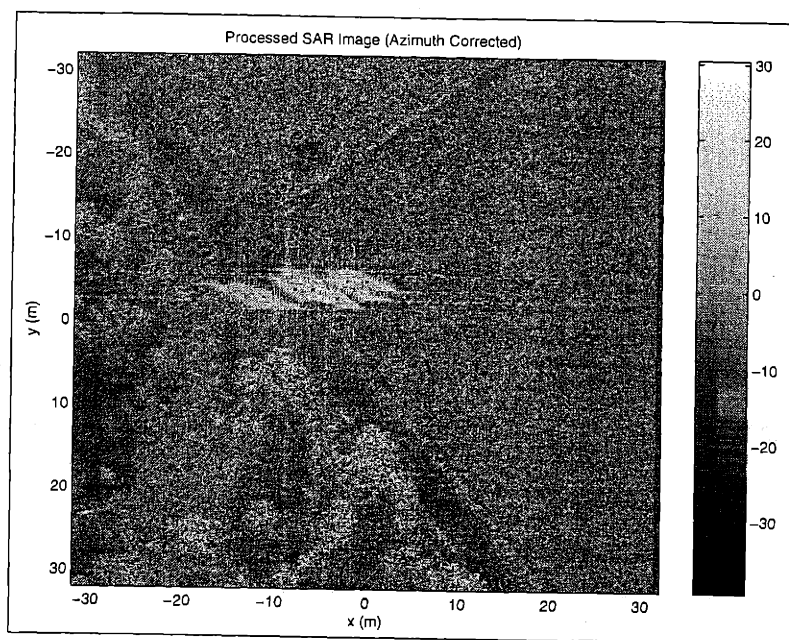
Figure 4.109: Exact-Velocity Azimuth-Displacement Compensated Matched-Filter SAR Image for Non-Rigid Body Motion with a Scatterer Spacing of $1m$
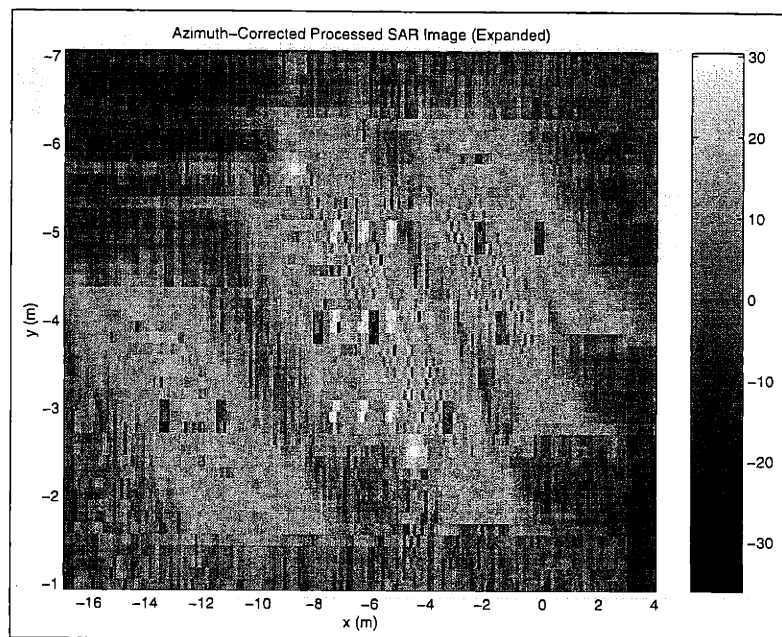
Figure 4.110: Exact-Velocity Azimuth-Displacement Compensated Matched-Filter SAR Image for Non-Rigid Body Motion with a Scatterer Spacing of $1m$
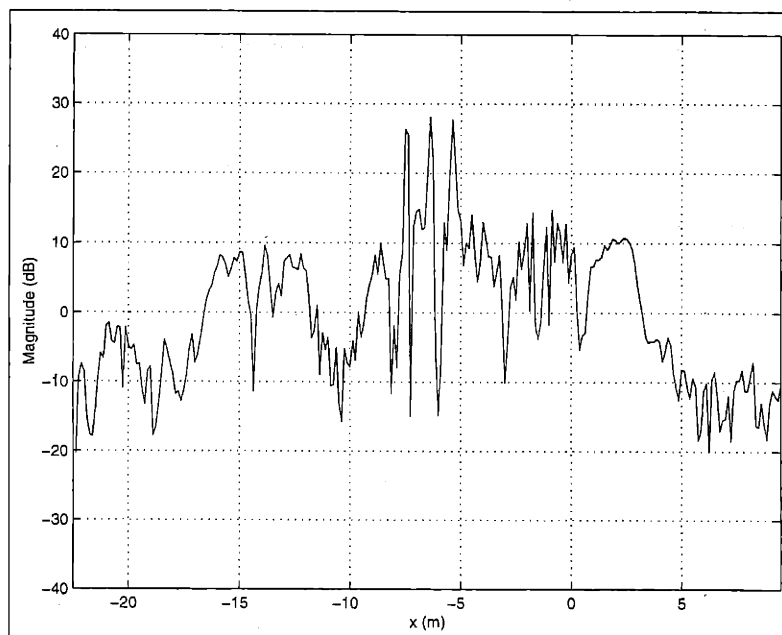
Figure 4.111:　Cross-Section of Exact-Velocity Azimuth-Displacement Compensated Matched-Filter SAR Image (at $y = -4m$) for Non-Rigid Body Motion with a Scatterer Spacing of $1m$

4.7.2 Synthetic-Motion Real Target Embedded in Real Clutter

For this example, we used a 128×128 pixel *stationary* SAR scene (with an approximate resolution in range and azimuth of of $\delta_y = 0.25m$ and $\delta_x = 0.25m$) consisting of a T-72 tank from the former Soviet Union, in a grass clutter background (shown in Figure 4.112 and Figure 4.113). An azimuthal cross-section (at a range of $0.45m$) of the target image is shown in Figure 4.114 (which shows some of the feature scatterers corresponding to the tank's treads centered at approximately $(x,y) = (-1m, 0.45m)$). This particular image was part of a spotlight-mode SAR data set collected by Sandia National Laboratory in 1995 under DARPA's Moving and Stationary Target Acquisition and Recognition (MSTAR) program. For these examples, we first (manually) segmented the MSTAR SAR scene into a target portion and a clutter portion, as shown in Figure 4.115 and Figure 4.116. (where the target portion was chosen such as to include as many of the dominant scatterers of the tank as possible). We then used the target portion of the MSTAR SAR scene and used it as an input into our general-motion estimation-theoretic model in order to generate the synthetic-motion moving-target SAR data. For this example, we gave all the target scatterers a velocity of $(\dot{x}[n_x, n_y], \dot{y}[n_x, n_y]) = (2m/s, 2.304m/s)$. The parameters of the estimation-theoretic model were again chosen to be as similar as possible to the 33.5 GHz Lincoln Laboratory Advanced Detection and Tracking System (ADTS) system operating in spotlight mode (as shown in Table 4.10).

The synthetic-motion moving-target SAR data was then re-embedded into the stationary clutter SAR image as shown in the conventional SAR images of Figure 4.117 and Figure 4.118 (along with the azimuthal cross-section (at a range of $0.45m$) shown in Figure 4.119). Here, we see that the added synthetic motion has seriously degraded the image of the target, as compared to the original MSTAR target-chip stationary image.

For the matched-filter, we used the clutter-nulling cross-interference reduction algorithm with a threshold of of $A_T[n_x, n_y] = 10|\hat{A}_{CONV}[n_x, n_y]|$, which was identical to the threshold used for the previous synthetic-target examples. The resulting matched-filter target-detection statistic, $\chi[n_x, n_y]$, is shown in Figure 4.120. Here, we see that the locations of only the relatively "bright" moving-target scatterers are apparent (corresponding to the tread and turret of the T-72 tank). For this example, we used a detection-statistic threshold χ_{MAX} of 2, which was much lower than the threshold χ_{MAX} of 6 used in the previous examples. Again, the detection scheme picked many of the relatively bright moving-target scatterers, but it also picked substantially more spurious false-alarm target locations, as shown in Figure 4.121. Unfortunately, we found that increasing the threshold would cause the matched-filter detection scheme to miss an unacceptable number of target scatterers.

For the median-prefiltering, we used median filters with a spatial region-of-interest (ROI) of $0.5m \times 0.5m$. For the reduced-order L_1-Norm based velocity-estimation algorithm, we used an L_1 weighting of $\gamma_A = 1.1$ (which was identical to the previous examples). The resulting azimuth and range velocity estimates are shown in Figure 4.122 and Figure 4.123 and in the cross-sections of Figure 4.122 and Figure 4.123. We see from these cross-sections that the matched filter gave a reasonable estimate of the range velocities of the "brighter" moving target-scatterers (such as the scatterer located at $(x,y) = (-1m, 0.45)$). However, the matched-filter gave much poorer estimates of the azimuth velocities. This is consistent with the first and second synthetic-target examples (rigid-body motion, with a scatterer

spacing of $1m$ and $0.75m$), where we observed that the azimuth velocity estimate was more affected by a closer scatterer spacing than the range velocity.

The resulting images generated by the least-squares algorithm are shown in Figure 4.126 and Figure 4.127. Again, we see that the matched-filter based SAR processing algorithm was able to image only the brighter of the moving target-scatterers (such as the scatterer located at $(x, y) = (-1m, 0.45)$). Again, this is due to the azimuth-velocity estimation errors caused by cross-scatterer interference. If we knew the velocities exactly, as illustrated by the exact-velocity case in Figure 4.132 and Figure 4.133 (which was nearly identical to the original stationary MSTAR image), we are able to image nearly all of the target scatterers.

For the azimuth-displacement compensation, we averaged the range velocity over a set of "bright" scatterer locations where both the target-detection statistic, $\chi[n_x, n_y]$, was greater than 7, and where the magnitude of estimated range-velocity was greater than $0.5m/s$, as shown in Figure 4.129. For this example, the average range velocity for these scatterer locations was computed to be $1.7562m/s$, which was significantly worse than the average-velocities computed for the synthetic target examples (since even the range-velocity estimates for the brighter scatterers had significant variation). We then used this velocity to compensate the scatterers at the previous "target" spatial locations (with $\chi[n_x, n_y] \leq 6$) which had an estimated range-velocity with a magnitude greater than $0.5m/s$. As shown in Figure 4.130 and Figure 4.131, because of the larger range-velocity, the resulting azimuth-displacement error for the moving target was approximately $15m$, which nearly "wrapped" the target completely to its initial position in the image.

From this example, we see that the velocity-performance of the matched filter is severely affected by cross-scatterer interference when the scatterers are relatively close (as with a real target), even if the velocities are similar. We also see that the azimuth-compensation is also severely affected by cross-scatterer interference (due to the larger range-velocity errors). Thus we see the need for some type of regularization upon the scatterer velocities in order to improve the imaging of closely-spaced scatterers.

F_c	Center Frequency	33.5 GHz
λ_c	Center Wavelength	0.009 m
αT_p	Chirp Bandwidth	1.2 GHz
f_{PRF}	Pulse Repetition Frequency	128 pulse/s
N	Complex Samples per Range Profile	128
$2K$	Pulses per Synthetic Aperture	128
R_o	Center Slant-Range	2778 M
v	SAR Platform Velocity	100 m/s
$\dot{\theta}$	Look-Angle Rotation Rate	0.036 rad/s
$2T$	Dwell Time	1.0 s
L	Synthetic-Aperture Length	100 m
δ_y	Range Resolution	0.25 m
δ_x	Azimuth Resolution	0.25 m
Δ_y	Range Sampling Interval	0.125 m
Δ_x	Azimuth Sampling Interval	0.125 m
$\Delta_{\dot{y}}$	MF Range-Velocity Quantization	0.25 m/s
$\Delta_{\dot{x}}$	MF Azimuth-Velocity Quantization	0.5 m/s
Δ_{W_y}	Range Width of MF Image-Window	4 m
Δ_{W_x}	Azimuth Width of MF Image-Window	8 m

Table 4.10: System Parameters for Matched-Filter SAR Processing Example (Synthetic-Motion Real Target Embedded in Real Clutter)
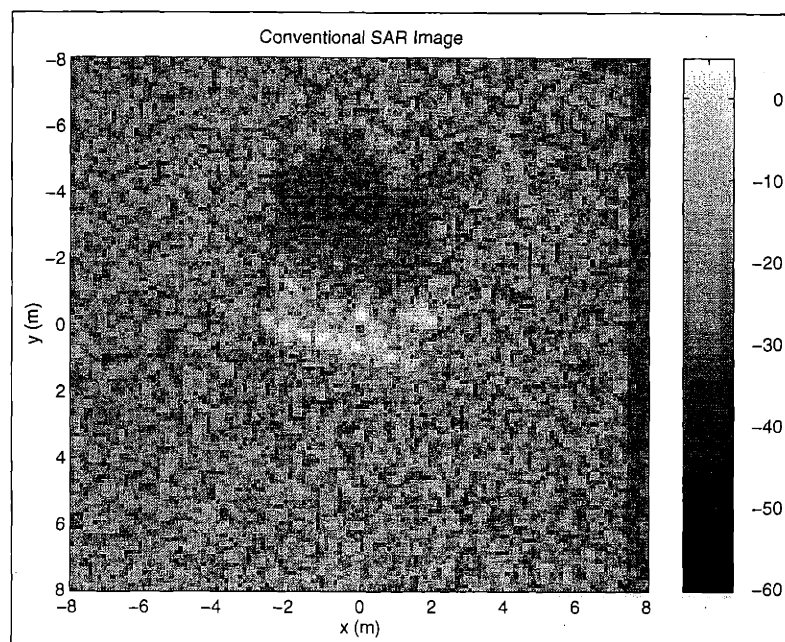
Figure 4.112: Stationary MSTAR Target Chip for Synthetic-Motion Real Moving-Target Example
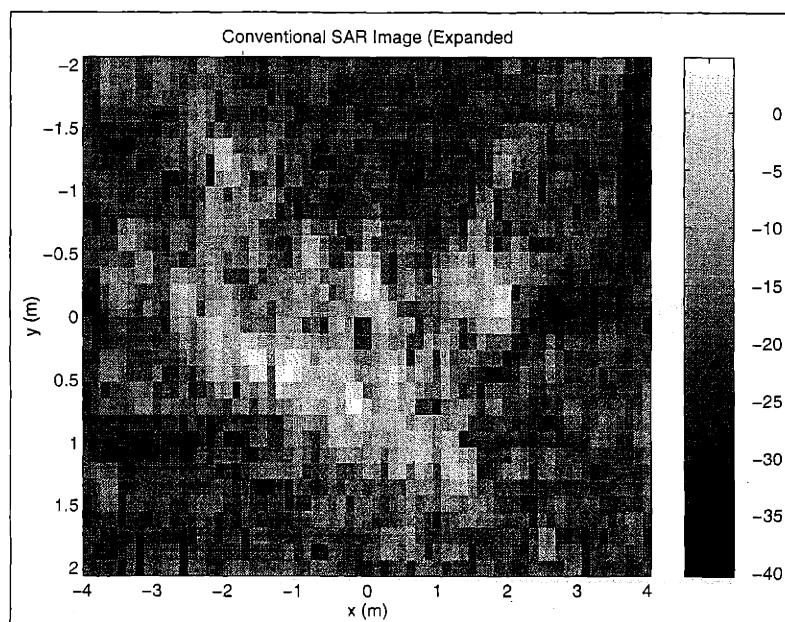
Figure 4.113: MSTAR Target Chip for Synthetic-Motion Real Moving-Target Example (expanded)
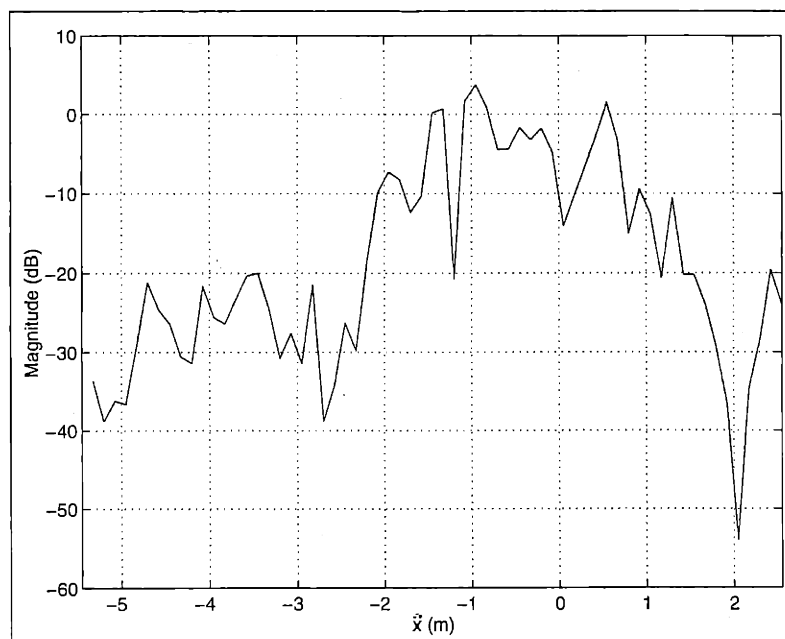
Figure 4.114: Azimuthal Cross-section of MSTAR Target Chip Image at $y = 0.45m$
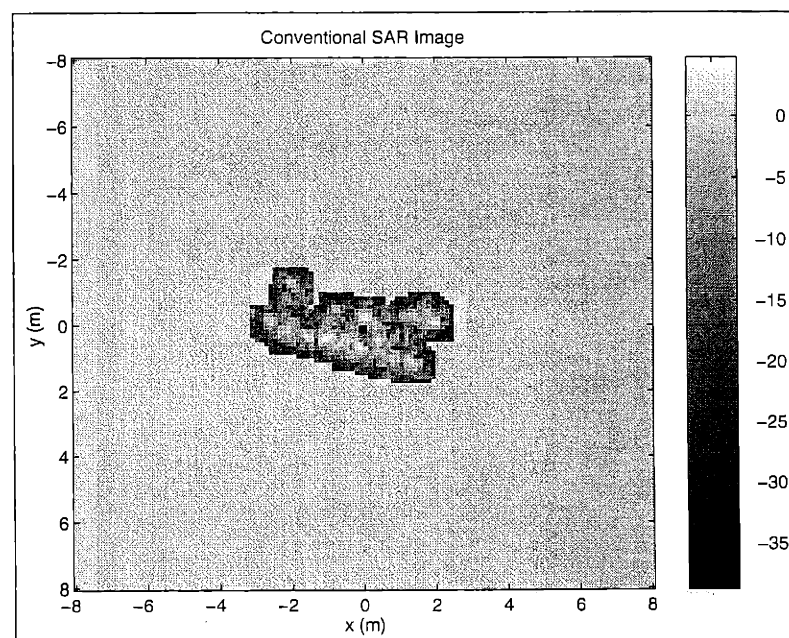
Figure 4.115: Target Portion of MSTAR Target Chip ("Non-White" Part)
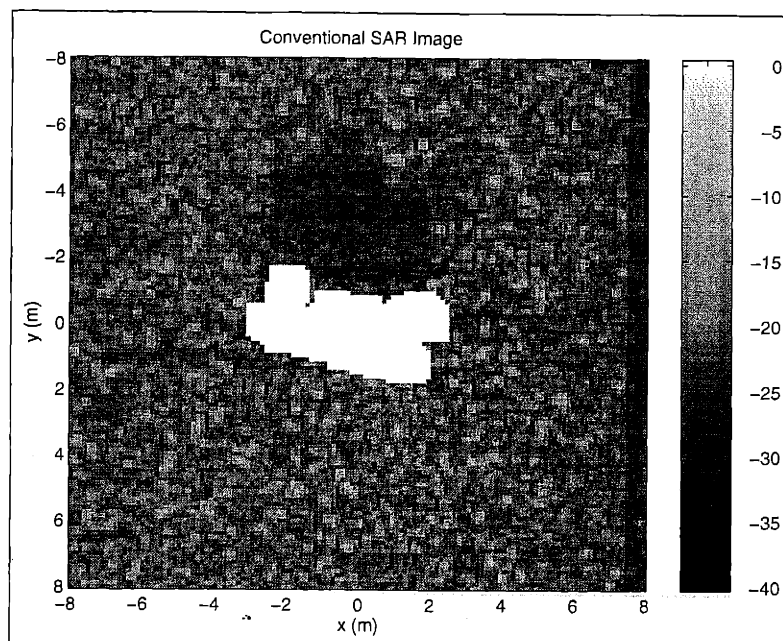
Figure 4.116: Clutter Portion of MSTAR Target Chip ("Non-White" Part)
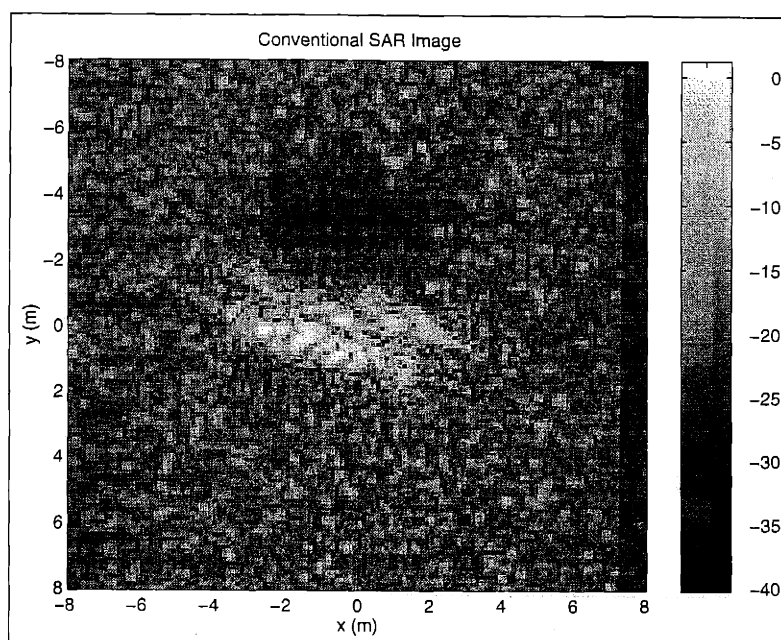
Figure 4.117: Conventional SAR Image for Synthetic-Motion Real Moving-Target Example
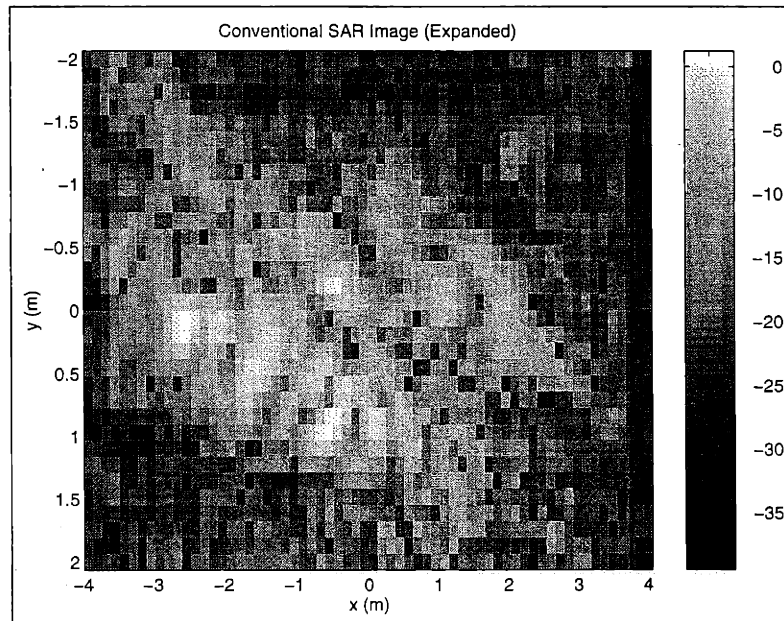
Figure 4.118: Expanded Conventional SAR Image for Synthetic-Motion Real Moving-Target Example
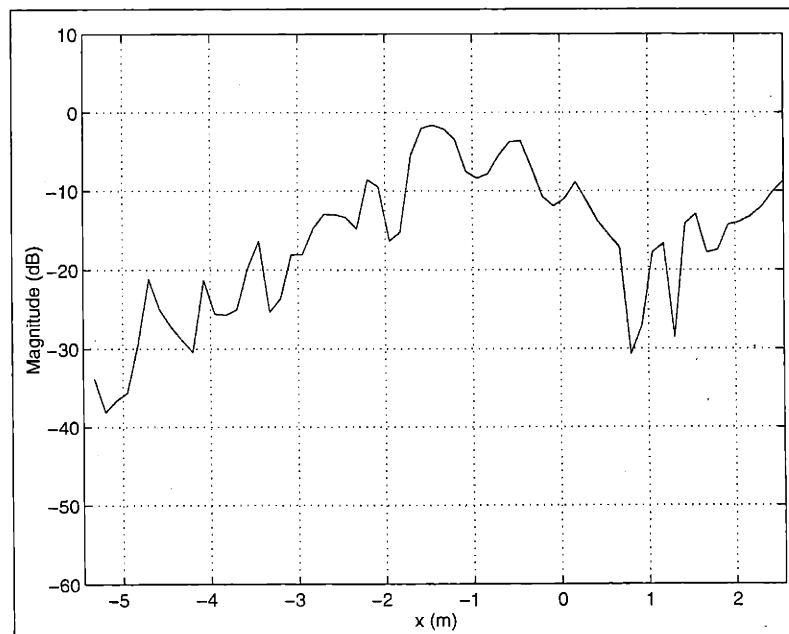
Figure 4.119: Cross-Section of Conventional SAR Image (at $y = 0.45m$) for Synthetic-Motion Real Moving-Target Example
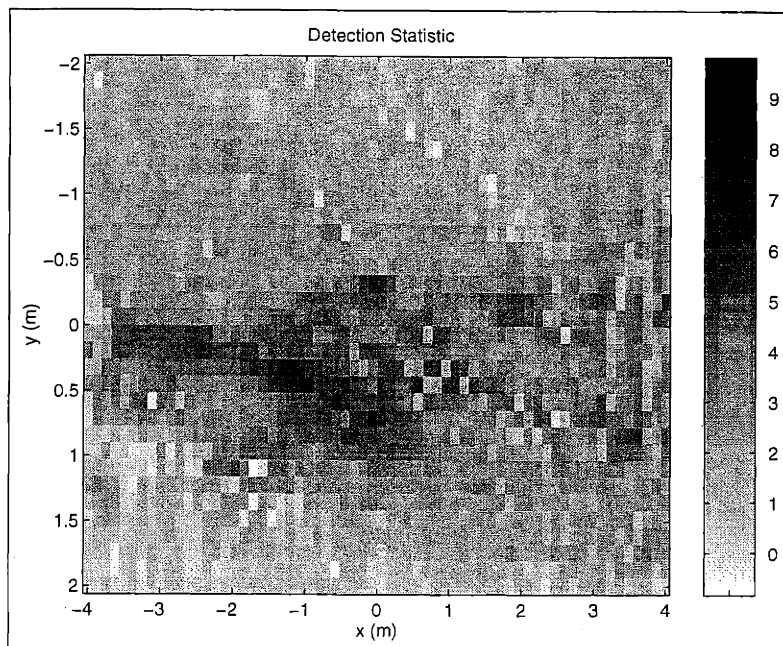
Figure 4.120: Detection Statistic for Synthetic-Motion Real Moving-Target Example
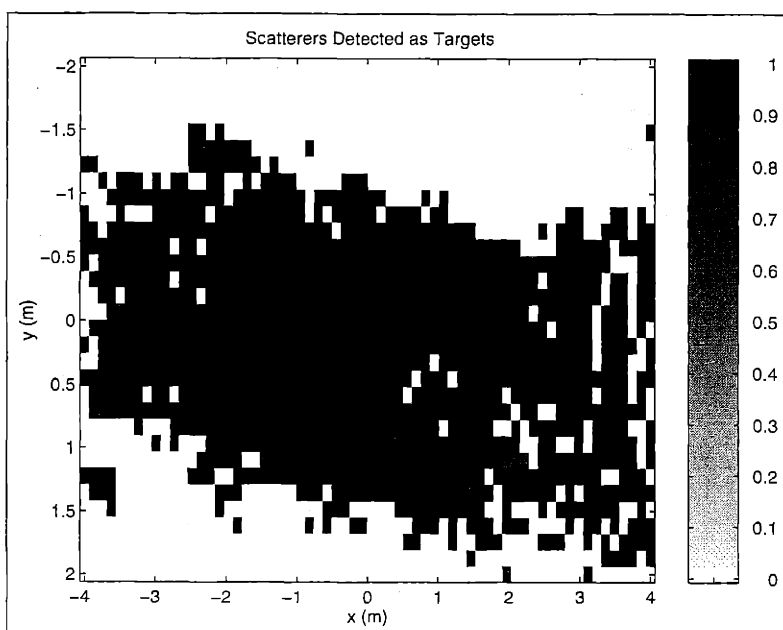
Figure 4.121: Selected Target Scatterers for Synthetic-Motion Real Moving-Target Example
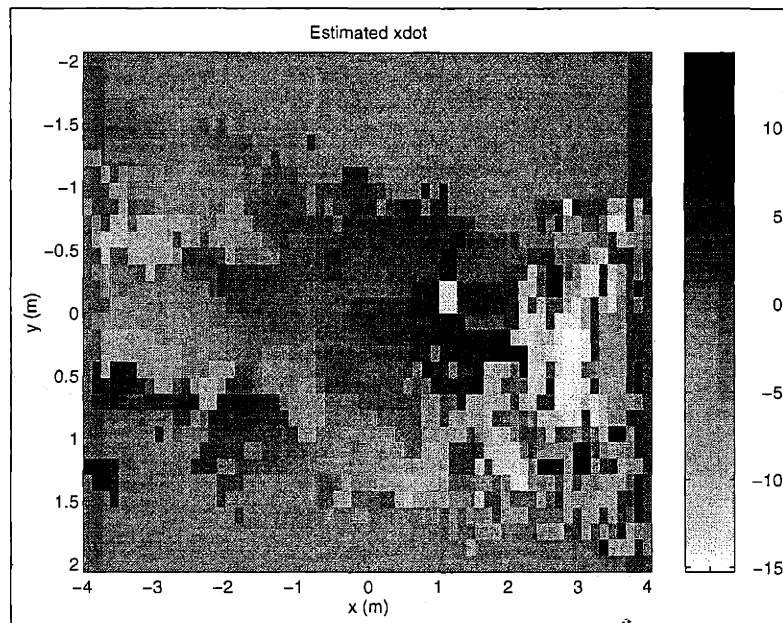
Figure 4.122: Estimated Azimuth-Velocity Field $\dot{x}$ for Synthetic-Motion Real Moving-Target Example
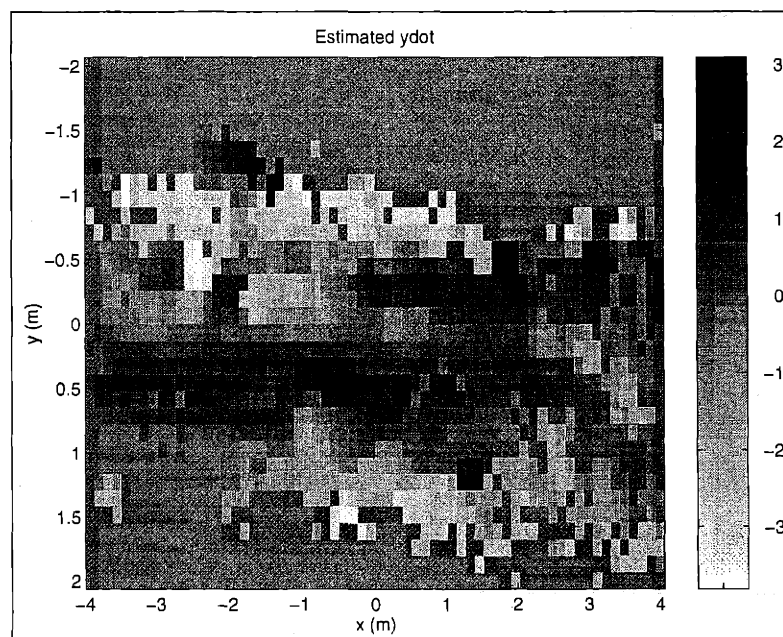
Figure 4.123: Estimated Range-Velocity Field $\dot{y}$ for Synthetic-Motion Real Moving-Target Example
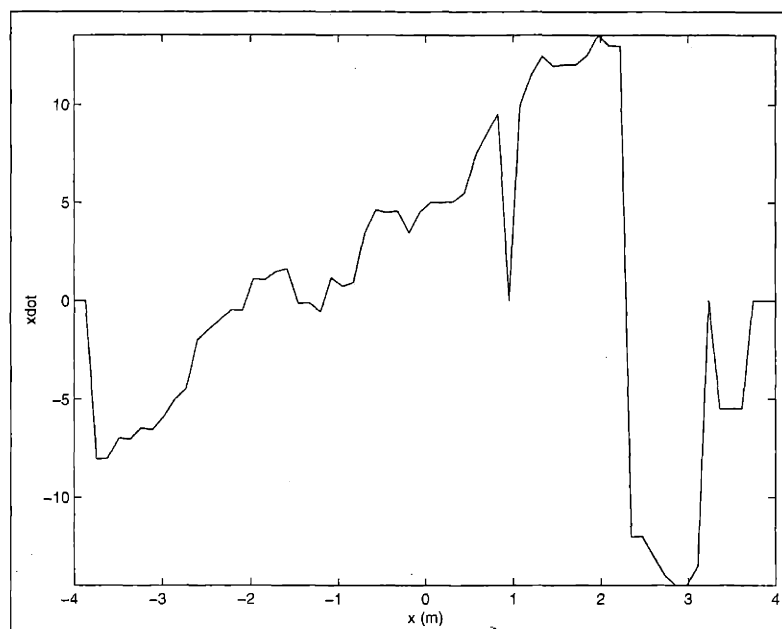
Figure 4.124: Cross-Section of Estimated Azimuth-Velocity Field $\dot{x}$ (at $y = 0.45m$) for Synthetic-Motion Real Moving-Target Example
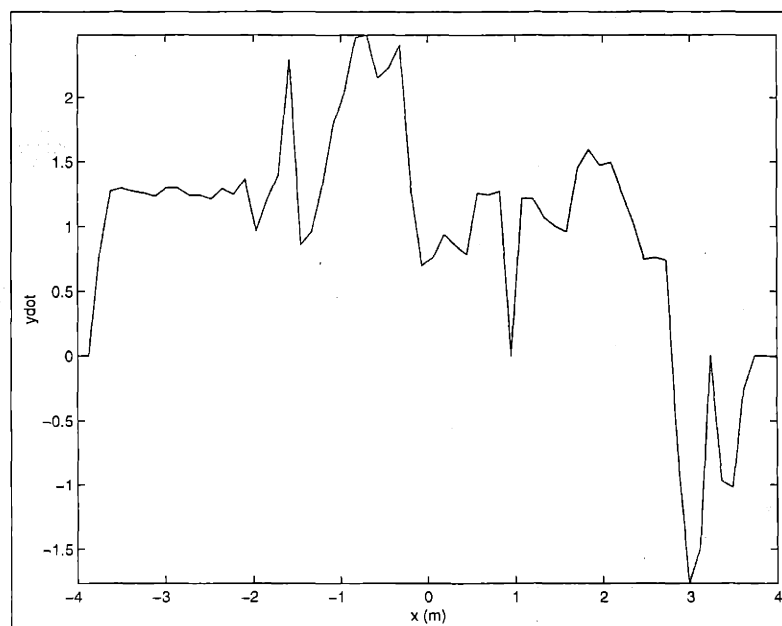
Figure 4.125: Cross-Section of Estimated Range-Velocity Field $\dot{y}$ (at $y = 0.45m$) for Synthetic-Motion Real Moving-Target Example
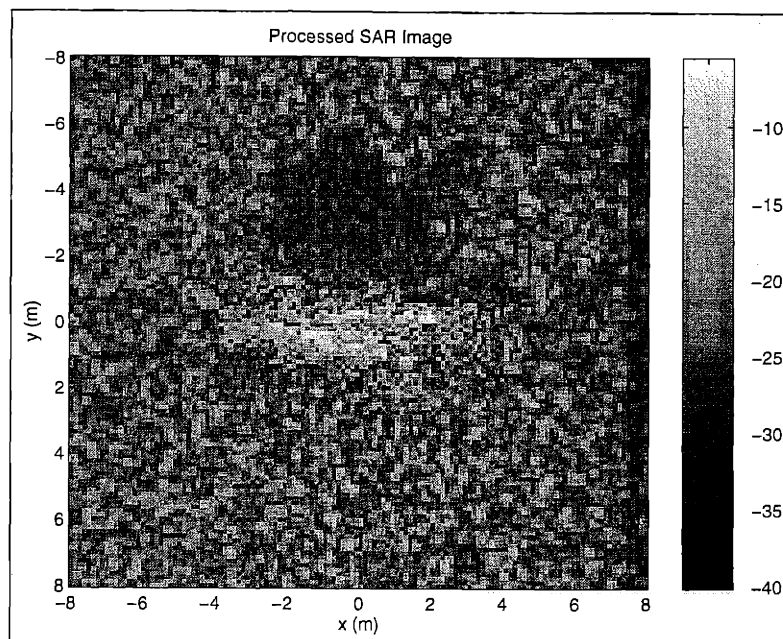
Figure 4.126: Matched-Filter SAR Image for Synthetic-Motion Real Moving-Target Example
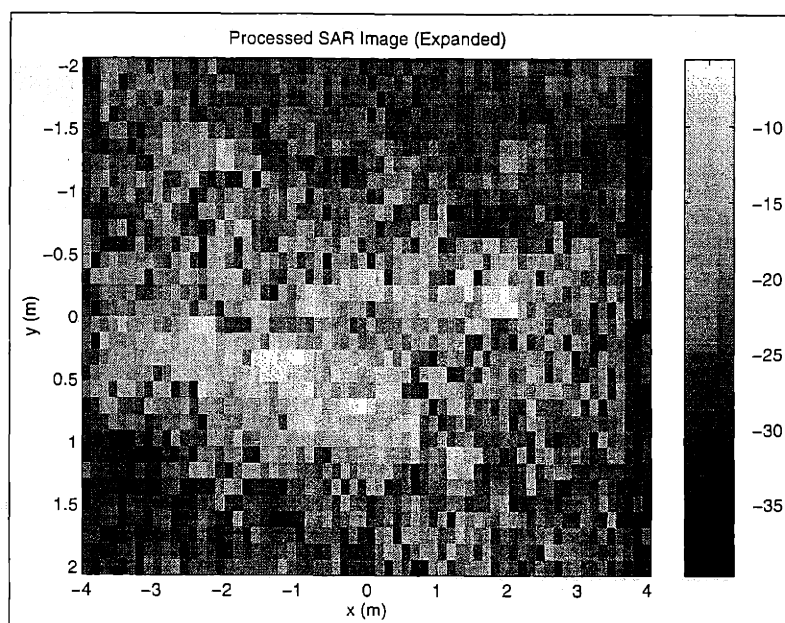
Figure 4.127: Expanded Matched-Filter SAR Image for Synthetic-Motion Real Moving-Target Example
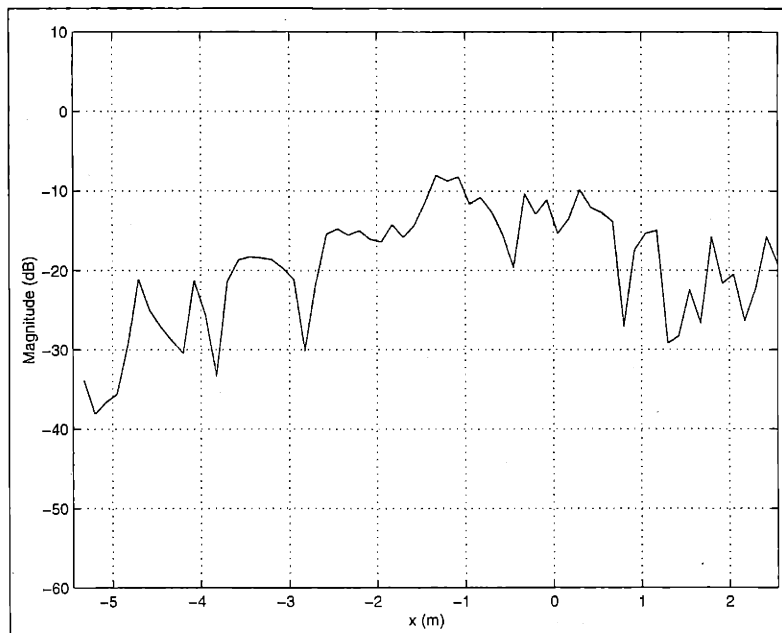
Figure 4.128: Cross-Section of Matched-Filter SAR Image (at $y = 0.45m$) for Synthetic-Motion Real Moving-Target Example
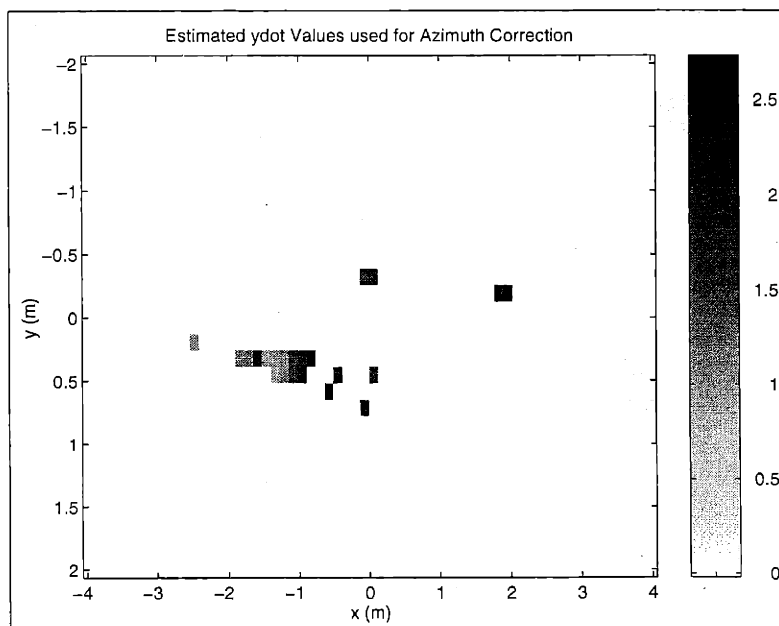
Figure 4.129: Estimated Range-Velocity Values used for Azimuth-Correction of Synthetic-Motion Real Moving-Target Example
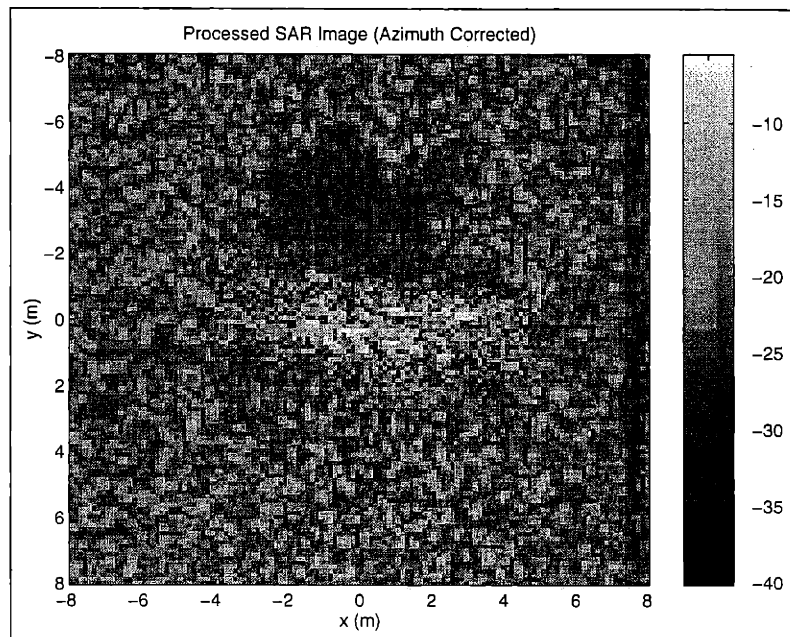
Figure 4.130: Azimuth-Corrected Matched-Filter SAR Image for Synthetic-Motion Real Moving-Target Example
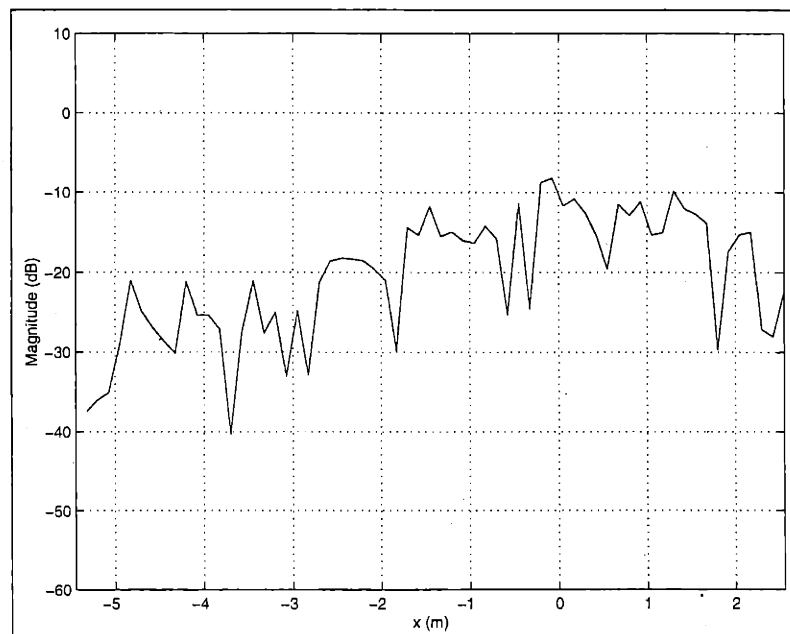
Figure 4.131: Cross-Section of Azimuth-Corrected Matched-Filter SAR Image (at $y = 0.45m$) for Synthetic-Motion Real Moving-Target Example
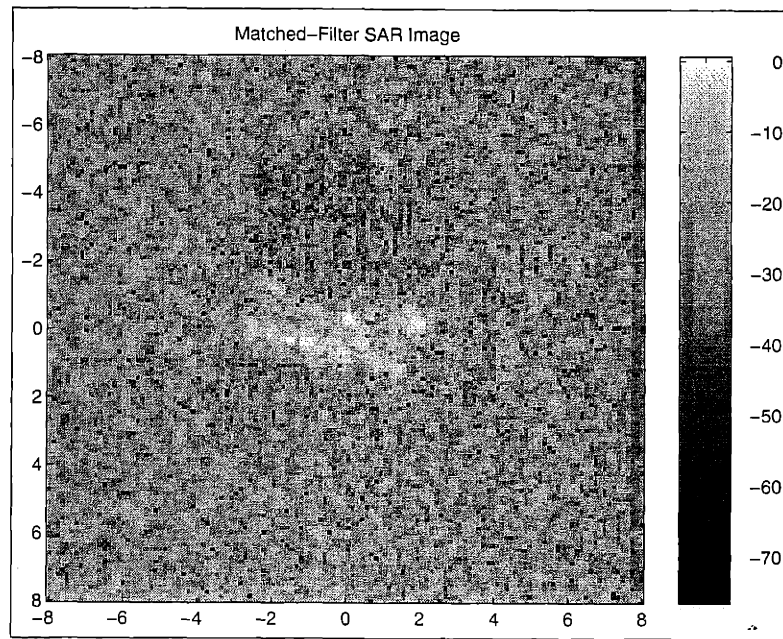
Figure 4.132: Exact-Velocity Matched-Filter SAR Image for Synthetic-Motion Real Moving-Target Example
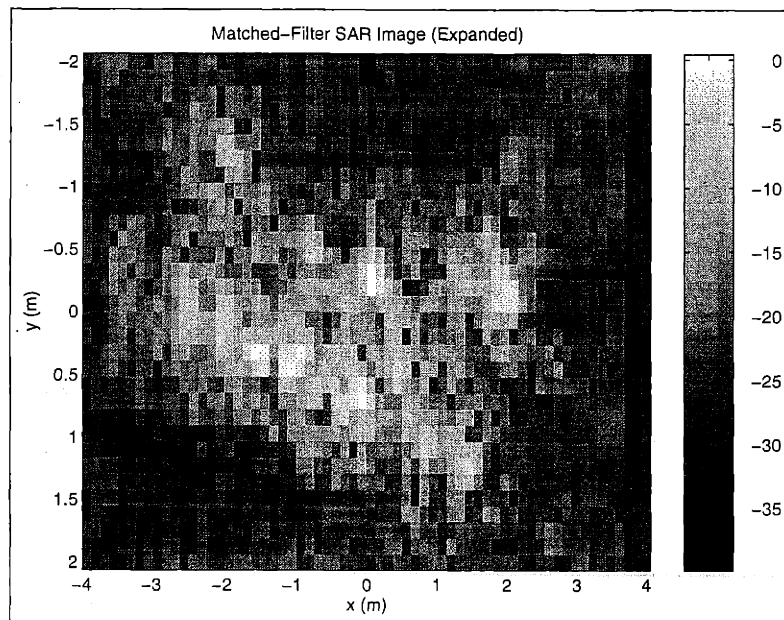
Figure 4.133: Expanded Exact-Velocity Matched-Filter SAR Image for Synthetic-Motion Real Moving-Target Example
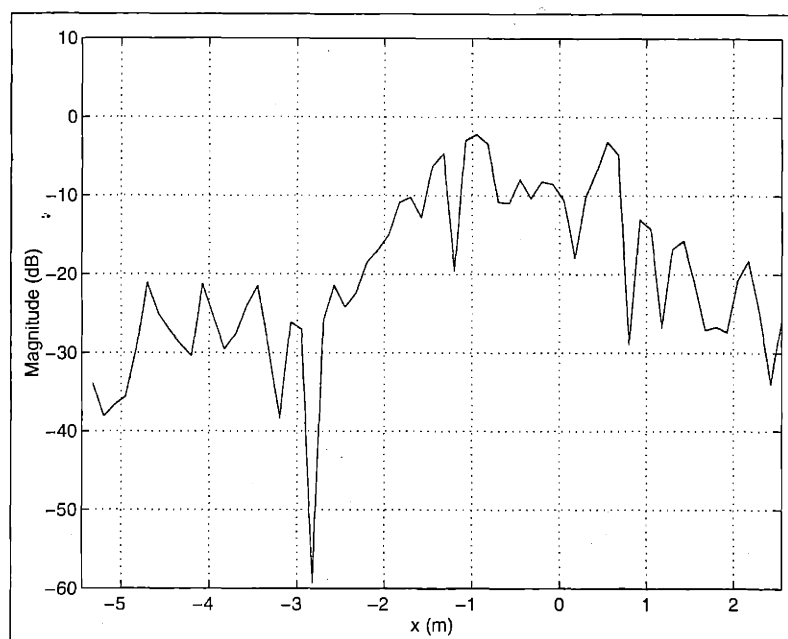
Figure 4.134: Cross-Section of Exact-Velocity Matched-Filter SAR Image (at $y = 0.45m$) for Synthetic-Motion Real Moving-Target Example

Chapter 5

Rigid-Body L_1-Norm SAR Processing

IN the previous chapter, we presented a matched-filter based estimation-theoretic technique for imaging moving targets. Recall that the matched-filter SAR processing technique used a multi-dimensional matched-filter as a means of computing a set of scatterer-velocity estimates which were used as initial conditions for an L_1-norm based estimation algorithm derived for the spatially-varying temporally-constant velocity (SVTCV) SAR model (which assumes that the target field consists of a $2-D$ array of ideal point scatterers with spatially independent velocities). Also, recall that this technique works reasonably well for simultaneously imaging both high-amplitude moving point scatterers and "nearby" high-amplitude stationary clutter. However, this matched-filter technique gave poor results for closely-spaced scatterers (due to cross-scatterer interference), even if the scatterers have similar velocities. This occurs because the matched-filter is optimized for estimating the parameters of a *single* point scatterer in the presence of circularly-complex Gaussian white noise. Therefore, it may give poor results for some real moving targets. One possible means of alleviating this problem is to add some type of velocity regularization to the SVTCV L_1-Norm based algorithm.

For some of the motion-compensated SAR imaging techniques presented in the literature [39], the spatially *coarse-scale* motions of many moving targets-of-interest are modeled by a *3-D rotating, translating rigid-body* (assuming that there is only one target with no nearby surrounding high-amplitude clutter scatterers, and assuming that there are not spatially fine-scale motions such as target-articulation and vibration). In addition (at least for these particular techniques), it has been shown [39] that for a slant-plane type of SAR data model (such as the SAR data model presented in this thesis in Chapter 2), the SAR data corresponding to a $3-D$ rigid-body target model can be well-approximated by a data set corresponding to a simpler $2-D$ rigid-body model (with the assumption that the "out-of-plane" rotation of the target is small). Therefore, *we can use a parameterized $2-D$ rigid-body kinematic model as a means of regularizing the target-scatterer motions when imaging moving targets.*

In this chapter, we present an estimation-theoretic L_1-Norm based approach which exploits a parameterized $2-D$ rigid-body temporally-constant velocity kinematic model (which was presented earlier in Chapter 2) as a means of imaging closely-spaced multiple

moving scatterers over a given spatial region. In Section 5.1, we detail the development of a "full" rigid-body L_1-Norm based SAR processing algorithm from the fore-mentioned rigid-body SAR model of Chapter 2. We also discuss in this section some of the implementation issues associated with this algorithm. In Section 5.2, we present a simplified purely-translational version of the rigid-body L_1-Norm based SAR processing algorithm. Unlike the "full" rigid-body algorithm presented in Section 5.2, this algorithm does not estimate rigid-body target's rotation rate. In Section 5.3, we present some results for both synthetic moving point scatterers embedded in real clutter and synthetic-motion real targets embedded in real clutter.

5.1   Full Rigid-Body L$_1$-Norm SAR Processing Algorithm

From Chapter 2, the demodulated (noise-free) SAR data, $f[n,k]$, for a $2-D$ array of point-scatterers (corresponding to a rigid-body target) can be expressed by the following relation

$$f[n,k] \quad = \sum_{n_x} \sum_{n_y} A[n_x, n_y] \, e^{\, j \, \left[(\phi_x[n,k] - \phi_{\dot{y}}[n,k]\dot{\psi}_{RB})\Delta_x n_x + (\phi_y[n,k] + \phi_{\dot{x}}[n,k]\dot{\psi}_{RB})n_y \Delta_y \, \right]}$$

$$\times e^{\, j \, \left[\phi_{\dot{x}}[n,k]\dot{x}_{RB} + \phi_{\dot{y}}[n,k]\dot{y}_{RB} \, \right]} \, . \tag{5.1}$$

Here, $(\Delta_x n_x, \Delta_y n_y)$ are the initial positions (at $t = 0$) of the point-scatterers belonging to the $2-D$ rigid-body target. The parameters $\dot{x}_{RB}$ and $\dot{y}_{RB}$ are the translational velocities of the target's center-of-rotation, while $\dot{\psi}_{RB}$ is the target's rotation rate. Given this model, we can write an estimation-theoretic model for the rigid-body temporally-constant velocity SAR data by including a (zero-mean circularly-complex Gaussian) additive-noise term $\eta[n,k]$,

$$
\boxed{
\begin{array}{c}
\textit{Rigid-Body Temporally-Constant Velocity (RBTCV)} \\
\underline{\textit{Estimation-Theoretic SAR Data Model}} \\[4pt]
f[n,k] = \quad \sum_{n_x} \sum_{n_y} A[n_x, n_y] s_{\dot{\psi}_{RB}}[n_x, n_y, n, k] s_{\dot{x}_{RB}\,\dot{y}_{RB}}[n,k] + \eta[n,k] \, . \\[4pt]
-\frac{N}{2} \le n \le \frac{N}{2} \quad -K \le k \le K
\end{array}
}
\tag{5.2}
$$

From Chapter 2, we can express the RBTCV estimation-theoretic model in the following matrix form

$$\mathbf{f} = \mathbf{F(v)A} + \eta \, . \tag{5.3}$$

Here, $\mathbf{f}$ is the SAR data, and $\mathbf{A}$ is the vector of scatterer intensities, given by

$$\mathbf{A} = \begin{bmatrix} \vdots \\ A[0,0] \\ A[0,1] \\ \vdots \end{bmatrix} \, . \tag{5.4}$$

The vector $\mathbf{v}$ is the vector of the rigid-body scatterer-velocity parameters

$$\mathbf{v} = \begin{bmatrix} \dot{x}_{RB} \\ \dot{y}_{RB} \\ \dot{\psi}_{RB} \end{bmatrix} \, , \tag{5.5}$$

and η is the additive Gaussian noise. The matrix $\mathbf{F}(\mathbf{v})$ has the form

$$\mathbf{F}(\mathbf{v}) = \begin{bmatrix} \ldots & \mathbf{s_v}[0,0] & \mathbf{s_v}[0,1] & \ldots \end{bmatrix} \, . \tag{5.6}$$

Each column vector $\mathbf{s_v}[n_x, n_y]$ corresponds to a lexicographical reordering of the complex exponential basis-function given by $s_{\dot{\psi}_{RB}}[n_x, n_y, n, k] s_{\dot{x}_{RB} \, \dot{y}_{RB}}[n, k]$. Since we assume that the additive noise η is spatially statistically-independent (and isotropic), its spatial-correlation matrix is given by

$$\mathbf{K}_\eta = E\left[\eta \eta^H\right] = \sigma_\eta^2 \mathbf{I} \, . \tag{5.7}$$

Given the rigid-body estimation-theoretic model $\mathbf{f} = \mathbf{F}(\mathbf{v})\mathbf{A} + \eta$, *the fundamental objective of the rigid-body L_1-norm based SAR processing algorithm is to find the set of scatterer amplitudes $\hat{\mathbf{A}}$ and scatterer velocity-parameters $\hat{\mathbf{v}} = [\ \hat{\dot{x}}_{RB}\ \hat{\dot{y}}_{SC}\ \hat{\dot{\psi}}_{RB}\ ]^T$ which minimizes the following L_1-norm regularized cost function $J(\mathbf{A}, \mathbf{v})$*

$$J(\mathbf{A}, \mathbf{v}) \;=\; ||\mathbf{f} - \mathbf{F}(\mathbf{v})\mathbf{A}||^2_{\mathbf{K}_\eta^{-1}} + \gamma_A ||\mathbf{A}||_1 \, . \tag{5.8}$$

From our discussion of the general L_1-norm based SAR processing algorithm in Chapter 3, this cost function is a standard least-squares cost function for $\mathbf{f} = \mathbf{F}(\mathbf{v})\mathbf{A} + \eta$, augmented by an L_1 penalty upon the scatterer amplitudes. As compared to the more standard L_2-based quadratic-regularization penalties (e.g. $\gamma_A \mathbf{A}^H \mathbf{A}$), this type of penalty tends toward sparse representations of $\hat{\mathbf{A}}$ (i.e., $\hat{\mathbf{A}}$ can be represented by a small number of zero elements).

Given that we assume that the additive noise η is spatially statistically-independent and isotropic, the L_1 cost function can be simplified to

$$J(\mathbf{A}, \mathbf{v}) \;=\; \frac{1}{\sigma_\eta^2} ||\mathbf{f} - \mathbf{F}(\mathbf{v})\mathbf{A}||^2_2 + \gamma_A ||\mathbf{A}||_1 \, . \tag{5.9}$$

For the purposes of estimating $\hat{\mathbf{A}}$ and $\hat{\mathbf{v}}$, we see from this expression that varying the assumed noise variance σ_η^2 is equivalent to varying the L_1 weighting γ_A (since the location of the minimum of the simplified version of the cost function $J(\mathbf{A}, \mathbf{v})$ is not affected by multiplying the simplified cost function by a constant). Therefore, for the results presented in this chapter, we normalized the noise variance to $\sigma_\eta^2 = 1$ and just varied the L_1 weighting γ_A, i.e.,

$$J(\mathbf{A}, \mathbf{v}) \;=\; ||\mathbf{f} - \mathbf{F}(\mathbf{v})\mathbf{A}||^2_2 + \gamma_A ||\mathbf{A}||_1 \, . \tag{5.10}$$

5.1.1 Coordinate-Descent Line-Minimization Implementation of Full Rigid-Body L₁-Norm Algorithm

As discussed in Chapter 3, the most straightforward method for minimizing the L_1 cost function (for the spatially statistically-independent additive-noise case) is to use the following recursive gradient-descent algorithm

$$
\begin{aligned}
\hat{\mathbf{A}}_{m+1} &= \hat{\mathbf{A}}_m - \alpha_A \left[\frac{\partial J(\mathbf{A}, \mathbf{v})}{\partial \mathbf{A}} \right]^H \Bigg|_{\mathbf{A}=\hat{\mathbf{A}}_m,\, \mathbf{v}=\hat{\mathbf{v}}_m} \\
&= \hat{\mathbf{A}}_m + \alpha_A \mathbf{F}^H(\hat{\mathbf{v}}_m)[\mathbf{f} - \mathbf{F}(\hat{\mathbf{v}}_m)\hat{\mathbf{A}}_m] - \alpha_A \gamma_A sgn[\hat{\mathbf{A}}_m]
\end{aligned}
\tag{5.11}
$$

$$
\begin{aligned}
\hat{\mathbf{v}}_{m+1} &= \hat{\mathbf{v}}_m - \alpha_{\mathbf{v}} \frac{1}{2} \Re \left[\frac{\partial J(\mathbf{A}, \mathbf{v})}{\partial \mathbf{v}} \right] \Bigg|_{\mathbf{A}=\hat{\mathbf{A}}_m,\, \mathbf{v}=\hat{\mathbf{v}}_m} \\
&= \hat{\mathbf{v}}_m + \alpha_{\mathbf{v}} \Re \left[\hat{\mathbf{A}}_m^H \frac{\partial \mathbf{F}^H(\hat{\mathbf{v}}_m)}{\partial \mathbf{v}} [\mathbf{f} - \mathbf{F}(\hat{\mathbf{v}}_m)\hat{\mathbf{A}}_m] \right] .
\end{aligned}
\tag{5.12}
$$

Here, we are simultaneously estimating both $\mathbf{A}$ and $\mathbf{v}$. The constants α_A and $\alpha_{\mathbf{v}}$ control the rate of convergence (and stability) of the gradient-descent algorithm.

Recall that the gradient, sgn[$\mathbf{A}$], of the L_1-norm of $\mathbf{A}$ is discontinuous at $\mathbf{A} = \mathbf{0}$. Therefore, for the the gradient-descent algorithm, we use the following continuous approximation (denoted by asgn[$\mathbf{A}$])

$$
\begin{aligned}
[asgn[\mathbf{A}]]_{n_x n_y} &= asgn(A[n_x, n_y]) \\
&= \frac{A[n_x, n_y]}{\sqrt{A[n_x, n_y] A^*[n_x, n_y] + \epsilon_A^2}} ,
\end{aligned}
\tag{5.13}
$$

where the parameter ϵ_A is an L_1 approximation constant. This continuous approximation is simply the gradient of the following approximation to the L_1-norm of $\mathbf{A}$

$$
\begin{aligned}
||\mathbf{A}||_1 &= \sum_{n_x} \sum_{n_y} |A[n_x, n_y]| \\
&\approx \sum_{n_x} \sum_{n_y} \sqrt{A[n_x, n_y] A^*[n_x, n_y] + \epsilon_A^2} .
\end{aligned}
\tag{5.14}
$$

From the previously-mentioned discussion of Chapter 3, one major disadvantage of the gradient-descent implementation is its sensitivity to the presence of local minima in the cost function $J(\mathbf{A}, \mathbf{v})$. For our SAR imaging application, this implies that the gradient-descent algorithm may converge to a solution set $\hat{\mathbf{A}}$ and $\hat{\mathbf{v}}$ where the gradient of $J(\mathbf{A}, \mathbf{v})$ is locally small, but where the SAR image is not focused. From Chapter 3, we saw that one way of reducing this sensitivity to local minima is by using the following *coordinate-descent line minimization* based algorithm.

For this algorithm (given the L_1 cost function $J(\mathbf{A}, \mathbf{v})$), we first define the following set of velocity-dependent target-scatterer amplitudes, $\mathbf{A}(\mathbf{v})$

$$
\mathbf{A}(\mathbf{v}) = \arg \min_{\mathbf{A}} [J(\mathbf{A}, \mathbf{v})] .
\tag{5.15}
$$

In other words, for a given set of rigid-body velocity parameters $\mathbf{v}$, $\mathbf{A}(\mathbf{v})$ is defined as the set of scatterer amplitudes which minimizes the L_1 cost function $J(\mathbf{A}, \mathbf{v})$. We can evaluate $\mathbf{A}(\mathbf{v})$ (for a given $\mathbf{v}$) by the following version of the previously-presented gradient-descent algorithm (which incorporates the continuous approximation, $asgn[\mathbf{A}]$, to the gradient of the L_1 norm of $\mathbf{A}$)

$$\hat{\mathbf{A}}_{m+1}(\mathbf{v}) \;=\; \hat{\mathbf{A}}_m(\mathbf{v}) + \alpha_A \mathbf{F}^H(\mathbf{v})[\mathbf{f} - \mathbf{F}(\mathbf{v})\hat{\mathbf{A}}_m(\mathbf{v})] - \alpha_A \gamma_A \, asgn[\hat{\mathbf{A}}_m(\mathbf{v})] \quad (5.16)$$

For a given set of rigid-body velocity parameters $\mathbf{v}$ (and velocity-dependent target-scatterer amplitudes $\mathbf{A}(\mathbf{v})$), the real part of the gradient (with respect to the velocity parameters $\mathbf{v}$) of the L_1 cost-function $J(\mathbf{A}, \mathbf{v})$ evaluated at $\mathbf{A} = \mathbf{A}(\mathbf{v})$ is given by

$$\Re\left[\frac{\partial J(\mathbf{A}, \mathbf{v})}{\partial \mathbf{v}} \right]\bigg|_{\mathbf{A}=\mathbf{A}(\mathbf{v})} \;=\; -2\Re\left[\mathbf{A}^H(\mathbf{v}) \frac{\partial \mathbf{F}^H(\mathbf{v})}{\partial \mathbf{v}} [\mathbf{f} - \mathbf{F}(\mathbf{v})\mathbf{A}(\mathbf{v})] \right] . \quad (5.17)$$

The coordinate-descent line-minimization algorithm uses this gradient to minimize the L_1 cost function in the following manner:

I. For a set of given initial rigid-body velocity-parameters $\mathbf{v}_0$, we first compute the following search direction, $\mathbf{d}_0$, given by the negative of the real part of the gradient (with respect to the rigid-body velocity parameters) of the L_1 cost-function $J(\mathbf{A}, \mathbf{v})$ evaluated at $\mathbf{A} = \mathbf{A}(\mathbf{v}_0)$ and $\mathbf{v} = \mathbf{v}_0$

$$\mathbf{d}_0 = -\frac{1}{2}\Re\left[\frac{\partial J(\mathbf{A}, \mathbf{v})}{\partial \mathbf{v}} \right]\bigg|_{\mathbf{A}=\mathbf{A}(\mathbf{v}_0), \mathbf{v}=\mathbf{v}_0} . \quad (5.18)$$

This quantity is then used as the initial condition for a set of recursive *coordinate-descent 1-D line minimizations*[5, 15].

II. For each iteration m (given the corresponding set of rigid-body velocity-parameters, $\mathbf{v}_m$, and given the corresponding direction vector $\mathbf{d}_m$):

A. We perform the following $1-D$ minimization over the scalar λ

$$\hat{\lambda}_m = \arg \min_{\lambda} \left[J(\mathbf{A}(\mathbf{v}_m + \lambda \mathbf{d}_m), \mathbf{v}_m + \lambda \mathbf{d}_m) \right] . \quad (5.19)$$

Essentially, we are searching the velocity-parameter space $\mathbf{v}$ along a $1-D$ line (parameterized by the scalar λ) defined by $\mathbf{v} = \mathbf{v}_m + \lambda \mathbf{d}_m$ for a new value of $\mathbf{v}$ which minimizes the L_1 cost function.

B. Once we obtain this new minimum, given by

$$\mathbf{v}_{m+1} = \mathbf{v}_m + \hat{\lambda}_m \mathbf{d}_m , \quad (5.20)$$

we then compute a new direction vector, $\mathbf{d}_{m+1}$, which we use in the next iteration of this algorithm to start a new search for a lower minimum.

$$\mathbf{d}_{m+1} = -\frac{1}{2}\Re\left[\frac{\partial J(\mathbf{A}, \mathbf{v})}{\partial \mathbf{v}} \right]\bigg|_{\substack{\mathbf{A}=\mathbf{A}(\mathbf{v}_{m+1}), \\ \mathbf{v}=\mathbf{v}_{m+1}}} + \mu_m \mathbf{d}_m . \quad (5.21)$$

In the literature[5, 15], the scalar μ_m for the coordinate-descent line-minimization algorithm is generally given by the following ratio of vector inner products

$$\mu_m = \frac{\left(\frac{1}{2}\Re\left[\frac{\partial J(\mathbf{A},\mathbf{v})}{\partial \mathbf{v}}\right]\Big|_{\substack{\mathbf{A}=\mathbf{A}(\mathbf{v}_{m+1}),\\ \mathbf{v}=\mathbf{v}_{m+1}}}\right)^T \frac{1}{2}\Re\left[\frac{\partial J(\mathbf{A},\mathbf{v})}{\partial \mathbf{v}}\right]\Big|_{\substack{\mathbf{A}=\mathbf{A}(\mathbf{v}_{m+1}),\\ \mathbf{v}=\mathbf{v}_{m+1}}}}{\left(\frac{1}{2}\Re\left[\frac{\partial J(\mathbf{A},\mathbf{v})}{\partial \mathbf{v}}\right]\Big|_{\substack{\mathbf{A}=\mathbf{A}(\mathbf{v}_{m}),\\ \mathbf{v}=\mathbf{v}_{m}}}\right)^T \frac{1}{2}\Re\left[\frac{\partial J(\mathbf{A},\mathbf{v})}{\partial \mathbf{v}}\right]\Big|_{\substack{\mathbf{A}=\mathbf{A}(\mathbf{v}_{m}),\\ \mathbf{v}=\mathbf{v}_{m}}}} . \tag{5.22}$$

However, for the results presented in this chapter, we used the following alternative form for μ_m (which has been shown in the literature [5] to be less sensitive to the presence of local minima in the L_1 cost function)

$$\mu_m =$$

$$\frac{\left(\frac{1}{2}\Re\left[\frac{\partial J(\mathbf{A},\mathbf{v})}{\partial \mathbf{v}}\right]\Big|_{\substack{\mathbf{A}=\mathbf{A}(\mathbf{v}_{m+1}),\\ \mathbf{v}=\mathbf{v}_{m+1}}}\right)^T \left(\frac{1}{2}\Re\left[\frac{\partial J(\mathbf{A},\mathbf{v})}{\partial \mathbf{v}}\right]\Big|_{\substack{\mathbf{A}=\mathbf{A}(\mathbf{v}_{m+1}),\\ \mathbf{v}=\mathbf{v}_{m+1}}} - \frac{1}{2}\Re\left[\frac{\partial J(\mathbf{A},\mathbf{v})}{\partial \mathbf{v}}\right]\Big|_{\substack{\mathbf{A}=\mathbf{A}(\mathbf{v}_{m}),\\ \mathbf{v}=\mathbf{v}_{m}}}\right)}{\left(\frac{1}{2}\Re\left[\frac{\partial J(\mathbf{A},\mathbf{v})}{\partial \mathbf{v}}\right]\Big|_{\substack{\mathbf{A}=\mathbf{A}(\mathbf{v}_{m}),\\ \mathbf{v}=\mathbf{v}_{m}}}\right)^T \frac{1}{2}\Re\left[\frac{\partial J(\mathbf{A},\mathbf{v})}{\partial \mathbf{v}}\right]\Big|_{\substack{\mathbf{A}=\mathbf{A}(\mathbf{v}_{m}),\\ \mathbf{v}=\mathbf{v}_{m}}}} . \tag{5.23}$$

For the coordinate-descent line-minimization algorithm, it can be shown[5, 15] that each new direction vector $\mathbf{d}_{m+1}$ is approximately orthogonal to the previous direction vector $\mathbf{d}_m$. As compared to the direct gradient-descent algorithm, we see that this algorithm has a somewhat more robust "global" minima search strategy.

Once we have obtained a convergent estimate $\hat{\mathbf{v}}$ of the velocity-parameters, the focused SAR image is given by $\hat{\mathbf{A}} = \mathbf{A}(\hat{\mathbf{v}})$. Recall from Chapter 3 that for higher values of the L_1 weighting γ_A, the L_1 imaging technique tends to attenuate most of the target scatterers, except for the "brighter" feature scatterers (which would be advantageous for some automatic target recognition applications). However, for the results presented in this chapter, we computed the scatterer amplitudes by finding the $\hat{\mathbf{A}}$ which minimized the original standard least-squares cost function (given that we have obtained a convergent estimate $\hat{\mathbf{v}}$ of the velocity-parameters from the fore-mentioned coordinate-descent line-minimization algorithm),i.e.,

$$\hat{\mathbf{A}} = \arg \min_{\mathbf{A}} [J(\mathbf{A}, \hat{\mathbf{v}})] = \arg \min_{\mathbf{A}} \left[||\mathbf{f} - \mathbf{F}(\hat{\mathbf{v}})\mathbf{A}||_2^2\right] . \tag{5.24}$$

Note that this is equivalent to $\gamma_A = 0$. We computed the scatterer amplitudes in this manner such that as few of the target scatterers as possible were attenuated (for the sake of comparison to the conventional SAR imaging techniques). This computation was done by the following recursive gradient-descent algorithm (with $\hat{\mathbf{A}}_0 = \mathbf{0}$)

$$\begin{aligned}\hat{\mathbf{A}}_{m+1} &= \hat{\mathbf{A}}_m - \alpha \left[\frac{\partial J(\mathbf{A}, \hat{\mathbf{v}})}{\partial \mathbf{A}}\right]^H\Bigg|_{\mathbf{A}=\hat{\mathbf{A}}_m} \\ &= \hat{\mathbf{A}}_m + \alpha \mathbf{F}^H(\hat{\mathbf{v}})[\mathbf{f} - \mathbf{F}(\hat{\mathbf{v}})\hat{\mathbf{A}}_m] .\end{aligned} \tag{5.25}$$

For the least-squares cost function, we again normalized the noise variance to $\sigma_\eta^2 = 1$ (since we assumed that the additive noise was spatially statistically-independent and isotropic).

5.1.2   Fast Computation of the L_1 Cost-Function and its Gradient

In the previous section, we presented a coordinate-descent line-minimization technique for finding estimates of $\mathbf{A}$ and $\mathbf{v}$ which minimizes the (normalized noise-variance) L_1 cost function $J(\mathbf{A}, \mathbf{v}) = \|\mathbf{f} - \mathbf{F}(\mathbf{v})\mathbf{A}\|_2^2 + \gamma_A \|\mathbf{A}\|_1$. This involves evaluating both the cost-function and its gradient, which first involves computation of the following estimate of the SAR data (given estimates of the scatterer amplitudes $\hat{\mathbf{A}}$ and the scatterer velocities $\hat{\mathbf{v}}$)

$$\hat{\mathbf{f}} = \mathbf{F}(\hat{\mathbf{v}})\hat{\mathbf{A}} . \tag{5.26}$$

In terms of the rigid-body SAR model, this quantity can alternately be expressed by

$$\hat{f}[n,k] = \sum_{n_x}\sum_{n_y} \hat{A}[n_x, n_y]\, e^{j\left[(\phi_x[n,k]-\phi_{\dot{y}}[n,k]\hat{\dot{\psi}}_{RB})\Delta_x n_x + (\phi_y[n,k]+\phi_{\dot{x}}[n,k]\hat{\dot{\psi}}_{RB})\Delta_y n_y\right]}$$
$$\times e^{j\left[\phi_{\dot{x}}[n,k]\hat{\dot{x}}_{RB}+\phi_{\dot{y}}[n,k]\hat{\dot{y}}_{RB}\right]} . \tag{5.27}$$

Then the gradients of the cost function with respect to both $\mathbf{A}$ and $\mathbf{v}$ (at $(\mathbf{A}, \mathbf{v}) = (\hat{\mathbf{A}}, \hat{\mathbf{v}})$) are given by the following expressions (where $\tilde{\mathbf{f}} = \mathbf{f} - \hat{\mathbf{f}}$)

$$\left[\frac{\partial J(\hat{\mathbf{A}}, \hat{\mathbf{v}})}{\partial \mathbf{A}}\right]^H = -\mathbf{F}^H(\hat{\mathbf{v}})\tilde{\mathbf{f}} + \gamma_A \operatorname{asgn}[\hat{\mathbf{A}}] = -\mathbf{F}^H(\hat{\mathbf{v}})(\mathbf{f} - \hat{\mathbf{f}}) + \gamma_A \operatorname{asgn}[\hat{\mathbf{A}}] \tag{5.28}$$

$$\Re\left[\frac{\partial J(\hat{\mathbf{A}}, \hat{\mathbf{v}})}{\partial \mathbf{v}}\right] = -2\Re\left[\hat{\mathbf{A}}^H \frac{\partial \mathbf{F}^H(\hat{\mathbf{v}})}{\partial \mathbf{v}}\tilde{\mathbf{f}}\right] = -2\Re\left[\hat{\mathbf{A}}^H \frac{\partial \mathbf{F}^H(\hat{\mathbf{v}})}{\partial \mathbf{v}}(\mathbf{f} - \hat{\mathbf{f}})\right] . \tag{5.29}$$

In terms of the rigid-body SAR model (with $\tilde{f}[n,k] = f[n,k] - \hat{f}[n,k]$), these gradients can alternately be expressed by

$$\left[\frac{\partial J(\hat{\mathbf{A}}, \hat{\mathbf{v}})}{\partial \mathbf{A}}\right]^H_{n_x n_y} = -\sum_k \sum_n \tilde{f}[n,k]e^{-j\left[\phi_{\dot{x}}[n,k]\hat{\dot{x}}_{RB}+\phi_{\dot{y}}[n,k]\hat{\dot{y}}_{RB}\right]}$$
$$\times e^{-j\left[(\phi_x[n,k]-\phi_{\dot{y}}[n,k]\hat{\dot{\psi}}_{RB})\Delta_x n_x + (\phi_y[n,k]+\phi_{\dot{x}}[n,k]\hat{\dot{\psi}}_{RB})\Delta_y n_y\right]} + \gamma_A \operatorname{asgn}(\hat{A}[n_x, n_y]) \tag{5.30}$$

$$\Re\left[\frac{\partial J(\hat{\mathbf{A}}, \hat{\mathbf{v}})}{\partial \dot{x}_{RB}}\right] =$$
$$-2\Re\left[\sum_{n_x}\sum_{n_y} \hat{A}^*[n_x, n_y] \sum_k \sum_n \tilde{f}[n,k]\,(-j\phi_{\dot{x}}[n,k])\, e^{-j\left[\phi_{\dot{x}}[n,k]\hat{\dot{x}}_{RB}+\phi_{\dot{y}}[n,k]\hat{\dot{y}}_{RB}\right]}\right.$$
$$\left.\times e^{-j\left[(\phi_x[n,k]-\phi_{\dot{y}}[n,k]\hat{\dot{\psi}}_{RB})\Delta_x n_x + (\phi_y[n,k]+\phi_{\dot{x}}[n,k]\hat{\dot{\psi}}_{RB})\Delta_y n_y\right]}\right] \tag{5.31}$$

$$\Re \left[\frac{\partial J(\hat{\mathbf{A}}, \hat{\mathbf{v}})}{\partial \hat{y}_{RB}} \right] =$$

$$-2\Re \left[\sum_{n_x} \sum_{n_y} \hat{A}^*[n_x, n_y] \sum_{k} \sum_{n} \tilde{f}[n, k] \, (-j\phi_{\dot{y}}[n, k]) \, e^{-j \left[\phi_{\dot{x}}[n,k]\hat{\dot{x}}_{RB} + \phi_{\dot{y}}[n,k]\hat{\dot{y}}_{RB} \right]} \right.$$

$$\left. \times e^{-j \left[(\phi_x[n,k] - \phi_{\dot{y}}[n,k]\hat{\dot{\psi}}_{RB})\Delta_x n_x + (\phi_y[n,k] + \phi_{\dot{x}}[n,k]\hat{\dot{\psi}}_{RB})\Delta_y n_y \right]} \right] \tag{5.32}$$

$$\Re \left[\frac{\partial J(\hat{\mathbf{A}}, \hat{\mathbf{v}})}{\partial \hat{\psi}_{RB}} \right] =$$

$$-2\Re \left[\sum_{n_x} \sum_{n_y} \hat{A}^*[n_x, n_y] \sum_{k} \sum_{n} \tilde{f}[n, k] e^{-j \left[\phi_{\dot{x}}[n,k]\hat{\dot{x}}_{RB} + \phi_{\dot{y}}[n,k]\hat{\dot{y}}_{RB} \right]} \right.$$

$$\times (-j \left[\phi_{\dot{x}}[n, k]\Delta_y n_y \Delta_y - \phi_{\dot{y}}[n, k]\Delta_x n_x \right])$$

$$\left. \times e^{-j \left[(\phi_x[n,k] - \phi_{\dot{y}}[n,k]\hat{\dot{\psi}}_{RB})\Delta_x n_x + (\phi_y[n,k] + \phi_{\dot{x}}[n,k]\hat{\dot{\psi}}_{RB})\Delta_y n_y \right]} \right] . \tag{5.33}$$

Rather than evaluating these quantities directly (which can be computationally prohibitive), the following "fast" and easily implementable solutions can be used (with equivalent performance). Let $f_{\hat{A}}[k_x, k_y]$ be the following discrete Fourier Transform of $\hat{A}[n_x, n_y]$ (which can be computed by standard Fast-Fourier Transform techniques)

$$f_{\hat{A}}[k_x, k_y] = \sum_{n_x} \sum_{n_y} \hat{A}[n_x, n_y] e^{-j \left[k_x \Delta_{k_x} \Delta_x n_x + k_y \Delta_{k_y} \Delta_y n_y \right]} .$$

$$\tag{5.34}$$

Then the quantity $\hat{f}[n, k]$ is equivalent to

$$\hat{f}[n, k] \quad = f_{\hat{A}} \left[\frac{(\phi_x[n, k] - \phi_{\dot{y}}[n, k]\hat{\dot{\psi}}_{RB})}{\Delta_{k_x}}, \frac{(\phi_y[n, k] + \phi_{\dot{x}}[n, k]\hat{\dot{\psi}}_{RB})}{\Delta_{k_y}} \right]$$

$$\times e^{j \left[\phi_{\dot{x}}[n,k]\hat{\dot{x}}_{RB} + \phi_{\dot{y}}[n,k]\hat{\dot{y}}_{RB} \right]} . \tag{5.35}$$

Here, we are essentially using the rotational-velocity dependent phase-relations $(\phi_x[n, k] - \phi_{\dot{y}}[n, k]\hat{\dot{\psi}}_{RB})$ and $(\phi_y[n, k] + \phi_{\dot{x}}[n, k]\hat{\dot{\psi}}_{RB})$ as coordinates for performing a $2-D$ interpolation within $f_{\hat{A}}[k_x, k_y]$. The constants Δ_{k_x} and Δ_{k_y} control the sampling of these phase-relations to k_x and k_y.

Let the discrete space-time multi-dimensional signals $\tilde{f}[k_x, k_y, n, k]$, $\tilde{f}_{\dot{x}_{RB}}[k_x, k_y, n, k]$, and $\tilde{f}_{\dot{y}_{RB}}[k_x, k_y, n, k]$ be given by

$$\tilde{f}[k_x, k_y, n, k] \quad = \tilde{f}[n, k] e^{-j \left[\phi_{\dot{x}}[n,k]\hat{\dot{x}}_{RB} + \phi_{\dot{y}}[n,k]\hat{\dot{y}}_{RB} \right]}$$

$$\times \delta \left[k_x - \frac{(\phi_x[n, k] - \phi_{\dot{y}}[n, k]\hat{\dot{\psi}}_{RB})}{\Delta_{k_x}}, k_y - \frac{(\phi_y[n, k] + \phi_{\dot{x}}[n, k]\hat{\dot{\psi}}_{RB})}{\Delta_{k_y}} \right]$$

$$\tag{5.36}$$

$$\tilde{f}_{\dot{x}_{RB}}[k_x, k_y, n, k] \quad = \tilde{f}[n, k]\, (-j\phi_{\dot{x}}[n, k])\, e^{-j\left[\phi_{\dot{x}}[n,k]\hat{\dot{x}}_{RB} + \phi_{\dot{y}}[n,k]\hat{\dot{y}}_{RB}\right]}$$

$$\times \delta\left[k_x - \frac{(\phi_x[n, k] - \phi_{\dot{y}}[n, k]\hat{\dot{\psi}}_{RB})}{\Delta_{k_x}}, k_y - \frac{(\phi_y[n, k] + \phi_{\dot{x}}[n, k]\hat{\dot{\psi}}_{RB})}{\Delta_{k_y}}\right]$$

$$(5.37)$$

$$\tilde{f}_{\dot{y}_{RB}}[k_x, k_y, n, k] \quad = \tilde{f}[n, k]\, (-j\phi_{\dot{y}}[n, k])\, e^{-j\left[\phi_{\dot{x}}[n,k]\hat{\dot{x}}_{RB} + \phi_{\dot{y}}[n,k]\hat{\dot{y}}_{RB}\right]}$$

$$\times \delta\left[k_x - \frac{(\phi_x[n, k] - \phi_{\dot{y}}[n, k]\hat{\dot{\psi}}_{RB})}{\Delta_{k_x}}, k_y - \frac{(\phi_y[n, k] + \phi_{\dot{x}}[n, k]\hat{\dot{\psi}}_{RB})}{\Delta_{k_y}}\right],$$

$$(5.38)$$

where $\delta[k_x, k_y]$ is the usual two-dimensional Kronecker delta-function. Then the gradients of the cost function with respect to both $\mathbf{A}$ and $\mathbf{v}$ (at $(\mathbf{A}, \mathbf{v}) = (\hat{\mathbf{A}}, \hat{\mathbf{v}})$) are equivalent to the following functions of the discrete space-time Fourier Transforms of $\tilde{f}[k_x, k_y, n, k]$, $\tilde{f}_{\dot{x}_{RB}}[k_x, k_y, n, k]$, and $\tilde{f}_{\dot{y}_{RB}}[k_x, k_y, n, k]$

$$\left[\frac{\partial J(\hat{\mathbf{A}}, \hat{\mathbf{v}})}{\partial \mathbf{A}}\right]_{n_x n_y}^H = -\sum_{k_x}\sum_{k_y}\sum_{k}\sum_{n} \tilde{f}[k_x, k_y, n, k] e^{-j\left[k_x \Delta_{k_x} \Delta_x n_x + k_y \Delta_{k_y} \Delta_y n_y\right]} \quad (5.39)$$

$$\Re\left[\frac{\partial J(\hat{\mathbf{A}}, \hat{\mathbf{v}})}{\partial \dot{x}_{RB}}\right] \quad = -2\Re\left[\sum_{n_x}\sum_{n_y} \hat{A}^*[n_x, n_y]\right.$$

$$\left.\times \sum_{k_x}\sum_{k_y}\sum_{k}\sum_{n} \tilde{f}_{\dot{x}_{RB}}[k_x, k_y, n, k] e^{-j\left[k_x \Delta_{k_x} \Delta_x n_x + k_y \Delta_{k_y} \Delta_y n_y\right]}\right] (5.40)$$

$$\Re\left[\frac{\partial J(\hat{\mathbf{A}}, \hat{\mathbf{v}})}{\partial \dot{y}_{RB}}\right] \quad = -2\Re\left[\sum_{n_x}\sum_{n_y} \hat{A}^*[n_x, n_y]\right.$$

$$\left.\times \sum_{k_x}\sum_{k_y}\sum_{k}\sum_{n} \tilde{f}_{\dot{y}_{RB}}[k_x, k_y, n, k] e^{-j\left[k_x \Delta_{k_x} \Delta_x n_x + k_y \Delta_{k_y} \Delta_y n_y\right]}\right] (5.41)$$

$$\Re\left[\frac{\partial J(\hat{\mathbf{A}}, \hat{\mathbf{v}})}{\partial \dot{\psi}_{RB}}\right] \quad = -2\Re\left[\sum_{n_x}\sum_{n_y} \hat{A}^*[n_x, n_y]\Delta_y n_y\right.$$

$$\times \sum_{k_x}\sum_{k_y}\sum_{k}\sum_{n} \tilde{f}_{\dot{x}_{RB}}[k_x, k_y, n, k] e^{-j\left[k_x \Delta_{k_x} \Delta_x n_x + k_y \Delta_{k_y} \Delta_y n_y\right]}$$

$$+ \sum_{n_x}\sum_{n_y} \hat{A}^*[n_x, n_y]\Delta_x n_x$$

$$\left.\times \sum_{k_x}\sum_{k_y}\sum_{k}\sum_{n} \tilde{f}_{\dot{y}_{RB}}[k_x, k_y, n, k] e^{-j\left[k_x \Delta_{k_x} \Delta_x n_x + k_y \Delta_{k_y} \Delta_y n_y\right]}\right] .(5.42)$$
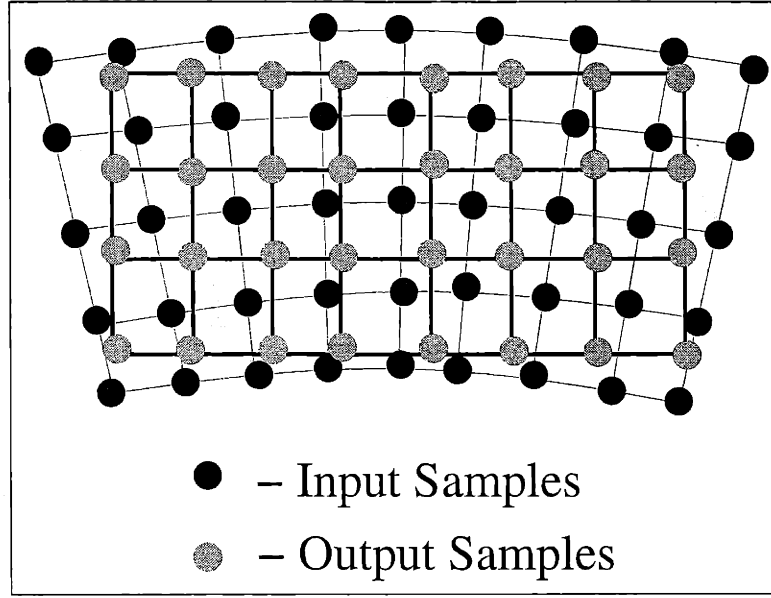
Figure 5.1: Polar Format Resampling

Essentially, this part of the implementation scheme performs a set of discrete Fourier Transforms (which can be computed by standard Fast-Fourier Transform techniques) upon phase-compensated versions of the SAR data which have been "remapped" according to the rotational-velocity dependent phase-relations $(\phi_x[n,k] - \phi_{\dot{y}}[n,k]\hat{\dot{\psi}}_{RB})$ and $(\phi_y[n,k] + \phi_{\dot{x}}[n,k]\hat{\dot{\psi}}_{RB})$. In many ways, this is very similar to the Polar-Format Resampling technique discussed in Section 3.1 (which is used in conventional SAR imaging for compensating for range-walk without sacrificing range resolution). From this viewpoint, we are resampling the phase-compensated SAR data set by interpolating from a polar grid to a rectangular grid, as shown in Figure 5.1. The angular extent of the polar grid is approximately proportional to the estimated relative SAR-platform-to-target rotation rate, which is given by the sum of the SAR's look-angle rotation rate and the estimated target rotation rate, i.e., $\dot{\theta} + \hat{\dot{\psi}}_{RB}$.

5.1.3 Azimuth-Rescaling and Azimuth-Displacement Compensation

Recall from Chapter 2 that the polynomial approximation to the RBTCV phase functions were given by

$$\phi_x[n,k] = -\frac{4\pi}{\lambda_c}\left(1 + \frac{\alpha T_p}{f_c}\frac{n}{N}\right)\left[\frac{1}{6}\dot{\theta}^3\left(\frac{Tk}{K}\right)^3 - \dot{\theta}\left(\frac{Tk}{K}\right)\right] \tag{5.43}$$

$$\phi_y[n,k] = -\frac{4\pi}{\lambda_c}\left(1 + \frac{\alpha T_p}{f_c}\frac{n}{N}\right)\left[1 - \frac{1}{2}\dot{\theta}^2\left(\frac{Tk}{K}\right)^2\right] \tag{5.44}$$

$$\phi_{\dot{x}}[n,k] = \frac{4\pi}{\lambda_c}\left(1 + \frac{\alpha T_p}{f_c}\frac{n}{N}\right)\left[\dot{\theta}\left(\frac{Tk}{K}\right)^2\right] \tag{5.45}$$

$$\phi_{\dot{y}}[n,k] = -\frac{4\pi}{\lambda_c}\left(1 + \frac{\alpha T_p}{f_c}\frac{n}{N}\right)\left[\left(\frac{Tk}{K}\right) - \frac{1}{2}\dot{\theta}^2\left(\frac{Tk}{K}\right)^3\right]. \tag{5.46}$$

Upon closer inspection, we see that for $\dot{\theta}$ "small", the range-velocity phase-function is approximately a linear function of the azimuth-position phase function, i.e., $\phi_{\dot{y}}[n,k] \approx -\phi_x[n,k]/\dot{\theta}$. This implies that for a given rigid-body target (consisting of a 2-D array of scatterers with initial spatial positions given by $(\Delta_x n_x, \Delta_y n_y)$), a *rigid-body imaging algorithm based upon these phase functions will have difficulty distinguishing between the initial azimuth position* $\Delta_x n_x$ *and the range-velocity induced displacement* $x_{DISP}(\dot{y}[n_x, n_y]) = -\dot{y}_{RB}/\dot{\theta}$. This is identical to the ambiguity problem (between the initial azimuth position and the range-velocity induced displacement) we originally encountered with the matched-filter phase-functions presented in Chapter 4.

In addition, this approximately-linear relationship between $\phi_{\dot{y}}[n,k]$ and $\phi_x[n,k]$ implies that the rotational-velocity dependent phase-relation $(\phi_x[n,k] - \phi_{\dot{y}}[n,k]\dot{\psi}_{RB})$ is approximately given by

$$\phi_x[n,k] - \phi_{\dot{y}}[n,k]\dot{\psi}_{RB} \approx \left(1 + \frac{\dot{\psi}_{RB}}{\dot{\theta}}\right)\phi_x[n,k]. \tag{5.47}$$

This essentially says that a rotating moving target (with a rotation rate of $\dot{\psi}_{RB}$) will appear to be scaled in azimuth by $1 + \dot{\psi}_{RB}/\dot{\theta}$. This relation also implies that *a rigid-body imaging algorithm based upon these phase functions will have difficulty distinguishing between a given rotating (with a rotation rate of* $\dot{\psi}_{RB}$*) and a non-rotating version of the rotating-target scaled by* $1 + \dot{\psi}_{RB}/\dot{\theta}$. In other words, this implies that the rigid-body imaging algorithm will exhibit very poor target rotation-rate estimation performance.

In an identical fashion to the matched-filter algorithm presented in Chapter 4, we can alleviate both of these problems for the rigid-body algorithm by first removing the "linear" portion of the polynomial approximation to the range-velocity phase function, $\phi_{\dot{y}}[n,k]$ (such that this function is no longer an approximately-linear function of the azimuth-position phase-function for $\dot{\theta}$ small). This leaves the following "leftover" dominant term

$$\phi_{\dot{y}}[n,k] \approx -\frac{4\pi}{\lambda_c}\left(\frac{\alpha T_p}{f_c}\frac{n}{N}\right)\left[\left(\frac{Tk}{K}\right)\right]. \tag{5.48}$$

This dominant "cross-phase" term between n and k corresponds to motion-induced *range-walk* (i.e., when we perform a Fourier Transform with respect to the "fast-time" index n, we have a displacement in range proportional to the "slow-time" index k). Next, we use the rigid-body algorithm (with the modified range-velocity phase function) to obtain estimates, $\hat{\dot{y}}_{RB}$ and $\hat{\dot{\psi}}_{RB}$, of the target range velocity and the target rotation rate, respectively. Once we obtain this estimate, we then rescale the resulting SAR image of the target in azimuth by the inverse of $1 + \hat{\dot{\psi}}_{RB}/\dot{\theta}$, (since we know the "look-angle" rotation rate $\dot{\theta}$). Lastly, we use the range-velocity estimate to correct the target scatterer reflectivity estimates for the range-velocity induced azimuth displacement

$$\hat{A}[n_x, n_y] = \hat{A}_U\left[n_x - \frac{1}{\Delta_x}\frac{1}{\dot{\theta}}\hat{\dot{y}}_{RB}, n_y\right]. \tag{5.49}$$

5.1.4   Azimuth Resolution

In Chapter 3, we derived values for the spatial sampling intervals, Δ_x and Δ_y. Recall from this chapter that these sampling intervals were some fraction of the corresponding approximate "inherent" azimuth and range resolutions, δ_x and δ_y (whose values we derived in Chapter 3), of the conventional SAR imaging system. Here, we derive an approximate value for the inherent azimuth resolution of the rigid-body imaging algorithm, assuming that we have $\gamma_A = 0$ (since this is the L_1 weighting we use to form the final focused SAR image) and assuming that we have "perfect" knowledge of the rigid-body velocity parameters, $\dot{x}_{RB}$, $\dot{y}_{RB}$, and $\dot{\psi}_{RB}$.

Suppose we are given a rigid-body moving target consisting of a $2-D$ array of ideal point-scatterers with initial positions at $(\delta_x n_x', \delta_y n_y')$ (where $\{n_x', n_y'\} \in Target$). For $\dot{\theta}$ "small", the noiseless SAR data set $f[n,k]$ for this rigid-body target (with known velocity-parameters, $\dot{x}_{RB}$, $\dot{y}_{RB}$, and $\dot{\psi}_{RB}$) is approximately given by

$$f[n,k] \approx$$

$$\sum_{n_x'} \sum_{n_y'} A[n_x', n_y'] \, e^{\, j \, \frac{4\pi}{\lambda_c} \left[(\dot{\theta} + \dot{\psi}_{RB}) \left(\frac{Tk}{K} \right) \delta_x n_x' \right]} \, e^{\, -j \, \frac{4\pi}{\lambda_c} \left[\frac{\alpha T_p}{f_c} \frac{n}{N} \delta_y n_y' \right]} \, e^{\, j \left[\phi_{\dot{x}}[n,k]\dot{x}_{RB} + \phi_{\dot{y}}[n,k]\dot{y}_{RB} \right]} .$$

$$-\frac{N}{2} \leq n \leq \frac{N}{2} \qquad -K \leq k \leq K$$

$$(5.50)$$

We see that the noiseless data set is essentially given by a scaled Fourier Transform of the imaged target field reflectivity (distorted by a translational-velocity dependent complex phase term). The noiseless SAR data can also be expressed in the following form

$$f[n,k] = \sum_{n_x'} \sum_{n_y'} A[n_x', n_y'] \, e^{\, j \, k\Delta\omega_x \left(1 + \frac{\dot{\psi}_{RB}}{\dot{\theta}} \right) \delta_x n_x'} \, e^{\, -j \, n\Delta\omega_y \delta_y n_y'} \, e^{\, j \left[\phi_{\dot{x}}[n,k]\dot{x}_{RB} + \phi_{\dot{y}}[n,k]\dot{y}_{RB} \right]} ,$$

$$-\frac{N}{2} \leq n \leq \frac{N}{2} \qquad -K \leq k \leq K$$

$$(5.51)$$

where the *discrete spatial frequencies* $(k\Delta\omega_x, n\Delta\omega_y)$ are given by

$$k\Delta\omega_x \;=\; \frac{4\pi\dot{\theta}t_T[k]}{\lambda_c} = \frac{4\pi\dot{\theta}}{\lambda_c}\left[\frac{k(2T)}{2K}\right] \tag{5.52}$$

$$n\Delta\omega_y \;=\; \frac{4\pi}{\lambda_c}\left[\frac{\alpha T_p}{f_c}\frac{\hat{t}[n]}{T_p}\right] = \frac{4\pi\alpha\hat{t}[n]}{c} = \frac{4\pi\alpha}{c}\left[\frac{nT_p}{N}\right] . \tag{5.53}$$

This equation essentially says that *the SAR data is a (phase-distorted) subset of the target-field's 2-D Fourier Transform*, where the dimensions of this subset, $2K(1+\dot{\psi}_{RB}/\dot{\theta})\Delta\omega_x$ and $N\Delta\omega_y$, are given by

$$2K\left(1 + \frac{\dot{\psi}_{RB}}{\dot{\theta}}\right)\Delta\omega_x \;=\; \left(1 + \frac{\dot{\psi}_{RB}}{\dot{\theta}}\right)\frac{8\pi\dot{\theta}T}{\lambda_c} \tag{5.54}$$

$$N\Delta\omega_y \;=\; \frac{4\pi\alpha T_p}{c} . \tag{5.55}$$

In matrix notation, if $\mathbf{v}_o$ is the vector of known velocity parameters, the noiseless SAR data is given by $\mathbf{f} = \mathbf{F}(\mathbf{v}_o)\mathbf{A}$. This implies that for an L_1 weighting of $\gamma_A = 0$, the maximum-likelihood estimate $\hat{\mathbf{A}}_{ML}$ for $\mathbf{A}$ is approximately given by the following expression

$$
\begin{aligned}
\hat{\mathbf{A}}_{ML} &= \left(\mathbf{F}^H(\mathbf{v}_o)\mathbf{F}(\mathbf{v}_o)\right)^{-1}\mathbf{F}^H(\mathbf{v}_o)\mathbf{f} \\
&\approx \mathbf{F}^H(\mathbf{v}_o)\mathbf{f} .
\end{aligned}
\tag{5.56}
$$

This implies that for known velocity parameters, $\dot{x}_{RB}$, $\dot{y}_{RB}$, and $\dot{\psi}_{RB}$, the noiseless-data maximum-likelihood estimate, $\hat{A}[n_x, n_y]$ (which is a phase-compensated discrete scaled inverse Fourier Transform of $f[n,k]$) is approximately given by the following set of scaled *sampled 2-D sinc functions* (where the spatial sampling intervals are again given by Δ_x and Δ_y)

$$
\begin{aligned}
\hat{A}[n_x, n_y] \quad &= \frac{1}{(2K)(N)} \sum_{k=-K}^{K} \sum_{n=-\frac{N}{2}}^{\frac{N}{2}} f[n,k] e^{-j\left[\phi_{\dot{x}}[n,k]\dot{x}_{RB} + \phi_{\dot{y}}[n,k]\dot{y}_{RB}\right]} \\
&\times e^{-j\, k\Delta\omega_x\left(1+\frac{\dot{\psi}_{RB}}{\dot{\theta}}\right)\Delta_x n_x} \, e^{j\, n\Delta\omega_y \Delta_y n_y} \\
&\approx \sum_{n_x'} \sum_{n_y'} A[n_x', n_y'] \text{sinc}\left(\frac{2K\left(1 + \frac{\dot{\psi}_{RB}}{\dot{\theta}}\right)\Delta\omega_x(\Delta_x n_x - \delta_x n_x'))}{2}\right) \\
&\times \text{sinc}\left(\frac{N\Delta\omega_y(\Delta_y n_y - \delta_y n_y'))}{2}\right) .
\end{aligned}
\tag{5.57}
$$

Note that we are implicitly including the target rotation-rate dependent azimuth scale factor $1 + \dot{\psi}_{RB}/\dot{\theta}$. In order for the sinc-function mainlobe "peaks"(corresponding to each point scatterer) to be distinct, the initial positions $(\delta_x n_x', \delta_y n_y')$ of the ideal point scatterers must be separated by an azimuth distance and a range distance equal to the respective azimuth width and range width of the mainlobes of the scaled sampled sinc functions. This implies that the azimuth resolution δ_x of the rigid-body SAR imaging algorithm is approximately given by the following expression

$$
\boxed{
\begin{aligned}
&\underline{\textit{Rigid-Body Azimuth Resolution}} \\[4pt]
&\delta_x \approx 2\,\frac{\pi}{\left(\frac{2K(1+\dot{\psi}_{RB}/\dot{\theta})\Delta\omega_x}{2}\right)} = \frac{\lambda_c}{2(\dot{\theta}+\dot{\psi}_{RB})T} .
\end{aligned}
}
\tag{5.58}
$$

We see that *the azimuth resolution of the SAR system for a rotating target is directly dependent upon the target's rotation rate*. For positive values of $\dot{\psi}_{RB}$, we have increased target resolution, while for negative values of $\dot{\psi}_{RB}$ we have decreased target resolution. In the literature[18], the spatial sampling-interval constants, Δ_x and Δ_y, are usually chosen to be some fraction of δ_x and δ_y (e.g., $\Delta_x = 0.5\delta_x$ and $\Delta_y = 0.5\delta_y$). Note that the approximate range resolution of the rigid-body algorithm is identical to the approximate range resolution

of the conventional algorithm presented in Chapter 3, given by

$$
\boxed{
\begin{array}{c}
\underline{\textit{Rigid-Body Range Resolution}} \\[2mm]
\delta_y \approx 2\,\dfrac{\pi}{\left(\frac{N\Delta\omega_y}{2}\right)} = \dfrac{c}{\alpha T_p}\ .
\end{array}
}
\tag{5.59}
$$

5.2 Purely-Translational Rigid-Body L_1-Norm SAR Processing Algorithm

In this section, we present a simplified version of the rigid-body L_1-norm SAR processing algorithm we derived for the purely-translational case (where we assumed that the rigid-body rotation rate $\dot{\psi}_{RB}$ was equal to zero). For this case, the rigid-body demodulated (noise-free) SAR data $f[n,k]$ is given by

$$
f[n,k] = \sum_{n_x}\sum_{n_y} A[n_x,n_y]\, e^{\,j\,[\phi_x[n,k]\Delta_x n_x + \phi_y[n,k]n_y\Delta_y\,]}\, e^{\,j\,[\phi_{\dot{x}}[n,k]\dot{x}_{RB} + \phi_{\dot{y}}[n,k]\dot{y}_{RB}\,]}\ ,
\tag{5.60}
$$

where $(\Delta_x n_x, \Delta_y n_y)$ are the initial positions (at $t=0$) of the point-scatterers. We are essentially assuming that the velocities of all of the scatterers of the target are equal to the translational velocities $(\dot{x}_{RB}, \dot{y}_{RB})$ of the target's center-of-rotation. For the matrix form of the RBTCV model, given by

$$
\mathbf{f} = \mathbf{F}(\mathbf{v})\mathbf{A} + \eta,
\tag{5.61}
$$

the scatterer-velocity parameter vector $\mathbf{v}$ is now simply given by

$$
\mathbf{v} = \left[\begin{array}{c} \dot{x}_{RB} \\ \dot{y}_{RB} \end{array}\right]\ .
\tag{5.62}
$$

Given this simplified RBTCV model and the corresponding normalized-noise L_1 cost function $J(\mathbf{A},\mathbf{v}) = ||\mathbf{f} - \mathbf{F}(\mathbf{v})\mathbf{A}||_2^2 + \gamma_A||\mathbf{A}||_1$, we can use the gradient-directed line minimization algorithm to compute an estimate $\hat{\mathbf{v}}$ of the velocity parameters, just as with the full rigid-body algorithm presented previously. Recall from the discussion of the Fourier-Transform implementation-method in Section 5.1.2 that this involves computing the following estimate of the SAR data (given estimates of the scatterer amplitudes $\hat{\mathbf{A}}$ and the scatterer velocities $\hat{\mathbf{v}}$)

$$
\hat{\mathbf{f}} = \mathbf{F}(\hat{\mathbf{v}})\hat{\mathbf{A}}\ .
\tag{5.63}
$$

For the purely-translational case, this quantity can alternately be expressed by

$$
\hat{f}[n,k] = \sum_{n_x}\sum_{n_y} \hat{A}[n_x,n_y]\, e^{\,j\,[\phi_x[n,k]\Delta_x n_x + \phi_y[n,k]\Delta_y n_y\,]}\, e^{\,j\,[\phi_{\dot{x}}[n,k]\dot{\hat{x}}_{RB} + \phi_{\dot{y}}[n,k]\dot{\hat{y}}_{RB}\,]}\ .
$$

$$
\tag{5.64}
$$

The corresponding gradients of the normalized-noise L_1 cost function $J(\mathbf{A}, \mathbf{v})$ (at $(\mathbf{A}, \mathbf{v}) = (\hat{\mathbf{A}}, \hat{\mathbf{v}})$) for the purely-translational case are given by the following expressions (with $\tilde{f}[n, k] = f[n, k] - \hat{f}[n, k]$)

$$\left[\frac{\partial J(\hat{\mathbf{A}}, \hat{\mathbf{v}})}{\partial \mathbf{A}}\right]^H_{n_x n_y} = -\sum_k \sum_n \tilde{f}[n, k] e^{-j \left[\phi_{\dot{x}}[n,k]\hat{\dot{x}}_{RB} + \phi_{\dot{y}}[n,k]\hat{\dot{y}}_{RB}\right]}$$
$$\times e^{-j \left[\phi_x[n,k]\Delta_x n_x + \phi_y[n,k]\Delta_y n_y\right]} \tag{5.65}$$

$$\Re\left[\frac{\partial J(\hat{\mathbf{A}}, \hat{\mathbf{v}})}{\partial \dot{x}_{RB}}\right] =$$
$$-2\Re\left[\sum_{n_x}\sum_{n_y} \hat{A}^*[n_x, n_y] \sum_k \sum_n \tilde{f}[n, k] (-j\phi_{\dot{x}}[n, k]) e^{-j \left[\phi_{\dot{x}}[n,k]\hat{\dot{x}}_{RB} + \phi_{\dot{y}}[n,k]\hat{\dot{y}}_{RB}\right]}\right.$$
$$\left.\times e^{-j \left[\phi_x[n,k]\Delta_x n_x + \phi_y[n,k]\Delta_y n_y\right]}\right] \tag{5.66}$$

$$\Re\left[\frac{\partial J(\hat{\mathbf{A}}, \hat{\mathbf{v}})}{\partial \dot{y}_{RB}}\right] =$$
$$-2\Re\left[\sum_{n_x}\sum_{n_y} \hat{A}^*[n_x, n_y] \sum_k \sum_n \tilde{f}[n, k] (-j\phi_{\dot{y}}[n, k]) e^{-j \left[\phi_{\dot{x}}[n,k]\hat{\dot{x}}_{RB} + \phi_{\dot{y}}[n,k]\hat{\dot{y}}_{RB}\right]}\right.$$
$$\left.\times e^{-j \left[\phi_x[n,k]\Delta_x n_x + \phi_y[n,k]\Delta_y n_y\right]}\right] . \tag{5.67}$$

In terms of the "fast" Fourier-Transform based implementation method presented in Section 5.1.2, the estimate of the SAR data (given estimates of the scatterer amplitudes $\hat{\mathbf{A}}$ and the scatterer velocities $\hat{\mathbf{v}}$) is given by the following simplified expression

$$\hat{f}[n, k] = f_{\hat{A}}\left[\frac{\phi_x[n, k]}{\Delta_{k_x}}, \frac{\phi_y[n, k]}{\Delta_{k_y}}\right] e^{j \left[\phi_{\dot{x}}[n,k]\hat{\dot{x}}_{RB} + \phi_{\dot{y}}[n,k]\hat{\dot{y}}_{RB}\right]} , \tag{5.68}$$

where $f_{\hat{A}}[k_x, k_y]$ is the following discrete Fourier Transform of $\hat{A}[n_x, n_y]$ (which can be computed by standard Fast-Fourier Transform techniques)

$$f_{\hat{A}}[k_x, k_y] = \sum_{n_x}\sum_{n_y} \hat{A}[n_x, n_y] e^{-j\left[k_x \Delta_{k_x} \Delta_x n_x + k_y \Delta_{k_y} \Delta_y n_y\right]} . \tag{5.69}$$

Recall that we can compute the gradients of the L_1 cost function by the following Fourier transforms of the discrete space-time multi-dimensional signals $\tilde{f}[k_x, k_y, n, k]$, $\tilde{f}_{\dot{x}_{RB}}[k_x, k_y, n, k]$, and $\tilde{f}_{\dot{y}_{RB}}[k_x, k_y, n, k]$

$$\left[\frac{\partial J(\hat{\mathbf{A}}, \hat{\mathbf{v}})}{\partial \mathbf{A}}\right]^H_{n_x n_y} = -\sum_{k_x}\sum_{k_y}\sum_k \sum_n \tilde{f}[k_x, k_y, n, k] e^{-j\left[k_x \Delta_{k_x} \Delta_x n_x + k_y \Delta_{k_y} \Delta_y n_y\right]} \tag{5.70}$$

$$\Re\left[\frac{\partial J(\hat{\mathbf{A}}, \hat{\mathbf{v}})}{\partial \dot{x}_{RB}}\right] \quad = -2\Re\left[\sum_{n_x}\sum_{n_y}\hat{A}^*[n_x, n_y]\right.$$

$$\left.\times \sum_{k_x}\sum_{k_y}\sum_k\sum_n \tilde{f}_{\dot{x}_{RB}}[k_x, k_y, n, k]e^{-j\left[k_x\Delta_{k_x}\Delta_x n_x + k_y\Delta_{k_y}\Delta_y n_y\right]}\right] \quad (5.71)$$

$$\Re\left[\frac{\partial J(\hat{\mathbf{A}}, \hat{\mathbf{v}})}{\partial \dot{y}_{RB}}\right] \quad = -2\Re\left[\sum_{n_x}\sum_{n_y}\hat{A}^*[n_x, n_y]\right.$$

$$\left.\times \sum_{k_x}\sum_{k_y}\sum_k\sum_n \tilde{f}_{\dot{y}_{RB}}[k_x, k_y, n, k]e^{-j\left[k_x\Delta_{k_x}\Delta_x n_x + k_y\Delta_{k_y}\Delta_y n_y\right]}\right] \quad .(5.72)$$

For the purely-translational case, these signals are given by the following (simplified) expressions

$$\tilde{f}[k_x, k_y, n, k] = \tilde{f}[n, k]e^{-j\left[\phi_{\dot{x}}[n,k]\hat{\dot{x}}_{RB} + \phi_y[n,k]\hat{\dot{y}}_{RB}\right]}\delta\left[k_x - \frac{\phi_x[n,k]}{\Delta_{k_x}}, k_y - \frac{\phi_y[n,k]}{\Delta_{k_y}}\right] \quad (5.73)$$

$$\tilde{f}_{\dot{x}_{RB}}[k_x, k_y, n, k] \quad = \tilde{f}[n, k]\left(-j\phi_{\dot{x}}[n, k]\right)$$

$$\times e^{-j\left[\phi_{\dot{x}}[n,k]\hat{\dot{x}}_{RB} + \phi_y[n,k]\hat{\dot{y}}_{RB}\right]}\delta\left[k_x - \frac{\phi_x[n,k]}{\Delta_{k_x}}, k_y - \frac{\phi_y[n,k]}{\Delta_{k_y}}\right] \quad (5.74)$$

$$\tilde{f}_{\dot{y}_{RB}}[k_x, k_y, n, k] \quad = \tilde{f}[n, k]\left(-j\phi_{\dot{y}}[n, k]\right)$$

$$\times e^{-j\left[\phi_{\dot{x}}[n,k]\hat{\dot{x}}_{RB} + \phi_{\dot{y}}[n,k]\hat{\dot{y}}_{RB}\right]}\delta\left[k_x - \frac{\phi_x[n,k]}{\Delta_{k_x}}, k_y - \frac{\phi_y[n,k]}{\Delta_{k_y}}\right] \quad .$$

$$(5.75)$$

In a similar fashion to the previous rigid-body L_1 processing algorithm (which included rotation), we see that this part of the implementation scheme performs a set of discrete Fourier Transforms (which can be computed by standard Fast-Fourier Transform techniques) upon phase-compensated versions of the SAR data which have been "remapped" according to the phase-relations $\phi_x[n, k]$ and $\phi_y[n, k]$. This is essentially equivalent to the standard Polar-Format Resampling algorithm presented in Chapter 3.

The approximate azimuth resolution of the purely-translational algorithm is identical to the full rigid-body case

$$\delta_x = \frac{\lambda_c}{2\left(\dot{\theta} + \dot{\psi}_{RB}\right)T} . \quad (5.76)$$

We see that the azimuth resolution is still directly dependent upon the target's (actual) rotation rate (even if the algorithm assumes that the target is not rotating). If the target is actually rotating, we cannot rescale the resulting SAR image in azimuth (since the purely-translational algorithm does not generate an estimate of the rotation rate $\dot{\psi}_{RB}$). However, we can still compensate for the range-velocity induced azimuth-displacement, since the algorithm does estimate the range-velocity $\dot{y}_{RB}$.

5.3   Experimental Results

Here, we present some examples of the motion-compensated imaging capabilities of both
the full rigid-body L_1-norm based algorithm (presented in Section 5.1) and the purely-
translational rigid-body L_1-norm based algorithm (presented in Section 5.2). In Section
5.3.1, we present some examples where we have a "synthetic" moving target (composed of
a 2-D array of ideal point scatterers) embedded in an actual stationary-clutter conventional
SAR image. In Section 5.3.2, we present some examples where we manually segmented the
conventional SAR image of an actual stationary target into a target portion and a clutter
portion, and used the target portion to generate a synthetic-motion moving target. In
Section 5.3.3, we present a brief summary of the velocity-parameter estimation-performance
of these two algorithms.

From the synthetic-target experimental results of Chapter 4, we found that the imag-
ing performance of the matched-filter SAR processing algorithm presented in that chapter
begins to degrade for closely spaced target scatterers (specifically for a target scatterer
2-D array spacing of $0.75m$), even if they have identical velocities. This was true for the
synthetic-motion moving-target example presented in this chapter as well (where all the
scatterers had identical velocities). In order to show the clear utility of the rigid-body
algorithm for imaging closely-spaced scatterers, the synthetic-target experimental exam-
ples we present in this chapter have a *closer* scatterer 2-D array spacing of $0.5m$. For
comparison purposes, we also include in our synthetic-motion moving-target experiments a
purely-translational motion example identical to the synthetic-motion real-target example
in Chapter 4.

As with the experimental examples presented in Chapter 3 and Chapter 4, we assumed
that we were only given the conventional moving-target (complex) SAR images (in the
discrete $2-D$ form $A_{CONV}[n_x, n_y]$). These images were converted into "raw" demodulated
SAR data $\mathbf{f}$ by normalizing the images (by their respective maximum magnitude over n_x
and n_y , denoted by A_{MAX}) and performing a scaled Fourier Transform corresponding to
the "conventional" zero-velocity SAR model, i.e.,

$$\mathbf{f} = \frac{1}{A_{MAX}}\mathbf{F}\mathbf{A}_{CONV} . \tag{5.77}$$

Once we obtained a focused image from either of the L_1 SAR processing algorithms, we
then post-multiplied this image by A_{MAX}.

5.3.1   Synthetic Point-Scatterers Embedded in Real Clutter

In this section, we present a set of experimental examples where we have a synthetic moving-
target (consisting of a $2-D$ array of ideal point-scatterers) embedded in a real stationary
clutter scene. For comparison purposes, we used a clutter scene that was identical to
the clutter scene used for the synthetic-target matched-filter examples in Chapter 4. This
particular scene consisted mainly of trees and grass, as shown in the conventional SAR image
of Figure 5.2 (with an approximate resolution in range and azimuth of of $\delta_y = 0.25m$ and
$\delta_x = 0.25m$). In addition, the clutter scene had two man-made high-amplitude scatterers
with a magnitude of about $35dB$.

We generated the SAR data for these examples by first performing a scaled Fourier Transform (corresponding to the conventional zero-velocity SAR model) upon the conventional SAR image of the clutter scene. This transformed data was then added to the SAR data corresponding to the synthetic target (which as stated earlier, consisted of a $2-D$ array of moving ideal point scatterers). As with the matched-filter experimental results presented in Chapter 4, the synthetic-target portion of the SAR data sets was generated using the general-motion estimation-theoretic SAR data model presented in Chapter 2, with parameters chosen to be as similar as possible to the 33.5 GHz Lincoln Laboratory Advanced Detection and Tracking System (ADTS)[16] system operating in spotlight mode (as shown in Table 5.1 for the synthetic target).

For all of the synthetic-target examples presented here, the $2-D$ target-scatterer array consisted of nine synthetic moving point-scatterers, just as with the synthetic-data examples presented in Chapter 4. The initial positions of these scatterers were centered near the two "man-made" high-amplitude scatterers in the following configuration about the point $(x, y) = (-6.5m, -4m)$:

Scatterer #0: $(n_x \Delta_x, n_y \Delta_y) = (-6.5m, -4m)$

Scatterer #1: $(n_x \Delta_x, n_y \Delta_y) = (-7m, -4.5m)$

Scatterer #2: $(n_x \Delta_x, n_y \Delta_y) = (-7m, -4m)$

Scatterer #3: $(n_x \Delta_x, n_y \Delta_y) = (-7m, -3.5m)$

Scatterer #4: $(n_x \Delta_x, n_y \Delta_y) = (-6m, -4.5m)$

Scatterer #5: $(n_x \Delta_x, n_y \Delta_y) = (-6m, -4m)$

Scatterer #6: $(n_x \Delta_x, n_y \Delta_y) = (-6m, -3.5m)$

Scatterer #7: $(n_x \Delta_x, n_y \Delta_y) = (-6.5m, -4.5m)$

Scatterer #8: $(n_x \Delta_x, n_y \Delta_y) = (-6.5m, -3.5m)$

We see that the synthetic-target array for this examples had a spatial spacing of $0.5m$ with respect to both range and azimuth, which as stated previously, was *closer* than the closest-spacing example of $0.75m$ for the synthetic-target experiments presented in Chapter 4.

For comparison purposes, we show in Figure 5.3 and Figure 5.4 the conventional SAR images of these synthetic point-scatterers for the case where we have *zero velocity* (after we embedded these scatterers in the real clutter SAR image). A cross-section of the zero-velocity conventional SAR image (at $y = -4m$) is shown in Figure 5.5 (corresponding to synthetic-target scatterers #'s 0, 2, and 5). We see that these scatterers have a "relative" mainlobe peak (which correspond to the depth of the "nulls" between the scatterers) of about $15dB$.

F_c	Center Frequency	33.5 GHz
λ_c	Center Wavelength	0.009 m
αT_p	Chirp Bandwidth	1.2 GHz
f_{PRF}	Pulse Repetition Frequency	512 pulse/s
N	Complex Samples per Range Profile	512
$2K$	Pulses per Synthetic Aperture	512
R_o	Center Slant-Range	2778 M
v	SAR Platform Velocity	100 m/s
θ	Look-Angle Rotation Rate	0.036 rad/s
$2T$	Dwell Time	1.0 s
L	Synthetic-Aperture Length	100 m
Δ_y	Range Sampling Interval	0.125 m
Δ_x	Azimuth Sampling Interval	0.125 m
δ_y	Range Resolution	0.25 m
δ_x	Azimuth Resolution	0.25 m

Table 5.1: System Parameters for Synthetic-Target L_1 SAR Processing Examples

First Example: Purely Translational Motion

For the first synthetic-target example, all of the nine moving point-scatterers in the 2-D synthetic-target array had a velocity of $(\dot{x}_{RB}, \dot{y}_{RB}) = (2m/s, 2.304m/s)$. In order to illustrate the performance of the range-velocity induced azimuth-displacement compensation portion of the L_1 SAR processing algorithm, we chose the range velocity $\dot{y}_{RB}$ such the synthetic-target scatterers "wrapped around" to their actual position in the SAR image. This was done for all of the experimental examples presented in this chapter. Each of these scatterers had an amplitude of $40dB$, which was slightly greater than the amplitude of the man-made scatterers in the clutter image. The conventional SAR images of these moving synthetic point-scatterers after being embedded in the background-clutter SAR image are shown in Figure 5.6 and Figure 5.7. A cross-section of the conventional SAR image (at $y = -4m$) is shown in Figure 5.8 (corresponding to synthetic-target scatterers #'s 0, 2, and 5). We see that the image of the moving point-scatterers has degraded to an unacceptable level for the purposes of automatic-target recognition.

For the full rigid-body L_1-norm SAR processing algorithm, we used an L_1 weighting of $\gamma_A = 1$ for the velocity-parameter estimation. The 2-D target scatterer array was assumed to be over a rectangular spatial region centered at $(x, y) = (-6.5m, -4m)$, with an azimuth width of $8m$ and a range width of $4m$.

The results of the full rigid-body L_1-norm SAR processing algorithm are shown in Figures 5.9 through 5.15. For this example, we obtained estimates of $(\hat{\dot{x}}_{RB}, \hat{\dot{y}}_{RB}, \hat{\dot{\psi}}_{RB}) = (1.75m/s, 2.28m/s, -0.0023rad/s)$. As shown in the image of Figure 5.11, the SAR image of the moving-target scatterers is greatly improved, as compared to the conventional SAR image shown in Figure 5.7. However, we still see a slight blurring caused by the azimuthal-velocity estimation error. In the azimuth cross-section plot in Figure 5.12, the three target scatterers 0, 2, and 5, are focused and distinct, with a relative mainlobe peak of about $12dB$. This is comparable to the results shown in Figure 5.5 for the cross-section

of the conventional SAR image of the *zero-velocity* scatterers . Since the algorithm assumes a rigid-body velocity model over the rectangular target spatial-region, we see in Figure 5.11 that the two stationary man-made clutter scatterers are blurred out, unlike the corresponding synthetic-target results for the matched-filter presented in Chapter 4 (since the matched-filter algorithm allows the scatterer velocities within the target spatial-region to be independent from scatterer to scatterer).

The results from the purely-translational algorithm are shown in Figures 5.16 through 5.22. The assumed target spatial-region was identical to the rectangular assumed target spatial region of the full-rigid body algorithm (with an azimuth width of $8m$ and a range width of $4m$, centered at $(x, y) = (-6.5m, -4m)$). We used an L_1 weighting of $\gamma_A = 0.8$ for the velocity-parameter estimation.

For this example, we obtained velocity estimates of $(\hat{\dot{x}}_{RB}, \hat{\dot{y}}_{RB}) = (1.86m/s, 2.40m/s)$. We see that the purely-translational algorithm has a slightly smaller azimuthal-velocity estimation error, as compared to the full rigid-body algorithm (but a slightly larger range-velocity estimation error). The moving scatterers in the resulting SAR image of Figure 5.18 are slightly more focused in azimuth than the moving scatterers in the resulting SAR image generated by the full rigid-body algorithm in Figure 5.11. This due to the smaller azimuthal-velocity estimation error. In the azimuth cross-section plot shown in Figure 5.19, we see that the three target scatterers are focused and distinct. We also see that the smaller azimuthal-velocity estimation-error gives us a slightly higher relative mainlobe peak of about $15dB$, just like the full rigid-body algorithm. These results are also comparable to the results shown in the cross-section of the conventional SAR image of the zero-velocity scatterers in Figure 5.5.

Recall from Section 5.1.3 that the range-velocity induced azimuth displacement is proportional to the target's range-velocity divided by the SAR's look-angle rotation rate. Also recall from this section that the corresponding azimuth-displacement compensation is similarly proportional to the *estimated* range-velocity divided by the SAR's look-angle rotation rate, as given by Equation 5.49. This implies that the resulting error in the target's azimuth displacement after the azimuth-displacement compensation will be proportional to the range-velocity estimation-error divided by the SAR's look-angle rotation rate. Because the purely-translational algorithm has a larger range-velocity estimation error for this example than the full rigid-body algorithm, it exhibits a correspondingly larger azimuth-displacement compensation-error (by about $2m$, as shown in the azimuth-compensated results of Figures 5.20 and 5.22, as compared to the full rigid-body azimuth-compensated results shown in Figures 5.13 and 5.15).
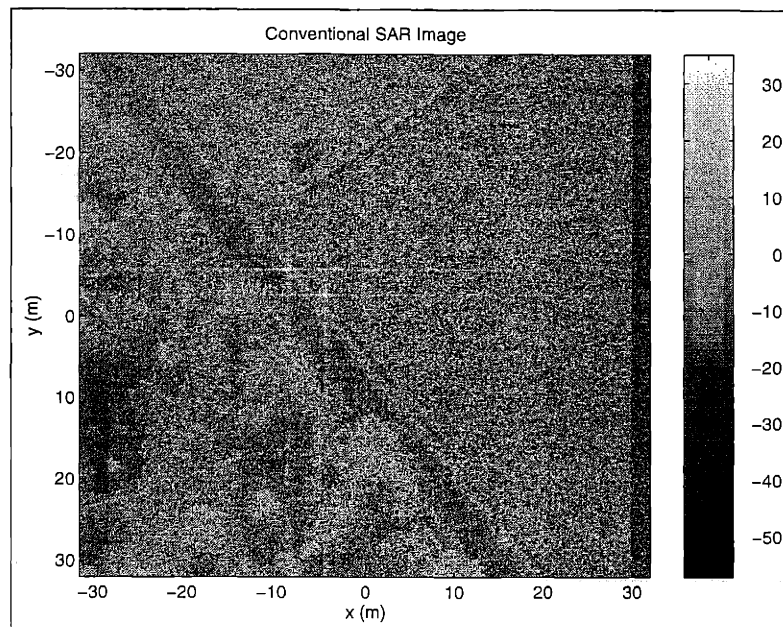
Figure 5.2: Conventional SAR Image of Stationary Clutter Scene used for Rigid-Body L_1 SAR-Processing Synthetic-Target Experimental Examples
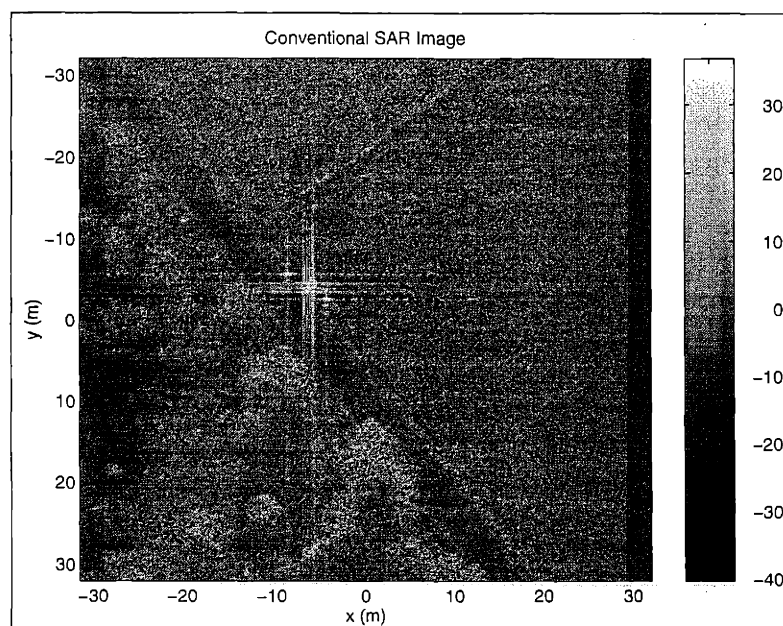
Figure 5.3: Conventional SAR Image of Synthetic Target with Zero Velocity

Figure 5.4: Target Region of Conventional SAR Image of Synthetic Target with Zero Velocity
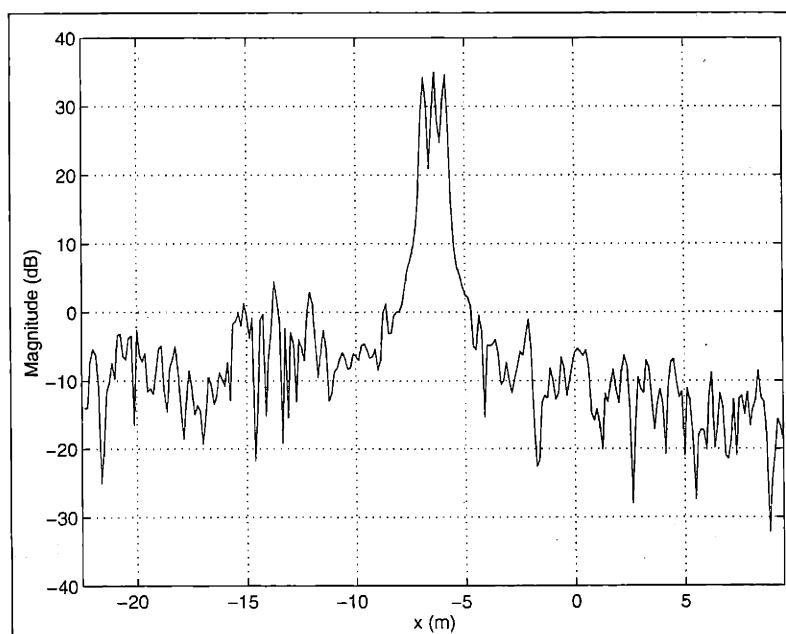
Figure 5.5: Cross-Section of Conventional SAR Image (at $y = -4m$) of Synthetic Target with Zero Velocity
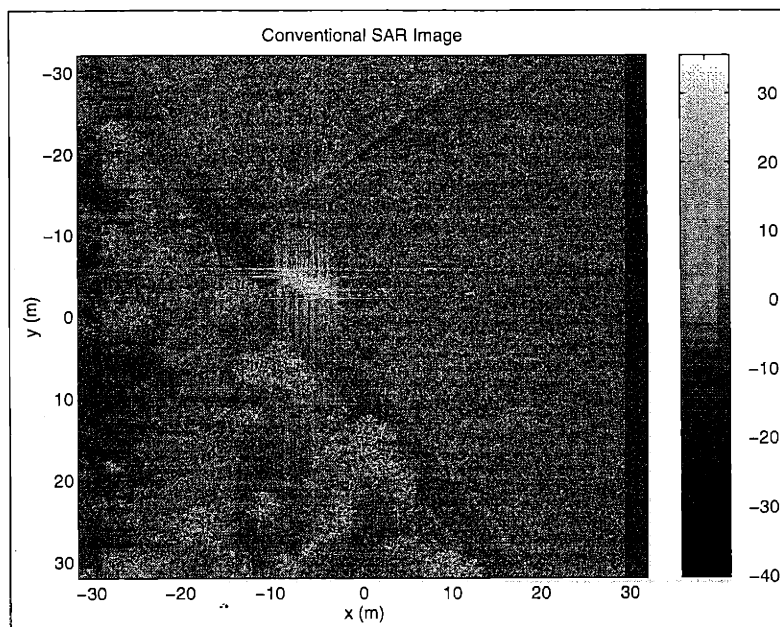
Figure 5.6: Conventional SAR Image for First Synthetic-Target Example
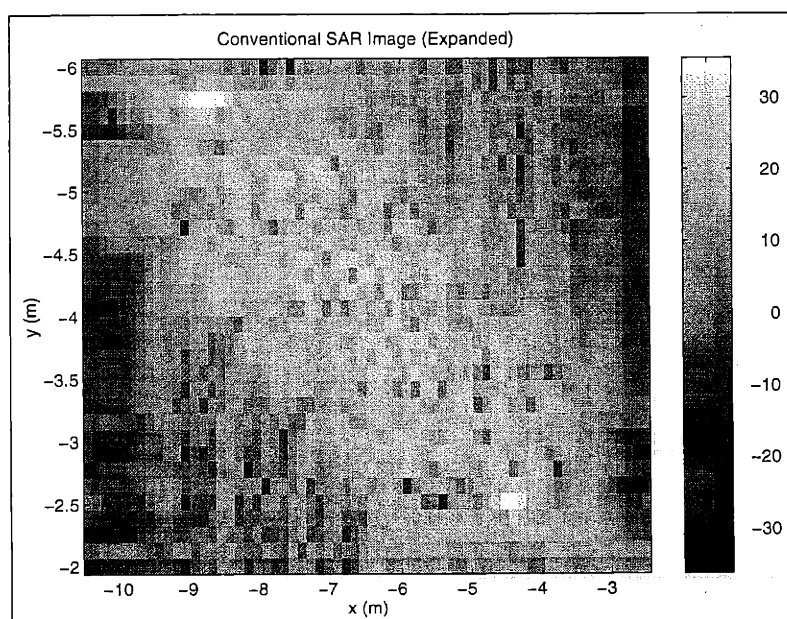
Figure 5.7: Target Region of Conventional SAR Image for First Synthetic-Target Example
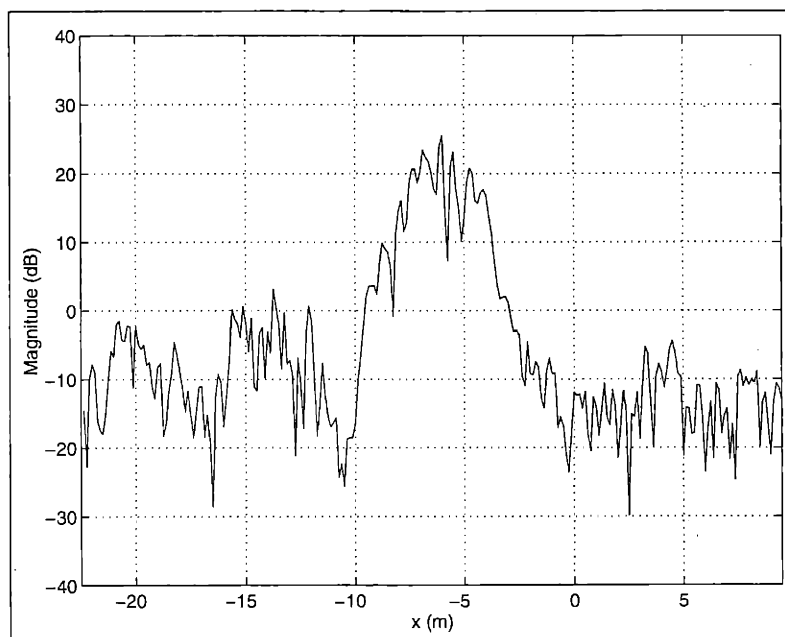
Figure 5.8: Cross-Section of Conventional SAR Image (at $y = -4m$) for First Synthetic-Target Example

Figure 5.9: Estimated Target-Velocity Parameters for First Synthetic-Target Example using Full Rigid-Body Processing Algorithm

Figure 5.10: L_1 SAR Image for First Synthetic-Target Example using Full Rigid-Body Processing Algorithm (Before Azimuth Rescaling and Azimuth-Displacement Compensation)

Figure 5.11: Target Region of L_1 SAR Image for First Synthetic-Target Example using Full Rigid-Body Processing Algorithm (Before Azimuth Rescaling and Azimuth-Displacement Compensation)

Figure 5.12: Cross-Section of L_1 SAR Image (at $y = -4m$) for First Synthetic-Target Example using Full Rigid-Body Processing Algorithm (Before Azimuth Rescaling and Azimuth-Displacement Compensation)

Figure 5.13: L_1 SAR Image for First Synthetic-Target Example using Full Rigid-Body Processing Algorithm (After Azimuth Rescaling and Azimuth-Displacement Compensation)

Figure 5.14: Target Region of L_1 SAR Image for First Synthetic-Target Example using Full Rigid-Body Processing Algorithm (After Azimuth Rescaling and Azimuth-Displacement Compensation)

Figure 5.15: Cross-Section of L_1 SAR Image (at $y = -4m$) for First Synthetic-Target Example using Full Rigid-Body Processing Algorithm (After Azimuth Rescaling and Azimuth-Displacement Compensation)

Figure 5.16: Estimated Target-Velocity Parameters for First Synthetic-Target Example using Purely-Translational Processing Algorithm
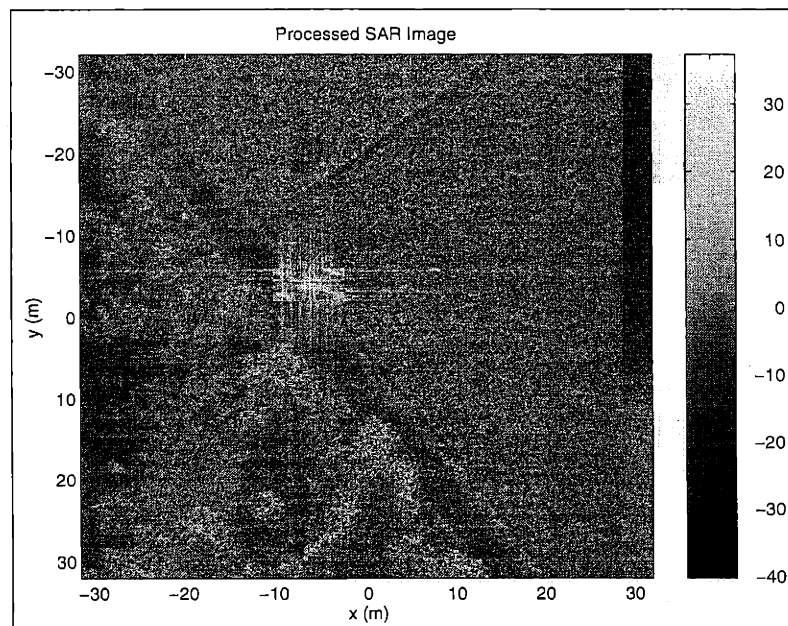
Figure 5.17: L_1 SAR Image for First Synthetic-Target Example using Purely-Translational Processing Algorithm (Before Azimuth-Displacement Compensation)

Figure 5.18: Target Region of L_1 SAR Image for First Synthetic-Target Example using Purely-Translational Processing Algorithm (Before Azimuth-Displacement Compensation)

Figure 5.19: Cross-Section of L_1 SAR Image (at $y = -4m$) for First Synthetic-Target Example using Purely-Translational Processing Algorithm (Before Azimuth-Displacement Compensation)
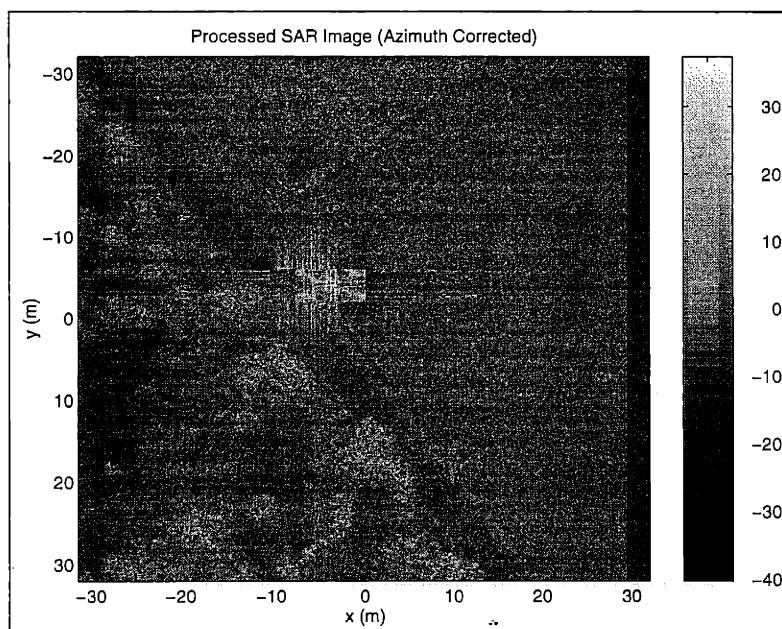
Figure 5.20: L_1 SAR Image for First Synthetic-Target Example using Purely-Translational Processing Algorithm (After Azimuth-Displacement Compensation)

Figure 5.21: Target Region of L_1 SAR Image for First Synthetic-Target Example using Purely-Translational Processing Algorithm (After Azimuth-Displacement Compensation)
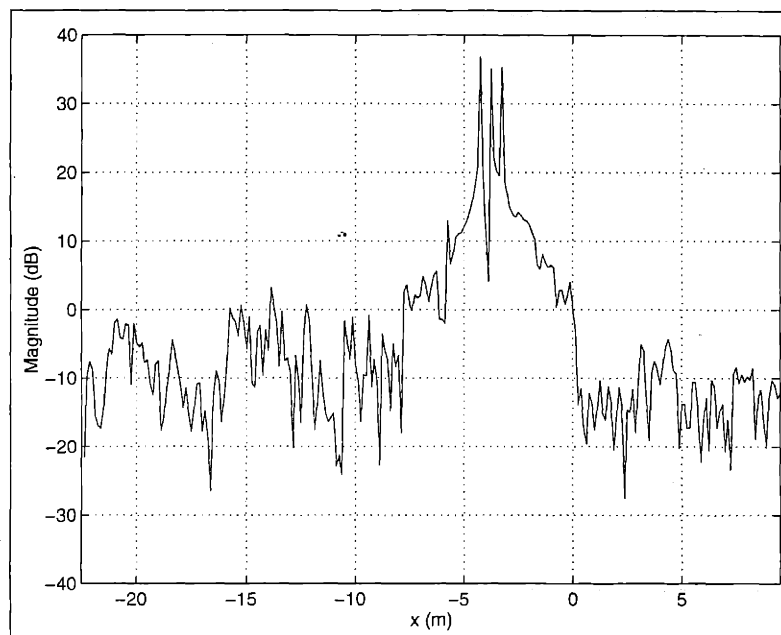
Figure 5.22: Cross-Section of L_1 SAR Image (at $y = -4m$) for First Synthetic-Target Example using Purely-Translational Processing Algorithm (After Azimuth-Displacement Compensation)

Second Example: Purely Translational Motion with Reduced Effective Signal-to-Clutter Ratio (SCR)

For our next synthetic-target example, we illustrate the effects of lowering the target's effective Signal-to-Clutter Ratio (SCR) (i.e., lowering the amplitudes of the moving synthetic-target scatterers, in relation to the amplitudes of the stationary clutter scatterers). Here, the moving-target scatterer amplitudes were reduced from $40dB$ to $34dB$, which was slightly less than the amplitudes of the two nearby man-made "bright" stationary scatterers in the background clutter image.

As with the first example, the synthetic-target consisted of a 2-D array of nine ideal point-scatterers (with a spatial spacing of $0.5m$ with respect to both range and azimuth) with initial positions centered around the point $(x, y) = (-6.5m, -4m)$, near the two "man-made" high-amplitude scatterers. We again gave the target a purely-translational velocity of $(\dot{x}_{RB}, \dot{y}_{RB}) = (2m/s, 2.304m/s)$.

For the sake of comparison, the L_1 weighting of $\gamma_A = 1$ used for the velocity-parameter estimation was identical to the L_1 weighting used for the first example. For the "first-trial" results of this algorithm, we used an assumed target spatial-region identical to the rectangular spatial region used by the full rigid-body algorithm for the first example, with an azimuth width of $8m$ and a range width of $4m$ (centered at $(x, y) = (-6.5m, -4m)$). Later in this example, we will present results generated by this algorithm where we reduced the range width of the assumed target region (in order to reduce the influence of the two bright man-made clutter scatterers).

The "first-trial" results obtained by the full rigid-body L_1-norm SAR processing algorithm are shown in Figures 5.26 through 5.29. For this example, we obtained velocity-parameter estimates of $(\hat{\dot{x}}_{RB}, \hat{\dot{y}}_{RB}, \hat{\dot{\psi}}_{RB}) = (-0.036m/s, 0.068m/s, -0.0001rad/s)$. Because of the reduced SCR, *the rigid-body algorithm now tries to focus the stationary clutter scatterers rather than the moving target* (though the clutter scatterers are still slightly blurred in range). From these first-trial results, we can conclude that the full rigid-body algorithm can only focus targets with a SCR greater than $0dB$, i.e., the target scatterers are "brighter" than the surrounding clutter scatterers.

The purely-translational algorithm used an L_1 weighting of $\gamma_A = 0.8$, which was identical to the weighting used by this algorithm for the first synthetic-target example. The "first-trial" target spatial-region was also identical, with an azimuth width of $8m$ and a range width of $4m$ (centered at $(x, y) = (-6.5m, -4m)$). Just as with the full rigid-body algorithm, we will later show results where we reduced the range width of this assumed target region.

The "first-trial" results generated by the purely-translational algorithm are shown in Figures 5.30 through 5.33. Here, we obtained velocity estimates of $(\hat{\dot{x}}_{RB}, \hat{\dot{y}}_{RB}) = (0.135m/s, 0.004m/s)$. In a similar fashion to the full rigid-body algorithm, this algorithm now tries to focus the stationary clutter scatterers rather than the synthetic moving target (due to the reduced SCR). In fact, we see from the SAR image of Figure 5.32 an improvement in the focusing of the clutter scatterers in comparison to the conventional SAR image of Figure 5.23. One explanation for this improvement is that fact that this algorithm estimates the velocity-parameters so as to minimize the L_1-norm of the SAR image (where a smaller L_1-norm implies a sharpening of the image focusing).

Next, we present results generated by the full rigid-body algorithm when we reduced the range width of the target spatial region from $4m$ to $2m$. The two bright man-made clutter scatterers *now lie outside of the assumed target region*, which sharply reduces their influence upon the performance of the SAR imaging algorithm. The azimuth width of this region was kept at $8m$, and the L_1 weighting was kept at $\gamma_A = 1$. Essentially, we *increased* the effective SCR of the target by reducing the mean amplitude of the clutter scatterers in the target spatial region.

The results generated by the full rigid-body L_1-norm SAR processing algorithm with the reduced target spatial-region are shown in Figures 5.34 through 5.37. For this example, we now obtained velocity-parameter estimates of $(\hat{\dot{x}}_{RB}, \hat{\dot{y}}_{RB}, \hat{\dot{\psi}}_{RB}) = (1.71m/s, 2.24m/s,$ $0.00002rad/s)$, which are *much improved* as compared to those obtained by this algorithm using the larger target spatial region. However, the velocity-parameter estimation-errors are slightly greater than the corresponding velocity-parameter estimation-errors of this algorithm for the first synthetic-target example (where we had both a higher SCR and a larger assumed target spatial-region). As shown in Figure 5.36, we see that the focusing of the moving-target scatterers is greatly improved, as compared to the "first-trial" full rigid-body L_1 SAR image shown in Figure 5.28 (where the algorithm tried to focus the two bright man-made clutter scatterers rather than the moving target). In the SAR image of Figure 5.35, the two bright man-made stationary clutter scatterers are essentially unchanged from the conventional SAR image of Figure 5.23 (since they now lie outside of the assumed target spatial region). In the azimuth cross-section plot of Figure 5.37, we see that the three target scatterers are focused and distinct, with a relative mainlobe peak of about $10dB$.

We also present results generated by the purely-translational algorithm (with a reduced target spatial region identical to the full rigid-body algorithm) in Figures 5.41 through 5.44. For this example, we kept the L_1 weighting at $\gamma_A = 0.8$.

From this example, we obtained velocity estimates of $(\hat{\dot{x}}_{RB}, \hat{\dot{y}}_{RB}) = (1.98m/s, 2.45m/s)$. Similarly to the reduced spatial-region results generated by the full rigid-body algorithm, these results are much improved as compared to the "first-trial" results generated by the purely-translational algorithm for this example (using the larger target spatial region). As shown in Figure 5.43, the focusing of the moving-target scatterers is greatly improved, as compared to the first-trial results in Figure 5.32. In the azimuth cross-section plot in Figure 5.44, the three target scatterers are focused and distinct, with a relative mainlobe peak of about $13dB$.

As compared to the estimation-performance of the full rigid-body algorithm with the reduced target spatial region, the purely-translational algorithm appears to have better azimuthal-velocity ($\dot{x}_{RB}$) estimation-performance, but worse range-velocity ($\dot{y}_{RB}$) estimation performance (which was exactly the case as with the previous synthetic-target example). Since we have essentially eliminated the influence of the two "bright" stationary scatterers (because of the reduced target spatial-region), one remaining explanation for these differences in the estimation-performance is the presence of the "extra" velocity-parameter $\dot{\psi}$ in the full rigid-body algorithm. This implies that the full rigid-body algorithm's L_1 cost function will have a somewhat different functional form than the purely-translational algorithm's L_1 cost function. Consequently, these two cost functions will not have the same local minima. Recall from Section 3.1.1 that the primary motivation for using the coordinate-descent line-minimization routine for the velocity-parameter estimation was to reduce the
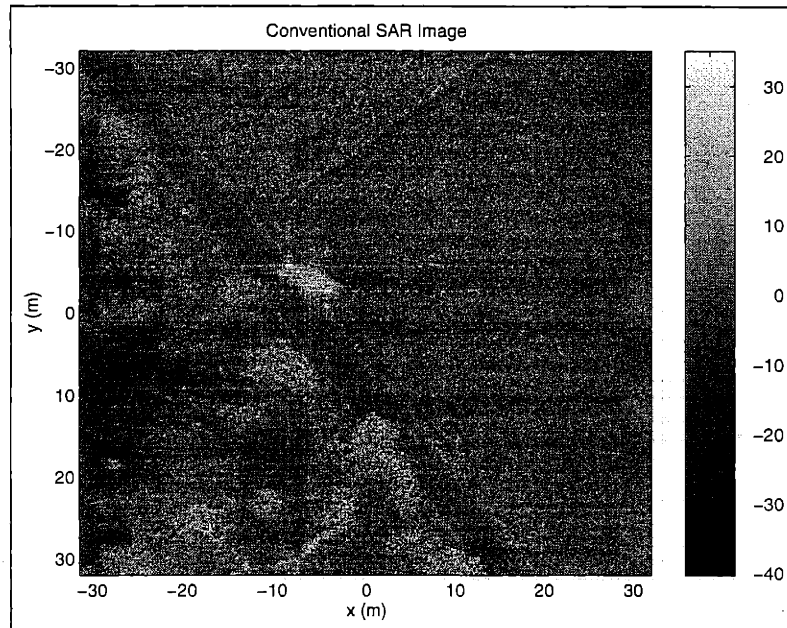
Figure 5.23: Conventional SAR Image for Second Synthetic-Target Example

sensitivity of the estimation-performance to local minima in the L_1 cost function. However, the parameter estimation-performance of the coordinate-descent line-minimization routine is still somewhat sensitive to local minima "near" the true global minimum of the L_1 cost function. As stated previously, the full rigid-body algorithm's L_1 cost function and the purely-translational algorithm's L_1 cost function will not have the same local minima. This ultimately implies that the respective coordinate-descent line-minimization routines of these two algorithms may converge to slightly different values of the translational-velocity parameters $(\hat{\dot{x}}_{RB}, \hat{\dot{y}}_{RB})$.

Recall from the previous discussion of the first synthetic-target example that the error in the azimuth-displacement after azimuth-displacement compensation is proportional to the range-velocity error. Therefore, we see a larger azimuth-displacement error after the azimuth-displacement compensation for the target scatterers in Figure 5.47, as compared to the corresponding results shown in Figure 5.40 generated by the full rigid-body algorithm with the reduced target spatial-region.
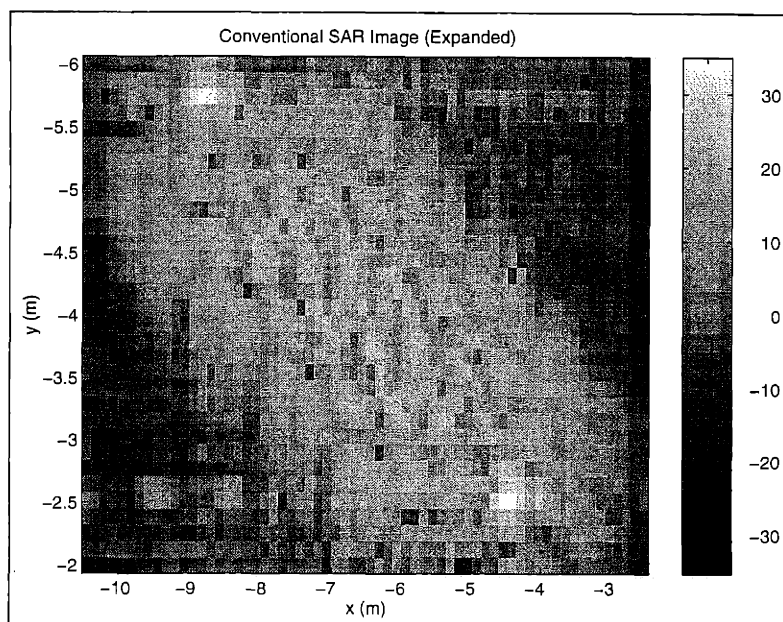
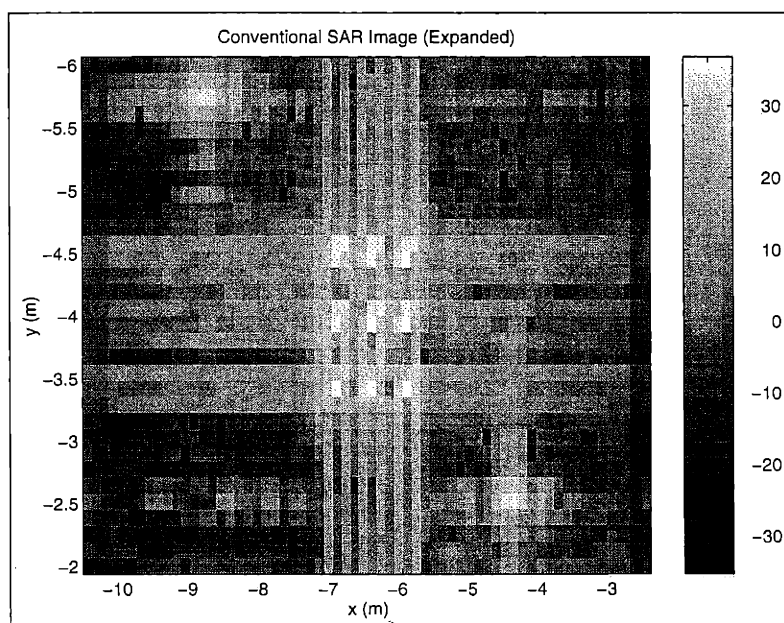Figure 5.24: Target Region of Conventional SAR Image for Second Synthetic-Target Example

Figure 5.25: Cross-Section of Conventional SAR Image (at $y = -4m$) for Second Synthetic-Target Example

Figure 5.26: Estimated Target-Velocity Parameters for Second Synthetic-Target Example using Full Rigid-Body Processing Algorithm

Figure 5.27: L_1 SAR Image for Second Synthetic-Target Example using Full Rigid-Body Processing Algorithm (Before Azimuth Rescaling and Azimuth-Displacement Compensation)
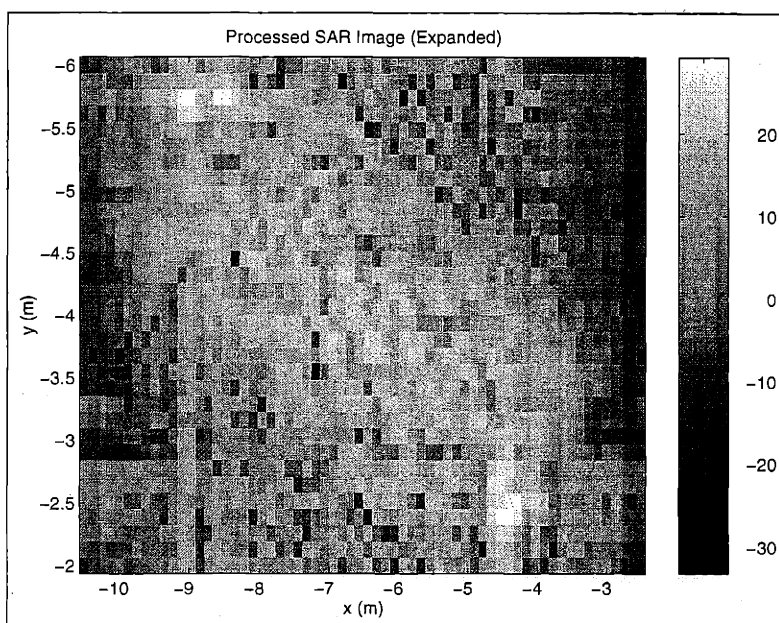
Figure 5.28: Target Region of L_1 SAR Image for Second Synthetic-Target Example using Full Rigid-Body Processing Algorithm (Before Azimuth Rescaling and Azimuth-Displacement Compensation)
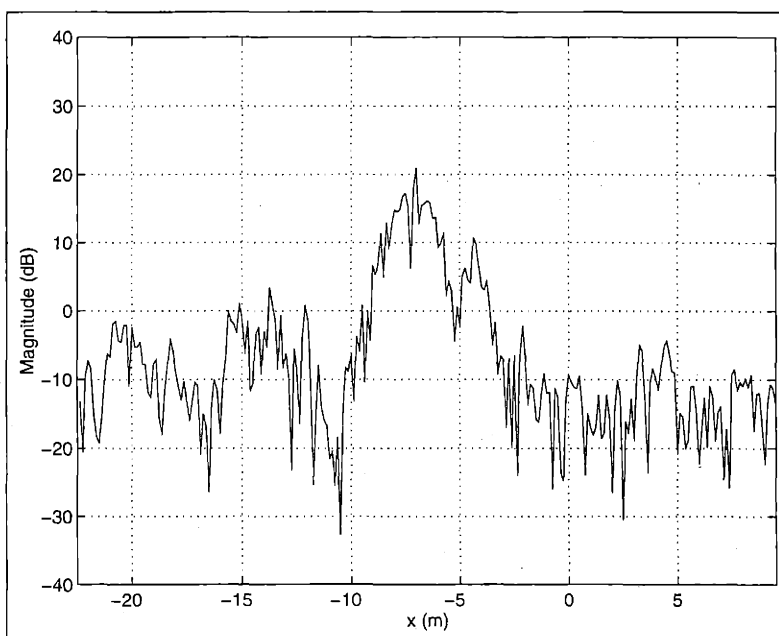
Figure 5.29: Cross-Section of L_1 SAR Image (at $y = -4m$) for Second Synthetic-Target Example using Full Rigid-Body Processing Algorithm (Before Azimuth Rescaling and Azimuth-Displacement Compensation)

Figure 5.30: Estimated Target-Velocity Parameters for Second Synthetic-Target Example using Purely-Translational Processing Algorithm
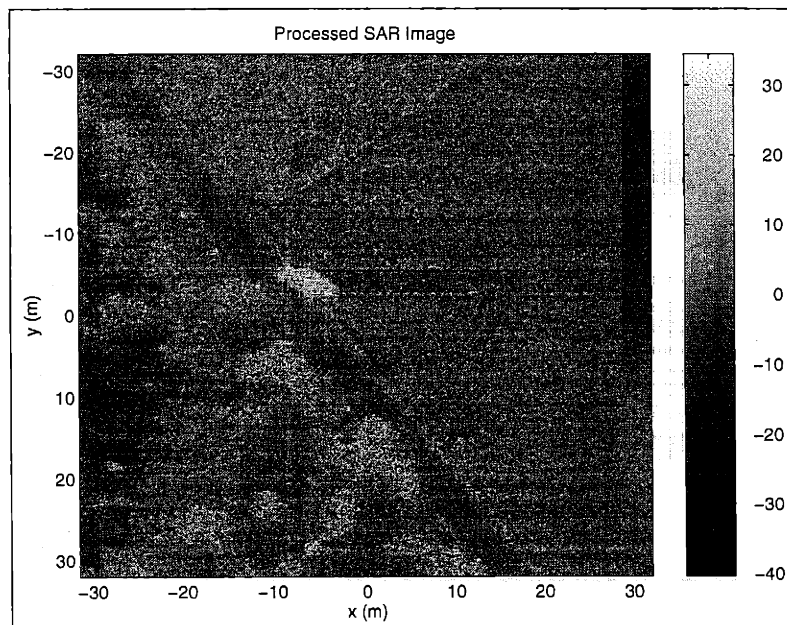
Figure 5.31: L_1 SAR Image for Second Synthetic-Target Example using Purely-Translational Processing Algorithm (Before Azimuth-Displacement Compensation)
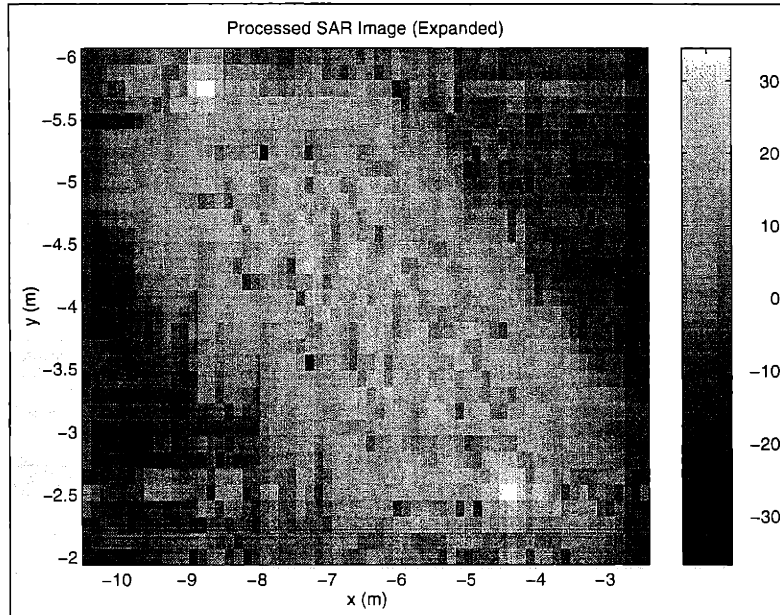
Figure 5.32: Target Region of L_1 SAR Image for Second Synthetic-Target Example using Purely-Translational Processing Algorithm (Before Azimuth-Displacement Compensation)
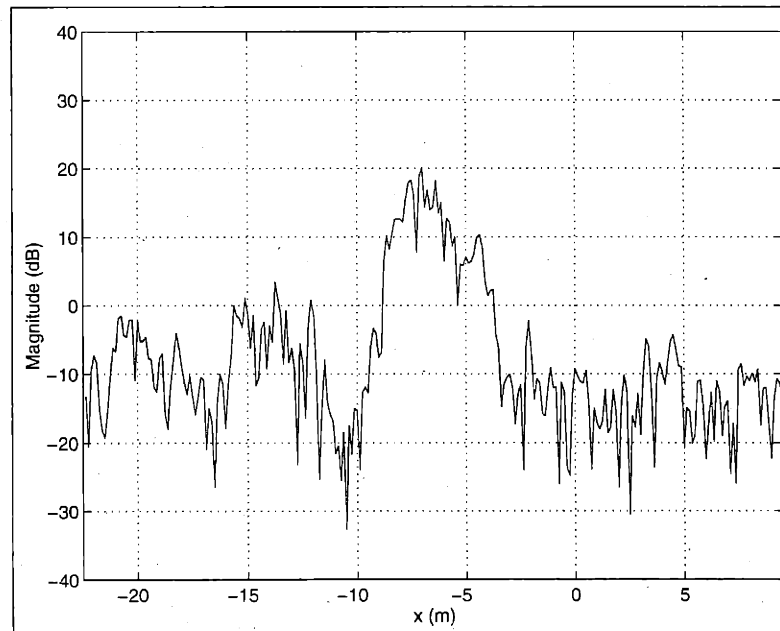
Figure 5.33: Cross-Section of L_1 SAR Image (at $y = -4m$) for Second Synthetic-Target Example using Purely-Translational Processing Algorithm (Before Azimuth-Displacement Compensation)
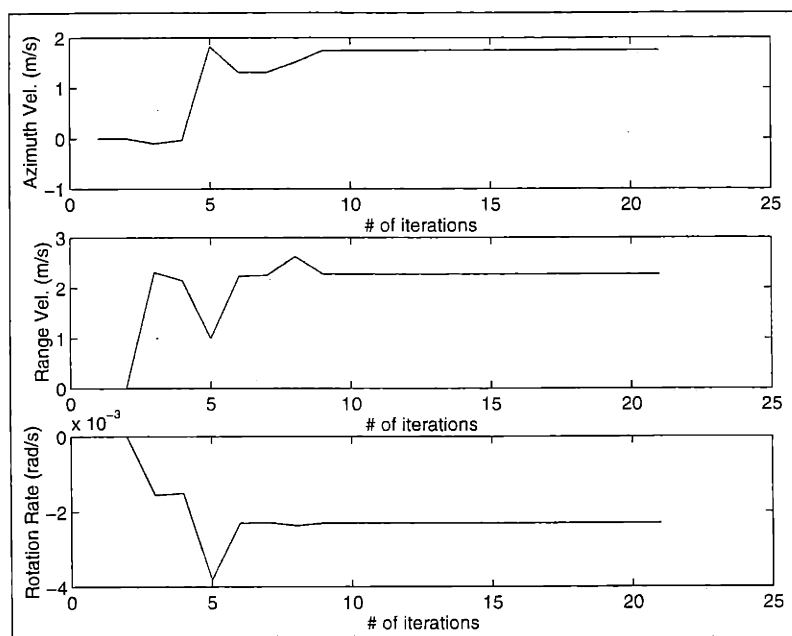
Figure 5.34: Estimated Target-Velocity Parameters for Second Synthetic-Target Example using Full Rigid-Body Processing Algorithm (with Reduced Target Spatial Region)
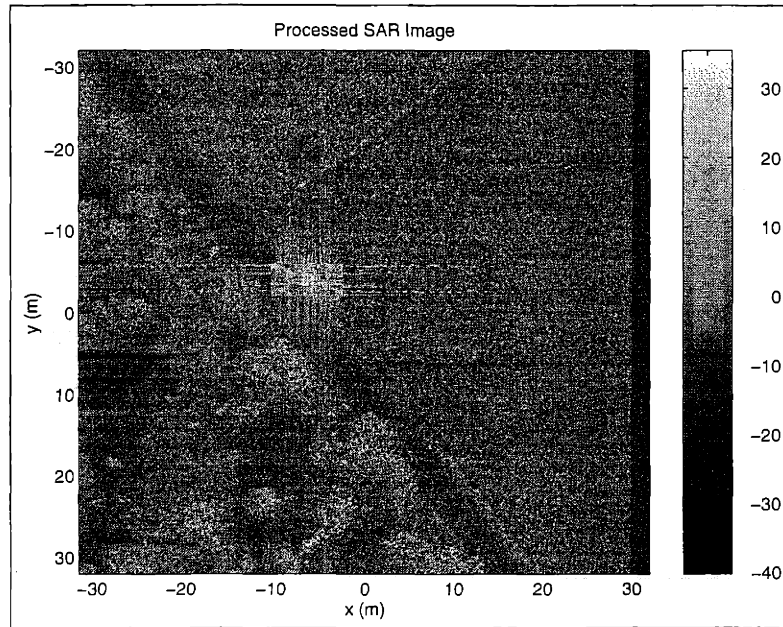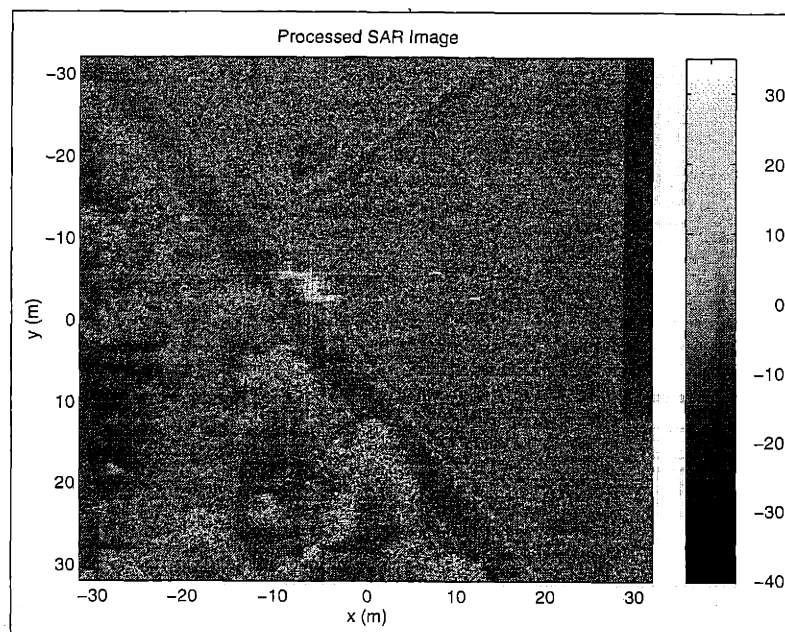

Figure 5.35: L_1 SAR Image for Second Synthetic-Target Example (with Reduced Target Spatial Region) using Full Rigid-Body Processing Algorithm (Before Azimuth Rescaling and Azimuth-Displacement Compensation)
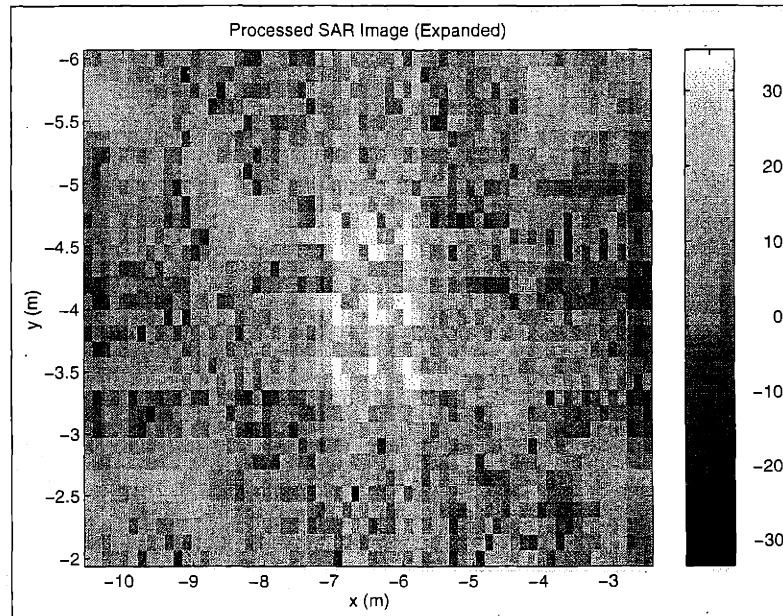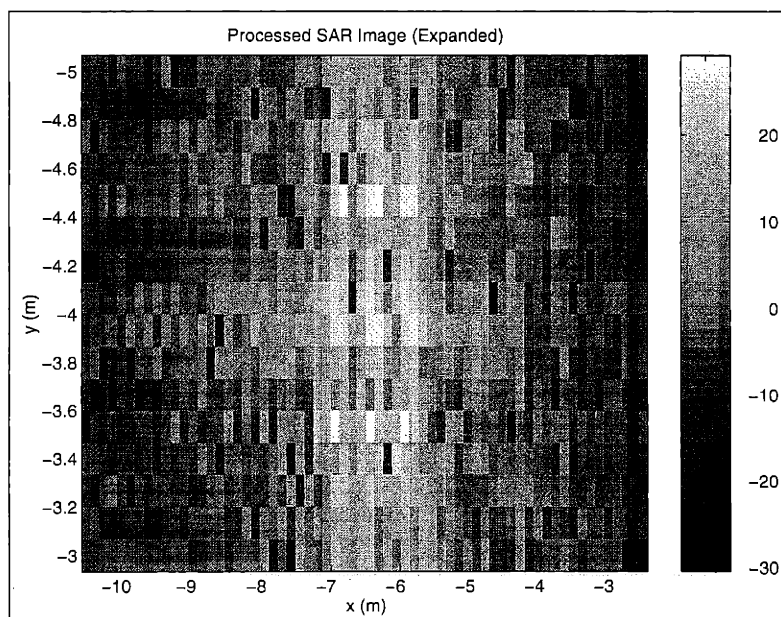
Figure 5.36: Target Region of L_1 SAR Image for Second Synthetic-Target Example (with Reduced Target Spatial Region) using Full Rigid-Body Processing Algorithm (Before Azimuth Rescaling and Azimuth-Displacement Compensation)
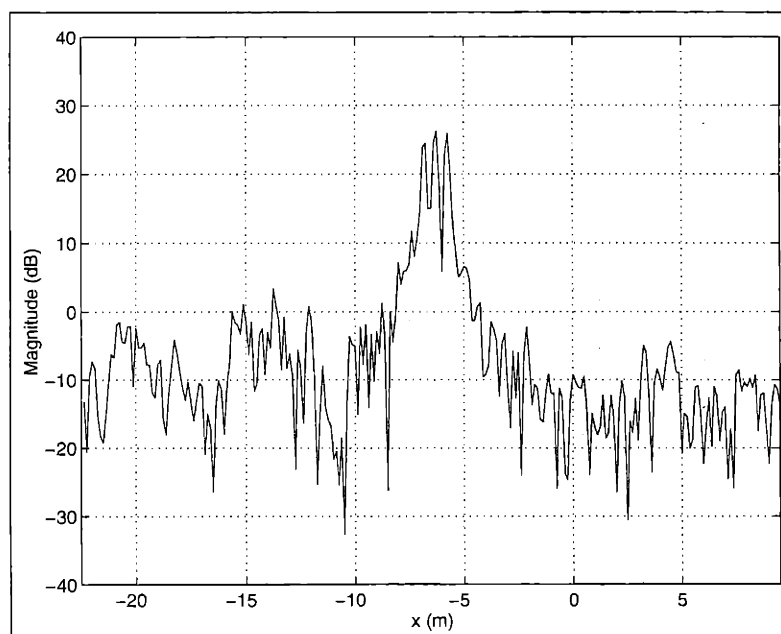
Figure 5.37: Cross-Section of L_1 SAR Image (at $y = -4m$) for Second Synthetic-Target Example (with Reduced Target Spatial Region) using Full Rigid-Body Processing Algorithm (Before Azimuth Rescaling and Azimuth-Displacement Compensation)
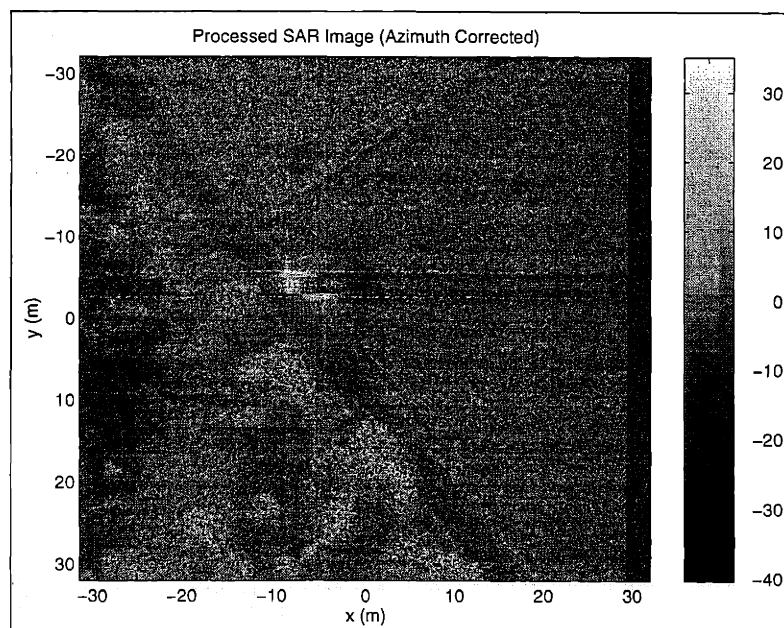
Figure 5.38: L_1 SAR Image (with Reduced Target Spatial Region) for Second Synthetic-Target Example using Full Rigid-Body Processing Algorithm (After Azimuth Rescaling and Azimuth-Displacement Compensation)
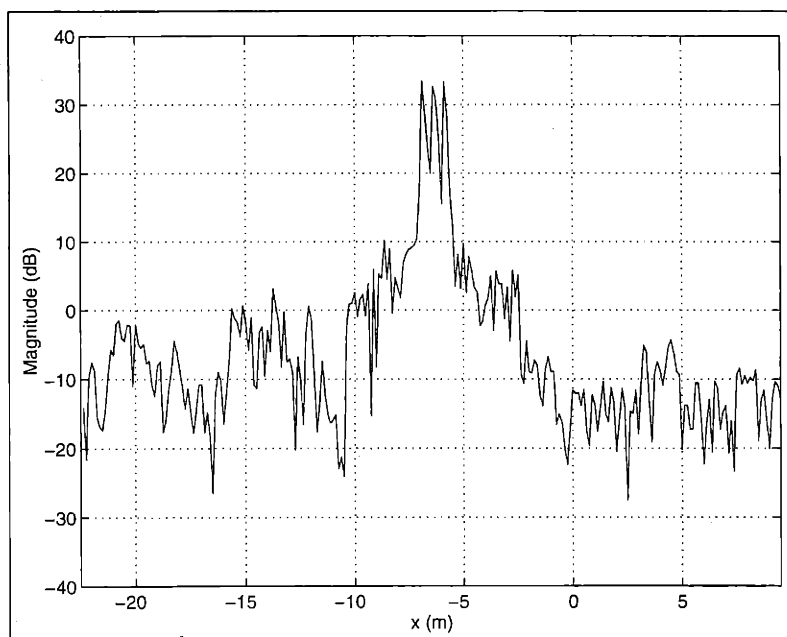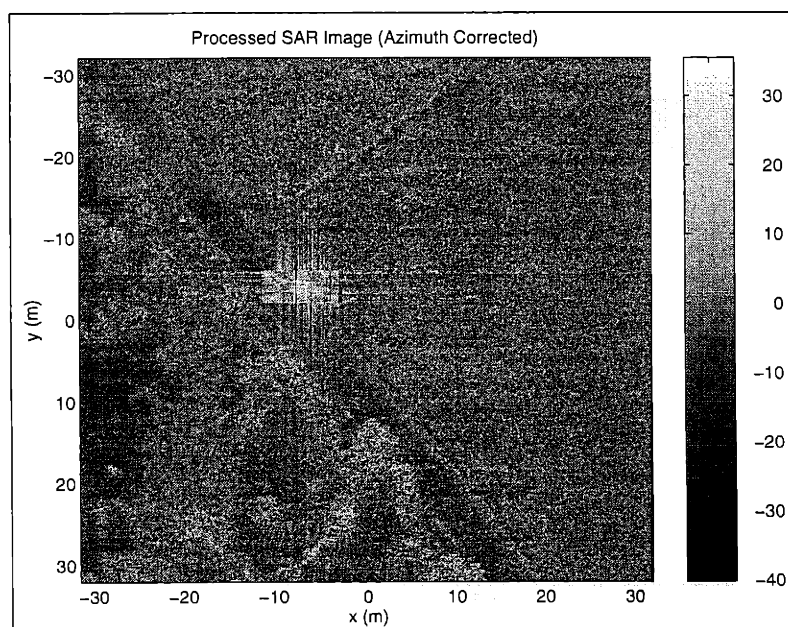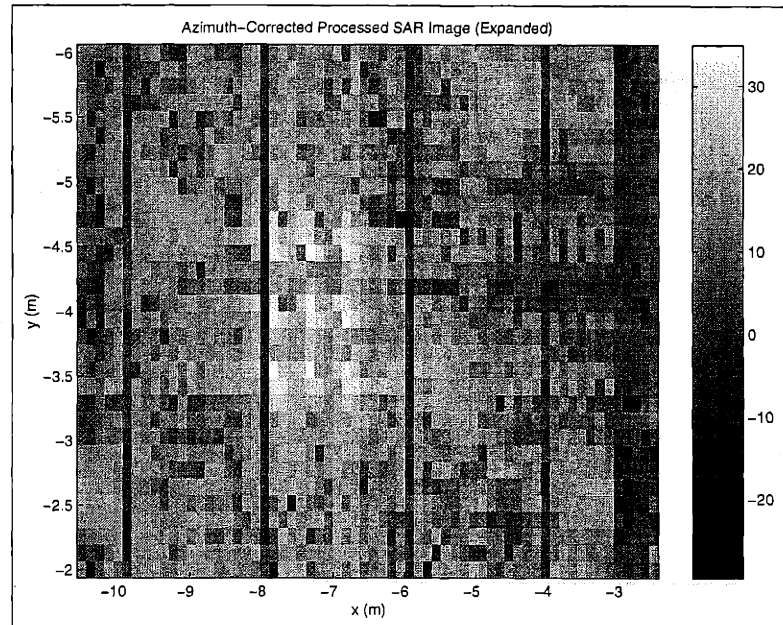

Figure 5.39: Target Region of L_1 SAR Image for Second Synthetic-Target Example (with Reduced Target Spatial Region) using Full Rigid-Body Processing Algorithm (After Azimuth Rescaling and Azimuth-Displacement Compensation)
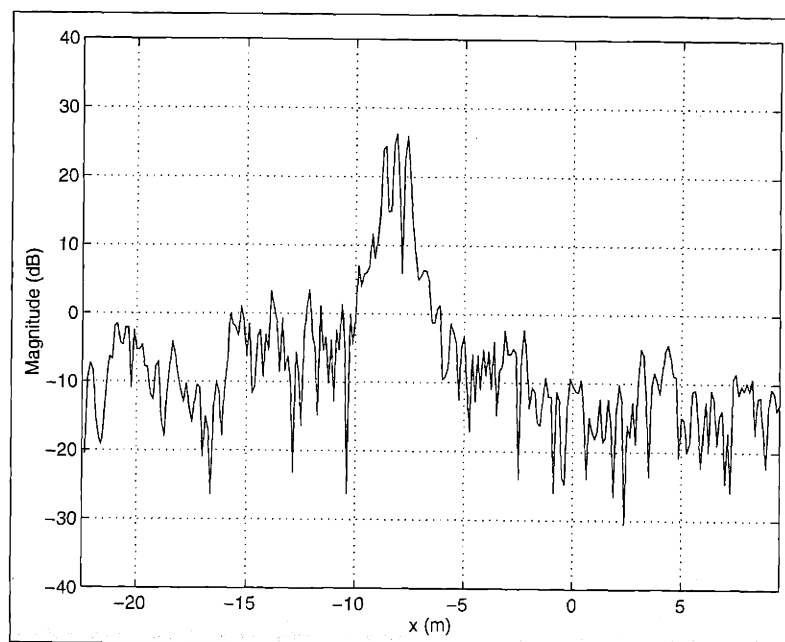
Figure 5.40: Cross-Section of L_1 SAR Image with Reduced Target Spatial Region (at $y = -4m$) for Second Synthetic-Target Example using Full Rigid-Body Processing Algorithm (After Azimuth Rescaling and Azimuth-Displacement Compensation)
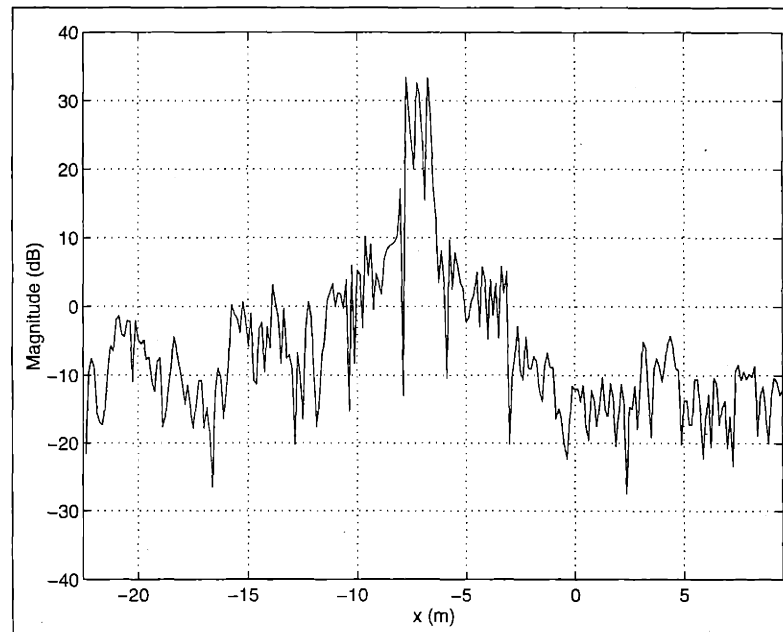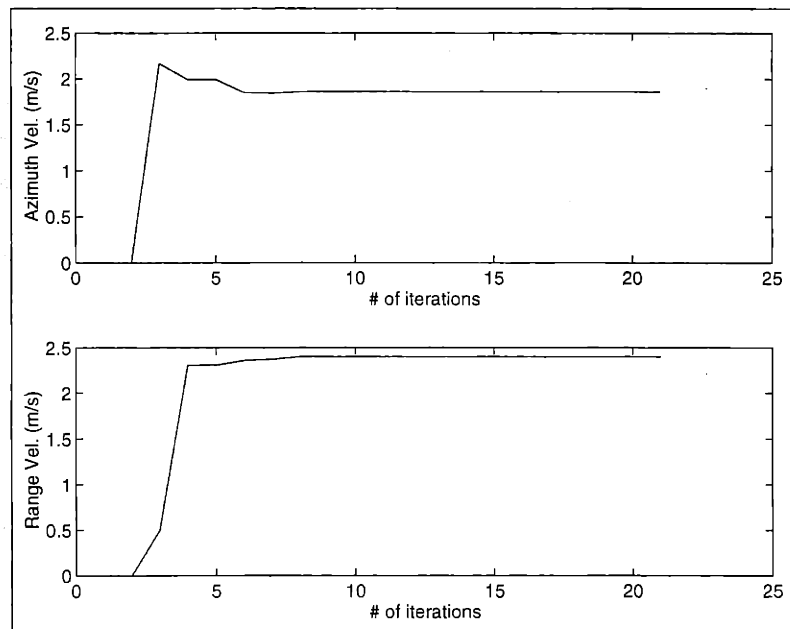

Figure 5.41: Estimated Target-Velocity Parameters for Second Synthetic-Target Example using Purely-Translational Processing Algorithm (with Reduced Target Spatial Region)
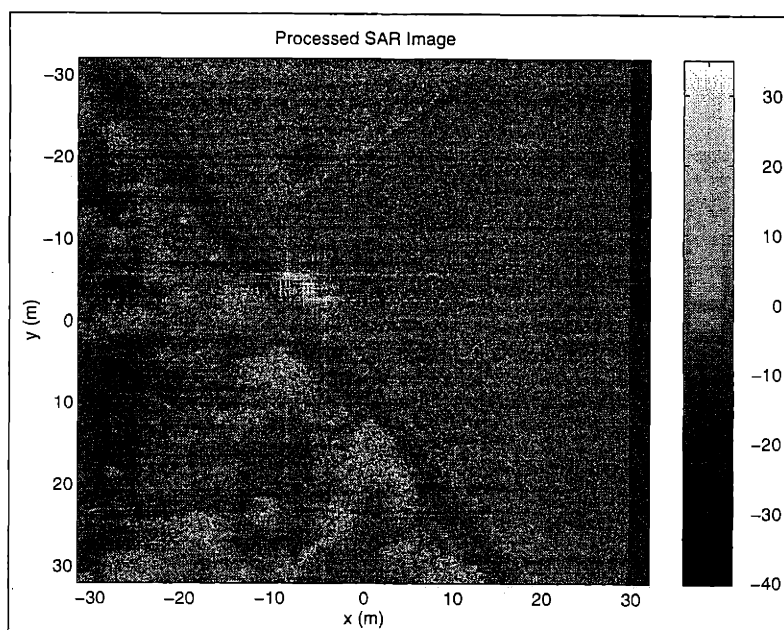
Figure 5.42: L_1 SAR Image for Second Synthetic-Target Example using Purely-Translational Processing Algorithm with Reduced Target Spatial Region (Before Azimuth-Displacement Compensation)
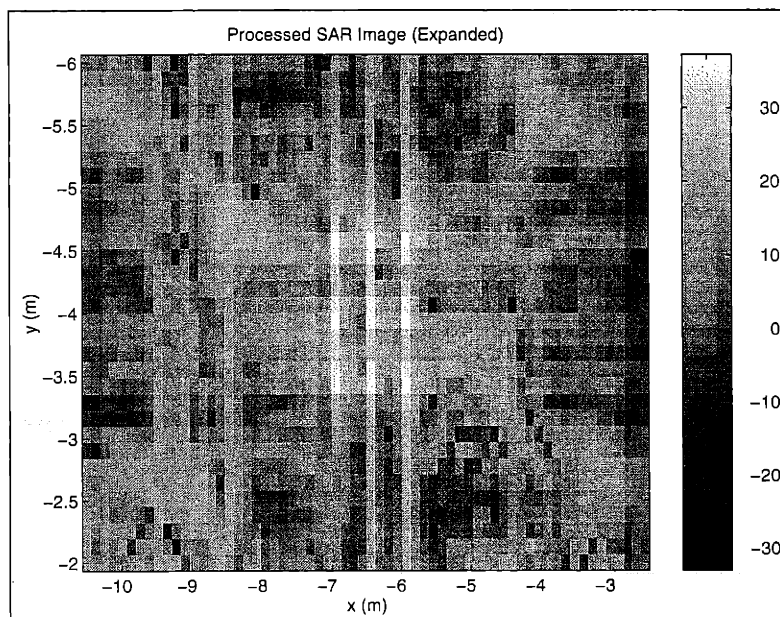

Figure 5.43: Target Region of L_1 SAR Image for Second Synthetic-Target Example using Purely-Translational Processing Algorithm with Reduced Target Spatial Region (Before Azimuth-Displacement Compensation)
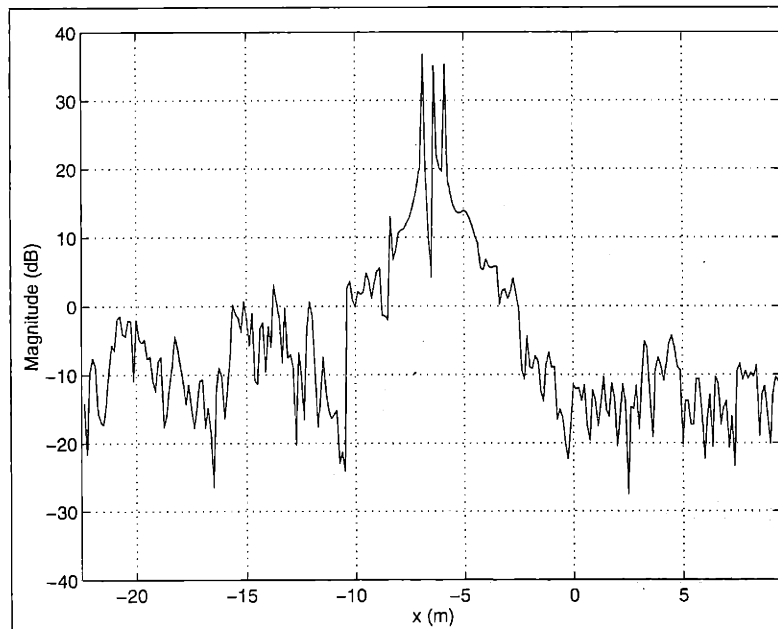
Figure 5.44: Cross-Section of L_1 SAR Image (at $y = -4m$) for Second Synthetic-Target Example using Purely-Translational Processing Algorithm with Reduced Target Spatial Region (Before Azimuth-Displacement Compensation)

Figure 5.45: L_1 SAR Image for Second Synthetic-Target Example (with Reduced Target Spatial Region) using Purely-Translational Processing Algorithm (After Azimuth-Displacement Compensation)

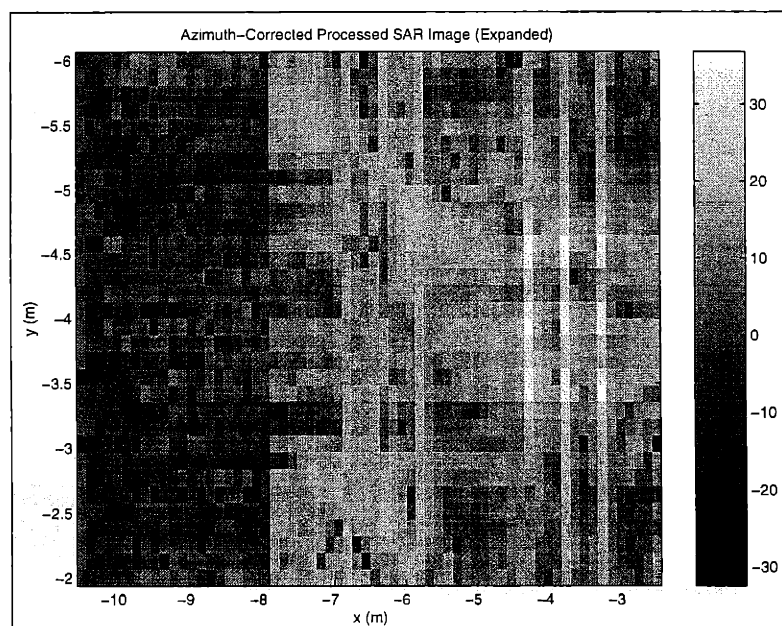Figure 5.46: Target Region of L_1 SAR Image for Second Synthetic-Target Example using Purely-Translational Processing Algorithm with Reduced Target Spatial Region (After Azimuth-Displacement Compensation)
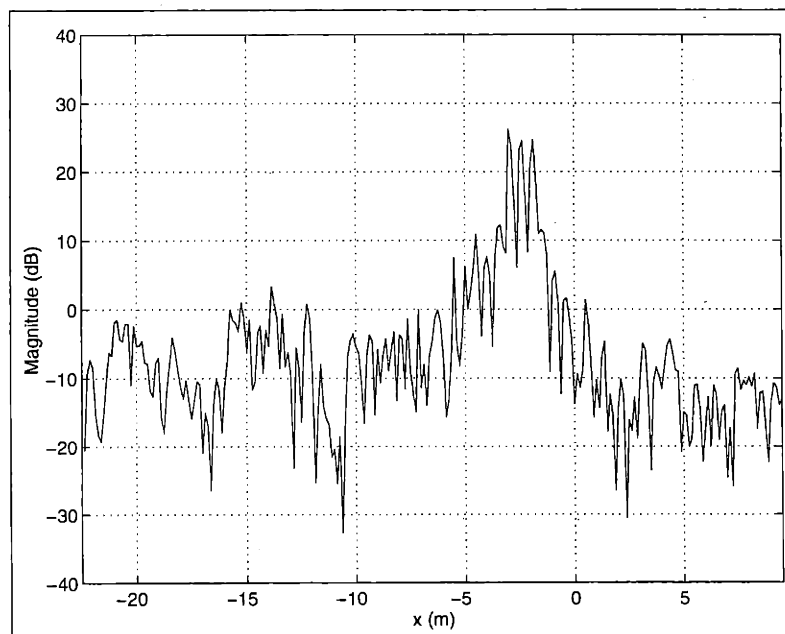
Figure 5.47: Cross-Section of L_1 SAR Image (at $y = -4m$) for Second Synthetic-Target Example (with Reduced Target Spatial Region) using Purely-Translational Processing Algorithm (After Azimuth-Displacement Compensation)

Third Example: Translational and Rotational Motion

For the next synthetic-target example, we illustrate some of the effects of rotational target motion upon the performance of both the full rigid-body L_1-norm SAR processing algorithm and the purely-translational L_1-norm SAR processing algorithm. As with the two previous purely-translational examples, we used as our synthetic target a 2-D array of nine synthetic moving point-scatterers with an amplitude of $40dB$. We gave the array of target scatterers a translational velocity of $(\dot{x}_{RB}, \dot{y}_{RB}) = (2m/s, 2.304m/s)$. But we also gave the synthetic target a positive rotational velocity of $\dot{\psi}_{RB} = 0.036rad/s$ about the point $(x, y) = (-6.5m, -4m)$. This rotation rate was equal to the SAR system's "look-angle" rotation rate of $\dot{\theta} = 0.036rad/s$. The conventional SAR image of the synthetic-target scatterers (after they are embedded in the background-clutter SAR image) is shown in Figure 5.48 (and in Figure 5.49). A cross-section of the conventional SAR image (at $y = -4m$) is shown in Figure 5.50. Just with the previous purely-translational motion examples, we see that the conventional image has degraded to a level unacceptable for most SAR ATR applications. In the image of Figure 5.48, we see a "spreading" of the target blur area with respect to azimuth, caused by the rotation-rate dependent azimuth scale factor $1 + \dot{\psi}_{RB}/\dot{\theta}$.

For the full rigid-body algorithm, we used an L_1 weighting of $\gamma_A = 0.95$ for the velocity-parameter estimation. We also assumed a target spatial-region (centered at $(x, y) = (-6.5m, -4m)$) identical to the target spatial-region used by this algorithm for the first synthetic-target example, with an azimuth width of $8m$ and a range width of $4m$. Note that the assumed target region included the two "bright" stationary man-made clutter scatterers. In spite of the azimuth spreading (due to the effects of the target's rotation), the target blur area was still contained within the boundaries of the assumed target spatial-region.

The results generated by the full rigid-body L_1-norm SAR processing algorithm are shown in Figure 5.51 through 5.57. For this rigid-body example, we obtained estimates of $(\hat{\dot{x}}_{RB}, \hat{\dot{y}}_{RB}, \hat{\dot{\psi}}_{RB}) = (1.85m/s, 2.40m/s, 0.025rad/s)$. As compared to the results generated by this algorithm for first synthetic-target example (using an identical target spatial region), we see a smaller error in the estimated azimuth velocity, but a larger error in both the estimated range velocity and the estimated rotation rate. One hypothesis for the differences in these errors is the interaction between the two bright stationary man-made clutter scatterers and the moving synthetic target scatterers. Later, we will test this hypothesis by reducing the range extent of the assumed target spatial region (such that the two "bright" stationary targets were excluded from this region, just as with the previous reduced-SCR purely-translational motion synthetic-target example).

In the "first-trial" L_1 SAR image of Figure 5.53, all of the target scatterers are focused and distinct, with a relative mainlobe height of about $13dB$. However, the stationary man-made clutter scatterers are blurred out, in a similar fashion to the results obtained by this algorithm for the first synthetic-target example. We also see the effects of the rotation-rate dependent azimuth scale factor $1 + \dot{\psi}_{RB}/\dot{\theta}$. In both the SAR image of Figure 5.53 and the cross-section plot of Figure 5.54, the synthetic-target scatterers appear to be separated in azimuth by approximately $1m$, since the synthetic moving-target is scaled in azimuth by $1 + \dot{\psi}_{RB}/\dot{\theta} = 2$. Recall that the full rigid-body algorithm gave a larger error in the estimated target rotation rate $\hat{\dot{\psi}}_{RB}$ (as compared to its results for the first synthetic-target

example). Therefore, when we rescaled the target portion of the SAR image by the inverse of $1 + \hat{\dot{\psi}}_{RB}/\dot{\theta}$ (as shown in the cross-section plot of Figure 5.57 of the azimuth-rescaled and azimuth-displacement compensated image of Figure 5.55), we obtained a target scatterer spacing in azimuth of approximately $0.6m$ (as compared to the original target azimuth spacing of $0.5m$). We also see in the cross-section plot of Figure 5.57 that we have an azimuth-displacement error of about $2m$, due to the error in the range-velocity estimate.

For the purely-translational algorithm, we used an L_1 weighting identical to the weighting of $\gamma_A = 0.8$ used by this algorithm for the first synthetic-target example. The target spatial region was also identical to the first synthetic-target example (with an azimuth width of $8m$ and a range width of $4m$, centered at $(x,y) = (-6.5m, -4m)$). Note that this target region included the two stationary man-made clutter scatterers. Later, we will reduce the range extent of the assumed target spatial region, such that the two "bright" stationary targets were excluded from this region (just as with the previous reduced-SCR purely-translational motion synthetic-target example).

The "first-trial" results for the purely-translational algorithm are shown in Figures 5.58 through 5.61. We obtained velocity estimates of $(\hat{\dot{x}}_{RB}, \hat{\dot{y}}_{RB}) = (1.86m/s, 2.40m/s)$, which were identical to the velocity estimates obtained by the purely-translational algorithm for the first synthetic-target example. We see that this velocity estimates were comparable to the estimates obtained by the full rigid-body algorithm for this example. In Figure 5.60, all of the target scatterers are focused and distinct, with a relative mainlobe height of about $15dB$ (as shown in the cross-section plot of Figure 5.61). However, because this algorithm assumes a zero target rotation rate, the scatterers at the "perimeter" of the moving target are not as sharply focused in the range direction y as the corresponding scatterers in the full rigid-body L_1 SAR image shown in Figure 5.53. After the azimuth-displacement compensation, we see an azimuth-displacement error of about $2m$ in the cross-section plot of Figure 5.64, This azimuth-displacement error was caused by the range-velocity estimation-error, which was comparable to the full rigid-body range-velocity estimation-error. The scatterers still appeared to be separated in azimuth by about $1m$, since we can not rescale the image in azimuth when using the purely-translational algorithm.

As stated earlier, the full rigid-body algorithm exhibited larger estimation-errors in both the range velocity $\dot{y}_{RB}$ and the rotation rate $\dot{\psi}_{RB}$, in comparison to the corresponding full rigid-body estimation-errors for the first purely-translational motion case. Recall that one hypothesis for these larger errors was the interaction of the rotating synthetic target with the two "bright" stationary scatterers contained within the assume target spatial region. In order to test this hypothesis, we reduced the range width of the assumed target spatial region (centered at $(x,y) = (-6.5m, -4m)$) from $4m$ to $2m$. This excluded the two stationary "bright" scatterers (just as with the previous reduced SCR purely-translational motion synthetic-target example). The azimuth width of the assumed target area was kept at $8m$, and the L_1 weighting was kept at $\gamma_A = 0.95$.

The results generated by the full rigid-body L_1-norm SAR processing algorithm with the reduced target spatial region are shown in Figures 5.65 through 5.71. For this example, we obtained velocity-parameter estimates of $(\hat{\dot{x}}_{RB}, \hat{\dot{y}}_{RB}, \hat{\dot{\psi}}_{RB}) = (1.83m/s, 2.31m/s, 0.0016\ rad/s)$. As compared to the first-trial results for the full rigid-body algorithm (with the larger assumed target area), we see that the exclusion of the two "bright" man-made clutter

scatterers significantly improved the range-velocity estimation-error performance. However, since the smaller assumed target spatial region excluded a portion of the moving target blur area (as shown in Figure 5.66), we now have a larger rotation-rate estimation error.

In Figure 5.67, the target scatterers are focused and distinct, with a relative mainlobe height of about $13dB$ (as shown in the cross-section plot of Figure 5.68). However, because of the larger estimation-error in the rotation rate, we see in Figure 5.68 that the scatterers do not appear to be as sharply focused as they are in the corresponding full rigid-body SAR image of Figure 5.54 (with the larger assumed target spatial region). After we rescale the SAR image in azimuth (as shown in Figure 5.69 and Figure 5.71), the scatterers still appear to be separated in azimuth by approximately $1m$, which is due to the larger rotation-rate estimation-error. However, because of the much smaller range-velocity estimation-error (in comparison to the range-velocity estimation-error of the full rigid-body algorithm with the larger assumed target spatial region), we see a correspondingly smaller azimuth-displacement error.

We next present results obtained by the purely-translational algorithm when the range width of the assumed target spatial region (centered at $(x, y) = (-6.5m, -4m)$) was reduced from $4m$ to $2m$, which excluded the two stationary "bright" scatterers. The azimuth width of the assumed target area was kept at $8m$, and the L_1 weighting was kept at $\gamma_A = 0.8$.

The results for the purely-translational algorithm are shown in Figures 5.72 through 5.75. We obtained velocity-parameter estimates of $(\hat{\dot{x}}_{RB}, \hat{\dot{y}}_{RB}) = (1.90m/s, 2.42m/s)$, which were comparable to the velocity-parameter estimates obtained by the purely-translational algorithm with the larger target region (as well as comparable to the estimates obtained by this algorithm for the previous purely-translational motion examples). Therefore, we can conclude that the performance of the purely-translational algorithm is less affected by the presence of the stationary scatterers than the full rigid-body algorithm, even though the overall range-velocity estimation-error performance is somewhat poorer. In Figure 5.74, all of the target scatterers are focused and distinct, with a relative mainlobe height of about $15dB$ (as shown in the cross-section plot of Figure 5.75). Just like the previous results generated for this example by this algorithm (with the larger target spatial region), the scatterers at the "perimeter" of the moving target are not as sharply focused in the range direction y as they are in the corresponding full rigid-body L_1 SAR image shown in Figure 5.53 (since the purely-translational algorithm assumes that the target rotation is zero). But these results were comparable to the results produced by the full rigid-body algorithm with an identical smaller assumed target region (shown in Figure 5.67 and Figure 5.68). However, the full rigid-body algorithm with the smaller assumed target region exhibited relatively poor rotation-rate estimation-performance for this example.

After the azimuth-displacement compensation, we see in Figure 5.76 (and in the cross-section plot of Figure 5.78) an azimuth displacement error of approximately $2m$ (caused by the range-velocity estimation-error), which was comparable to the azimuth displacement error of the full rigid-body algorithm. As with the first-trial results of this algorithm, the scatterers still appeared to be separated in azimuth by about $1m$ (since we can not rescale the image in azimuth).
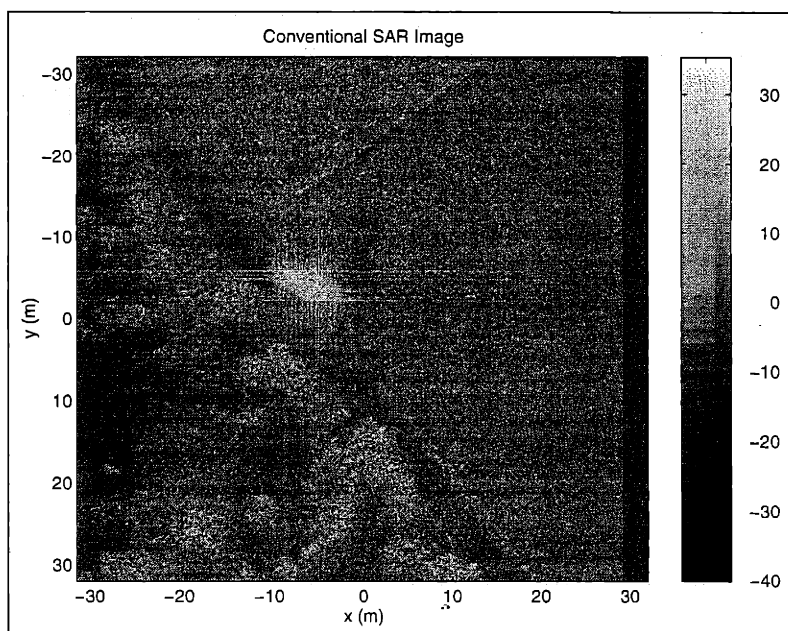
Figure 5.48: Conventional SAR Image for Third Synthetic-Target Example
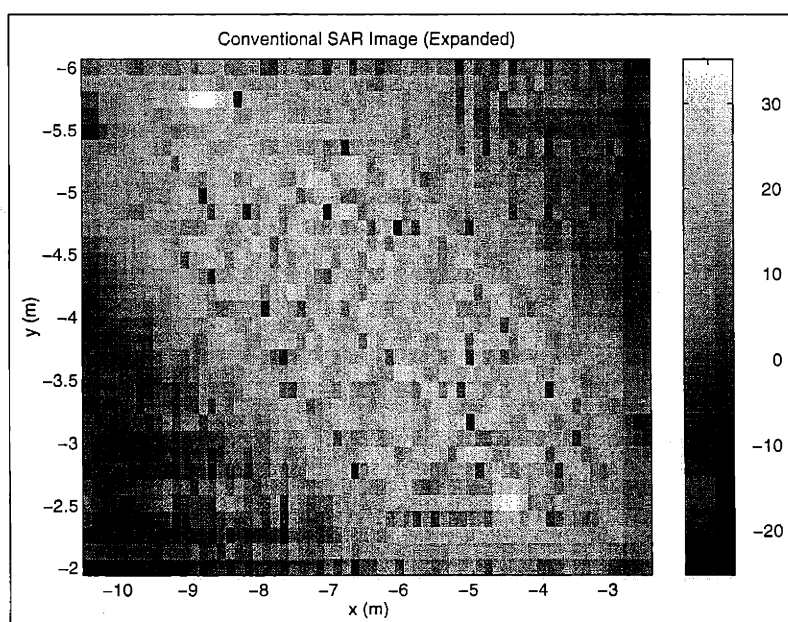
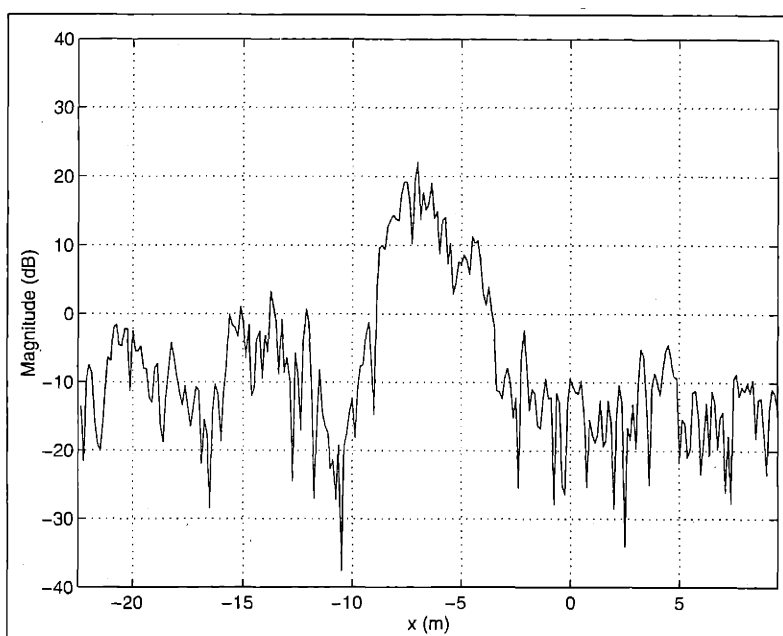Figure 5.49: Target Region of Conventional SAR Image for Third Synthetic-Target Example
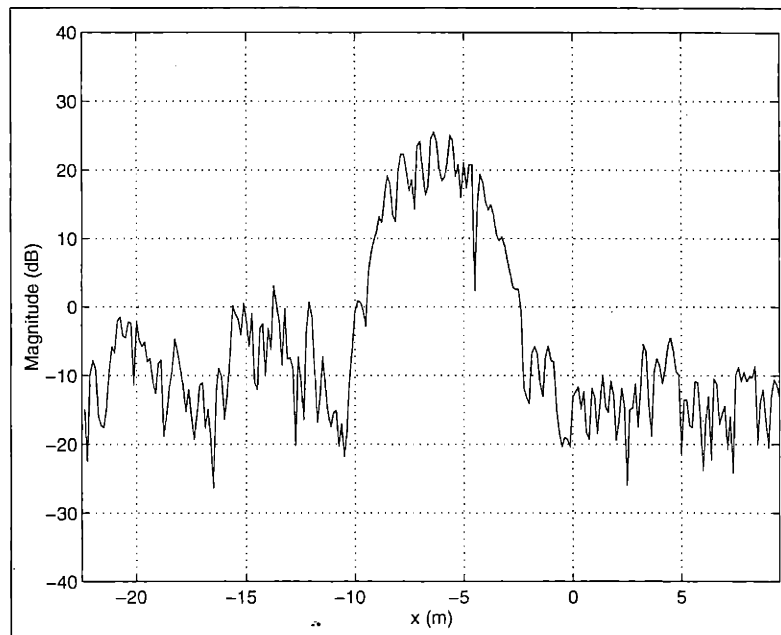
Figure 5.50: Cross-Section of Conventional SAR Image (at $y = -4m$) for Third Synthetic-Target Example
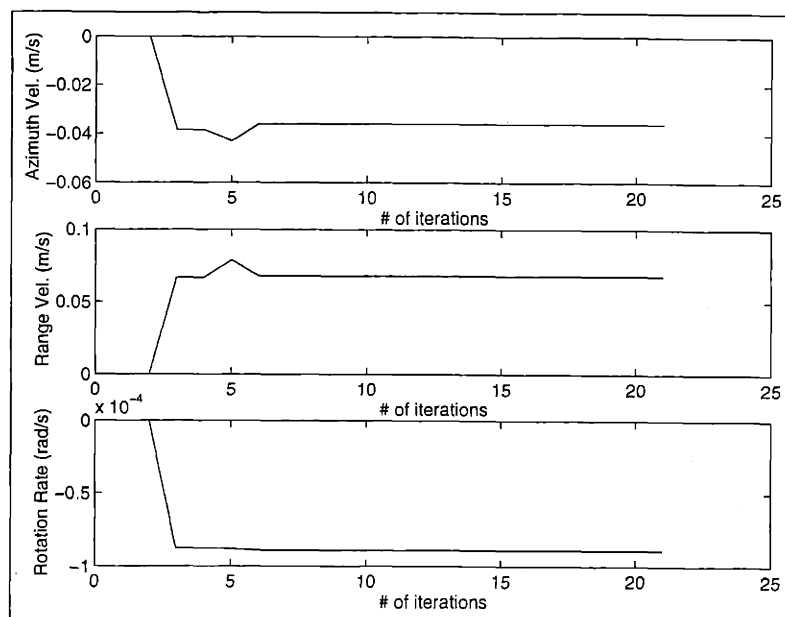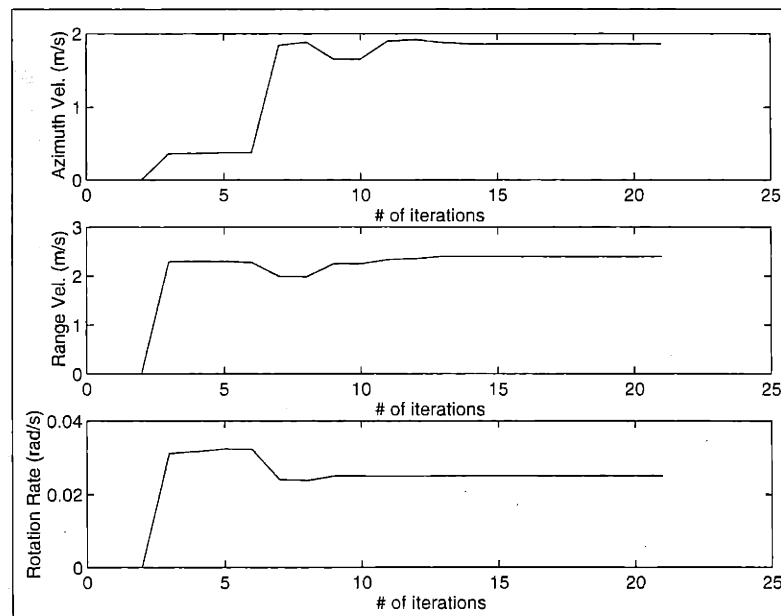

Figure 5.51: Estimated Target-Velocity Parameters for Third Synthetic-Target Example using Full Rigid-Body Processing Algorithm
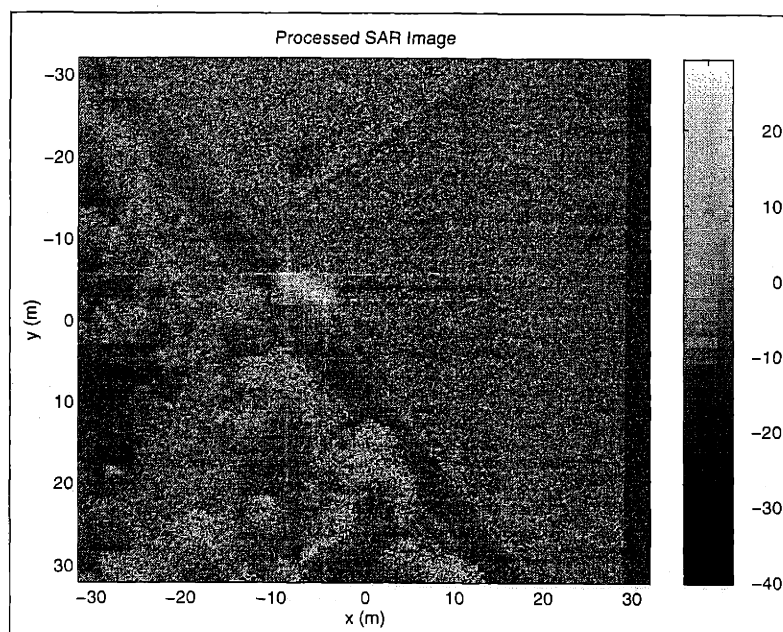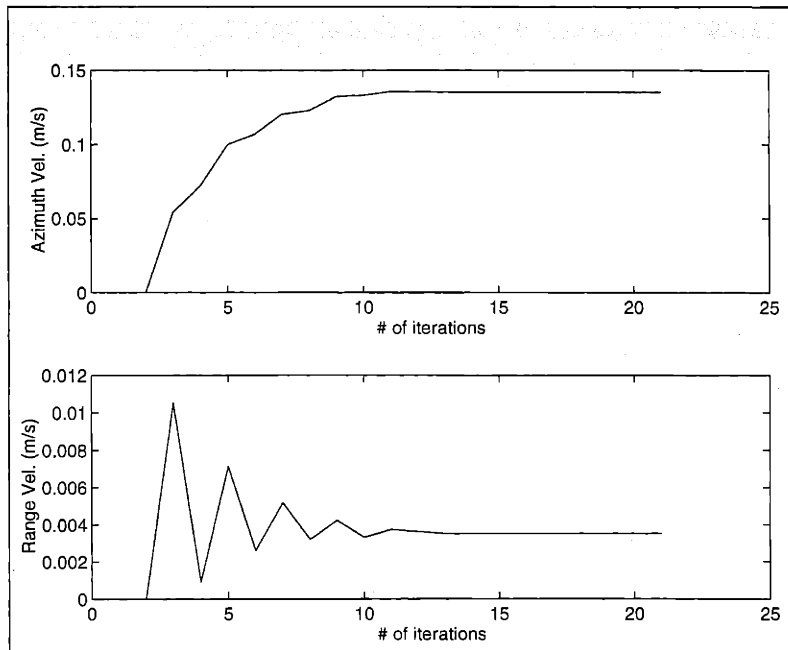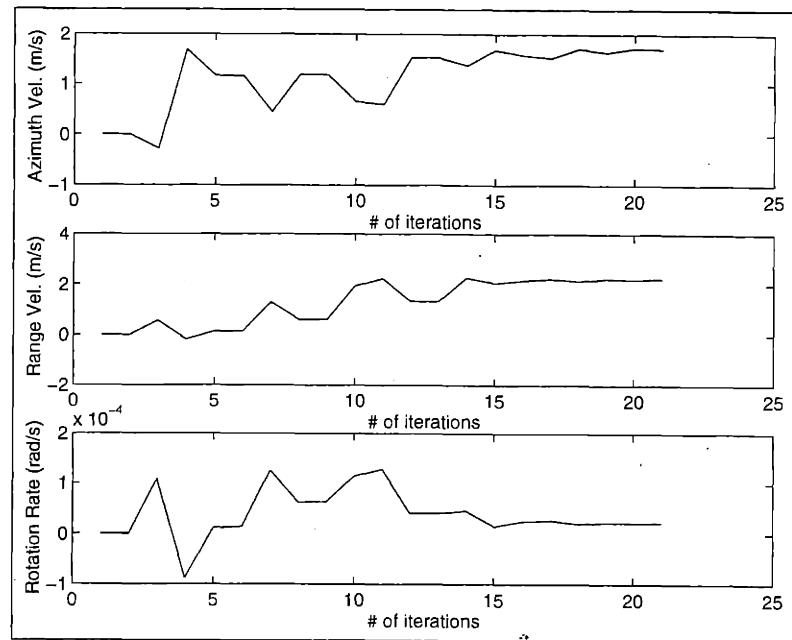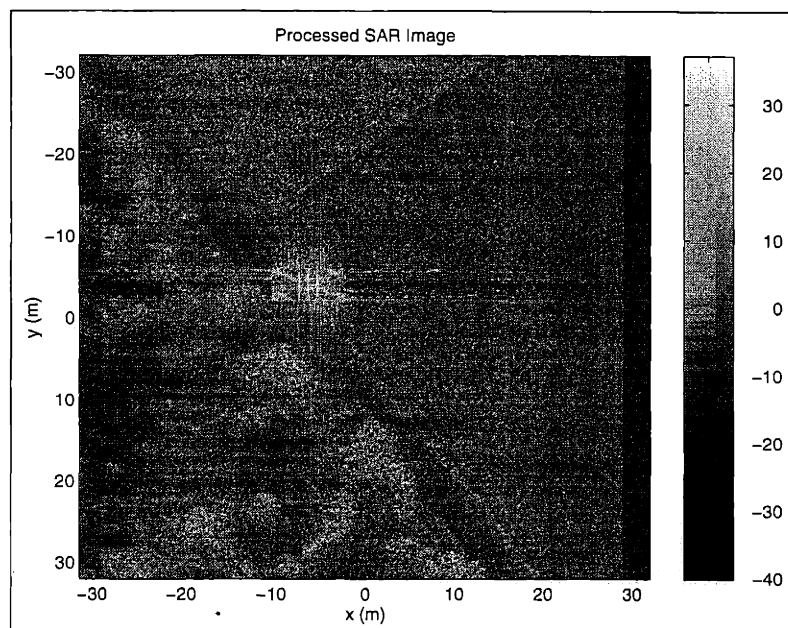
Figure 5.52: L_1 SAR Image for Third Synthetic-Target Example using Full Rigid-Body Processing Algorithm (Before Azimuth Rescaling and Azimuth-Displacement Compensation)
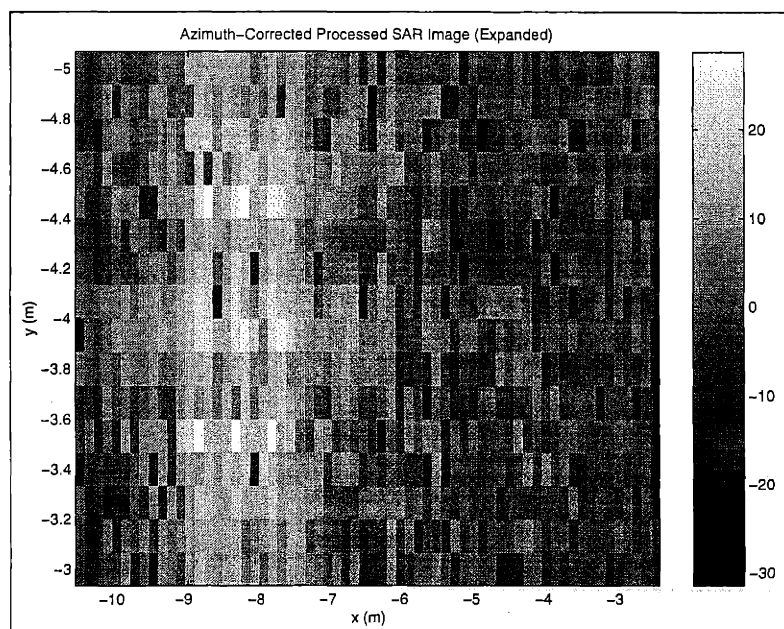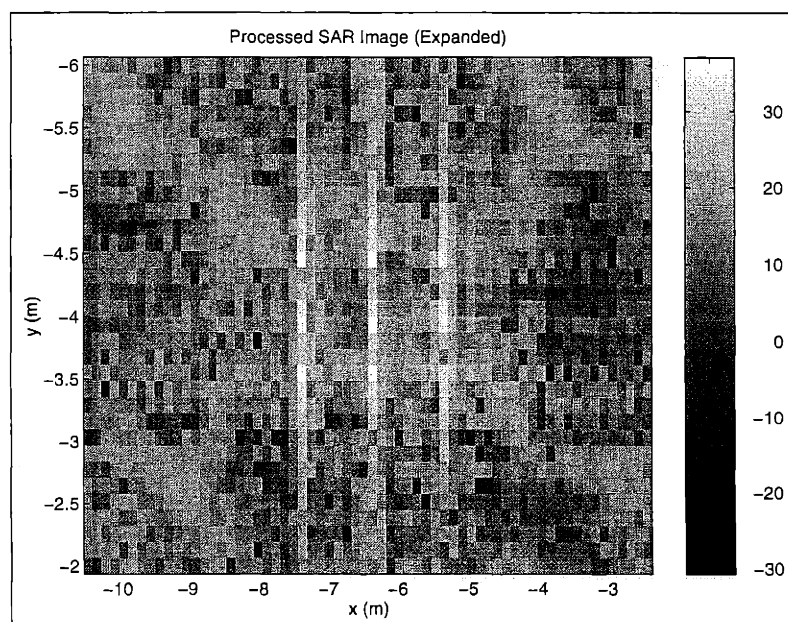

Figure 5.53: Target Region of L_1 SAR Image for Third Synthetic-Target Example using Full Rigid-Body Processing Algorithm (Before Azimuth Rescaling and Azimuth-Displacement Compensation)
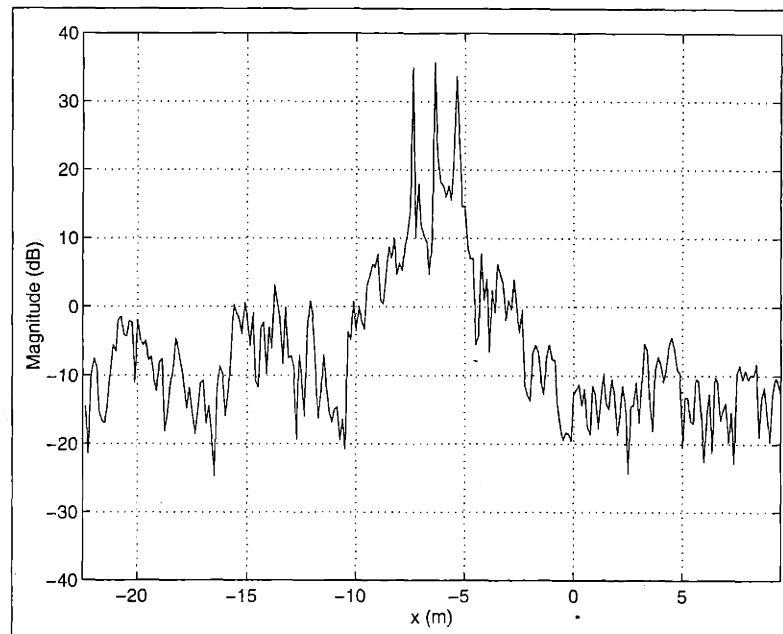
Figure 5.54: Cross-Section of L_1 SAR Image (at $y = -4m$) for Third Synthetic-Target Example using Full Rigid-Body Processing Algorithm (Before Azimuth Rescaling and Azimuth-Displacement Compensation)
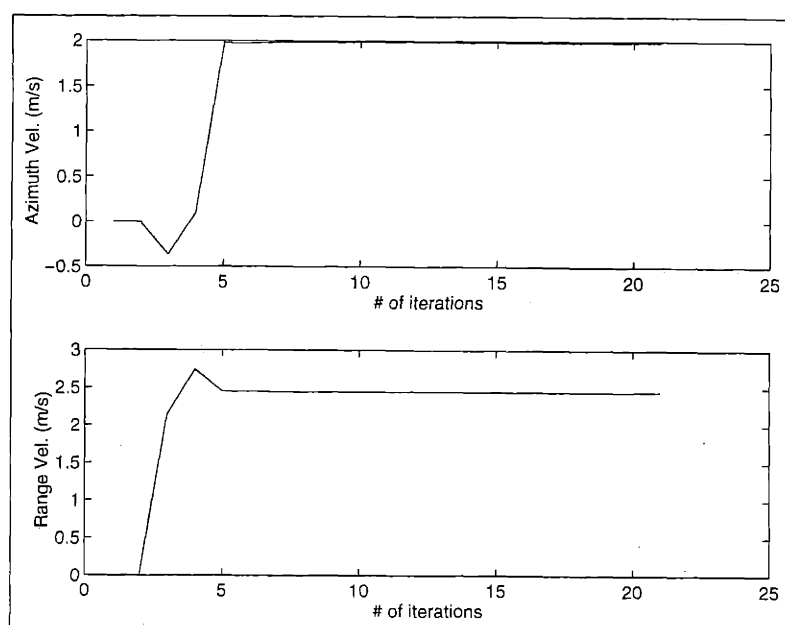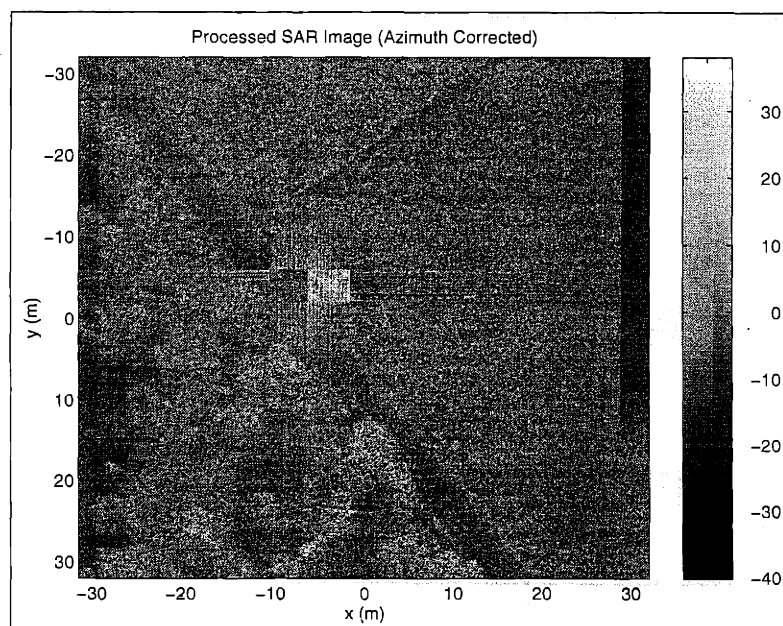

Figure 5.55: L_1 SAR Image for Third Synthetic-Target Example using Full Rigid-Body Processing Algorithm (After Azimuth Rescaling and Azimuth-Displacement Compensation)
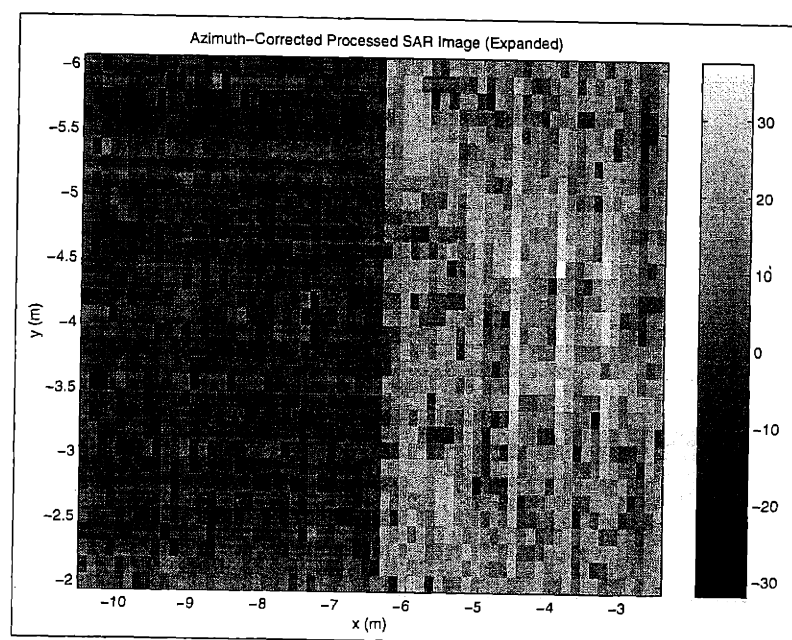
Figure 5.56: Target Region of L_1 SAR Image for Third Synthetic-Target Example using Full Rigid-Body Processing Algorithm (After Azimuth Rescaling and Azimuth-Displacement Compensation)
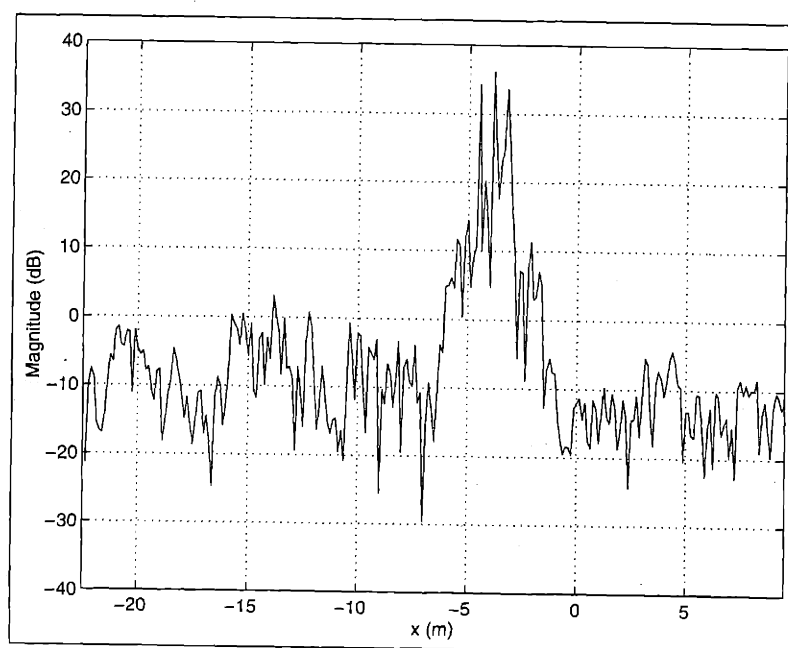
Figure 5.57: Cross-Section of L_1 SAR Image (at $y = -4m$) for Third Synthetic-Target Example using Full Rigid-Body Processing Algorithm (After Azimuth Rescaling and Azimuth-Displacement Compensation)
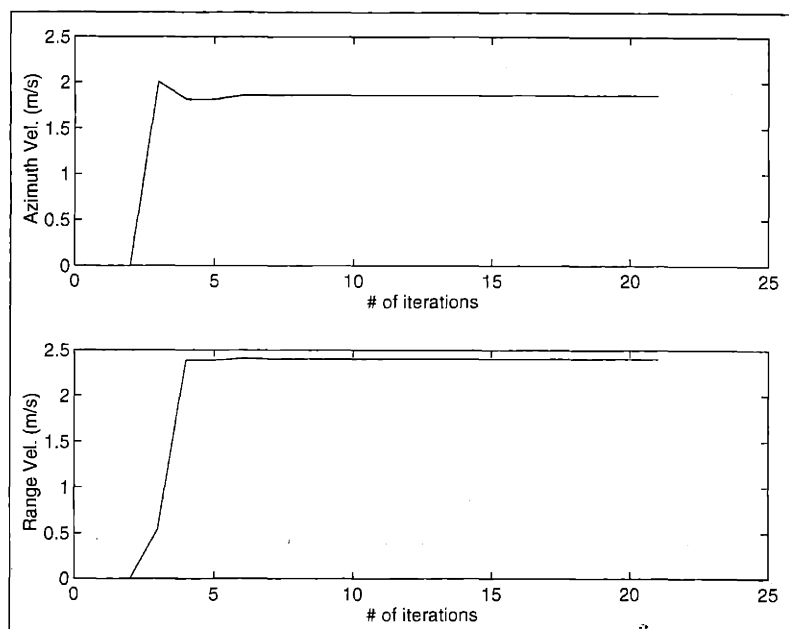
Figure 5.58: Estimated Target-Velocity Parameters for Third Synthetic-Target Example using Purely-Translational Processing Algorithm
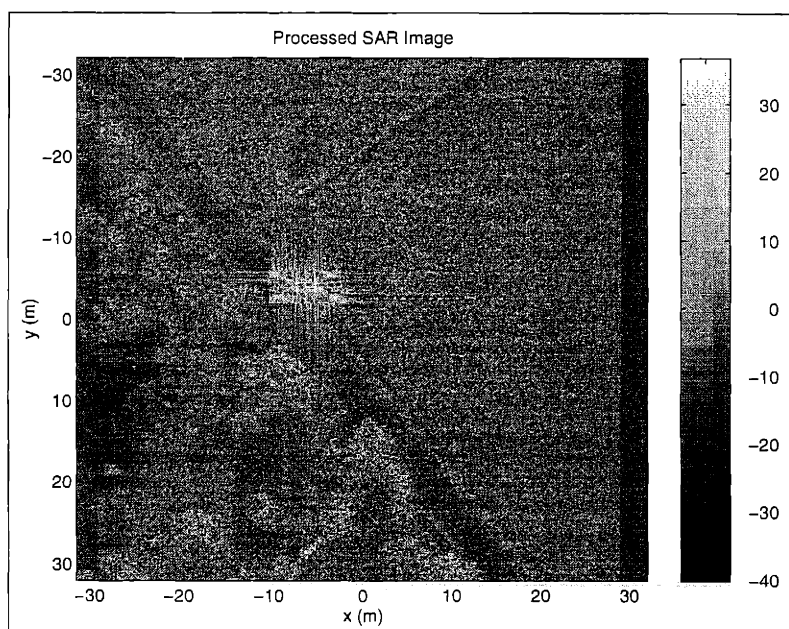
Figure 5.59: L_1 SAR Image for Third Synthetic-Target Example using Purely-Translational Processing Algorithm (Before Azimuth-Displacement Compensation)
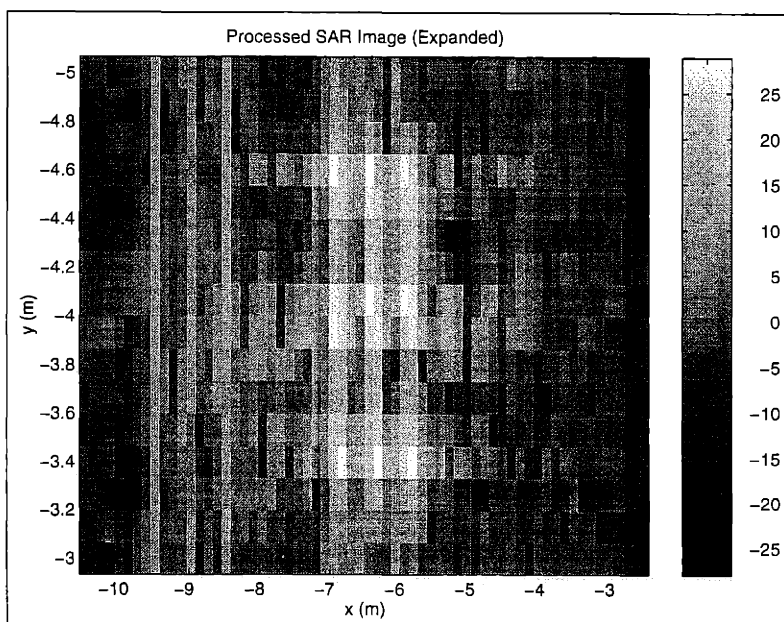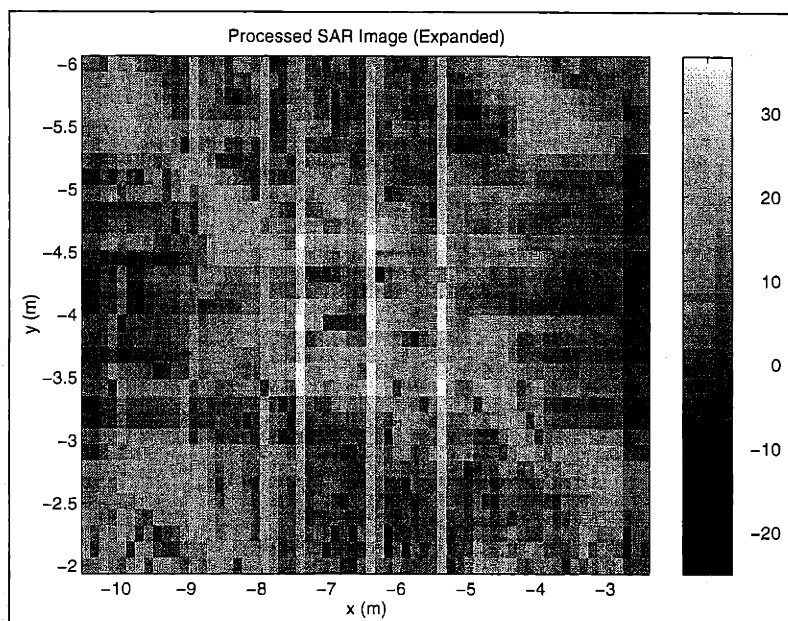
Figure 5.60: Target Region of L_1 SAR Image for Third Synthetic-Target Example using Purely-Translational Processing Algorithm (Before Azimuth-Displacement Compensation)
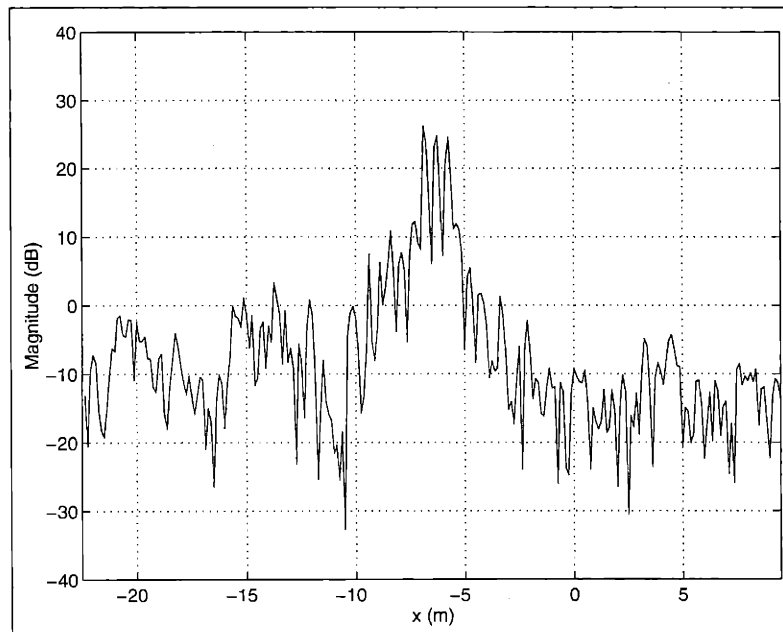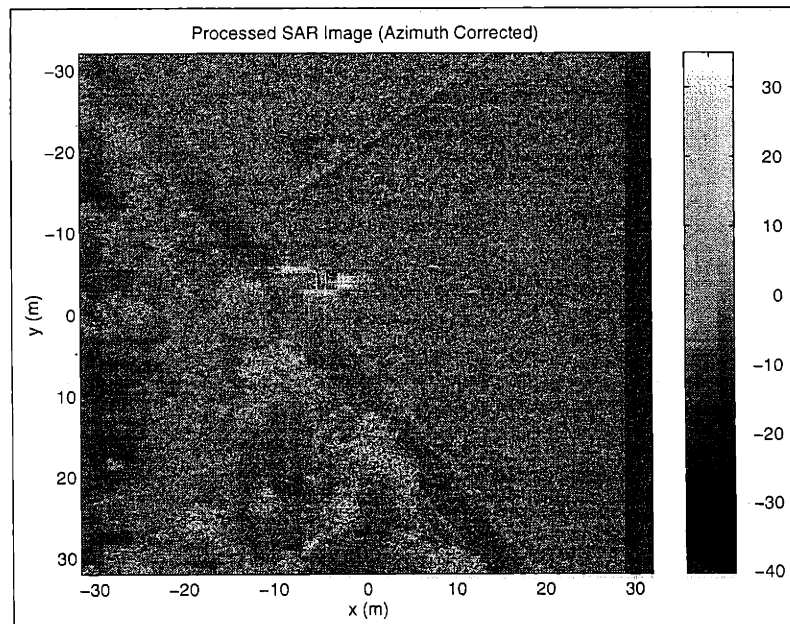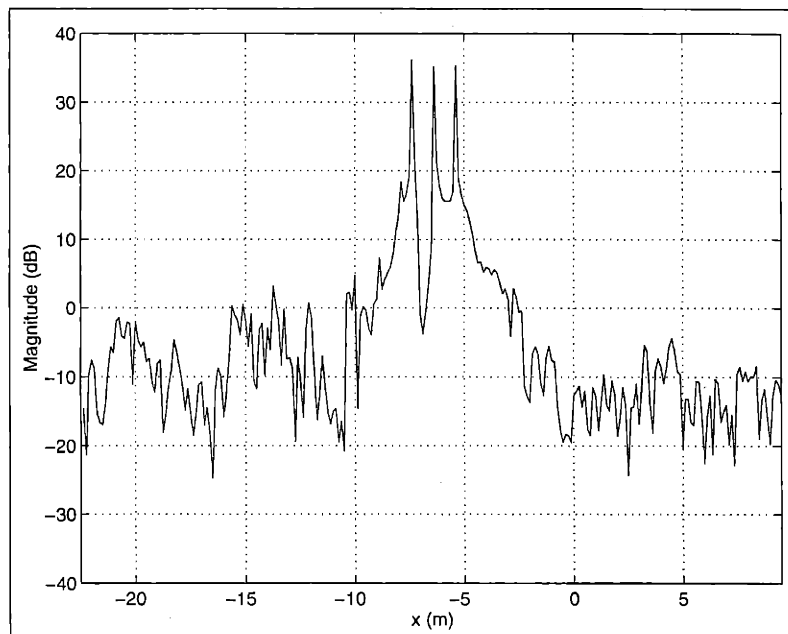

Figure 5.61: Cross-Section of L_1 SAR Image (at $y = -4m$) for Third Synthetic-Target Example using Purely-Translational Processing Algorithm (Before Azimuth-Displacement Compensation)
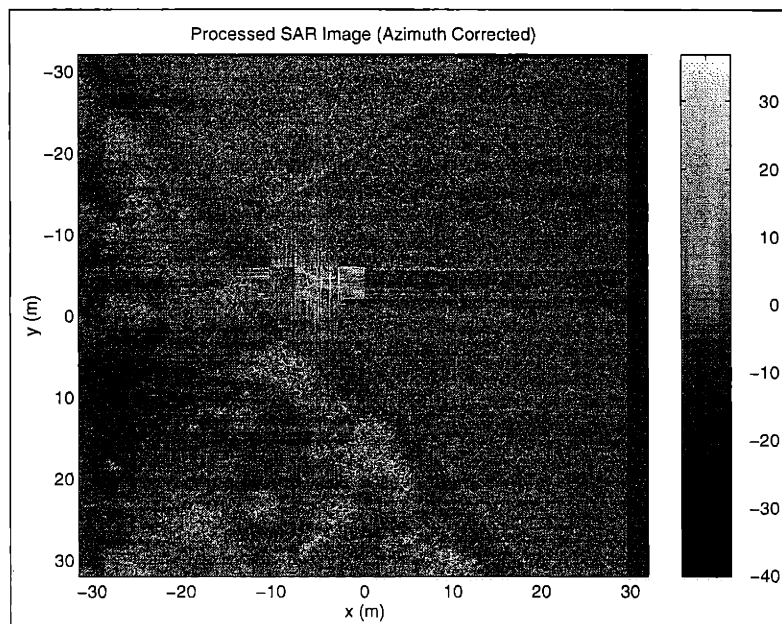
Figure 5.62: L_1 SAR Image for Third Synthetic-Target Example using Purely-Translational Processing Algorithm (After Azimuth-Displacement Compensation)
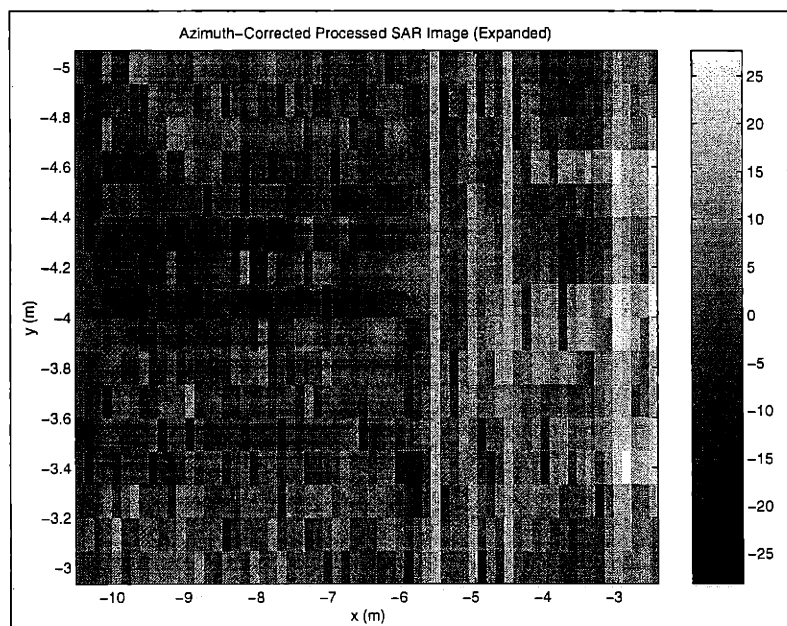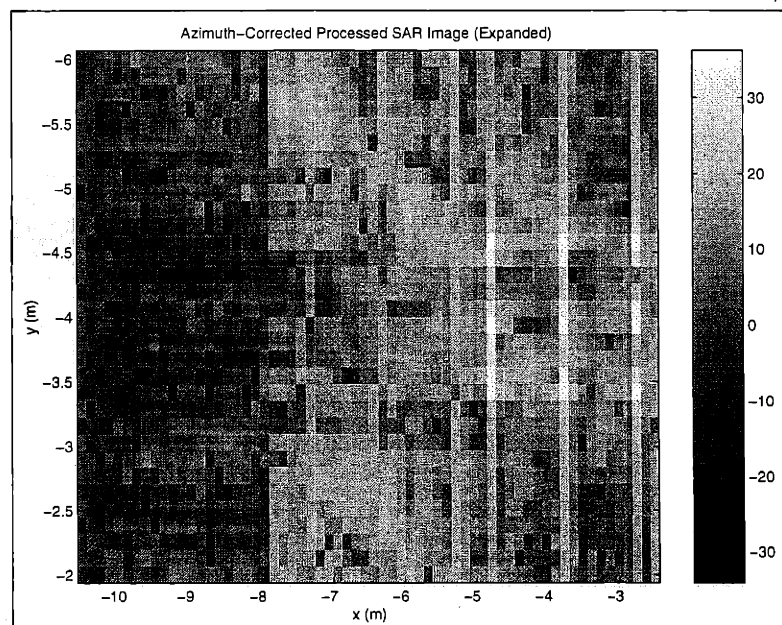

Figure 5.63: Target Region of L_1 SAR Image for Third Synthetic-Target Example using Purely-Translational Processing Algorithm (After Azimuth-Displacement Compensation)

Figure 5.64: Cross-Section of L_1 SAR Image (at $y = -4m$) for Third Synthetic-Target Example using Purely-Translational Processing Algorithm (After Azimuth-Displacement Compensation)


Figure 5.65: Estimated Target-Velocity Parameters for Third Synthetic-Target Example using Full Rigid-Body Processing Algorithm (with Reduced Target Spatial Region)
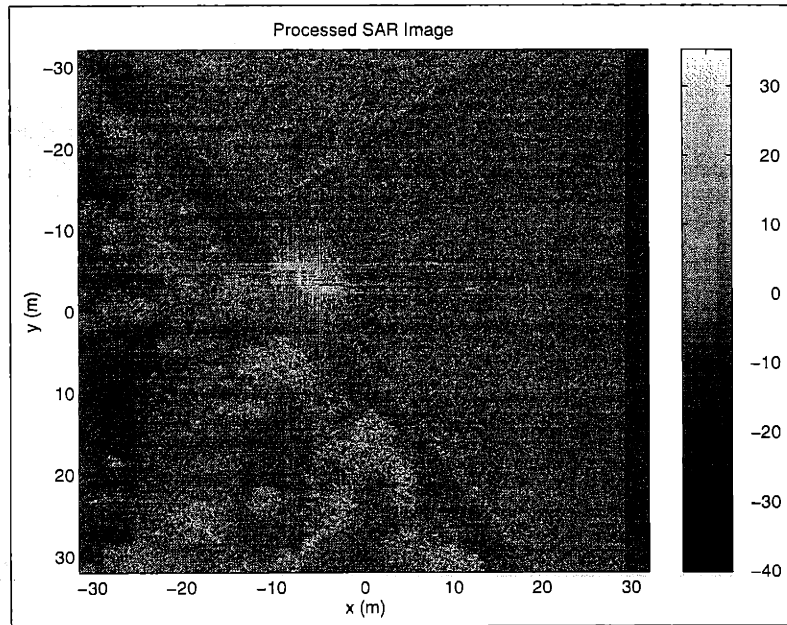
Figure 5.66: L_1 SAR Image for Third Synthetic-Target Example (with Reduced Target Spatial Region) using Full Rigid-Body Processing Algorithm (Before Azimuth Rescaling and Azimuth-Displacement Compensation)
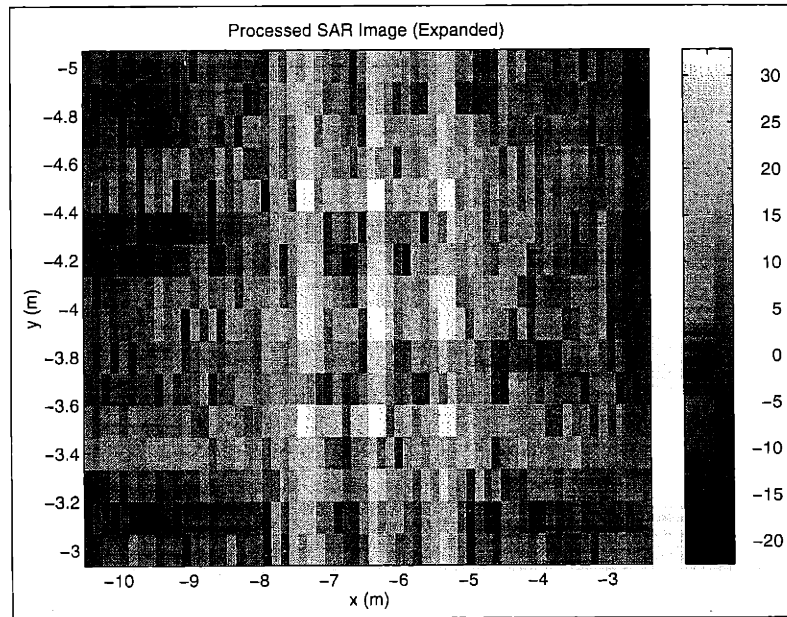
Figure 5.67: Target Region of L_1 SAR Image for Third Synthetic-Target Example (with Reduced Target Spatial Region) using Full Rigid-Body Processing Algorithm (Before Azimuth Rescaling and Azimuth-Displacement Compensation)

Figure 5.68: Cross-Section of L_1 SAR Image (at $y = -4m$) for Third Synthetic-Target Example (with Reduced Target Spatial Region) using Full Rigid-Body Processing Algorithm (Before Azimuth Rescaling and Azimuth-Displacement Compensation)
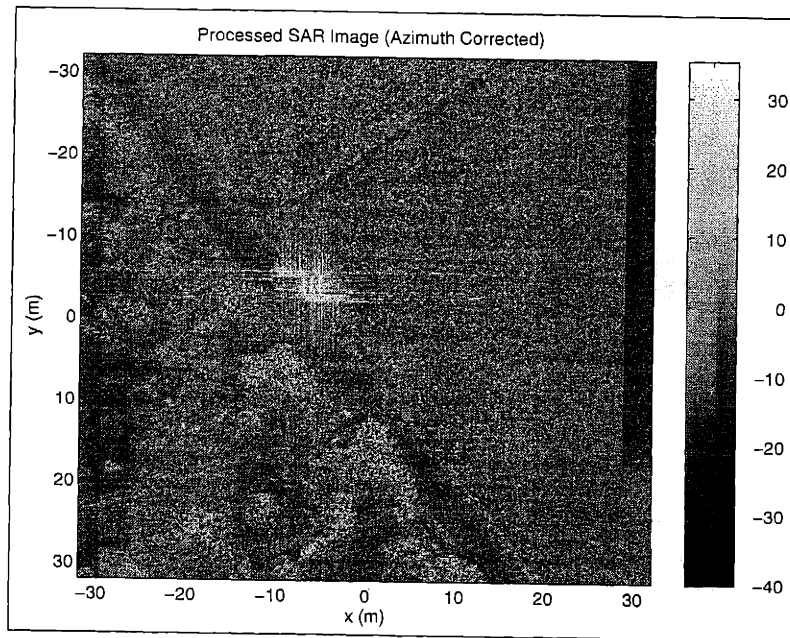
Figure 5.69: L_1 SAR Image (with Reduced Target Spatial Region) for Third Synthetic-Target Example using Full Rigid-Body Processing Algorithm (After Azimuth Rescaling and Azimuth-Displacement Compensation)
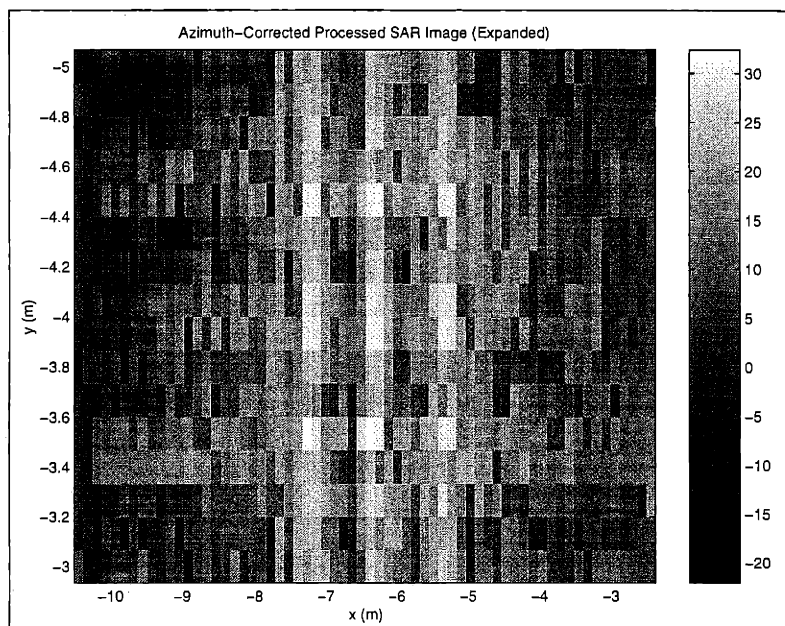
Figure 5.70: Target Region of L_1 SAR Image for Third Synthetic-Target Example (with Reduced Target Spatial Region) using Full Rigid-Body Processing Algorithm (After Azimuth Rescaling and Azimuth-Displacement Compensation)
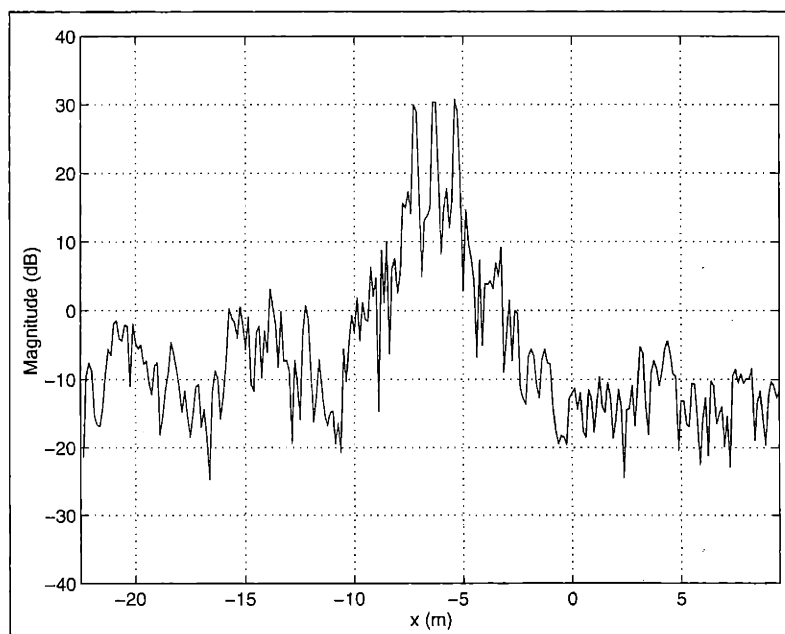
Figure 5.71: Cross-Section of L_1 SAR Image with Reduced Target Spatial Region (at $y = -4m$) for Third Synthetic-Target Example using Full Rigid-Body Processing Algorithm (After Azimuth Rescaling and Azimuth-Displacement Compensation)
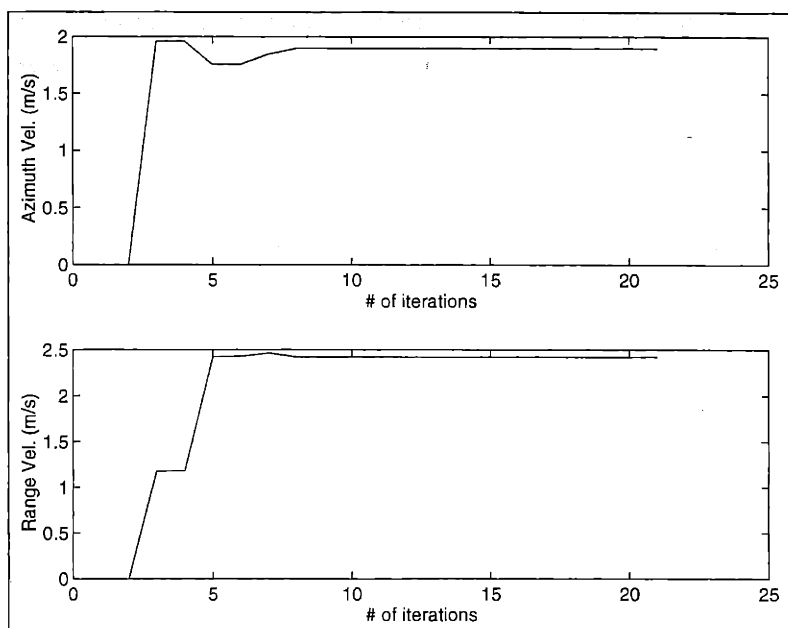
Figure 5.72: Estimated Target-Velocity Parameters for Third Synthetic-Target Example using Purely-Translational Processing Algorithm (with Reduced Target Spatial Region)
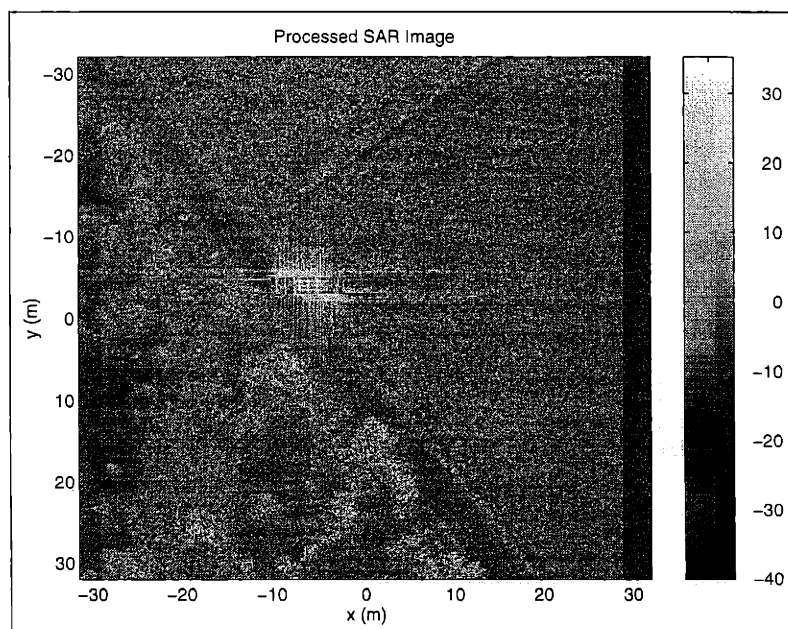
Figure 5.73: L_1 SAR Image for Third Synthetic-Target Example using Purely-Translational Processing Algorithm with Reduced Target Spatial Region (Before Azimuth-Displacement Compensation)
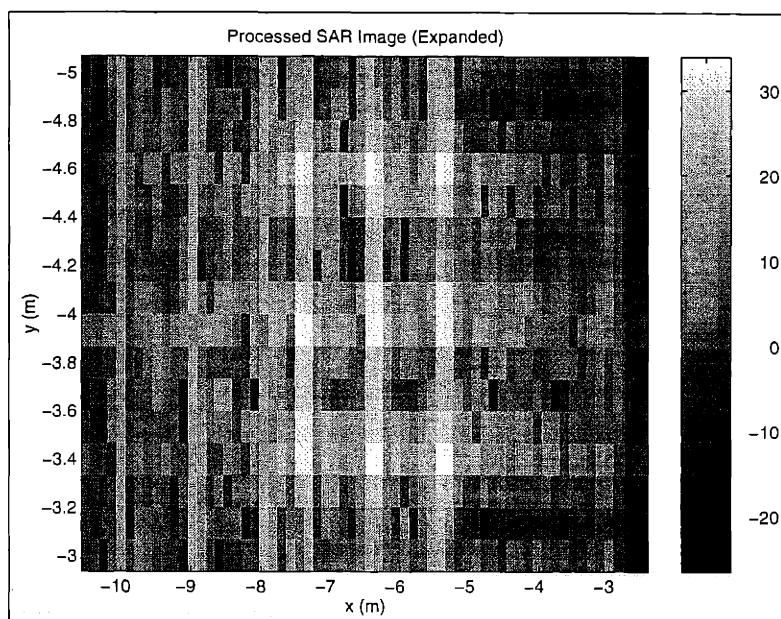
Figure 5.74: Target Region of L_1 SAR Image for Third Synthetic-Target Example using Purely-Translational Processing Algorithm with Reduced Target Spatial Region (Before Azimuth-Displacement Compensation)
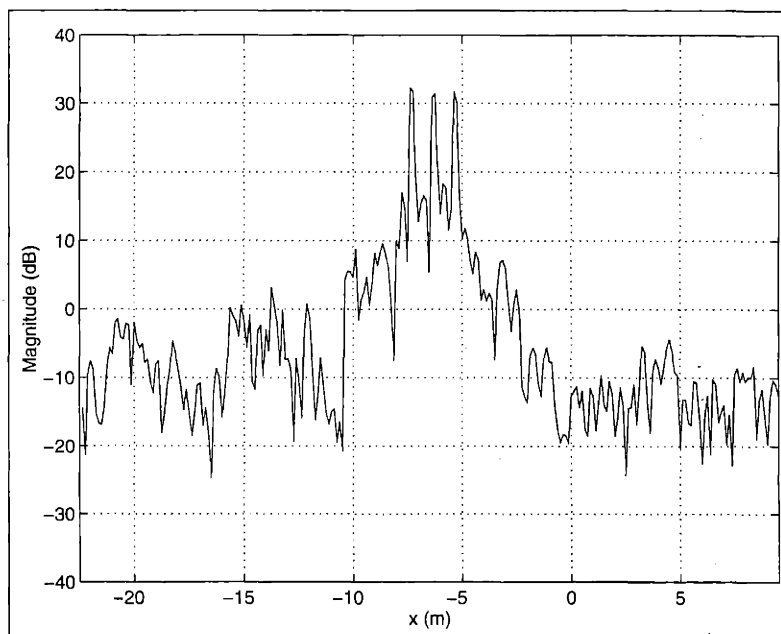
Figure 5.75: Cross-Section of L_1 SAR Image (at $y = -4m$) for Third Synthetic-Target Example using Purely-Translational Processing Algorithm with Reduced Target Spatial Region (Before Azimuth-Displacement Compensation)
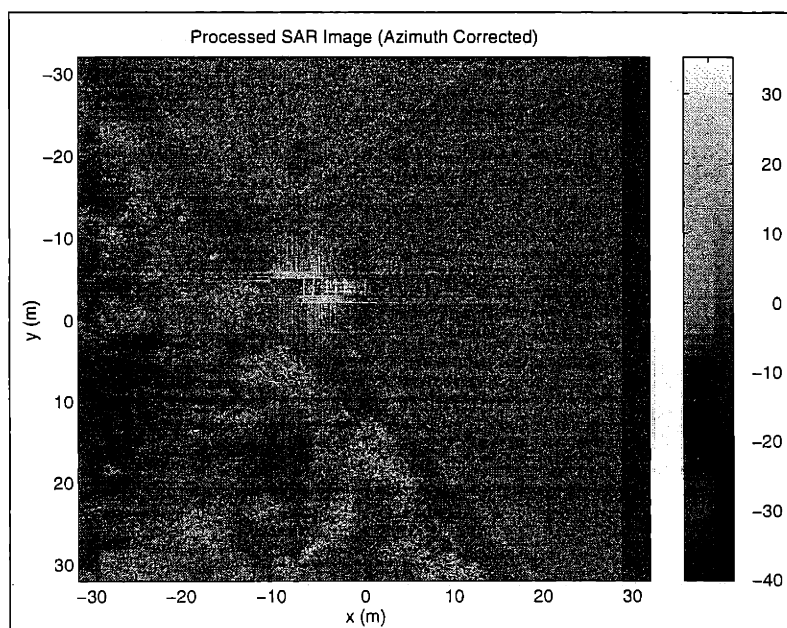
Figure 5.76: L_1 SAR Image for Third Synthetic-Target Example (with Reduced Target Spatial Region) using Purely-Translational Processing Algorithm (After Azimuth-Displacement Compensation)
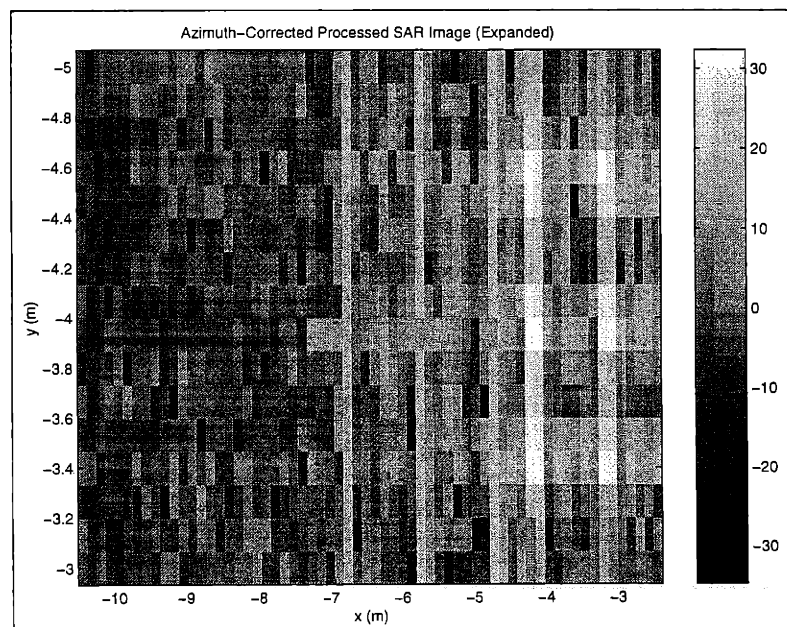
Figure 5.77: Target Region of L_1 SAR Image for Third Synthetic-Target Example using Purely-Translational Processing Algorithm with Reduced Target Spatial Region (After Azimuth-Displacement Compensation)
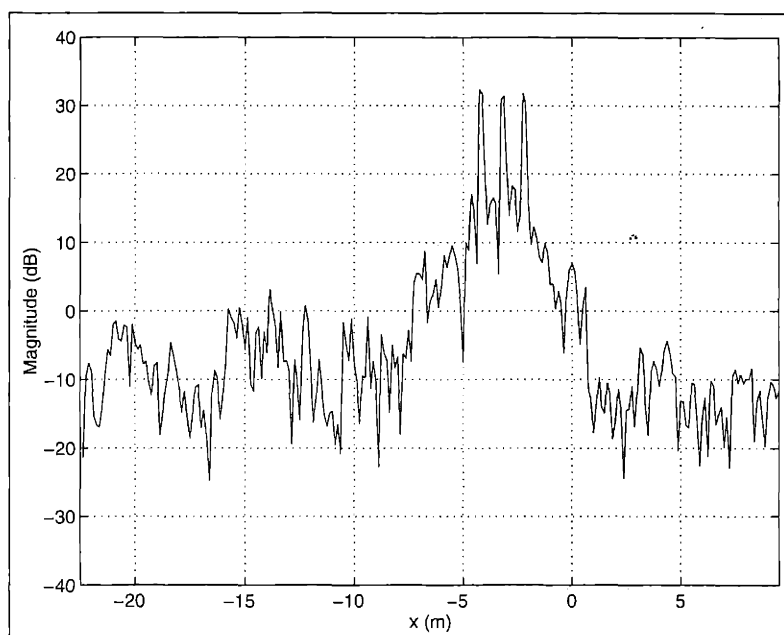
Figure 5.78: Cross-Section of L_1 SAR Image (at $y = -4m$) for Third Synthetic-Target Example (with Reduced Target Spatial Region) using Purely-Translational Processing Algorithm (After Azimuth-Displacement Compensation)

5.3.2 Synthetic-Motion Real Targets Embedded in Real Clutter

In this section, we present a series of experimental examples where we manually segmented the conventional SAR image of an actual stationary target into a target portion and a clutter portion, and used the target portion to generate a synthetic-motion moving target. For comparison purposes, we used a 128 × 128 pixel SAR image, with an approximate resolution in range and azimuth of of $\delta_y = 0.25m$ and $\delta_x = 0.25m$. This image was identical to the stationary-target SAR image used to generate the synthetic-motion real-target example presented in Chapter 4 for the matched-filter algorithm. It consisted of a T-72 tank from the former Soviet Union (in a grass clutter background), as shown in Figure 5.79. This particular image was part of a spotlight-mode SAR data set collected by Sandia National Laboratory in 1995 under DARPA's Moving and Stationary Target Acquisition and Recognition (MSTAR) program. An azimuthal cross-section (at a range of $0.45m$) of the target image is shown in Figure 5.81. In this cross-section, we observe some of the "dominant" feature scatterers corresponding to the tank's treads, (approximately located at $(x, y) = (-1m, 0.45m)$).

As with the synthetic-motion real-target example presented in Chapter 4, we manually segmented the MSTAR SAR scene into a target portion and a clutter portion, as shown in Figure 5.82 and Figure 5.83. The target portion was chosen such as to include as many of the "dominant" feature scatterers of the tank as possible. We the used this target portion as an input into our general-motion estimation-theoretic model in order to generate the synthetic-motion moving-target data. The moving target was then re-embedded back into the stationary clutter by adding this generated data to the scaled Fourier Transform of the stationary-clutter portion (where the scaled Fourier Transform corresponds to the zero-velocity SAR model). The parameters of the estimation-theoretic model were chosen to be as similar as possible to the 33.5 GHz Lincoln Laboratory Advanced Detection and Tracking System (ADTS) system operating in spotlight mode, as shown in Table 5.2.

First Example: Purely Translational Motion

For our first example, we consider the purely-translational motion case (i.e., $\dot\psi_{RB}$ equal to zero), where we have a target velocity of $(\dot x_{RB}, \dot y_{RB}) = (2m/s, 2.304m/s)$. This example was identical to the synthetic-motion real-target example presented in Chapter 4. As shown in Figure 5.84, the target motion has significantly degraded the conventional SAR image (in comparison to the original stationary-target MSTAR image of Figure 5.79). Therefore, we can assume that the target motion would cause a similar degradation in the performance of most SAR-image based ATR algorithms which attempt to use this conventional image of the moving target. We also see a similar degradation in the azimuthal cross-section of the conventional image in Figure 5.86 (in comparison to the corresponding azimuthal cross-section of the original stationary-target MSTAR image, shown in Figure 5.81).

For the full rigid-body L_1-norm SAR processing algorithm, we used an L_1 weighting of $\gamma_A = 0.7$ for the velocity-parameter estimation. We assumed a rectangular target spatial region with an azimuth width of $8m$ and a range width of $4m$, centered at $(x, y) = (0m, 0m)$.

The results of the full rigid-body L_1-norm SAR processing algorithm are shown in Figures 5.87 through 5.92. For this example, we obtained velocity-parameter estimates of $(\hat{\dot x}_{RB}, \hat{\dot y}_{RB}, \hat{\dot\psi}_{RB}) = (2.00m/s, 2.28m/s, 0.0002rad/s)$. As shown in Figure 5.88, the L_1 SAR

F_c	Center Frequency	33.5 GHz
λ_c	Center Wavelength	0.009 m
αT_p	Chirp Bandwidth	1.2 GHz
f_{PRF}	Pulse Repetition Frequency	128 pulse/s
N	Complex Samples per Range Profile	128
$2K$	Pulses per Synthetic Aperture	128
R_o	Center Slant-Range	2778 M
v	SAR Platform Velocity	100 m/s
$\dot{\theta}$	Look-Angle Rotation Rate	0.036 rad/s
$2T$	Dwell Time	1.0 s
L	Synthetic-Aperture Length	100 m
Δ_y	Range Sampling Interval	0.125 m
Δ_x	Azimuth Sampling Interval	0.125 m
δ_y	Range Resolution	0.25 m
δ_x	Azimuth Resolution	0.25 m

Table 5.2: System Parameters for the Synthetic-Motion Real-Target L_1 SAR Processing Examples

image is greatly improved, as compared to the conventional SAR image of Figure 5.84. In fact, the image of the T-72 tank is nearly identical to the image of the T-72 tank in the original MSTAR data of Figure 5.79 (except for sidelobe "streaks" near some of the "brighter" target feature scatterers). Therefore, we can assume that a SAR-image based ATR system which uses this image would probably see a similar improvement in performance (in comparison to its performance when using the conventional SAR image). The azimuthal cross-section of the L_1 SAR image In Figure 5.90 is also very similar to the cross-section of the original MSTAR stationary image shown in Figure 5.81. However, the nulls between the "dominant" feature scatterers corresponding to the tank treads are not quite as pronounced. After we performed the azimuth rescaling and azimuth-displacement compensation, the resulting azimuth displacement error was relatively small (approximately 0.75m), as shown in the azimuthal cross-section of Figure 5.92 (due to the relatively small range-velocity estimation-error).

We show the results from the purely-translational L_1-norm SAR processing algorithm in Figures 5.94 through 5.96. For this algorithm, we used an L_1 weighting of $\gamma_A = 0.98$ for the velocity-parameter estimation. Just as with the full rigid-body algorithm, we used a rectangular spatial target region with an azimuth width of $8m$ and a range width of $4m$, centered at $(x, y) = (0m, 0m)$.

For the purely-translational algorithm, we obtained velocity-parameter estimates of $(\hat{\dot{x}}_{RB}, \hat{\dot{y}}_{RB}) = (1.52m/s, 2.28m/s)$. We observe that the purely-translational algorithm has a somewhat larger azimuth-velocity estimation error, as compared to the azimuth-velocity estimation error of the full rigid-body algorithm. However, the resulting SAR image in Figure 5.95 is nearly identical to the original MSTAR image of Figure 5.79, except for the blurring of the target's "shadow" upon the clutter background. In fact, we see a slight improvement in this image, as compared to the corresponding SAR image of the full rigid-

body L_1-norm algorithm in Figure 5.89 (i.e., the sidelobe "streaks" appear to have been attenuated for some of the brighter feature scatterers). As shown in the azimuthal cross-section of Figure 5.96, the nulls between the feature scatterers corresponding to the tank treads are more pronounced, in comparison to the corresponding azimuthal cross-section for the full rigid-body algorithm, shown in Figure 5.90. As with the full rigid-body results shown in Figure 5.92, the resulting azimuth displacement error after azimuth-displacement compensation was relatively small (approximately $0.75m$), as shown in Figure 5.92 (due to the relatively small range-velocity estimation-error).

For the results of the L_1 full rigid-body algorithm presented in this chapter, we computed the scatterer amplitudes by minimizing the following standard least-squares cost function $J(\mathbf{A}, \hat{\mathbf{v}}) = ||\mathbf{f} - \mathbf{F}(\hat{\mathbf{v}})\mathbf{A}||_2^2$ (given that we obtained a convergent velocity-parameter estimate $\hat{\mathbf{v}}$ from the coordinate-descent line-minimization portion of this algorithm). Recall from Section 3.1.1 that the prime motivation for computing the scatterer amplitudes in this manner was to reduce the attenuation of the target scatterers as much as possible (for the sake of comparison to the conventional SAR imaging techniques). In order to examine the effects of velocity-parameter estimation errors upon the images generated by the full rigid-body L_1 algorithm, we include results generated by the standard least-squares cost-function minimization for this experimental case when the velocity parameters are known *exactly*. As shown in Figure 5.99, the SAR image produced by this minimization (using the exact velocity parameters) is slightly sharper (as would be expected) than the corresponding image produced by the full rigid-body algorithm using the estimated velocity-parameters (shown in Figure 5.88). However, as compared to the image produced in Figure 5.95 by the purely-translational algorithm, the sidelobe "streaks" near the bright target scatterers are still somewhat apparent. In the azimuthal cross-section of the "exact-velocity" SAR image (shown in Figure 5.101), the nulls between the feature scatterers corresponding to the tank treads are slightly more pronounced, in comparison to the corresponding cross-section (shown in Figure 5.90) of the rigid-body SAR image produced using the estimated velocity parameters.
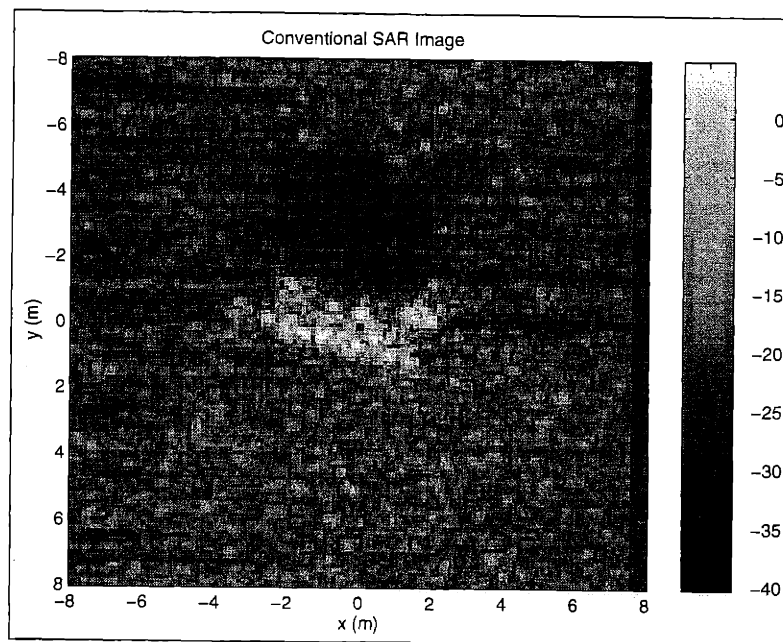
Figure 5.79: MSTAR Target Chip for Synthetic-Motion Real-Target Examples
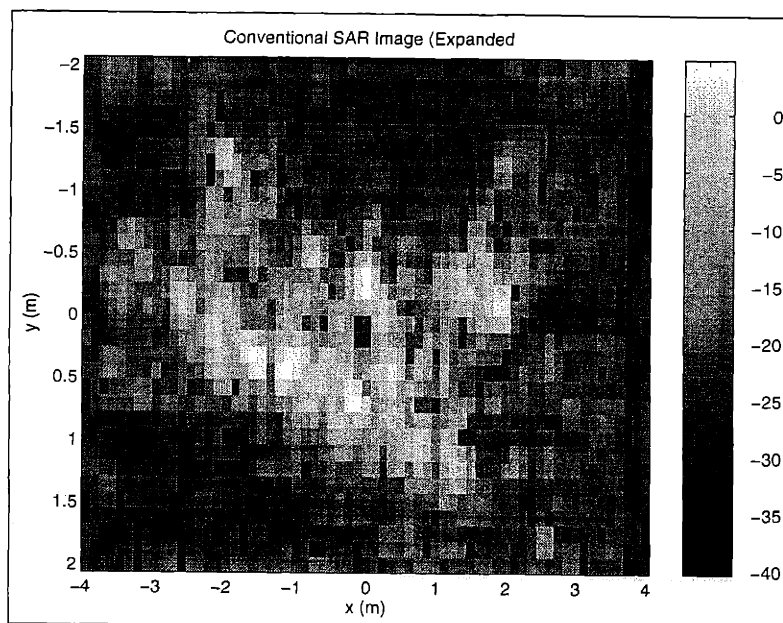
Figure 5.80: MSTAR Target Chip for Synthetic-Motion Real Moving-Target Examples (expanded)
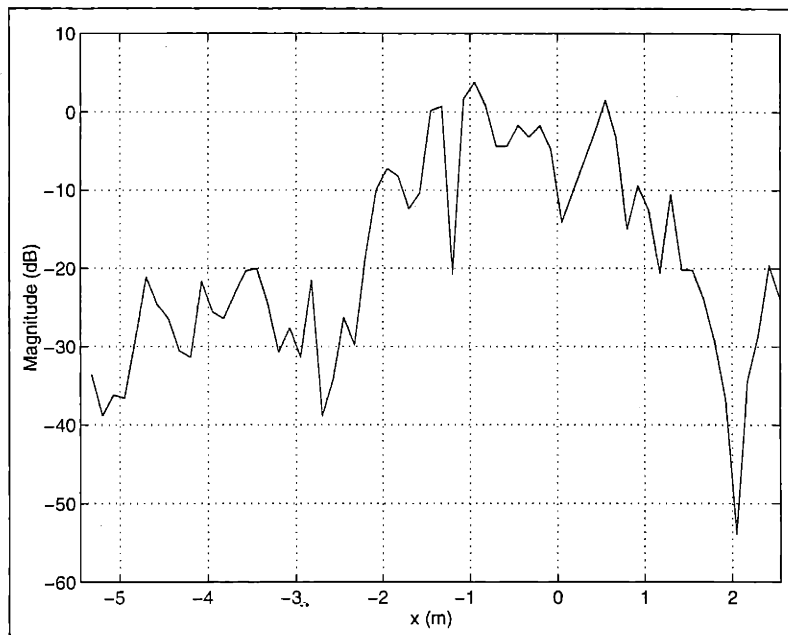
Figure 5.81: Azimuthal Cross-section of MSTAR Target Chip Image at $y = 0.45m$
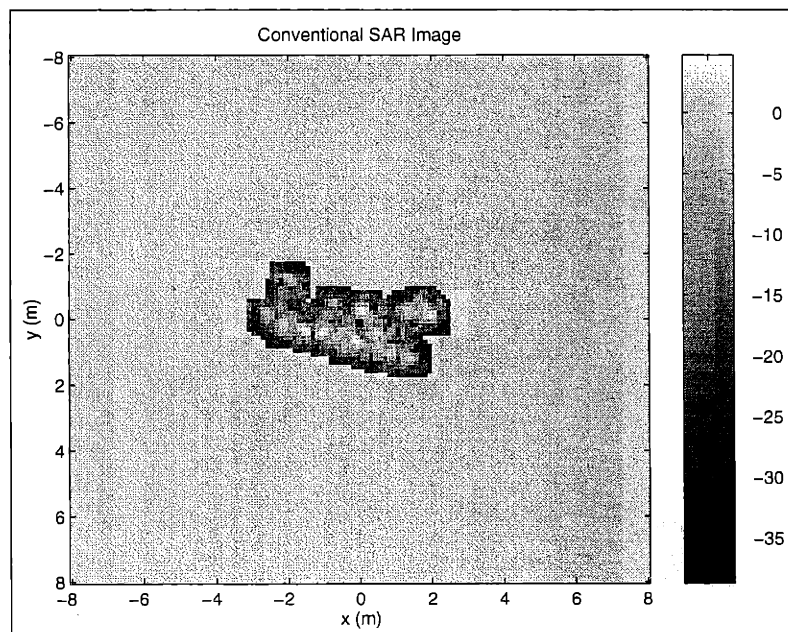
Figure 5.82: Target Portion of MSTAR Target Chip
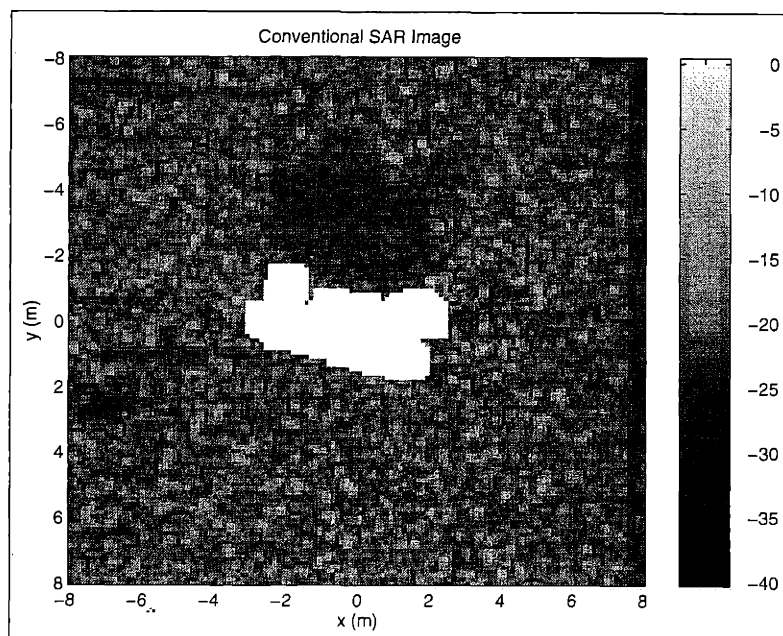
Figure 5.83: Clutter Portion of MSTAR Target Chip ("Non-white" Part)
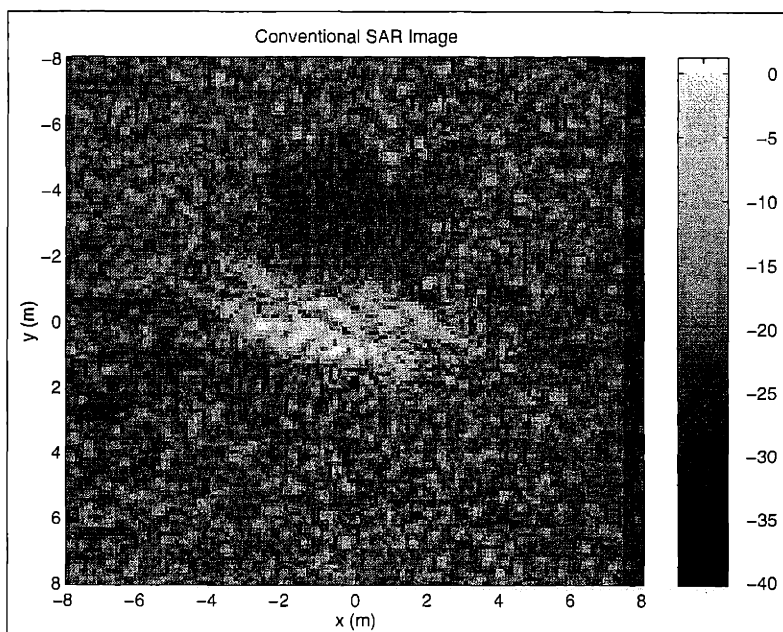
Figure 5.84: Conventional SAR Image for First Synthetic-Motion Real-Target Example
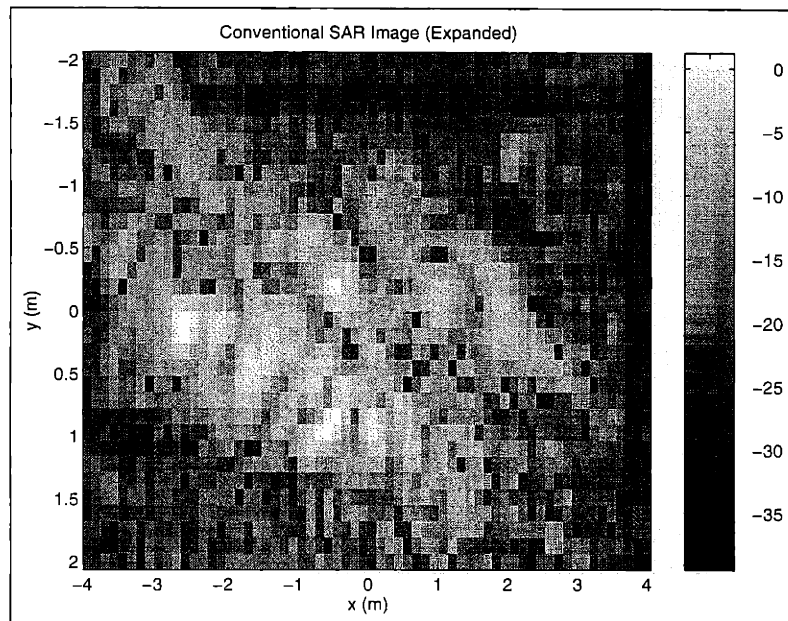
Figure 5.85: Target Region of Conventional SAR Image for First Synthetic-Motion Real-Target Example
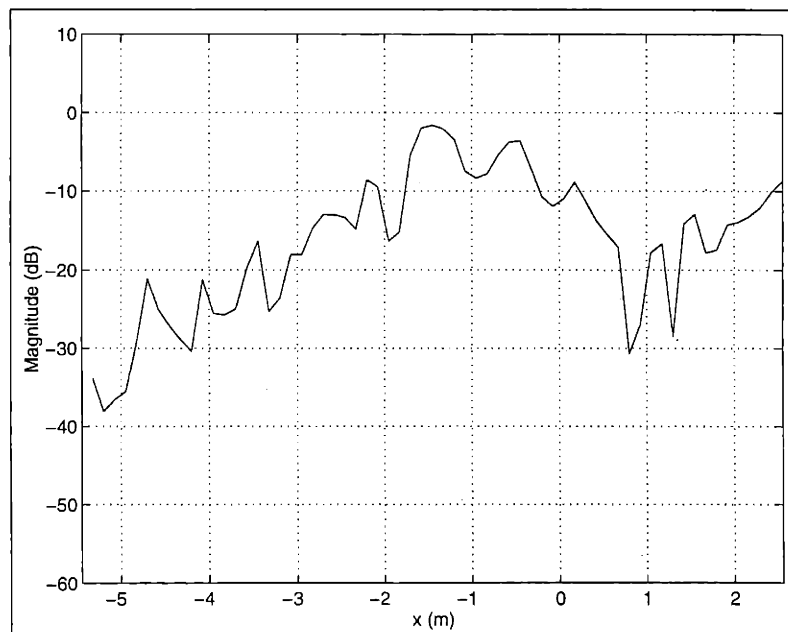
Figure 5.86: Cross-Section of Conventional SAR Image (at $y = 0.45m$) for First Synthetic-Motion Real-Target Example
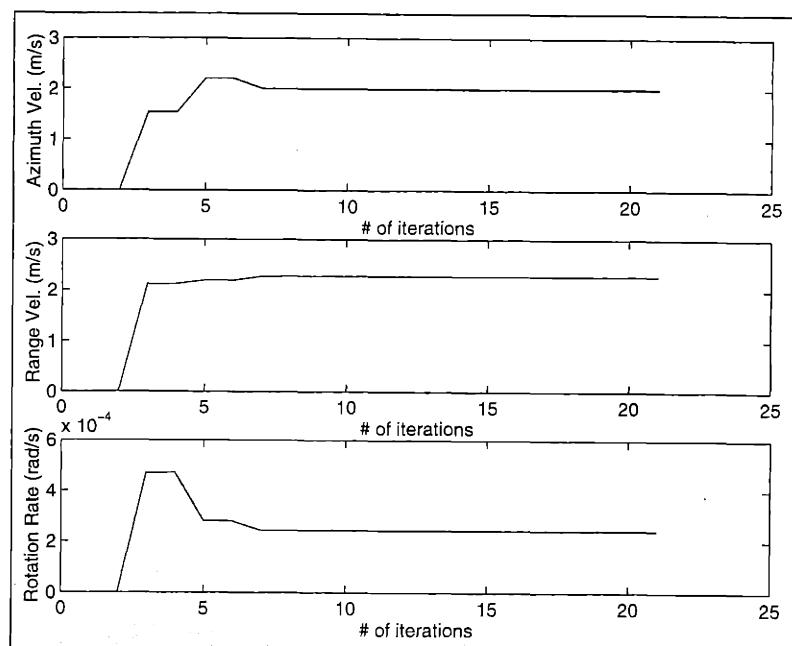
Figure 5.87: Estimated Target-Velocity Parameters for First Synthetic-Motion Real-Target Example using Full Rigid-Body Processing Algorithm
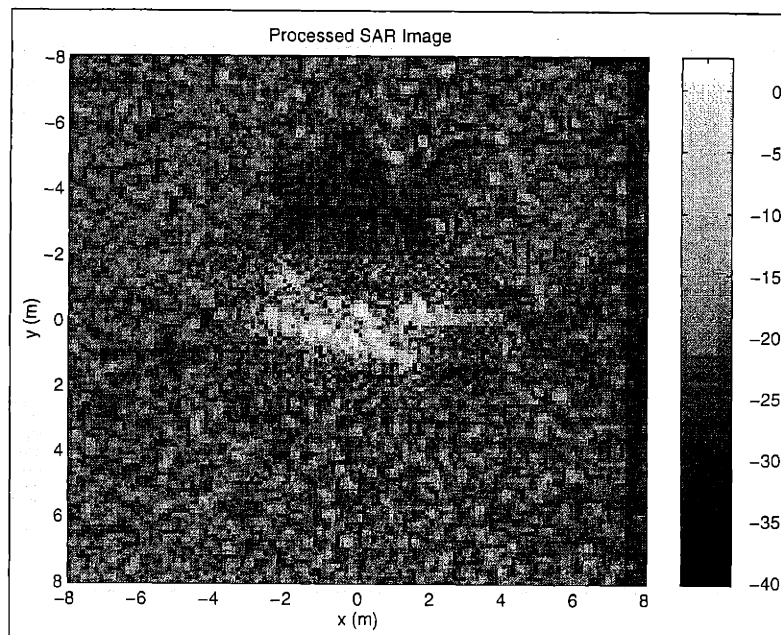
Figure 5.88: L_1 SAR Image for First Synthetic-Motion Real-Target Example using Full Rigid-Body Processing Algorithm (Before Azimuth Rescaling and Azimuth-Displacement Compensation)
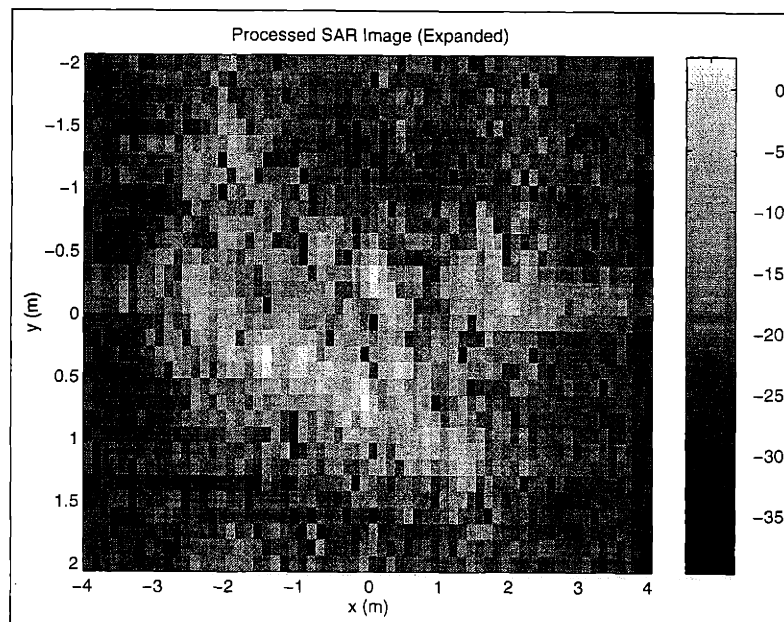
Figure 5.89: Target Region of L_1 SAR Image for First Synthetic-Motion Real-Target Example using Full Rigid-Body Processing Algorithm (Before Azimuth Rescaling and Azimuth-Displacement Compensation)
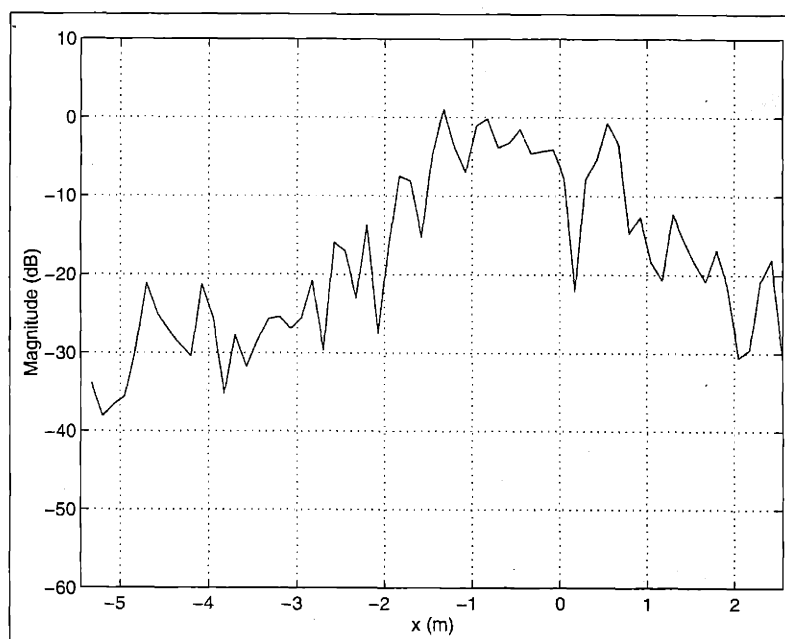
Figure 5.90: Cross-Section of L_1 SAR Image (at $y = 0.45m$) for First Synthetic-Motion Real-Target Example using Full Rigid-Body Processing Algorithm (Before Azimuth Rescaling and Azimuth-Displacement Compensation)
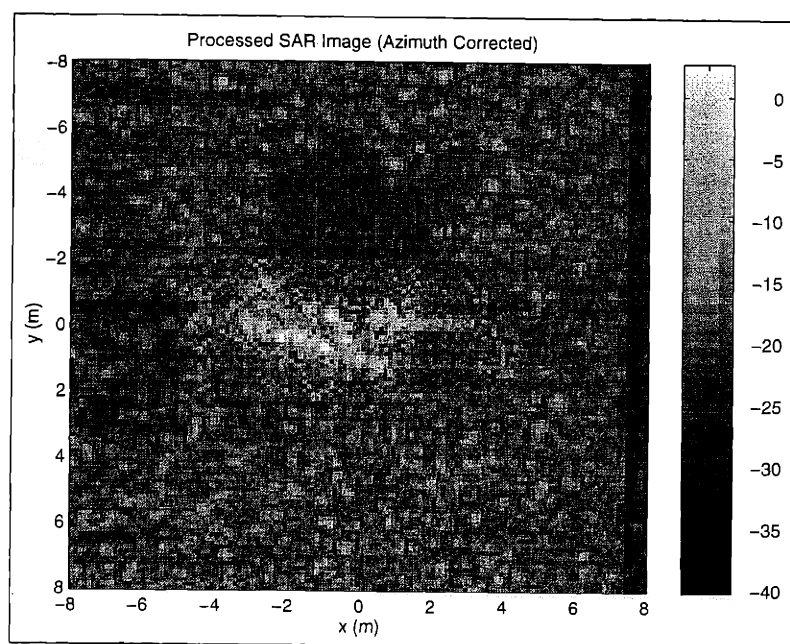
Figure 5.91: L_1 SAR Image for First Synthetic-Motion Real-Target Example using Full Rigid-Body Processing Algorithm (After Azimuth Rescaling and Azimuth-Displacement Compensation)
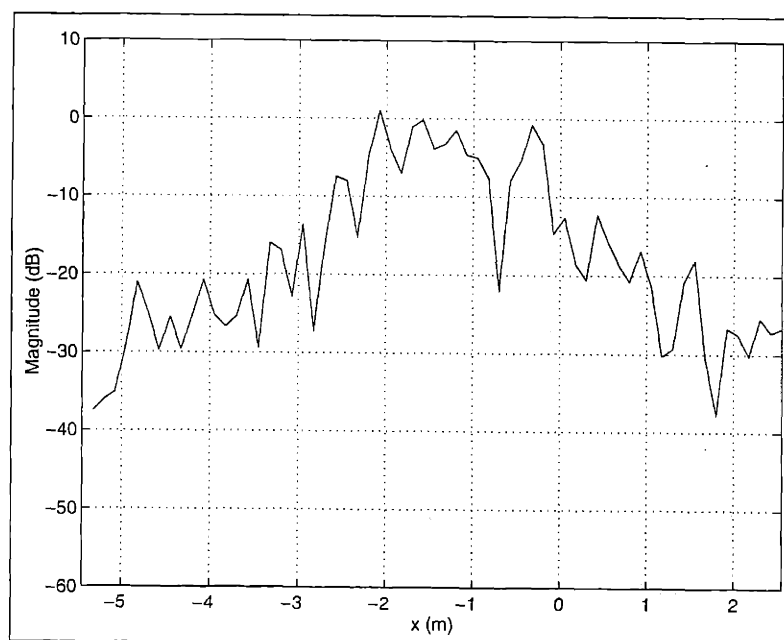
Figure 5.92: Cross-Section of L_1 SAR Image (at $y = 0.45m$) for First Synthetic-Motion Real-Target Example using Full Rigid-Body Processing Algorithm (After Azimuth Rescaling and Azimuth-Displacement Compensation)
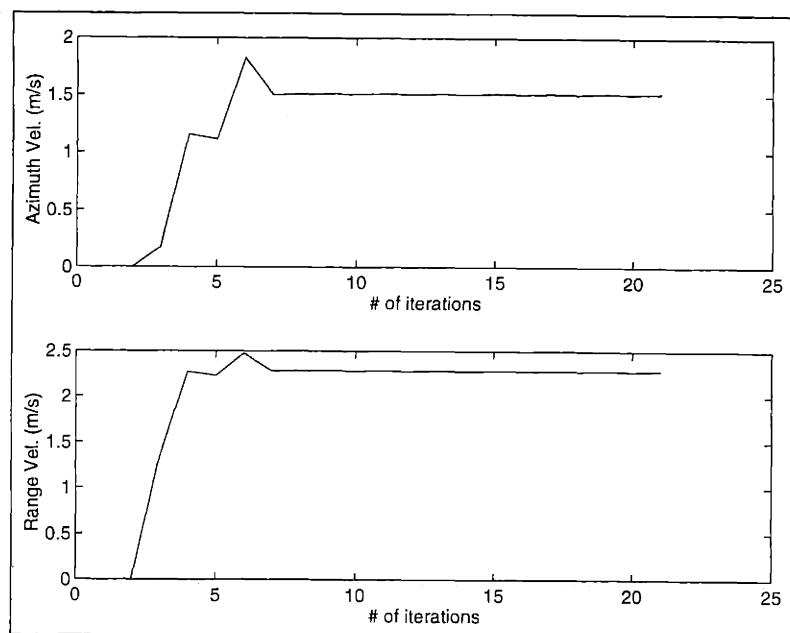
Figure 5.93: Estimated Target-Velocity Parameters for First Synthetic-Motion Real-Target Example using Purely-Translational Processing Algorithm
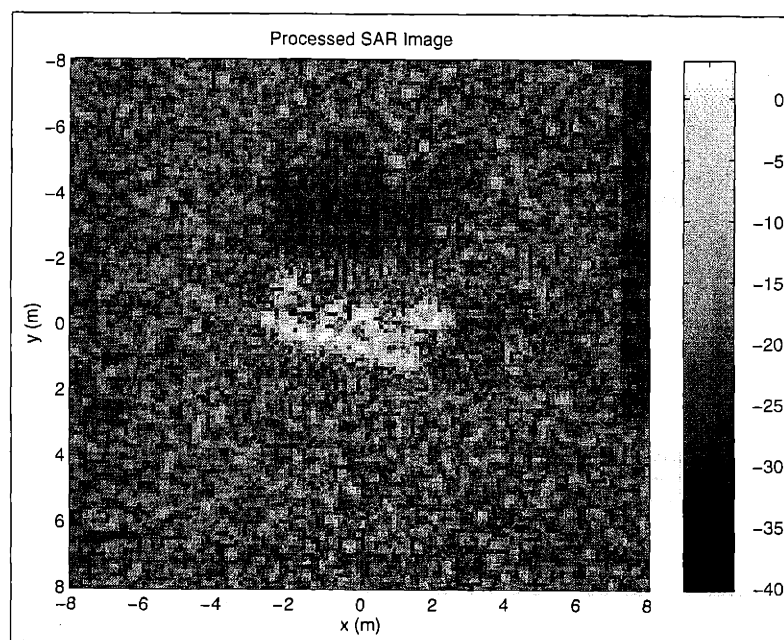
Figure 5.94: L_1 SAR Image for First Synthetic-Motion Real-Target Example using Purely-Translational Processing Algorithm (Before Azimuth-Displacement Compensation)
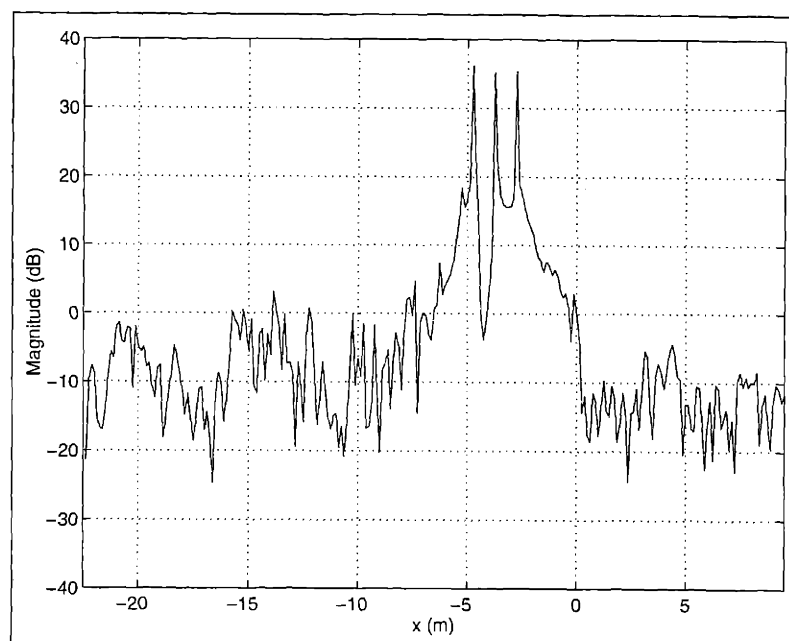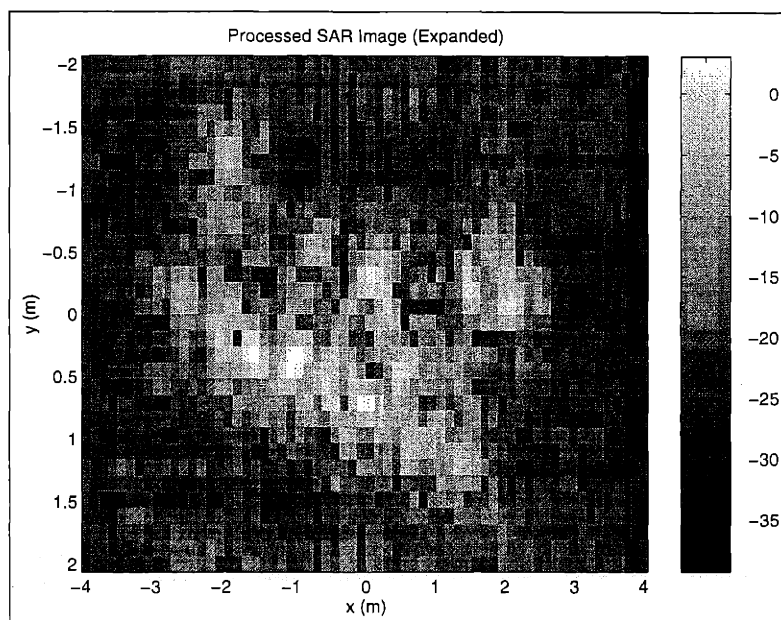
Figure 5.95: Target Region of L_1 SAR Image for First Synthetic-Motion Real-Target Example using Purely-Translational Processing Algorithm (Before Azimuth-Displacement Compensation)
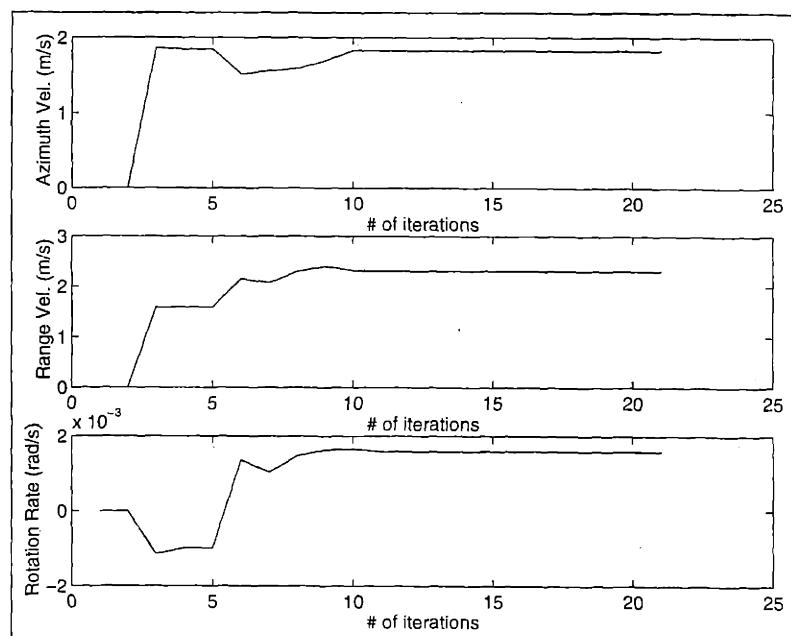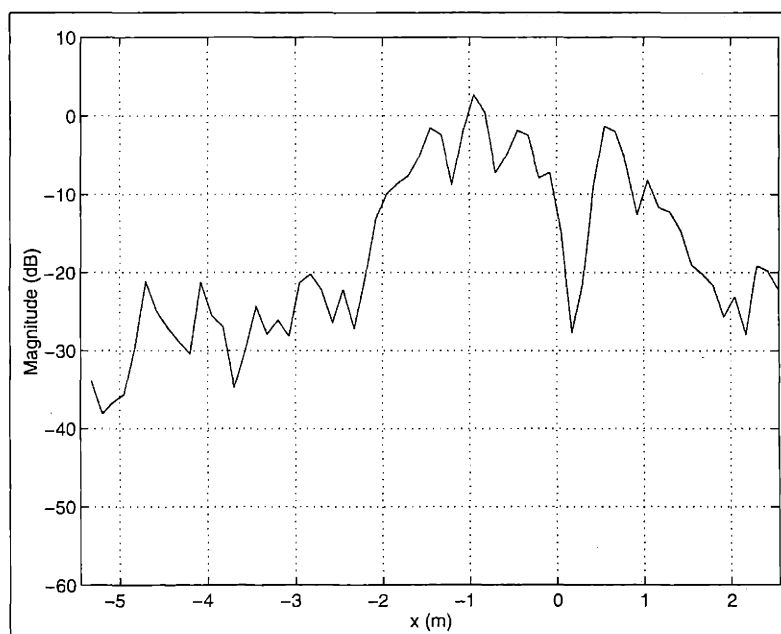

Figure 5.96: Cross-Section of L_1 SAR Image (at $y = 0.45m$) for First Synthetic-Motion Real-Target Example using Purely-Translational Processing Algorithm (Before Azimuth-Displacement Compensation)
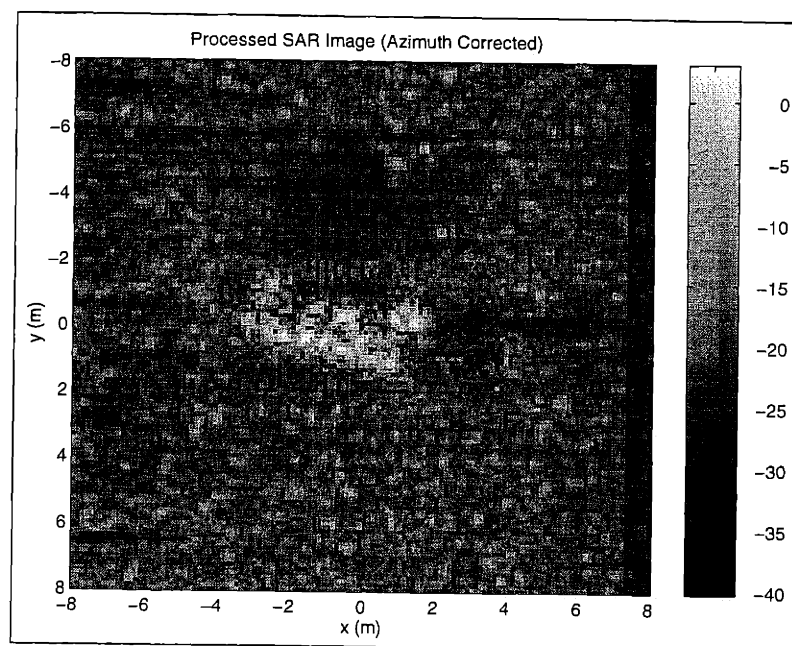
Figure 5.97: L_1 SAR Image for First Synthetic-Motion Real-Target Example using Purely-Translational Processing (After Azimuth-Displacement Compensation)
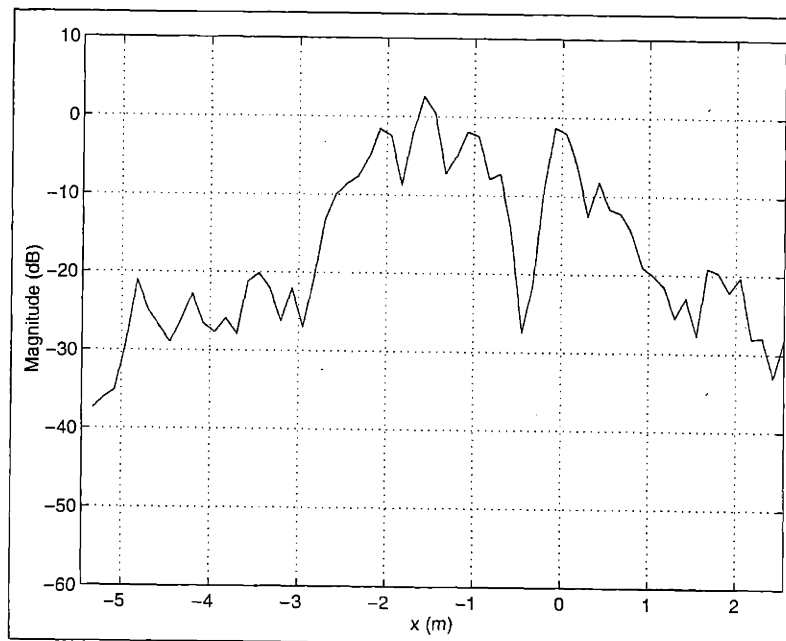
Figure 5.98: Cross-Section of L_1 SAR Image (at $y = 0.45m$) for First Synthetic-Motion Real-Target Example using Purely-Translational Processing (After Azimuth-Displacement Compensation)
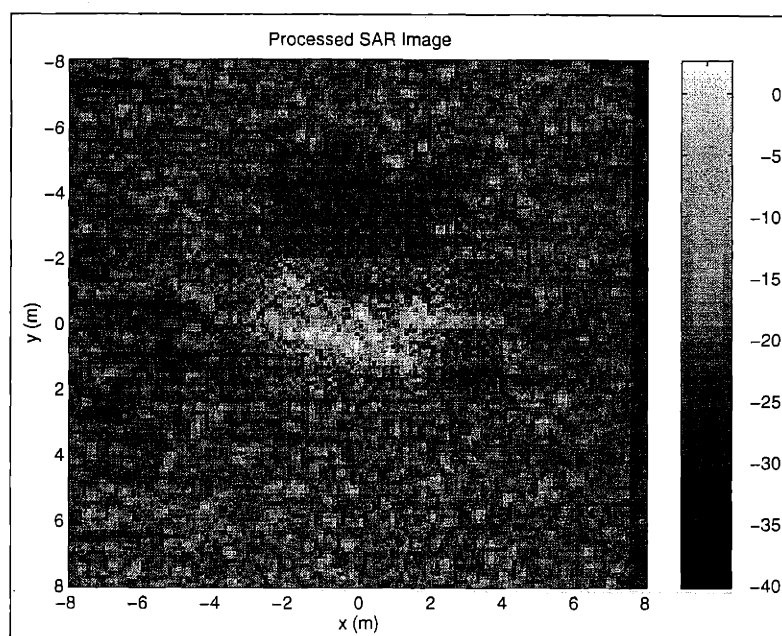
Figure 5.99: Exact-Velocity L_1 SAR Image for First Synthetic-Motion Real-Target Example using Full Rigid-Body Processing Algorithm (Before Azimuth Rescaling and Azimuth-Displacement Compensation)
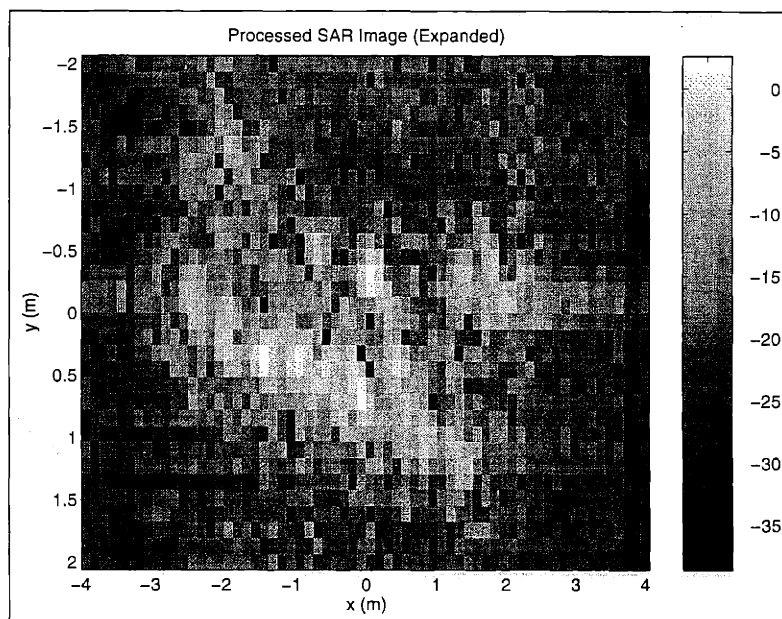
Figure 5.100: Target Region of Exact-Velocity L_1 SAR Image for First Synthetic-Motion Real-Target Example using Full Rigid-Body Processing Algorithm (Before Azimuth Rescaling and Azimuth-Displacement Compensation)
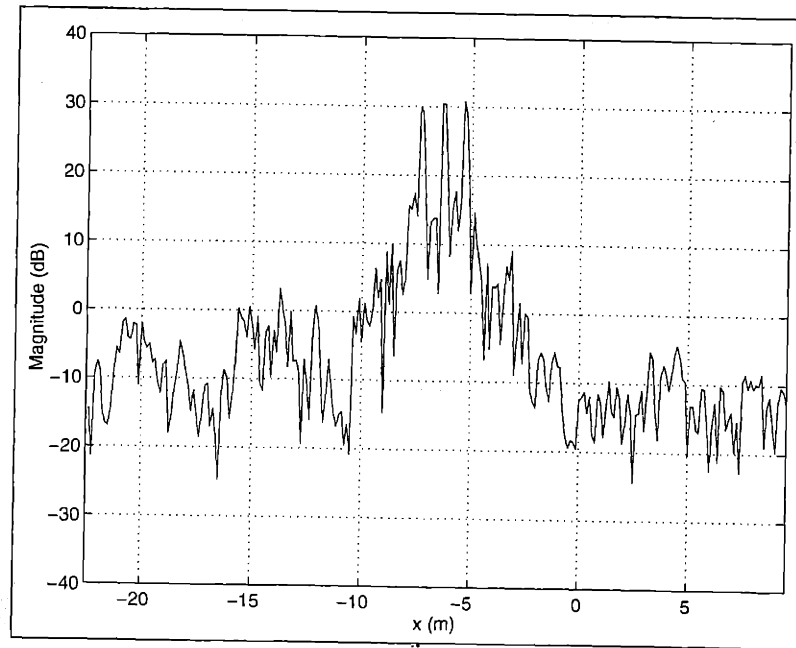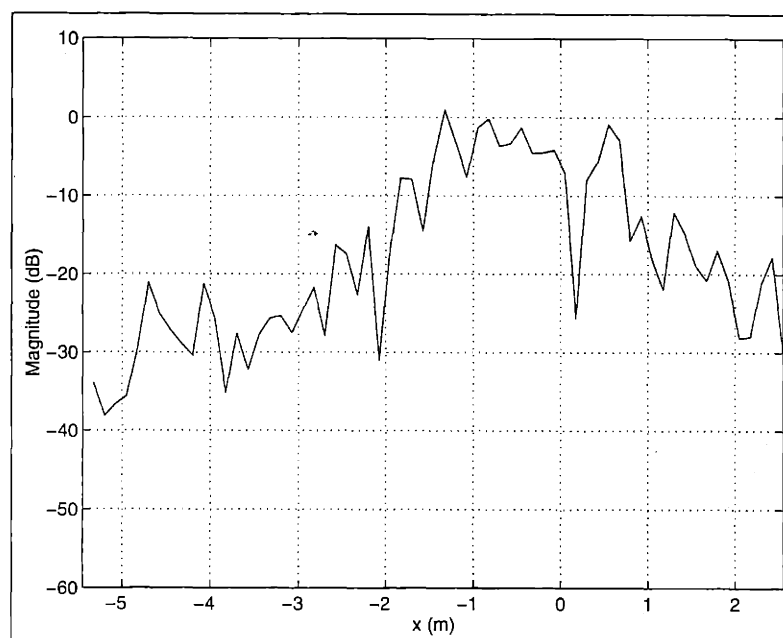
Figure 5.101: Cross-Section of Exact-Velocity L_1 SAR Image (at $y = 0.45m$) for First Synthetic-Motion Real-Target Example using Full Rigid-Body Processing Algorithm (Before Azimuth Rescaling and Azimuth-Displacement Compensation)

**Second Example: Translational and Rotational Motion (Positive Rotation)**

For the next synthetic-motion real-target example, we illustrate some of the effects of target rotation, just as with the third synthetic-target example presented in the previous section. We again have a translational target velocity of $(\dot{x}_{RB}, \dot{y}_{RB}) = (2m/s, 2.304m/s)$. However, we now have a *positive* target rotational rate equal to the SAR's look-angle rotational rate (i.e., $\dot{\psi}_{RB} = \dot{\theta} = 0.036rad/s$). Physically, this corresponds to the moving target rotating in the direction of negative "look" angle, which implies that the relative rotation rate between the target and the SAR platform is larger than $\dot{\theta}$. As shown in the conventional image of Figure 5.102, we again see that the target motion has seriously degraded the SAR image, as compared to the original stationary-target MSTAR image of Figure 5.79. Recall from Section 5.1.3 that the azimuth scaling of a rotating target is directly dependent upon the target rotation rate. For this case, the azimuth scale factor for the moving target is given by $1 + \dot{\psi}_{RB}/\dot{\theta} = 2$, which causes the target blur area to appear "spread out" in azimuth.

For the full rigid-body algorithm, we used an L_1 weighting of $\gamma_A = 1$ for estimating the velocity parameters. We assumed a rectangular target spatial region with an azimuth width of $16m$ and a range width of $4m$, centered at $(x, y) = (0m, 0m)$. Since we knew *a priori* that the rotating target was scaled in azimuth by a factor of two, we scaled the azimuth width of the target region of the full rigid-body algorithm by a corresponding factor of two (in comparison to the target region used in previous purely-translational motion example). For an actual SAR ATR system based upon this algorithm, the size and location of the assumed target spatial region would be determined by the size and location of the moving-target "blur" area in the conventional SAR image.

The results of the full rigid-body L_1-norm SAR processing algorithm are shown in Figures 5.105 through 5.110. For this example, we obtained velocity-parameter estimates of $(\hat{\dot{x}}_{RB}, \hat{\dot{y}}_{RB}, \hat{\dot{\psi}}_{RB}) = (1.97m/s, 2.19m/s, 0.037rad/s)$. As compared to the results of the full rigid-body algorithm for the previous purely-translational motion example, we see a relatively larger estimation error in the range velocity $\dot{y}_{RB}$. The focusing of the moving target in resulting SAR image of Figure 5.106 is still improved, in comparison to the conventional SAR image of Figure 5.102. However, this image does not appear to be as focused as the resulting full rigid-body SAR image for the previous purely-translational moving-target case in Figure 5.88. The target portion of the SAR image (i.e., the T-72 tank) is a scaled version of the target portion of the original MSTAR image of Figure 5.79, due to the rotation-rate dependent azimuthal scale factor $1 + \dot{\psi}_{RB}/\dot{\theta}$.

For the full rigid-body algorithm, the target portion of the resulting SAR image in Figure 5.106 exhibited "streaking" artifacts along the range direction y. As we will show later, these artifacts are caused by the presence of spatially-periodic "nulls" (with respect to the azimuth direction) between the target scatterers. An example of the effect of these nulls is shown in the azimuth cross-section of Figure 5.108. We will also show that the azimuth location of these nulls are highly spatially-correlated with respect to range. In addition, the scatterers from a "real" target (such as the T-72 tank) tend to be spatially-distributed (i.e., their amplitudes are spatially-correlated in both range and azimuth, as shown in the original MSTAR image of Figure 5.79). This implies that the amplitudes of the target scatterers between the nulls will also be correlated with respect to range. Therefore, the azimuth cross-sections (as a function of range) of any resulting SAR image will be correlated with

respect to range, thereby producing the streaking artifacts.

One hypothesis for the cause of the spatially-periodic nulls is the interaction between the rotation-rate dependent azimuthal scale factor $1 + \dot{\psi}_{RB}/\dot{\theta}$ and the azimuthal sampling interval Δ_x of the original conventional MSTAR image used to generate the SAR data. Later, we will discuss this hypothesis in more detail when we present the results produced by the full rigid-body algorithm when the velocity-parameters are known exactly.

The full rigid-body SAR image, (after azimuth-rescaling and azimuth-displacement compensation) is shown in Figure 5.109. The image of the T-72 moving target appears to have the correct scaling, though it is slightly blurred in comparison to the corresponding SAR image (shown in Figure 5.91) generated by this algorithm for the previous purely-translational motion example. However, we have an azimuth-displacement error of approximately $4m$, due to the range-velocity estimation-error. Note that the "streaking" artifacts exhibited in the uncompensated image of Figure 5.106 are no longer present. The azimuthal cross-section of the azimuth-compensated SAR image is shown in Figure 5.110. As with the previous purely-translational motion example, the azimuthal cross-section is similar to the azimuthal cross-section of the original MSTAR stationary image shown in Figure 5.81. However, the nulls between the "dominant" feature scatterers corresponding to the tank treads are not quite as pronounced. In addition, the spatially-periodic nulls with respect to the azimuth direction exhibited in the cross-section (shown in Figure 5.106) of the uncompensated image are no longer present in this cross-section.

We show the results of the purely-translational L_1-norm SAR processing algorithm in Figures 5.111 through 5.116. For this example, we used an L_1 weighting of $\gamma_A = 0.8$ for the velocity-parameter estimation. We assumed a rectangular target spatial region identical to the larger target region used by the full rigid-body algorithm for this experimental example (with an azimuth width of $16m$ and a range width of $4m$, centered at $(x, y) = (0m, 0m)$).

For this algorithm, we obtained velocity-parameter estimates of $(\hat{\dot{x}}_{RB}, \hat{\dot{y}}_{RB}) = (1.95m/s, 2.28m/s)$. We see that the purely-translational L_1-norm algorithm exhibits better estimation performance for these velocity parameters than the full rigid-body algorithm does for this example (even though the target is rotating). In fact, this algorithm exhibits better azimuth-velocity estimation performance for this example than it did for the previous purely-translational velocity experimental example. One hypothesis for this performance improvement is the increased azimuth spacing between the moving-target scatterers, due to the rotation-rate dependent azimuthal scale factor $1 + \dot{\psi}_{RB}/\dot{\theta}$ (which implies less cross-interference between these scatterers).

We see in Figure 5.112 that even with the target rotation, the purely-translational L_1-norm algorithm focuses the resulting SAR image almost as well as the full rigid-body L_1-norm algorithm did in Figure 5.106. However, the SAR image produced by the purely-translational algorithm exhibited streaking artifacts identical to the streaking artifacts exhibited by the SAR image produced by the full rigid-body algorithm. As with the full rigid-body SAR image, these artifacts are caused by the interaction between the range-correlated spatially-periodic "nulls" (with respect to the azimuth direction, as shown in the azimuth cross-section of Figure 5.114) and the spatially-distributed real-target scatterers. Recall that one hypothesis for the cause of these nulls is the interaction between the rotation-rate dependent azimuthal scale factor $1+\dot{\psi}_{RB}/\dot{\theta}$ and the azimuth sampling interval of the original conventional MSTAR image used to generate the SAR data. We will discuss

this hypothesis in more detail later when we present the exact-velocity results for the full rigid-body algorithm.

The SAR image produced by the purely-translational algorithm after azimuth displacement compensation is shown in Figure 5.115. In comparison to the compensated image produced by the full rigid-body algorithm in Figure 5.109, we see a smaller azimuth-displacement error (of approximately $1m$), due to a smaller range-velocity estimation-error. However, unlike the compensated full rigid-body image, the "streaking" artifacts are still present, since the image could not be rescaled in azimuth by this algorithm.

As with the previous purely-translational motion example, we include results produced by the minimization of the standard least-squares cost function $J(\mathbf{A}, \hat{\mathbf{v}}) = ||\mathbf{f} - \mathbf{F}(\hat{\mathbf{v}})\mathbf{A}||_2^2$ of the full rigid-body algorithm when the velocity parameters $\hat{\mathbf{v}}$ are known *exactly* (in order to illustrate the effects of velocity-parameter estimation-error upon the images produced by this algorithm). As shown in Figure 5.117, we see that the target portion of the SAR image (before azimuth compensation) is a scaled version of the target portion of the original MSTAR image of Figure 5.79, due to the rotation-rate dependent azimuth scale factor. However, this image is better focused (as would be expected) than the images produced with estimated velocity parameters by either the full rigid-body algorithm (in Figure 5.106) or the purely-translational algorithm (in Figure 5.112). The streaking artifacts along the range direction y are still apparent in the exact-velocity full rigid-body image. Recall that these artifacts are caused by the interaction of the range-correlated spatially-periodic nulls (with respect to the azimuth direction, as shown in the azimuthal cross-section of Figure 5.119) with the spatially-distributed real-target scatterers. We will discuss the cause of these nulls in more detail shortly.

After we perform the azimuth-rescaling (according to the exact target rotation rate), we see that the resulting SAR image in Figure 5.120 is better focused than the corresponding azimuth-rescaled full rigid-body SAR image of Figure 5.109 (produced using estimated velocity parameters). The streaking artifacts due to the spatially-periodic nulls have again disappeared. As shown in the azimuthal cross-section of Figure 5.121 the nulls between the feature scatterers corresponding to the tank treads are more pronounced, in comparison to the azimuthal cross-section of the azimuth-rescaled full rigid-body SAR image in Figure 5.110.

As stated previously, the uncompensated exact-velocity SAR image produced by the full-rigid body algorithm (shown in Figure 5.120) exhibited significant streaking artifacts in the range direction (as well as the corresponding full rigid-body SAR image produced using estimated velocity-parameters, shown in Figure 5.109). These artifacts are caused by the interaction of range-correlated spatially-periodic "nulls" in the SAR image (with respect to the azimuth direction, as shown in the cross-section of Figure 5.121) with the spatially-distributed real-target scatterers. Recall that one hypothesis for the cause of these nulls is the interaction between the rotation-rate dependent azimuthal scale factor $1 + \dot{\psi}_{RB}/\dot{\theta}$ and the azimuth image sampling-interval Δ_x of the original conventional MSTAR image used to generate the SAR data. Here, we present this hypothesis in more detail.

Let $A[n'_x, n'_y]$ (where $\{n'_x, n'_y\} \in$ Target) represent the (focused) target region of the conventional MSTAR image used to generate the moving-target SAR data. This target region is essentially assumed to consist of a $2 - D$ array of ideal point-scatterers with initial positions at $(\Delta_x n'_x, \Delta_y n'_y)$, where Δ_x and Δ_y are the azimuth and range image sampling-

intervals of the conventional MSTAR image. For a "small" look-angle rotation-rate $\dot{\theta}$, recall from Section 5.1.4 that the noiseless SAR data set $f[n,k]$ for a rigid-body moving-target (with *known* velocity-parameters, $\dot{x}_{RB}$, $\dot{y}_{RB}$, and $\dot{\psi}_{RB}$) is approximately given by

$$f[n,k] \approx$$

$$\sum_{n'_x} \sum_{n'_y} A[n'_x, n'_y] \, e^{j\frac{4\pi}{\lambda_c}\left[(\dot{\theta}+\dot{\psi}_{RB})\left(\frac{Tk}{K}\right)\Delta_x n'_x\right]} \, e^{-j\frac{4\pi}{\lambda_c}\left[\frac{\alpha T_p}{f_c}\frac{n}{N}\Delta_y n'_y\right]} \, e^{j\left[\phi_{\dot{x}}[n,k]\dot{x}_{RB}+\phi_{\dot{y}}[n,k]\dot{y}_{RB}\right]}$$

$$\approx \sum_{n'_x} \sum_{n'_y} A[n'_x, n'_y] \, e^{j\,k\Delta\omega_x\left(1+\frac{\dot{\psi}_{RB}}{\dot{\theta}}\right)\Delta_x n'_x} \, e^{-j\,n\Delta\omega_y\Delta_y n'_y} \, e^{j\left[\phi_{\dot{x}}[n,k]\dot{x}_{RB}+\phi_{\dot{y}}[n,k]\dot{y}_{RB}\right]} \ .$$

$$-\frac{N}{2} \le n \le \frac{N}{2} \qquad -K \le k \le K$$

$$(5.78)$$

In this expression, the discrete spatial frequencies $(k\Delta\omega_x, n\Delta\omega_y)$ are given by

$$k\Delta\omega_x = \frac{4\pi\dot{\theta}t_T[k]}{\lambda_c} = \frac{4\pi\dot{\theta}}{\lambda_c}\left[\frac{k(2T)}{2K}\right] \tag{5.79}$$

$$n\Delta\omega_y = \frac{4\pi}{\lambda_c}\left[\frac{\alpha T_p}{f_c}\frac{\hat{t}[n]}{T_p}\right] = \frac{4\pi\alpha\hat{t}[n]}{c} = \frac{4\pi\alpha}{c}\left[\frac{nT_p}{N}\right] \ . \tag{5.80}$$

We see that the exact-velocity SAR data set is essentially a scaled Fourier Transform of the imaged target field reflectivity (distorted by a translational-velocity dependent nonlinear complex phase term).

Recall from Section 5.1.4 that if $\mathbf{v}_o$ is the vector of known velocity parameters, the exact-velocity SAR data is given in matrix notation by $\mathbf{f} = \mathbf{F}(\mathbf{v}_o)\mathbf{A}$. This implies that the maximum-likelihood estimate $\hat{\mathbf{A}}$ (which minimizes the standard least-squares cost function $J(\mathbf{A}, \mathbf{v}_o) = ||\mathbf{f} - \mathbf{F}(\mathbf{v}_o)\mathbf{A}||_2^2$), is approximately given by the following expression

$$\hat{\mathbf{A}} = \left(\mathbf{F}^H(\mathbf{v}_o)\mathbf{F}(\mathbf{v}_o)\right)^{-1}\mathbf{F}^H(\mathbf{v}_o)\mathbf{f}$$

$$\approx \mathbf{F}^H(\mathbf{v}_o)\mathbf{f} \ . \tag{5.81}$$

In other words, for known velocity parameters, $\dot{x}_{RB}$, $\dot{y}_{RB}$, and $\dot{\psi}_{RB}$, the approximation to the maximum-likelihood SAR image (*before azimuth-rescaling*) $\hat{A}_U[n_x, n_y]$ is given by the following convolution of the conventional MSTAR image $A[n'_x, n'_y]$ with a scaled sampled 2-D sinc function (where the spatial sampling intervals are given by Δ_x and Δ_y)

$$\hat{A}_U[n_x, n_y] = \frac{1}{(2K)(N)} \sum_{k=-K}^{K} \sum_{n=-\frac{N}{2}}^{\frac{N}{2}} f[n,k] e^{-j\left[\phi_{\dot{x}}[n,k]\dot{x}_{RB}+\phi_{\dot{y}}[n,k]\dot{y}_{RB}\right]}$$

$$\times \, e^{-j\,k\Delta\omega_x\Delta_x n_x} \, e^{j\,n\Delta\omega_y\Delta_y n_y}$$

$$\approx \sum_{n'_x} \sum_{n'_y} A[n'_x, n'_y]\text{sinc}\left(\frac{2K\Delta\omega_x\Delta_x\left(n_x - \left(1+\frac{\dot{\psi}_{RB}}{\dot{\theta}}\right)n'_x\right)}{2}\right)\text{sinc}\left(\frac{N\Delta\omega_y\Delta_y(n_y - n'_y)}{2}\right) \ .$$

$$(5.82)$$

Essentially, this expression is equivalent to first removing the translational-velocity dependent nonlinear phase from the SAR data, then performing a scaled Fourier transform. If we include the "linear" portion of the phase function $\phi_{\tilde{y}}[n, k]$ (which was discussed in Section 5.1.3) in this calculation, we implicitly perform the compensation for the range-velocity induced azimuth-displacement.

For the MSTAR image used for the results of this chapter, the spatial sampling intervals Δ_x and Δ_y were chosen to be one-half the respective inherent spatial resolutions δ_x and δ_y of the conventional SAR imaging system. Recall from Chapter 3 that these spatial resolutions were given by

$$\delta_x = 2 \frac{\pi}{\left(\frac{2K\Delta\omega_x}{2}\right)} = \frac{\lambda_c}{2\dot{\theta}T} \tag{5.83}$$

$$\delta_y = 2 \frac{\pi}{\left(\frac{N\Delta\omega_y}{2}\right)} = \frac{c}{\alpha T_p} . \tag{5.84}$$

This implies that the approximation (before azimuth-rescaling) $\hat{A}_U[n_x, n_y]$ to the exact-velocity maximum-likelihood SAR image is given by

$$\hat{A}_U[n_x, n_y] \quad = \sum_{n'_x} \sum_{n'_y} A[n'_x, n'_y]\text{sinc} \left(\frac{2\pi\Delta_x \left(n_x - \left(1 + \frac{\dot{\psi}_{RB}}{\theta}\right) n'_x \right)}{\delta_x} \right) \text{sinc} \left(\frac{2\pi\Delta_y(n_y - n'_y)}{\delta_y} \right)$$

$$= \sum_{n'_x} \sum_{n'_y} A[n'_x, n'_y]\text{sinc} \left(\pi \left(n_x - \left(1 + \frac{\dot{\psi}_{RB}}{\dot{\theta}}\right) n'_x \right) \right) \text{sinc} \left(\pi(n_y - n'_y) \right) . \tag{5.85}$$

Since the variables n_x, n_y, n'_x, and n'_y are integer-valued, the unscaled SAR image can be simplified further to

$$\hat{A}_U[n_x, n_y] \approx \begin{cases} A[n'_x, n'_y] & \left| n_x - \left(1 + \frac{\dot{\psi}_{RB}}{\theta}\right) n'_x \right| \leq \frac{1}{2}, \quad \left| n_y - n'_y \right| \leq \frac{1}{2}, \\ & \{n'_x, n'_y\} \in \text{Target} \\ \\ 0 & \text{otherwise} \end{cases} . \tag{5.86}$$

For an azimuthal scale factor $1 + \dot{\psi}_{RB}/\dot{\theta}$ greater than unity (i.e., positive rotation), this expression implies that *the target region of the unscaled SAR image will exhibit spatially-periodic nulls in azimuth with an approximate period of* $(1 + \dot{\psi}_{RB}/\dot{\theta})\Delta_x$ *meters*. We also see that the spatial location of these nulls is not a function of the discrete-valued range-sampling variable n_y, which implies that *these locations will be highly-correlated with respect to the range direction*.

Another implication of this result is that if we estimate the period of these nulls (from the SAR image) we can then estimate the target rotation rate. However, for a real moving-target which is actually physically rotating (rather than the synthetic-motion real target used for this example), the spatially-periodic nulls may not necessarily be as clearly-defined in the SAR image, which implies that it may be difficult to estimate this period. However,

if we have a SAR image of the target when it is stationary, we can estimate the rotation rate by comparing the relative scaling in azimuth.

For this example, the positive target rotation-rate $\dot{\psi}_{RB}$ was equal to the SAR system's look-angle rotation-rate $\dot{\theta}$. This gave an azimuthal scale factor of $1+\dot{\psi}_{RB}/\dot{\theta} = 2$. Recall that the assumed azimuth sampling interval Δ_x of the MSTAR image was equal to $0.125m$. This implies that the exact-velocity SAR image (before azimuth rescaling) for the full rigid-body algorithm will exhibit spatially-periodic nulls in azimuth with a period of approximately $(1 + \dot{\psi}_{RB}/\dot{\theta})\Delta_x = 0.25m$. This indeed is the case, as shown by both the uncompensated exact-velocity SAR image of Figure 5.117 (where we see that the streaking artifacts are separated in azimuth by about $0.25m$) and the azimuthal cross-section of Figure 5.119. In addition, we see that the streaking artifacts in the uncompensated full rigid-body SAR image of Figure 5.106 (computed with estimated velocity-parameters) also had an approximate azimuth separation of $0.25m$ (as well as the streaking artifacts in the uncompensated SAR image of Figure 5.112, computed with the purely-translational algorithm).
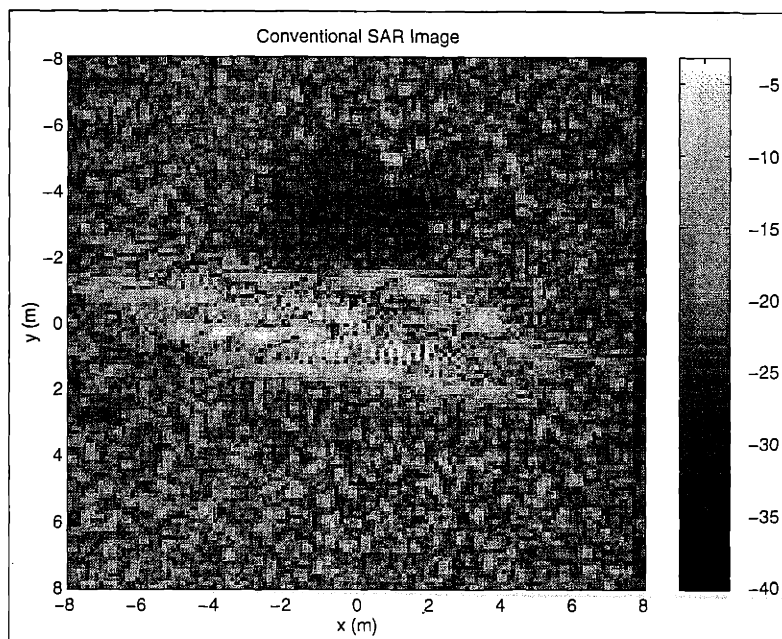
Figure 5.102: Conventional SAR Image for Second Synthetic-Motion Real-Target Example
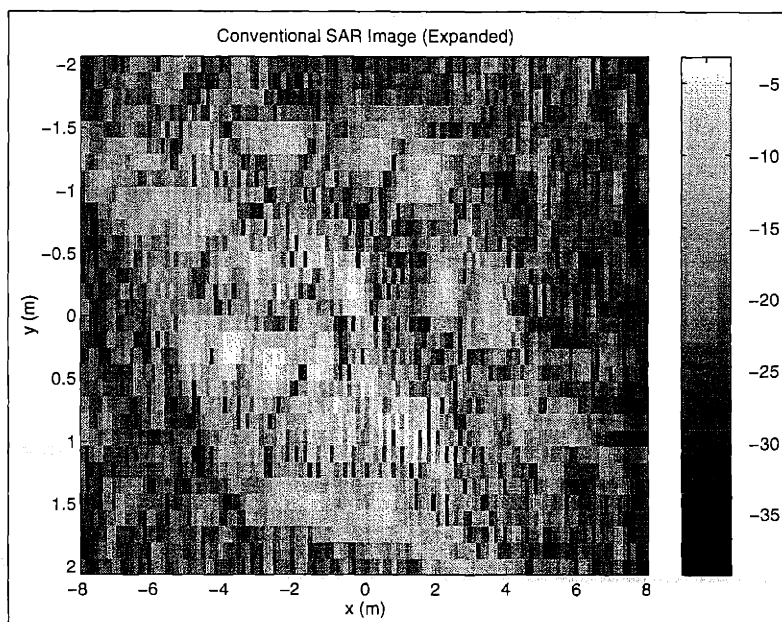
Figure 5.103: Target Region of Conventional SAR Image for Second Synthetic-Motion Real-Target Example
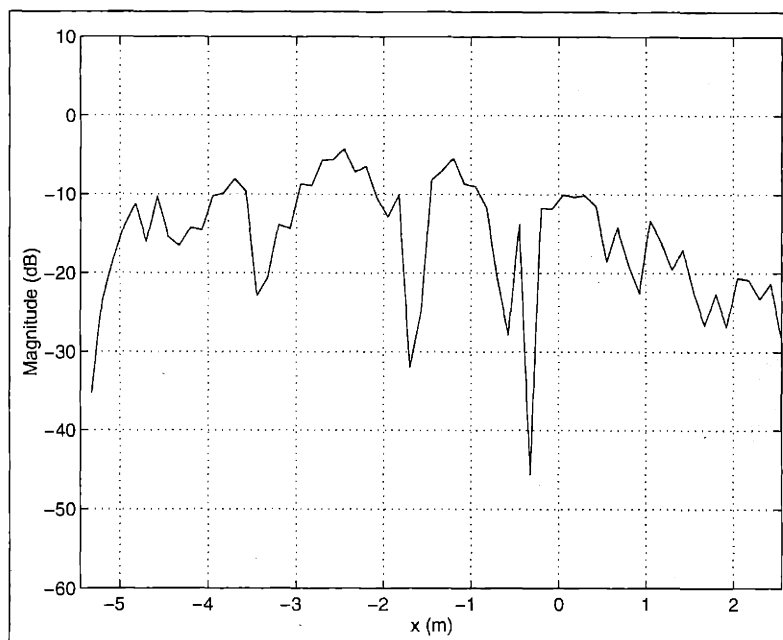
Figure 5.104: Cross-Section of Conventional SAR Image (at $y = 0.45m$) for Second Synthetic-Motion Real-Target Example
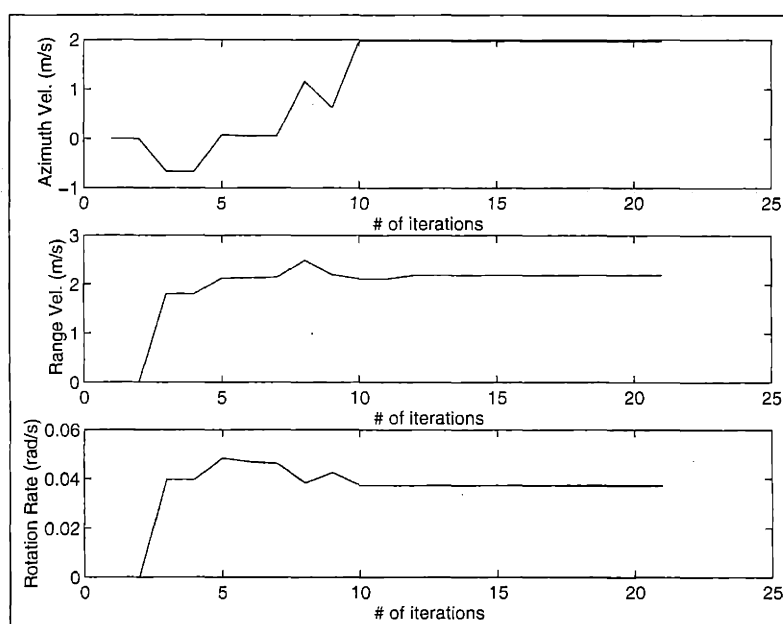
Figure 5.105: Estimated Target-Velocity Parameters for Second Synthetic-Motion Real-Target Example using Full Rigid-Body Processing Algorithm
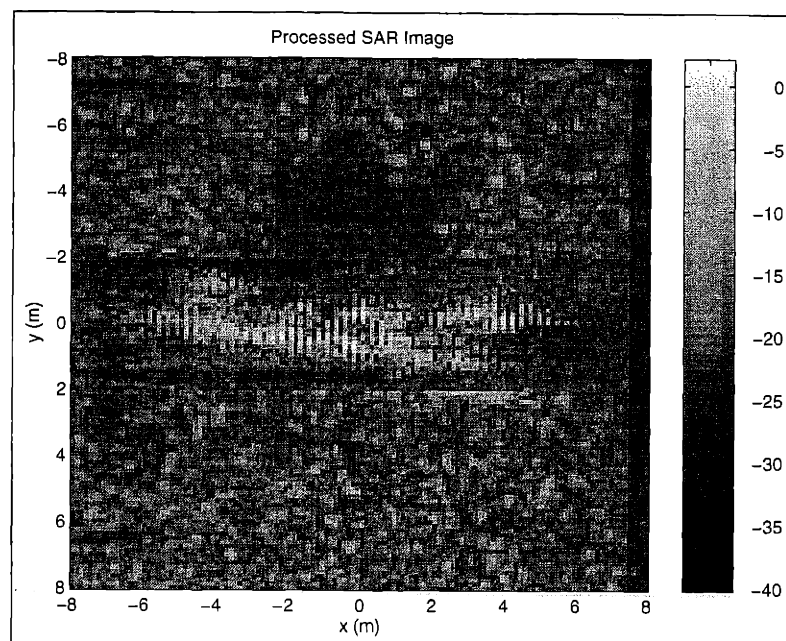
Figure 5.106: L_1 SAR Image for Second Synthetic-Motion Real-Target Example using Full Rigid-Body Processing Algorithm (Before Azimuth Rescaling and Azimuth-Displacement Compensation)
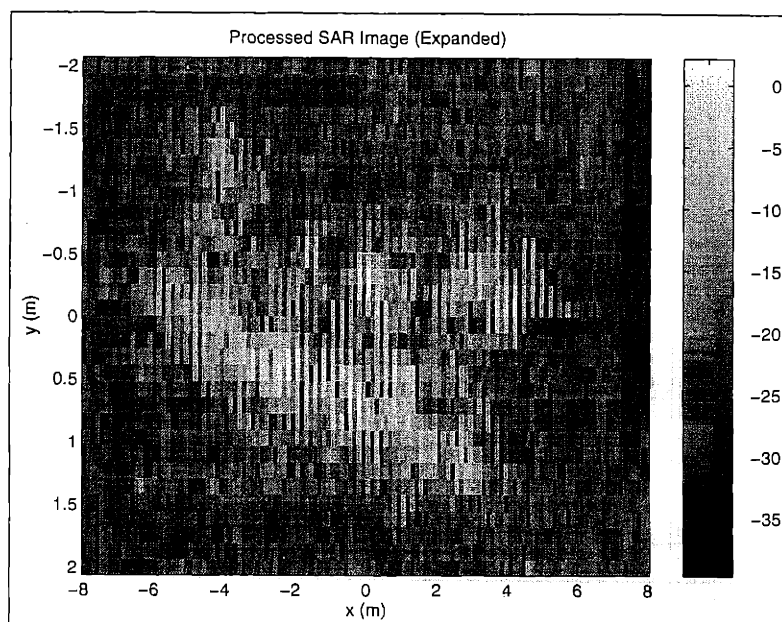
Figure 5.107: Target Region of L_1 SAR Image for Second Synthetic-Motion Real-Target Example using Full Rigid-Body Processing Algorithm (Before Azimuth Rescaling and Azimuth-Displacement Compensation)
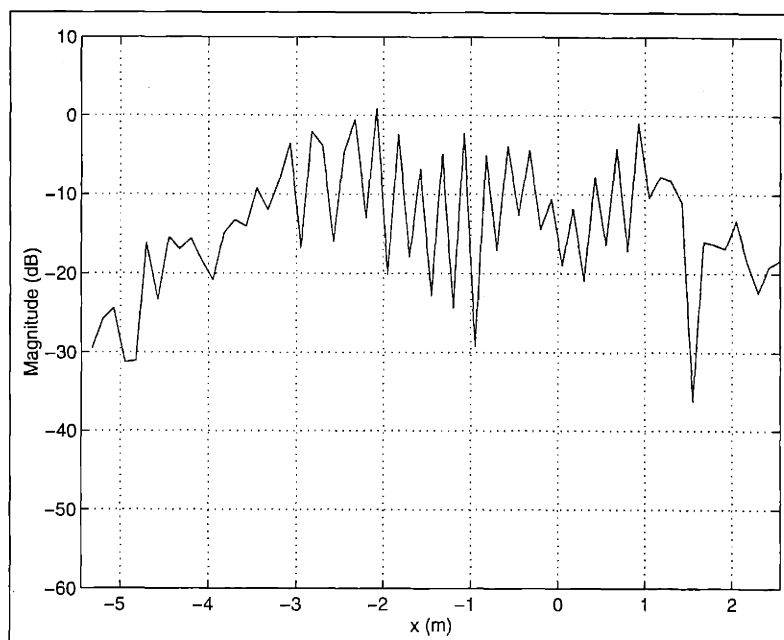
Figure 5.108: Cross-Section of L_1 SAR Image (at $y = 0.45m$) for Second Synthetic-Motion Real-Target Example using Full Rigid-Body Processing Algorithm (Before Azimuth Rescaling and Azimuth-Displacement Compensation)
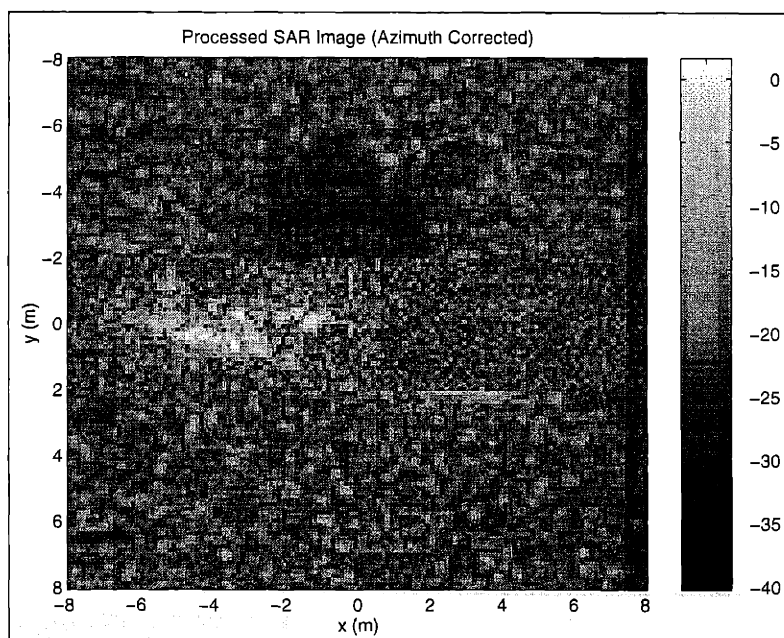
Figure 5.109: L_1 SAR Image for Second Synthetic-Motion Real-Target Example using Full Rigid-Body Processing Algorithm (After Azimuth Rescaling and Azimuth-Displacement Compensation)
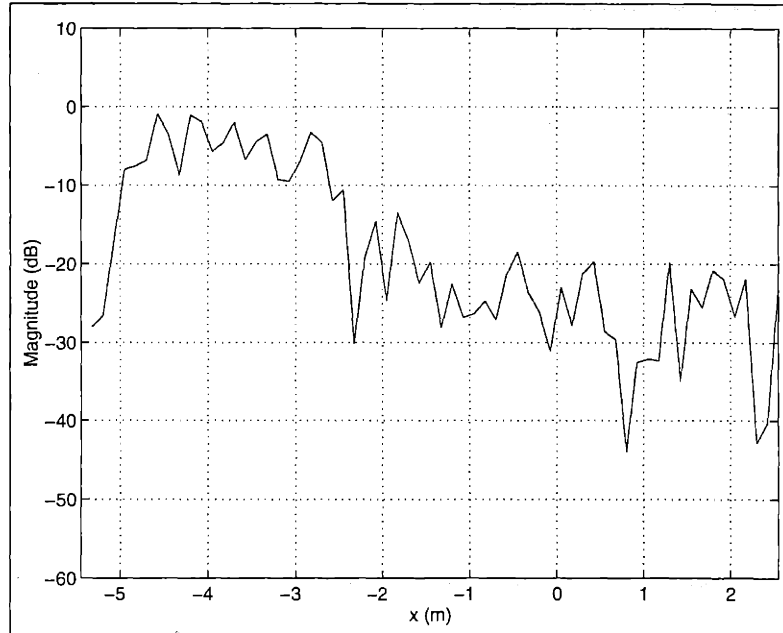
Figure 5.110: Cross-Section of L_1 SAR Image (at $y = 0.45m$) for Second Synthetic-Motion Real-Target Example using Full Rigid-Body Processing Algorithm (After Azimuth Rescaling and Azimuth-Displacement Compensation)
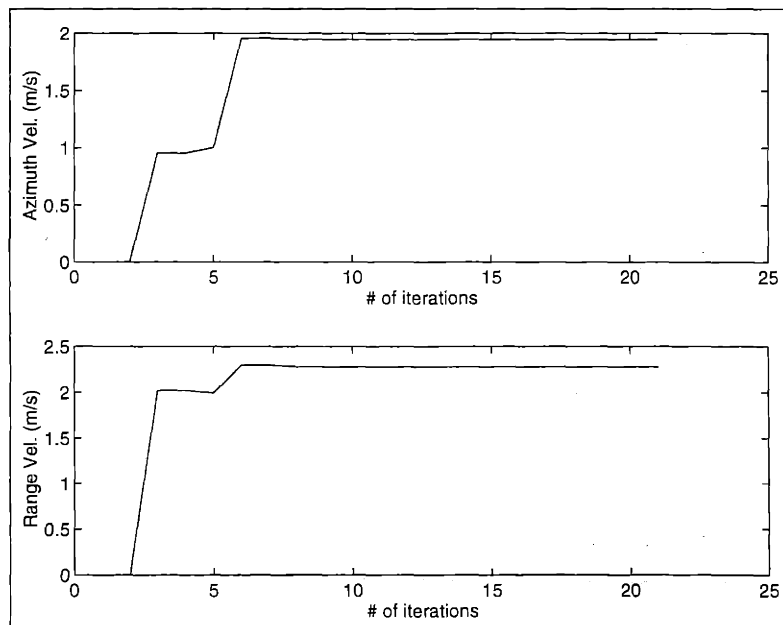
Figure 5.111: Estimated Target-Velocity Parameters for Second Synthetic-Motion Real-Target Example using Purely-Translational Processing Algorithm
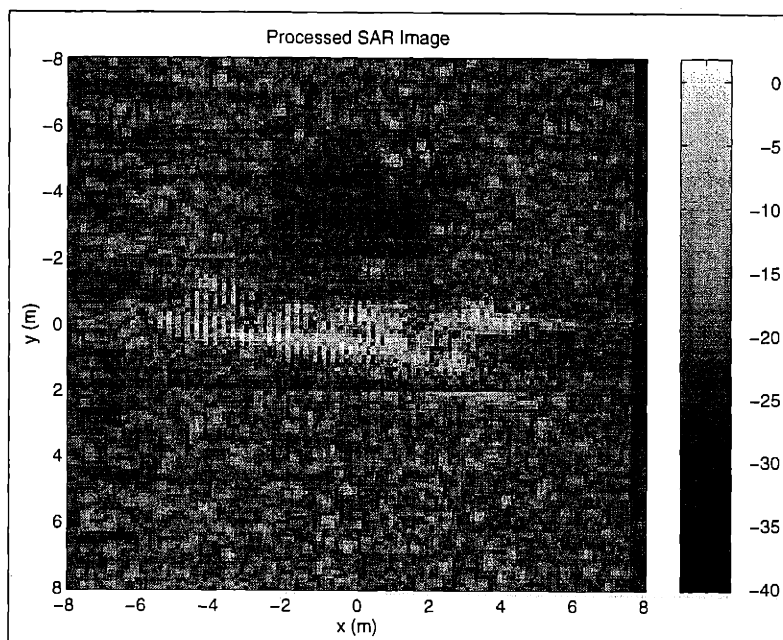
Figure 5.112: L_1 SAR Image for Second Synthetic-Motion Real-Target Example using Purely-Translational Processing Algorithm (Before Azimuth-Displacement Compensation)
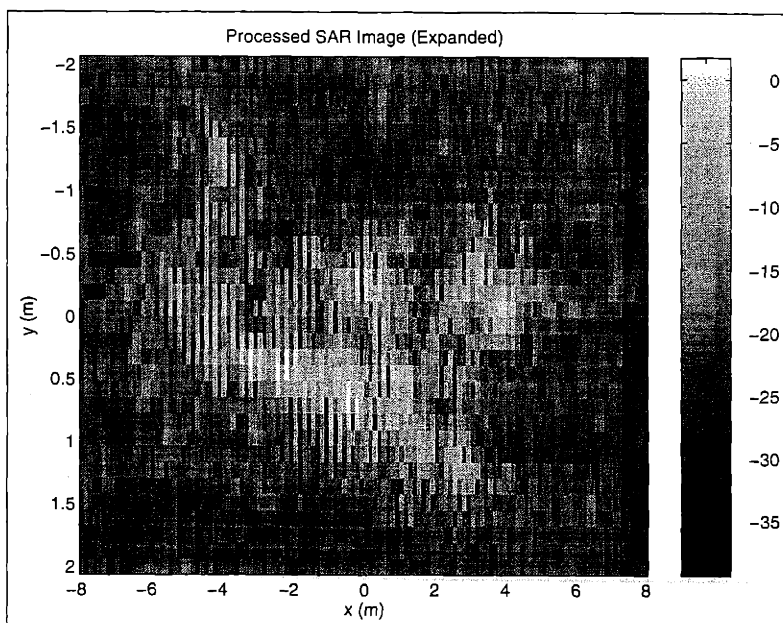
Figure 5.113: Target Region of L_1 SAR Image for Second Synthetic-Motion Real-Target Example using Purely-Translational Processing Algorithm (Before Azimuth-Displacement Compensation)
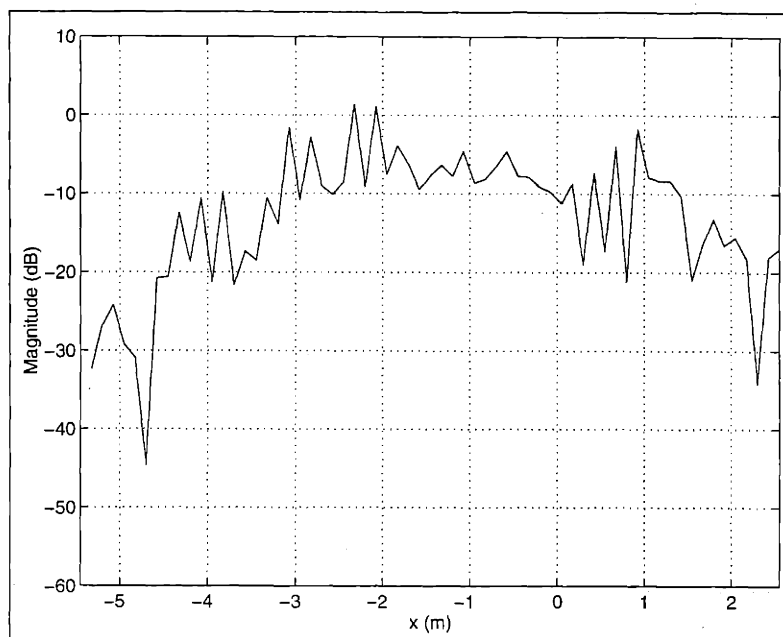
Figure 5.114: Cross-Section of L_1 SAR Image (at $y = 0.45m$) for Second Synthetic-Motion Real-Target Example using Purely-Translational Processing Algorithm (Before Azimuth-Displacement Compensation)
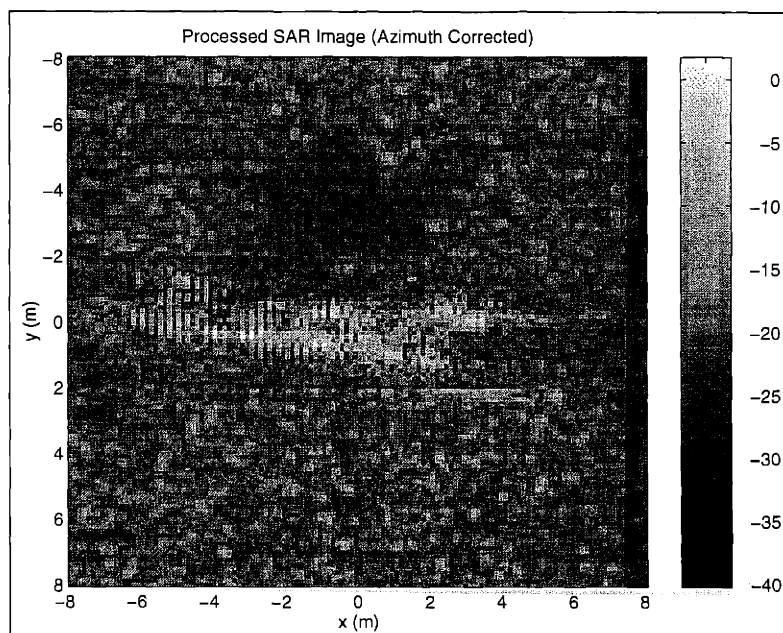
Figure 5.115: L_1 SAR Image for Second Synthetic-Motion Real-Target Example using Purely-Translational Processing (After Azimuth-Displacement Compensation)
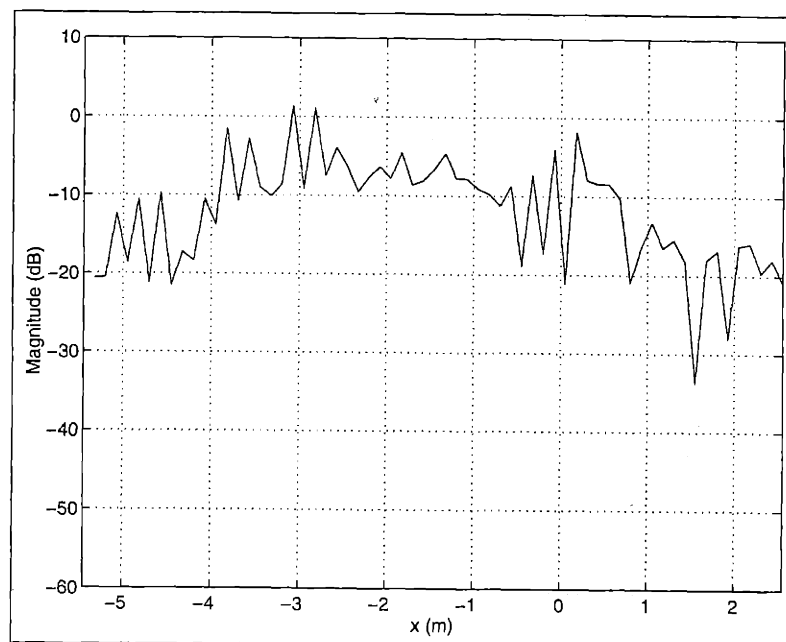
Figure 5.116: Cross-Section of L_1 SAR Image (at $y = 0.45m$) for Second Synthetic-Motion Real-Target Example using Purely-Translational Processing (After Azimuth-Displacement Compensation)

Figure 5.117: Exact-Velocity L_1 SAR Image for Second Synthetic-Motion Real-Target Example using Full Rigid-Body Processing Algorithm (Before Azimuth Rescaling and Azimuth-Displacement Compensation)

Figure 5.118: Target Region of Exact-Velocity L_1 SAR Image for Second Synthetic-Motion Real-Target Example using Full Rigid-Body Processing Algorithm (Before Azimuth Rescaling and Azimuth-Displacement Compensation)

Figure 5.119: Cross-Section of Exact-Velocity L_1 SAR Image (at $y = 0.45m$) for Second Synthetic-Motion Real-Target Example using Full Rigid-Body Processing Algorithm (Before Azimuth Rescaling and Azimuth-Displacement Compensation)

Figure 5.120: Exact-Velocity L_1 SAR Image for Second Synthetic-Motion Real-Target Example using Full Rigid-Body Processing Algorithm (After Azimuth Rescaling and Azimuth-Displacement Compensation
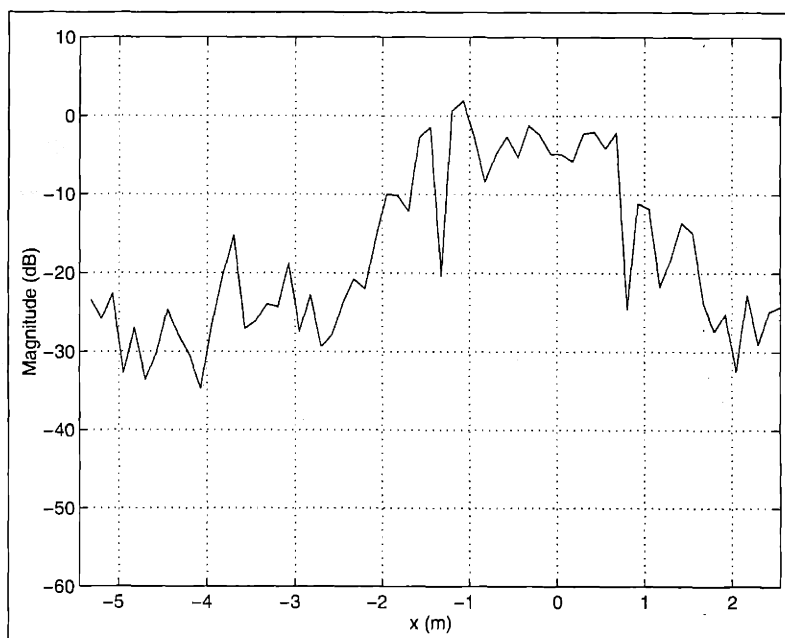
Figure 5.121: Cross-Section of Exact-Velocity L_1 SAR Image (at $y = 0.45m$) for Second Synthetic-Motion Real-Target Example using Full Rigid-Body Processing Algorithm (After Azimuth Rescaling and Azimuth-Displacement Compensation

Third Example: Translational and Rotational Motion (Negative Rotation)

For our next synthetic-motion real-target example, we illustrate the effects of *negative* target rotation upon the performance of the two L_1 SAR processing algorithm. For this example, the target's rotation rate is equal to minus one-half times the SAR's look-angle rotational rate (i.e., $\dot{\psi}_{RB} = -\frac{1}{2}\dot{\theta} = -0.018 rad/s$). Physically, this corresponds to the moving target rotating in the direction of positive "look" angle, which implies that the relative rotation rate between the target and the SAR platform is smaller than $\dot{\theta}$. As with the previous examples, we have a translational target velocity of $(\dot{x}_{RB}, \dot{y}_{RB}) = (2m/s, 2.304m/s)$.

As shown in the conventional image of Figure 5.122, the target motion has seriously degraded the SAR image, just as with the previous example with positive rotation. For this example, the rotation-rate dependent azimuth scale factor is given by $1 + \dot{\psi}_{RB}/\dot{\theta} = 0.5$. Therefore, the target blur area appears to be " shrunken" in azimuth (in comparison to the target blur area of the conventional SAR image shown in Figure 5.84 for the first purely-translational motion example).

For the full rigid-body L_1-norm SAR processing algorithm, we used an L_1 weighting of $\gamma_A = 0.9$ for the velocity-parameter estimation. We assumed a rectangular target spatial region identical to the region used by this algorithm for the first purely-translational motion example (with an azimuth width of $8m$ and a range width of $4m$, centered at $(x, y) = (0m, 0m)$).

The results of the rigid-body L_1-norm SAR processing algorithm are shown in Figures 5.125 through 5.130. For this case, we obtained velocity-parameter estimates of $(\hat{\dot{x}}_{RB}, \hat{\dot{y}}_{RB}, \hat{\dot{\psi}}_{RB}) = (1.94m/s, 2.21m/s, -0.013rad/s)$. As compared to the first synthetic-motion real-target example, we see a larger estimation- error in both the target rotation rate and the range velocity. One factor contributing to this increased error is the smaller effective look-angle extent for the SAR system, due to the negative target rotation rate. As shown in Figure 5.126, the SAR image is still improved, in comparison to the conventional SAR image of Figure 5.122, even with the larger estimation errors in both the range velocity and the rotation rate. We again see the effect of the rotation-rate dependent azimuth scale factor $1 + \dot{\psi}_{RB}/\dot{\theta}$, in that the target portion of the SAR image of Figure 5.126 is a (smaller) scaled version of the target portion of the original MSTAR image of Figure 5.79. Since we have an azimuth image sampling interval $\Delta_x = 0.125$ equal to the azimuth image sampling interval of the conventional image, the azimuth scale factor has the effect of "merging" (i.e., low-pass filtering and downsampling in azimuth) the target scatterers in the SAR image We will discuss this merging effect in more detail later when we present the "exact-velocity" results generated by this algorithm.

The L_1 SAR image after azimuth-rescaling and azimuth-displacement compensation is shown in Figure 5.129. The image of the T-72 moving-target has a scaling comparable to the original MSTAR image of Figure 5.79. It also has an azimuth-displacement error of approximately $3m$ (due to the range-velocity estimation-error). However, the target portion of this image appears to be modulated by spatially-periodic "nulls" with respect to the azimuth direction, which were also apparent in the previous positive rotation example (though in the previous example, the uncompensated focused image exhibited these nulls). As we will discuss in more detail later, these nulls are caused by the interaction between the azimuth-rescaling algorithm and the before-mentioned target-scatterer merging. We

will also show that since the result of the azimuth-rescaling algorithm is not a function of the discrete-valued range-sampling variable n_y, the spatially-periodic nulls will be highly-correlated in range.

The azimuth cross-section of the azimuth-compensated SAR image is shown in Figure 5.110. This cross-section appears to be a shifted version (modulated by the spatially-periodic nulls) of the azimuth cross-section of the original MSTAR stationary image shown in Figure 5.81.

For the purely-translational L_1-norm SAR processing algorithm, we used an L_1 weighting of $\gamma_A = 0.8$. We also assumed a rectangular target spatial region identical to the first purely-translational motion example (with an azimuth width of $8m$ and a range width of $4m$, centered at $(x, y) = (0m, 0m)$).

The results generated by the purely-translational L_1-norm SAR processing algorithm are shown in Figures 5.131 through 5.136. For this algorithm, we obtained velocity-parameter estimates of $(\hat{\dot{x}}_{RB}, \hat{\dot{y}}_{RB}) = (2.25m/s, 2.24m/s)$, which were comparable in accuracy to the results of the full rigid-body algorithm. We see in Figure 5.132 that even with the added target rotation, the purely-translational L_1-norm algorithm's moving-target image is nearly as focused as the full rigid-body L_1-norm algorithm's moving-target image (shown in Figure 5.126). As with the full rigid-body algorithm, the target portion of the SAR image appears to be a scaled version of the target portion of the the original MSTAR image shown in Figure 5.79, due to the rotation-rate dependent azimuth scale factor $1 + \dot{\psi}_{RB}/\dot{\theta}$. The azimuthal cross-section of the SAR image, shown in Figure 5.134, also appears to be a scaled version of the azimuth cross-section shown in Figure 5.81 of the original MSTAR stationary image.

As with the previous examples, we illustrate the effects of velocity-parameter estimation-error upon the full rigid-body algorithm by including results produced by the minimization of the standard least-squares cost function $J(\mathbf{A}, \hat{\mathbf{v}}) = ||\mathbf{f} - \mathbf{F}(\hat{\mathbf{v}})\mathbf{A}||_2^2$ (when the velocity parameters $\hat{\mathbf{v}}$ were known exactly). In Figure 5.137, we see that the (uncompensated) SAR image shown in Figure 5.81 is a (smaller) scaled version the original MSTAR image of Figure 5.79, due to the rotation-rate dependent azimuth scale factor. As with the full rigid-body results presented earlier in Figure 5.126, we see the merging of the target scatterers in the SAR image (which we will discuss in more detail shortly). However, this image is sharper (as would be expected) than the images produced using estimated velocity parameters by either the full rigid-body algorithm (in Figure 5.126), or the purely-translational algorithm (in Figure 5.132). The target region of the rescaled exact-velocity SAR image in Figure 5.140 still appears to be a modulated version of the target area of the original MSTAR image (shown in Figure 5.79), due to the interaction between the target-scatterer merging and the rescaling algorithm. The azimuthal cross-section of this rescaled image (shown in Figure 5.141) also appears to be a modulated version of the azimuthal cross-section of the original MSTAR image (shown in Figure 5.81).

As stated previously in this discussion, the rescaled exact-velocity image shown in Figure 5.140 appears to be modulated by a series of (range-correlated) spatially-periodic "nulls" with respect to the azimuth direction. These nulls are due to the interaction between the azimuth rescaling algorithm and the before-mentioned target-scatterer merging. Here, we discuss this interaction in more detail.

Recall from the previous positive-rotation example that the target region of the uncom-

pensated exact-velocity full rigid-body SAR image was approximately given by the following convolution of the target region of the conventional MSTAR image, $A[n'_x, n'_y]$, with a scaled sampled 2-D sinc function (for the case where the spatial sampling intervals, Δ_x and Δ_y, were equal to one-half the respective spatial resolutions δ_x and δ_y of the SAR system)

$$\hat{A}_U[n_x, n_y] = \sum_{n'_x} \sum_{n'_y} A[n'_x, n'_y] \text{sinc}\left(\pi\left(n_x - \left(1 + \frac{\dot{\psi}_{RB}}{\dot{\theta}}\right)n'_x\right)\right) \text{sinc}\left(\pi(n_y - n'_y)\right) \ .$$

(5.87)

For an azimuthal scale factor $1 + \dot{\psi}_{RB}/\dot{\theta}$ less than unity (corresponding to a negative target rotation rate with a magnitude less than $\dot{\theta}$), this expression implies that the target region of the uncompensated SAR image will be a scaled version of the target region of the conventional MSTAR image, (after low-pass filtering in azimuth by a sinc function with an azimuth width of $\Delta_x/(1 + \dot{\psi}_{RB}/\dot{\theta})$ (which is greater than Δ_x), then downsampled by a factor of $1/(1 + \dot{\psi}_{RB}/\dot{\theta})$). This is essentially the previously-mentioned target-scatterer merging exhibited in the uncompensated exact-velocity image of Figure 5.137.

For the full rigid-body algorithm, the exact-velocity azimuth-rescaled SAR image $\hat{A}[n_x, n_y]$ is given by

$$\hat{A}[n_x, n_y] = \hat{A}_U\left[\left(1 + \frac{\dot{\psi}_{RB}}{\dot{\theta}}\right)n_x, n_y\right] \ .$$

(5.88)

For an azimuthal scale factor $1 + \dot{\psi}_{RB}/\dot{\theta}$ less than unity, this implies that the rescaled SAR image is given by the following *subsampled* (with respect to azimuth) version of the uncompensated image (where n''_x is an integer-valued variable with the same domain as n_x)

$$\hat{A}[n_x, n_y] \quad \approx \quad \begin{cases} \hat{A}_U[n''_x, n_y] & \left|n_x - \dfrac{n''_x}{\left(1 + \frac{\dot{\psi}_{RB}}{\dot{\theta}}\right)}\right| < \frac{1}{2} \\[2ex] & n''_x \in \{\ldots, -2, -1, 0, 1, 2, \ldots\} \\[2ex] 0 & \text{otherwise} \end{cases} \ .$$

(5.89)

Since we have now corrected for the azimuthal scale factor $1 + \dot{\psi}_{RB}/\dot{\theta}$, this relation (along with the previous convolutional equation for $\hat{A}_U[n_x, n_y]$) implies that the rescaled SAR image is given by a subsampled version (with respect to azimuth) of the (low-pass filtered) conventional MSTAR image. Note that the azimuth rescaling is not a function of the the discrete-valued range-sampling variable n_y, which implies that the subsampling effects are highly correlated in range.

In a similar fashion to the uncompensated image for the previous positive rotation example, this has the effect of producing spatially-periodic "nulls" (with respect to azimuth) in the rescaled SAR image (with a period of $\Delta_x/(1 + \dot{\psi}_{RB}/\dot{\theta})$). For this negative-rotation example, the target rotation-rate $\dot{\psi}_{RB}$ was equal to one-half the negative of the SAR system's "look angle" rotation-rate $\dot{\theta}$, which gave an azimuth scale factor of $1 + \dot{\psi}_{RB}/\dot{\theta} = 0.5$. Since the azimuth sampling-rate constant Δ_x was equal to $0.125m$, this implies that

rescaled SAR image would exhibit (range-correlated) spatially-periodic nulls with a period of $\Delta_x/(1 + \dot{\psi}_{RB}/\dot{\theta}) = 0.25m$. This is indeed the case, as shown in the rescaled exact-velocity image of Figure 5.140, and the corresponding azimuthal cross-section in Figure 5.141.

For this negative-rotation experimental example, we see that the benefits of the the azimuth-rescaling algorithm are tempered by the presence of the spatially-periodic nulls in the resulting SAR image. This implies that *it is of questionable utility to use this algorithm for cases of negative target rotation* (unlike the previous positive-rotation case where the azimuth-rescaling algorithm actually removed the nulling artifacts from the SAR image). An alternative to this version of the azimuth-rescaling algorithm would be to use an algorithm which interpolates the amplitudes of the rescaled image, such that the nulls are less apparent. However, an interpolation-type algorithm may not necessarily be as straightforward as the present azimuth-rescaling algorithm.
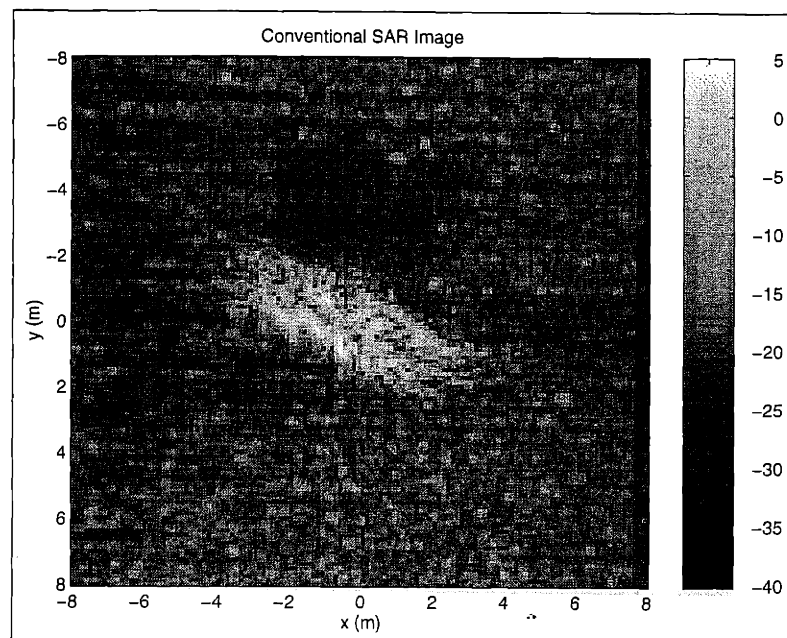
Figure 5.122: Conventional SAR Image for Third Synthetic-Motion Real-Target Example
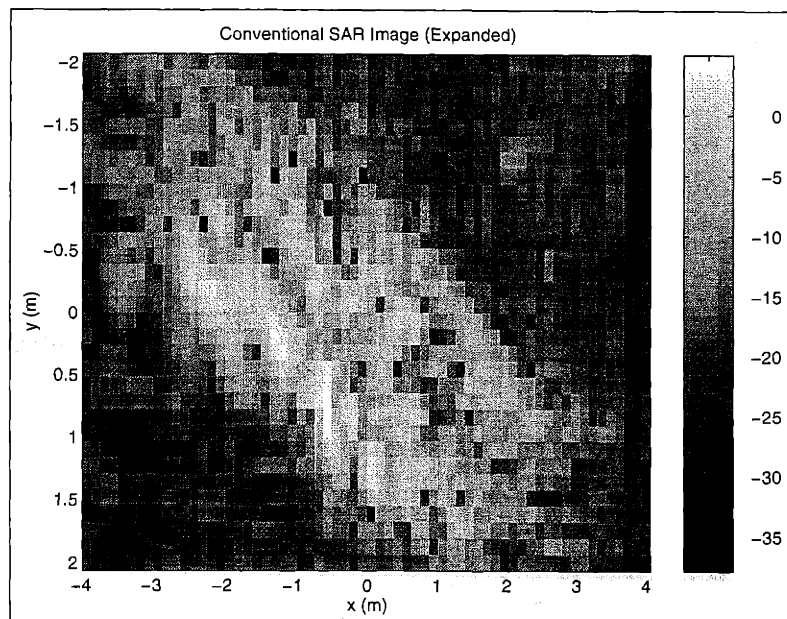
Figure 5.123: Target Region of Conventional SAR Image for Third Synthetic-Motion Real-Target Example
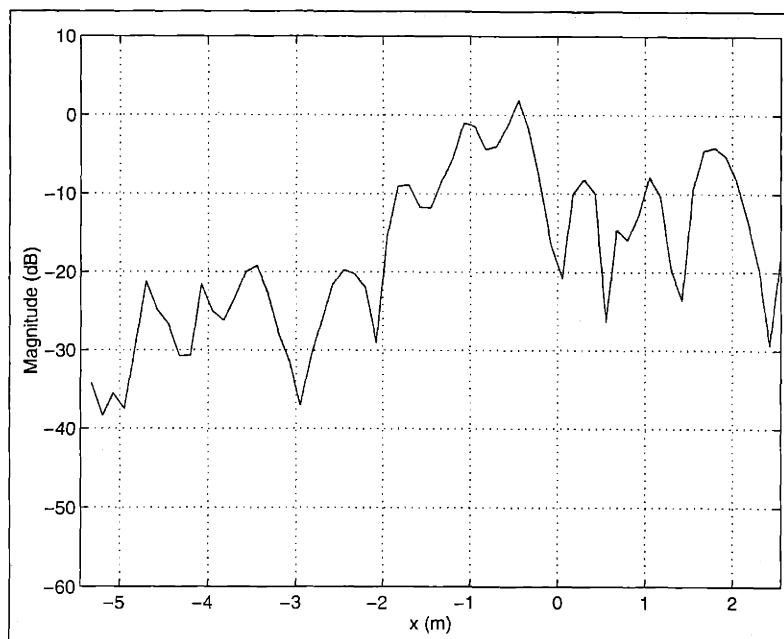
Figure 5.124: Cross-Section of Conventional SAR Image (at $y = 0.45m$) for Third Synthetic-Motion Real-Target Example
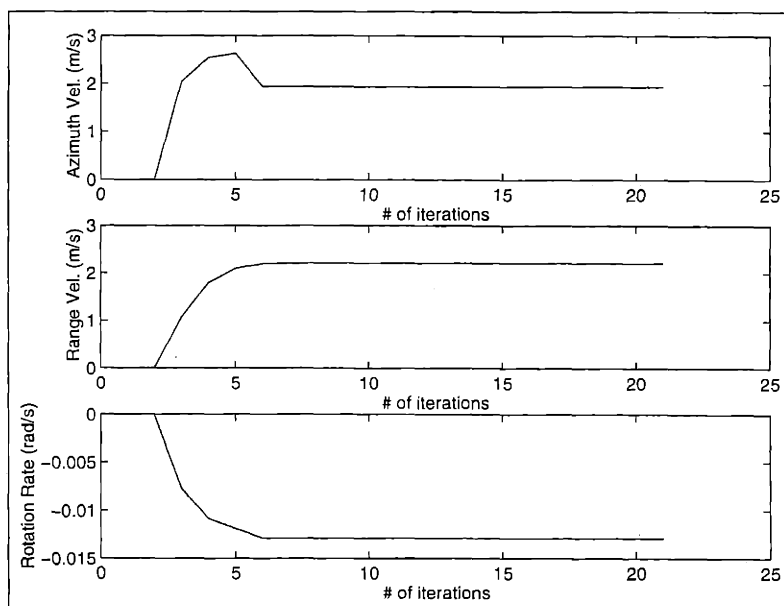
Figure 5.125: Estimated Target-Velocity Parameters for Third Synthetic-Motion Real-Target Example using Full Rigid-Body Processing Algorithm
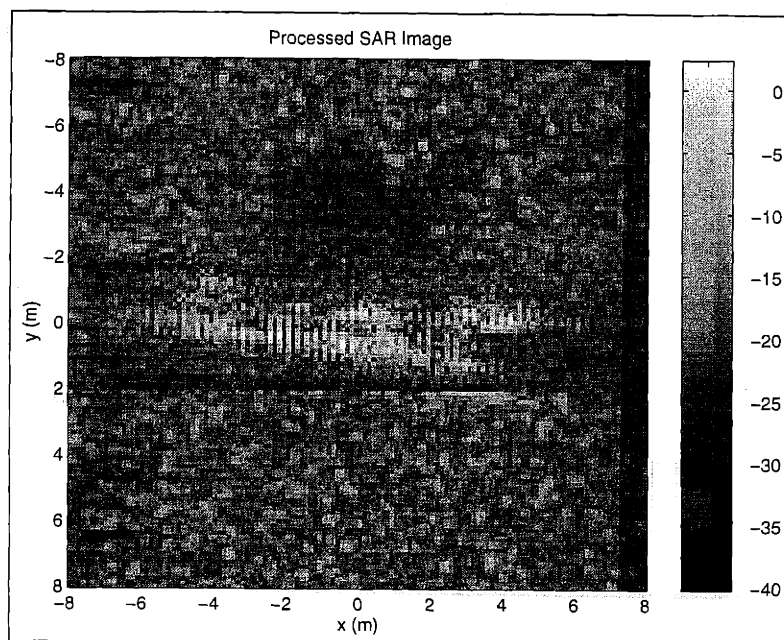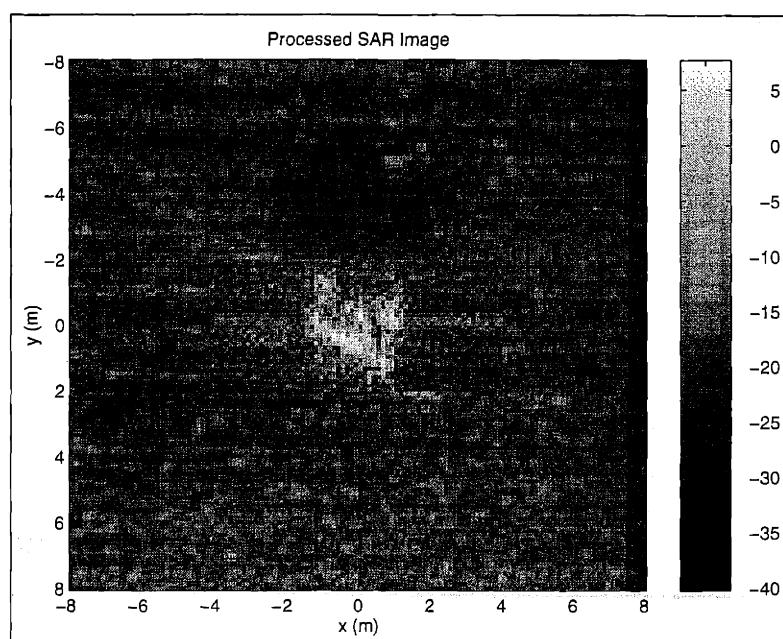
Figure 5.126: L_1 SAR Image for Third Synthetic-Motion Real-Target Example using Full Rigid-Body Processing Algorithm (Before Azimuth Rescaling and Azimuth-Displacement Compensation)
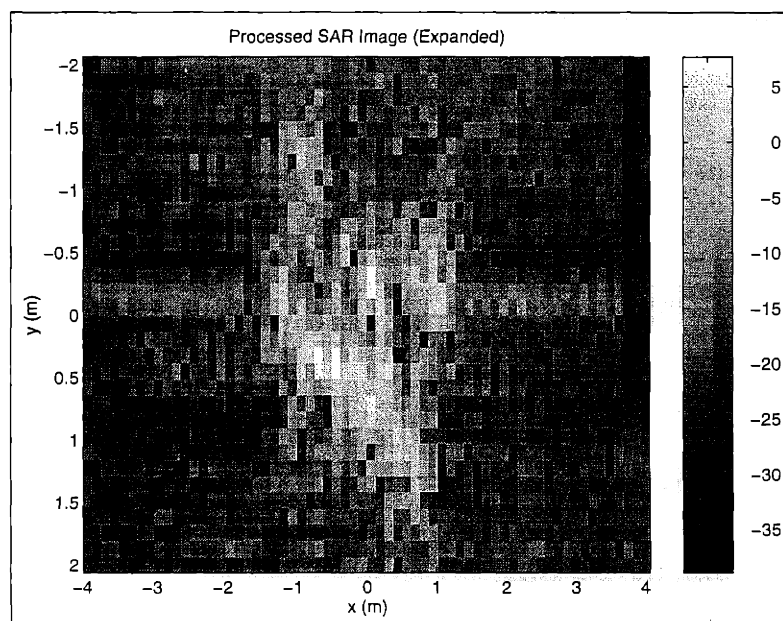
Figure 5.127: Target Region of L_1 SAR Image for Third Synthetic-Motion Real-Target Example using Full Rigid-Body Processing Algorithm (Before Azimuth Rescaling and Azimuth-Displacement Compensation)
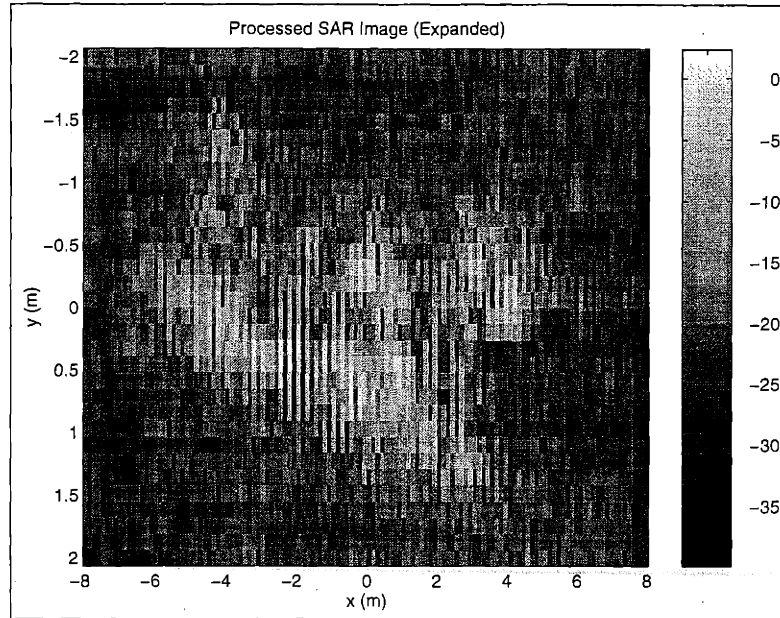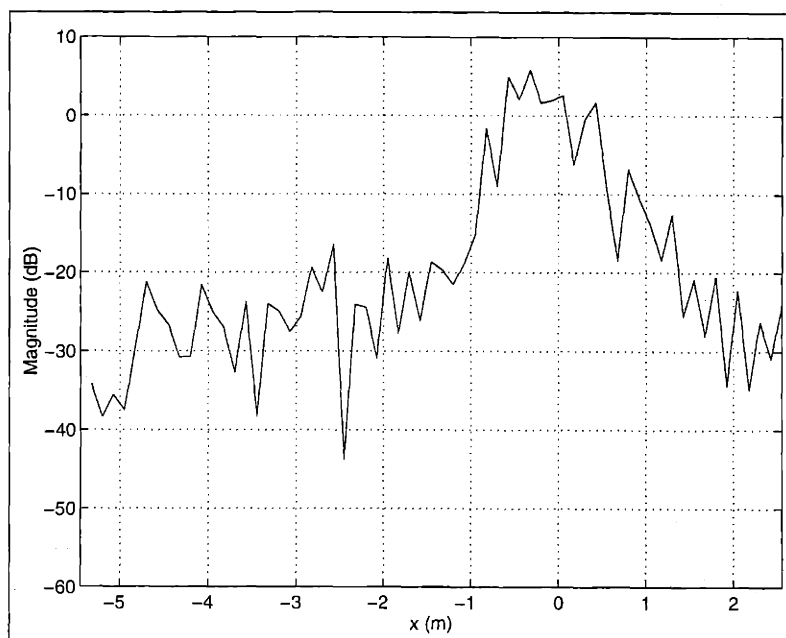
Figure 5.128: Cross-Section of L_1 SAR Image (at $y = 0.45m$) for Third Synthetic-Motion Real-Target Example using Full Rigid-Body Processing Algorithm (Before Azimuth Rescaling and Azimuth-Displacement Compensation)
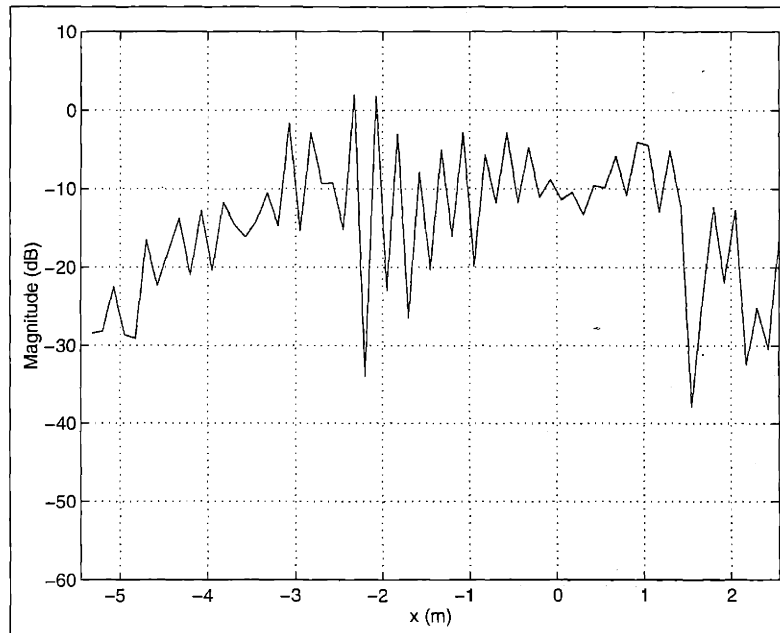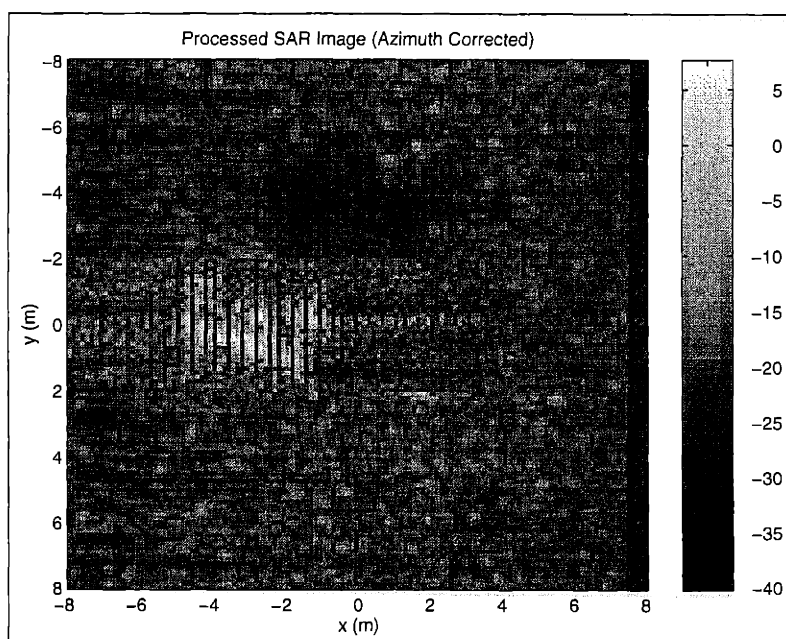

Figure 5.129: L_1 SAR Image for Third Synthetic-Motion Real-Target Example using Full Rigid-Body Processing Algorithm (After Azimuth Rescaling and Azimuth-Displacement Compensation)
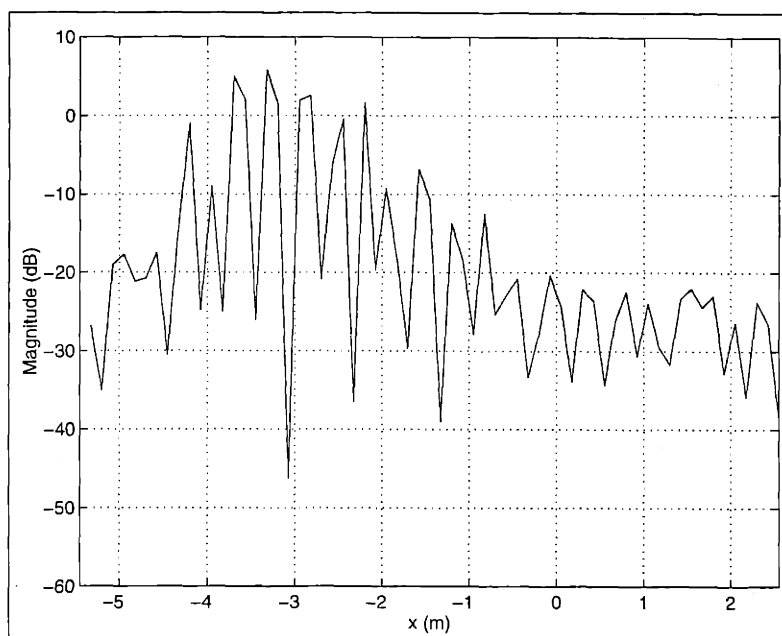
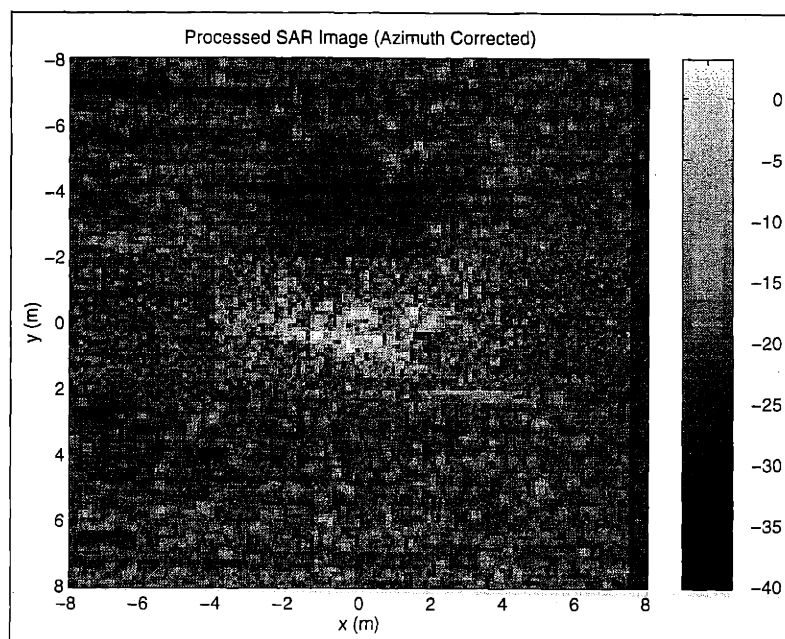Figure 5.130: Cross-Section of L_1 SAR Image (at $y = 0.45m$) for Third Synthetic-Motion Real-Target Example using Full Rigid-Body Processing Algorithm (After Azimuth Rescaling and Azimuth-Displacement Compensation)
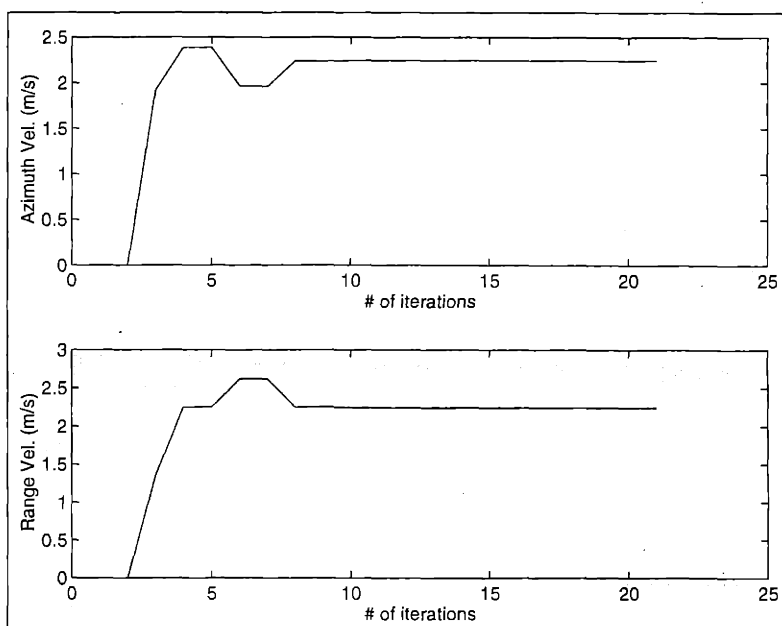

Figure 5.131: Estimated Target-Velocity Parameters for Third Synthetic-Motion Real-Target Example using Purely-Translational Processing Algorithm
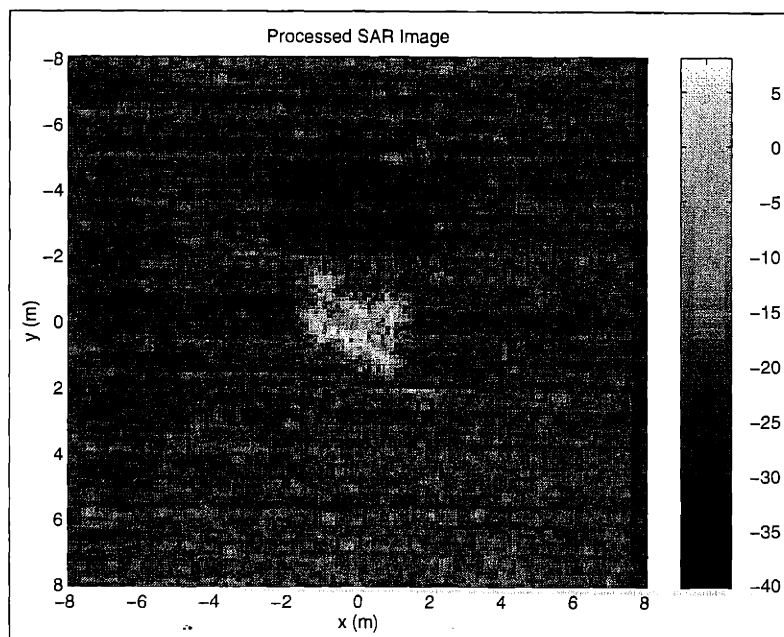
Figure 5.132: L_1 SAR Image for Third Synthetic-Motion Real-Target Example using Purely-Translational Processing Algorithm (Before Azimuth-Displacement Compensation)
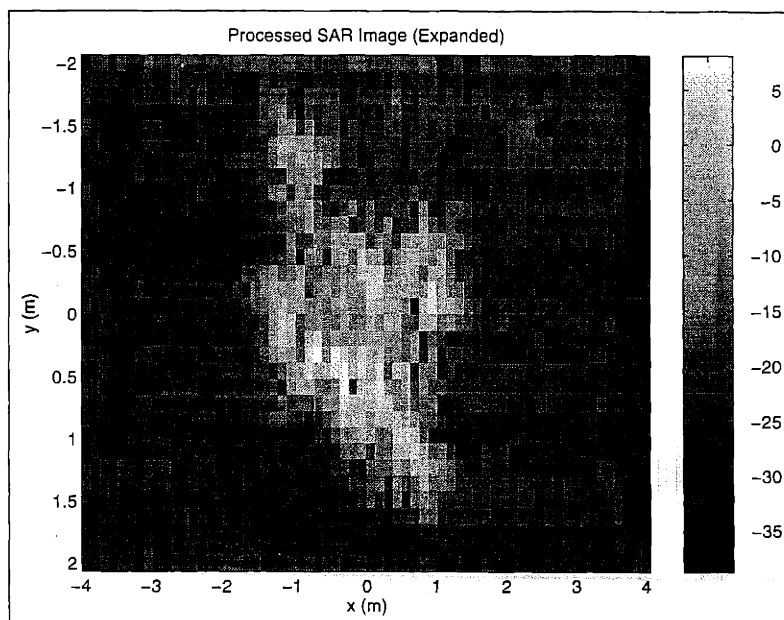
Figure 5.133: Target Region of L_1 SAR Image for Third Synthetic-Motion Real-Target Example using Purely-Translational Processing Algorithm (Before Azimuth-Displacement Compensation)
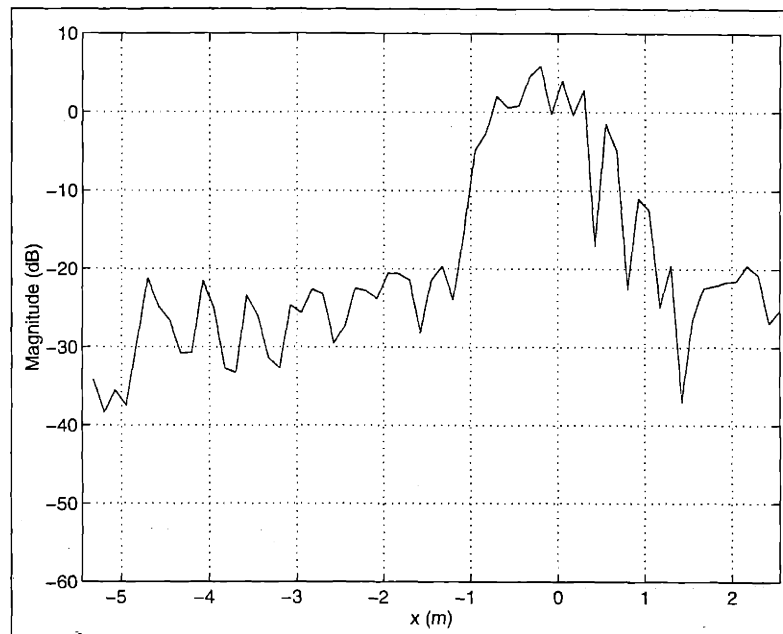
Figure 5.134: Cross-Section of L_1 SAR Image (at $y = 0.45m$) for Third Synthetic-Motion Real-Target Example using Purely-Translational Processing Algorithm (Before Azimuth-Displacement Compensation)
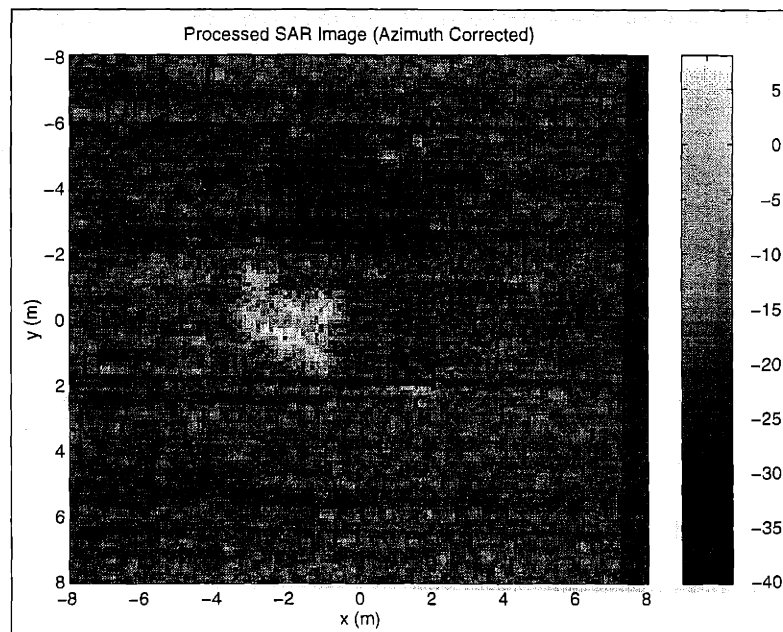
Figure 5.135: L_1 SAR Image for Third Synthetic-Motion Real-Target Example using Purely-Translational Processing (After Azimuth-Displacement Compensation)
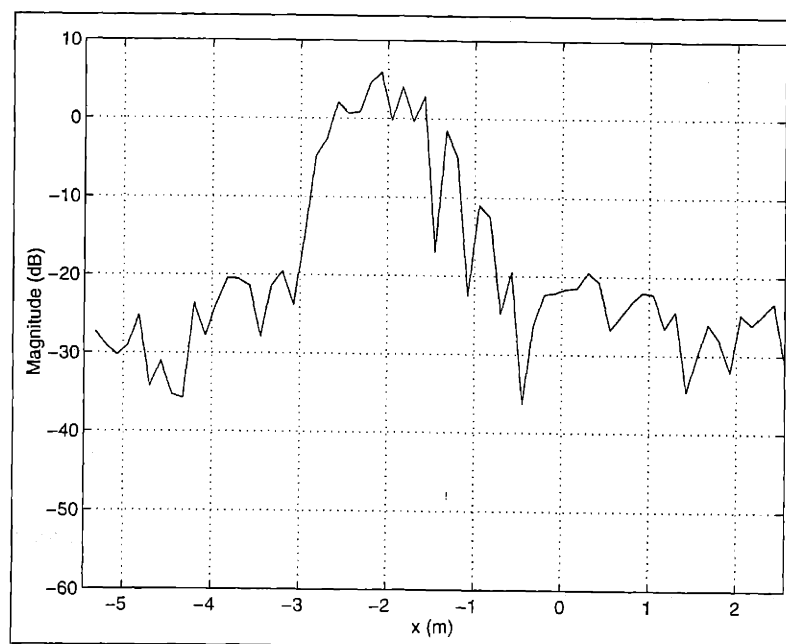
Figure 5.136: Cross-Section of L_1 SAR Image (at $y = 0.45m$) for Third Synthetic-Motion Real-Target Example using Purely-Translational Processing (After Azimuth-Displacement Compensation)
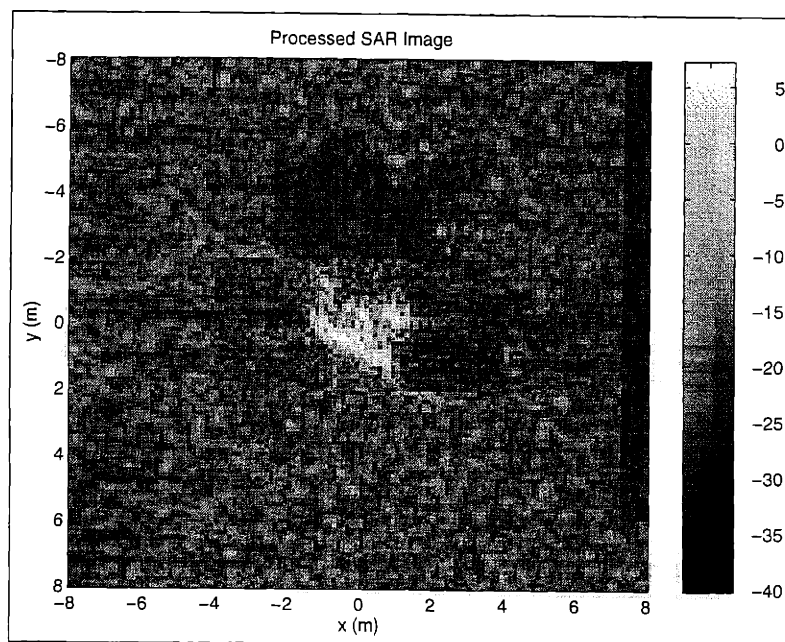
Figure 5.137: Exact-Velocity L_1 SAR Image for Third Synthetic-Motion Real-Target Example using Full Rigid-Body Processing Algorithm (Before Azimuth Rescaling and Azimuth-Displacement Compensation)
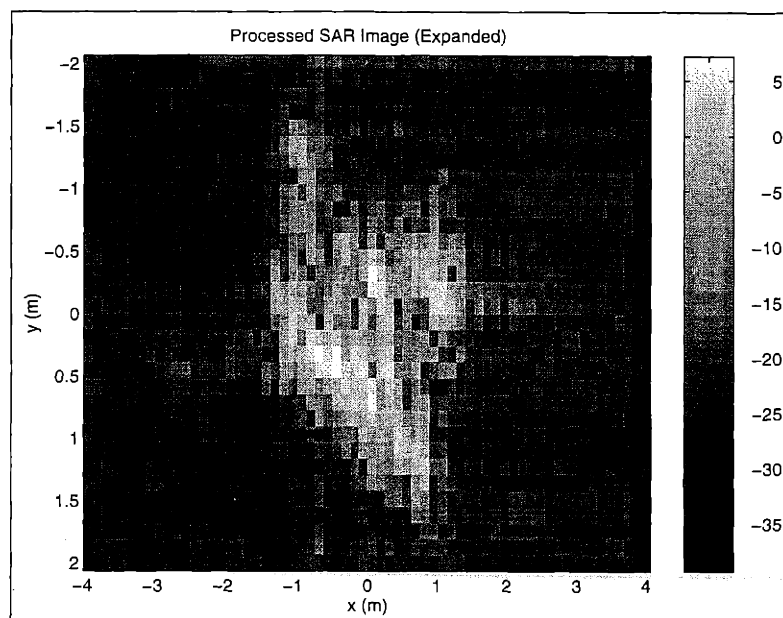
Figure 5.138: Target Region of Exact-Velocity L_1 SAR Image for Third Synthetic-Motion Real-Target Example using Full Rigid-Body Processing Algorithm (Before Azimuth Rescaling and Azimuth-Displacement Compensation)
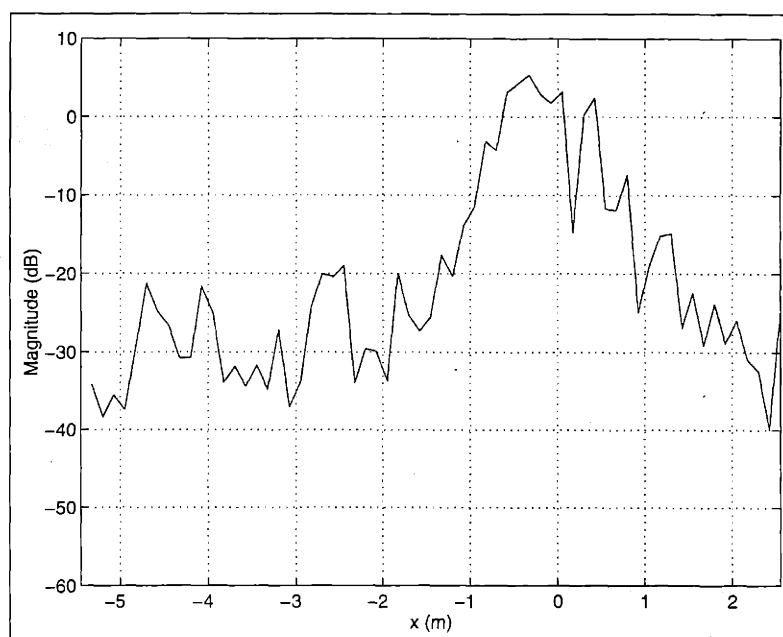
Figure 5.139: Cross-Section of Exact-Velocity L_1 SAR Image (at $y = 0.45m$) for Third Synthetic-Motion Real-Target Example using Full Rigid-Body Processing Algorithm (Before Azimuth Rescaling and Azimuth-Displacement Compensation)
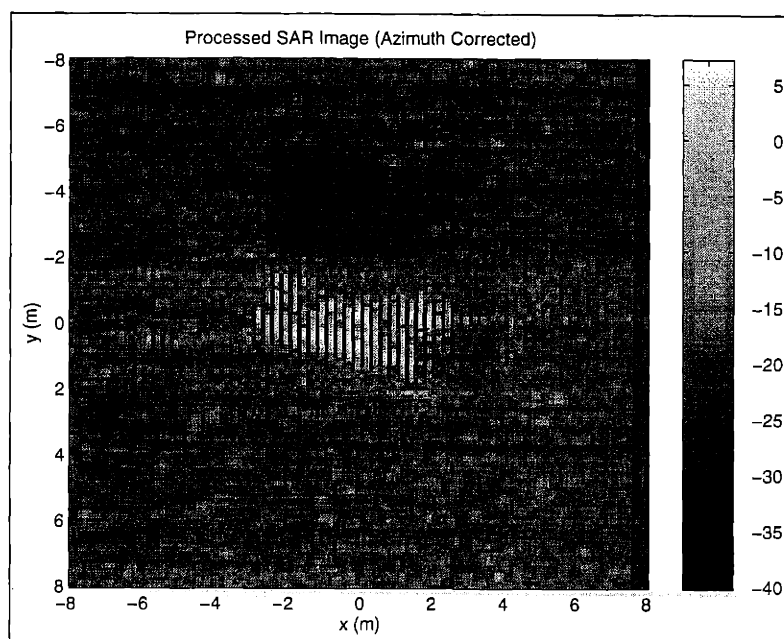
Figure 5.140: Exact-Velocity L_1 SAR Image for Third Synthetic-Motion Real-Target Example using Full Rigid-Body Processing Algorithm (After Azimuth Rescaling and Azimuth-Displacement Compensation
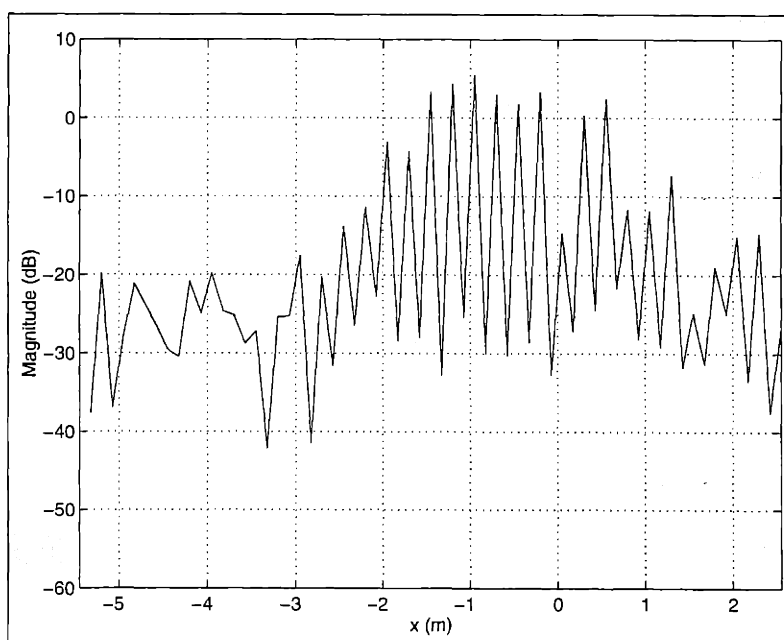
Figure 5.141: Cross-Section of Exact-Velocity L_1 SAR Image (at $y = 0.45m$) for Third Synthetic-Motion Real-Target Example using Full Rigid-Body Processing Algorithm (After Azimuth Rescaling and Azimuth-Displacement Compensation

Experiment	$|\hat{\dot{x}}_{RB} - \dot{x}_{RB}|$	$|\hat{\dot{y}}_{RB} - \dot{y}_{RB}|$	$|\hat{\dot{\psi}}_{RB} - \dot{\psi}_{RB}|$
1 (Purely-Translational Motion)	0.25 m/s	0.03 m/s	0.0023 rad/s
2 (Reduced SCR)	2.04 m/s	2.24 m/s	0.0001 rad/s
2b (Reduced SCR, Reduced T. Region)	0.29 m/s	0.07 m/s	0.00002 rad/s
3 (Positive Rotation)	0.15 m/s	0.10 m/s	0.011 rad/s
3b (Positive Rot., Reduced T. Region)	0.17 m/s	0.01 m/s	0.0344 rad/s

Table 5.3: Summary of Synthetic-Target Estimation-Performance Results for Full Rigid-Body Algorithm

Experiment	$|\hat{\dot{x}}_{RB} - \dot{x}_{RB}|$	$|\hat{\dot{y}}_{RB} - \dot{y}_{RB}|$
1 (Purely-Translational Motion)	0.14 m/s	0.10 m/s
2 (Reduced SCR)	1.87 m/s	2.30 m/s
2b (Reduced SCR, Reduced T. Region)	0.02 m/s	0.14 m/s
3 (Positive Rotation)	0.14 m/s	0.10 m/s
3b (Positive Rot., Reduced T. Region)	0.10 m/s	0.12 m/s

Table 5.4: Summary of Synthetic-Target Estimation-Performance Results for Purely-Translational Algorithm

5.3.3 Summary of Estimation Performance Results

In this section, we briefly summarize the velocity-parameter estimation-performance results presented in this chapter. As shown in Table 5.3, the full rigid-body algorithm appeared to have acceptable overall range-velocity estimation-error performance for the synthetic-target experimental examples, except for the reduced SCR example (with the larger target area) where it tried to focus the stationary clutter scatterers. For all of the other synthetic-target examples, the magnitude of the range-velocity estimation-error was less than $0.10m/s$. Recall from the previous sections that the azimuth-displacement error (after applying the azimuth-displacement compensation algorithm) was proportional to the range-velocity estimation-error divided by the look-angle rotation rate $\dot{\theta} = 0.036rad/s$. Therefore, the overall azimuth-displacement error of this algorithm was less than $3m$ for these examples. The overall azimuth-velocity estimation-error was somewhat larger, but the resulting SAR images of the synthetic-target scatterers still appeared to be sufficiently focused. In Table 5.3, we see an apparent improvement in the azimuth-velocity estimation performance for the case of positive target rotation. Recall that the target rotation caused an increase in the apparent azimuthal spacing between the synthetic-target scatterers (due to the rotation-rate dependent azimuth scale factor). This implies that the azimuth-velocity estimation-performance of this algorithm is somewhat sensitive to cross-scatterer interference (since this interference is lessened when the scatterers are further apart in azimuth). On the other hand, the rotation-rate estimation error increased for the positive-rotation case when we reduced the assumed target spatial region (even though this eliminated the bright man-made clutter scatterers from this region). This implied that the rotation-rate estimation performance of the full rigid-body algorithm was influenced by the amount of target "blur energy" included in the assumed target spatial region.

Experiment	$|\hat{\dot{x}}_{RB} - \dot{x}_{RB}|$	$|\hat{\dot{y}}_{RB} - \dot{y}_{RB}|$	$|\hat{\dot{\psi}}_{RB} - \dot{\psi}_{RB}|$
1 (Purely-Translational Motion)	0.003 m/s	0.02 m/s	0.0002 rad/s
2 (Positive Rotation)	0.03 m/s	0.11 m/s	0.0013 rad/s
3 (Negative Rotation)	0.06 m/s	0.10 m/s	0.0051 rad/s

Table 5.5: Summary of Synthetic-Motion Real-Target Estimation-Performance Results for Full Rigid-Body Algorithm

Experiment	$|\hat{\dot{x}}_{RB} - \dot{x}_{RB}|$	$|\hat{\dot{y}}_{RB} - \dot{y}_{RB}|$
1 (Purely-Translational Motion)	0.48 m/s	0.02 m/s
2 (Positive Rotation)	0.05 m/s	0.02 m/s
3 (Negative Rotation)	0.25 m/s	0.06 m/s

Table 5.6: Summary of Synthetic-Motion Real-Target Estimation-Performance Results for Purely-Translational Algorithm

As shown in Table 5.4, the purely-translational algorithm had a slightly worse overall range-velocity estimation performance for the synthetic-target experimental examples than the full rigid-body algorithm for these examples (as shown in Table 5.3). However, the resulting SAR images of the synthetic-target scatterers were still focused to an acceptable level. Because of this slightly worse range-velocity performance, the purely-translational algorithm also had slightly worse azimuth-displacement errors (about $4m$). On the other hand, the purely-translational algorithm had much better azimuth-velocity estimation performance, especially when we reduced the assumed target region.

In Table 5.5, we see that the overall range-velocity estimation performance (as well as the azimuth displacement errors) of the full rigid-body algorithm for the synthetic-velocity real-target examples was comparable to the performance of this algorithm for the previous synthetic-target examples in Table 5.3. For these examples, the full rigid-body algorithm had a range-velocity estimation-error magnitude of less than $0.11m/s$, which gave azimuth displacement errors of less than $3m$. On the other hand, the azimuth-velocity performance of the significantly improved for these examples. The most likely reason for this improvement was the absence of any "bright" stationary man-made clutter scatterers in this set of experimental examples (in comparison to the previous synthetic-target examples), which implied that we had a relatively higher SCR.

For the purely-translational algorithm, we see from Table 5.6 that the range-velocity estimation performance for the synthetic-velocity real-target examples significantly improved (in relation to the corresponding performance of this algorithm for the previous synthetic-target examples). Consequently, the azimuth displacement errors (after azimuth compensation) also significantly improved (with a magnitude less than $2m$). In a similar fashion to the full rigid-body algorithm, this improvement was most likely due to the absence of "bright" stationary man-made clutter scatterers in this set of experimental examples (in comparison to the previous examples). However, the overall azimuth-velocity estimation performance was somewhat worse. Since the target scatterers have a closer average azimuthal spacing for these examples than for the synthetic-target examples, this degradation in performance was most likely due to cross-scatterer interference effects.

Chapter 6

Contributions and Suggestions for Further Research

IN this thesis, we present research contributions made in the area of spotlight-mode synthetic-aperture radar (SAR) imaging, where this research was done from an estimation-theoretic perspective. For this research, we addressed the following issues:

- Reducing sidelobe imaging artifacts and improving resolution for stationary SAR scenes containing high-amplitude scatterers.

- Improving the spotlight-mode SAR image formation process in the presence of moving targets.

In this chapter, we briefly summarize the contributions of this thesis, and we present the overall conclusions which can be derived from the results of our research. We also present some suggestions for extending this work.

6.1 Contributions

Here, we briefly summarize the contributions of the research presented in this thesis. The main contributions of this work can be categorized as follows:

I. A Framework for SAR Imaging using L_1-Norm Based Regularization

II. A Framework for Simultaneous Imaging of Moving Targets and Nearby Stationary Clutter

6.1.1 A Framework for SAR Imaging using L_1-Norm Based Regularization

In Chapter 3 of this thesis, we developed a generalized SAR imaging framework which exploits the idea of L_1-norm regularization in order to address the limitations of conventional SAR imaging (e.g., blurring to motion, sidelobe artifacts, and loss of scatterer resolution). In that chapter, we first presented a estimation-theoretic justification for this idea, from the

context of the ill-posed over-complete basis-pursuit estimation problem. We then presented some results in order to demonstrate the utility of an L_1-norm regularized approach for reducing sidelobes and improving resolution for stationary SAR images. From these results, we especially saw the potential utility of this approach for enhancing feature scatterers in the stationary SAR images for the purposes of automatic-target recognition.

In Chapter 5, we presented a parameterized estimation-theoretic L_1-norm regularized approach for imaging rigid-body moving targets. We also present some results from using this rigid-body technique for both synthetic moving point-scatterers embedded in real clutter and synthetic-motion real targets embedded in real clutter. From these results, we show that this technique is able to compensate the SAR image of a single rigid-body moving target for the blurring due to a constant target translational-velocity and a constant target rotation-rate (even if the target scatterers are relatively closely-spaced). Unlike some of the rigid-body moving-target imaging techniques presented in the literature, the rigid-body L_1-norm regularized approach was able to estimate the rigid-body motion parameters and compensate for the motion-induced blurring without requiring the tracking of high-amplitude prominent-point target-scatterers. However, range-velocity induced azimuth-displacement compensation performance of this technique was significantly affected by range-velocity estimation errors (such as errors due to interference from nearby stationary scatterers and/or errors due to target rotation).

6.1.2 A Framework for Simultaneous Imaging of Moving Targets and Nearby Stationary Clutter

One fundamental limitation of many of the moving-target techniques presented in the literature (as well as the rigid-body L_1-norm regularized approach presented in Chapter 5) is the fact that they assume that the imaged target field is only composed of a single moving rigid-body target. Therefore, these techniques cannot image a moving target and nearby high-amplitude stationary clutter simultaneously.

In Chapter 4, we presented an estimation-theoretic moving-target SAR imaging technique which addresses this issue. This technique used a multi-dimensional matched-filter as a means of computing a set of scatterer-velocity estimates which are used as initial conditions for an L_1-norm-based estimation algorithm derived for a spatially-varying temporally-constant velocity (SVTCV) estimation-theoretic SAR model (which assumes that the target field consists of a $2 - D$ array of ideal point scatterers with spatially independent velocities). The matched filter also computed a target detection statistic for determining which spatial locations in a particular SAR scene correspond to actual moving scatterers (allowing a reduction in the computational intensity of the SVTCV L_1-norm based estimation algorithm).

In Chapter 4, we also presented some results using this technique for both synthetic point scatterers embedded in real clutter, and a synthetic-motion real target embedded in real clutter. From these results, we show that this approach can image a moving target and nearby high-amplitude stationary clutter simultaneously. We also show the potential of this technique for imaging targets with non-rigid body motion.

However, one significant issue with this technique was the influence of cross-scatterer interference (when we were imaging targets with closely-spaced scatterers) upon the range-

velocity induced azimuth-displacement compensation performance. In order to reduce this influence, we averaged the estimated range velocities of the relatively high-amplitude target scatterers. This scheme worked reasonably well for the examples where we had targets with purely-translational rigid-body motion (and sufficient spatial-separation between the target scatterers). However, this scheme was not able to correct for azimuth-position distortions due to non-rigid body target motion. This scheme also failed when the target scatterers were relatively closely-spaced (even if the scatterers had identical velocities).

6.2 Suggestions for Further Research

In this section, we present some suggestions for extending the research presented in this thesis.

6.2.1 L_1-Norm Based Imaging with Non-Rigid Body Scatterer-Velocity Regularization

In this thesis, we presented two estimation-theoretic techniques for moving-target SAR imaging. The matched-filter based approach was able to image a moving target and nearby high-amplitude stationary clutter simultaneously. This approach was also able to image a target with non-rigid body motion. However, we also found that the performance of the matched-filter was highly affected by cross-scatterer interference when the target-scatterers were relatively closely-spaced. On the other hand, the rigid-body L_1-norm regularized approach was able to image rigid-body moving targets, even when the target-scatterers were relatively closely-spaced. But this approach is not able to image both a moving target and nearby high-amplitude stationary clutter simultaneously. Thus, one extension of this research would be to find a technique which is able to make some type of (non-rigid body) velocity-regularization compromise between assuming a single rigid-body target and assuming that every scatterer has completely independent velocities (i.e., a trade-off between being able to image closely-spaced target scatterers and being able to image the moving target and nearby clutter simultaneously). Some possible avenues for this non-rigid body velocity-regularization include the use of cubic splines or Markov random-field models.

6.2.2 Improved Range-Velocity Induced Azimuth-Displacement Compensation

One important issue with the matched-filter based approach was the influence of range-velocity estimation-errors (due to cross-scatterer interference) upon its azimuth-displacement compensation performance. Recall that we used a relatively simple scheme which used the average of the estimated range-velocities of the brighter target-scatterers. However, this scheme gave poor results for non-rigid body target motion, and gave poor results for targets with closely-space scatterers. Therefore, one pressing area for further research is improving the azimuth-displacement compensation scheme for the matched filter.

For the present matched-filter azimuth-displacement compensation scheme, again recall that we averaged the estimated range velocities of a set of bright target scatterers. An possible alternative to averaging would be to set up a random field estimation inverse-problem

for the range-velocity field $\ddot{y}[n_x, n_y]$ where the bright-scatterer range-velocity estimates are sparse noisy measurements. Once this range-velocity field is estimated, it is then used for the azimuth compensation.

6.2.3 Imaging of Moving targets with Temporally-Varying Velocities

One fundamental assumption of the two estimation-theoretic techniques for moving-target SAR imaging presented in this thesis is that the velocity of each scatterer in the imaged SAR scene does not change over the dwell time (which was a reasonable assumption for the relatively short dwell times used for the results presented in this thesis). However, for longer dwell times, these techniques may give unacceptable results for target with temporally-varying motions, such as acceleration. Therefore, an extension of this research would be to develop algorithms for imaging targets with temporally-varying motions. For example, one possible avenue for doing this for the rigid-body L_1-norm regularized approach would be to add a set of acceleration parameters to the SAR model.

Appendix A

Current Motion-Compensated SAR Techniques

IN Chapter 1, we briefly described some of the current approaches to the moving-target SAR problem. These approaches can be divided into four distinct subclasses: *prominent-point* techniques, *phase-estimation* techniques, *space-time-frequency* techniques, and *polynomial phase* techniques. Here, we present an overview of the prominent-point techniques and the phase-estimation techniques (since they are the most closely related to the techniques presented in this thesis). The prominent-point class of SAR motion-compensation algorithms essentially correct for target motion by tracking a number of bright (i.e., high signal-to-noise ratio) target scatterers. On the other hand, the phase-estimation techniques do not require the tracking of bright prominent-point scatterers. However, these techniques assume that each target scatterer has the same velocity (and they assume that this velocity is purely in azimuth). A common characteristic of both the prominent-point techniques and the phase-estimation techniques is that they assume that the target-field reflectivity consists of a 2-D array of point scatterers that belong to a single *rigid-body* moving target. In Chapter 2, we derived a rigid-body temporally-constant velocity (RBTCV) estimation-theoretic model (i.e., we assumed that both the target's center-of-rotation translational velocities and the target's rotation rate were constant). For this presentation, we first derive a generalized rigid-body estimation-theoretic model for the SAR data (where we can have both a non-constant center-of-rotation translational velocity and a non-constant rotation rate).

A.1   Generalized Rigid-Body SAR Data Model

In Chapter 2, we derived the following general-motion model for the demodulated spotlight-mode SAR data $f[n, k]$ (given that we have a moving target which consists of a $2 - D$ array of ideal point scatterers)

$$
\begin{aligned}
\underline{General\text{-}Motion\ SAR\ Data\ Model} \\
f[n,k] \;=\; \sum_{n_x}\sum_{n_y} A[n_x,n_y] \\
\times e^{-j\,\frac{4\pi}{\lambda_c}\left[\left(1+\frac{\alpha T_p}{f_c}\frac{\hat{t}[n]}{T_p}\right)\left(y_{n_x n_y}(t_T[k])\cos(\dot\theta t_T[k])-x_{n_x n_y}(t_T[k])\sin(\dot\theta t_T[k])\right)\right]} \\
=\; \sum_{n_x}\sum_{n_y} A[n_x,n_y]\, e^{-j\,\frac{4\pi}{\lambda_c}\left[\left(1+\frac{\alpha T_p}{f_c}\frac{\hat{t}[n]}{T_p}\right)y'[n_x,n_y,k]\right]} \; . \\[2mm]
-K \le k \le K \qquad -\frac{N}{2}\le n\le \frac{N}{2}
\end{aligned}
\tag{A.1}
$$

In this expression, $\hat{t}[n]=\frac{T_p n}{N}$ is the "fast" (pulse-relative) sampling time, while $t_T[k]=\frac{2Tk}{2K}$ is the "slow" sampling (pulse-transmit) time [7, 10]. The corresponding trajectories of the point-scatterers in the 2-D array are given by $(x_{n_x n_y}(t), y_{n_x n_y}(t))$, while the "relative" range is given by $y'[n_x,n_y,k]$. The SAR system's look-angle rotation-rate is given by $\dot\theta$.

For a rigid-body target with a translational trajectory given by $(x_{RB}(t_T[k]), y_{RB}(t_T[k]))$ and a rotational trajectory given by $\psi_{RB}(t_T[k])$, the motion model for the scatterer trajectories is given by

$$
\begin{aligned}
\underline{Rigid\text{-}Body\ Motion\ Model} \\
x_{n_x n_y}(t_T[k]) \;=\; \Delta_x n_x \cos(\psi_{RB}(t_T[k])) + \Delta_y n_y \sin(\psi_{RB}(t_T[k])) + x_{RB}(t_T[k]) \\[2mm]
y_{n_x n_y}(t_T[k]) \;=\; \Delta_y n_y \cos(\psi_{RB}(t_T[k])) - \Delta_x n_x \sin(\psi_{RB}(t_T[k])) + y_{RB}(t_T[k]).
\end{aligned}
\tag{A.2}
$$

Here, Δ_x and Δ_y are the respective azimuth and range spatial sampling-interval constants of the $2-D$ target scatterer array. Usually, these constants are picked to be some fraction (e.g., one-half) of the respective azimuth and range spatial-resolutions, δ_x and δ_y, of the conventional SAR imaging technique presented in Chapter 3, i.e.,

$$
\begin{aligned}
\textit{Conventional SAR Azimuth Resolution and Range Resolution} \\
\delta_x = \frac{\lambda_c}{2\theta T} \\[2mm]
\delta_y = \frac{c}{\alpha T_p} \; .
\end{aligned}
\tag{A.3}
$$

If we substitute the rigid-body motion model into the SAR relative-range equation, given by

$$
y'[n_x,n_y,k] = y_{n_x n_y}(t_T[k])\cos(\dot\theta t_T[k]) - x_{n_x n_y}(t_T[k])\sin(\dot\theta t_T[k]) \;,
\tag{A.4}
$$

and simplify, we get the following expression

$$
\begin{aligned}
y'[n_x, n_y, k] &= y'_{RB}[k] + \Delta_y n_y \cos((\dot{\theta} t_T[k] + \psi_{RB}(t_T[k]))) \\
&\quad - \Delta_x n_x \sin((\dot{\theta} t_T[k] + \psi_{RB}(t_T[k]))) \; .
\end{aligned}
\tag{A.5}
$$

In this expression, $y'_{RB}[k]$ refers to the relative range of the target's center of rotation, given by

$$
y'_{RB}[k] = y_{RB}(t_T[k]) \cos(\dot{\theta} t_T[k]) - x_{RB}(t_T[k]) \sin(\dot{\theta} t_T[k]) \; .
\tag{A.6}
$$

For $\theta[k] + \psi_{RB}(t_T[k]) = \dot{\theta} t_T[k] + \psi_{RB}(t_T[k])$ "small", we can approximate the relative-range relation by

$$
\begin{aligned}
y'[n_x, n_y, k] &= y'_{RB}[k] + \Delta_y n_y - \Delta_x n_x [\dot{\theta} t_T[k] + \psi_{RB}(t_T[k])] \\
&= y_{RB}(t_T[k]) - x_{RB}(t_T[k]) \dot{\theta} t_T[k] + \Delta_y n_y \\
&\quad - \Delta_x n_x [\dot{\theta} t_T[k] + \psi_{RB}(t_T[k])] \; .
\end{aligned}
\tag{A.7}
$$

Next, we substitute this expression into the general-motion SAR data equation, given by

$$
f[n, k] = \sum_{n_x} \sum_{n_y} A[n_x, n_y] \, e^{-j \frac{4\pi}{\lambda_c}(1 + \frac{\alpha T_p}{f_c} \frac{\hat{t}[n]}{T_p}) y'[n_x, n_y, k]} \; . \qquad -\frac{N}{2} \le n \le \frac{N}{2}
$$

$$
-K \le k \le K
\tag{A.8}
$$

If we assume that the center frequency f_c of the SAR's transmitted "chirp" signal is much greater than its bandwidth $BW = \alpha T_p$, we can simplify this expression to

$$
\begin{aligned}
f[n, k] &= \sum_{n_x} \sum_{n_y} A[n_x, n_y] \, e^{-j \frac{4\pi}{\lambda_c} \frac{\alpha T_p}{f_c} \frac{\hat{t}[n]}{T_p} \Delta_y n_y} \, e^{j \frac{4\pi}{\lambda_c} [\dot{\theta} t_T[k] + \psi_{RB}(t_T[k])] \Delta_x n_x} e^{-j(\phi_r[n,k] + \phi_a[k])}
\end{aligned}
$$

$$
-\frac{N}{2} \le n \le \frac{N}{2} \quad -K \le k \le K \; ,
\tag{A.9}
$$

where the *range phase-error* $\phi_r[n, k]$ and the *azimuth phase-error* $\phi_a[k]$ are given by

$$
\begin{aligned}
\phi_r[n, k] &= \frac{4\pi}{\lambda_c} \frac{\alpha T_p}{f_c} \frac{\hat{t}[n]}{T_p} \left[y'_{RB}(t_T[k]) \right] \\[2mm]
&= \frac{4\pi}{\lambda_c} \frac{\alpha T_p}{f_c} \frac{\hat{t}[n]}{T_p} \left[y_{RB}(t_T[k]) - x_{RB}(t_T[k]) \dot{\theta} t_T[k] \right] \\[2mm]
&\approx \frac{4\pi}{\lambda_c} \frac{\alpha T_p}{f_c} \frac{\hat{t}[n]}{T_p} \left[y_{RB}(t_T[k]) \right]
\end{aligned}
\tag{A.10}
$$

$$
\begin{aligned}
\phi_a[k] &= \frac{4\pi}{\lambda_c} \left[y'_{RB}(t_T[k]) \right] \\[2mm]
&= \frac{4\pi}{\lambda_c} \left[y_{RB}(t_T[k]) - x_{RB}(t_T[k]) \dot{\theta} t_T[k] \right] \\[2mm]
&= \frac{4\pi}{\lambda_c} \left[(\dot{y}_{RB}(0) - x_{RB}(0)\dot{\theta}) t_T[k] \right] \\[2mm]
&\quad + \frac{4\pi}{\lambda_c} \left[(y_{RB}(t_T[k]) - \dot{y}_{RB}(0) t_T[k]) - (x_{RB}(t_T[k]) - x_{RB}(0)) \dot{\theta} t_T[k] \right] \\[2mm]
&= \phi_{DISP}[k] + \phi_{BLUR}[k] \; .
\end{aligned}
\tag{A.11}
$$

Here, we see that for $\dot{\theta}$ "small", the range phase-error $\phi_r[n,k]$ is approximately proportional to the translational range displacement $y_{RB}(t_T[k])$. We also see that we can decompose the azimuth phase-error term $\phi_a[k]$ into a (linear with respect to $t_T[k]$) "displacement" term $\phi_{DISP}[k]$ (dependent upon the range translational-velocity), and a (nonlinear with respect to $t_T[k]$) "blurring" term $\phi_{BLUR}[k]$ (dependent upon the azimuth translational-velocity). In addition, we see (embedded in the data equation) a *spatially-varying phase-error proportional to the product of the azimuth position* $\Delta_x n_x$ *and the target rotational trajectory* $\psi_{RB}(t_T[k])$.

Let the vectors $\mathbf{x}_{RB}, \mathbf{x}_{RB}$, and $\mathbf{\Psi}_{RB}$ be given by

$$\mathbf{x}_{RB} = \begin{bmatrix} x_{RB}(t_T[-K]) \\ \vdots \\ x_{RB}(t_T[0]) \\ \vdots \\ x_{RB}(t_T[K]) \end{bmatrix} \tag{A.12}$$

$$\mathbf{y}_{RB} = \begin{bmatrix} y_{RB}(t_T[-K]) \\ \vdots \\ y_{RB}(t_T[0]) \\ \vdots \\ y_{RB}(t_T[K]) \end{bmatrix} \tag{A.13}$$

$$\mathbf{\Psi}_{RB} = \begin{bmatrix} \psi_{RB}(t_T[-K]) \\ \vdots \\ \psi_{RB}(t_T[0]) \\ \vdots \\ \psi_{RB}(t_T[K]) \end{bmatrix} . \tag{A.14}$$

Then we can express the rigid-body SAR data in the following form

$$
\begin{aligned}
f[n,k] &= \sum_{n_x}\sum_{n_y} A[n_x,n_y] \left(e^{-j\frac{4\pi}{\lambda_c}\frac{\alpha T_p}{f_c}\frac{t[n]}{T_p}\Delta_y n_y} e^{j\frac{4\pi}{\lambda_c}[\dot{\theta}t_T[k]+\psi_{RB}(t_T[k])]\Delta_x n_x} \right) e^{-j(\phi_r[n,k]+\phi_a[k])} \\
&= \sum_{n_x}\sum_{n_y} A[n_x,n_y] s_{\mathbf{\Psi}_{RB}}[n_x,n_y,n,k] s_{\mathbf{x}_{RB},\mathbf{y}_{RB}}[n,k] \; . \\
&\qquad -\frac{N}{2} \le n \le \frac{N}{2} \quad -K \le k \le K
\end{aligned}
\tag{A.15}
$$

Therefore, the resulting estimation-theoretic model of the rigid-body SAR data is given by

---

Estimation-Theoretic Rigid-Body SAR Data Model

$$f[n,k] = \sum_{n_x}\sum_{n_y} A[n_x,n_y] s_{\psi_{\mathbf{RB}}}[n_x,n_y,n,k] s_{\mathbf{x}_{RB},\mathbf{y}_{RB}}[n,k] + \eta[n,k]$$
$$-\frac{N}{2} \le n \le \frac{N}{2} \quad -K \le k \le K \; ,$$

$$\tag{A.16}$$

---

where the additive noise is zero-mean circularly-complex Gaussian, i.e.,

$$\mathrm{Re}\,[\,\eta[n,k]\,] \sim \mathrm{N}(0,\sigma_\eta^2/2) \tag{A.17}$$

$$\mathrm{Im}\,[\,\eta[n,k]\,] \sim \mathrm{N}(0,\sigma_\eta^2/2) \tag{A.18}$$

$$\mathrm{E}\,[\mathrm{Re}\,[\,\eta[n,k]\,]\,\mathrm{Im}\,[\,\eta[n,k]\,]] = 0\;. \tag{A.19}$$

We can also express the rigid-body estimation-theoretic model in the following matrix form

$$\mathbf{f} = \mathbf{F}(\mathbf{x}_{RB},\mathbf{y}_{RB})\mathbf{F}(\mathbf{\Psi}_{RB})\mathbf{A} + \eta\;. \tag{A.20}$$

Here, $\mathbf{f}$ is the SAR data, $\mathbf{A}$ is the vector of scatterer intensities, given by

$$\mathbf{A} = \begin{bmatrix} \vdots \\ A[0,0] \\ A[0,1] \\ \vdots \end{bmatrix}\;. \tag{A.21}$$

and η is the additive Gaussian noise. The matrix $\mathbf{F}(\psi_{\mathbf{RB}})$ has the form

$$\mathbf{F}(\mathbf{\Psi}_{RB}) = \begin{bmatrix} \cdots & \mathbf{s}_{\mathbf{\Psi}_{RB}}[0,0] & \mathbf{s}_{\mathbf{\Psi}_{RB}}[0,1] & \cdots \end{bmatrix}\;, \tag{A.22}$$

where each column vector $\mathbf{s}_{\mathbf{\Psi}_{RB}}[n_x,n_y]$ corresponds to a lexicographical ordering of the complex exponential basis-function given by $s_{\mathbf{\Psi}_{RB}}[n_x,n_y,n,k]$. The matrix $\mathbf{F}(\mathbf{x}_{RB},\mathbf{y}_{RB})$ is a diagonal matrix given by

$$\mathbf{F}(\mathbf{x}_{RB},\mathbf{y}_{RB}) = \mathrm{diag}\,[\mathbf{s}(\mathbf{x}_{RB},\mathbf{y}_{RB})]\;, \tag{A.23}$$

where the vector $\mathbf{s}(\mathbf{x}_{RB},\mathbf{y}_{RB})$ corresponds to a lexicographical ordering of the complex exponential basis-function given by $s_{\mathbf{x}_{RB},\mathbf{y}_{RB}}[n,k]$. If we also assume that the additive noise η is spatially statistically-independent and isotropic, its spatial-correlation matrix is given by

$$\mathbf{K}_\eta = E\left[\eta\eta^H\right] = \sigma_\eta^2\mathbf{I}\;. \tag{A.24}$$

A.2 Prominent-Point SAR Motion-Compensation Techniques

A.2.1   Range-Migration ISAR (RMI)

The Range-Migration ISAR (RMI) technique [16] developed by Lincoln Laboratory focuses the SAR image by subtracting out the phase of the brightest scatterer, which is assumed to be the center-of-rotation of the moving target. This technique can compensate for both *unknown, purely-translational* motion and *known, constant-rate rotational* motion (i.e., $\psi_{RB}(t_T[k]) = \dot{\psi}_{RB}t_T[k]$, with positive $\dot{\psi}_{RB}$ defined in the opposite direction of the positive direction of the look-angle rotation-rate θ). This implies that estimation-theoretic model for the RMI technique has the following form

$$\boxed{\begin{array}{c} \underline{\textit{RMI Estimation-Theoretic Model}} \\[4pt] \mathbf{f} = \mathbf{F}(\mathbf{x}_{RB},\mathbf{y}_{RB})\mathbf{F}(\dot{\psi}_{RB})\mathbf{A} + \eta\;. \end{array}} \tag{A.25}$$

The RMI procedure consists of several steps. First, the sampled demodulated SAR data, $f[n,k]$ is compressed in range by a scaled Fourier Transform to form a series of Relative-Range Profiles (RRP) $R[n'_y, k]$, exactly as with the conventional spotlight-mode SAR processing technique. Recall from the previous section that the demodulated SAR data can be expressed by the following relation

$$f[n,k] \;=\; \sum_{n_x}\sum_{n_y} A[n_x, n_y]\, e^{-j\frac{4\pi}{\lambda_c}(1+\frac{\alpha T_p}{f_c}\frac{t[n]}{T_p})(y'[n_x,n_y,k])} \;, \tag{A.26}$$

where the "rigid-body" relative range $y'[n_x, n_y, k]$ (for $\theta(t_T[k]) + \psi_{RB}(t_T[k]) = (\dot{\theta}t_T[k] + \psi_{RB}(t_T[k]))$ "small") is given by

$$
\begin{aligned}
y'[n_x, n_y, k] \;=&\; y'_{RB}[k] + \Delta_y n_y - \Delta_x n_x[\dot{\theta}t_T[k] + \psi_{RB}(t_T[k])] \\
=&\; y_{RB}(t_T[k]) - x_{RB}(t_T[k])\dot{\theta}t_T[k] \\
&+ \Delta_y n_y - \Delta_x n_x[\dot{\theta}t_T[k] + \psi_{RB}(t_T[k])] \;.
\end{aligned}
\tag{A.27}
$$

This implies that the sampled RRP $R[n'_y, k]$ for the rigid-body estimation-theoretic SAR data model is approximately given by

$$
\begin{aligned}
R[n'_y, k] \;=&\; \sum_{n=-\frac{N}{2}}^{\frac{N}{2}} f[n,k]\, e^{j\frac{4\pi}{\lambda_c}(\frac{\alpha T_p}{f_c}\frac{t[n]}{T_p})n'_y\Delta_y} \\
=&\; \sum_{n=-\frac{N}{2}}^{\frac{N}{2}} \sum_{n_x}\sum_{n_y} A[n_x, n_y]\, e^{-j\frac{4\pi}{\lambda_c}(1+\frac{\alpha T_p}{f_c}\frac{t[n]}{T_p})(y'[n_x,n_y,k])}\, e^{j\frac{4\pi}{\lambda_c}(\frac{\alpha T_p}{f_c}\frac{t[n]}{T_p})n'_y\Delta_y} \\
=&\; \sum_{n_x}\sum_{n_y} A[n_x, n_y]\, e^{-j\frac{4\pi}{\lambda_c}(y'[n_x,n_y,k])}\mathrm{sinc}\left(\frac{\pi}{\delta_y}\left(n'_y\Delta_y - y'[n_x, n_y, k]\right)\right) \;,
\end{aligned}
\tag{A.28}
$$

where Δ_y is the SAR's range spatial-sampling interval. The bright (i.e., high amplitude) prominent-point scatterers appear as "tracks" in the RRP data, as shown in Figure A.1.

The RMI technique assumes that the brightest prominent-point track corresponds to the center-of-rotation of the moving target. For each SAR "slow-time" sampling instant $t_T[k]$, the complex RRP data samples are shifted in range by the relative-range position $\hat{y}'_{RB}[k]$ of this track, as shown in Figure A.1. (in order to correct for target-motion induced range-walk). This produces $R'[n_y, k]$, given by

$$
\begin{aligned}
R'[n'_y, k] \;=&\; R\left[n'_y + \frac{\hat{y}'_{RB}[k]}{\Delta_y}, k\right] \\
=&\; \sum_{n_x}\sum_{n_y} A[n_x, n_y]\, e^{-j\frac{4\pi}{\lambda_c}(y'[n_x,n_y,k])}\mathrm{sinc}\left(\frac{\pi}{\delta_y}\left(n'_y\Delta_y - (y'[n_x, n_y, k] - \hat{y}'_{RB}[k])\right)\right) \\
\approx&\; \sum_{n_x}\sum_{n_y} A[n_x, n_y]\, e^{-j\frac{4\pi}{\lambda_c}(y'[n_x,n_y,k])}
\end{aligned}
$$
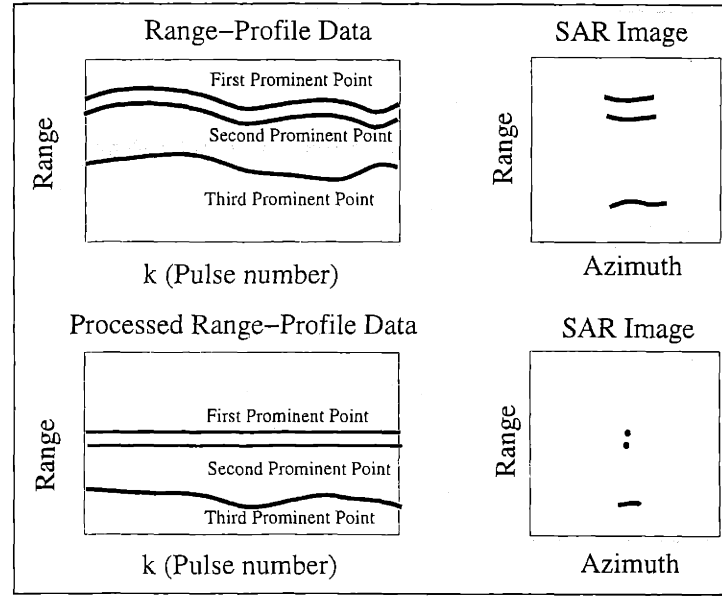
Figure A.1: Range-Migration ISAR Prominent-Point SAR Processing

$$\times \mathrm{sinc}\left(\frac{\pi}{\delta_y}\left(n_y'\Delta_y - (\Delta_y n_y - \Delta_x n_x[\dot\theta t_T[k] + \psi_{RB}(t_T[k])])\right)\right)$$

$$\approx \sum_{n_x}\sum_{n_y} A[n_x, n_y]\, e^{-j\frac{4\pi}{\lambda_c}(y'[n_x,n_y,k])} \mathrm{sinc}\left(\frac{\pi}{\delta_y}\left(n_y'\Delta_y - \Delta_y n_y\right)\right)\ .$$

$$(A.29)$$

It can be shown that the range shift operation upon $R[n_y', k]$ is equivalent to multiplying its *inverse* Fourier Transform (namely the original rigid-body SAR data $f[n, k]$) by the complex-conjugate of the rigid-body range phase-error term

$$\left[e^{j\phi_r[n,k]}\right]^* \approx e^{+j\frac{4\pi}{\lambda_c}\left(\frac{\alpha T_p}{f_c}\frac{t[n]}{T_p}\right)\hat{y}'_{RB}[k]}\ .$$

$$(A.30)$$

The next step in the RMI algorithm is to adjust the complex phase of range-walk compensated RRP data $R'[n_y', k]$ by the conjugate of the "phase history" of the complex data (approximately given by $e^{-j\frac{4\pi}{\lambda_c}\hat{y}'_{RB}[k]}$) along the track corresponding to the brightest prominent-point scatterer (which is assumed to be the center of rotation of the target). This produces the final RMI-compensated RRP data $R''[n_y', k]$, given by

$$\begin{aligned}
R''[n_y', k] &= R'[n_y', k] e^{j\frac{4\pi}{\lambda_c}\hat{y}'_{RB}[k]}\\
&= R\left[n_y' + \frac{\hat{y}'_{RB}[k]}{\Delta_y}, k\right] e^{j\frac{4\pi}{\lambda_c}\hat{y}'_{RB}[k]}\\
&= \sum_{n_x}\sum_{n_y} A[n_x, n_y]\, e^{-j\frac{4\pi}{\lambda_c}(y'[n_x,n_y,k] - \hat{y}'_{RB}[k])} \mathrm{sinc}\left(\frac{\pi}{\delta_y}\left(n_y'\Delta_y - n_y\Delta_y\right)\right)
\end{aligned}$$

$$= \sum_{n_x} \sum_{n_y} A[n_x, n_y] \, e^{-j\frac{4\pi}{\lambda_c}(\Delta_y n_y - \Delta_x n_x[\dot{\theta} t_T[k] + \psi_{RB}(t_T[k])])}$$

$$\times \mathrm{sinc}\left(\frac{\pi}{\delta_y}\left(n'_y \Delta_y - n_y \Delta_y\right)\right) \, . \tag{A.31}$$

By inspection, we see that this step of the RMI algorithm is equivalent to multiplying the original rigid-body SAR data $f[n, k]$ by the complex-conjugate of the rigid-body azimuth phase-error term

$$\left[e^{-j\phi_a[k]}\right]^* \approx e^{j\frac{4\pi}{\lambda_c}(\hat{y}'_{RB}[k])} \, . \tag{A.32}$$

Since we assume that the rigid-body target has a *known, constant rotation-rate* $\dot{\psi}_{RB}$, i,e,

$$\begin{aligned} y'[n_x, n_y, k] - y'_{RB}[k] &= n_y \Delta_y - n_x \Delta_x [\dot{\theta} t_T[k] + \psi_{RB}(t_T[k])] \\ &= n_y \Delta_y - n_x \Delta_x [(\dot{\theta} + \dot{\psi}_{RB}) t_T[k]] \, , \end{aligned} \tag{A.33}$$

we can Fourier-transform the sampled processed data $R''[n'_y, k]$ with respect to the "slow time" k (just as with the conventional SAR processing technique presented in Chapter 3) to form the following SAR image

$$\hat{A}[n'_x, n'_y] = \frac{1}{2K} \sum_{k=-K}^{K} R''[n'_y, k] e^{-j\frac{4\pi}{\lambda_c}[n'_x \Delta_x (\dot{\theta} + \dot{\psi}_{RB}) t_T[k]]}$$

$$= \frac{1}{2K} \sum_{k=-K}^{K} R''[n'_y, k] e^{-j\frac{4\pi}{\lambda_c}[n'_x \Delta_x \dot{\theta}(1 + \frac{\dot{\psi}_{RB}}{\dot{\theta}}) t_T[k]]}$$

$$= \sum_{n_x} \sum_{n_y} A[n_x, n_y] \, e^{-j\frac{4\pi}{\lambda_c} n_y \Delta_y} \mathrm{sinc}\left(\frac{\pi}{\delta_x}\left(1 + \frac{\dot{\psi}_{RB}}{\dot{\theta}}\right)(n'_x \Delta_x - n_x \Delta_x)\right)$$

$$\times \mathrm{sinc}\left(\frac{\pi}{\delta_y}\left(n'_y \Delta_y - n_y \Delta_y\right)\right) \, . \tag{A.34}$$

The RMI technique compensates for the spatially-varying phase error due to the known target rotation rate $\dot{\psi}_{RB}$ by essentially rescaling the azimuth Fourier Transform by $1 + \dot{\psi}_{RB}/\dot{\theta}$. When the processed data is Fourier-transformed in azimuth, the bright prominent-point target scatterer is now in focus at the center of the resulting SAR image. If the moving-target is rigid and rotating at a constant rate, it would then appear be in focus (since all of its scatterers would have the same translational trajectory, once we account for the effect of $\dot{\psi}_{RB}$). However, this technique would tend to defocus scatterers that do not have the same trajectory as the prominent point. In matrix form, the RMI technique is equivalent to the following estimate

$$\hat{\mathbf{A}} = \mathbf{F}^H(\dot{\psi}_{RB}) \mathbf{F}^H(\hat{\mathbf{x}}_{RB}, \hat{\mathbf{y}}_{RB}) \mathbf{f} \, , \tag{A.35}$$

where $\mathbf{F}^H(\hat{\mathbf{x}}_{RB}, \hat{\mathbf{y}}_{RB})$ corresponds to the range-shift and phase-history compensation operations upon the RRP data, and $\mathbf{F}^H(\dot{\psi}_{RB})$ corresponds to the scaled azimuthal Fourier Transform with respect to k.

Recall that the azimuth resolution for the conventional SAR imaging algorithm was given by

$$\delta_x = \frac{\lambda_c}{2\dot{\theta}T} .$$

(A.36)

This implies that the effective azimuth resolution for the RMI algorithm is approximately given by

$$\frac{\delta_x}{\left(1 + \frac{\dot{\psi}_{RB}}{\dot{\theta}}\right)} = \frac{1}{\left(1 + \frac{\dot{\psi}_{RB}}{\dot{\theta}}\right)} \frac{\lambda_c}{2\dot{\theta}T} = \frac{\lambda_c}{2(\dot{\theta} + \dot{\psi}_{RB})T} .$$

(A.37)

In other words, *the effective RMI azimuth resolution is directly dependent upon the target's rotation rate.* Since the range resolution δ_y is not a function of $\dot{\theta}$, it is unaffected by $\dot{\psi}_{RB}$.

A.2.2   Geometric-Analysis Automated Imaging

The Geometric-Analysis Automated Imaging (GAI) technique [39], developed by the Environmental Research Institute of Michigan (ERIM), is a somewhat more sophisticated multiple prominent-point cousin of the Lincoln Lab Range-Migration ISAR algorithm. Whereas the Lincoln Lab algorithm only compensates for pure translational motion (and known rotational motion), the Geometric Analysis technique also compensates for *unknown* rotational motion $\psi_{RB}(t_T[k])$ and other complicated target motions (where the target is assumed to be rigid). In other words, the GAI techniques uses the "full" estimation-theoretic rigid-body model

$$\boxed{\begin{array}{c} \underline{GAI\ Estimation\text{-}Theoretic\ Model} \\[4pt] \mathbf{f} = \mathbf{F}(\mathbf{x}_{RB}, \mathbf{y}_{RB})\mathbf{F}(\mathbf{\Psi}_{RB})\mathbf{A} + \eta . \end{array}}$$

(A.38)

In the literature, the "full-order" version of this algorithm requires four prominent-point scatterers, and can compensate for motions in 3-D. Here, we present a simplified 2-D version (requiring only three prominent-point scatterers).

As with the Lincoln Lab algorithm, the first step in the Geometric Analysis technique is to Fourier Transform the demodulated SAR data, $f[n, k]$ with respect to n to form the Relative-Range Profiles (RRP) $R[n'_y, k]$, given by

$$
\begin{aligned}
R[n'_y, k] &= \sum_{n=-\frac{N}{2}}^{\frac{N}{2}} f[n, k]\, e^{j\frac{4\pi}{\lambda_c}\left(\frac{\alpha T_p}{f_c}\frac{t[n]}{T_p}\right)n'_y\Delta_y} \\[6pt]
&= \sum_{n=-\frac{N}{2}}^{\frac{N}{2}} \sum_{n_x} \sum_{n_y} A[n_x, n_y]\, e^{-j\frac{4\pi}{\lambda_c}\left(1+\frac{\alpha T_p}{f_c}\frac{t[n]}{T_p}\right)(y'[n_x,n_y,k])}\, e^{j\frac{4\pi}{\lambda_c}\left(\frac{\alpha T_p}{f_c}\frac{t[n]}{T_p}\right)n'_y\Delta_y} \\[6pt]
&= \sum_{n_x} \sum_{n_y} A[n_x, n_y]\, e^{-j\frac{4\pi}{\lambda_c}(y'[n_x,n_y,k])}\mathrm{sinc}\left(\frac{\pi}{\delta_y}\left(n'_y\Delta_y - y'[n_x, n_y, k]\right)\right) .
\end{aligned}
$$

(A.39)

The bright high-amplitude prominent points again appear as "tracks" in the RRP data.

The next step in the Geometric-Analysis Imaging technique is to compensate for translational target motion. This procedure is exactly the same as the Lincoln Laboratory RMI technique. First, we shift the complex RRP data samples by the range location $\frac{\hat{y}'_{RB}(t_T[k])}{\Delta y}$ of the track of the brightest prominent-point scatterer (in order to correct for target-motion induced range-walk). This produces $R'[n'_y, k]$, given by

$$
R'[n'_y, k] = R\left[n'_y + \frac{\hat{y}'_{RB}[k]}{\Delta_y}, k \right]
$$

$$
= \sum_{n_x} \sum_{n_y} A[n_x, n_y]\, e^{-j \frac{4\pi}{\lambda_c}(y'[n_x, n_y, k])} \mathrm{sinc}\left(\frac{\pi}{\delta_y}\left(n'_y \Delta_y - (y'[n_x, n_y, k] - \hat{y}'_{RB}[k]) \right) \right) ,
$$

$$(A.40)$$

where the rigid-body relative range (*before* the "small-angle" simplification) is given by

$$
\begin{aligned}
y'[n_x, n_y, k] \;&=\; y'_{RB}[k] + \Delta_y n_y \cos((\dot{\theta}t_T[k] + \psi_{RB}(t_T[k]))) \\
&\quad - \Delta_x n_x \sin((\dot{\theta}t_T[k] + \psi_{RB}(t_T[k]))) .
\end{aligned}
$$

$$(A.41)$$

Next, we adjust the phase of range-walk compensated RRP data $R'[n'_y, k]$ by the "phase history" of the complex data along the first prominent-point track. This produces the translation-compensated RRP data $R''[n'_y, k]$, given by

$$
\begin{aligned}
R''[n'_y, k] \;&= R'[n'_y, k] e^{j \frac{4\pi}{\lambda_c}\hat{y}'_{RB}[k]} \\[4pt]
&= R\left[n'_y + \frac{\hat{y}'_{RB}[k]}{\Delta_y}, k \right] e^{j \frac{4\pi}{\lambda_c}\hat{y}'_{RB}[k]} \\[4pt]
&= \sum_{n_x} \sum_{n_y} A[n_x, n_y]\, e^{-j \frac{4\pi}{\lambda_c}(y'[n_x, n_y, k] - \hat{y}'_{RB}[k])} \\[4pt]
&\quad \times \mathrm{sinc}\left(\frac{\pi}{\delta_y}\left(n'_y \Delta_y - (y'[n_x, n_y, k] - \hat{y}'_{RB}[k]) \right) \right) .
\end{aligned}
$$

$$(A.42)$$

Again, the bright prominent-point target-scatterers appear as tracks in the compensated RRP data.

Recall that the 2-D version of the GAI technique needs at least three prominent-point scatterers. Therefore the next step is to choose two additional prominent-point tracks, with relative-range trajectories given by $y'[n_x, n_y, k] = y'_1[k]$ and $y'[n_x, n_y, k] = y'_2[k]$, respectively. The Geometric-Analysis algorithm now "unwraps" the phase information along these prominent-point tracks in the translation-compensated data to order to extract two high-precision relative-range paths, $\hat{y}'_1[k] - \hat{y}'_{RB}[k]$ and $\hat{y}'_2[k] - \hat{y}'_{RB}[k]$, approximately given by

$$
\hat{y}'_1[k] - \hat{y}'_{RB}[k] \approx \frac{\lambda_c}{4\pi} \angle \left[R'' \left[\frac{y'_1[k] - y'_{RB}[k]}{\Delta_y}, k \right] \right]
$$

$$(A.43)$$
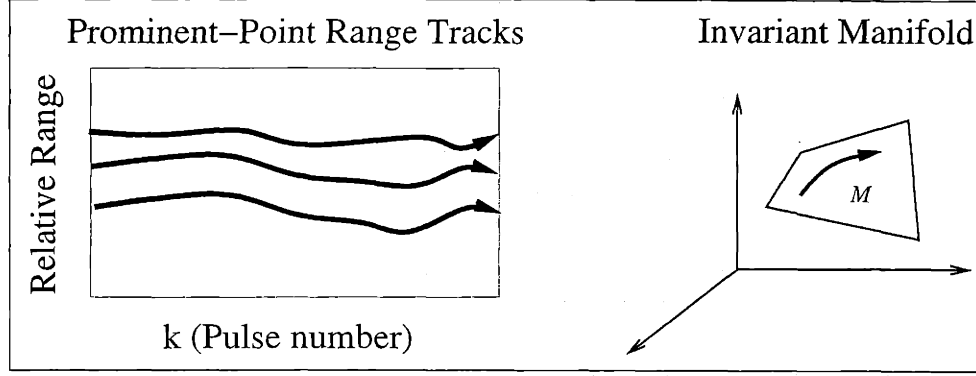
Figure A.2: Invariant Manifold for Geometric-Analysis SAR Processing

$$\hat{y}'_2[k] - \hat{y}'_{RB}[k] \approx \frac{\lambda_c}{4\pi} \angle \left[R'' \left[\frac{y'_2[k] - y'_{RB}[k]}{\Delta_y}, k \right] \right] . \tag{A.44}$$

After the range paths are obtained, the algorithm now estimates both the geometry (up to 2-D isometrics) and the motion history of the rigid moving target by the Invariant-Manifold Theorem (from two-dimensional Euclidean geometry). From this theorem, it can be shown that the relative-range measurements corresponding to the rigid moving-target prominent points satisfy the following invariant equation

$$\boxed{\begin{array}{c} \textit{2-D Invariant Equation} \\ I_1[y'_1[k] - y'_{RB}[k]]^2 + I_2[y'_2[k] - y'_{RB}[k]]^2 \\ +J[(y'_1[k] - y'_{RB}[k])(y'_2[k] - y'_{RB}[k])] = 1 . \end{array}} \tag{A.45}$$

In essence, this equation states that the rigid-body prominent-point range measurements are constrained to lie within a curved sub-manifold of the 3-D space of relative-range tracks $(y'_{RB}[k], y'_1[k], y'_2[k])$, as shown in Figure A.2. Let A_{12} be the area of the $2-D$ triangle formed by the three prominent scatterers, and let r_1 and r_2 be the relative distances from the brightest prominent-point scatterer to the first and second additional prominent-point scatterers, respectively. Then the invariant parameters (I_1, I_2, J) are given by the following geometric equations

$$I_1 = \frac{r_1^2}{(2A_{12})^2} \tag{A.46}$$

$$I_2 = \frac{r_2^2}{(2A_{12})^2} \tag{A.47}$$

$$J = -\frac{2r_1 r_2 \cos(\beta)}{(2A_{12})^2} , \tag{A.48}$$

where β is the inscribed angle of the triangle vertex corresponding to the brightest prominent-point. Since these parameters enter the invariant equation in a linear fashion, they can be

estimated from the previously obtained range paths $\hat{y}_1'[k] - \hat{y}_{RB}'[k]$ and $\hat{y}_2'[k] - \hat{y}_{RB}'[k]$ by using least-squares techniques.

After the invariant parameters (I_1, I_2, J) are estimated, we can obtain the geometric parameters (r_1, r_2, β) for the rigid target. It can be shown that the area of the triangle formed by the three prominent-point scatterers can be expressed by $A_{12} = \frac{1}{2} r_1 r_2 \sin(\beta)$. Substituting this expression into the geometric equations, and solving for (r_1, r_2, β), the parameters of this triangle are given by

$$r_1 \; = \; \sqrt{\frac{4I_1}{4I_1 I_2 - J^2}} \tag{A.49}$$

$$r_2 \; = \; \sqrt{\frac{4I_2}{4I_1 I_2 - J^2}} \tag{A.50}$$

$$\beta \; = \; \cos^{-1}\left(\frac{-J}{2\sqrt{I_1 I_2}}\right) . \tag{A.51}$$

These parameters can be used along with the prominent-point range observations to estimate the rotational motion of the target. In terms of the parameters (r_1, r_2, β), the relative-ranges $y_1'[k] - y_{RB}'[k]$ and $y_2'[k] - y_{RB}'[k]$ of the prominent-point scatterers are given by

$$y_1'[k] - y_{RB}'[k] \;\; = \;\; r_1 \cos(\dot{\theta} t_T[k] + \psi_{RB}(t_T[k])) \tag{A.52}$$

$$y_2'[k] - y_{RB}'[k] \;\; = \;\; r_2 \cos(\dot{\theta} t_T[k] + \psi_{RB}(t_T[k]) - \beta) . \tag{A.53}$$

Using these two equations, we can estimate the rotational trajectory $\psi_{RB}(t_T[k])$ from the high-precision prominent-point range tracks $\hat{y}_1[k] - \hat{y}_{RB}[k]$ and $\hat{y}_2[k] - \hat{y}_{RB}[k]$.

Once an estimate of the rotational-motion trajectory is obtained, it is then used to focus the resulting SAR image. Since the angle $\dot{\theta} t_T[k] + \psi_{RB}(t_T[k])$ gives a measure of the *relative* rotation between the target and the SAR antenna, it can be shown [7, 39] that we can focus the SAR image by performing an operation similar to Polar Format Resampling (discussed in Section 3.1.3) upon $f''[n, k]$ (the *inverse* Fourier Transform of the translation-compensated RRP data $R''[n_y', k]$ with respect to n_y'). However, rather than using an uniform angular spacing (given by $\dot{\theta} t_T[k]$), we now use a *non-uniform* angular spacing (given by $\dot{\theta} t_T[k] + \psi_{RB}(t_T[k]) - \psi_{RB}(t_T[0])$), as shown in Figure A.3. Note that since we subtracting $\psi_{RB}(t_T[0])$, we are essentially imaging the target with its angular orientation at $t_T[0] = 0$. In matrix form, the GAI technique is equivalent to the following estimate

$$\hat{\mathbf{A}} = \mathbf{F}^H(\hat{\boldsymbol{\Psi}}_{RB}) \mathbf{F}^H(\hat{\mathbf{x}}_{RB}, \hat{\mathbf{y}}_{RB}) \mathbf{f} , \tag{A.54}$$

where $\mathbf{F}^H(\hat{\mathbf{x}}_{RB}, \hat{\mathbf{y}}_{RB})$ corresponds to the range-shift and phase-history compensation operations upon the RRP data, and $\mathbf{F}^H(\hat{\boldsymbol{\Psi}}_{RB})$ corresponds to the data resampling and scaled Fourier Transform operations.
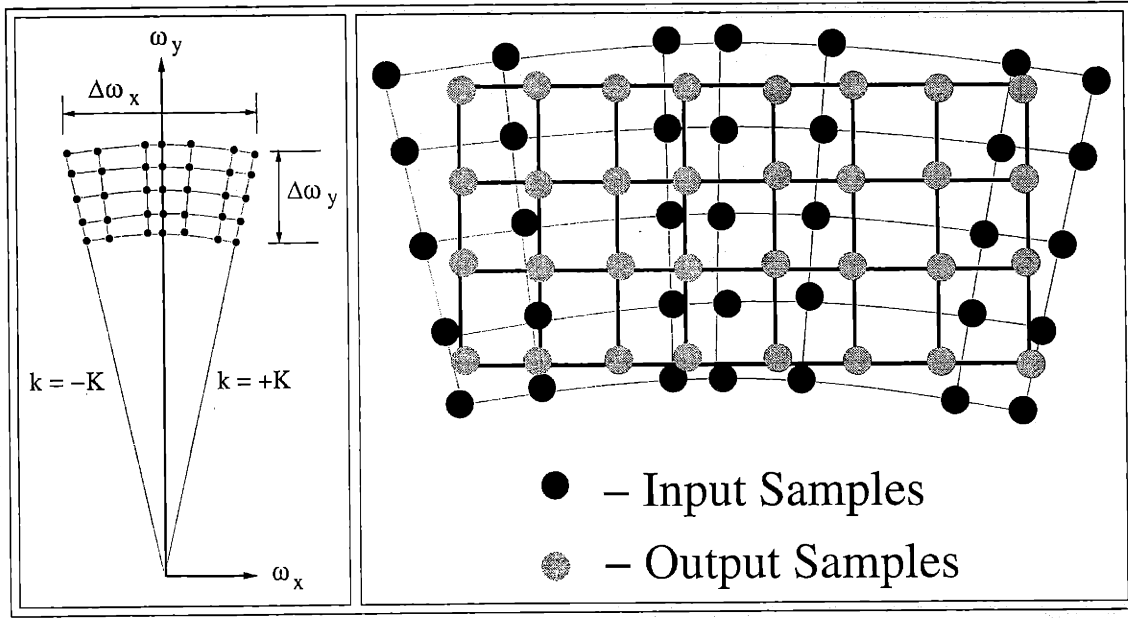
Figure A.3: Non-Uniform Polar Format Resampling For Geometric-Analysis Imaging

A.3   Phase-Estimation SAR Motion-Compensation Techniques

A.3.1   Phase-Gradient Autofocusing (PGA)

Phase-Gradient Autofocusing (PGA)[7], developed by Sandia Laboratory, is an imaging technique where the *derivative* of the motion-induced phase error is first estimated from the SAR data. Once the phase error is obtained by integrating the estimated phase-error derivative, it is then used to correct the original SAR imagery. Compared to the previously-presented techniques, PGA does not require the tracking of "bright" prominent-point scatterers, which implies that it tends to be more robust to noise.

In terms of our estimation-theoretic rigid-body SAR data model, the PGA technique corresponds to the case where we assume that each target scatterer has the same motion-induced phase error (i.e., $\psi(t_T[k]) = 0$). In addition,, PGA assumes that the target motion is purely in azimuth (i.e., $y(t_T[k]) = 0$ and $\phi_r[n,k] = 0$). Therefore, the PGA estimation-theoretic model is given by

$$\underline{PGA\ Estimation\text{-}Theoretic\ Model}$$
$$\mathbf{f} = \mathbf{F}(\mathbf{x}_{RB}, \mathbf{0})\mathbf{F}(\mathbf{0})\mathbf{A} + \eta \ .$$

(A.55)

Note that $\mathbf{F}(\mathbf{0})$ is essentially the conventional SAR scaled Fourier Transform.

Now, the azimuth phase-error $\phi_a(t_T[k])$ for $y(t_T[k]) = 0$ is given by

$$\phi_a[k] \quad = \quad \frac{4\pi}{\lambda_c} \left[y'_{RB}(t_T[k]) \right]$$

$$= \frac{4\pi}{\lambda_c} \Big[y_{RB}(t_T[k]) - x_{RB}(t_T[k])\dot{\theta} t_T[k] \Big]$$

$$= -\frac{4\pi}{\lambda_c} \Big[x_{RB}(t_T[k])\dot{\theta} t_T[k] \Big]$$

$$= -\frac{4\pi}{\lambda_c} \Big[x_{RB}(0)\dot{\theta} t_T[k] \Big] - \frac{4\pi}{\lambda_c} \Big[(x_{RB}(t_T[k]) - x_{RB}(0))\dot{\theta} t_T[k] \Big]$$

$$= \phi_{DISP}[k] + \phi_{BLUR}[k] \,.$$

$$(A.56)$$

However, as we will see later, the PGA technique does not compensate for *linear* phase errors, which implies that that it does not compensaate for the "displacement" part of the azimuthal phase-error. In other words, PGA assumes that $x_{RB}(0) = 0$.

For the PGA technique, we assume that the azimuth phase error is "bandlimited, i.e., the scaled Fourier Transform $\hat{A}_a[n'_x, n'_y]$ of $e^{-j\phi_a[k]}$ is approximately given by the following spatially-limited complex-valued *point-spread* function

$$\hat{A}_a[n'_x, n'_y] = \sum_k \sum_n e^{-j\phi_a[k]} \, e^{j \frac{4\pi}{\lambda_c} \frac{\alpha T_p}{f_c} \frac{\hat{t}[n]}{T_p} \Delta_y n'_y} \, e^{-j \frac{4\pi}{\lambda_c} \dot{\theta} t_T[k] \Delta'_x n_x}$$

$$= \begin{cases} \hat{A}_{ax}[n'_x] \mathrm{sinc}\left(\frac{\pi}{\delta_y} n'_y \Delta_y \right) & -\frac{\Delta_{x_a}}{2} \le n'_x \Delta_x \le \frac{\Delta_{x_a}}{2} \\ 0 & \text{otherwise} \end{cases}$$

$$\approx \begin{cases} \hat{A}_{ax}[n'_x] & n'_y = 0 \quad -\frac{\Delta_{x_a}}{2} \le n'_x \Delta x \le \frac{\Delta_{x_a}}{2} \\ 0 & \text{otherwise} \end{cases} \,.$$

$$(A.57)$$

This implies that a conventional SAR image $\hat{A}_{CONV}[n'_x, n'_y]$ of the moving target is approximately given by the *convolution* of $\hat{A}_a[n'_x, n'_y]$ with the 2-D target scatterer-amplitude array $A[n'_x, n'_y]$ (corresponding to a "perfect" SAR image with no phase error)

$$\hat{A}_{CONV}[n'_x, n'_y] \approx \hat{A}_a[n'_x, n'_y] \star A[n'_x, n'_y] \,.$$

$$(A.58)$$

Since we assume that we are imaging ideal point scatterers (i.e., $\Delta_x \ll \Delta_{x_a}$), we can approximate $\hat{A}_{CONV}[n'_x, n'_y]$ by the following sum of shifted and scaled versions of the phase-error point-spread function $\hat{A}_{ax}[n_x]$

$$\hat{A}_{CONV}[n'_x, n'_y] \approx \sum_{n_x} A[n_x, n'_y] \hat{A}_{ax}[n'_x - n_x] \,.$$

$$(A.59)$$

After we obtain $\hat{A}_{CONV}[n'_x, n'_y]$ by conventional SAR processing, we then select a peak-amplitude (i.e., largest magnitude) scatterer for each range location $n'_y \Delta_y$. The corresponding azimuth locations of these scatterers are given by

$$x_{peak}[n'_y] = \Delta_x n_{peak}[n'_y]$$

$$= \Delta_x \arg\left[\max_{n'_x} \left| \hat{A}_{CONV}[n'_x, n'_y] \right| \right] \,.$$

$$(A.60)$$

Once we obtain the peak-amplitude scatterer locations, we now shift the conventional image $\hat{A}_{CONV}[n'_x, n'_y]$ with respect to azimuth such that these scatterers are now located at $n'_x \Delta_x =$

0. In other words, we shift $\hat{A}_{CONV}[n'_x, n'_y]$ for each n'_y by $n_{peak}[n'_y]$ to form the image $\hat{A}_{CONV}[n'_x + n_{peak}[n'_y], n'_y]$, given by

$$\hat{A}_{CONV}[n'_x + n_{peak}[n'_y], n'_y] \quad = \quad \sum_{n_x} A[n_x, n'_y]\hat{A}_{ax}[n'_x + n_{peak}[n'_y] - n_x] \; . \quad (A.61)$$

The next step in the PGA technique is to symmetrically window the shifted azimuth profile $\hat{A}_{CONV}[n'_x + n_{peak}[n'_y], n'_y]$ about $n'_x = 0$ (the new azimuth location of the peak-amplitude scatterers) with an unity-magnitude rectangular window $w[n'_x]$ of width Δ_{x_a} (which is the same width as the phase-error point-spread function) to produce $\hat{A}_w[n'_x, n'_y] = \hat{A}_{CONV}[n'_x + n_{peak}[n'_y], n'_y]w[n'_x]$. If the amplitude $A[n_{peak}[n'_y], n'_y]$ of the peak-amplitude scatterer for a given range $n'_y\Delta_y$ is significantly greater than the amplitude of the rest of scatterers at that range, $\hat{A}_w[n'_x, n'_y]$ can be approximated by the following expression (where $\delta[n_x]$ is the usual Kronecker delta function)

$$\begin{aligned} \hat{A}_w[n'_x, n'_y] \quad &= \hat{A}_{CONV}[n'_x + n_{peak}[n'_y], n'_y]w[n'_x] \\ &\approx \sum_{n_x} A[n_{peak}[n'_y], n'_y]\delta[n_x - n_{peak}[n'_y]]\hat{A}_{ax}[n'_x + n_{peak}[n'_y] - n_x]w[n'_x] \\ &= A[n_{peak}[n'_y], n'_y]\sum_{\bar{n}_x} \delta[n_x - n_{peak}[n'_y]]\hat{A}_{ax}[n'_x + n_{peak}[n'_y] - n_x]w[n'_x] \\ &\approx \begin{cases} A[n_{peak}[n'_y], n'_y]\hat{A}_{ax}[n'_x] & -\frac{\Delta_{x_a}}{2} \le n'_x\Delta x \le \frac{\Delta_{x_a}}{2} \\ 0 & \text{otherwise} \end{cases} \; . \end{aligned}$$

$$(A.62)$$

In other words, we approximately have only *one* moving-target point-spread function for each range location $n'_y\Delta_y$.

From this expression, the inverse scaled Fourier Transform $R_w[n'_y, k']$ of $\hat{A}_w[n'_x, n'_y]$ (with respect to n'_x) is approximately given by

$$R_w[n'_y, k'] \approx \begin{cases} A[n_{peak}[n'_y], n'_y]e^{-j\,\phi_a[k']} \\ 0 & \text{otherwise} \end{cases} \; . \quad (A.63)$$

This implies that *the phase of $R_w[n'_y, k']$ with respect to k' is approximately equal to (within a constant) the phase of $e^{-j\,\phi_a[k']}$*. However, because of the azimuth shift operation, the phase of $R_w[n'_y, k']$ with respect to k' does not contain the linear portion $\phi_{DISP}[k']$ of the azimuth phase-error $\phi_a[k']$. This implies that the phase of $R_w[n'_y, k']$ with respect to k' only contains the nonlinear portion $\phi_{BLUR}[k']$, i.e.,

$$R_w[n'_y, k'] \approx \begin{cases} A[n_{peak}[n'_y], n'_y]e^{-j\,\phi_{BLUR}[k']} \\ 0 & \text{otherwise} \end{cases} \; . \quad (A.64)$$

The derivative of $R_w[n'_y, k']$ with respect to the "slow-time" variable k' (given by the inverse FT of $j\frac{4\pi}{\lambda_c}\dot{\theta}n'_x\Delta_x[\hat{A}_w[n'_x, n'_y]]$) is approximately equal to j times the derivative of the phase times $R_w[n'_y, k']$. Therefore, we can estimate the the nonlinear portion $\phi_{BLUR}[k']$ of the azimuth phase error for the range location $n'_y\Delta_y$ by the following (numerical) integral

$$\hat{\phi}_{BLUR}[k'] \approx -\int_{k''=0}^{k'} \frac{Im[(\frac{d}{dk''}R_w[n'_y, k''])(R^*_w[n'_y, k''])]}{|R_w[n'_y, k'']|^2}dk'' \; . \quad (A.65)$$

If we want a more robust estimate of the phase-error derivative, we can average both the numerator and the denominator of the previous equation over many range locations in the following manner

$$\hat{\phi}_{BLUR}[k'] \approx -\int_{k''=0}^{k'} \frac{\sum_{n'_y} Im[(\frac{d}{dk''}R_w[n'_y,k''])(R_w^*[n'_y,k''])]}{\sum_{n'_y} |R_w[n'_y,k'']|^2} . \qquad (A.66)$$

Note that this averaging operation follows from our assumption that each scatterer has the same phase error, i.e., purely translational motion.

Once this estimate of the phase error is obtained, the final motion-compensated SAR image is given by the scaled (conventional SAR) Fourier Transform of the original SAR data $f[n,k]$ (after multiplication by the complex-conjugate of $e^{-j\,\hat{\phi}_{BLUR}[k']}$). In terms of the estimation-theoretic model, this operation is equivalent to

$$\hat{\mathbf{A}} = \mathbf{F}^H(\mathbf{0})\mathbf{F}^H(\hat{\mathbf{x}}_{RB},\mathbf{0})\mathbf{f} , \qquad (A.67)$$

where $\mathbf{F}^H(\hat{\mathbf{x}}_{RB},\mathbf{0})$ corresponds to the phase-error compensation operation upon the SAR data, and $\mathbf{F}^H(\mathbf{0})$ corresponds to the scaled (conventional SAR) Fourier Transform.

In 1993, Jakowaltz and Wahl[22] developed a maximum-likelihood PGA method for calculating the azimuth phase error, based upon the Singular-Value Decomposition (SVD). Here, $R_w[n'_y,k']$ is lexicographically ordered into the following $N \times 2K+1$ matrix $\mathbf{R}_w$ (where N is the number of "fast-time" data samples per transmitted SAR pulse, and $2K+1$ is the total number of transmitted SAR pulses)

$$\mathbf{R}_w = \begin{bmatrix} R_w[-\frac{N}{2},-K] & \ldots & R_w[-\frac{N}{2},0] & \ldots & R_w[-\frac{N}{2},K] \\ R_w[-\frac{N}{2}+1,-K] & \ldots & R_w[-\frac{N}{2}+1,0] & \ldots & R_w[-\frac{N}{2}+1,K] \\ R_w[-\frac{N}{2}+2,-K] & \ldots & R_w[-\frac{N}{2}+2,0] & \ldots & R_w[-\frac{N}{2}+2,K] \\ \vdots & & \vdots & \ddots & \vdots \\ R_w[\frac{N}{2},-K] & \ldots & R_w[\frac{N}{2},0] & \ldots & R_w[\frac{N}{2},K] \end{bmatrix} . \qquad (A.68)$$

The SVD of this matrix is given by

$$\begin{aligned} \mathbf{R}_w &= \mathbf{U}_{R_w}\mathbf{\Sigma}_{R_w}\mathbf{V}_{R_w}^H \\ &= \sum_q \sigma_q \mathbf{u}_q \mathbf{v}_q^H . \end{aligned} \qquad (A.69)$$

It can be shown that the maximum-likelihood estimate of the azimuth phase error at each "slow-time" sampling instance $t_T[k]$ is given by the phase argument of the corresponding k-th element of the $1 \times (2K+1)$ maximum right singular vector, i.e.

$$\begin{bmatrix} \hat{\phi}_{BLUR}[-K] & \ldots & \hat{\phi}_{BLUR}[k] & \ldots & \hat{\phi}_{BLUR}[K] \end{bmatrix} = -\angle \begin{bmatrix} \mathbf{v}_1^H \end{bmatrix} . \qquad (A.70)$$

A.3.2   Shear-Averaging

Shear-Averaging [14], is an imaging technique where the pulse-to-pulse *difference* of the motion-induced phase error is first estimated from the SAR data. Once the phase error is obtained by a recursive sum of the estimated phase-error differences, it is then used to correct the original SAR imagery. As with the PGA algorithm discussed in the previous section, the Shear-Averaging technique corresponds to the case where we assume that each target scatterer has the same phase error. The target motion is again assumed to purely in azimuth (no range-walk). In other words, our estimation-theoretic model is exactly the same as the PGA model

$$
\boxed{
\begin{array}{c}
\underline{\textit{Shear-Averaging Estimation-Theoretic Model}} \\[4pt]
\mathbf{f} = \mathbf{F}(\mathbf{x}_{RB}, \mathbf{0})\mathbf{F}(\mathbf{0})\mathbf{A} + \eta \ .
\end{array}
}
\qquad (A.71)
$$

Also, we again assume that the phase error is "bandlimited", i.e., the scaled Fourier Transform $\hat{A}_a[n'_x, n'_y]$ of $e^{-j\phi_a[k]}$ is approximately given by the following spatially-limited complex-valued *point-spread* function

$$
\begin{aligned}
\hat{A}_a[n'_x, n'_y] &= \sum_k \sum_n e^{-j\phi_a[k]}\, e^{j\frac{4\pi}{\lambda_c}\frac{\alpha T_p}{f_c}\frac{\dot{t}[n]}{T_p}\Delta_y n'_y}\, e^{-j\frac{4\pi}{\lambda_c}\dot{\theta}t_T[k]\Delta'_x n_x} \\[6pt]
&= \begin{cases} \hat{A}_{ax}[n'_x]\operatorname{sinc}\left(\frac{\pi}{\delta_y}n'_y\Delta_y\right) & -\frac{\Delta_{xa}}{2} \le n'_x\Delta_x \le \frac{\Delta_{xa}}{2} \\ 0 & \text{otherwise} \end{cases} \\[6pt]
&\approx \begin{cases} \hat{A}_{ax}[n'_x] & n'_y = 0 \quad -\frac{\Delta_{xa}}{2} \le n'_x\Delta x \le \frac{\Delta_{xa}}{2} \\ 0 & \text{otherwise} \end{cases} ,
\end{aligned}
\qquad (A.72)
$$

which again implies that a conventional SAR image $\hat{A}_{CONV}[n'_x, n'_y]$ of the moving target is approximately given by the convolution of $\hat{A}_a[n'_x, n'_y]$ with the 2-D target scatterer-amplitude array $A[n'_x, n'_y]$ (corresponding to a "perfect" SAR image with no phase error)

$$
\hat{A}_{CONV}[n'_x, n'_y] \approx \hat{A}_a[n'_x, n'_y] \star A[n'_x, n'_y] \ .
\qquad (A.73)
$$

The first step in the Shear-Averaging technique is to compute the conventional SAR image $\hat{A}_{CONV}[n'_x, n'_y]$ from the demodulated SAR data $f[n, k]$ by using a scaled Fourier Transform (exactly the same as PGA). We again select the peak-amplitude (i.e., largest magnitude) scatterers for each range location $n'_y\Delta_y$, where the azimuth locations of these scatterers are given by

$$
\begin{aligned}
x_{peak}[n'_y] &= \Delta_x n_{peak}[n'_y] \\[4pt]
&= \Delta_x \arg\left[\max_{n'_x}\left|\hat{A}_{CONV}[n'_x, n'_y]\right|\right] \ .
\end{aligned}
\qquad (A.74)
$$

Once we obtain the peak-amplitude scatterer locations, we again shift the conventional image $\hat{A}_{CONV}[n'_x, n'_y]$ with respect to azimuth such that these scatterers are now located

at $n'_x \Delta_x = 0$. In other words, we shift $\hat{A}_{CONV}[n'_x, n'_y]$ for each n'_y by $n_{peak}[n'_y]$ to form the image $\hat{A}_{CONV}[n'_x + n_{peak}[n'_y], n'_y]$, given by

$$\hat{A}_{CONV}[n'_x + n_{peak}[n'_y], n'_y] = \sum_{n_x} A[n_x, n'_y]\hat{A}_{ax}[n'_x + n_{peak}[n'_y] - n_x] . \quad (A.75)$$

The next step in the shear-averaging technique is to symmetrically window the shifted azimuth profile $\hat{A}_{CONV}[n'_x + n_{peak}[n'_y], n'_y]$ about $n'_x = 0$ (the new azimuth location of the peak-amplitude scatterers) with an unity-magnitude rectangular window $w[n'_x]$ of width Δ_{x_a} (which is the same width as the phase-error point-spread function) to produce $\hat{A}_w[n'_x, n'_y] = \hat{A}_{CONV}[n'_x + n_{peak}[n'_y], n'_y]w[n'_x]$ (which is also exactly the same as the PGA technique). Recall that if the amplitude $A[n_{peak}[n'_y], n'_y]$ of the peak-amplitude scatterer for a given range $n'_y \Delta_y$ is significantly greater than the amplitude of the rest of scatterers at that range, $\hat{A}_w[n'_x, n'_y]$ can be approximated by the following expression (where $\delta[n_x]$ is the usual Kronecker delta function)

$$\begin{aligned} \hat{A}_w[n'_x, n'_y] &= \hat{A}_{CONV}[n'_x + n_{peak}[n'_y], n'_y]w[n'_x] \\ &\approx \sum_{n_x} A[n_{peak}[n'_y], n'_y]\delta[n_x - n_{peak}[n'_y]]\hat{A}_{ax}[n'_x + n_{peak}[n'_y] - n_x]w[n'_x] \\ &= A[n_{peak}[n'_y], n'_y]\sum_{n_x} \delta[n_x - n_{peak}[n'_y]]\hat{A}_{ax}[n'_x + n_{peak}[n'_y] - n_x]w[n'_x] \\ &\approx \begin{cases} A[n_{peak}[n'_y], n'_y]\hat{A}_{ax}[n'_x] & -\frac{\Delta_{x_a}}{2} \le n'_x\Delta x \le \frac{\Delta_{x_a}}{2} \\ 0 & \text{otherwise} \end{cases} \end{aligned}$$
$$(A.76)$$

Therefore, the phase of $R_w[n'_y, k']$, the inverse azimuth Fourier Transform of $\hat{A}_w[n'_x, n'_y]$, is again approximately equal to the nonlinear blurring portion $\phi_{BLUR}[k]$ of the corresponding motion-induced azimuth phase error, $\phi_a[k]$, i.e.,

$$R_w[n'_y, k'] \approx \begin{cases} A[n_{peak}[n'_y], n'_y]e^{-j \phi_{BLUR}[k']} \\ 0 & \text{otherwise} \end{cases} \quad (A.77)$$

The phase-error differences are obtained in the following manner. For a shift-index of Δ_k, the shear average is defined as the following sum over the range locations

$$S[k, \Delta_k] = \sum_{n'_y} R_w[n'_y, k']R_w[n'_y, k' - \Delta_k]^* . \quad (A.78)$$

Since we shifted each peak-amplitude scatterer to $n'_x = 0$, any phase variations in $R_w[n'_y, k']$ as a function of k' are due solely to the phase error (i.e., the uncorrupted signal $R_w[n'_y, k']$ is DC with respect to k'). This implies that we can write the shear average as

$$\begin{aligned} S[k, \Delta_k] &\approx e^{j(\phi_{BLUR}[k'] - \phi_{BLUR}[k' - \Delta_k])} \sum_{n'_y} \left| R_w[n'_y, k'] \right|^2 \\ &\approx e^{j(\phi_{BLUR}[k'] - \phi_{BLUR}[k' - \Delta_k])} \sum_{n'_y} \left| A[n_{peak}[n'_y], n'_y] \right|^2 . \end{aligned} \quad (A.79)$$

For a shift-index $\Delta_k = 1$, we see that the phase of the shear average is approximately equal to the pulse-to-pulse phase-error difference. If we define the phase error to be zero at $t_T[k] = t_T[-K] = -T$ (the transmit time of the first SAR pulse), then the phase error can be calculated by the following recursion

$$
\begin{aligned}
\hat{\phi}_{BLUR}[-K] &= 0 \\
\hat{\phi}_{BLUR}[-K+1] &= \angle\,[S[-K,1]] \\
&\vdots \\
\hat{\phi}_{BLUR}[k] &= \hat{\phi}_{BLUR}[k-1] + \angle\,[S[k,1]]\ .
\end{aligned}
\tag{A.80}
$$

Once this estimate of the phase error is obtained, the final motion-compensated SAR image is given by the scaled (conventional SAR) Fourier Transform of the original SAR data $f[n,k]$ (after multiplication by the the complex-conjugate of $e^{-j\,\hat{\phi}_{BLUR}[k']}$). In terms of the estimation-theoretic model, this operation is equivalent to

$$
\hat{\mathbf{A}} = \mathbf{F}^H(\mathbf{0})\mathbf{F}^H(\hat{\mathbf{x}}_{RB},\mathbf{0})\mathbf{f}\ ,
\tag{A.81}
$$

where $\mathbf{F}^H(\hat{\mathbf{x}}_{RB},\mathbf{0})$ corresponds to the phase-error compensation operation upon the SAR data, and $\mathbf{F}^H(\mathbf{0})$ corresponds to the scaled (conventional SAR) Fourier Transform.

It can be shown [22] that the shear-averaging algorithm is essentially equivalent to the maximum-likelihood singular-value decomposition PGA algorithm discussed in the previous section (for the case where we estimate the phase error at time $t_T[k]$ by only using the data from the two consecutive pulses at times $t_T[k]$ and $t_T[k] - \Delta_k\frac{T}{K}$).

Bibliography

[1] Barbarossa, S., "Detection and Imaging of Moving Objects with Synthetic Aperture Radar, Part 1:Optimal Detection and Parameter Estimation Theory", *Proceedings of the IEE*, vol. 139, no. 1, February 1992

[2] Barbarossa, S., Farina, A., "Detection and Imaging of Moving Objects with Synthetic Aperture Radar, Part 1:Joint Time-Frequency Analysis by Wigner-Ville Distribution", *Proceedings of the IEE*, vol. 139, no. 1, February 1992

[3] Barbarossa, S., Farina, A., "Space-Time-Frequency Processing of Synthetic Aperture Radar Signals", *IEEE Trans. on Aero. and Elect. Systems*, vol. 30, no. 2, April 1994

[4] Barbarossa, S., Scaglione, A., "Autofocusing of SAR Images Based on the Product High-Order Ambiguity Function", *Proceedings of the IEE:Radar, Sonar, and Navigation*, vol. 145, no. 5, October 1998

[5] Bertsekas, Dimitri, P., *Nonlinear Programming*, Athena Scientific, Belmont, MA, 1995

[6] Bhatia, Mickey, *Wavelet Transform-Based Multi-Resolution Techniques for Tomographic Reconstruction and Detection*, PhD thesis, Department of Electrical Engineering and Computer Science, Massachusetts Institute of Technology, August 1994

[7] Carrara, W. G., Goodman, R. S., Majewski, R. M., *Spotlight Synthetic Aperture Radar: Signal Processing Algorithms*, Artech House, Norwood, MA, 1995

[8] Chen, S. S., Donoho, D. L., and Saunders, M. A., "Atomic Decomposition by Basis Pursuit", Technical Report, Department of Statistics, Stanford University, May 1995. Available via ftp at playfair.stanford.edu

[9] Chen, S. S., and Donoho, D. L., "Basis Pursuit", Technical Report, Department of Statistics, Stanford University, 1994. Available via ftp at playfair.stanford.edu

[10] Curlander, John C., and McDonough, Robert N., *Synthetic Aperture Radar:Systems and Signal Processing*, John Wiley and Sons, Inc., New York, 1991

[11] Donoho, D. L., "Sparse Components of Images and Optimal Atomic Decompositions", Technical Report, Department of Statistics, Stanford University, December 1998. Available via ftp at playfair.stanford.edu

[12] Dudgeon, D. E., and Lacoss, R. T., (editors) *Lincoln Laboratory Journal-Special Issue on Automatic Target-Recognition*, Vol. 6, No. 1, Spring 1993

[13] Fleck, P. L., "A SAR Tutorial", MIT Lincoln Laboratory Memo 47M-1330

[14] Fienup, J. R., "Phase-Error Correction by Shear-Averaging", *Signal Recovery and Synthesis II*, vol. 5 of 1989 OSA Technical Digest Series, Optical Society of America, Washington, D.C., 1989, pp. 134-137

[15] Freund, R., "6.252 Class Notes", Massachusetts Institute of Technology, Spring 1998

[16] Henry, J. C. and Murphy, T. J., "Lincoln Laboratory Technique for the Ultrahigh-Resolution Imaging of Moving Targets", *Algorithms for Synthetic-Aperture Radar Imagery II, Proc. SPIE*, vol. 2487, pp. 359-370, April 1995

[17] Henry, J. C., Murphy, T. J., and Carusone, K. M., "The Lincoln Laboratory Millimeter-Wave Synthetic Aperture Radar (SAR) Imaging System", *Proc. SPIE*, vol. 1630, pp. 35-52, 1992

[18] Irving, W. W., "Introduction to Spotlight-Mode Synthetic Aperture Radar", Area Exam Report, Department of Electrical Engineering and Computer Science, Massachusetts Institute of Technology, 1993

[19] Irving, W. W., *Multiscale Stochastic Realization and Model Identification with Applications to Large-Scale Estimation Problems* PhD thesis, Department of Electrical Engineering and Computer Science, Massachusetts Institute of Technology, August 1995

[20] Jaggi, S, *Multiscale Geometric Feature Extraction and Object Recognition* PhD thesis, Department of Electrical Engineering and Computer Science, Massachusetts Institute of Technology, February 1997

[21] Johnson, Don H. and Dudgeon, Dan E., *Array Signal Processing:Concepts and Techniques*, Prentice Hall, Englewood Cliffs, NJ, 1993

[22] Jakowaltz, Jr., C. V., and Wahl, D. E., "Eigenvector Method for Maximum-Likelihood Estimation of Phase Errors in Synthetic-Aperture-Radar Imagery", *Journal of the Optical Society of America, A*, vol. 10, no. 12, pp. 2539-2546, December 1993

[23] Kreithen, D.E., Halversen, S.D., and Owirka, G.J., "Discriminating Targets from Clutter", *Lincoln Laboratory Journal* vol. 6, 1993

[24] Lim, Jae S., *Two-Dimensional Signal and Image Processing* Prentice Hall, Englewood Cliffs, NJ, 1990

[25] Logan, C. L., Krim, H., and Willsky, A.S., "A Matched-Filter Method for Motion-Compensated Spotlight-Mode SAR Processing", *Proc. 1996 IEEE ICASSP*, Atlanta, GA, 1996

[26] Logan, C. L., Krim, H., and Willsky, A.S., "A Estimation-Theoretic Technique for Motion-Compensated Synthetic-Aperture Array Imaging", *Proc. 1998 IEEE ICIP*, Chicago, IL, October 1998

[27] Luettgen, Mark R., *Image Processing with Multiscale Stochastic Models*, PhD thesis, Department of Electrical Engineering and Computer Science, Massachusetts Institute of Technology, May 1993

[28] Munson, D. C., O'Brien, J. D., and Jenkins, W. K., "A Tomographic Formulation of Spotlight-Mode Synthetic-Aperture Radar", *Proc. IEEE*, vol. 72, pp. 917-925, August 1983

[29] Novak, L.M., Burl, M.C., Chaney, R., and Owirka, G.J., "Optimal Processing of Polarimetric Synthetic-Aperture Radar Imagery", *Lincoln Laboratory Journal* vol. 3, 1990

[30] Novak, L.M., Burl, M.C., and Irving, W.W., "'Optimal Polarimetric Processing for Enhanced Target Detection", *IEEE Trans. on Aero. and Elect. Systems*, vol. 29, pp. 234, 1993

[31] Novak, L.M., Halversen, S.D., Owirka, G.J., and Hiett, M., "Effects of Polarization and Resolution on the Performance of a SAR Automatic Target Recognition System", *Lincoln Laboratory Journal* vol. 8, 1995

[32] Osher, S., and Rudin, L., "Feature-Oriented Signal Processing using Nonlinear Partial Differential Equations", AFOSR Report F49620-90-C-0011

[33] Peleg, S., Porat, P., and Friedlander, B., "The Achievable Accuracy in Estimating the Instantaneous Phase and Frequency of a Constant Amplitude Signal", *IEEE Trans. Signal Processing*, vol. 41, no. 6, pp. 2216-2224, 1993

[34] Perry, R.P., DiPietro, R. C., Johnson, B. L., Kozma, A, and Vaccaro, J. J., "Planar Subarray Processing for SAR Imaging", *The Record of the 1995 IEEE International Radar Conference*, pp. 473-478, May 1995

[35] Rudin, L.I., Osher, S., and Fatemi, E., " Nonlinear Total Variation Based Noise Removal Algorithms", *Physica D.*, 1992

[36] Rudin, L.I., Osher, S., and Fu, C., "Total Variation Based Restoration of Noisy Blurred Images", submitted to *SIAM J. on Numer. Analy.*, 1992

[37] Soumekh, Mehrdad, *Fourier Array Imaging*, Prentice Hall, Englewood Cliffs, NJ, 1994

[38] Stockburger, Edward and Orwig, Lawrence, "Autofocusing of Ground Moving-Target Imagery", *Algorithms for Synthetic-Aperture Radar Imagery II, Proc. SPIE*, vol. 2487, pp. 314-324, April 1995

[39] Stuff, M. A., Sullivan, R. C., Thelen, B. J., and Werness, S. A., "Automated Two and Three Dimensional, Fine-Resolution, Radar Imaging of Rigid Targets with Arbitrary Unknown Motion", *Algorithms for Synthetic-Aperture Radar Imagery I, Proc. SPIE*, vol. 2230, pp. 180-189, April 1994

[40] Van Trees, H. L., *Detection, Estimation and Modulation Theory: Part I*, Wiley, New York, NY, 1968

[41] Van Trees, H. L., *Detection, Estimation and Modulation Theory: Part II*, Wiley, New York, NY, 1968

[42] Van Trees, H. L., *Detection, Estimation and Modulation Theory: Part III*, Wiley, New York, NY, 1968

[43] Van Trees, H. L., *Detection, Estimation and Modulation Theory: Part IV*, Wiley, New York, NY, 1968

[44] Verbout, S.M., Irving, W.W., and Hanes, A.S., "Improving a Template-Based Classifier in a SAR Automatic Target Recognition System by Using 3-D Target Information", *Lincoln Laboratory Journal* vol. 6, 1993

[45] Wahl, D. E., Eichel, P. H., Ghiglia, D. C., and Jakowaltz, Jr., C. V., "Phase Gradient Autofocus - A Robust Tool for High-Resolution SAR Phase Correction", *IEEE Trans. on Aero. and Elect. Systems*, vol. 30, no. 3, pp. 827-835, July 1994

[46] Willis, N. Parker and Bresler, Yoram, "Optimal Scan for Time-Varying Tomography II: Efficient Design and Experimental Validation", *IEEE Transactions on Image Processing*, vol. 4, no. 3, May 1995

ABOUT THE AUTHOR

Cedric Leonard Logan was born in Montgomery, AL, USA, on March 31, 1968. He was raised in rural Lowndes County, AL, and attended Central High School of Hayneville, AL. In 1985, Mr. Logan was admitted to The University of Alabama, Tuscaloosa, AL, where he received the B.S.E.E. degree (*magna cum laude*) in 1989. While at The University of Alabama, Mr. Logan was voted Outstanding Senior in Electrical Engineering by The University of Alabama chapter of Eta Kappa Nu.

He received the S.M. and E.E. degrees from the Massachusetts Institute of Technology (MIT), Cambridge, MA, in 1993, with a thesis titled "Robust Controller Design and Evaluation for a Small Underwater Vehicle", which was supervised by Professor Michael Athans and Mr. Bill Bonnice. While at MIT, Mr. Logan was supported in part by Draper Laboratory as a Draper Fellow (1989-1993), by Schlumberger Well Services as a GEM Fellow (1989-1990), and by MIT Lincoln Laboratory as a Research Assistant (1994-1996).

Mr. Logan is a member of Tau Beta Pi, Eta Kappa Nu, and Sigma Xi.

FREE AT LAST. FREE AT LAST.
THANK GOD ALMIGHTY,
I AM FREE AT LAST.